Conformal Antenna Array

This conformal antenna array design handbook summarizes information available on such antenna configurations based primarily on the research sponsored by the Research Administrator's Office, AIR-310B, of the Naval Air Systems Command. Significant guidance and encouragement of this research effort was provided by the late Dr. H. J. MUELLER, formerly the Research Administrator.

The assistance of Dr. R. C. HANSEN, editor of this handbook, is gratefully acknowledged.

JAMES W. WILLIS
Technical Monitor

CONFORMAL ANTENNA ARRAY

DESIGN HANDBOOK

Contract N00019-81-M-0094

387195

A

CONFORMAL ARRAY HANDBOOK

Contributors:

P. T. Bargeliotes
J. Boersma
Z. W. Chang
K. E. Golden
A. Hessel
W. H. Kummer
R. Mather
H. E. Mueller
D. C. Pridmore-Brown
E. L. Rope
J. Shapiro
G. E. Stewart
G. Tricoles
A. T. Villeneueve
M. C. Behnke
J. E. Boyns
G. Deschamps
R. C. Hansen
J. K. Hsiao
S. H. Lee
R. Mittra
A. D. Munger
J. B. L. Rao
A. F. Seaton
S. M. Sterling
F. G. Terrio
G. Vaughn

J. W. Willis, Technical Monitor

(10) R. C. Hansen, Editor

CONFORMAL ARRAY HANDBOOK

TABLE OF CONTENTS

PREFACE

Starting in the late 1960's the Naval Air Systems Command foresaw a need for development of antenna arrays that could mount flush with the skin of an airframe or missile, and the Conformal Array Antenna (CAA) program was started. Not only can a CAA eliminate the conventional radome and its structural problems, but the mechanical steering/gimballing is replaced by rapid inertialess electronic scanning. At that time planar phased array mutual impedance effects such as 'blind spots' were being vigorously investigated. It was recognized that the CAA development cycle could profit from much of the planar array work, but that there were problems unique to curved surfaces that must be solved. As expected, a satisfactory understanding of mutual coupling in planar arrays was developed by the early 1970's, including compensation techniques for both wide angle scan and wide bandwidth, along with the necessary computational tools. Subsequent work on planar arrays has been concentrated on components and feed techniques.

The CAA program had as an initial goal the understanding of radiation processes from an array of slots on a conical metal surface and the computation of these effects. This initial goal was perhaps overly ambitious but it served as a useful vehicle for attacking the geometry, lattice, and polarization problems. In the next several years an understanding of these facets of the overall problem was developed for cylinders and cones. But the computation of mutual coupling and its effects proved to be extremely difficult. The calculation of patterns, although mathematically simpler, involves some of the same computational difficulties. And a satisfactory solution for both mutual coupling and radiation patterns is essential to allow effective design of arrays. Satisfactory results were finally obtained in a combination of harmonic series solutions and GTD solutions,

with each used in the regime of variables where it is most accurate. The CAA program has concluded with measurements on experimental antennas.

During these developments, several symposia were held to facilitate technical interchange among those working on CAA. The first was a Conformal Array Antenna Conference (1970) held in January at NELC (now NOSC), San Diego. A closely related symposium on Phased Array Antennas (1972) was sponsored by ABMDA in 1970 at PIB, Farmingdale, New York; a session on conformal arrays was included. Another meeting was the February Array Antenna Conference, (1972) held again at NELC. This meeting also had much material on CAA. The most recent was held in April at Crystal City, Virginia, a workshop on Conformal Antennas (1975).

The organizations that have been involved in the Naval Conformal Antenna Array program are listed here, in an approximate chronological order.

Naval Air Systems Command

J. W. Willis, Project Manager
H. J. Mueller

Hughes Aircraft, Culver City

W. H. Kummer
A. T. Villeneueve
P. T. Bargeliotes
A. F. Seaton
M. C. Behnke
F. G. Terrio

General Dynamics, San Diego

G. Tricoles
E. L. Rope

Polytechnic Institute of New York

A. Hessel
L. B. Felsen
J. Shapira
Z. W. Chang

Naval Ocean Systems Center

J. H. Provencher
Guy Vaughn
A. D. Munger
J. E. Boyns
R. L. Mather
S. M. Sterling
W. V. King

Naval Research Laboratories

J. K. Hsiao
J.B.L. Rao

Aerospace Corporation

G. E. Stewart
D. C. Pridmore-Brown
K. E. Golden

University of Illinois, Electromagnetic Lab.

S. H. Lee
R. Mittra
G. Deschamps
J. Boersma

The purpose of this Handbook is to make available in one place the design information developed under the CAA program. As feasible, this information has been supplemented by other related unclassified material and references.

CHAPTER 1

CONFORMAL GEOMETRY

CHAPTER 2

APERTURE SYNTHESIS

CHAPTER 3

SLOTS ON CYLINDER: PATTERN AND ADMITTANCE

CHAPTER 4

MODAL CALCULATION OF SLOTS ON CONE

CHAPTER 5

GTD CALCULATION OF PATTERN AND ADMITTANCE

CHAPTER 6

CONICAL ARRAY EXPERIMENTS

INTRODUCTION

Conformal arrays are valuable whenever an antenna must be located on a surface, be it the skin of a missile, an RPV or aircraft, or the nose of an artillery round or re-entry vehicle. Even ships have large curved surfaces that can mount array antennas. Conforming the array to the surface not only saves space and allows rapid inertialess scan but often is essential for structural reasons. A number of different CAA types are possible, but these seem to fit roughly three categories:

(1) low gain antennas for small missiles and artillery rounds;
(2) fuselage mounted ECM arrays for aircraft;
(3) electronically scanned arrays covering wide angles.

In the first of these CAA's, typically a pair of printed circuit 'wrap around' slots with shallow cavities are emplaced around the cylinder; two or more are used to give adequate circumferential response (Schaubert et al, 1979). The second is also a CAA, and is typically a small array located on the side or belly of an aircraft. Limited scanning is used. The fuselage curvature here is a minor factor in the array design and performance (Mailloux, 1977). With the third type, with which this handbook is exclusively concerned, the curvature of the body plays a pervasive role, and the azimuth scan is large, often 360 deg. It is useful to compare such arrays with planar arrays, to sharpen up the differences between conformal and planar, as these are the subjects of the chapters that follow. First a brief sketch of planar array design technology is given.

Array synthesis for pencil beam patterns is best done using the Taylor one-parameter modified sin x/x line source space factor or the Taylor $\bar{n}$ space factor; for small arrays an iterative adjustment is recommended. Higher Q distributions for equal

level sidelobes can use Chebyshev designs or Taylor with large $\bar{n}$. Shaped beams, e.g., $\csc^2 \theta$ are readily done with the Woodward-Lawson series of sinc beams. In realizing these distributions the mutual coupling between all elements must be taken into account, and of course these effects change with beam position (scan angle) and frequency. For single mode elements, such as dipoles, narrow slots, and patches, the Carter thin wire dipole mutual impedance (or the Babinet equivalent admittance) is adequate. Infinite ground plane effects are introduced by use of image elements. Finite ground plane modifications may be added to mutual impedance using GTD. Finally, the actual currents (voltages) are related to impressed voltages (currents) through complex simultaneous equations over the finite array, where the coefficients are the mutual impedances (admittances). Thus edge effects, where edge element impedance varies differently from that of center elements, are displayed. The pattern of the array of actual currents is then multiplied by the isolated element pattern to get the overall pattern. Multimode elements such as open ended waveguides present a much more difficult problem. In principle, equations could be solved where the number of equations is the number of elements times the number of external modes used. Since the latter is often over 100, this scheme is impractical even with powerful computers. Large arrays can be analyzed by assuming that most elements behave as if imbedded in an infinite array. This assumption of an infinite array allows an immediate simplification in that a unit cell can be constructed about each element with the unit cell boundaries adjusted so that the single unit cell represents the entire array performance. The real part of active impedance is given by the sum of propagating modes, where one mode exists for the main beam and an additional mode for each grating lobe (if any). Thus the resistance for a dipole array, or conductance for a slot array can be readily written in closed form. Unfortunately the reactive component requires an infinite series as all modes including

evanescent modes contribute to reactance. Nonetheless, the unit cell approach yields insights into array behavior with scan angle unattainable from other approaches. The output of the unit cell analysis is active impedance versus scan angle and frequency, and active element pattern versus frequency. The (active) reflection coefficient may be used with the array factor (the pattern of the array with isotropic elements) and the isolated element pattern to get the overall pattern. Alternatively the array factor and the active element pattern may be used to get the overall pattern. The powerful unit cell approach allows scan compensation devices such as waveguide plugs and dielectric sheets to be analyzed and designed. Thus the 'blind spot' produced near grating lobe incidence when a trapped wave* is set up along the surface of a large array is suppressed. Edge effects in multimode arrays can be examined approximately by analyzing an infinite array, then obtaining the coupling coefficients which are Fourier coefficients of the unit cell mode voltages and reflection coefficient. These coefficients are then summed over the finite array to give a set of mode voltages and reflection coefficient for each element. Useful references on phased arrays are Hansen (1964, 1966), Hansen (1968), Ma (1968), Oliner and Knittel (1972), Amitay, Galindo and Wu (1972), Hansen (1973), Tsandoulas and Knittel (1973), Ma (1974), and Hansen (1981).

New features are introduced by conformal arrays, and are discussed in the chapters that follow. A special issue on conformal arrays (Kummer, 1974) is useful. These new features are:

element lattice - some geometries cannot be covered by a uniform rectangular or hexagonal lattice

* This is somewhat analogous to Brewster's angle in reflection at a dielectric, and to Wood's anomalies in optical gratings.

element polarization - a fixed pattern polarization projected on the surface may vary from element to element, and each may vary with main beam angles θ, ϕ

distribution separability - for some geometries the aperture (array) distribution is not constant; for example, as θ changes both θ and ϕ distributions may change.

difference pattern - variability: boresight may vary as θ is changed, for example.

mutual coupling - curved surfaces may enhance or degrade coupling, but the calculation thereof is much more difficult than for flat surfaces.

pattern synthesis - even with the actual excitation known (coupling fully included), the element pattern may vary from element to element, and is difficult to calculate. Only brute force numerical synthesis techniques will give precise results.

In all the work on CAA, it is tacitly assumed that the coordinates are separable, at least in ϕ, the azimuth angle. Non-separable coordinates present essentially an intractable problem. Although most conformal arrays consist of antenna elements located upon a metallic surface, curved arrays in free space are sometimes used and are worthy of study as prototypes. Perhaps

the simplest curved array is the ring array, a set of elements disposed on a circle. The term 'circular array' is denigrated as it can mean both a ring array and a planar array of circular outline. Ring arrays with more than one concentric ring, or with a center element are not considered as CAA; they are special types of planar arrays. Earth or ground effects are not considered in this Handbook; it is assumed that the CAA is in free space.

The Handbook is in six chapters. Chapter One treats conformal geometry and the analysis of conformal arrays of isotropic elements. Projective aperture synthesis, where a known planar distribution is projected onto the conformal surface is the subject of Chapter Two. Harmonic modal function series are utilized in Chapters Three and Four to calculate patterns and active admittance of a CAA on a cylinder and on a cone. The modal series calculation becomes unwieldy for large radii; Geometric Theory of Diffraction is used to calculate pattern and admittance for large radii in Chapter Five. Finally Chapter Six describes some measurements made on conical arrays. Material for this Handbook was supplied by the listed contributors; it was the pleasant task of the editor to assemble and edit this work.

CHAPTER 1

CONFORMAL GEOMETRY

1.0 INTRODUCTION

This Chapter is concerned with the calculation of patterns of arrays of elements located on a (virtual) curved surface. Effects of a metallic surface will be considered in later Chapters. In this Chapter the emphasis is on lattice, grating lobe, and polarization features of a conformal array. Planar arrays can be constructed with elements located on a regular lattice; this allows the behavior of grating lobes and active element impedance to be extensively studied in terms of element spacing. Conformal can mean any curved surface, but only a few separable surfaces (sphere, cylinder, cone) can be analyzed for all dimensions. In practice, the general curved surface can be analyzed for element impedance only when curvatures are large in wavelengths. Thus this Handbook will be limited to arrays on cylindrical and conical surfaces.

Because the ring array is a building block of both the cylindrical array and the conical array, it is first discussed in Section 1.1. Most of the early work on conformal arrays was on ring arrays. The ring array is also a constituent of a spherical array, but since most surfaces of practical interest are represented by a cylinder or a cone rather than by a sphere, the only attention paid to the latter consists of listing references on spherical arrays. Section 1.2 covers cylindrical array work, with Section 1.3 concerned with conical arrays. A general purpose conformal array pattern code is the subject of the last Section.

1.1 Ring Array Space Factor

Analytical efforts on ring arrays existed before 1940, but significant progress was made during World War II by Page (1948 a,b) who considered a single azimuthal Fourier mode, and by Knudsen (1951, 1953, 1956) who analyzed a ring array as a series of Bessel function terms and showed that the azimuthal mode number and ring diameter must be compatible to avoid superdirectivity. The properties of individual azimuthal modes were pursued by Tillman and colleagues (Hickman et al, 1961; Hilburn and Hickman, 1968; Hilburn, 1969; Tillman, 1968). The last entry is a book containing extensive modal data, both pattern and impedance. Beam cophasal excitation, in which all elements contribute to the main beam in phase, is almost always used. The harmonic (Bessel) series analysis has been used for sidelobe control through excitation tapering, and for pattern synthesis (James, 1965; Fenby, 1965; Royer, 1966; Longstaff et al, 1967; Biswell and Butler, 1968; Redlich, 1970; and Lim and Davies, 1975). A harmonic analysis without explicit Bessel functions has also been used (Blass, 1974) as has a polynomial approach (Gerlin, 1974). DuHamel developed a procedure for producing Chebyshev patterns for ring arrays (1951). Effects of ground for HF ring arrays have been reported by Tillman et al (1955) and by Ma and Walters (1970). An examination of current distribution on dipoles in a ring array via moment method has been made by Sinnott and Harrington (1973).

Circular arc arrays, which are what result in practice from using tapered excitation, are reported by Lo and colleagues (Lo and Hsuan, 1965; Lee and Lo, 1965). Gobert and Yang (1974) consider a ring array of non-parallel dipoles, as well as conical arrays. Geometry, pattern coverage, and grating lobes in spherical arrays have been investigated by Hoffman (1963), MacPhie (1968), Chan et al (1968), Sengupta et al (1968 a and b), and Schrank (1972). Thinned arrays on a sphere have been probabilistically evaluated by Panicali and Lo (1969). Finally before

moving on to a brief analysis of ring arrays, the IEEE Trans. on Antennas and Propagation Special Issue on Conformal Antennas, W. H. Kummer ed., (1974) should be mentioned.

1.1.1 Continuous Ring Antenna

Assume a local 'element' pattern G where ϕ is the azimuth angle, and α is the angular location of the local element. A continuous current density I then produces the space factor (pattern):

$$E(\phi,\theta) = \frac{M}{2\pi} \int_0^{2\pi} I(\alpha)\ G(\phi-\alpha,\theta)\ d\alpha \qquad (1)$$

M is the number of elements which the continuous distribution replaces. If $I(\alpha)$ is symmetric, it may be written:

$$I(\alpha) = \sum_{n=0}^{\infty} I_n \cos n\alpha \qquad (2)$$

The I_n are the complex current mode amplitudes. The element factor $G(\phi-\alpha,\theta)$ may also be expanded as:

$$G(\phi-\alpha,\theta) = f(\theta) \sum_{n=0}^{\infty} F_{in}(\theta) \cos m(\phi-\alpha) \qquad (3)$$

Substitution of (2) and (3) into (1) and integrating yields:

$$E(\phi,\theta) = Mf(\theta) \sum_{n=0}^{\infty} \frac{1}{\epsilon_n}\ I_n F_n(\theta) \cos n\phi \qquad (4)$$

where $\epsilon_n = 1$ if $n = 0$, $\epsilon_n = 2$ if $n \neq 0$. The I_n are determined from the desired azimuth pattern expanded in a Fourier series. Call the desired pattern $T_n(\phi)$ to indicate an N^{th} -order Chebyshev pattern, though any pattern may be used if it can be put in the following form:

$$T_N(\phi) = \sum_{n=0}^{\infty} C_n{}^N \cos n\phi \qquad (5)$$

The computation of coefficients C_n^N was developed by DuHamel (1951) but his algorithm has poor accuracy for large N. Better formulas are given by Munger (1967), and in a forthcoming book (Hansen, 1981).

Equating (4) and (5) at $\theta = \theta_0$ yields

$$I_n^{(\theta_0)} = \frac{\varepsilon_n C_n^N}{Mf(\theta) F_n(\theta)} \tag{6a}$$

and

$$I^{(\theta_0)}(\alpha) = \sum_{n=0}^{\infty} I_n^{(\theta_0)} \cos n\alpha \tag{6b}$$

The superscript (θ_0) has been introduced to emphasize that I_n and $I(\alpha)$ give the optimum azimuth pattern $T_n(\phi)$ only in the cone $\theta = \theta_0$. At a general elevation angle θ the pattern is

$$E^{(\theta_0)}(\phi,\theta) = Mf(\theta) \sum_{n=0}^{\infty} I_n^{(\theta_0)} F_n(\theta) \cos n\phi \tag{7}$$

The choice of $N_0 = k\rho \sin\theta_0$ avoids superdirectivity, and allows efficient excitation of azimuthal modes. Thus $N^{(\theta_0)} = N \cos\theta_0$, where $N_0 \approx k\rho$ is N at $\theta_0 = 0$. This selection of $N^{(\theta_0)}$ gives approximately the same amplitude distribution for all θ_0, and a cophasal beam. For a given sidelobe level, the beamwidth is approximately proportional to $\frac{1}{N}$. Thus

$$\text{azimuth beamwidth} \approx \text{beamwidth at broadside}/\cos\theta_0 \tag{8}$$

This broadening of the beamwidth is only apparent, however. It is due to the fact that the azimuth pattern is measured on a cone

$\theta = \theta_0$, and the ratio of the perimeter of the cone base at θ_0 to that at $\theta = 0$ is just $(\cos \theta_0)^{-1}$. The actual spatial extent of the beam in the plane perpendicular to the $\phi = 0$ plane remains approximately constant to near zenith.

Figures 1 and 2 show the behavior of (8) for $\theta_0 = 0$ and $\theta_0 = 45^\circ$. The distribution is for a -50-dB Chebyshev pattern, so only the beam shape appears in the plot (all sidelobes are at -50 dB for $\theta = \theta_0$). The extensive beam broadening (beyond the $(\cos \theta_0)^{-1}$ factor) and gain loss for $\theta \neq \theta_0$ are due to the deviation of the phase from the optimum (which is essentially $-jk \cos \theta_0 \cos \alpha_p$. Figure 3 shows elevation patterns through the beam $\phi = 0$ direction with the azimuth pattern optimized at various θ_0. They are compared with the element elevation pattern, since this represents the maximum possible for each curve. For a linear array the curves would all coincide with the elevation element pattern. For the ring array they coincide with the elevation element pattern only at θ_0, where all elements add in phase to form the beam.

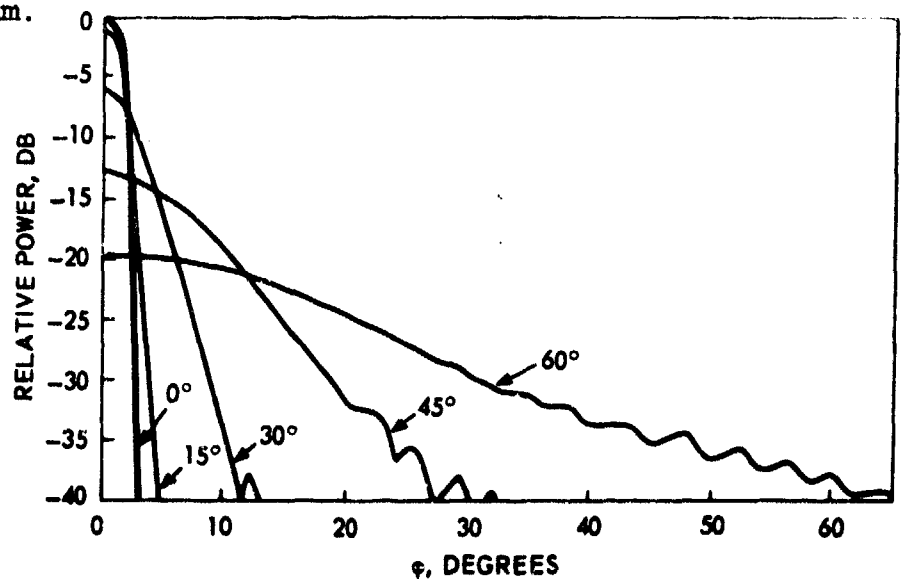

Figure 1. Ring-array pattern for $\theta_0 = 0^\circ$, -50-dB continuous Chebyshev distribution. $N^{(\theta_0)} = N_0 \cos \theta_0$, $N_0 = 128$, and element is axial slot in cylinder of radius $\rho = 26.3\lambda$

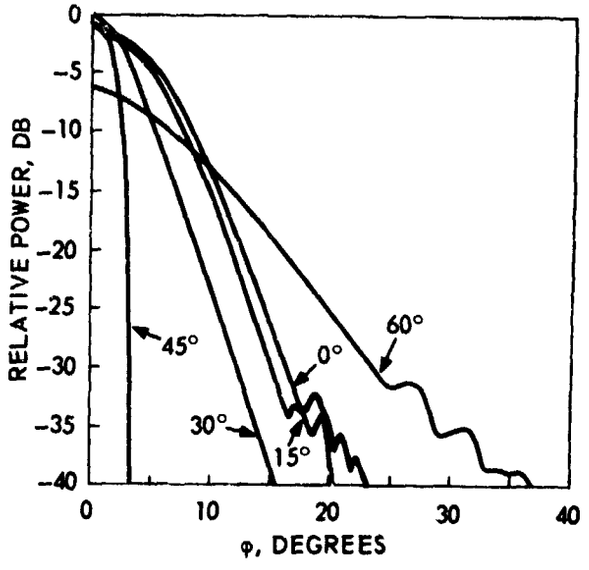

Figure 2. Ring-array pattern for $\theta_0 = 45^\circ$.

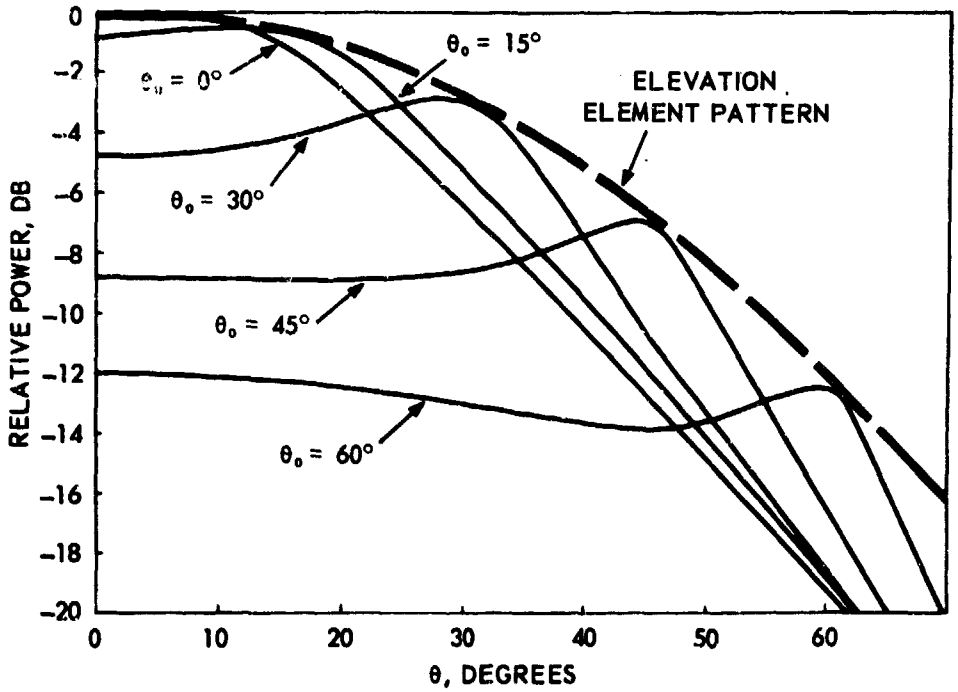

Figure 3. Ring-array elevation patterns through the beam for azimuth pattern optimized at various θ_0 compared with element elevation pattern. Parameters same as in Figure 1.

1.1.2 Discrete Ring Array

The continuous distribution can be replaced by M elements located at

$$\alpha_p = \frac{2\pi}{M}(p+f) \qquad p = 0,1,2,\ldots, M-1$$

where f is a fraction that indicates the position of the beam with respect to the first element. It can be shown (see Appendix A) that

$$E(\phi,\theta) = M \sum_{n=0}^{N} \frac{1}{\varepsilon_n} I_n^{(\theta_0)} \left| F_n(\theta) \cos n\phi + \sum_{r=1}^{\infty} F_{rM-n}(\theta) \cos\left[(rM-n)\phi - 2\pi r f\right] \right| \qquad (9)$$

(9) is the desired pattern plus an error term. For spacing $s = 2\pi p/m$ of less than a half wavelength, only the $r = 0$ term is significant. For spacing less than one wavelength, only $r = 0$ and $r = 1$ contribute, and so forth. The error term's primary contribution to the pattern is in the form of a grating lobe.

1.1.3 Grating Lobes

A convenient way of evaluating the grating lobe is to represent the terms in (9) by integrals and evaluate by the method of stationary phase (Biswell, 1968). An early approximation was given by Walsh (1951).

The pattern for an arc array of 2P + 1 active elements is

$$E(\phi,\theta) = \sum_{p=-P}^{P} I_p \, G(\phi-\alpha_p,\theta) \tag{10}$$

This may be written as a series of integrals according to the Poisson sum formula.

$$E(\phi,\theta) = \sum_{r=-\infty}^{\infty} \int_{-P}^{P} I(\alpha_p) \, G(\phi-\alpha_p,\theta) \, e^{j2\pi rp} \, dp \tag{11}$$

By change of variable $\alpha = \frac{2\pi}{M} p$:

$$E(\phi,\theta) = \frac{M}{2\pi} \sum \int I(\alpha) \, G(\phi-\alpha,\theta) \, e^{jrM\alpha} \, d\alpha \tag{12}$$

$$= \frac{M}{2\pi} \sum \varepsilon_r \int I(\alpha) \, G(\phi-\alpha,\theta) \cos(rM\alpha) \, d\alpha$$

where $2\alpha(P)$ is the active segment of the ring, M is the number of elements on the full ring, and $I(\alpha)$ is a continuous representation of the distribution $I(\alpha_p)$.

Now substitute (10) and (6b) into (12), and let $\alpha(P) = \pi$; it may be shown that the r^{th} term of (12) is identical to the r^{th} term of (10). The $r = 0$ term is just the pattern due to the continuous distribution $I(\alpha)$, and the higher terms are the error introduced by letting $p = \frac{2\pi}{M}(p+f)$.

The method of stationary phase can be applied to evaluate approximately the integrals in (12) - in particular to find the contribution to the grating lobe. From (22) and (25b) the r^{th} integral of (12) is

$$I_r(\phi,\theta) = \int_{-\alpha(p)}^{\alpha(p)} |I(\alpha)|\,|G(\phi-\alpha,\theta)| \exp jk\rho u(\alpha)\,d\alpha \qquad (13)$$

where

$$u(\alpha) = \cos\theta\cos(\phi-\alpha) - \cos\theta_0\cos\alpha + \frac{r\alpha}{s}$$

and $s = k\rho/M$ is the interelement spacing.

The integral is to be evaluated under the assumption that the largest contribution is from the neighborhood of the point(s) α_0 where the phase term $u(\alpha)$ is constant. This assumption is best for $k\rho$ large. The condition for α_0 is now $u'(\alpha) = 0$, or

$$\cos\theta\sin(\phi-\alpha_0) + \cos\theta_0\sin\alpha_0 + \frac{r}{s} = 0 \qquad (14)$$

In the region around α_0 since $u'(\alpha_0) = 0$,

$$u(\alpha) \approx u(\alpha_0) + \frac{1}{2!}(\alpha-\alpha_0)^2 u''(\alpha_0) \qquad (15)$$

Furthermore, if α_0 is well inside the range $-\alpha(P)$ to $\alpha(P)$, the limits may be extended to $-\infty$ and ∞. Finally, assume that $I(\alpha)$

and $G(\phi-\alpha, \theta)$ are reasonably constant over the region near α_0 so that they may be taken out of the integral. The integral is now in a standard form and becomes

$$I_r(\phi,\theta) = \left| I(\alpha_0) \right| \left| G(\theta-\alpha_0, \theta) \right| \sqrt{\frac{2\pi}{k\rho|u'(\alpha_0)|}} \quad (16)$$

with

$$u''(\alpha_0) = -\cos\theta \cos(\phi-\alpha_0) + \cos\theta_0 \cos\alpha_0 \quad (17)$$

For simplicity, consider $\theta = \theta_0$. Now $u''(\alpha_0) = 0$ for $\phi_0 = 2\alpha_0$. This gives the maximum of (16) corresponding to a grating lobe. The position of the grating lobe is now given by (14), which becomes

$$\sin\frac{\phi_0}{2} = \frac{-r}{2s}\cos\theta_0 \quad (18)$$

$r = 0$ gives the main beam at $\phi_0 = 0$, while positive and negative r give grating lobes at positive and negative ϕ_0 angles under the condition

$$\left| \frac{r}{2s\cos\theta_0} \right| \leq 1 \quad (19)$$

However, (16) is not a valid representation of the integral at $u'(\alpha_0) = u''(\alpha_0) = 0$, for (15) must be replaced by:

$$u(\alpha) = u(\alpha_0) + \frac{1}{3!}(\alpha-\alpha_0)^3 u'''(\alpha_0)$$

Now evaluating the integral thus obtained at $\phi_0 = 2\alpha_0$

$$I_n(\varphi,\theta_0) = |I(\alpha_0)|\,|G(\varphi_0-\alpha_0;\theta_0)|\left(\frac{6}{k\rho|u'''(\alpha_0)|}\right)^{1/3}\frac{\Gamma(1/3)}{\sqrt{3}}\exp[jk\rho u(\alpha_0)]\ \text{or}$$

$$|I_r(\varphi_0,\theta_0)| = \left|I\left(\frac{\varphi_0}{2}\right)G\left(\frac{\varphi_0}{2},\theta_0\right)\frac{\Gamma(1/3)}{\sqrt{3}}\left(\frac{12}{k}\right)^{1/3}\left(\frac{s\cos\theta_0}{r\rho}\right)^{1/3}\right| \qquad (20)$$

Equation (20) is subject to the restrictions that I (α) and $G(\phi-\alpha,\theta)$ are slowly varying, $k\rho$ is large, and α_0 is not near 0 but is inside the range $-\alpha(P)$ to $+\alpha(P)$. To compute the grating lobe height compared with the main beam height, compare the grating lobe computed from (20) with the main beam computed from

$$I_0 = \int_{-\alpha(p)}^{\alpha(p)} |I(\alpha)|\,|G(\alpha,\theta)|\,d\alpha \qquad (21)$$

Figure 4 shows the grating lobe height relative to the beam as a function of spacing ($s\cos\theta_0$) for various $\cos^n$ amplitude tapers, with $\rho = 26\lambda$ and $G(\phi-\alpha,\theta_0) = \cos(\phi-\alpha)$. $\alpha(P) = \frac{\pi}{2}$ was used to assure that $0<\alpha_0<\alpha(P)$. For comparison, actual patterns were computed from (10 and the grating lobe heights are shown. The maximum difference between the actual grating lobe and that computed from (20) is 2 dB. Since the approximation from (20) represents the worst case, it appears to be a useful guide for controlling the grating lobe as a function of spacing, current distribution, element pattern, radius, and arc length. The position of the grating lobe (for $r = -1$ and $\theta_0 = 0$) predicted by (18) is shown in Figure 5 in comparison with the actual position, with good agreement.

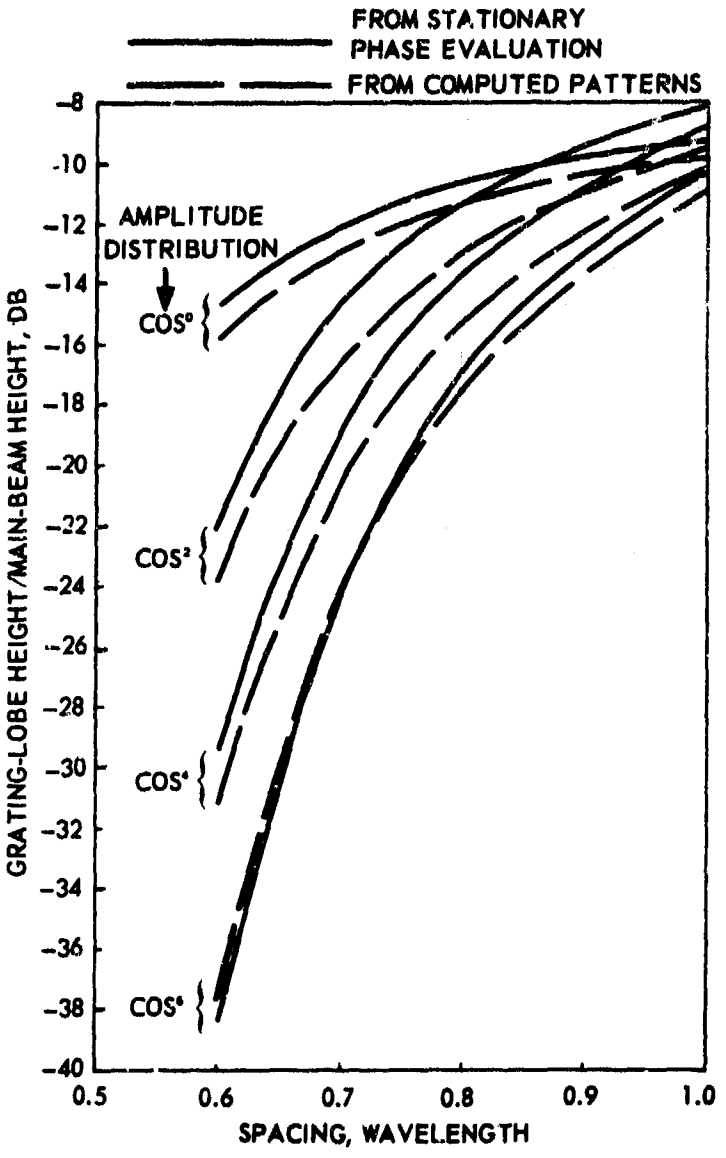

Figure 4. Grating lobe height versus spacing for various $\cos^n$ amplitude tapers; comparison of approximate stationary phase evaluation with exact computation.

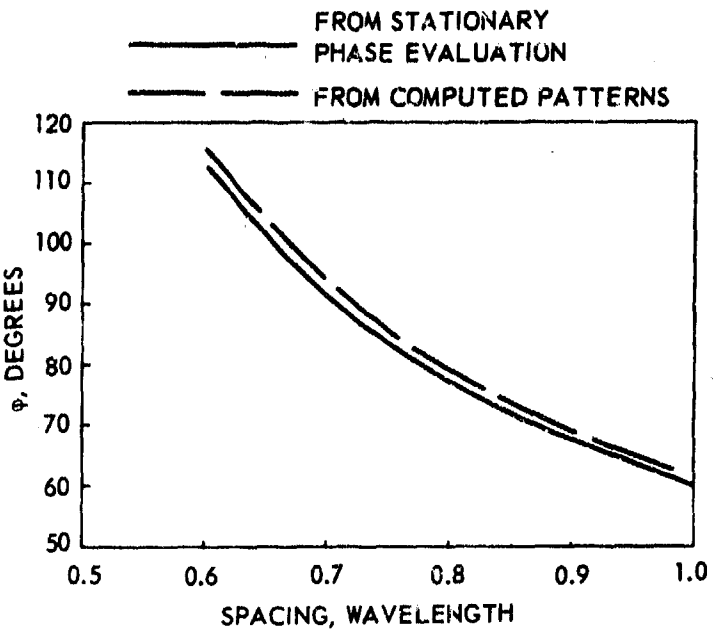

Figure 5. Position of grating lobe for stationary phase approximation and exact computation. The exact location is nearly independent of amplitude taper (to 1 degree), so the average is represented.

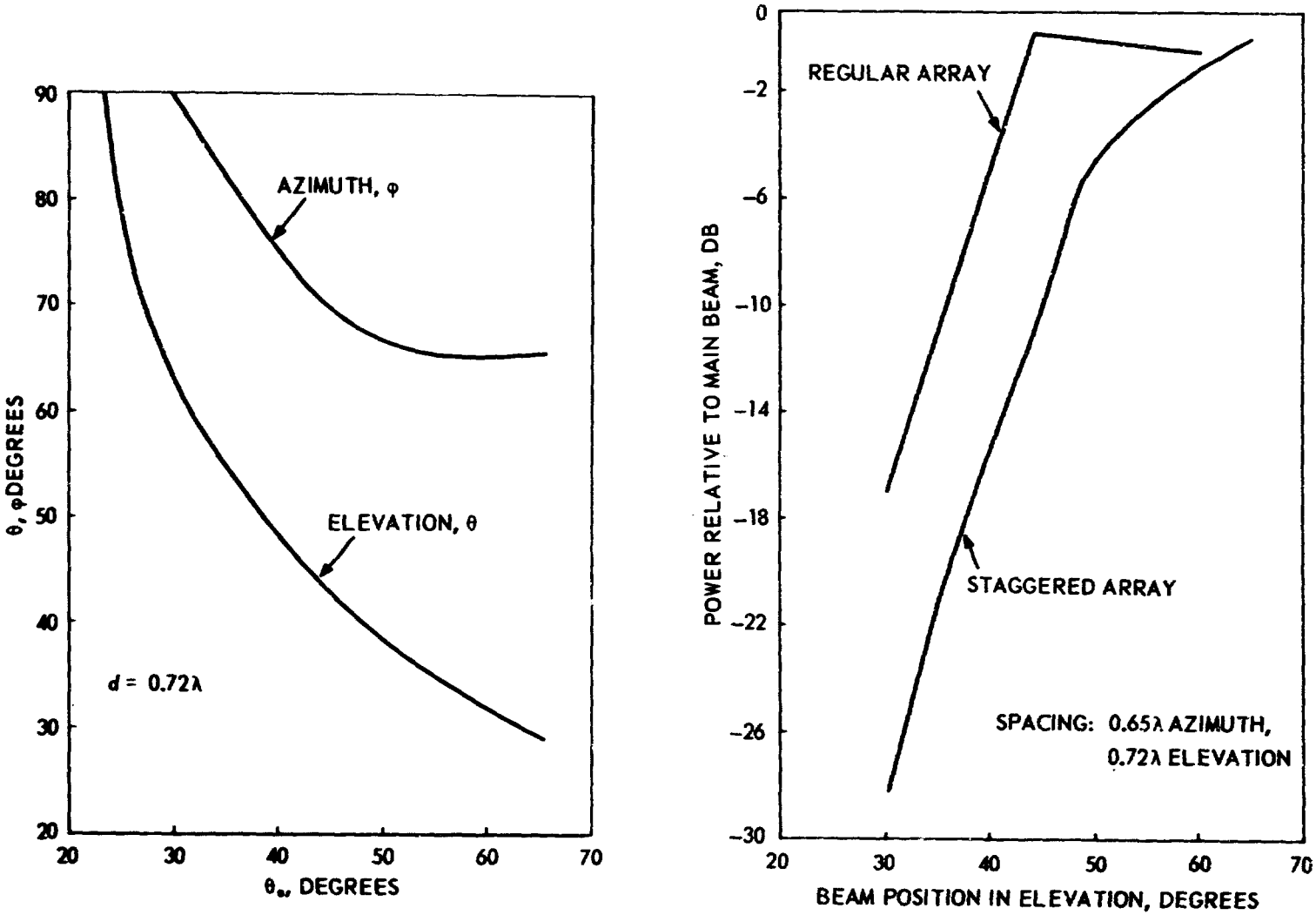

Figure 6. Grating lobe position in elevation and azimuth for staggered-array lobe (left), and grating lobe height as a function of scan angle for regular and staggered configurations (right).

1.1.4 Equivalence Between Continuous and Array Distributions

The basic equivalence between discrete and continuous distributions on a planar surface was described by Ksienski (1961). Using the same size aperture, a good approximation may be given by the pattern produced by the discrete (array) distribution to the continuous distribution patterns provided the element spacing is suitably small. In general, element spacing is controlled by grating lobes and by the pattern in invisible space, which affects the aperture Q. In some shaped beam cases, the optimum element spacing may be below $\lambda/2$. Most pencil beam patterns are satisfactorily realized by keeping all grating lobes well away from visible space. For all small arrays and for shaped beam patterns, the discrete approximation may not be adequate, especially for some element patterns. Thus it may be necessary to numerically adjust the distribution, which is best done by adjusting the zeroes of the array polynomial. The array zeroes can be made the same as those of the continuous distribution pattern (Elliott, 1977). A better way used by Winter (1977) numerically adjusts the discrete distribution to optimize the pattern. All these results have been developed for linear/planar distributions. For conformal surfaces, it can be expected that the results generally apply. Related material will be found in Chapter 2.

1.2 The Cylindrical Array

The cylindrical array can be considered to consist of a stack of identical ring arrays. Denote the complex excitation of the p^{th} element in the q^{th} ring by $I_{pq} = I(\alpha_p, z_q)$, where α_p is the angular location of the p^{th} and z_q is the z-axis location of the q^{th} ring. The coordinate system is shown in Figure 7. The beam is assumed to be pointed in the $\phi = 0$ direction in azimuth, corresponding to the $\alpha = 0$ reference point of the element location. The beam is stepped around the cylinder by redefining the $\alpha = 0$ reference to the desired position.

All elements are assumed identical, symmetrical, equally spaced, and pointed along the radius vector. Thus, the azimuth element pattern can be expressed as a function of $|\phi - \alpha|$. In general, the azimuth pattern depends on the elevation angle θ. The complex element pattern is denoted by $G(\phi-\alpha,\theta)$, with the phase referenced to the center of the ring in which it lies. Thus, if it is assumed that the phase center is at the element,*

$$G(\phi-\alpha,\theta) = |G(\phi-\alpha,\theta)| \exp[jk\rho \cos\theta \cos(\phi-\alpha)] \tag{22}$$

The far field is

$$E(\phi,\theta) = \sum_p \sum_q I_{pq} G(\phi-\alpha_p,\theta) \exp[jqu] \tag{23}$$

where

$u = kd \sin\theta$

d = spacing between elements in vertical direction

$k = 2\pi/\lambda$

*This is not strictly true for an element on a ground plane, but the deviation is significant only where the amplitude is small - that is, past 90^0 - so the assumption has negligible effect on computed results.

A beam can be formed in the direction $\phi = 0$, $\theta = \theta_o$ by exciting all elements to add in phase in that direction (beam cophasal excitation). Thus, in view of (22) and (23):

$$I_{pq} = \left| I_{pq} \right| \exp \left[-jk \rho \cos \theta_o \cos \alpha_p - jqu_o \right] \qquad (24)$$

where $u_o = kd \sin \theta_o$.

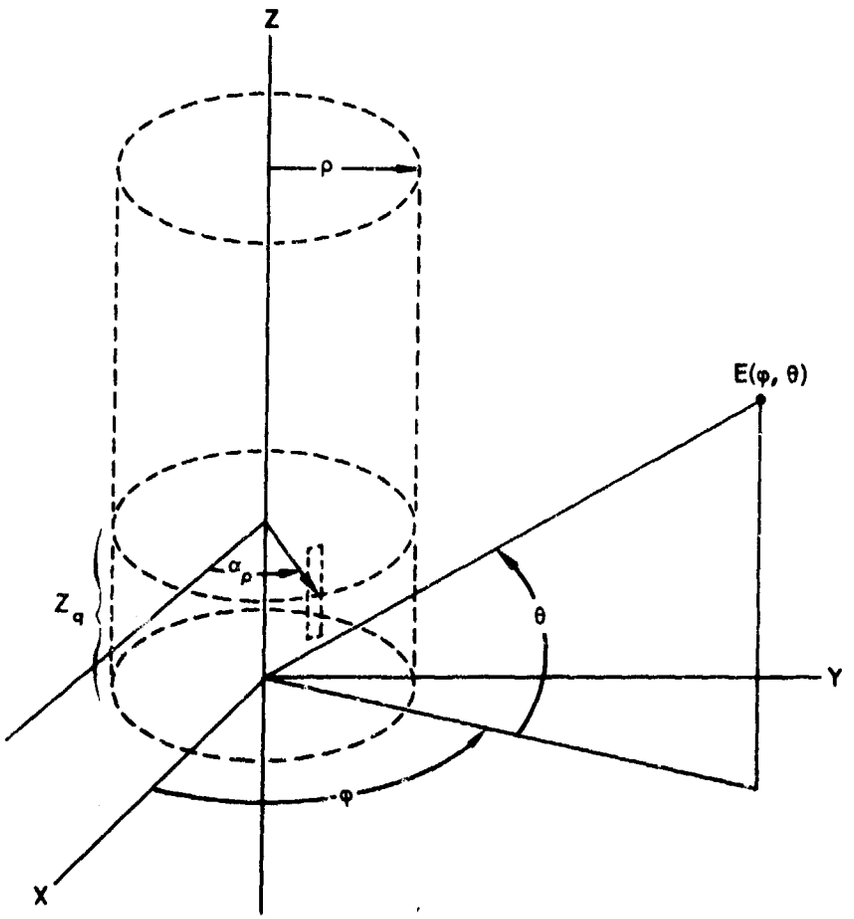

Figure 7. Coordinate system.

In (24) the phase terms are separated in α_p and z_q, where $z_q = qd$. This allows assuming a current distribution of the form

$$I(\alpha_p, z_q) = I^{(a)}(\alpha_p)\, I^{(e)}(z_q) = I_p^{(a)}\, I_q^{(e)} \tag{25a}$$

with

$$I_p^{(e)} = I_p^{(a)}[\exp - jk\rho\cos\theta_o \cos\alpha_p] \tag{25b}$$

and

$$I_q^{(e)} = I_q^{(e)} \exp[-jqu_o] \tag{25c}$$

The superscripts (a) and (e) indicate azimuth and elevation distributions, respectively. Note that the azimuth distribution depends on the beam-pointing angle in both azimuth and elevation, whereas $I_q^{(e)}$ depends only on θ_o. Writing the current distribution in the form (25a) allows the pattern (23) to be written in the form

$$E(\phi,\theta) = E^{(a)}(\phi,\theta)\, E^{(e)}(\theta) \tag{26a}$$

where

$$E^{(a)}(\phi,\theta) = \sum_p I_p^{(a)}\, G(\phi-\alpha_p,\theta) \tag{26b}$$

and

$$E^{(e)}(\theta) = \sum_q I_q^{(e)} \exp[jqu] \tag{26c}$$

$E^{(a)}(\phi,\theta)$ is just the pattern of a single ring excited by $I_p^{(a)}$. $E^{(e)}(\theta)$ is the space factor of a single vertical column of elements excited by $I_q^{(e)}$.

Thus, the analysis can be simplified by assuming the separable aperture distribution and considering the cylindrical-array pattern to be the product of a ring array pattern and a linear array pattern. A pencil beam can be formed by selecting $I_p^{(a)}$ to form a beam at $\phi = 0$ in the azimuth cone $\theta = \theta_o$, and by selecting $I_q^{(e)}$ to form a beam at θ_o in the elevation plane $\phi = 0$. Since the pencil beam is the product of two fan beams, the principal sidelobes will lie on the cone and plane in which the fan beams were shaped.

The patterns do not include the effects of mutual coupling. Active element patterns, which do, and the corresponding element efficiencies have been calculated by Schwartzman and Kahn (1964) and by Kahn (1971).

1.2.1 Grating Lobes and Patterns

A cylinder can be covered with a regular lattice but the projection in any direction produces unequal spacing in azimuth. In elevation however the projected element spacings are uniform, so that conventional grating lobe theory can be used for elevation. There are no sharply defined, high amplitude grating lobes due to azimuth spacing, but the sidelobes of a low sidelobe design may be raised if the element spacing is too large. Since the cylinder must have elements "all around" to allow 360 deg azimuth scanning, there are two variables involved in grating lobe type calculations; element spacing and cylinder radius. In addition each element pattern usually has its axis in a radial direction so that the element pattern cannot be factored out. Amplitude tapering is typically used to produce moderately low sidelobes, so that any meaningful pattern calculation must include element spacing, cylinder radius, element pattern, and amplitude taper. For this reason there are no simple grating lobe type results for the cylindrical array. Cylindrical arrays that are phased to produce narrow beams tend to be more susceptible

to grating lobe problems than do comparable planar arrays because of two factors: (1) On the sides of the active portion of the array the element patterns do not point in the direction of the beam; and (2) in this same region it is necessary to introduce a large interelement phase shift into the excitation to compensate for the curvature of the cylinder. The latter factor is equivalent to scanning the side portion of the array to some angle off the normal to the cylinder at that point; hence, the interelement spacing must be kept correspondingly small to prevent the formation of grating lobes.

Elevation scan to θ_o is achieved by adding the phase -qkd sin θ_o to the q^{th} ring. The performance of the array pattern in the plane $\phi = 0$ is now the same as for a linear array with ring array "elements" with patterns such as those in Figure 2. In particular, a grating lobe appears at θ when

$$\frac{d}{\lambda} (\sin \theta - \sin \theta_o) = \pm m \qquad m = 1,2,... \qquad (27)$$

The lobe is at $\phi = 0$ in azimuth because $E^{(a)}(\phi,\theta)$ has its maximum at $\phi = 0$ (or nearly so) for all θ. The grating lobe as it arises from $E^{(e)}(\theta)$ has unit magnitude (equal to main beam), but is reduced by $E^{(a)}(\phi = 0,\theta)$.

Staggering alternate columns of elements on the cylinder is an effective means of extending the elevation scanning angle for a given ring-to-ring spacing d and maintaining a small grating lobe. Consider the staggered array as a superposition of two regular arrays, each with the normal number of rings Q but only half the number of elements in each ring $\frac{M}{2}$. The subarrays are identical except one is rotated by half a spacing in azimuth and is raised by half a spacing in the vertical direction, with the phase compensating for the dislocation. The ring-array patterns for the subarrays can be written (see Appendix A):

Array I - The beam in the direction of the first element; that is, f = 0.

$$EI = f(\theta) \sum_n I_n^{(\theta_o)} F_n(\theta) \cos n\phi + f(\theta) \sum_n I_n^{(\theta_o)} F_{\frac{M}{2} - n}(\theta)$$

$$\cdot \cos\left(\frac{M}{2} - n\right) \phi + f(\theta) \sum_n I_n^{(\theta_o)} F_{M-n} \cos (M - n)\phi \qquad (28)$$

The r = 2 term, which ordinarily would not contribute (for $s<\lambda$) is included, because the spacing is now double the normal spacing.

Array II - The beam is in a direction halfway between two elements; that is, f = 0.5.

$$EII = f(\theta) \sum_n I_n^{(\theta_o)} F_n(\theta) \cos n\phi - f(\theta) \sum_n I_n^{(\theta_o)} F_{\frac{M}{2} - n}(\theta)$$

$$\cdot \cos\left(\frac{M}{2} - n\right) \phi + f(\theta) \sum_n I_n^{(\theta_o)} F_{M-n} \cos (M - n)\phi \qquad (29)$$

If the array were not staggered, each ring would have M elements and a pattern

$$E^{(a)}(\phi, \theta) = f(\theta) \sum_n I_n^{(\theta_o)} F_n(\theta) \cos\phi n + f(\theta) \sum_n I_n^{(\theta_o)} F_{M-n}(\theta)$$

$$\cdot \cos (M - n)\phi \qquad (30)$$

The grating-lobe term that arises because of the doubling of the spacing is

$$E_{g\ell}(\phi, \theta) = \sum_n I_n F_{\frac{M}{2} - n} \cos\left(\frac{M}{2} - n\right) \phi \qquad (31)$$

Assume Array II is raised with respect to Array I by $\frac{d}{2}$ and multiplied by $\exp\left[jk\frac{d}{2}(\sin\theta - \sin\theta_o)\right]$ to account for the phase. The patterns of cylindrical Arrays I and II are then

$$EI(\phi,\theta) = \sum_{q=1}^{Q} \left|I_q\right| \exp\left[jqkd(\sin\theta - \sin\theta_o)\right] \cdot \left[E^{(a)}(\phi,\theta) + E_{g\ell}(\phi,\theta)\right]$$

and

$$EII(\phi,\theta) = \exp\left[jk\frac{d}{2}(\sin\theta - \sin\theta_o)\right] \sum_{q=1}^{Q} \left|I_q\right| \exp\left[jqkd(\sin\theta \sin\theta_o)\right] \left[E^{(a)}(\phi,\theta) - E_{g\ell}(\phi,\theta)\right] \quad (32)$$

The sum of EI and EII is the pattern of the staggered array. It may be put in the form

$$E(\phi,\theta) = \left\{\sum_{q=1}^{2Q} I_q \exp\left[jqk\frac{d}{2}(\sin\theta - \sin\theta_o)\right]\right\} \cdot E^{(a)}(\phi,\theta) + \left\{\sum_{q=1}^{Q} I_q \exp\left[jqkd(\sin\theta - \theta_o)\right]\right\} \cdot \left\{1 - \exp\left[jk\frac{d}{2}(\sin\theta - \sin\theta_o)\right]\right\} \cdot E_{g\ell}(\phi,\theta) \quad (33)$$

The first term of (33) is the pattern of an array of 2Q rings spaced at half the normal spacing with M elements on each ring; that is, the staggered array with the "holes" filled in. This term should give no grating lobe because of the half spacing in elevation and the normal spacing in azimuth.

The second term accounts for the grating lobe. The factor

$$\sum_{q=1}^{Q} \left| I_q \right| \exp\left[jqkd\,(\sin\theta - \sin\theta_o)\right]$$

is the linear array pattern for normal elevation spacing, and gives a grating lobe when

$$\frac{d}{\lambda}\,(\sin\theta - \sin\theta_o) = \pm 1 \tag{34}$$

This gives

$$1 - \exp\left[jk\frac{d}{2}\,(\sin\theta - \sin\theta_o)\right] = 2$$

Thus, the grating lobe of the cylindrical staggered array is equal to the grating lobe of the linear array, with spacing d, times the grating lobe of a ring array, with spacing 2s. The elevation and azimuth positions of the product lobe are the positions of the linear and ring array lobes, respectively. The staggered-array lobe appears at the same elevation angle as the lobe of the regular array but is removed from $\phi = 0$ to $\phi = \phi_{g\ell}$ as determined from a ring array with every other element removed. The advantage gained is the amount the grating lobe of the ring subarrays is down from the main beam.

Figure 6 shows the grating lobe height as a function of scan angle for regular and staggered configurations, and the position in elevation and azimuth for the staggered array lobe. The parameters are $N_0 = 128$, $\theta_0 = 0^\circ$ and a-50dB Chebyshev distribution.

In obtaining (33) equation (9) was the start. However, the start could equally well have been (13), using $\alpha = \frac{2\pi}{M}(p + f)$. Also, it was assumed that $f = 0$ for Array I and $f = 0.5\lambda$ for Array II. (33) depends only on the fact that $E_{g\ell}\ (\phi,\theta)$ for

Array I is equal to $-E_{g\ell}(\phi,\theta)$ for Array II, which is true for any orientation of the first element with respect to the main beam. Thus, (33) is valid for cylindrical arc arrays in general. Furthermore, $E_{g\ell}(\phi,\theta)$ may easily be identified from patterns computed directly from (10) with alternate elements excited.

Figure 8 shows $E^{(a)}(\phi,\theta) + E_{g\ell}(\phi,\theta)$ and for comparison $E^{(a)}(\phi,\theta)$ for various θ_o. These patterns are computed from (10) and the contribution from $E_{g\ell}(\phi,\theta)$ is easily identified. The effect of staggering is easily seen. For example, if the rings are spaced at $d = 0.72\lambda$, a beam at $\theta_o = 30^o$ gives a grating lobe at about -60^o. From Figure 8C a regular array gives the grating lobe height at -11 dB, which is the difference between the beams at $\theta = 30^o$ and $\theta = 60^o$. For a staggered array, the grating lobe height is the difference between the beam at $\theta = 30^o$ and the grating lobe at $\theta = 60^o$, or about -28 dB.

1.2.2 Principal Sidelobes

For the regular array the principal sidelobes will lie on the plane $\phi = 0$ and the cone $\theta = \theta_0$, because the regular-array pattern, for the separable distribution, can be thought of as the product of two fan beams.

For the staggered array we can consider equation (33). The first term is the product of a linear array fan beam and a ring array fan beam, giving principal sidelobes as a regular array on the plane $\phi = 0$ and the cone $\theta = \theta_0$. The second term gives another set of axes, however. The first two factors of the second term give the linear array grating lobe (without the main beam); the third factor gives the ring array grating lobe (with double spacing). Thus, another set of principal sidelobes lies on the cone $\theta = \theta_{g\ell}$ and the warped plane $\phi = \theta_{g\ell}(\theta)$ where $\theta_{g\ell}$ is given by (34) and $\phi_{g\ell}(\theta)$ gives a maximum to $E_{g\ell}(\phi,\theta)$.

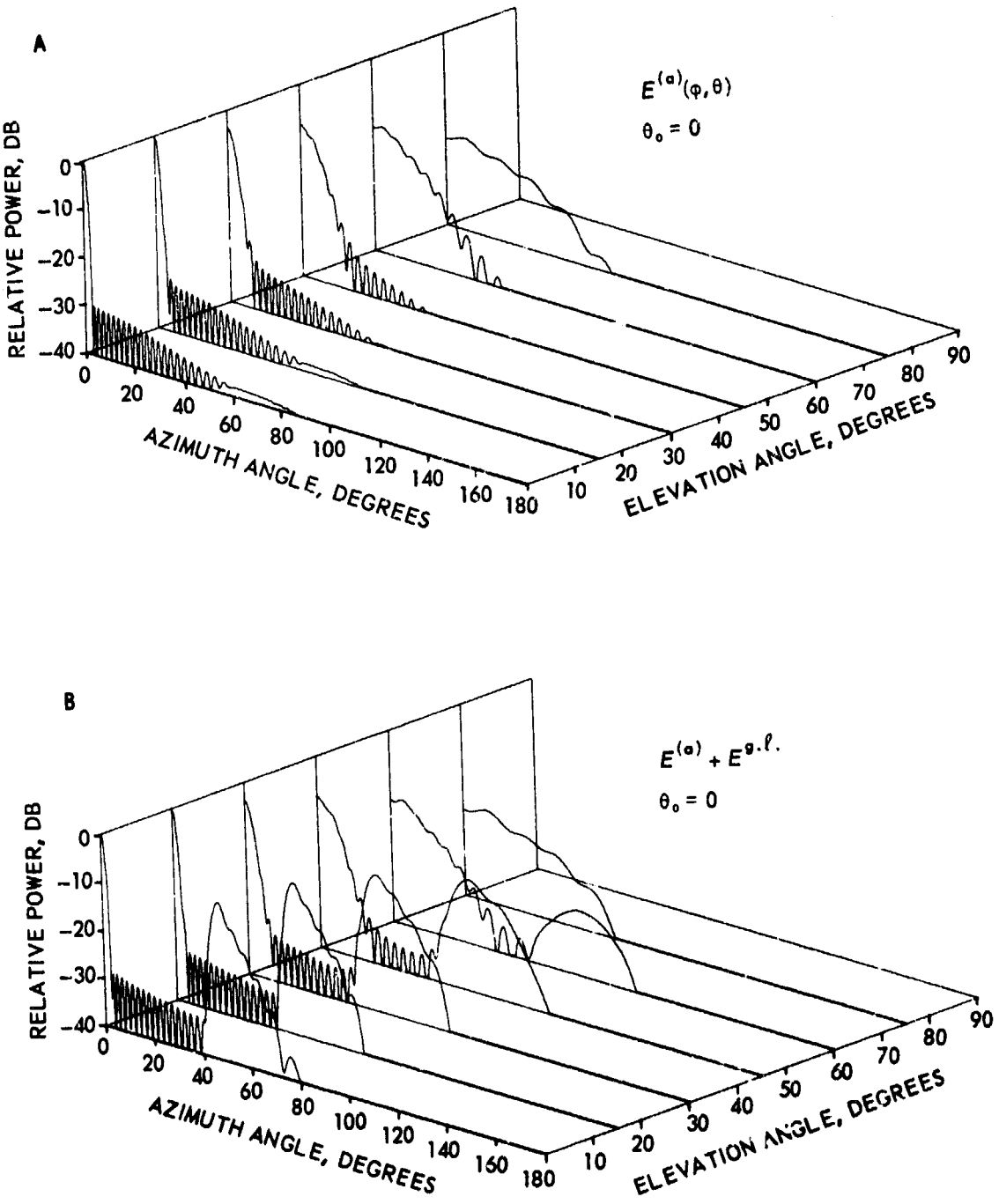

Figure 8. $E^{(a)}(\phi,\theta) + E_{g\ell}(\phi,\theta)$ and $E^{(a)}(\phi,\theta)$ for various θ_0. Forty-four active elements spaced at 0.65λ on a radius of 26.3λ, with a projected 30-dB Chebyshev distribution and cosine element pattern.

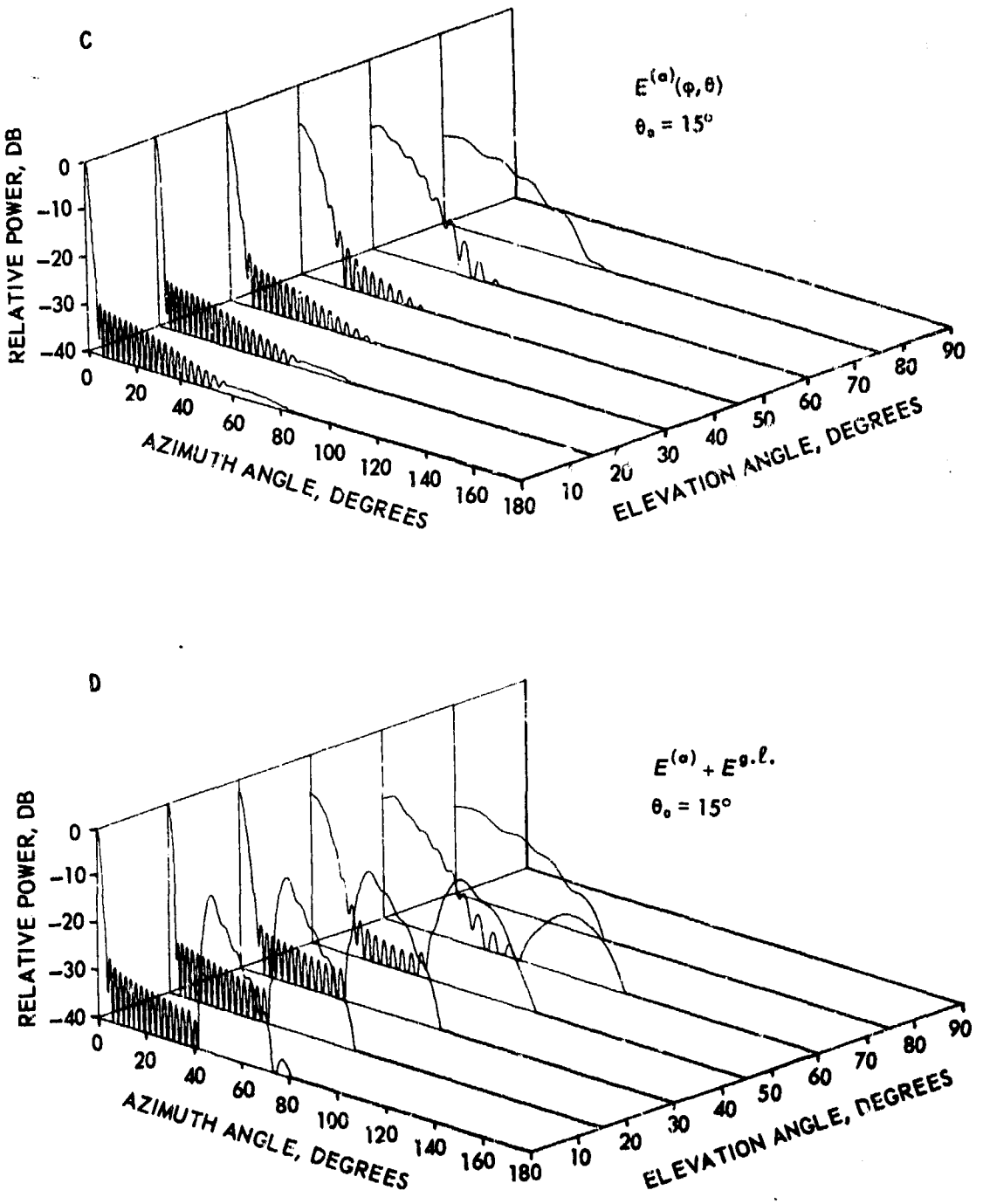

Figure 8 (continued)

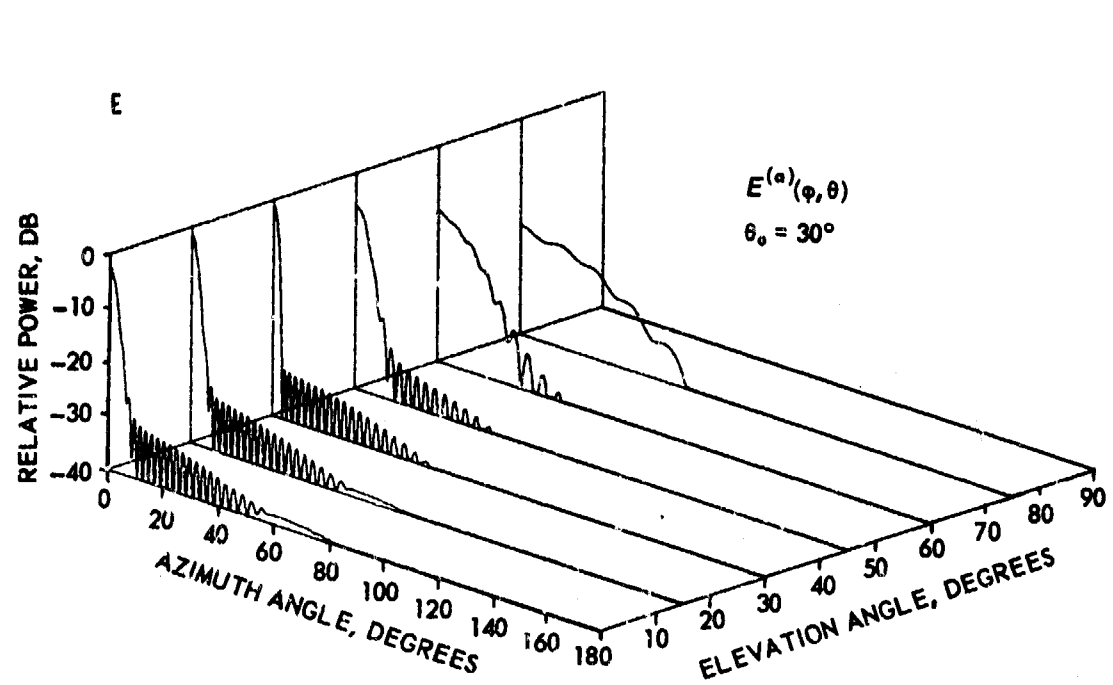

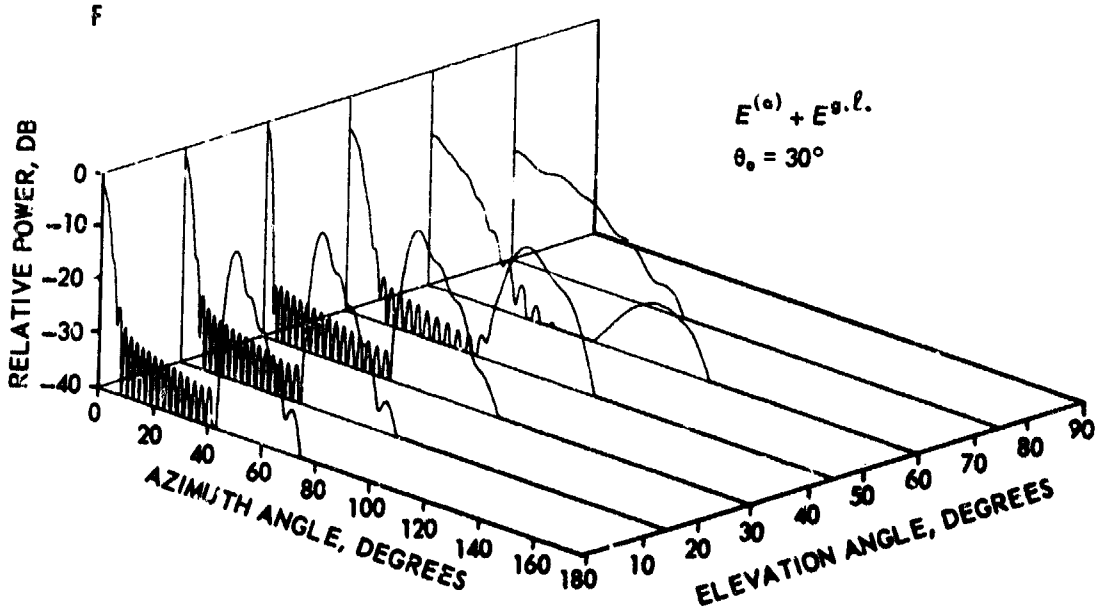

Figure 8 (continued)

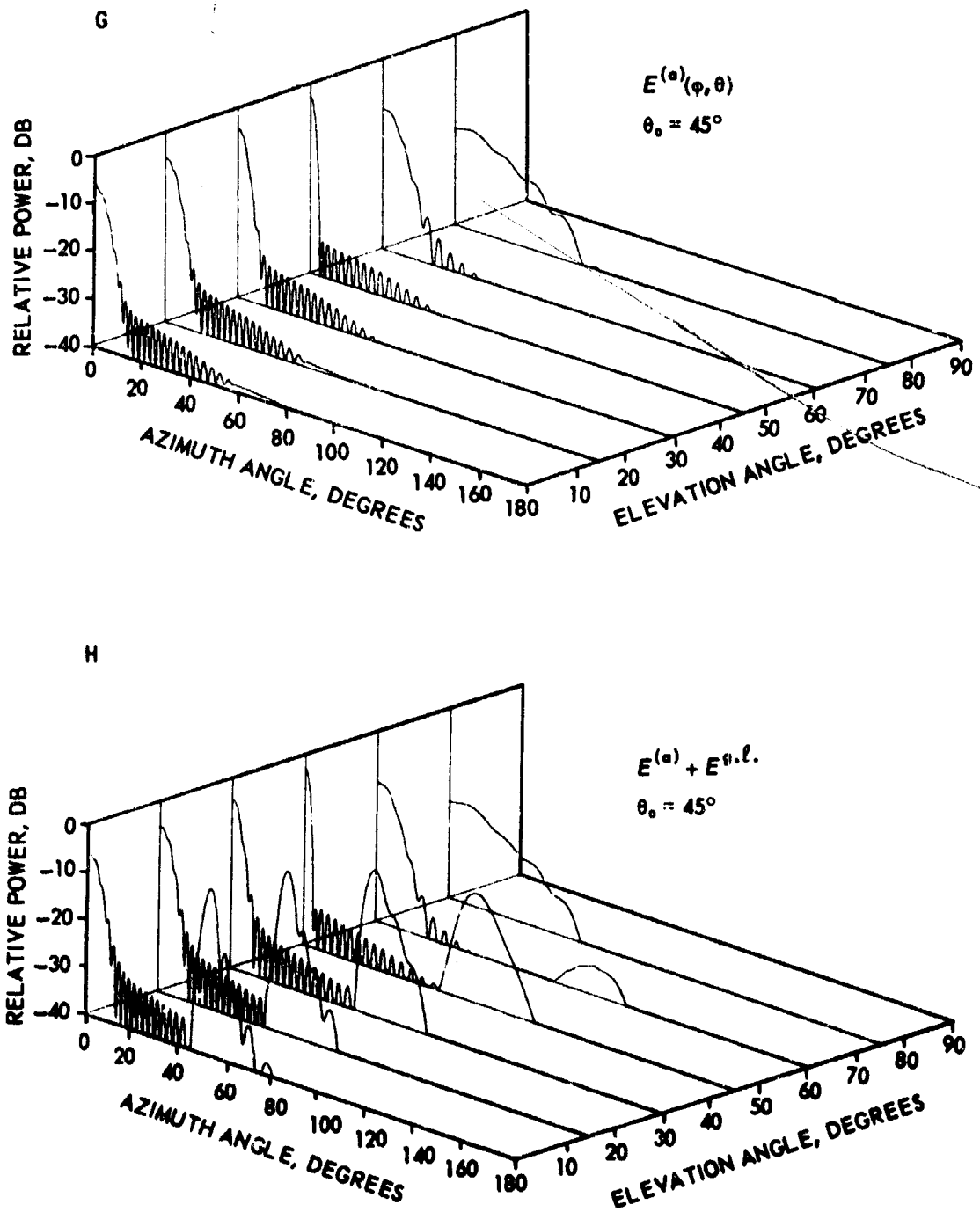

Figure 8 (continued)

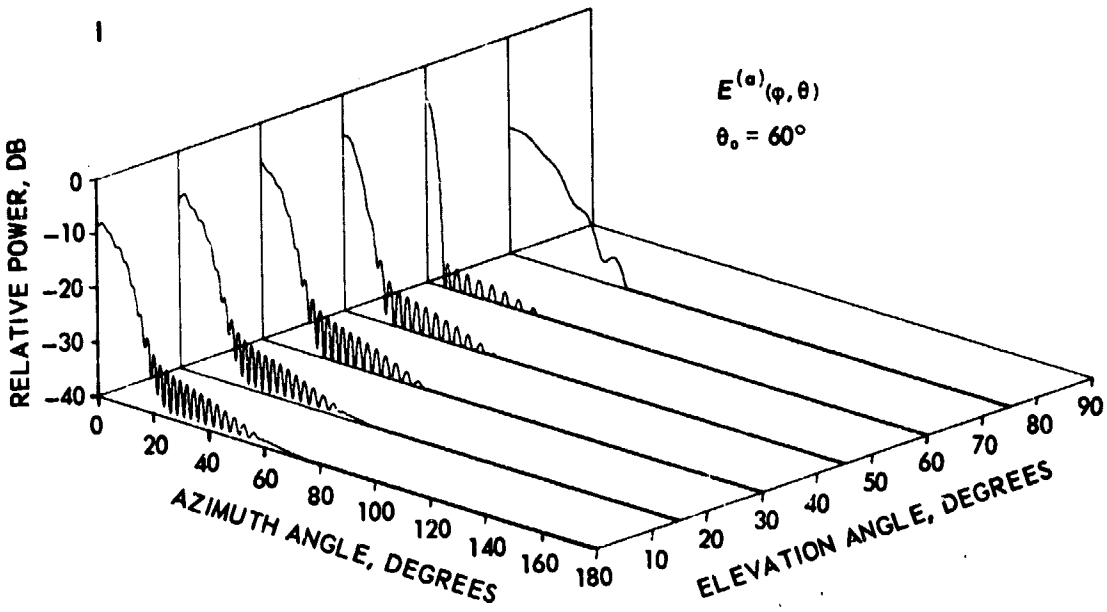

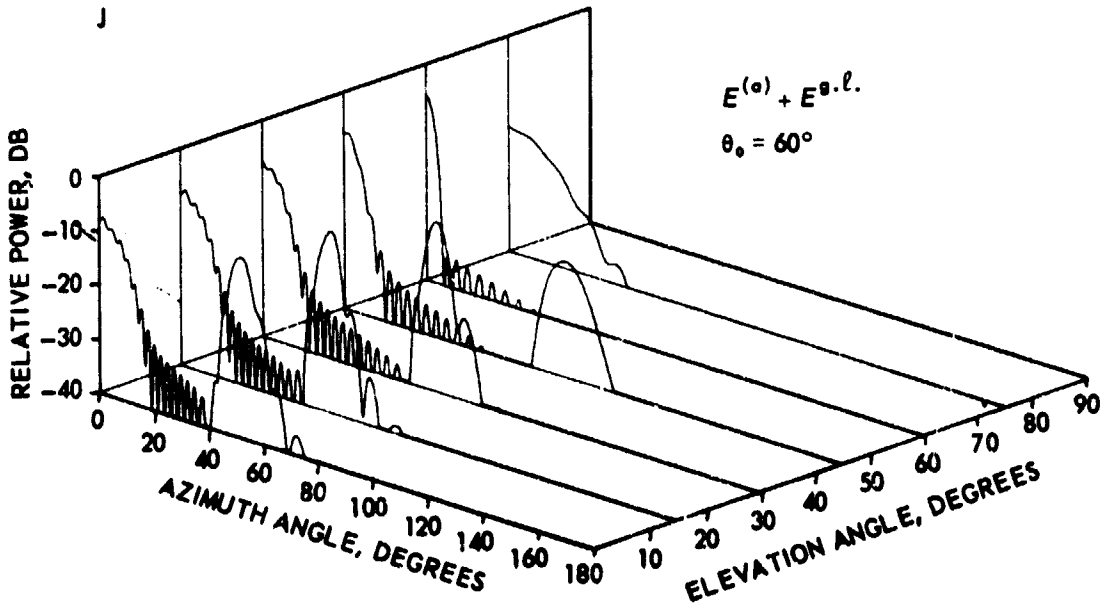

Figure 8 (continued)

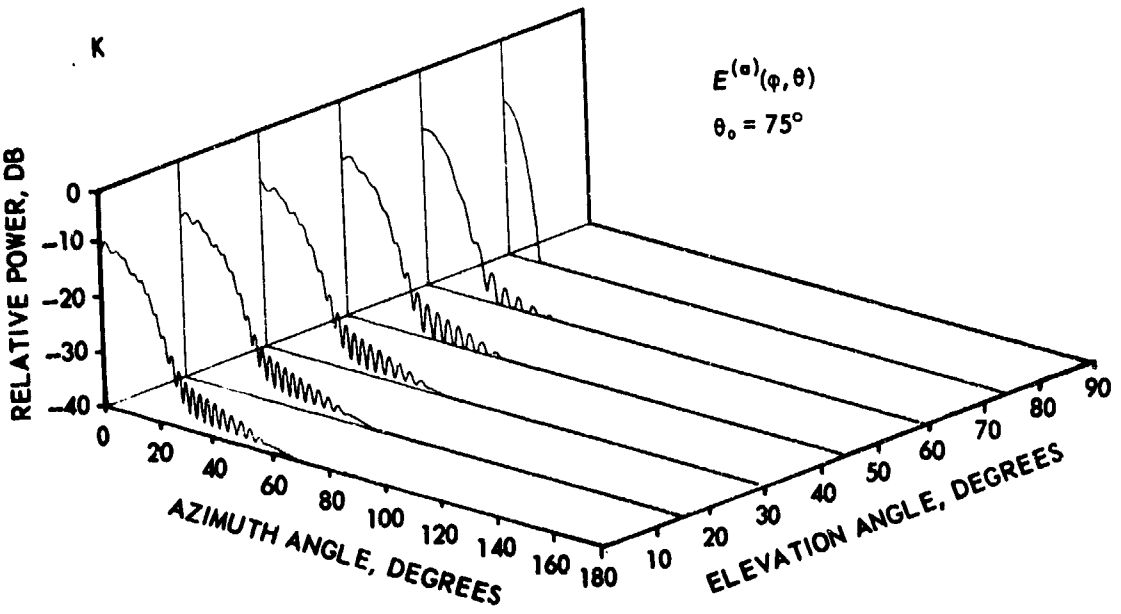

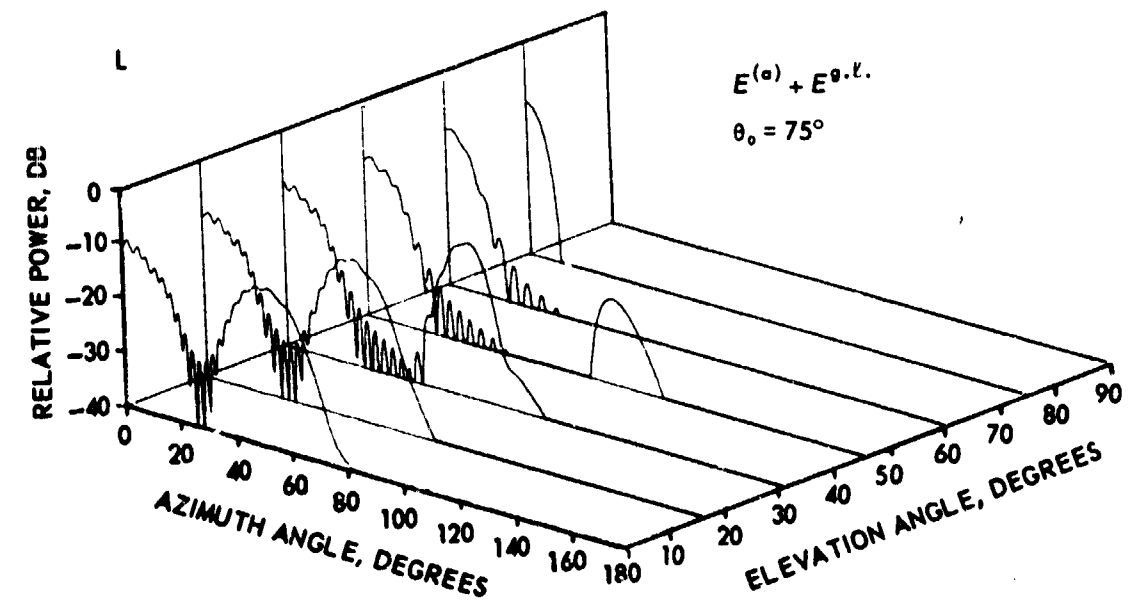

Figure 8 (continued)

For the regular array, then, the full cylindrical array pattern is well represented by two contours through ϕ,θ space, (ϕ,θ_0) and $(0,\theta)$. For the staggered array, the full pattern is well represented by the four contours (ϕ,θ_0), $(0,\theta)$, $(\phi,\theta_{g\ell})$ and $(\phi_{g\ell}\ (\theta),\ \theta)$. Figure 9 presents the patterns for regular and staggered arrays at various θ_0. The same single ring parameters are assumed as for Figure 8; in addition, 32 rings spaced at 0.72λ are used with a 30-dB Chebyshev distribution for $I_q(e)$. The contour $(\phi_{g\ell}\ (\theta),\ \theta)$ was determined from the patterns of Figure 8 by interpolation between the maximum points on the grating lobe.

The grating lobe can be reduced and elevation scan extended by reducing the azimuth and/or elevation spacing of the staggered array. For example, reducing the azimuth spacing from 0.65λ to 0.5λ (with $d = 0.72\lambda$) increases the scan-angle limit from 30° to about 40° to maintain a grating lobe of 30 dB, and further reduction to 0.4λ allows scanning to above 75° with the grating lobe below 40 dB. Reduction of elevation spacing (with $s = 0.65\lambda$) from 0.72 to 0.6λ allows scanning to above 50° for a grating lobe below 40 dB. In the array being implemented, however, the elevation spacing is restricted to a minimum of 0.72λ because of the element size.

1.2.3 Cylindrical Depolarization

The cylindrical surface like any curved surface depolarizes an incident wave. For example, if a linearly polarized wave is incident in the plane of incidence (the plane containing the cylinder axis and the direction of incidence), polarizations that are parallel or normal to this plane behave differently. With electric field parallel to the plane of incidence, the axial component of field on the cylindrical surface is in the same direction but the circumferential components oppose. Of course, at normal incidence the latter are zero. For normal

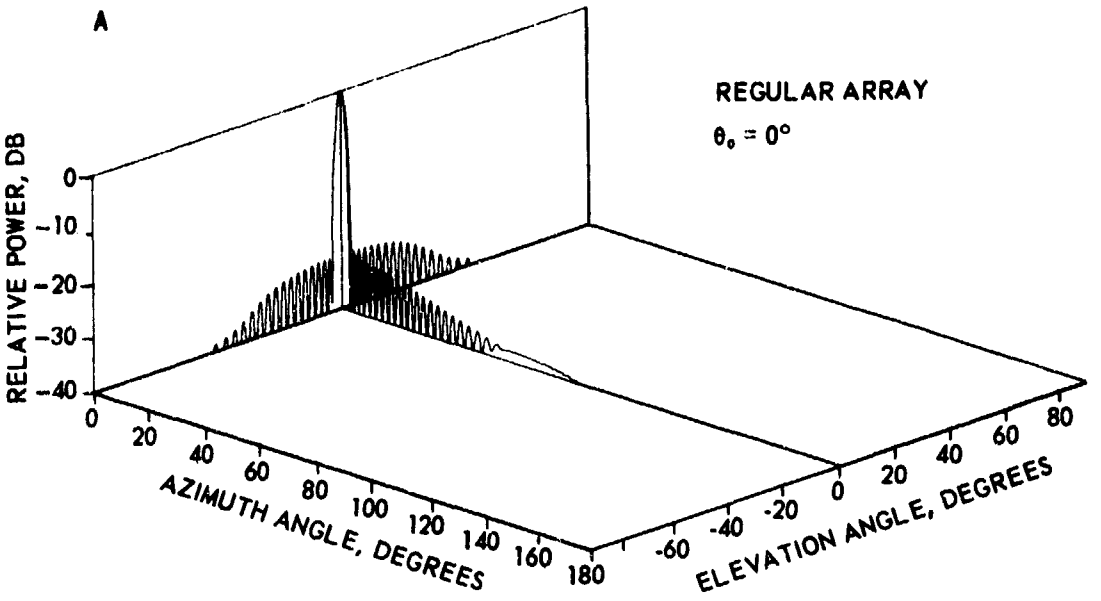

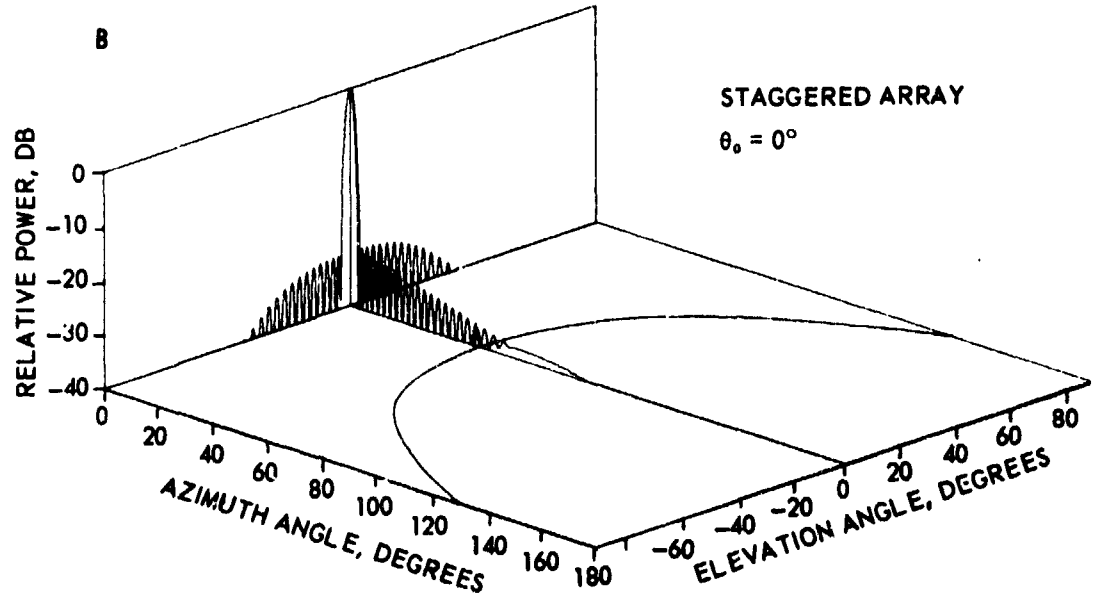

Figure 9. Patterns for regular and staggered arrays at various θ_0. Ring-array elements as in Figure 8. Vertical spacing is 0.72λ, and 32 rings are assumed with a 30-dB Chebyshev distribution.

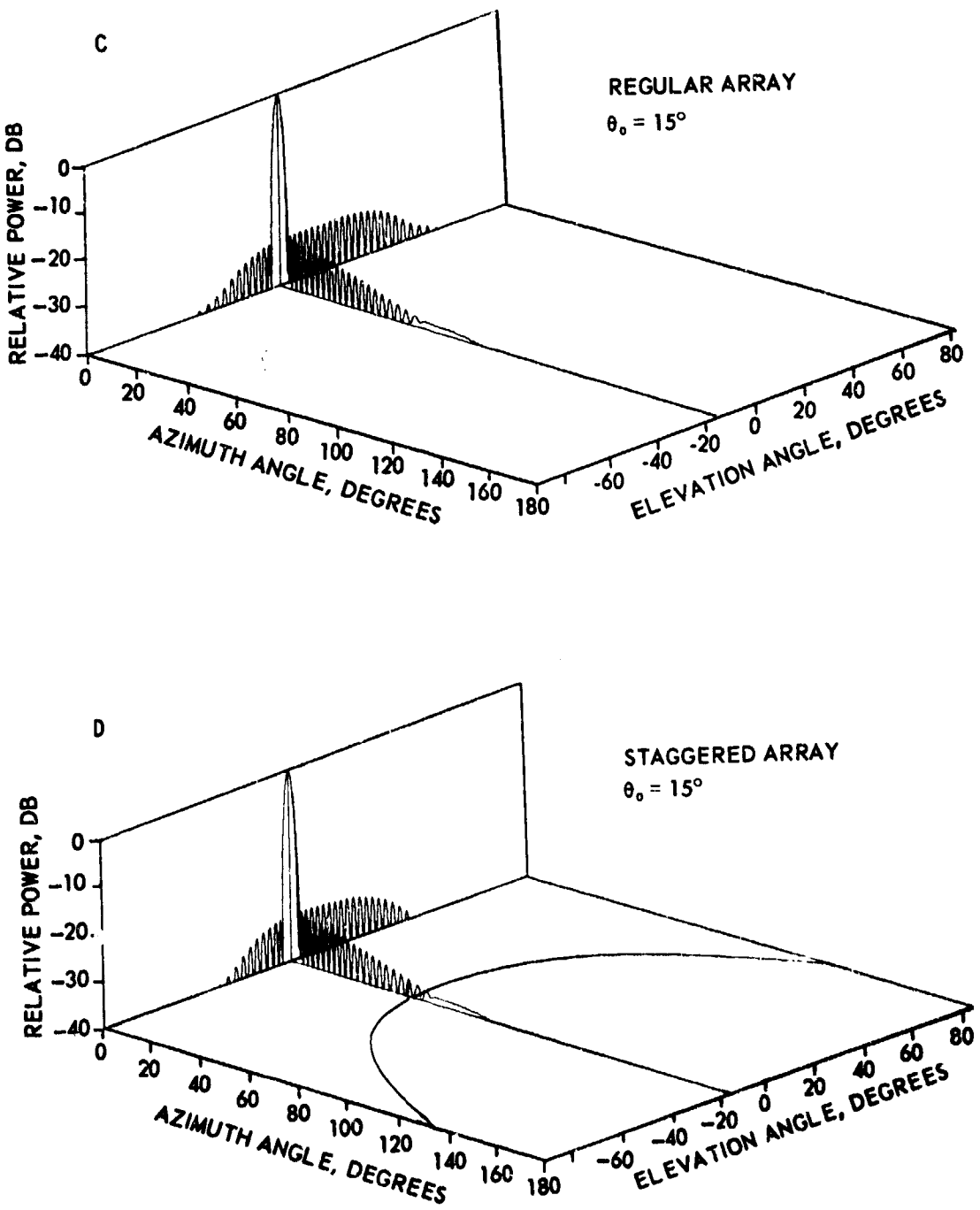

Figure 9 (continued)

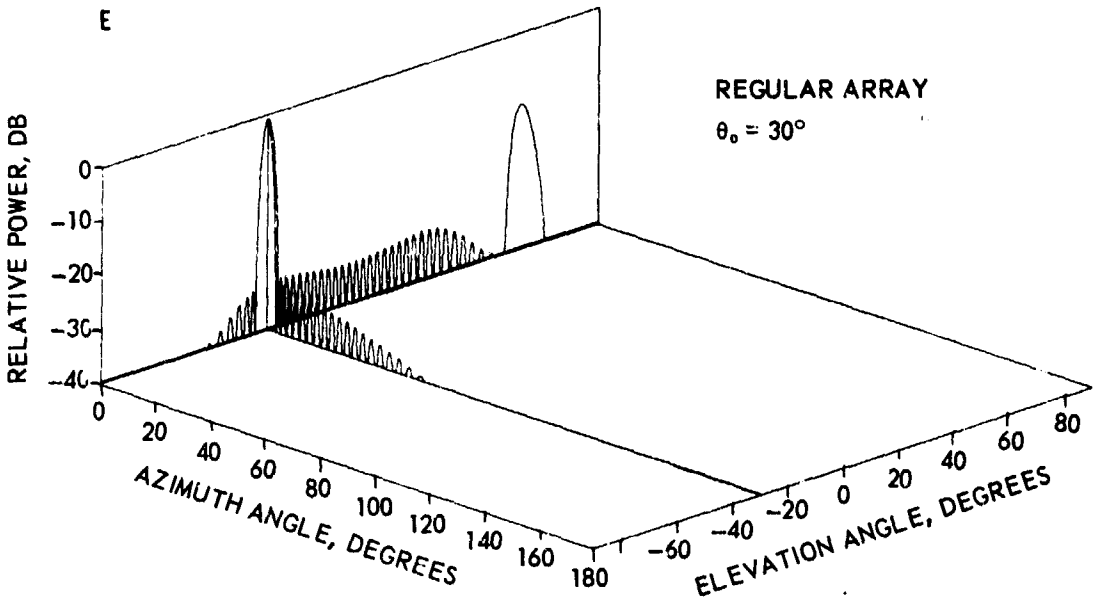

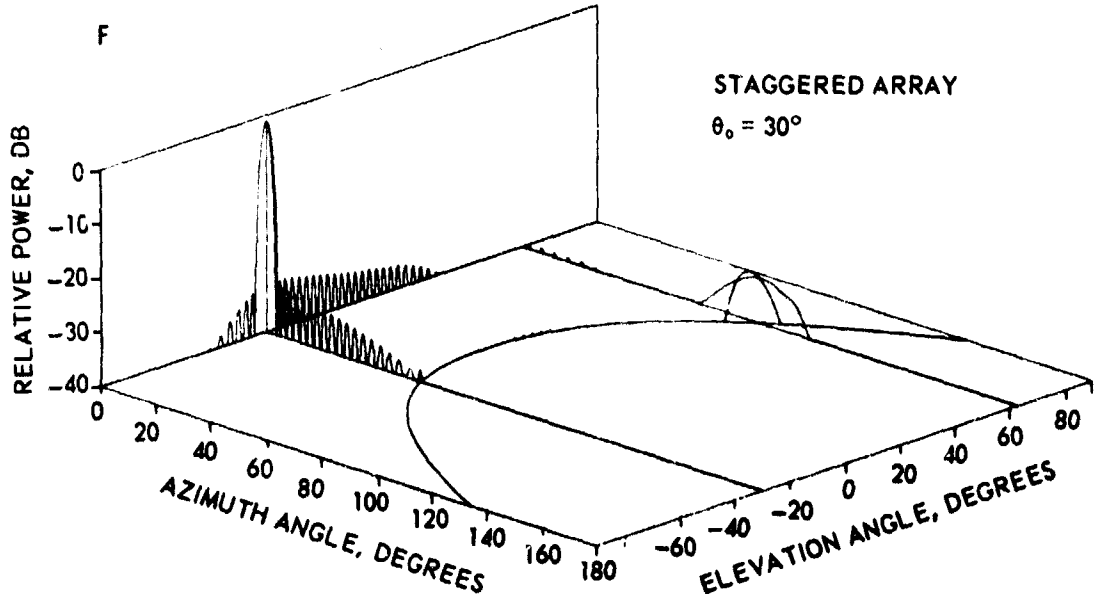

Figure 9 (continued)

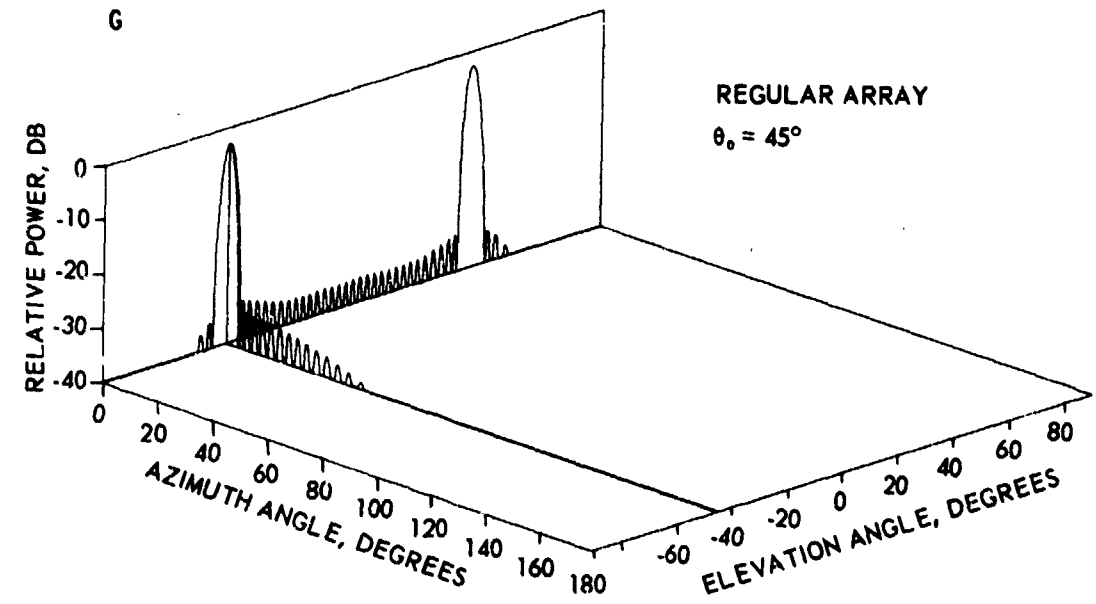

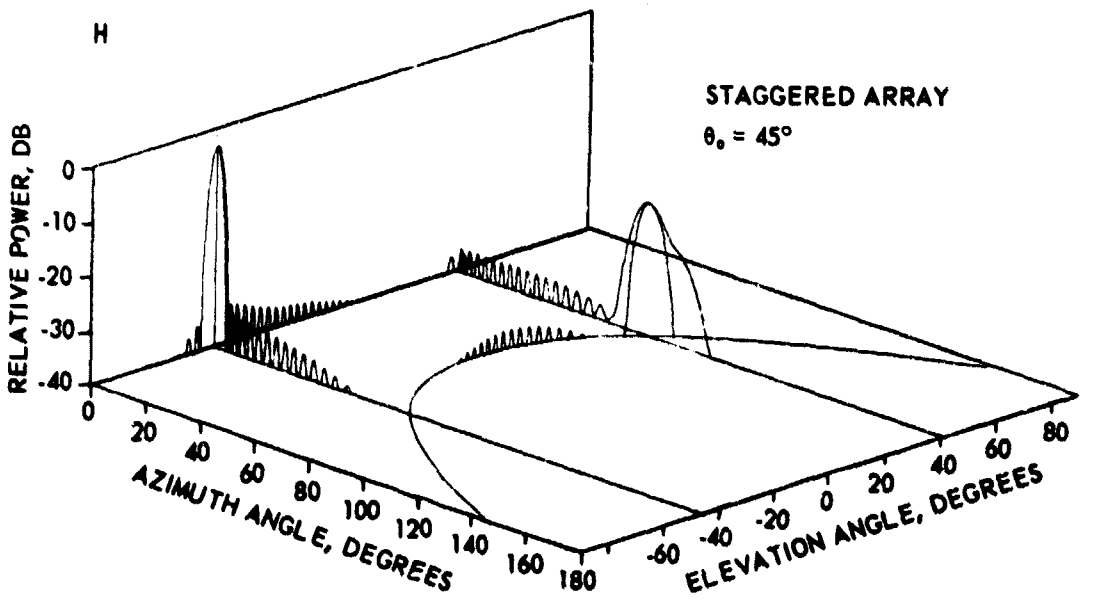

Figure 9 (continued)

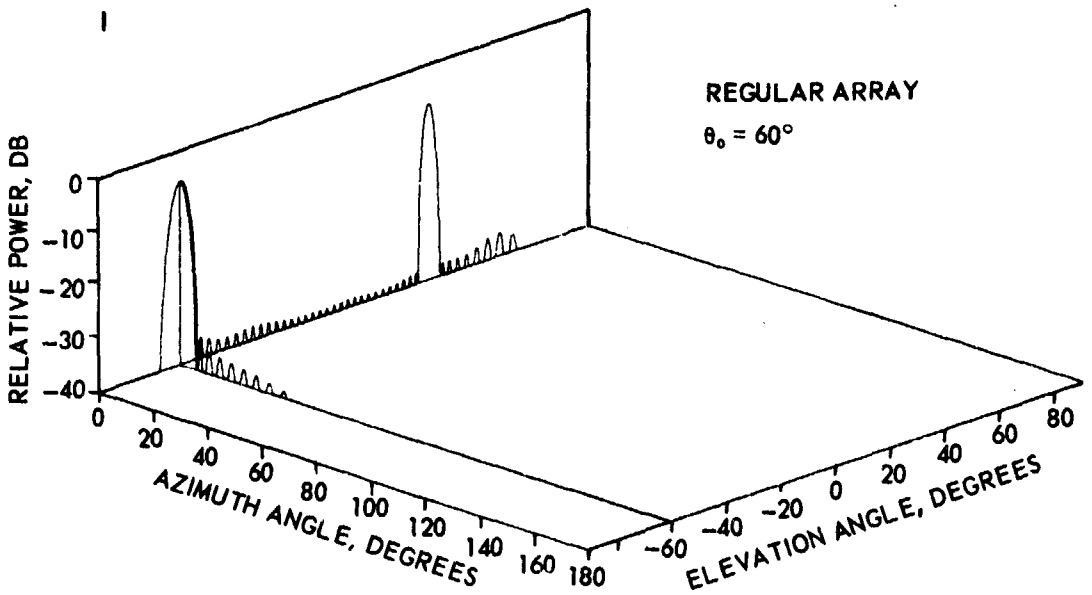

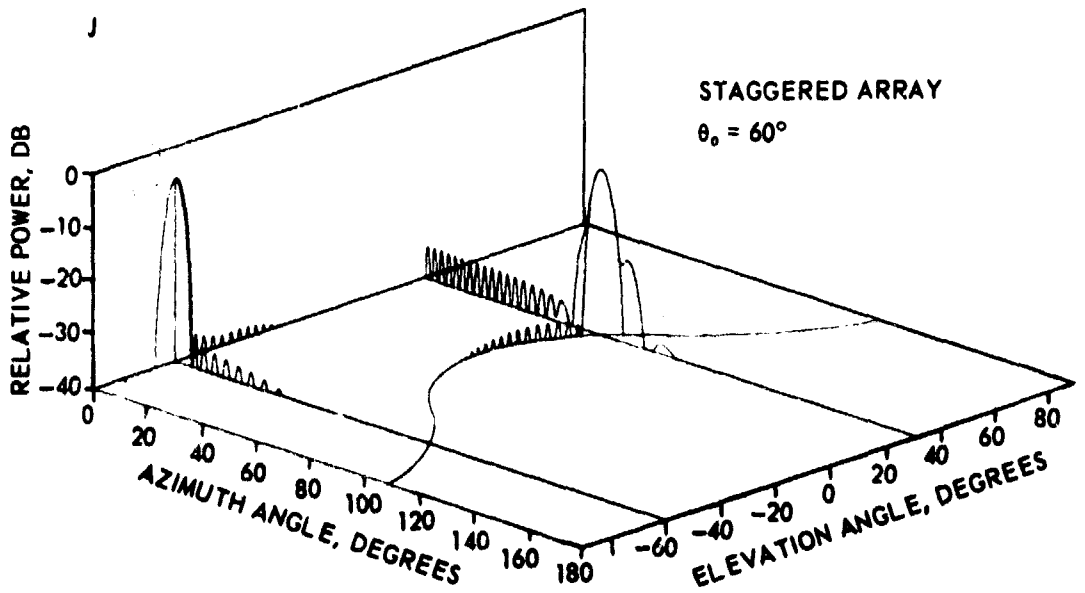

Figure 9 (continued)

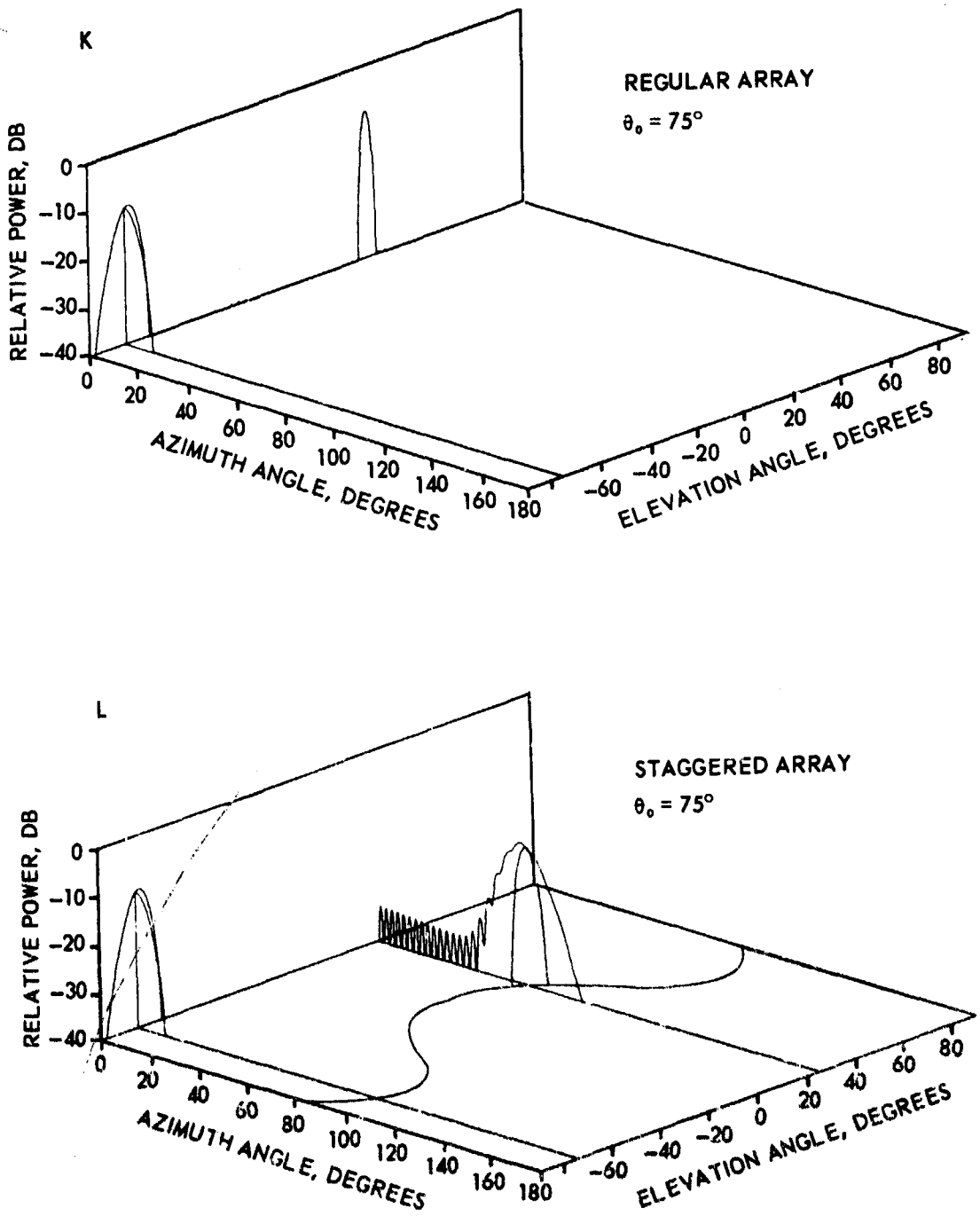

Figure 9 (continued)

polarization, the axial components are in the same direction; and the circumferential components are also in the same circumferential direction. Thus incident circular polarization produces fields that have the polarization axes oriented right on one side, and left on the other side, with all polarizations elliptical except at points of incidence. Thus a cylindrical array should use elements that radiate both axial and circumferential components. Further, the ratio of these components in general for any given element will change as the angle of incidence changes. Arrays on large (in wavelengths) cylinders with tapered circumferential distributions will experience a lower and perhaps negligible level of depolarization as the amplitude at elements significantly away from a projected aperture plane may be small. Conical arrays do not share this advantage unless only the large diameter portion of the surface is utilized. The general conical case will be discussed later.

1.2.4 Comparison of Planar and Cylindrical Arrays

The question often arises whether the cylindrical array makes efficient use of aperture and hardware -- in particular, when compared with the standard planar-array approach. For 360-degree azimuth coverage, four planar arrays, each scanning ± 45 degrees, are generally used, so the cylinder is compared with the four-sided planar configuration. Identical elements are assumed. For elevation scanning and elevation pattern, the two configurations give nearly identical results, assuming that both use a separable cophasal distribution and identical distributions in elevation. The planar array elevation pattern is the array factor multiplied by the elevation element pattern, while the cylindrical array elevation pattern is the array factor multiplied by the "ring array element" elevation pattern. Figure 3, for example, shows the "ring array element" elevation patterns compared with the element elevation pattern. If anything, it is

an advantage of the cylinder that the ring array elevation patterns tend to suppress sidelobes more than does the element pattern alone.

The comparison, then, can be reduced to a comparison of the ring array azimuth pattern to the linear array azimuth pattern.

Assume that no more than 180° of the arc will be excited on the ring. Then the amplitude excitation of a linear array can be projected* onto an arc whose chord is equal to the length of the linear array, with the phase of the elements on the arc corrected to give a linear phase front. For small angles off broadside -- that is, the main beam and first few sidelobes, the arc can be expected to give about the same results as the linear array, because for small angles the curvature has a negligible effect on the phased contribution from each element. Also, effects of element spacing become apparent only at larger angles. By this reasoning, the projection of, say, a Chebyshev distribution is a convenient means for forming the desired beamwidth and constraining the inner sidelobes of an arc array. Computations bear this out. Furthermore, the farther-out sidelobes tend naturally to be lower, with the exception of the grating lobe. Computations indicate that if the grating lobe is controlled, all sidelobes will be below the inner sidelobes.

The relative performance of the linear and arc arrays can be evaluated in terms of the number of elements and the overall antenna size required. Consider Figure 10. The active apertures are shown in dark lines, and are of the same projected length.

*The increased element density as a function of α on the arc means the amplitude should be reduced by $1/\cos \alpha$; however, this is exactly compensated by the assumed cosine element pattern.

The element spacing on the linear array can be fixed at $d = 0.586\lambda$, which is the spacing required to scan to $\pm 45^{\circ}$ with the grating lobe just coming in at $\pm 90^{\circ}$. For the arc, the grating lobe can be controlled by placing the stationary point outside the active arc, say at $\alpha_0 = (P) + \delta$. Then from (18) with $\theta_0 = 0$ and $r = -1$, since δ is small

$$s = 1/2 \sin (\alpha(P) + \delta) \simeq 1/[\sin \alpha(P) + \delta \cos \alpha(p)] \qquad (35)$$

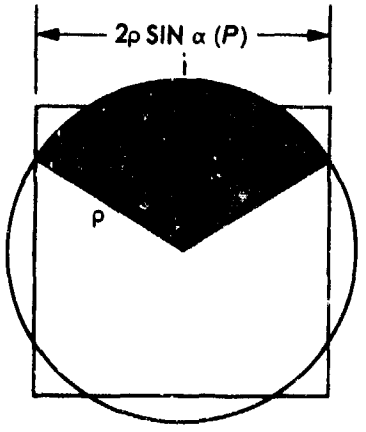

Figure 10. Four-sided linear array compared to equivalent circular array.

The total number of elements on the four-sided array is about

$$8 \rho \sin \alpha(P)/0.586\lambda$$

The total number on the ring is

$$2\pi\rho/s = 4\pi\rho(\sin \alpha(P) + \delta \cos \alpha(P))$$

The ratio is

$$\frac{\text{number of ring elements}}{\text{number of linear elements}} = 0.920 \ (1 + \delta \cot \alpha(P)) \qquad (36)$$

From this one may conclude that about 92 to 100 percent of the elements required for a four-sided linear array are required to obtain the equivalent ring array. Table 1 and Figure 11 show results and patterns for a 40-element linear array with uniform and Chebyshev amplitude distributions, in comparison with arc arrays of equivalent projected aperture. A cosine element pattern is assumed for all cases. The directivity is that of the azimuth patterns numerically integrated. It is not the actual directivity, since elevation directivity is not considered, but it is valid for comparison purposes.

TABLE 1. BEAMWIDTH, SIDELOBE LEVEL, AND DIRECTIVITY

Distribution	Linear Array (fig. 11.1)	90° Arc (fig. 11.2)	118° Arc (fig. 11.3)
Uniform			
beamwidth*	2.5° (3.04°)	2.19°	2.17°
sidelobe**	-13.3 dB	-13.3 dB	-13.4 dB
gain	21.7 dB	21.3 dB	21.4 dB
Chebyshev (-20 dB)			
beamwidth*	2.22° (3.14°)	2.28°	2.28°
sidelobe**	-20.0 dB	-20.0 dB	-20.2 dB
gain	21.2 dB	20.7 dB	20.8 dB
Chebyshev (-26 dB)			
beamwidth*	2.47° (3.50°)	2.52°	2.52°
sidelobe**	-26.0 dB	-25.8 dB	-25.2 dB
gain	21.3 dB	21.1 dB	21.1 dB
Chebyshev (-30 dB)			
beamwidth*	2.62° (3.71°)	2.38°	2.66°
sidelobe**	-30.0 dB	-29.4 dB -28.8 dB g.ℓ.	-28.6 dB
gain	21.2 dB	21.0 dB	21.0 dB

*The beamwidth for the linear array scanned to 45° is shown in parentheses.
**The grating lobe is below the sidelobe level except where indicated (g.ℓ.).

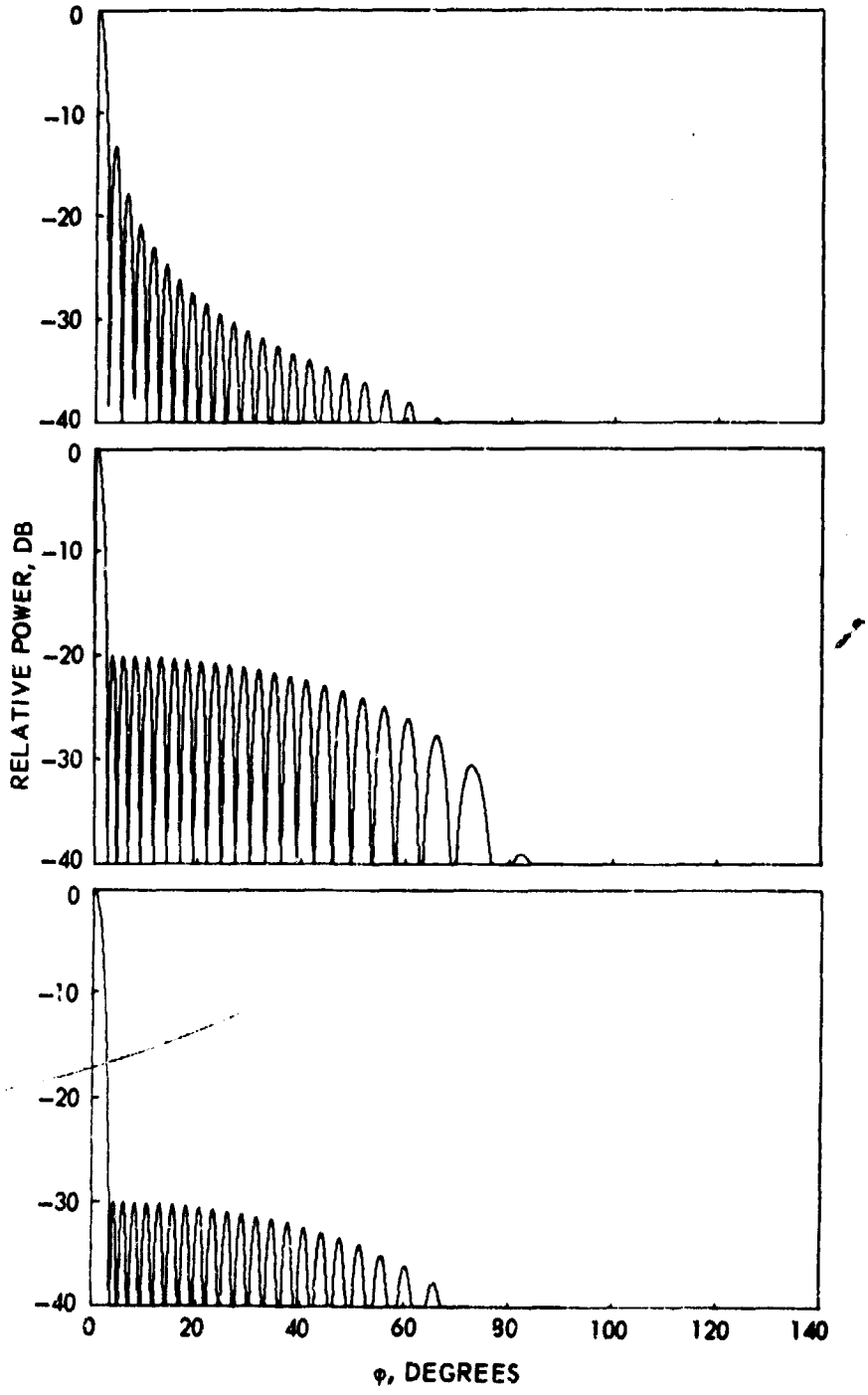

Figure 11.1. Forty-element linear-array patterns for uniform (top), -20-dB Chebyshev (middle), and -30-dB Chebyshev (bottom) distributions. Broadside only, with spacing 0.59λ and cosine element pattern.

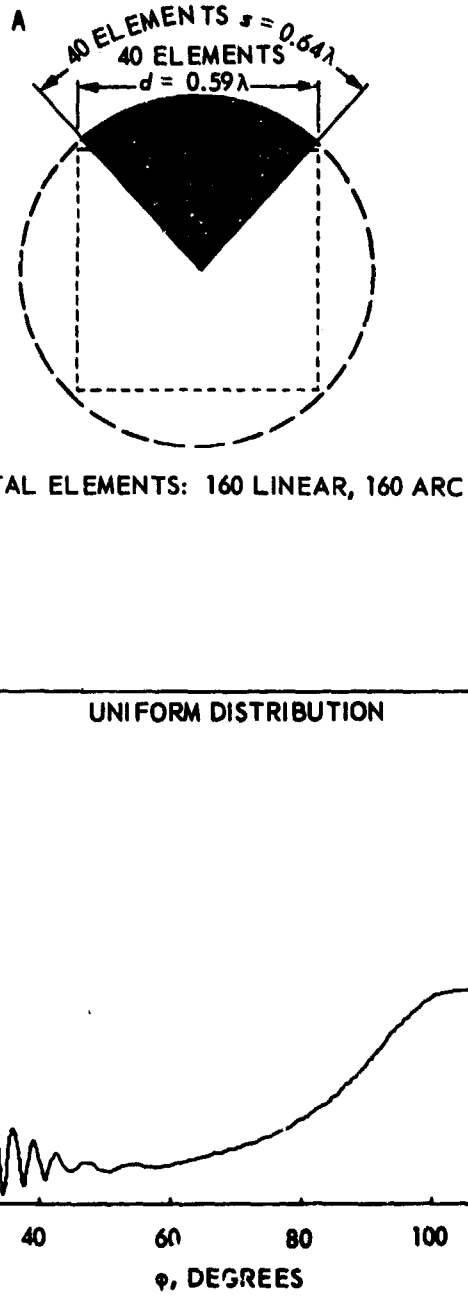

Figure 11.2. Ninety-degree arc-array analogous to the linear array, with patterns for analogous distributions.

C

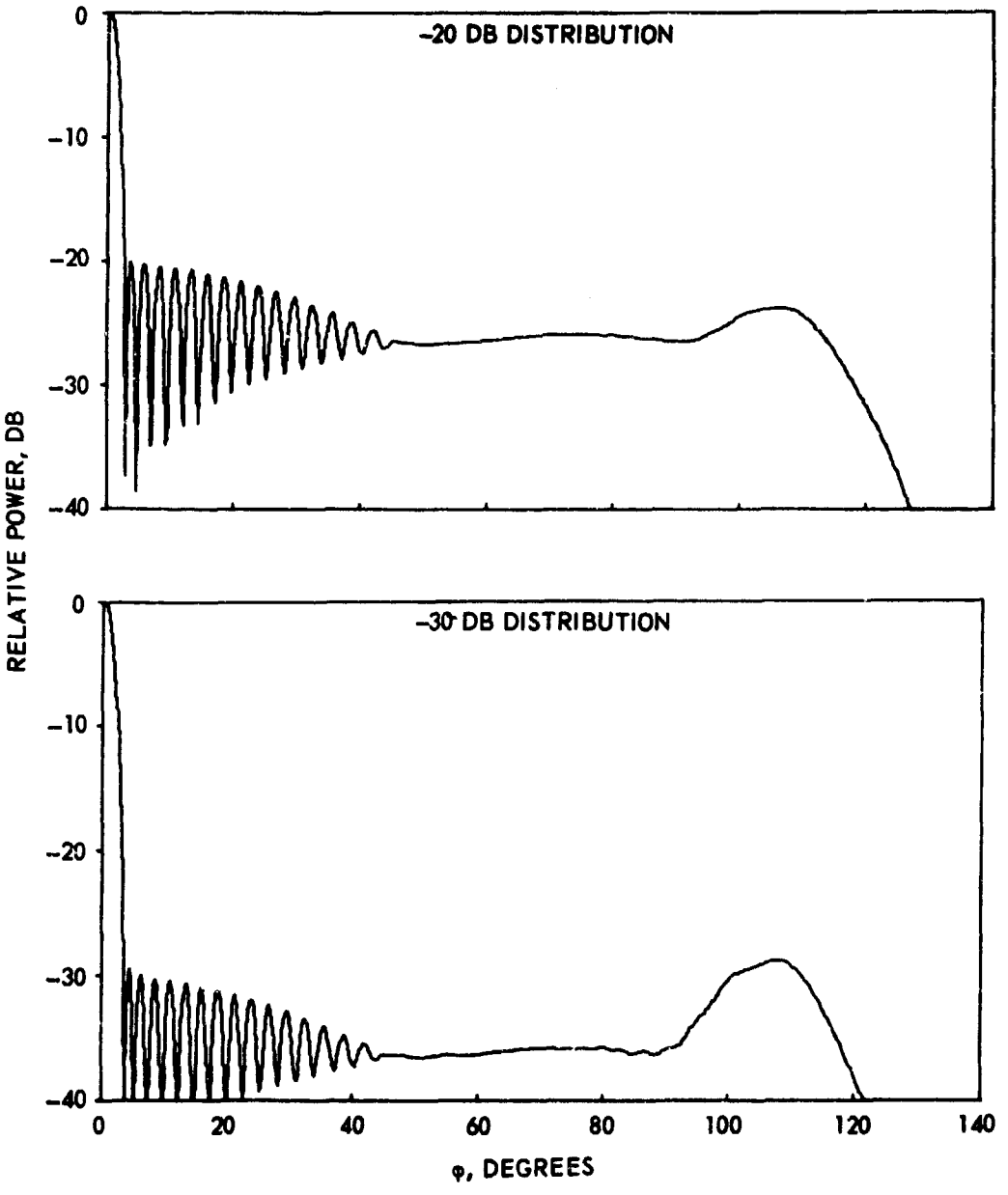

Figure 11.2 (continued)

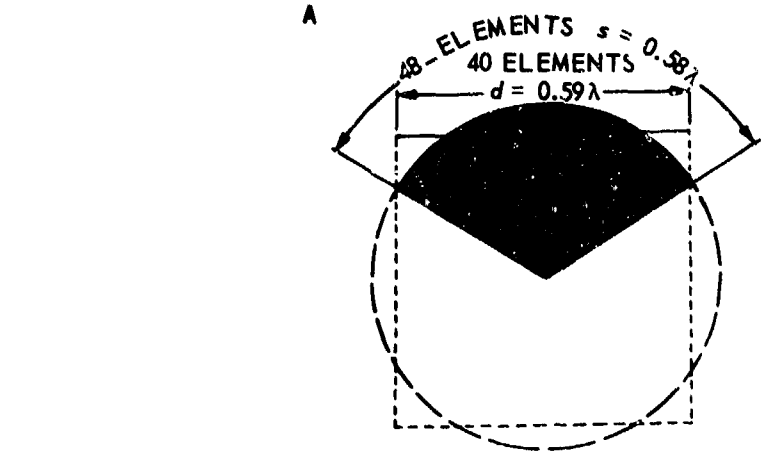

TOTAL ELEMENTS: 160 LINEAR, 148 ARC

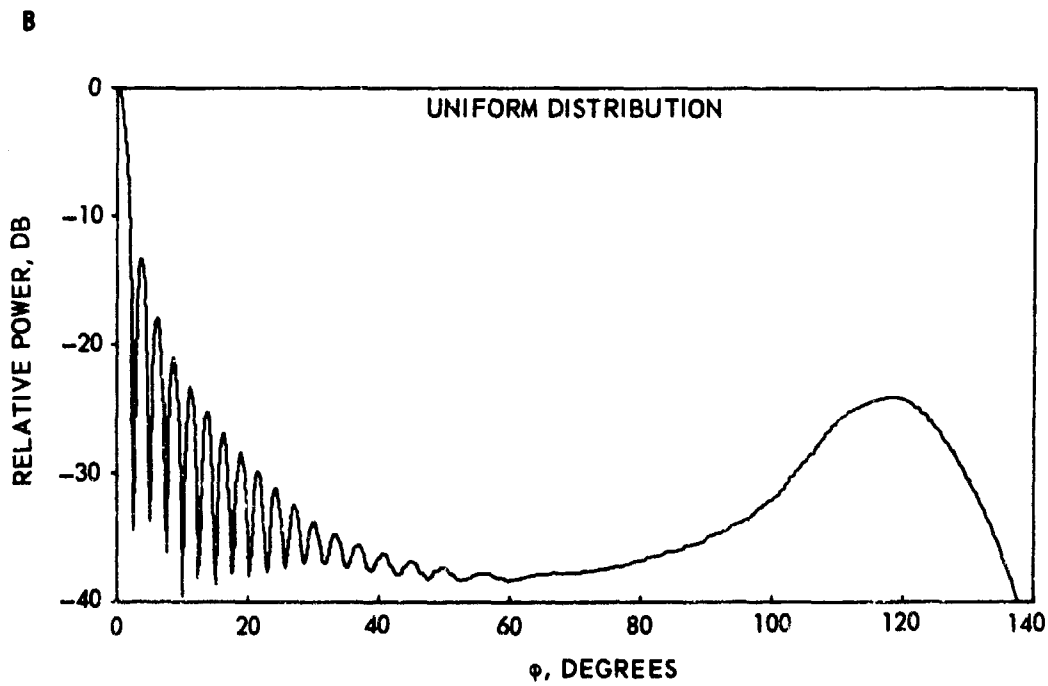

Figure 11.3. One-hundred-eighteen-degree arc array analogous to the linear array, with patterns for analogous distributions.

C

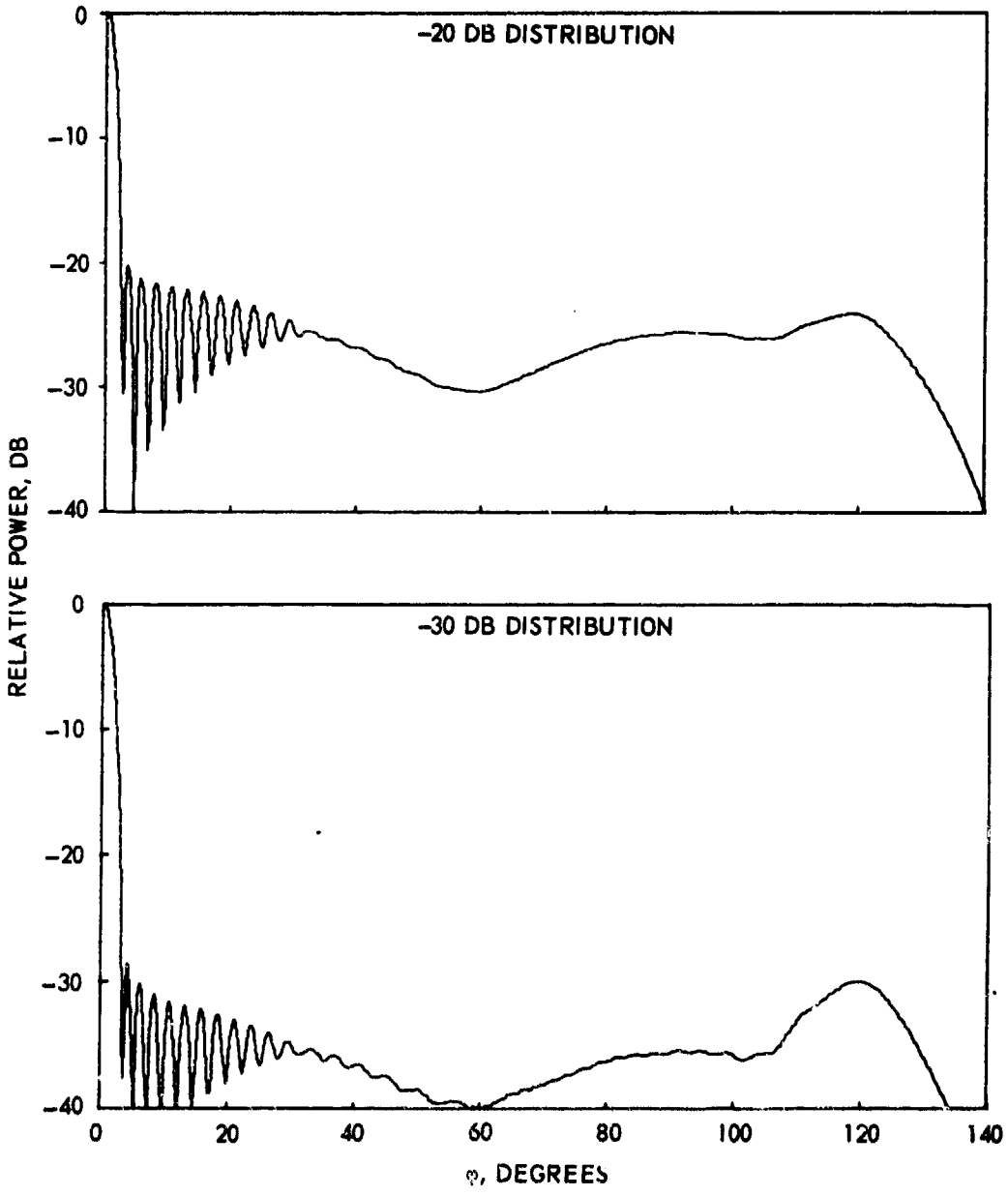

Figure 11.3 (continued)

Figure 11.1 shows 40-element linear-array patterns for uniform, and -26- and -30-dB-sidelobe Chebyshev patterns with the cosine element pattern. Figures 11.2 and 11.3 show arc arrays corresponding to the linear array of Figure 11.1, with patterns for the various distributions. Size and number of elements are shown.

The results in Figure 11 indicate that the circular array of size and number of elements equivalent to a four-sided linear array can be made approximately equivalent in broadside performance. Since the linear array beam broadens for scan off broadside, however, the overall performance of the ring array is superior.

In addition, there are some disadvantages of the planar array which the cylindrical array inherently avoids. The ring array beam is identical for all beam positions, while the planar array beam is broader in scanning off broadside. As the ring array beam is scanned by, in effect, commuting the distribution, it is always formed by a distribution which is symmetrical in phase and amplitude. This results in superior beam pointing accuracy independent of frequency change. Finally, the cylindrical array gives 360° coverage in azimuth with none of the hand-over problems associated with the use of several planar arrays. In some applications these advantages can be very important.

The cylindrical array, however, has some disadvantages. For scanning, the amplitude as well as the phase must be switched in azimuth, and a feeding systems results that may be more complex than that of a planar array system. (However, computer control is not a problem in view of the separable aperture.) The greatest disadvantage would appear to be that the cylindrical array cannot be physically separated as can the four planar arrays. This means that the cylinder must be in a position to look 360°, while each planar array need see only a 90° sector.

More important, it means that the cylinder cannot be tilted back to increase the elevation coverage, as is common practice with planar arrays. For this reason, a truncated cone might be considered to extend the elevation coverage and still retain the advantages of circular symmetry.

1.3 The Conical Array

In the design of electronically scanned conical arrays, problems arise that are different than those for arrays on planar surfaces. The gain of conical arrays changes as a function of the scan angle, and also depends on the part of the radiating structure that is visible from the far field at the beam pointing position. The polarization in the far field changes as a function of scan angle for radiating elements whose polarization is fixed with respect to the surface of the cone. Sum and difference patterns become sensitive to the incident polarization. The manner in which these quantities vary with scan angle will be discussed. The problem of pattern synthesis and analysis is also examined, and several techniques are discussed. In addition, the control circuitry and phase shifters required for these arrays are described. The general configuration for conical arrays consists of a set of radiating elements placed on a conical surface. The far-field patterns to be radiated from this array are pencil beams with suitably controlled sidelobes. Difference patterns are generated to improve tracking accuracy. The pencil beam is summed from a direction perpendicular to the generatrices through the axis of the cone. The radiating elements comprising the conical array are assumed to have symmetry in the plane perpendicular to the axis of the cone, the ϕ plane. The array placed on the conical surface is assumed to have symmetry in the ϕ plane. Whatever the shape of the active part of the array, the projected aperture of the active part will be a function of the position angle defining the beam pointing direction in the plane defined by the axis of the cone and a generatrix, (the θ plane). The active part is defined as that part that is turned ON to receive (or transmit) energy. The projected aperture will be constant for any ϕ scan at constant θ because of the symmetry mentioned above. Assume for the moment that the conical surface will be used in its entirety, that is, the active part of the array will

go from the tip to a cone diameter of, say, 10 inches. To establish the theoretical upper limit of performance, further assume that the area is used perfectly in the electromagnetic sense. The projected area of the active part of the area will be directly proportional to the achievable gain. For purposes of comparison, normalize this area to that of a planar aperture of a diameter of 10 inches. Thus the conformal array is compared with a mechanically scanned parabola or planar array located at the maximum diameter of the conformal array.

The graph in Figure 12 is shown for a cone angle of 20 degrees. Except for the first 12 degrees of a scan (from 0 to 12 degrees) the conformal array has a larger area gain. This fact may be used as follows.

(a) Assume that the same gain is wanted for all θ scans. The active part of the conformal array will then have a constant projected area. This could, for instance, reduce the prime power required for scan directions other than on-axis.

(b) The minimum gain of the conformal array can be decreased for the on-axis direction and increased for other directions as compared with that of the mechanically scanned antenna.

The beamwidth of a planar array changes as a function of the beam pointing in direct proportion to the projected aperture perpendicular to the beam pointing direction. This relation is an approximation but is quite accurate for angles between broadside and 50 to 60 degrees. In a conformal array the beamwidth is not so easily related to the geometry of the array because both the shape of the active part of the array and its projected area change as a function of the beam pointing direction. An estimate of the beam and sidelobe shapes will be given below.

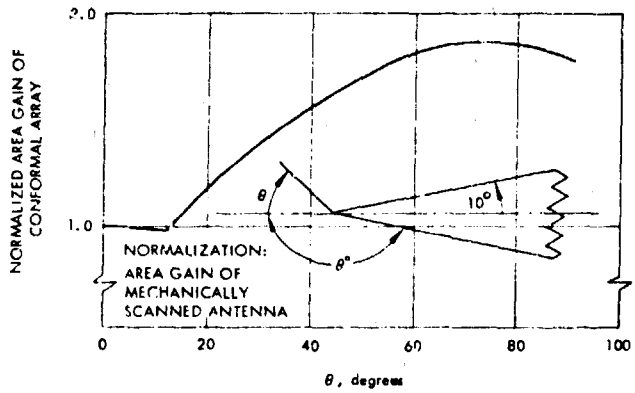

Figure 12. Normalized area gain of conformal array as a function of scan angle.

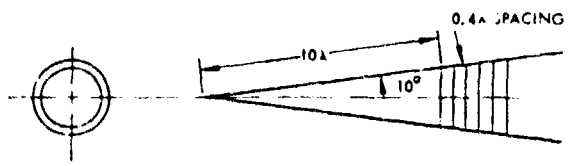

Figure 13. Layout of ring array with six rings.

For the beam pointed perpendicular to the generatrix of the cone, the radiation characteristics may be approximated using an equivalent planar array whose area is the projected area of the active part of the conformal array. Thus one would expect beamwidths commensurate with the projected aperture dimensions shown in Figure 12 and near-in sidelobes below 15 dB.

At the other extreme, a beam pointed along the axis of the cone, a different condition exists. For small angles near the cone axis, the array when projected forward would look approximately like a concentric ring array. The center rings of the array are missing, since the extreme tip of the cone is probably not usable in practice. For a 6 ring by 24 element/ring array as shown in Figure 13, the pattern would be somewhat as shown in Figure 14. For comparison, Figure 14 also shows the pattern of an array of the same size on the same cone but with the center rings filled. The latter is the usual pattern for a uniform circular array. It will be noted that the ring array has a narrower beamwidth and higher sidelobes than the filled array. This narrower beamwidth can be explained with reference to an interferometer which has a beamwidth one-half of that of a completely filled linear array of the same length. The "sidelobes" are as high as the main beam. This particular case is an intermediate one. Thus it can be seen that there is a trade-off between array filling, beamwidth, and sidelobe level.

1.3.1 Lattices on a Cone

In a conical (and also a cylindrical) array, advantage can be taken of the circular symmetry of the surface to reduce the steering problem essentially to that of scanning in one dimension only. Figure 15 shows an end-on view of the cone with the shaded portion representing the excited area of the surface. If the beam lies in the plane perpendicular to the cone axis, its position will be as shown in the figure - and symmetrical with

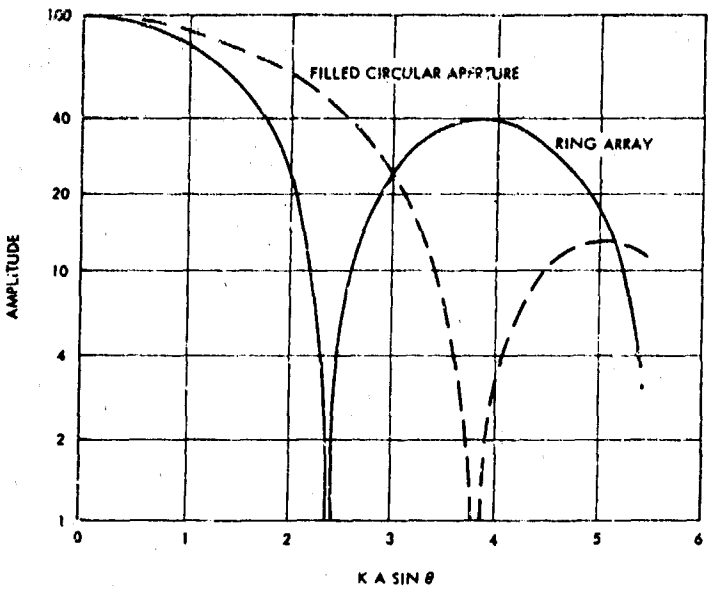

Figure 14. Patterns of circular apertures.

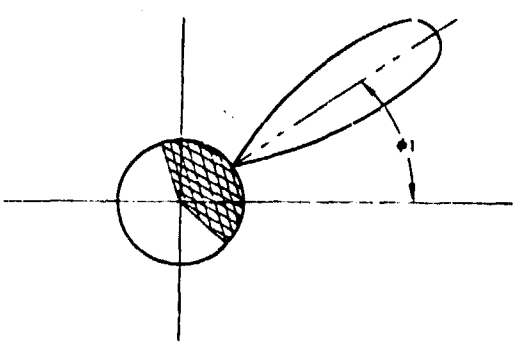

Figure 15. Excited portion of cone for beam pointing to ϕ_1.

respect to the active area of the array. If the beam is scanned toward endfire while ϕ_1 is held fixed, it can be seen that the projection of the beam onto the plane of the paper will still fall at ϕ_1. Hence the active area is still symmetrically located with respect to the beam. The beam can be thought of as being broadside to the cone in the ϕ plane and capable of being electronically scanned in the plane that passes through the cone axis (the θ plane).

If the beam is now steered around in the ϕ plane to ϕ_2, ideally the active portion of the array will follow it to maintain a symmetrical relationship with the new beam pointing direction as shown in Figure 16. Here also, the beam can be electronically steered toward endfire without changing the angle ϕ_2 or disturbing the symmetry conditions. Hence, it may be concluded that for any angle of ϕ, in the ideal case of a continuously illuminated aperture, the beam can be considered to be broadside to the cone in the ϕ plane and need be electronically scanned only in the θ plane.

With a discrete number of elements on the cone, the ideal situation outlined above can only be approximated. However, if a reasonably large number of elements is used, the approximation will be quite close. For example, if 16 elements are used in the larger rings around the cone, the largest portion of the area of excitation can be switched in 22-1/2-degree steps. Thus, it is necessary to electronically scan the beam only $\pm$11-1/4-degrees off the perpendicular to the excited area to achieve full coverage around the axis of the cone by a sequence of switching and phasing operations. Since any one active area of the cone scans only $\pm$11-1/4-degrees in the ϕ plane, the interelement spacing in that plane need be only slightly less than the spacing required for an array that does not scan at all in that plane. Hence, the interelement spacing problem is reduced approximately to that associated with scanning in the θ plane only. It may also be

attractive to provide amplitude and phase control at each element instead of switching.

The conical array can be thought of as a set of cylindrical arrays of different radii as a first-order approximation. Hence, it is to be expected that it, too, will have a tendency to have grating lobes in the ϕ plane. Therefore, it is anticipated that the interelement spacing in that plane will have to be kept smaller than would normally be necessary for an equivalent planar array. However, the fact that each circle of elements on the cone nearer the tip is smaller than the previous one may tend to alleviate this problem by introducing a modest amount of quasi-randomness into the element placement.

A more nearly continuous illumination in both principal axes of the cone can be achieved by staggering the elements in alternate circles as shown in Figure 17. Thus, although the actual spacing between any two elements on a circle with an 8-inch diameter is $1.2\lambda_0$ (assuming 16 elements per circle), the effective spacing is only one-half that value. An interelement spacing of $0.6\lambda_0$ is rather large for a circular array; however, each circle nearer the tip of the cone will bring the elements closer together until the point of physical interference is reached. The average interelement spacing in the ϕ plane for the section of the cone that has 16 elements per ring should thus be less than $0.5\lambda_0$.

In the smaller regions of the cone, fewer elements will be needed per circle. The type of element to be used will influence the decision on just how many should be used in each circle. The crossed waveguide elements (Kummer, 1972) can be fitted together quite closely on a flat surface provided that they are rotated at an angle of approximately 20 to 25 degrees, depending on wall thickness, to the principal axes of the lattice (see Figure 18). They can be brought most closely together on a curved surface if they still maintain that angle. When the elements in alternate

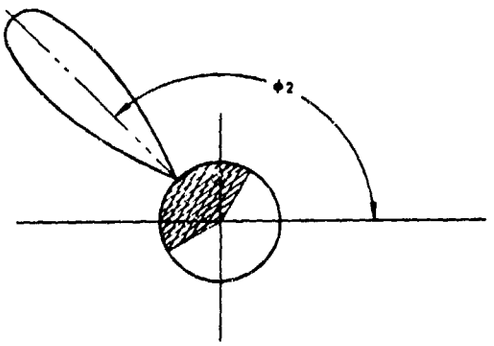

Figure 16. Excited portion of cone for beam pointing to ϕ_2.

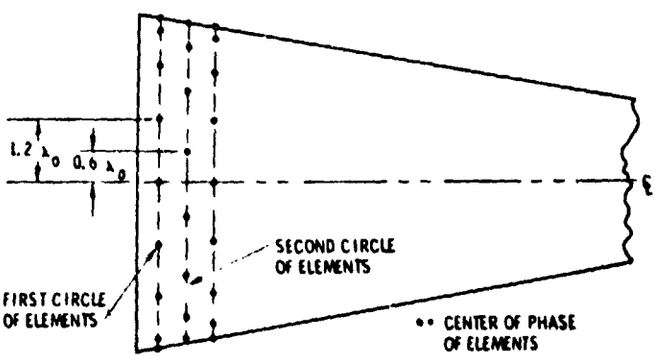

Figure 17. Effect of staggering elements in alternate circles on cone.

circles are staggered in a symmetrical fashion, the lattice is rotated 45 degrees as shown in Figure 19.

The unusual geometry of the cone requires special consideration of the coordinate system used to represent the patterns. It has been found that in some coordinate systems it is impossible to properly define the two principal planes of the beam when they are scanned to the nose-fire position. (Howard et al, 1969). Hence, a special coordinate system was devised that follows the peak of the beam as it is scanned. (Howard, 1969). The major requirement for the new coordinate system is that two fixed planes of the new system intersect the main beam of the antenna pattern at right angles. This requirement is satisfied by a variable spherical coordinate system, with angular coordinates ϕ' and θ'. The system is positioned so that $\phi' = 0$, $\theta' = 90$ degrees corresponds to the main beam pointing direction $\phi = \phi_1$, $\theta = \theta_1$. This variable coordinate system can be related to the fixed conventional coordinate system through the transformations presented in Villeneuve (1968). In this reference,

$$\cos \theta = \cos \theta' \sin \theta_1 + \sin \theta' \cos \phi' \cos \theta_1$$

$$\sin \theta = \sqrt{\sin^2 \theta' \sin^2 \phi' + (\sin \theta' \cos \phi' \sin \theta_1 + \cos \theta' \cos \theta_1)^2}$$

$$\sin \phi = \sin \theta' \sin \phi'/\sin \theta$$

$$\cos \phi = (\sin \theta' \cos \phi' \sin \theta_1 - \cos \theta' \cos \phi_1)/\sin \theta$$

The transformations have little effect on the pattern representations for broadside beam pointing directions (θ_1 near 90 degrees), but have considerable effect for endfire beam pointing directions (θ_1 near 0 degree).

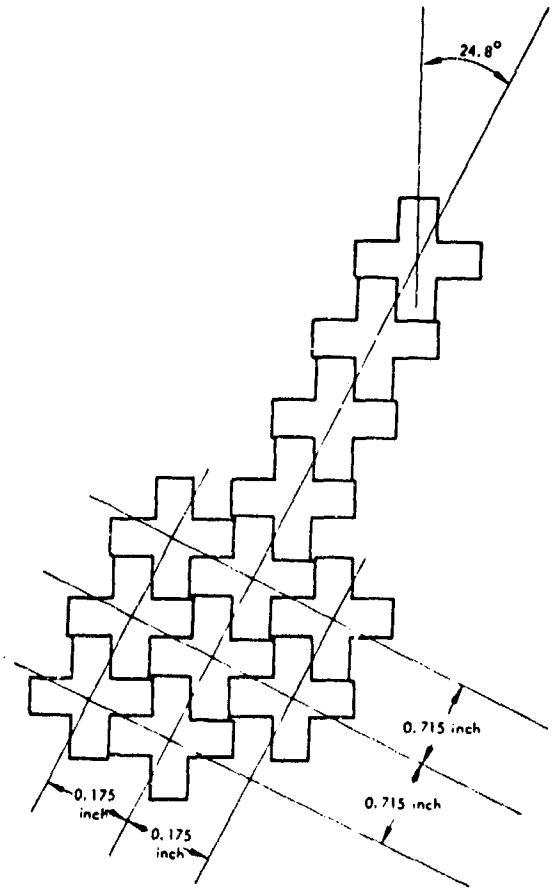

Figure 18. Tilted lattice for closest packing arrangement of crossed-waveguide elements.

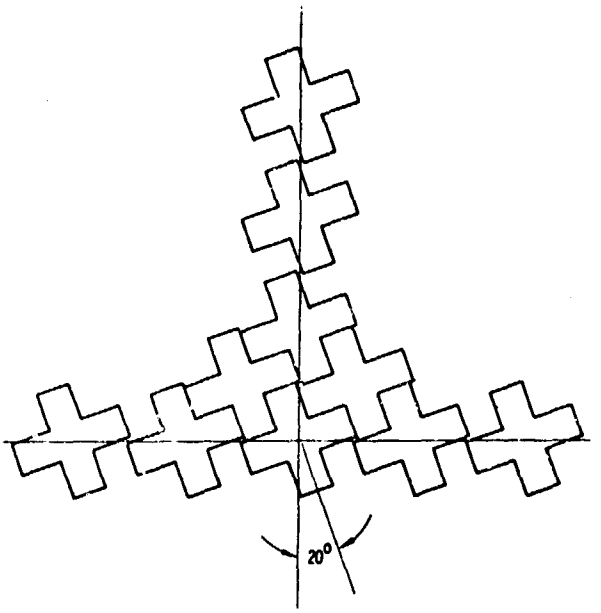

Figure 19. Crossed-waveguide elements tilted at angle of ~20 degrees in staggered arrangement to obtain closest packing.

Another transformation is necessary to preserve the polarization of the test point used to perform the pattern plots. The test point polarization must be fixed in the Cartesian frame of the physical antenna cone. Again using Villeneuve (1968), the new polarizations are related to the old polarizations through

$$\underline{1}_{\theta'} = \frac{1}{\sin\theta'}\left[\underline{1}_{\theta}\left(\cos\theta\cos\phi\cos\theta_1 + \sin\theta\sin\theta_1\right) - \underline{1}_{\phi}\sin\phi\cos\theta_1\right]$$

$$\underline{1}_{\phi'} = \frac{1}{\sin\theta'}\left[\underline{1}_{\theta}\sin\phi\cos\theta_1 + \underline{1}_{\phi}\left(\cos\theta\cos\phi\cos\theta_1 + \sin\theta\sin\theta_1\right)\right]$$

For convenience, the new coordinates were renormalized as $\phi = \phi'$ and $\theta = \theta' - 90$ degrees, so that the main beam peak is always centered at $\phi = 0$ degree, $\theta = 0$ degree.

Using these modifications to the coordinate system, a computer program was written and a series of patterns calculated for a crossed-slot configuration that partially filled a cone. The slot arrangement consisted of six rings of crossed slots with 24 slots per ring. The two arms of each crossed slot were fed in such amplitude and phase that linear polarization of the proper orientation resulted at the peak of the beam. The large end only of the cone was filled with elements, and the ring nearest the tip was 10 wavelengths from it. Total length of the cone was $12.2\lambda_0$ and the base had a diameter of $4.4\lambda_0$. The elements thus extended only about 20 percent of the way from the base of the cone to its tip, and the computer patterns only present a rough indication of those of a completely covered cone.

In the calculations each element was weighted by the gain that it has in the direction of the peak of the beam. It was determined that this weighting yields the highest signal-to-noise ratio when the array is operating in the receiving mode (Kummer

et al, 1969). Figure 20 presents a series of patterns computed for a beam steered 20 degrees off the nose-fire position (θ_1 = 20 degrees). These patterns represent only the desired component of polarization. There is a sizable cross-polarized component at some angles. The assymmetry of the conical geometry impedes a straightforward presentation of the antenna patterns, as evidenced by the complexity of the set of pattern plots presented in Figure 20. A complete description of the antenna requires three-dimensional models for clarity. In an attempt to remedy the inherent confusion, the sum and difference patterns are presented in isometric views in Figure 21. The computer program used for the previous pattern computations was then modified so that it would handle elements arranged in a staggered configuration similar to that shown in Figure 17. Sixteen elements per ring were assumed for the initial computation. With that number of elements in each ring, it was estimated that 10 rings would fit on the cone. Thus, a total of 160 elements "filled" the large end of the cone. The small end of the cone was then left "empty." The diameter of the base of the cone was 6.2 inches and its total length was 17.5 inches. The frequency was assumed to be 9.0 GHz and the spacing between rings to be $0.45\lambda_0$ to prevent grating lobes. The 10 rings of elements thus covered the lower 5.3 inches of the cone. In the nose-fire direction the projected radius of the empty area was over twice as large as the projected thickness of the annulus of the filled area.

The broadside patterns of an array of this type would be quite normal because the visible surface of the array at any one point is approximately rectangular. Further, the majority of the slots are "seen" from favorable angles in regard to polarization.

In the nose-fire direction, however, a marked difference in beamwidths for the two principal planes appears, as can be seen in Figure 22. Three reasons were determined to explain this difference:

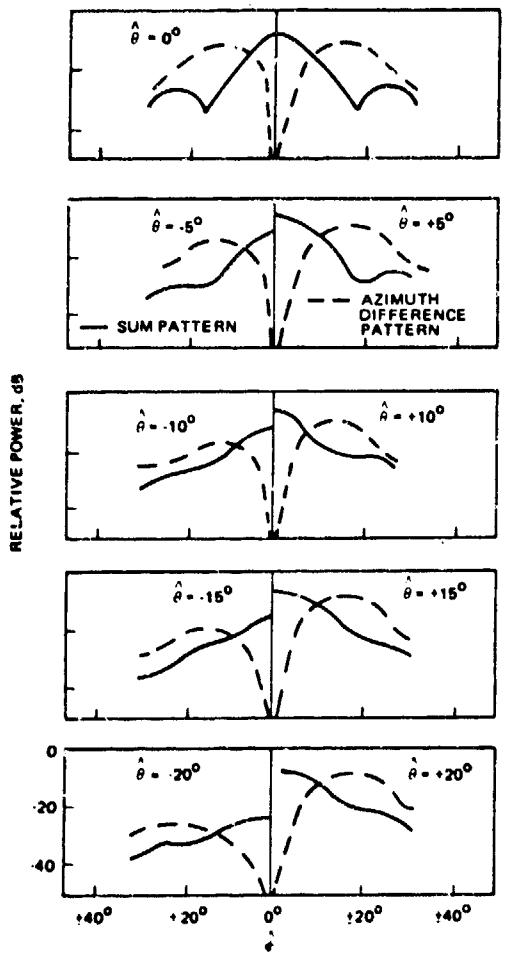

Figure 20. Two-dimensional antenna patterns for θ_1 = 20 degrees for $\hat{\phi}$-polarization optimized.

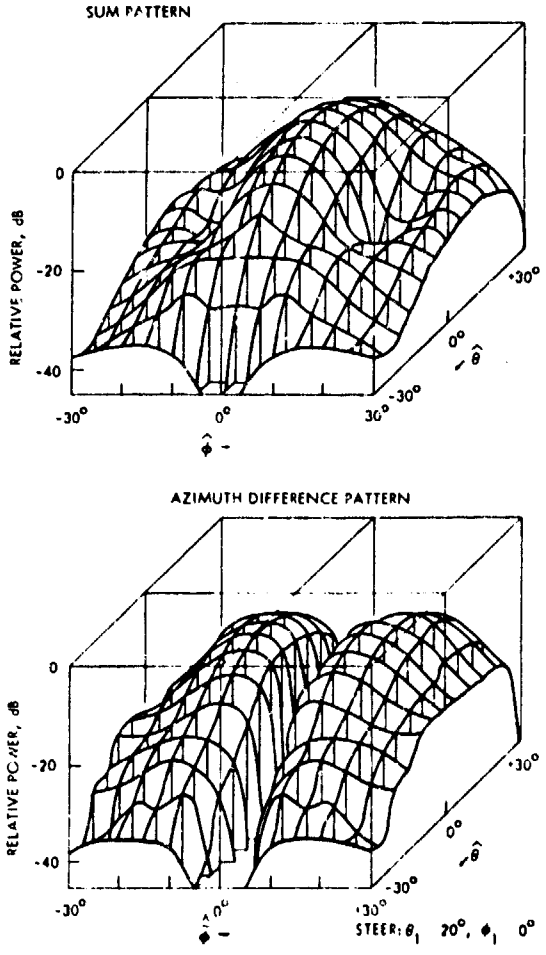

Figure 21. Three-dimensional antenna patterns for θ_1 = 20 degrees for $\hat{\phi}$-polarization optimized.

(a) The weighting applied to the elements tends to "turn off" the elements that are being viewed from an unfavorable angle. Slots in two areas of the annulus are excited at a much reduced level. This different excitation tends to create an interferometer effect in one principal plane while the effective width of the useful aperture in the other plane is reduced to considerably less than the full diameter of the base.

(b) The geometry of the cone is such that when the slots are oriented in a position to optimize the polarization of the signal in the nose-fire position, they are no longer optimum at any other angle. In the process of computing a pattern it is necessary to fix the polarizations of the slots so that there is no cross-polarized component at the peak of the beam. At other angles, more or less energy will go into this component depending on the steepness of the cone and the direction of the cut for the computed pattern. These two factors are related to the rapid change in polarization angle in the radiated pattern of a slot when viewed from a point close to either null in that pattern. This rapid change in polarization further aggravates the interferometer effect.

(c) The large empty area in the center of the "working" annulus is in essence aperture blockage which contributes also to the interferometer effect making it somewhat worse than in either of the other situations alone.

In a first step to alleviate the difference in beamwidths, the weighting applied to the elements was removed. Instead, each element was assumed driven with equal power although its element pattern was still taken into consideration when the far field patterns were computed. The differential in beamwidths between the ϕ and θ cuts was much reduced by this action (see Figure 23).

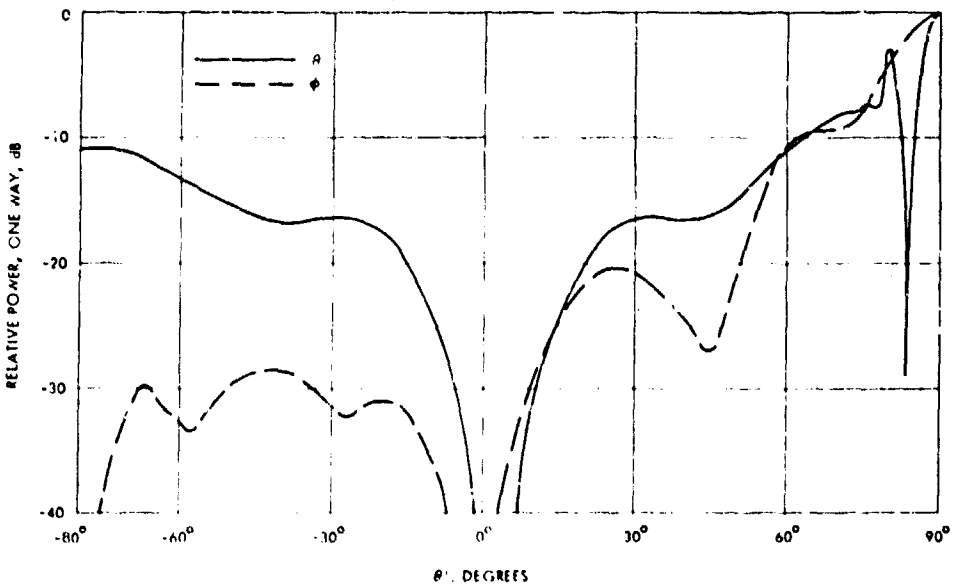

Figure 22. Computed patterns for staggered element arrangement similar to arrangement of Figure 18.

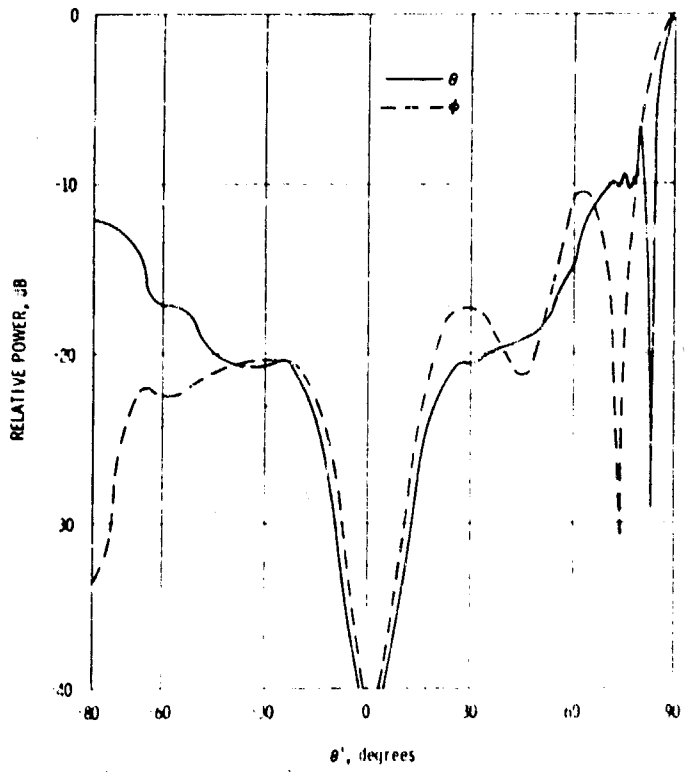

Figure 23. Patterns of same slot arrangement used for Figure 22 but with amplitude weighting suppressed.

The second step was to modify the computer program so that the remaining portion of the cone was filled with elements as much as was thought practical in such a sharp cone. The cone was made larger also to correspond to a physical cone with which experimental work currently was being done. The final arrangement of elements was:

Location on Cone	Number of Rings	Elements per Ring	Number of Elements
Base of cone	9	16	144
Center portion	12	8	96
Upper portion	8	4	32
Near tip (Loaded elements)	4	4	16
	Total		288 elements

The center portion of the cone was assumed to contain the same crossed-waveguide elements as those near the base of the cone. The upper portion contained a crossed-waveguide element similar to the others but of a shorter length. The difference in length made matching more difficult and tolerances had to be tighter, but the short length was necessary to permit the location of as many rings as possible in the narrow region of the cone. Near the tip, the upper four rings had to use loaded elements to make packaging feasible. Even with loaded elements, the first ring was 3 inches from the tip of the cone. The projected distance between two diametrically opposite elements in this first ring was 1.04 inch or $0.79\lambda_0$, so that a small "hole" still remained in the center of the aperture.

Computed patterns for this element arrangement with no weighting show that the ϕ and θ beamwidths are somewhat closer in value than in step (b), but that the largest improvement was obtained by eliminating the element weighting. Figure 24 shows the patterns for this final and best set of results for the nose-fire case. The difference between ϕ and θ is approximately 1.5 to 1, which should not be too large to be tolerated for most applications.

It is not possible with crossed slots or crossed-waveguide elements to eliminate the rapid change in polarization that appears

under certain conditions. The only solution visualized so far is the replacement of the crossed slots by crossed dipoles in certain areas of the cone. This solution is not a very attractive one because it introduces particular problems of its own.

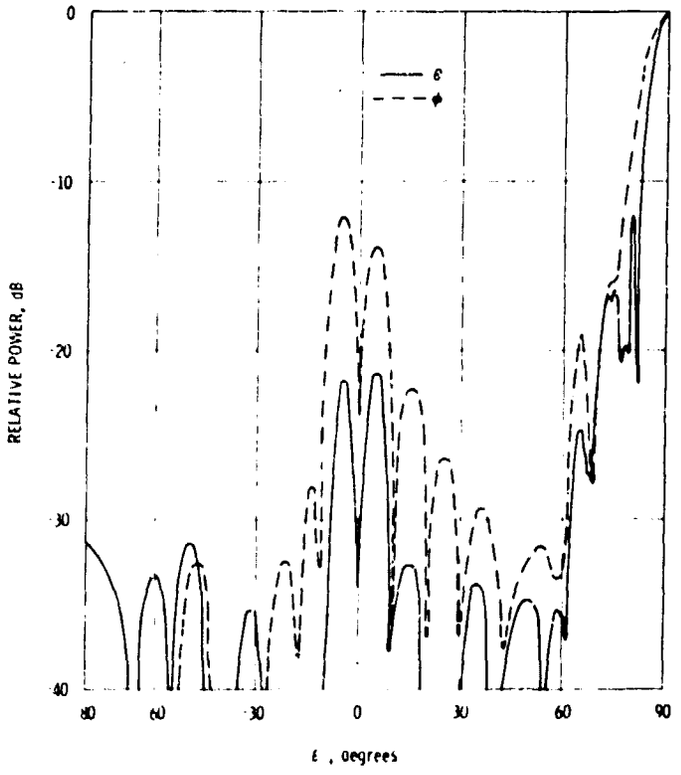

Figure 24. Patterns of cone fully covered with slots in staggered arrangement and amplitude weighting suppressed.

1.3.2 Conical Depolarization

A cone is less hospitable to an array in that its surface cannot be covered with a regular lattice. The question of orienting the radiators on the cone so that optimum performance in all directions is obtained involves the geometry of the radiator. The case of a beam pointing directly ahead is considered first. Since the array is conformal, some sort of flush-mounted radiator will be required. The slot and the open-ended waveguide are the two most commonly used flush-mounted radiators. The polarization of these radiators are nearly identical; hence the polarization of the slot radiator is considered.

The E-field in one quadrant of the far field of a slot is shown in Figure 25. In this figure the ground plane is assumed to be in the x-y plane. It can be seen that the polarization of the field is everywhere perpendicular to the ground plane in the immediate vicinity of that plane. If the slots are imagined to be placed on a ten-degree half-angle cone, then in the forward direction each slot will be viewed from an angle of ten degrees above its nominal ground plane. The polarization at that angle can be visualized by constructing a surface on Figure 25 that is ten degrees above the x-y plane. This surface is shown in the Figure by dashed lines.

It is instructive to start near the x-axis and note the change in polarization angle as the ten-degree surface is followed around to the y-axis. (The scale of angles in the x-y plane is used for convenience.) At 0 degree the polarization (shown by the dark arrows) is found to be parallel to the ground plane and, hence, is termed horizontal. As the progression continues around the quadrant toward the y-axis, the polarization vector at first turns quite rapidly downward, then turns increasingly more slowly in the same direction, until at the y-axis, it is vertical. At 45 degrees, the polarization is still very nearly

vertical instead of nearly 45 degrees as might be expected. The result of this unequal rate of rotation of the polarization vector is that, when the slots are placed on a cone, they must rotate at an uneven rate with their position around the cone in order for them to all have the same polarization directly ahead. It can be shown that, in the quadrants, the slots must be oriented so that their projections on the endfire view are also parallel with the projections of the principal axis slots. This requirement is due to the fact that the far-field polarization of the E-field of a slot is always perpendicular to the projection of the long dimension of the slot onto a plane perpendicular to the line-of-sight.

To obtain a picture of how the slots oriented to favor endfire operation would look from other angles in space, a paper cone was made with a number of slots drawn on it (Figure 26). When the cone is viewed from end-fire, the projections of all these slots are parallel as desired (see Figure 26a). When the slots are viewed from a broadside position nearest the axial slots, they are predominately lined up in an approximately axial fashion (Figure 26b); hence, cross-polarization would not be too much of a problem. However, when the slots are viewed from the broadside region nearest the transverse slots, they are not properly lined up at all (Figure 26c). With this slot arrangement, large amounts of the available power would go into cross-polarized lobes, and the effective aperture would be much smaller than the projected area of the cone in this direction.

There are a number of ways in which radiators providing variable polarization might be mounted on a cone, but complete symmetry cannot be maintained with a minimum number of elements or with simple control functions for beam formation and steering. To illustrate some of the configurations that might be used, several crossed-slot configurations were sketched on additional

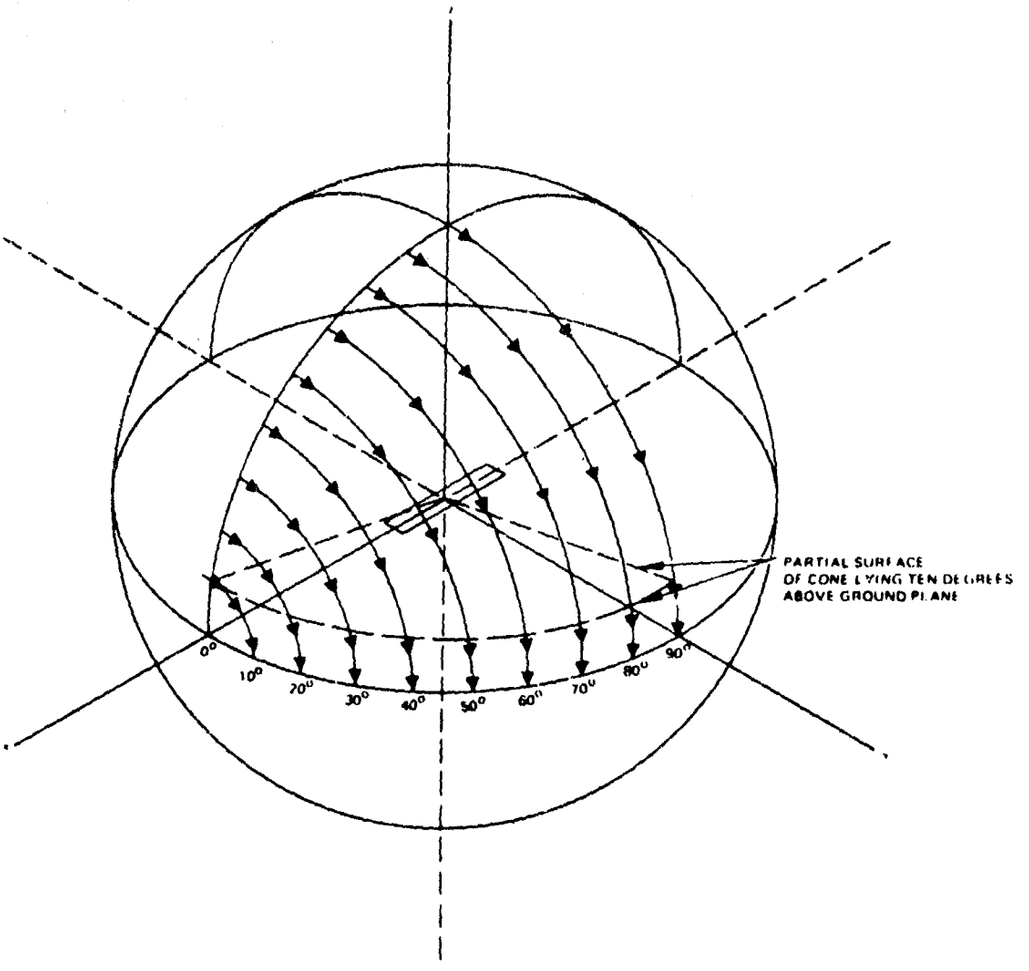

Figure 25. Polarization of field radiated by slot at locus of points ten degrees above ground plane.

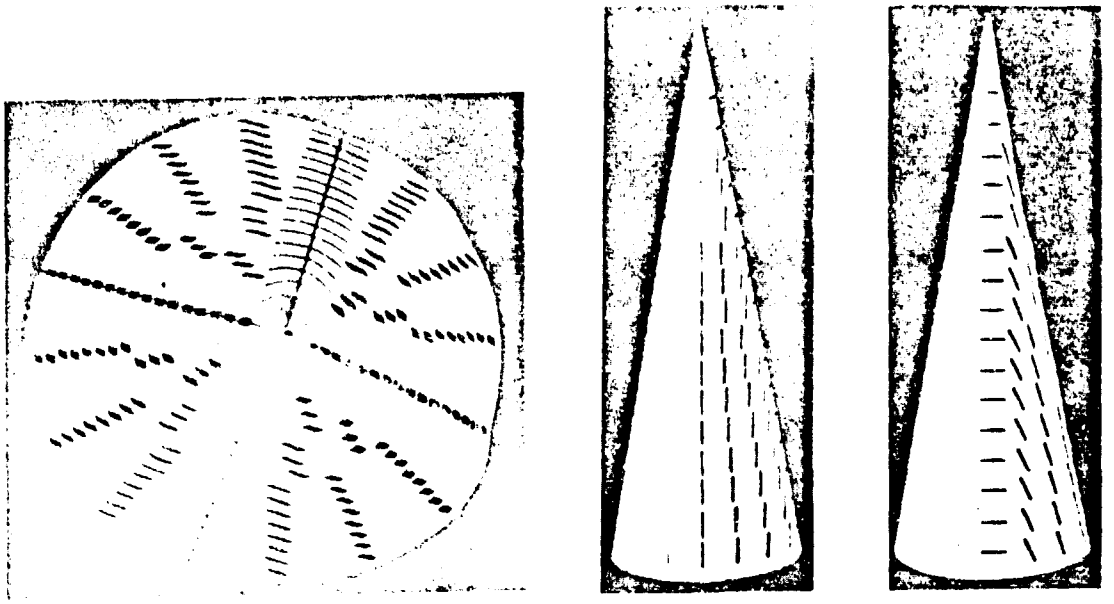

a. End-on View

b. Side View with Axial predominating

c. View of side opposite transverse slots

Figure 26. Cone on which slots have been placed to favor end-fire radiation.

cone models. Three views of each configuration are illustrated, a nose-view and views from two opposite sides (Figures 27, 29, and 29). In Figure 27 the elements are placed on the vertices of a square grid laid out on the developed cone. The slots are oriented circumferentially and along the cone generatrices. With this arrangement, only the radial and circumferential excitations required at any position must be determined.

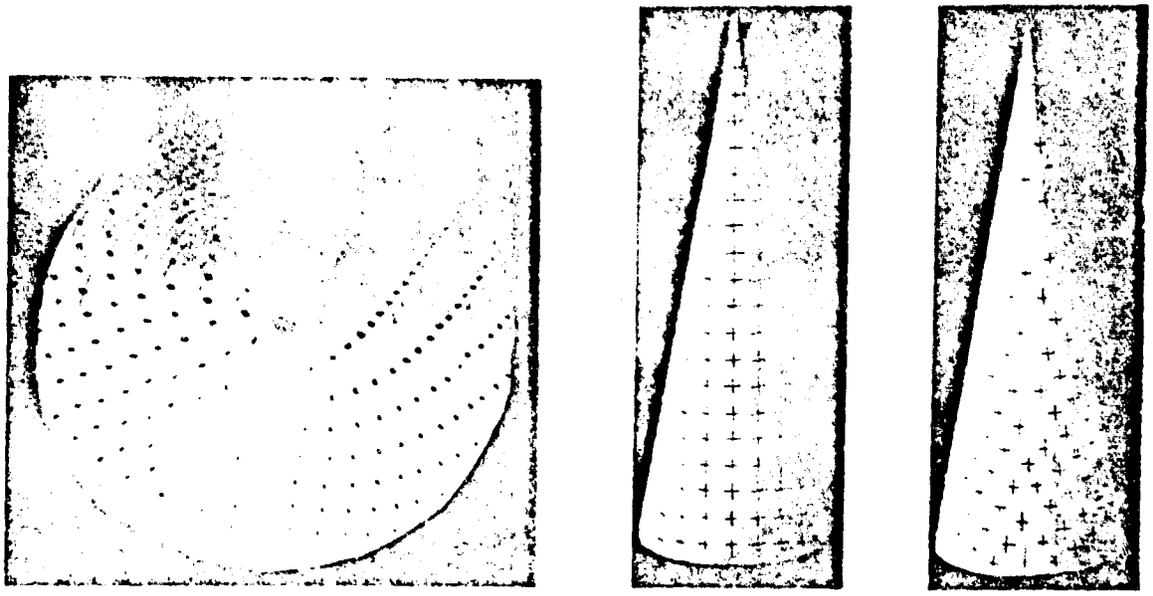

a. Nose View

b. Side view

c. Opposite side view

Figure 27. Cone with elements on square grid and slots oriented radially and circumferentially.

A third arrangement that further simplifies the control problem has the slots located on rings at fixed interelement spacings about each ring and oriented along generatrices and circumferentially (Figure 28). In this arrangement, only the radial and circumferential components of the excitation must be computed as in the second arrangement, but in addition, the computation of the phase function is also simplified.

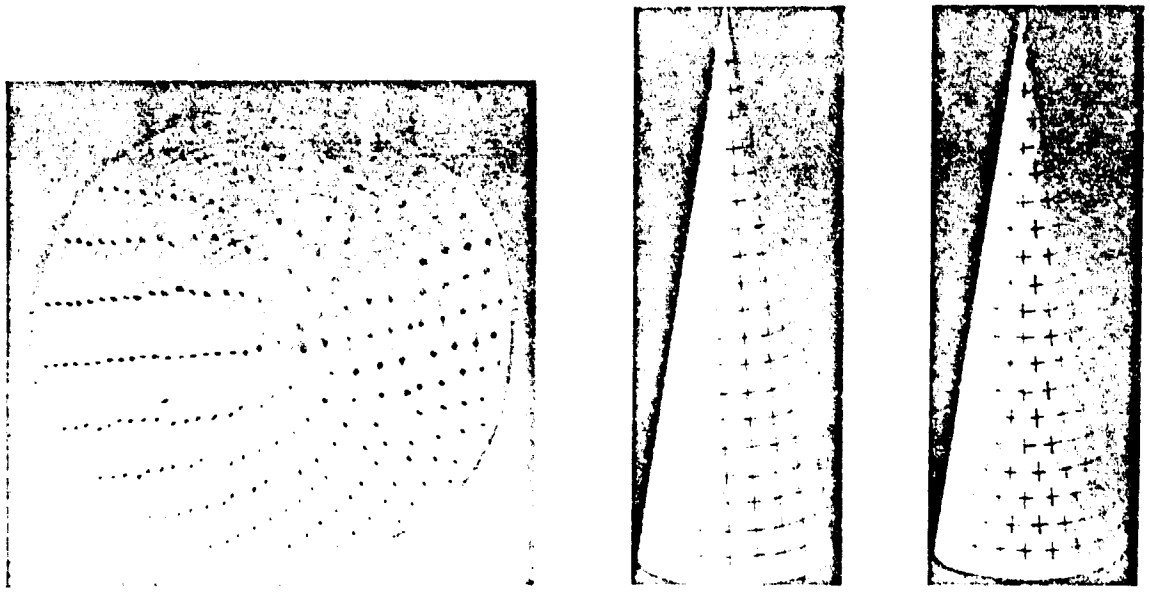

a. Nose view

b. Side view

c. Opposite side view

Figure 28. Cone with elements on rings.

Figure 29 shows a fourth arrangement in which elements are located on rings and, in addition, groups of rings are placed along the cone generatrices. Each ring of a group contains the same number of elements. When the spacing of elements in a ring exceeds a prescribed maximum value, an extra element is added to that ring. This new number of elements is used in succeeding rings until the element spacing again exceeds the prescribed maximum value. At that point, again another element is added. This arrangement results in a simpler control problem than in the other configurations because the phase control function for elements in any one group is simplified from that of the elements in the other configurations.

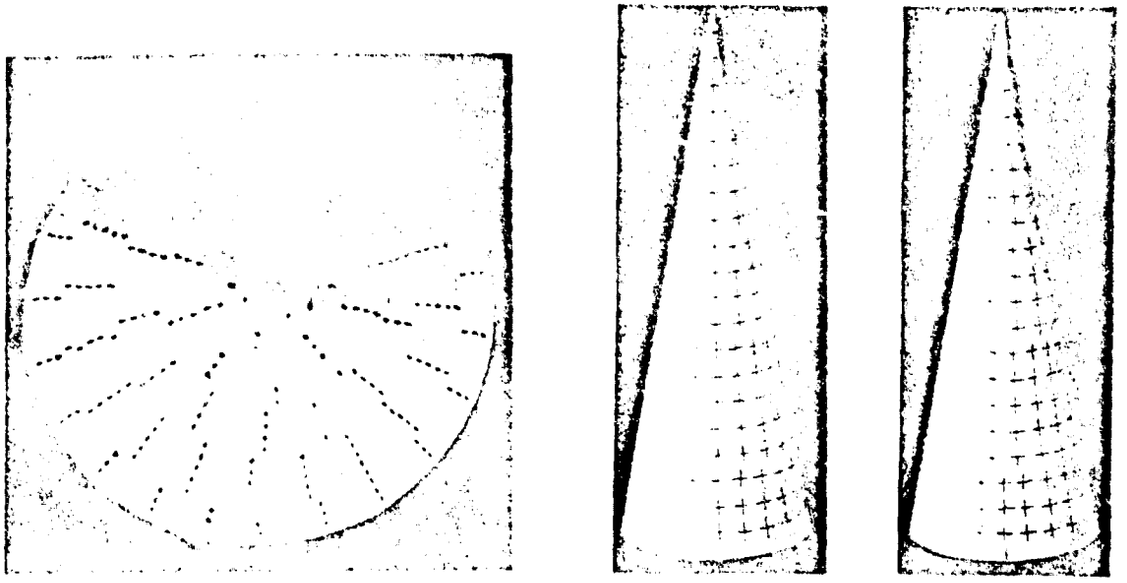

a. Nose view

b. Side view

c. Opposite side view

Figure 29. Cone with elements on rings and generatrices.

Other factors also influence the placement and orientation of elements on the cone. Physical feeding arrangements, ease of fabrication, and physical size, as well as requirements dictated by pattern specifications, must be considered before a final arrangement can be selected.

1.3.3 Quantization Effects on Conical Array Performance

The conical array computer program that has been used previously to compute patterns from several slot configurations on cones has been modified to simulate the use of digital phase-shifters and digital polarization-rotators.* In its original form of the program, the polarization of each element was rotated in such a way that no cross-polarized energy was radiated by any element in the direction of the peak of the beam. This condition, of course, can in general be met at only one point in the far-field pattern, and cross-polarized energy will exist elsewhere. Even satisfying the condition at the peak of the beam in a practical antenna using crossed slot (or equivalent) elements requires the use of a continuously adjustable variable power divider between the two orthogonal parts of each element.

The phase shifters, as well as the polarization rotators, will be digital devices in conical array systems. Modifications made in the program allow quantization at any number of bits desired in either the phase shift or the polarization rotation. With these modifications a series of patterns has been computed. In most of the patterns computed to date 4-bit devices have been assumed for each function; however, some of the results indicate that 3-bits may be adequate for the phase shifter. In a composite digital phase-shifter/polarization-rotator (Teeter & Bushore, 1951, Vaillancourt, 1958) two 3-bit digital phase shifters in a parallel arrangement produce both the effects of a 4-bit digital polarization-rotator and a 3-bit digital phase-shifter. The exact performance characteristics of this device have not yet been simulated in the computer program.

*See Appendix of Bargeliotes et al (1973) for a listing of the program and an explanation of many of its parameters. See Bargeliotes et al (1977) for a compilation of patterns.

The element configuration used for computing this series of patterns had a total of 432 crossed slots. Their phase centers were arranged in a staggered fashion similar to that shown in Figure 30 with the exception that 48 generatrices were used instead of 32 to bring the elements closer together in the circumferential plane. The generatrices in the 432 element configuration are spaced 7.5° apart in ϕ starting at 3.75°.

It is apparent from Figure 30 that if the beam is pointed in a direction in ϕ that is coincident with one of the generatrices that the elements will tend to be symmetrically disposed in relation to the beam pointing direction. Symmetry also tends to hold if the beam is pointed half-way between two generatrices, although not to such a high degree. Calculations to observe the effects of polarization-rotation quantization showed that these symmetries tended to mask the expected degradations in pattern characteristics. In an effort to avoid the symmetries, and to calculate the worse case, beam pointing directions in ϕ were chosen that differed from the angles of the generatrices by 1/4 of the angular separation between generatrices. Four such angles were determined and used for computing a series of patterns. The angles were ϕ = 5.625°, 9.375°, 13.125°, and 16.875°, and encompass a variety of asymmetries that should include the worst case.

A scan angle of θ_0 = 31.0° was chosen as being a typically difficult beam pointing direction for the conical array. θ° was held at this value for each of the four scan angles in ϕ mentioned above. For each beam point direction in ϕ a series of 8 patterns was computed. Four of these were ϕ cuts (ϕ = constant) for a θ polarized array and produce difference patterns in the longitudinal plane. Four of them were τ = 90° for a ϕ polarized array and produce difference patterns in the circumferential plane.

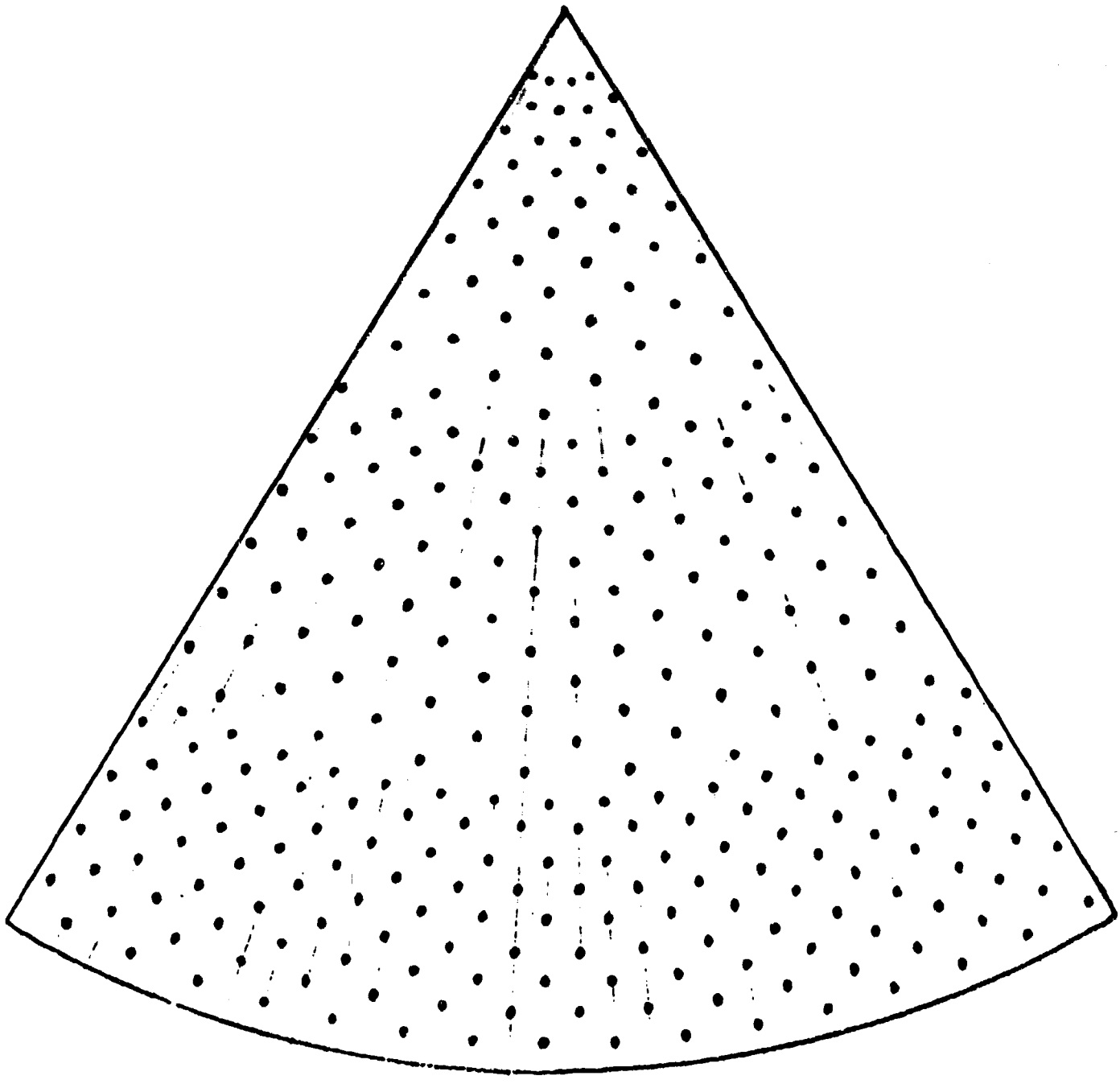

Figure 30. Scale Drawing of centers of phase of the elements on the cone in an "unrolled" view for 288 element configuration.

Of the four patterns for each cut, one was a reference pattern with neither polarization-rotation nor phase quantized, one had 4-bit polarization-rotation quantization only, one had 4-bit phase quantization only, and the last one had both 4-bit polarization-rotation and 4-bit phase quantization.

The results of these patterns are summarized in Tables 2 through 5. In the tables four quantities are recorded for each pattern, (1) the sum pattern nominal gain (the values given are relative gains only and are not intended to give an accurate estimate of array gain), (2) sum pattern 1st sidelobe level (or shoulder, in some cases), (3) sum pattern cross-polarized component (this is the highest value attained anywhere throughout the pattern and is given in dB below the peak of the sum pattern), (4) the difference pattern null depth (also in relation to the peak of the sum pattern).

A survey of the results shows that quantization effects are not severe; not even in regard to degrading the null-depth of the difference patterns as might be expected. The null depths are consistently lower for the ϕ cuts than for the τ cuts for reasons that are not clear. Computer round-off error as well as the different principal polarizations of the two cuts may be factors. The computer program needs to be further modified so that it will compute difference patterns in both principal planes for either θ polarized or ϕ polarized arrays.

The tables show that phase quantization at 4-bits has very little effect on the patterns. It shows up mostly on the 1st sidelobe level, and in the cross-polarized component. It appears that 3-bit phase shifters may be adequate for this array with its relatively large number of elements, and the possibility should be investigated.

TABLE 2

Effect of Quantization of Polarization Rotation and Phase Shift on Conical Array Performance:

Cone Half-Angle = 10.0°

Total No. of Slots = 432

Beam Point Direction: Theta = 31.0° Phi = 5.625°

PATTERN CUT	PRINCIPAL POLARIZATION	PARAMETER	NO QUANTIZATION	POLARIZATION ROTATION QUANTIZED: 4-BITS	PHASE QUANTIZED: 4-BITS	BOTH POLARIZATION ROT. AND PHASE QUANTIZED: 4-BIT
$\phi=5.625^{\circ}$	θ	Sum Pattern Nominal Gain	15.98dB	15.95dB	15.98dB	15.95dB
		Sum Pattern 1st. Sidelobe	-11.06dB	-11.06dB	-10.91dB	-10.90dB
		Sum Pattern Cross-Pol. Comp.	-43.84dB	-30.20dB	-38.49dB	-28.77dB
		Difference Pattern Null Depth	-57.59dB	-59.73dB	-57.59dB	-59.73dB
$\tau=90^{\circ}$	ϕ	Sum Pattern Nominal Gain	16.65dB	16.50dB	16.67dB	16.59dB
		Sum Pattern 1st. Sidelobe	-9.41dB	-9.31dB	-8.76dB	-8.76dB
		Sum Pattern Cross-Pol. Comp.	-14.46dB	-13.87dB	-13.85dB	-13.56dB
		Difference Pattern Null Depth	-33.61dB	-37.91dB	-31.70dB	-26.63dB

TABLE 3

Effect of Quantization of Polarization Rotation and Phase Shift on Conical Array Performance:

Cone Half-Angle = 10.0°

Total No. of Slots = 432

Beam Point Direction: Theta = 31.0° Phi = 9.375°

PATTERN CUT	PRINCIPAL POLARIZATION	PARAMETER	NO QUANTIZATION	POLARIZATION ROTATION QUANTIZED: 4-BITS	PHASE QUANTIZED: 4-BITS	BOTH POLARIZATION ROT. AND PHASE QUANTIZED: 4-BIT
$\phi=9.375^{\circ}$	θ	Sum Pattern Nominal Gain	15.98dB	15.95dB	15.98dB	15.95dB
		Sum Pattern 1st. Sidelobe	-11.06dB	-11.05dB	-11.29dB	-11.24dB
		Sum Pattern Cross-Pol. Comp.	-35.41dB	-30.07dB	-34.47dB	-28.63
		Difference Pattern Null Depth	-73.86dB	-50.41dB	-73.86dB	-50.41dB
$\tau=90^{\circ}$	ϕ	Sum Pattern Nominal Gain	16.47dB	16.35dB	16.47dB	16.35
		Sum Pattern 1st. Sidelobe	-9.63dB	-9.69dB	-9.04dB	-9.13dB
		Sum Pattern Cross-Pol. Comp.	-16.74dB	-16.98dB	-16.46dB	-16.78dB
		Difference Pattern Null Depth	-35.06dB	-31.49dB	-35.06dB	-31.49dB

TABLE 4

Effect of Quantization of Polarization Rotation and Phase Shift on Conical Array Performance:

Cone Half-Angle = 10.0°

Total No. of Slots = 432

Beam Point Direction: Theta = 31.0° Phi = 13.125°

PATTERN CUT	PRINCIPAL POLARIZATION	PARAMETER	NO QUANTIZATION	POLARIZATION ROTATION QUANTIZED: 4-BITS	PHASE QUANTIZED: 4-BITS	BOTH POLARIZATION ROT. AND PHASE QUANTIZED: 4-BIT
$\phi=13.125^{\circ}$	θ	Sum Pattern Nominal Gain	15.98dB	15.90dB	15.98dB	15.90dB
		Sum Pattern 1st. Sidelobe	-11.05dB	-11.04dB	-11.33dB	-11.35dB
		Sum Pattern Cross-Pol. Comp.	-36.05dB	-26.87dB	-33.59dB	-26.87dB
		Difference Pattern Null Depth	-62.52dB	-53.20dB	-62.52dB	-53.20
$\tau=90^{\circ}$	ϕ	Sum Pattern Nominal Gain	16.37dB	16.29dB	16.37dB	16.29db
		Sum Pattern 1st. Sidelobe	-9.96dB	-9.98dB	-9.37dB	-9.41dB
		Sum Pattern Cross-Pol. Comp.	-16.77dB	-16.03dB	-16.34dB	-15.63dB
		Difference Pattern Null Depth	-49.26dB	-45.59dB	-49.26dB	-45.59dB

TABLE 5

Effect of Quantization of Polarization Rotation and Phase Shift on Conical Array Performance:

Cone Half-Angle = 10.0°

Total No. of Slots = 432

Beam Point Direction: Theta = 31.0° Phi = 16.875°

PATTERN CUT	PRINCIPAL POLARIZATION	PARAMETER	NO QUANTIZATION	POLARIZATION ROTATION QUANTIZED: 4-BITS	PHASE QUANTIZED: 4-BITS	BOTH POLARIZATION ROT. AND PHASE QUANTIZED: 4-BIT
ϕ=16.875	θ	Sum Pattern Nominal Gain	15.98dB	15.91dB	15.98dB	15.91dB
		Sum Pattern 1st. Sidelobe	-11.05dB	-11.05dB	-11.11dB	-11.12dB
		Sum Pattern Cross-Pol. Comp.	-35.84dB	-32.56dB	-32.26dB	-29.37dB
		Difference Pattern Null Depth	-68.66dB	-54.52dB	-68.66dB	-54.52dB
τ=90°	ϕ	Sum Pattern Nominal Gain	16.39dB	16.19dB	16.39dB	16.19dB
		Sum Pattern 1st. Sidelobe	-10.00dB	-9.92dB	-9.35dB	-9.54dB
		Sum Pattern Cross-Pol. Comp.	-15.64dB	-15.07dB	-15.26dB	-14.72dB
		Difference Pattern Null Depth	-33.92dB	-32.67dB	-33.92dB	-32.67dB

A complete set of patterns for the $\phi = 9.375^{o}$ beam pointing direction is given as being representative of the 4 sets. They are presented in Figures 31 through 46. A study of these patterns indicates that degradation due to quantization of the polarization-rotation and phase shift is not severe.

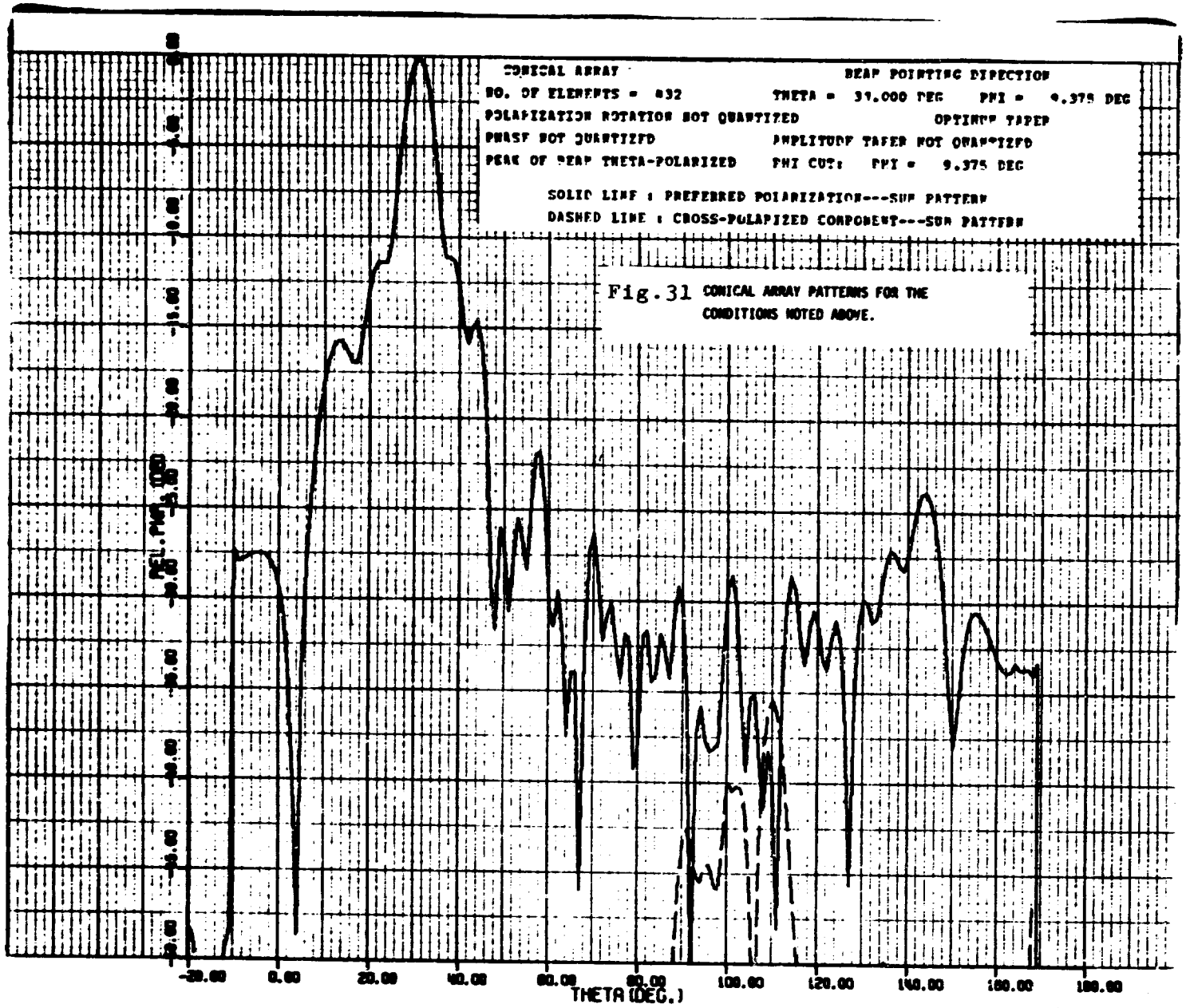

Fig.31 CONICAL ARRAY PATTERNS FOR THE CONDITIONS NOTED ABOVE.

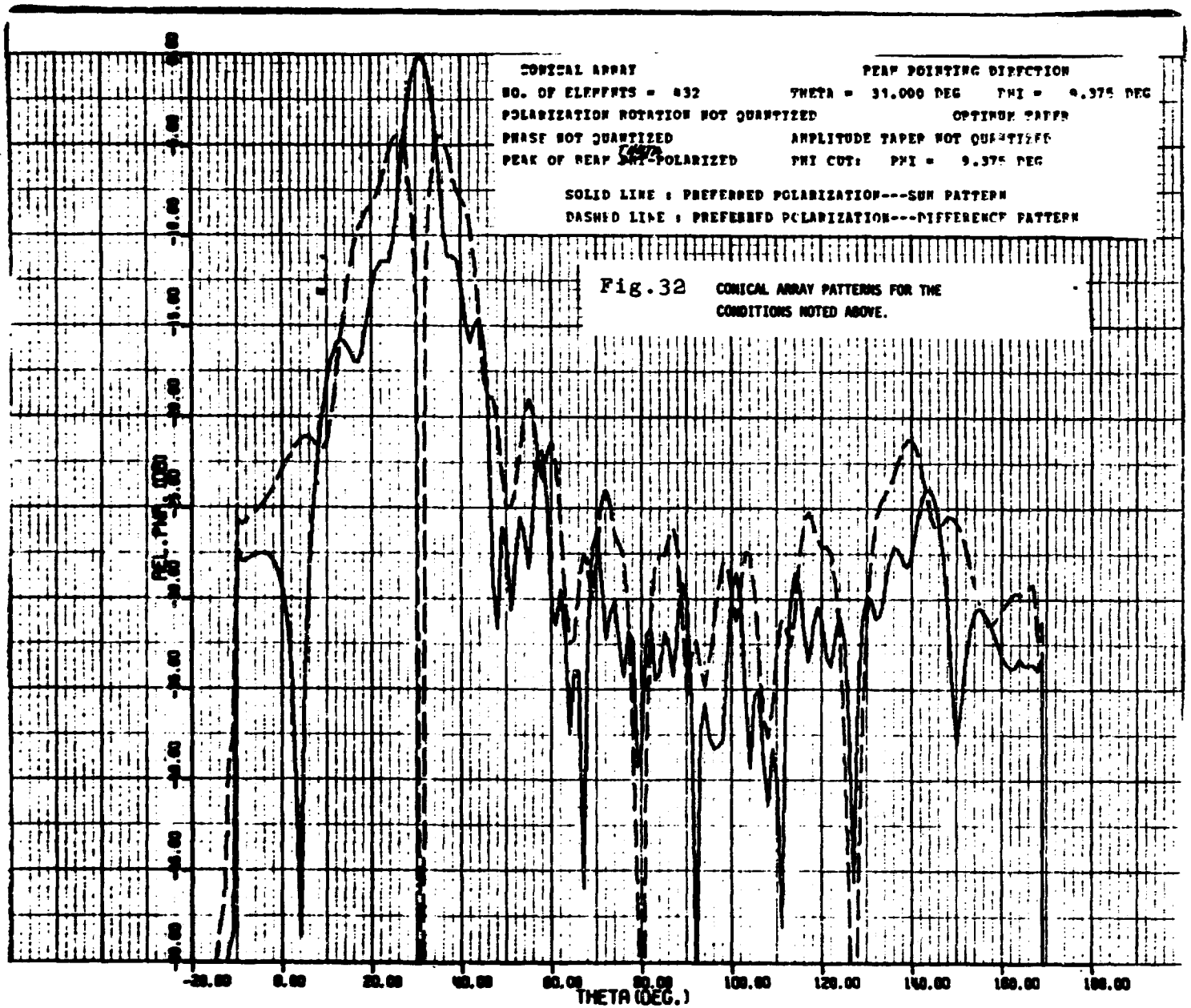

Fig.32 CONICAL ARRAY PATTERNS FOR THE CONDITIONS NOTED ABOVE.

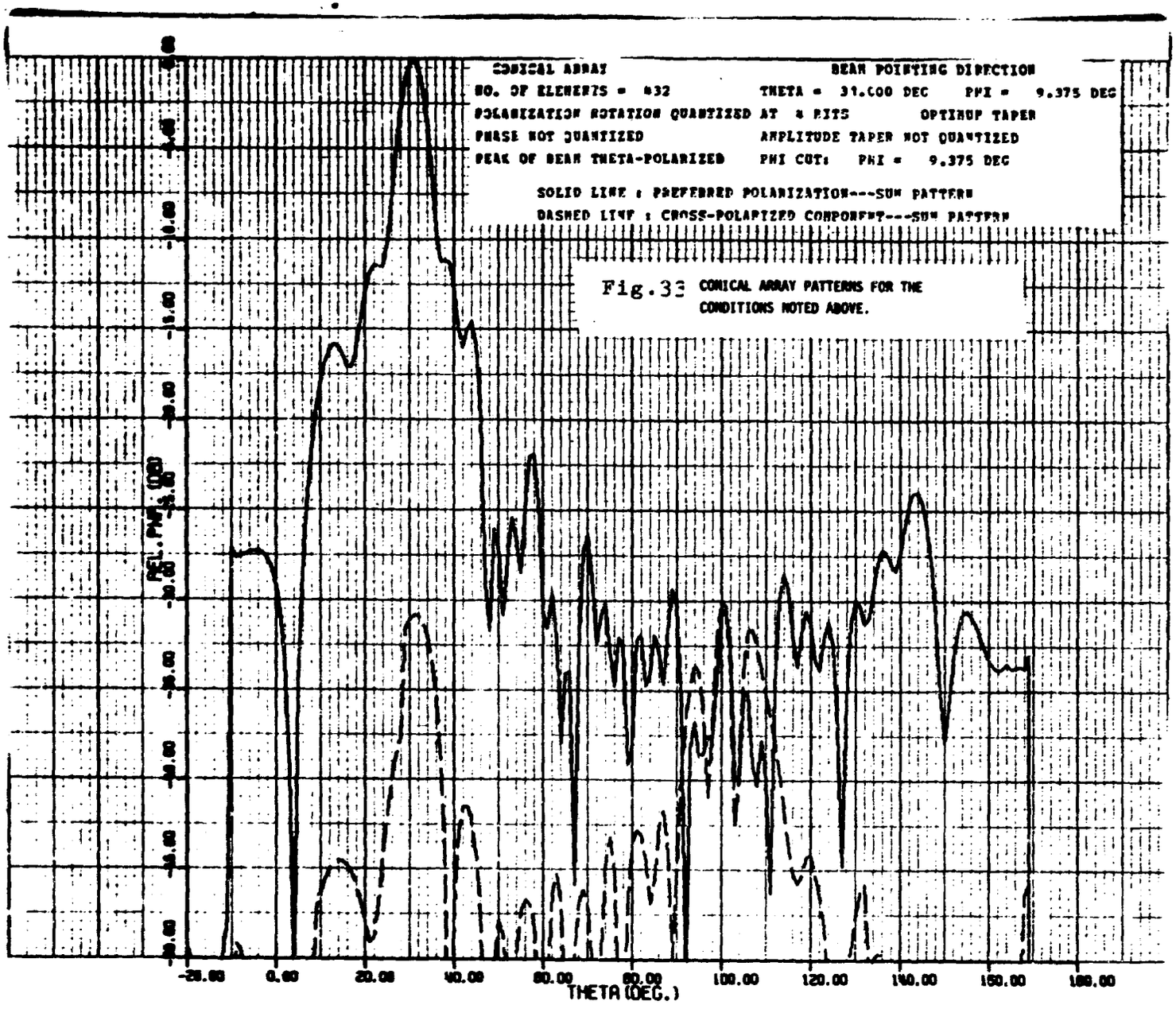

Fig.33 CONICAL ARRAY PATTERNS FOR THE CONDITIONS NOTED ABOVE.

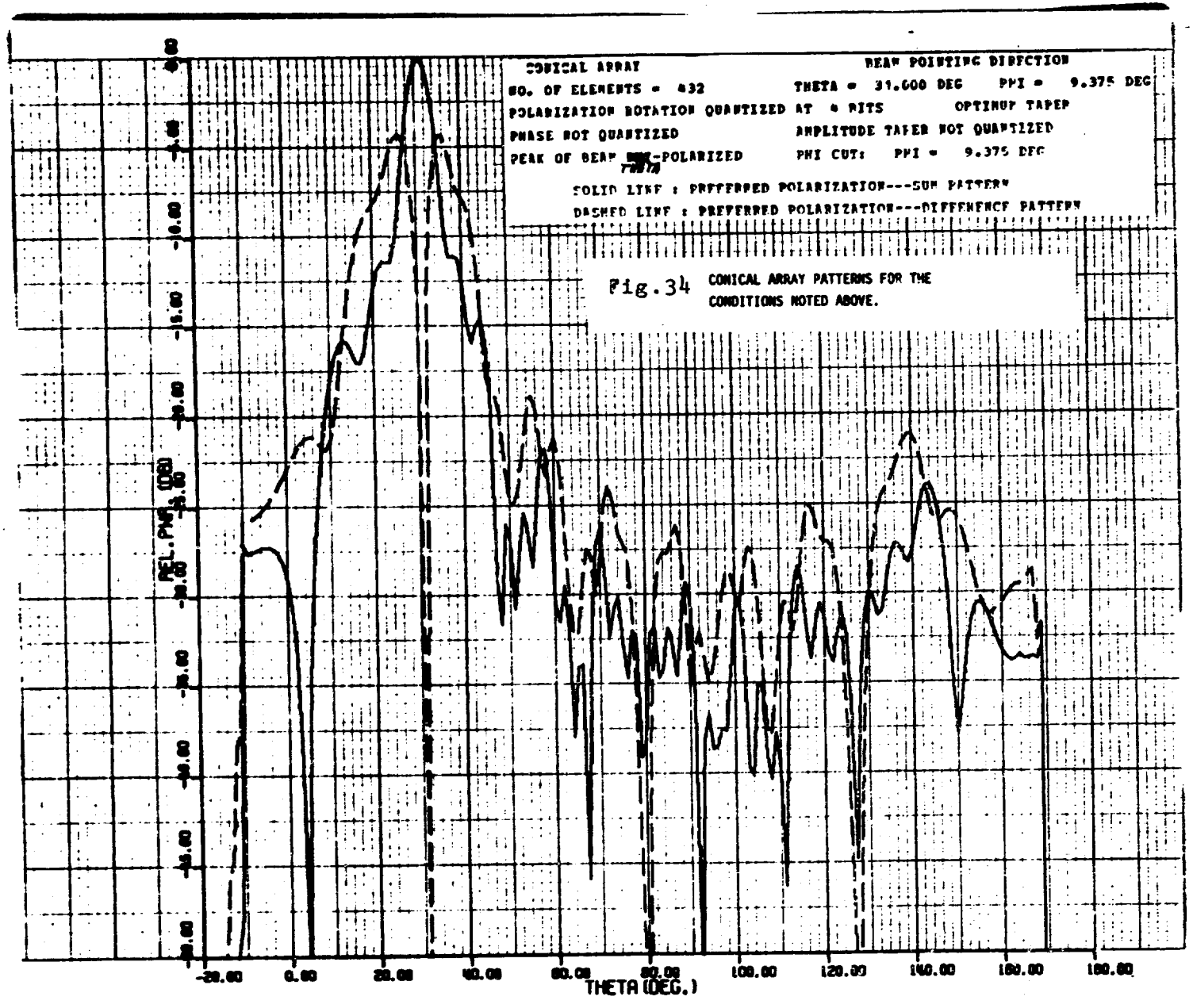

Fig.34 CONICAL ARRAY PATTERNS FOR THE CONDITIONS NOTED ABOVE.

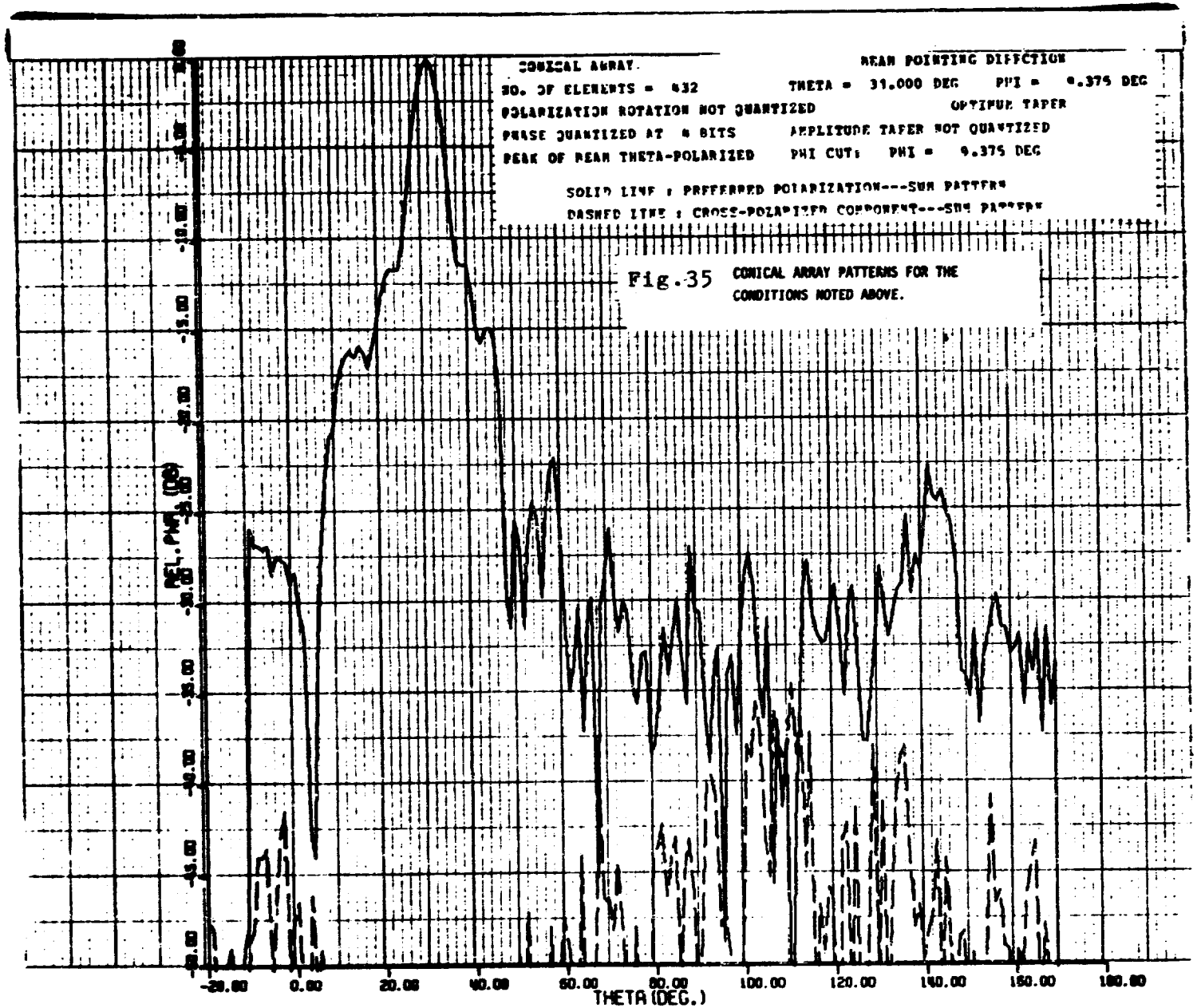

Fig.35 CONICAL ARRAY PATTERNS FOR THE CONDITIONS NOTED ABOVE.

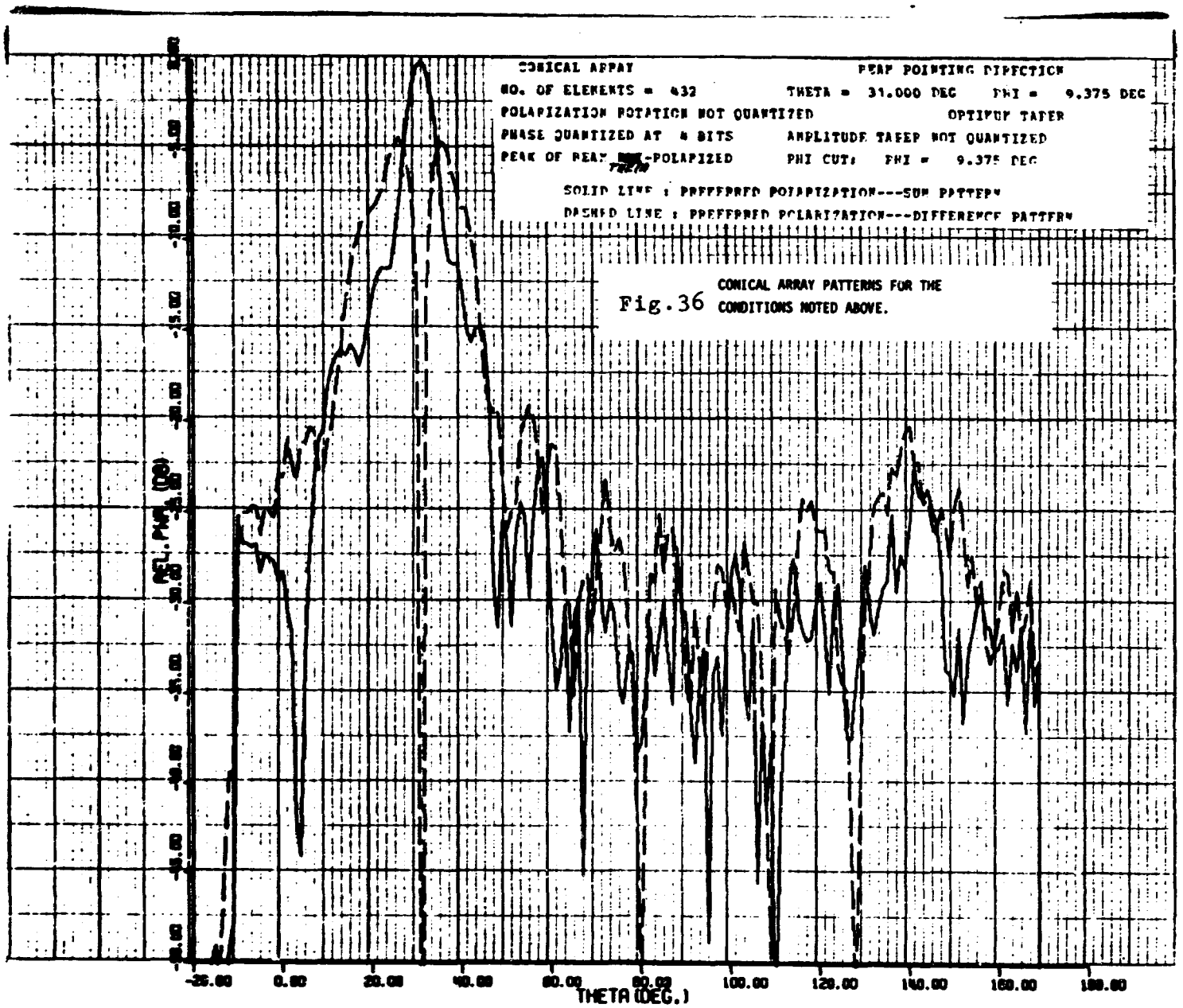

Fig.36 CONICAL ARRAY PATTERNS FOR THE CONDITIONS NOTED ABOVE.

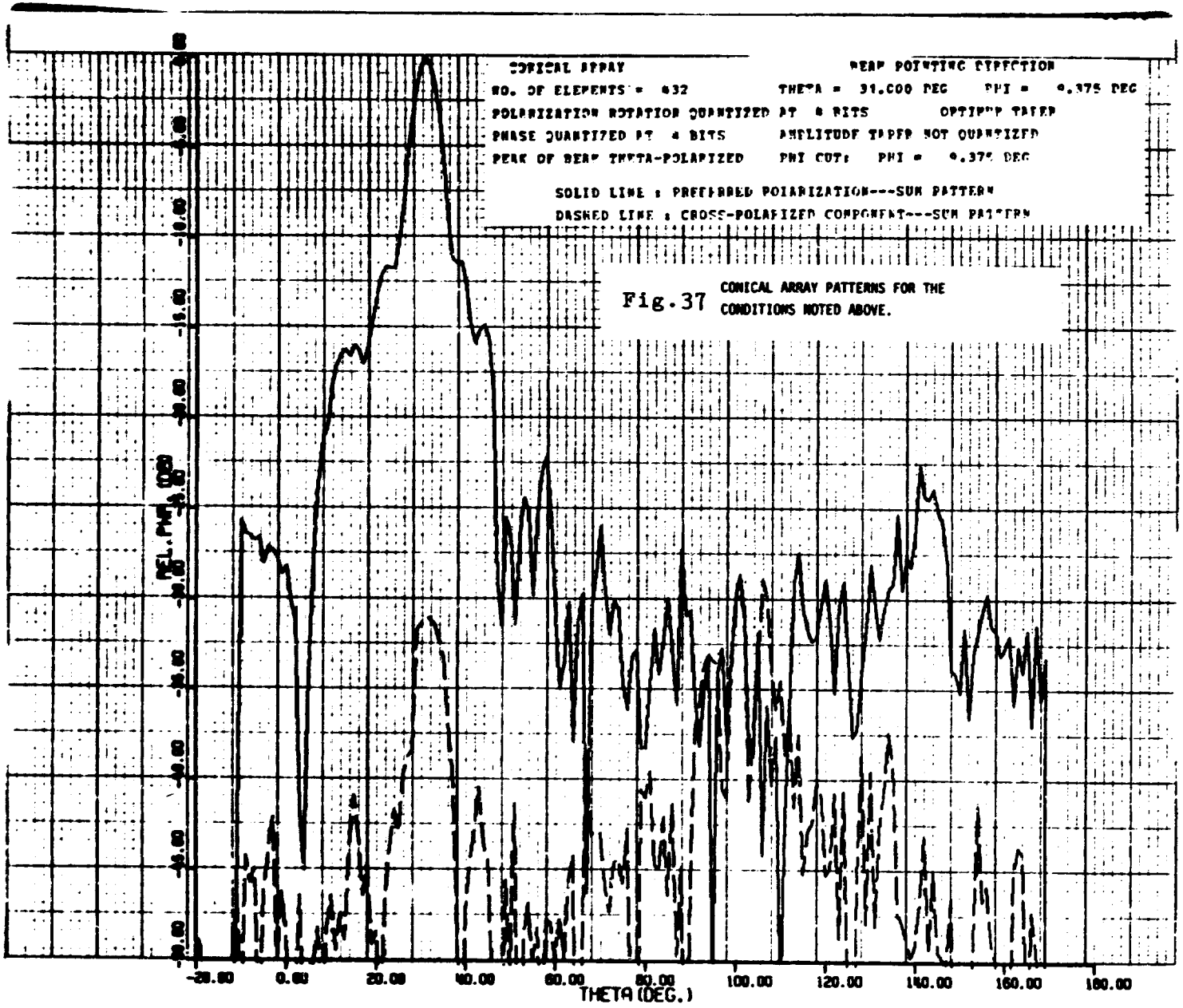

Fig.37 CONICAL ARRAY PATTERNS FOR THE CONDITIONS NOTED ABOVE.

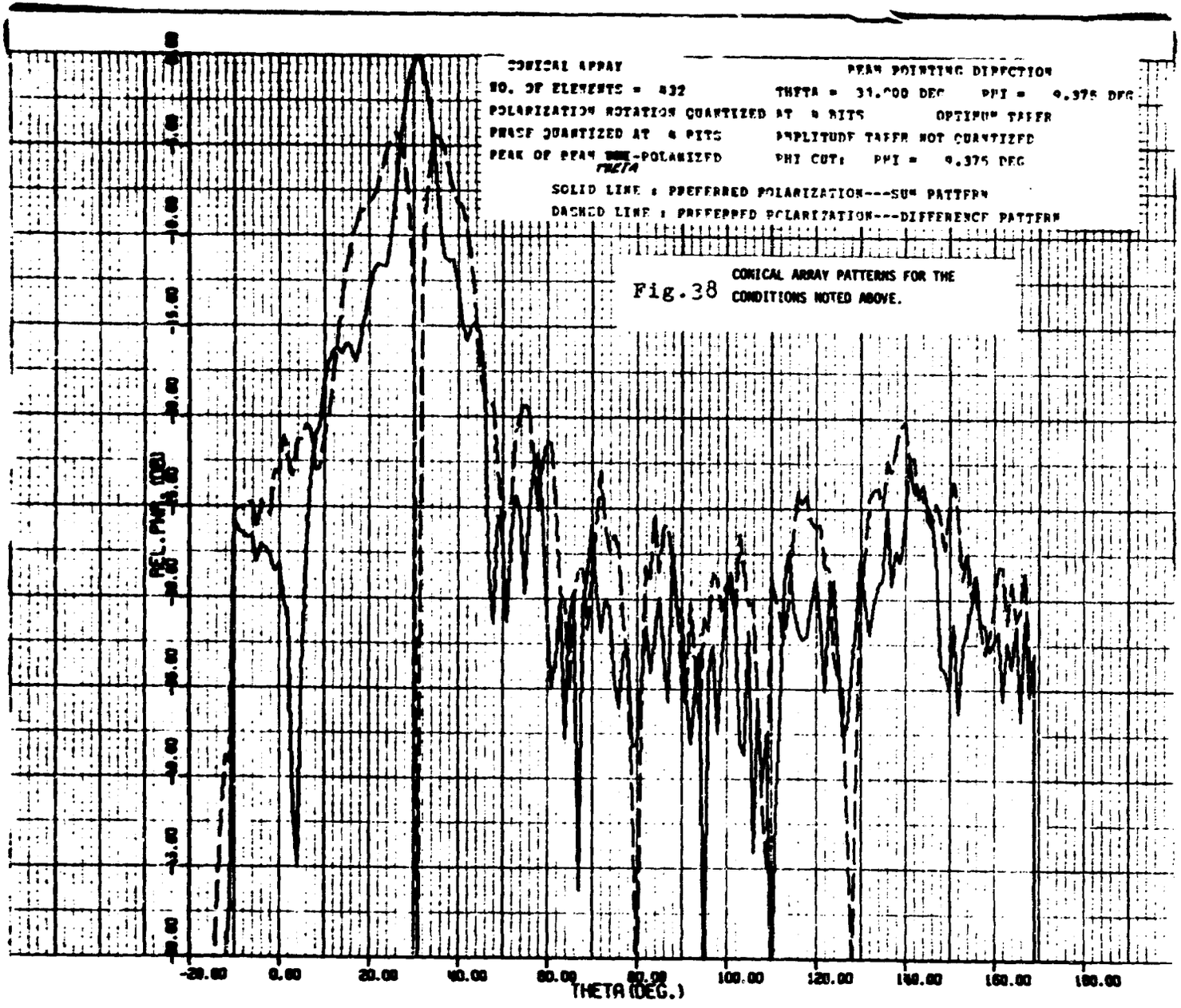

Fig.38 CONICAL ARRAY PATTERNS FOR THE CONDITIONS NOTED ABOVE.

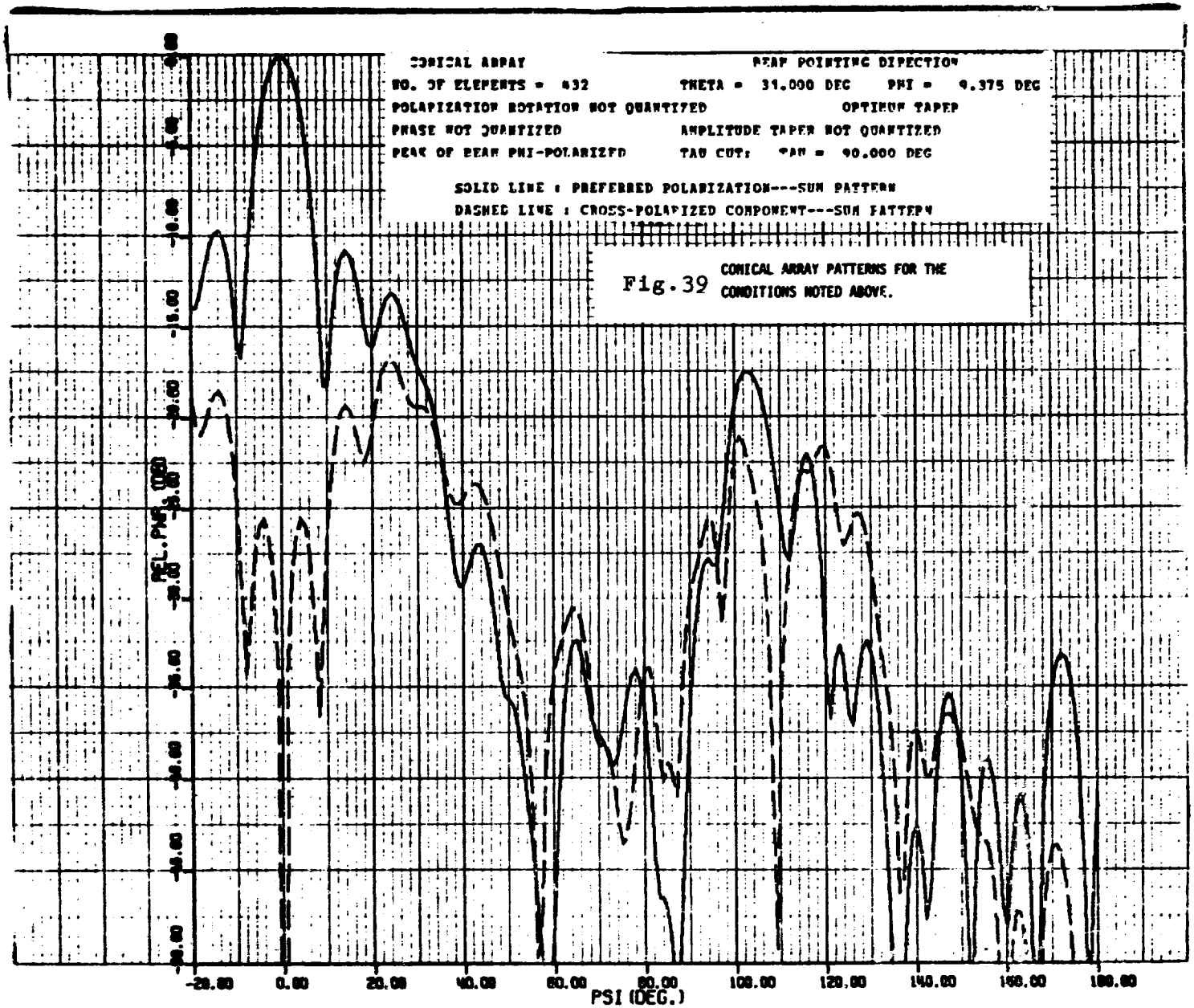

Fig.39 CONICAL ARRAY PATTERNS FOR THE CONDITIONS NOTED ABOVE.

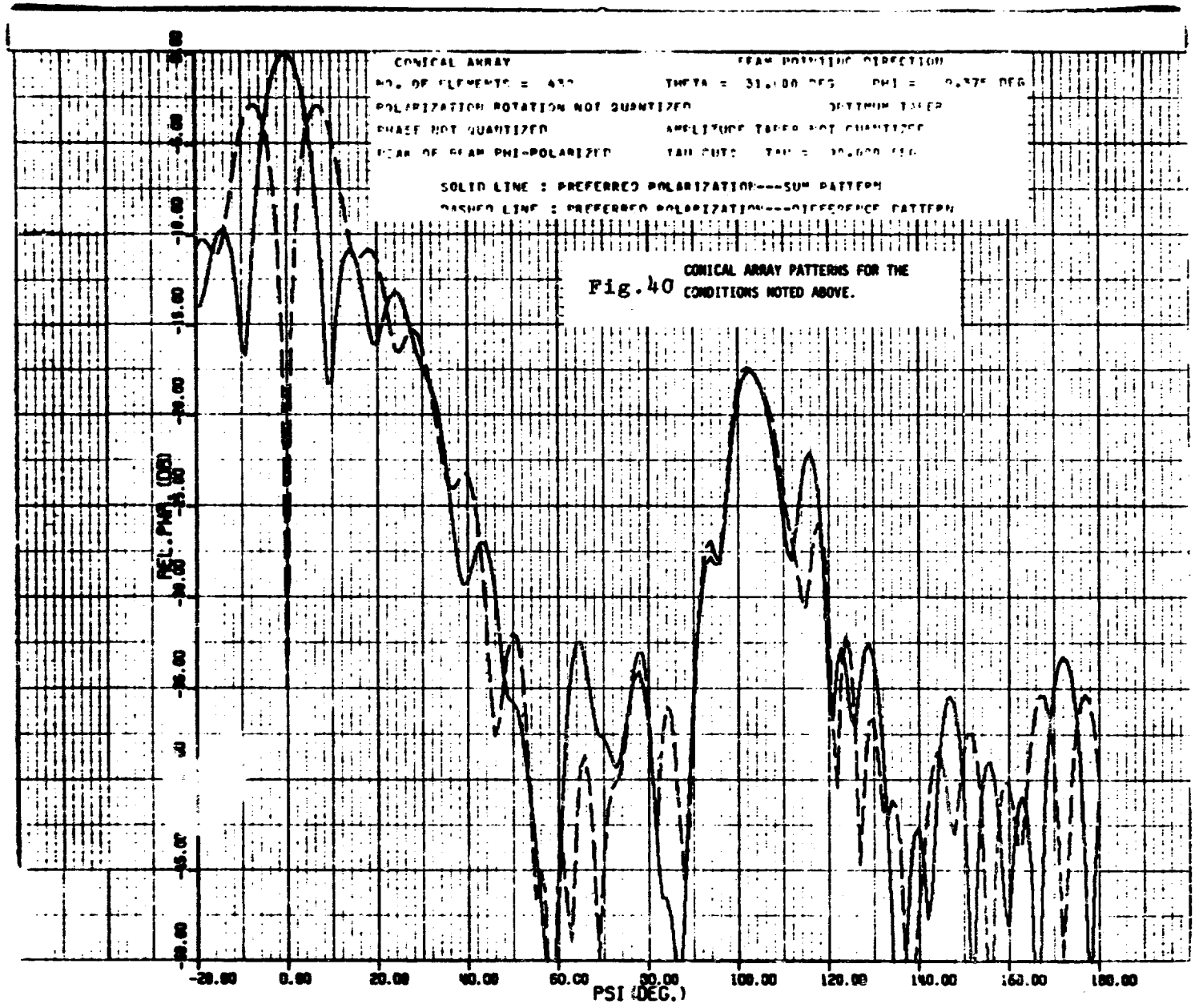

Fig.40 CONICAL ARRAY PATTERNS FOR THE CONDITIONS NOTED ABOVE.

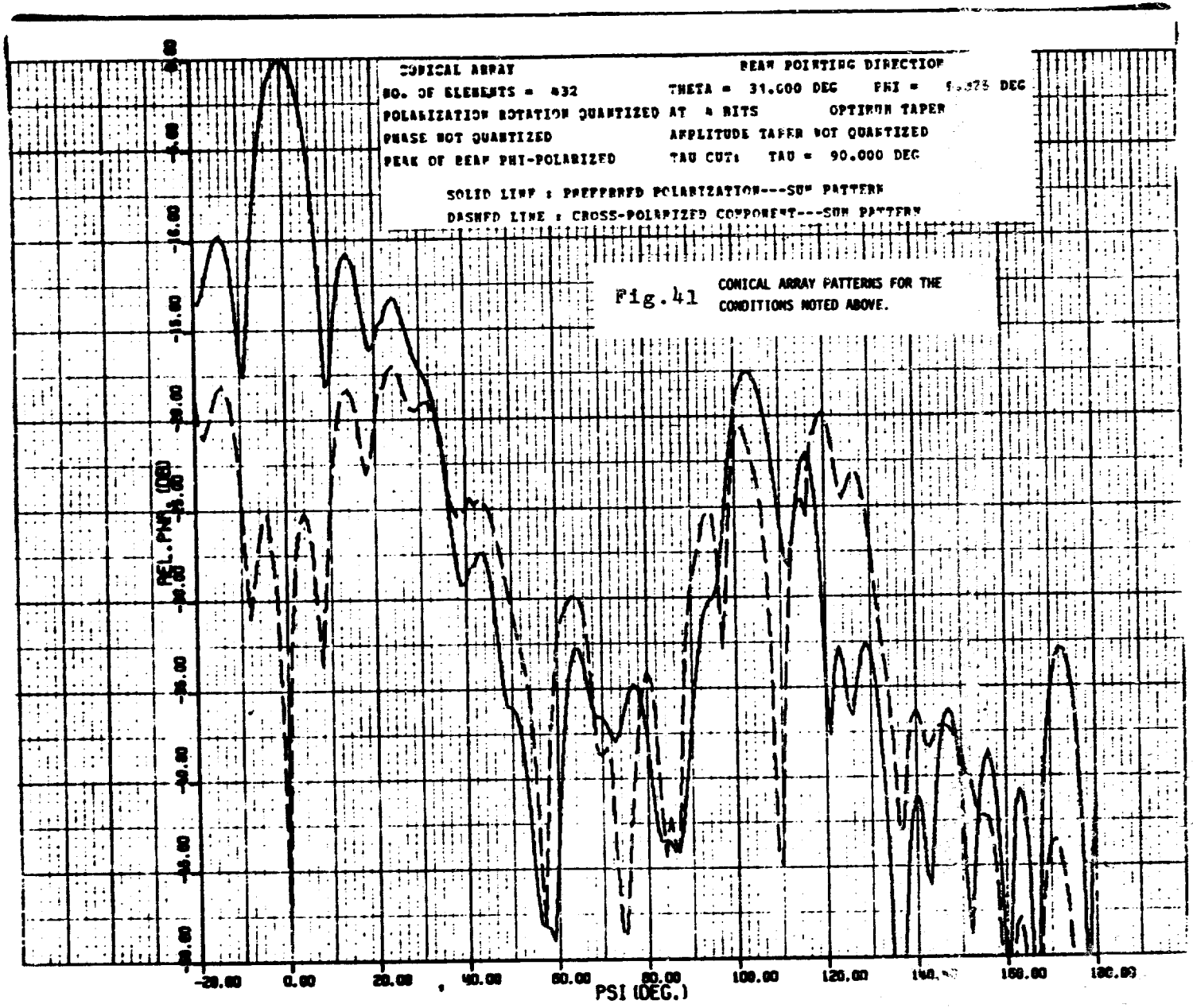

Fig.41 CONICAL ARRAY PATTERNS FOR THE CONDITIONS NOTED ABOVE.

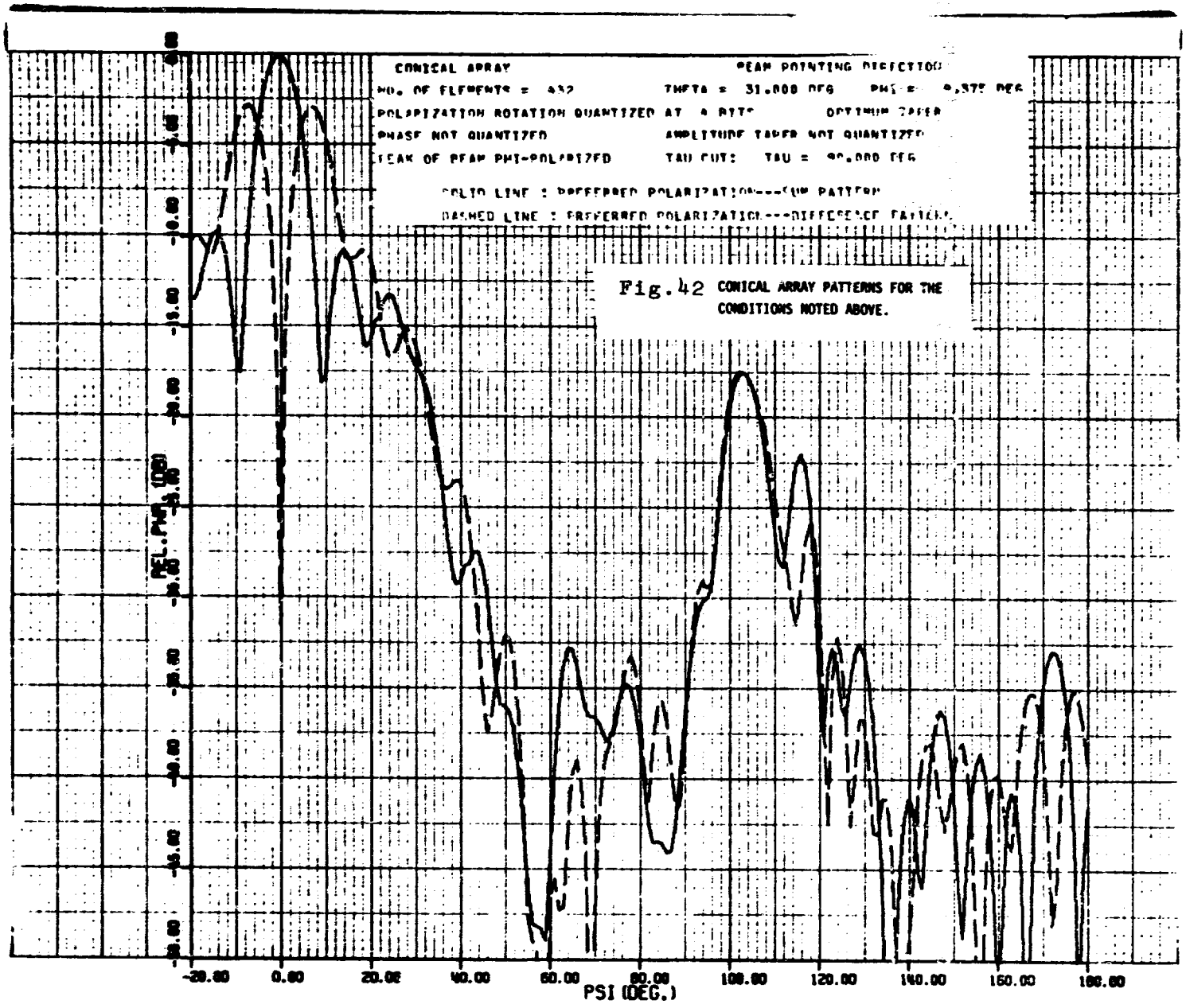

Fig.42 CONICAL ARRAY PATTERNS FOR THE CONDITIONS NOTED ABOVE.

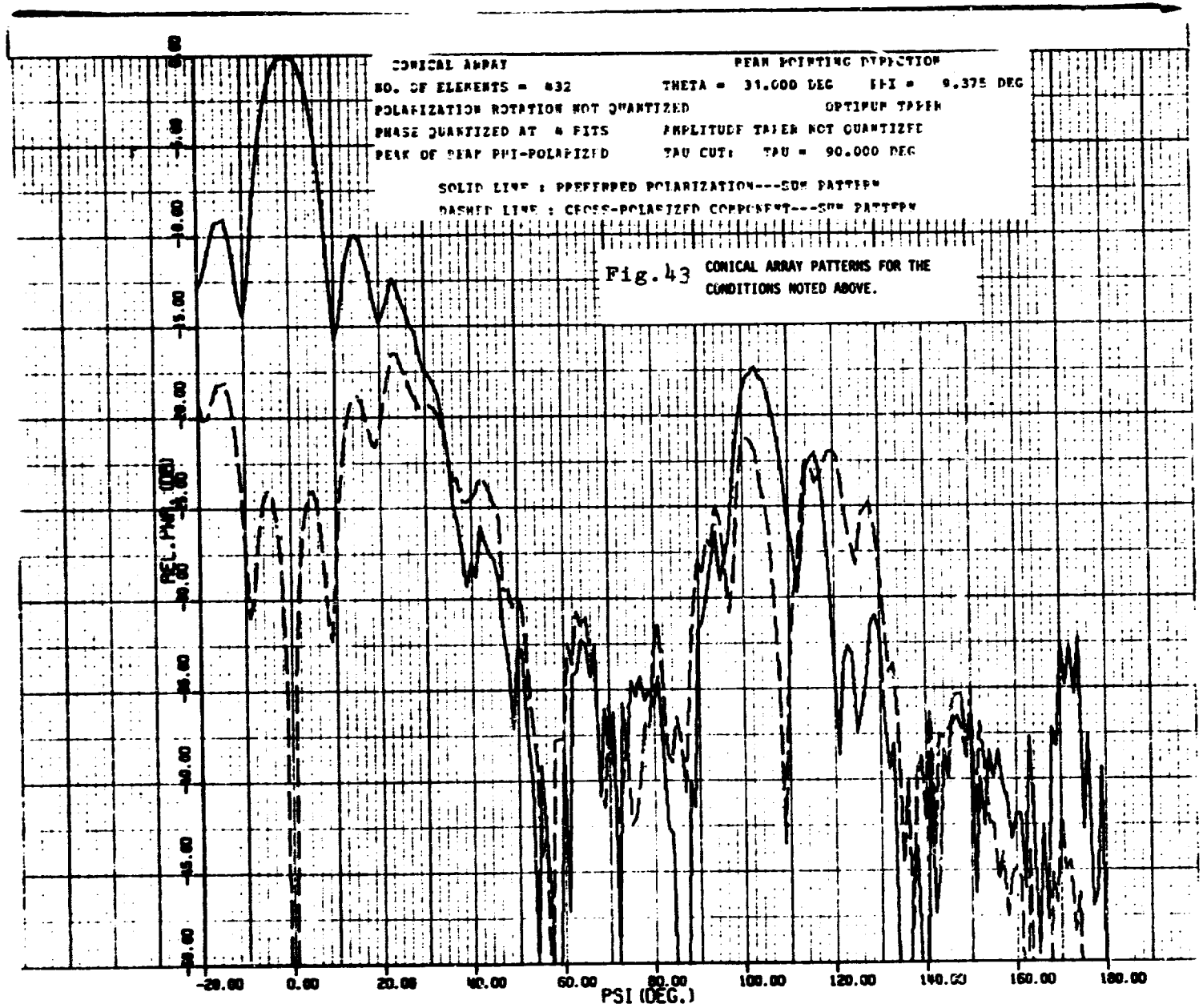

Fig.43 CONICAL ARRAY PATTERNS FOR THE CONDITIONS NOTED ABOVE.

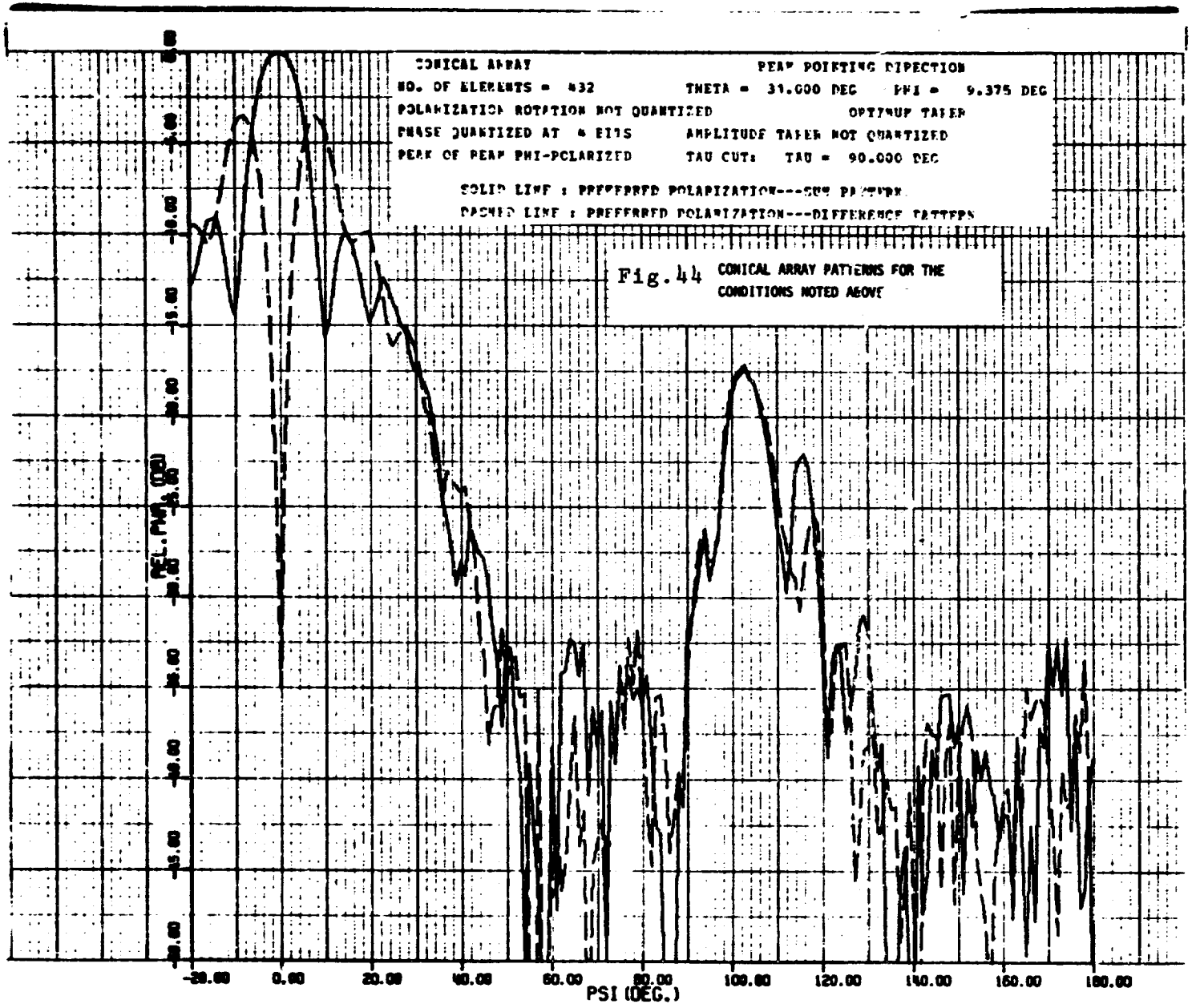

Fig. 44 CONICAL ARRAY PATTERNS FOR THE CONDITIONS NOTED ABOVE

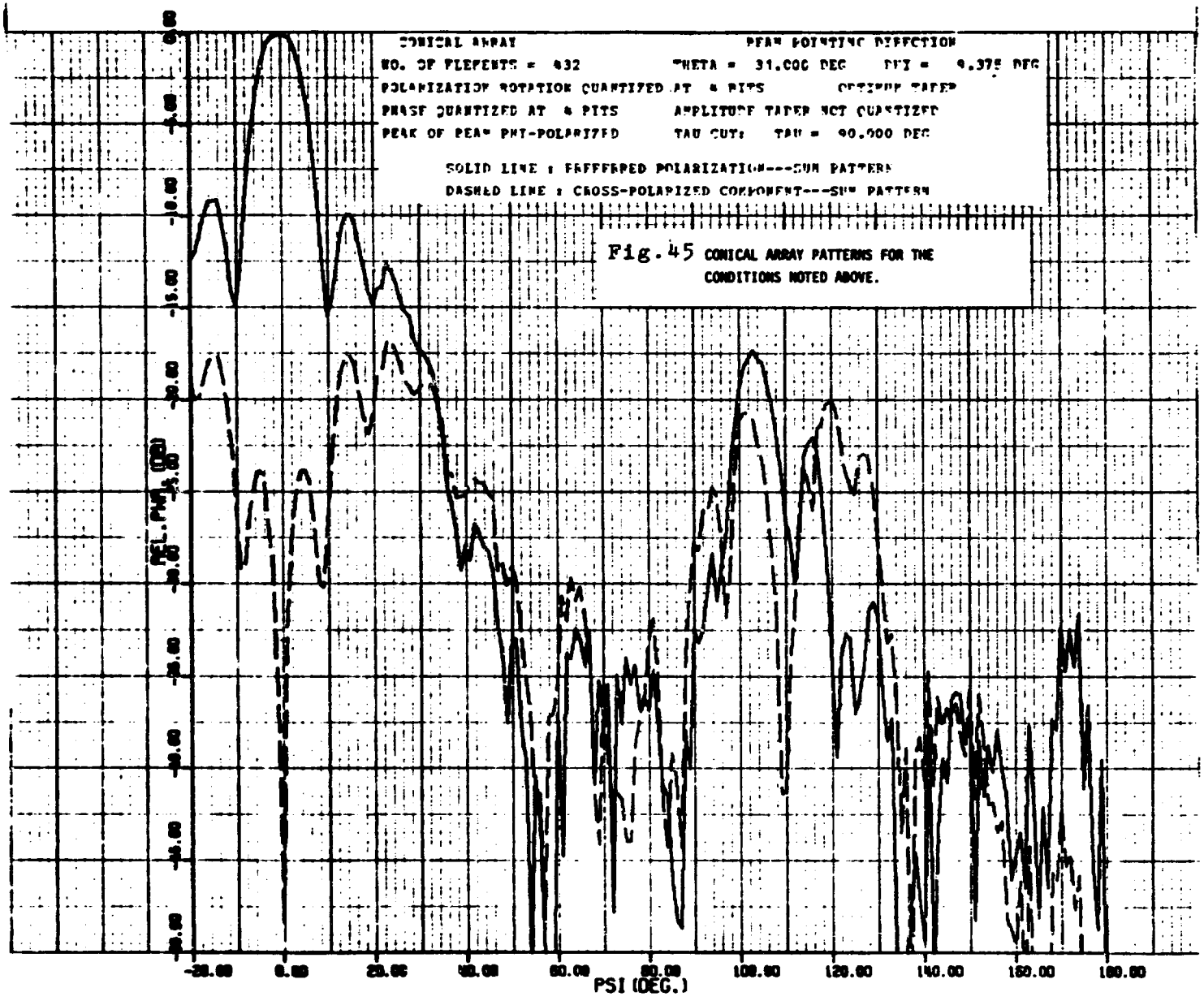

Fig. 45 CONICAL ARRAY PATTERNS FOR THE CONDITIONS NOTED ABOVE.

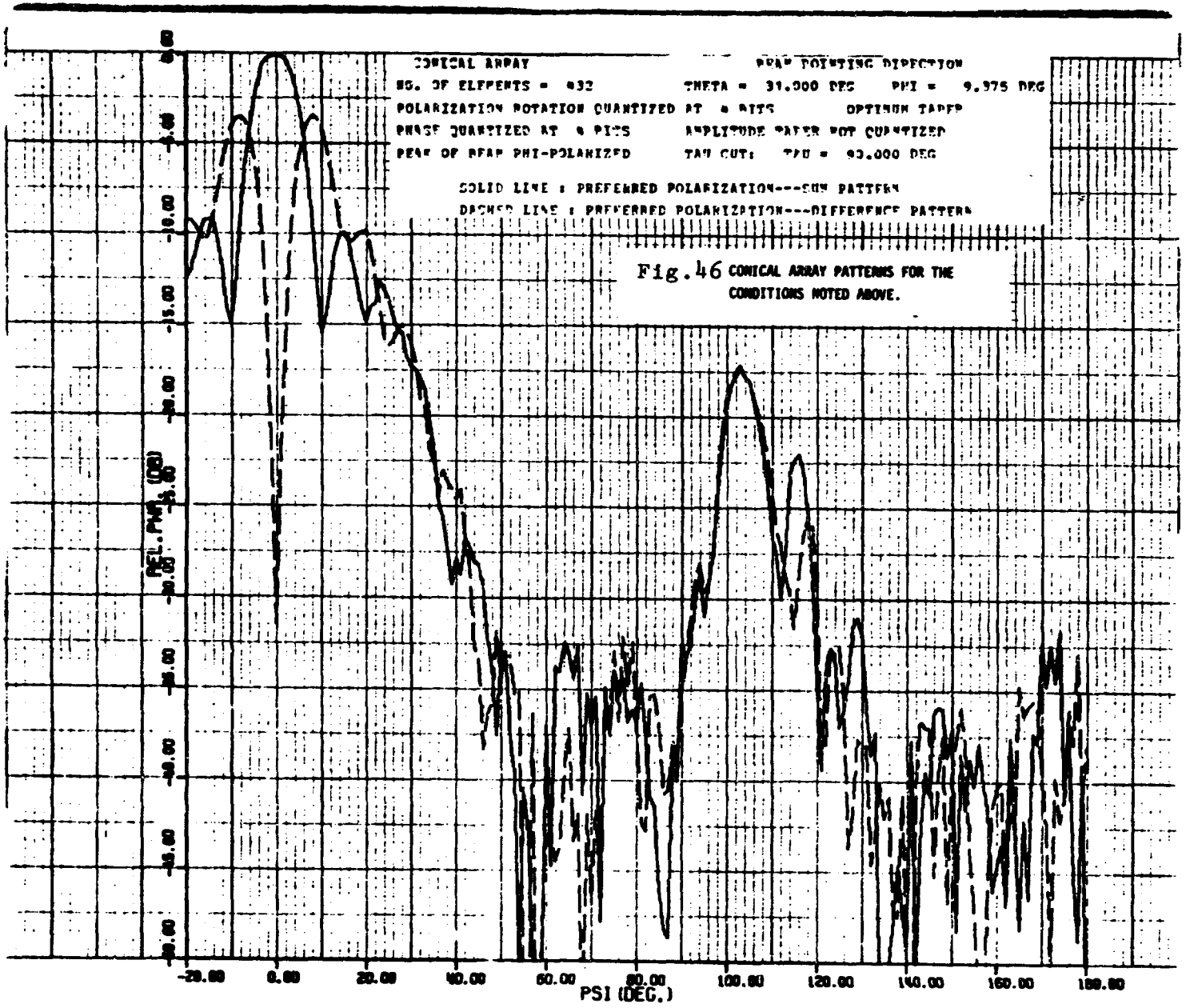

Fig.46 CONICAL ARRAY PATTERNS FOR THE CONDITIONS NOTED ABOVE.

1.4 A Conformal Array Pattern Code

A computer program has been developed (Hsiao and Rao, 1974, 1976) to calculate patterns of arrays located on singly or doubly curved surfaces. In this code all elements are assumed to have equal amplitude excitation although this restriction is easily removed. Elements are assumed to be identical, i.e. the element pattern is not affected by surface curvature. Each element pattern is appropriately rotated so its axis is normal to the array surface. The effects of a metallic surface, and mutual coupling effects are not included herein; see Chapters 3-4-5. The utility of this simple code is that it easily and quickly produces patterns from curved arrays; actual array patterns will be less good due to mutual coupling, metallic surface, and other effects. Code results are then sort of a best case.

Figure 47 shows the coordinate system of a general conformal array under consideration. The position of the nth element in the array is given by a radius vector R_n from the reference point as

$$R_n = (x_n, y_n, z_n), \tag{37}$$

and the element pattern is assumed known in a different primed coordinate system and is given by $E_n(\theta'_n, \phi'_n)$. The appropriate expression for the far-field pattern of a conformal array can be written as

$$F(\theta,\phi) = \sum_{n=1}^{N} I_n E_n(\theta'_n, \phi'_n) \exp\left[jkR_n \cdot (\hat{R} - \hat{R}_0)\right], \tag{38}$$

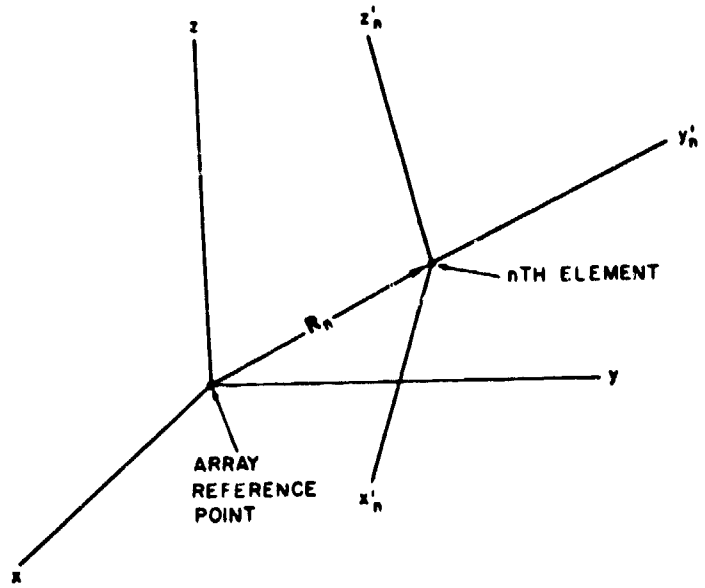

Figure 47. Coordinate system of the conformal array.

where

$\hat{R}$ = (sin θ cos ϕ, sin θ sin ϕ, cos θ),

$\hat{R}_0$ = (sin θ_0 cos ϕ_0, sin θ_0 sin ϕ_0, cos θ_0),

I_n = the excitation coefficient of the nth element,

θ, ϕ = the spherical polar coordinates of the conformal array,

θ'_n, ϕ'_n = the primed spherical coordinates in which the far-field, expression for the nth element is known,

and

θ_0, ϕ_0 = the direction of the pattern maximum in the unprimed coordinate system.

Equation (38) is expressed in mixed coordinates to conveniently represent the far-field pattern. However, to complete the radiation pattern $F(\theta,\phi)$ of a conformal array, it is first necessary to transform the element patterns to a common coordinate system (unprimed coordinate system) and then to express the element pattern in terms of the unprimed coordinates θ and ϕ. This can be done most conveniently using a coordinate transformation, as will be discussed in the next section.

The element pattern is assumed known in a primed coordinate system and has the general form

$$E(\theta',\phi') = E_{\theta'}(\theta',\phi')\,\hat{\theta}' + E_{\phi'}(\theta',\phi')\hat{\phi}', \qquad (39)$$

where $E_{\theta'}$ and $E_{\phi'}$ are θ' and ϕ' components. The radial component is not included in Equation (39) because the interest here is in the far-field radiation pattern. The subscript n is omitted in Equation (39) for brevity.

It is also assumed, as noted earlier, that the element position in the array is specified in rectangular coordinates with

respect to a reference point on the conformal surface and that each element orientation is specified by Euler angles ξ_x, ξ_y, ξ_z with respect to the unprimed rectangular coordinates x, y, and z. Therefore, to transform the element pattern given in Equation (39) from primed to unprimed coordinates, it is first necessary to transform the pattern into primed rectangular coordinates and finally to unprimed polar coordinates. These transformations can be represented by the following matrix formulation:

$$\begin{vmatrix} E_R(\theta,\phi) \\ E_\theta(\theta,\phi) \\ E_\phi(\theta,\phi) \end{vmatrix} = \left| D_{RP} \right| \left| R_M \right| \left| D'_{PR} \right| \begin{vmatrix} 0 \\ E_{\theta'}(\theta;\phi') \\ E_{\phi'}(\theta;\phi') \end{vmatrix}, \quad (40)$$

where $|D'_{PR}|$ is the matrix which transforms the primed polar coordinates to primed rectangular coordinates; the subscript PR means polar to rectangular coordinates. The matrix $|R_M|$ transforms primed to unprimed rectangular coordinates. The matrix D_{RP} transforms unprimed rectangular to polar coordinates; the subscript RP represents rectangular to polar coordinates. The form of these matrices is obtained next. It is well known that the transformation from polar to rectangular coordinates can be represented in matrix form as

$$\begin{vmatrix} E_{x'} \\ E_{y'} \\ E_{z'} \end{vmatrix} = \left| D'_{PR} \right| \begin{vmatrix} E_{R'} \\ E_{\theta'} \\ E_{\phi'} \end{vmatrix}, \quad (41)$$

where the transformation matrix $|D'_{PR}|$ is given as

$$\left|D'_{PR}\right| = \begin{vmatrix} \sin\theta'\cos\phi' & \cos\theta'\cos\phi' & -\sin\phi' \\ \sin\theta'\sin\phi' & \cos\theta'\sin\phi' & \cos\phi' \\ \cos\theta' & -\sin\theta' & 0 \end{vmatrix} \quad (42)$$

This matrix is known to be real orthogonal. If $\left|D'_{RP}\right|$ is the inverse of $\left|D'_{PR}\right|$, for an orthogonal matrix the following relation is known to be true:

$$\left|D'_{RP}\right| = \left|D'_{PR}\right|^{-1} = \left|D'_{PR}\right|^{T}, \quad (43)$$

where $\left|D'_{PR}\right|^{T}$ is the transpose of $\left|D'_{PR}\right|$. Therefore the transformation matrix $\left|D_{RP}\right|$ in Equation (40) is given by the transpose of the matrix given in Equation (42) with θ and ϕ replacing θ' and ϕ'.

As mentioned before, the matrix $\left|R_M\right|$ is used to transform a function from primed to unprimed rectangular coordinates. Since the far-field element pattern is a function of angular variables only, the coordinate transformation involves only the change in element orientation. This can be obtained by three successive rotations about the three coordinate axes. The first rotation is for angle ξ_x about the x axis. The orthogonal matrix between the primed and unprimed rectangular coordinate systems for this rotation is

$$\left|C\right| = \begin{vmatrix} 1 & 0 & 0 \\ 0 & \cos\xi_x & -\sin\xi_x \\ 0 & \sin\xi_x & \cos\xi_x \end{vmatrix} . \quad (44)$$

The second rotation is for an angle ξ_y about the y axis. The orthogonal matrix for this rotation is

$$|B| = \begin{vmatrix} \cos \xi_y & 0 & \sin \xi_y \\ 0 & 1 & 0 \\ -\sin \xi_y & 0 & \cos \xi_y \end{vmatrix} \tag{45}$$

The third and final rotation is for an angle ξ_z about the z axis. The orthogonal matrix for this rotation is

$$|A| = \begin{vmatrix} \cos \xi_z & -\sin \xi_z & 0 \\ \sin \xi_z & \cos \xi_z & 0 \\ 0 & 0 & 1 \end{vmatrix} \tag{46}$$

In all three rotations the angle of rotation is positive when the rotation is clockwise with respect to the axis of rotation. The overall transformation matrix may be written as

$$|R_M| = |A| \; |B| \; |C| \; . \tag{47}$$

One should note here that the order of matrix multiplication is not commutative; thus the sequence of these transformations is not interchangeable. Equation (38) can now be rewritten in the matrix form with the aid of Equation (40) as

$$\begin{vmatrix} E_R(\theta, \varphi) \\ E_\theta(\theta, \varphi) \\ E_\varphi(\theta, \varphi) \end{vmatrix} = \sum_{n=1}^{N} A_n \exp\left[jk\bar{R}_n \cdot (\hat{R} - \hat{R}_0)\right] |D_{RP}| \, |R_M| \, |D'_{PR}| \begin{vmatrix} 0 \\ E_{\theta'}(\theta', \varphi') \\ E_{\varphi'}(\theta', \varphi') \end{vmatrix} . \tag{48}$$

However, the right-hand side is still expressed in primed coordinate variables θ' and ϕ'. These variables can be eliminated

by considering the relations between the primed and unprimed coordinate variables. The relations between rectangular coordinate variables can be written as

$$\begin{vmatrix} x \\ y \\ z \end{vmatrix} = \left| R_M \right| \begin{vmatrix} x' \\ y' \\ z' \end{vmatrix} , \tag{49}$$

and the relations between the rectangular and polar coordinate variables are given by

$$\begin{vmatrix} x \\ y \\ z \end{vmatrix} = \begin{vmatrix} \sin\theta \cos\phi \\ \sin\theta \sin\phi \\ \cos\theta \end{vmatrix} \tag{50}$$

and

$$\begin{vmatrix} x' \\ y' \\ z' \end{vmatrix} = \begin{vmatrix} \sin\theta' \cos\phi' \\ \sin\theta' \sin\phi' \\ \cos\theta' \end{vmatrix} \tag{51}$$

Substituting Equations (47), (50), and (51) in Equation (49), it can be shown that

$$\theta' = \cos^{-1} z'(\theta,\phi) \tag{52}$$

$$\phi' = \tan^{-1} \frac{y'(\theta,\phi)}{x'(\theta,\phi)} \tag{53}$$

The ambiguity in the value of the arctangent function in Equation (53) is resolved by applying the same set of rules that one uses to determine the value of $\tan^{-1}(y/x)$, where x and y are the rectangular coordinate variables.

1.4.1 Description of the Computer Program

A computer program has been written in FORTRAN language which computes and plots the far-field pattern of a conformal array for a given set of array parameters and is included as the Appendix B. The program is divided into a main program and several subroutines to allow flexibility. The name of the main program is Coflaray (short name for conformal array). The array element orientations (angles) and positions can be supplied as input data or can be calculated using subroutine ELAGPO (short name for element angle and position). Three separate ELAGPO subroutines were developed. The first one is for a doubly curved surface with uniformly spaced elements; the second one is for a doubly curved surface with projected uniformly spaced elements; the third one is for an array on a conic surface. Therefore, depending on the conformal array under consideration, the corresponding ELAGPO subroutine should be used. It is also possible to write additional ELAGPO subroutines for any well-defined conformal array, and they can be substituted for the ones written for this report. Except for this ELAGPO subroutine, the other subroutines which should be included with the Coflaray program, given in the order in which they are called in the program, are:

CODTRF - This subroutine computes the elements of the R_M matrix, as given by Equation (47) for each array element.

DPRMAT - This subroutine computes the elements of the matrices $|D'_{PR}|$ and $|D_{PR}|$ for each array element, as given by Equations (42) and (43).

ANGTRF - This subroutine computes the relations between primed and unprimed coordinate variables, as given by Equations (52) and (53).

ELPAT - This subroutine is used to select the array element pattern as either that of a vertical dipole or a horizontal dipole.

MATMUT - This subroutine performs the matrix multiplication shown in Equation (40).

FRAME - This subroutine is used to establish the coordinate-system frame to plot the radiation patterns.

PENCHG - This subroutine is called in the FRAME subroutine to change to a different pen in plotting.

REZERO - This subroutine is used to reset the origin if more than one plot is desired in any given computer run.

The program requires four data cards. The first data card should contain six variables in an integer format of 6I5. These variables are:

NE - Number of elements in the array. If the subroutine ELAGPO is to be used, NE should be less than or equal to zero.

NC - Number of antenna pattern cuts required in ϕ plane.

NP - Number of points at which the antenna pattern is calculated and plotted.

LLL - Controls the amount of printout needed:
If LLL = 0, printout for diagnostic purpose;
LLL = 1, print element positions and rotation angles;
LLL = 2, print pattern function only;
LLL>2, no printout.

LBP - If it is zero, the scanning is obtained by using row-column planar-array phasing. If it is one, exact conformal-array phasing is used.

NBP - Number of phase-shift bits used in digital phase control. If NBP is greater than 10, analog phases are assumed.

The second data card (or set of cards) depends on whether or not the ELAGPO subroutine is needed. If it is needed, then which particular ELAGPO subroutine is used. First, we will discuss the set of data cards needed when the ELAGPO subroutine is not used. In that case the data cards should contain all the element positions, the element orientations (rotation angles), and the specification of the ground plane. The data cards should conform to the following read and format statements:

```
    READ 101, ((W(I,J), I = 1, NE), J = 1,3),
    READ 101, ((G(I,J), I = 1, NE), J = 1,3),
    READ 100, (LG(I), I = 1,3),
101 FORMAT (8F10.6),
100 FORMAT (615),
```

where

W(I,J) are the element positions,
G(I,J) are the element rotation angles,

and the

LG array specifies the ground plane of radiators as follows:

If LG(1) = 1,LG(2) = LG(3) = 0, the ground plane is the zy plane;
LG(1) = LG(3) = 0,LG(2) = 1, the ground plane is the xz plane;
LG(1) = LG(2) = 0,LG(3) = 1, the ground plane is the xy plane.

When the subroutine ELAGPO is used to compute the array element positions and orientations, the second data card contains the description of the conformal surface and the array dimensions. For a doubly curved surface (with uniformly or projected uniformly spaced elements), the second data card should contain seven variables conforming with the format of 2I5,4F10.6,I2. These variables are:

NCX - Number of columns in the x direction.
NRY - Number of rows in the y direction
AX - Aperture in the x direction, in wavelengths
AY - Aperture in the y direction, in wavelengths
RX - Radius of curvature in the x direction, in wavelengths
RY - Radius of curvature in the y direction, in wavelengths
LP - If LP = 0, the array element is a horizontal dipole; if LP = 1, it is a vertical dipole.

When the subroutine ELAGPO for a conic array is used, the second data card should contain eight variables conforming with the format I5,5F10.4,2I5. These variables are:

MM - Number of rows;
RB - Base radius in wavelengths;
ARC - Cone arc (in degrees) occupied by the array;
TC - Cone angle in degrees;
DX - Spacing in the x direction, in wavelengths;
DY - Spacing in the y direction, in wavelengths;
LP - If LP = 0, the array element is a horizontal dipole; if LP = 1, it is a vertical dipole;
LRT - If LRT = 0, the array element distribution is on a rectangular grid; if LRT = 1, it is on a triangular grid.

The third and the fourth (or last two) data cards should contain the angular range and the plane in which the radiation pattern is desired. The third data card should contain one or more values of ϕ [FI(I) in degrees] defining the plane or planes in which the radiation pattern is desired. This data should conform to the format 8F10.6. The last data card contains four variables conforming with the format 8F10.6; these variables are:

FIO - Scan angle ϕ_0 in degrees;
TAO - Scan angle θ_0 in degrees;
TAPI - Initial value of θ;
TAPF - Final value of θ over which the radiation pattern is desired.

1.4.2 Examples

A few examples of computing the radiation patterns of a conformal array are included here which illustrate several features of the program.

The first example considered is uniformly spaced circular-arc array with 32 elements, as shown in Figure 48. The individual elements are assumed to be vertical dipoles (dipoles normal to the array plane). The array aperture in the x direction (projection of the array arc onto the x axis) is assumed to 15.5λ, so that the average interelement spacing in the projected plane (x axis) is 0.5λ. The interest here is to find the radiation pattern when scanned to 15° in the array plane ($\phi = 0^\circ$ plane). Since the interest is in an uniformly spaced circular-arc array, the subroutine ELAGPO for a doubly curved surface with uniformly spaced elements is used. The four data cards for this example have the following values:

Data Card 1: NE=0, NC=1, NP=361, LLL=2, LBP=1, NBP=11
Data Card 2: NCX=32, NRY=1, AX=15.5, AY=0., RX=12.66333, RY=0., LP=1
Data Card 3: FI(I)=0.
Data Card 4: FIO=0., TAO=15°, TAPI=-90°, TAPF=90°.

Using these data cards, the computer prints (printout not included here) the values of the normalizing factor, the normalized values (expressed in dB) of the radiation field at 361 values of θ, with increments of 0.5° over the interval $-90<\theta<90^\circ$, and the steering phases used to scan the beam. In this example

it is specified (LBP = 1) to use correct steering phases. The computer output includes a plot of the radiation pattern which is shown in Figure 49.

The second example is the same as the first example except that the array elements are assumed to be projected uniformly spaced (when projected onto the x axis they have equal inter-element spacing) on the circular arc, as shown in Figure 50. The advantage of this type of distribution is that the pattern can be scanned using simpler row steering of a uniformly spaced linear array (Rao & Hsiao, 1974B), as will be illustrated in Example 3. The data cards for Example 2 are the same as those of Example 1. However, the subroutine ELAGPO for a doubly curved surface with projected uniformly spaced elements is used instead of the one used in Example 1. The computed radiation pattern is shown in Figure 51.

The third example is the same as the second example, except for the steering phases used to scan the array pattern. In this example, approximate steering (linear array steering) phases are used instead of the correct steering phases. So the data cards are the same as that of Example 2, except that the value of LBP in the first data card is changed from 1 to 0. The ELAGPO subroutine used is the same as that used in Example 2. The computed radiation pattern for this example is shown in Figure 52.

The fourth example considered is a 7-by-13-element, uniformly spaced array on a circular cylindrical surface, as shown in Figure 53. The array apertures are assumed to be 3λ in the x direction and 6λ in the y direction. The radius of curvature of the circular cylinder is assumed to be 5.186λ. To obtain a broadside pattern in the $\phi = 0$ plane (xz plane), the data cards should contain the following values:

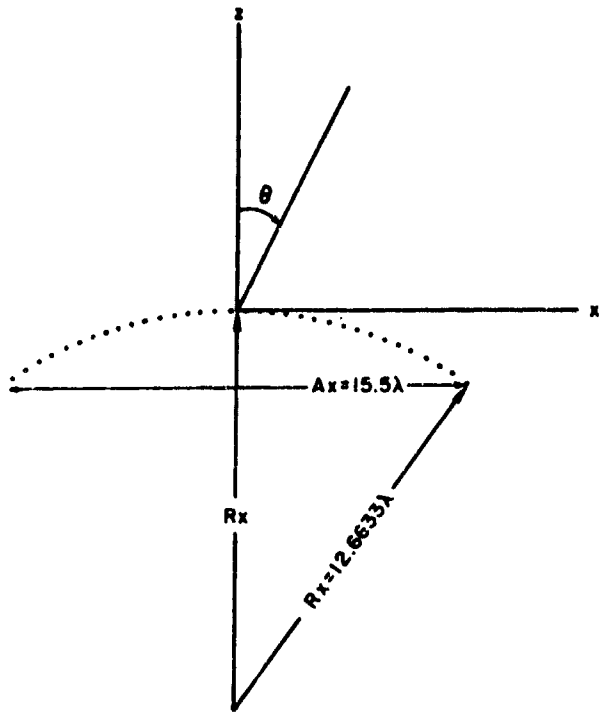

Fig.48 — Uniformly spaced circular-arc array

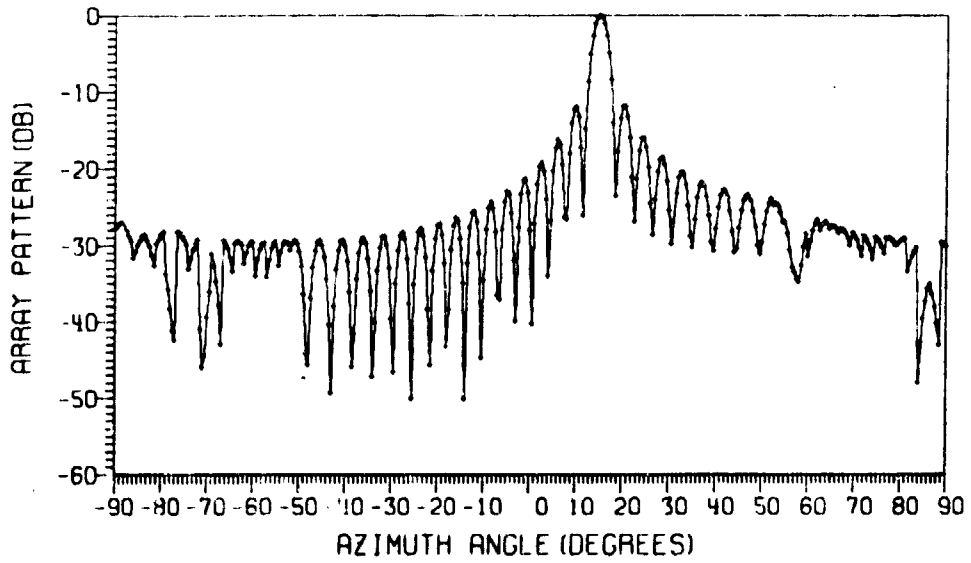

Fig.49 — Radiation pattern of a uniformly spaced circular-arc array

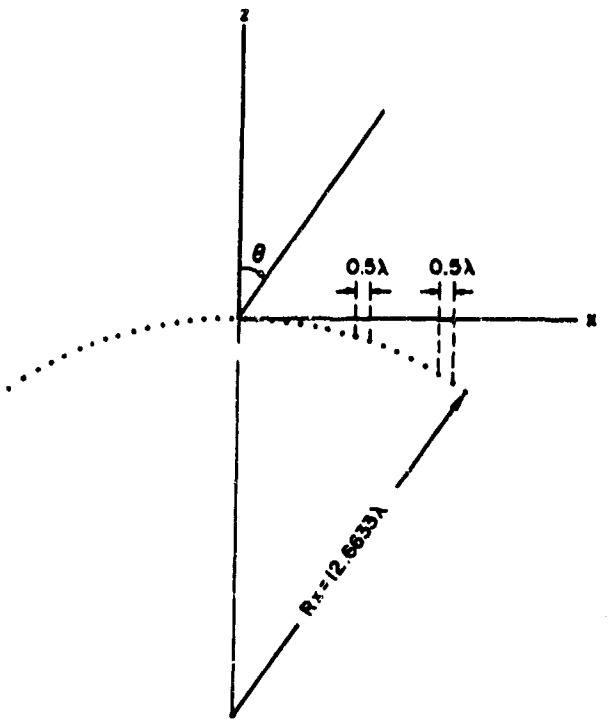

Fig. 50 — Projected uniformly spaced circular-arc array

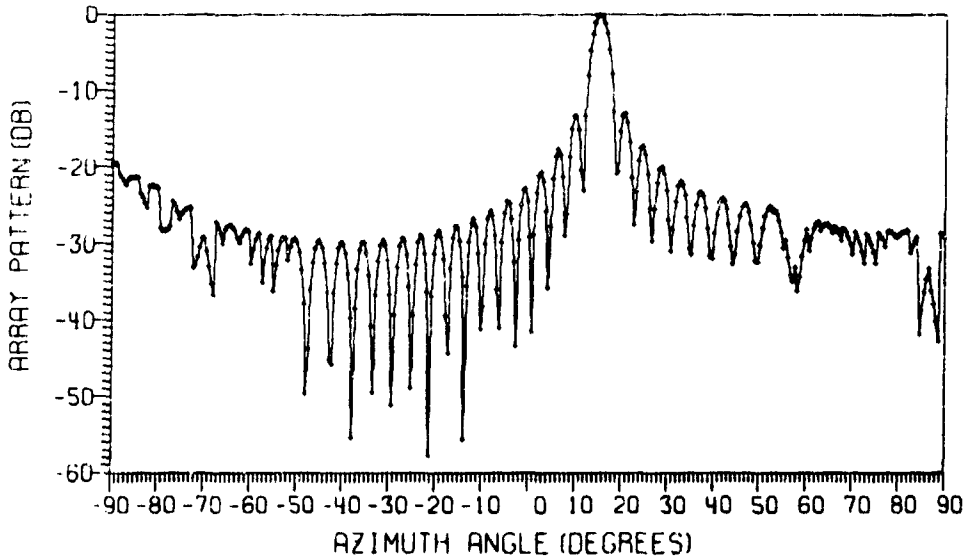

Fig. 51 — Radiation pattern of a projected uniformly spaced circular-arc array, scanned to 15° by applying exact phase steering

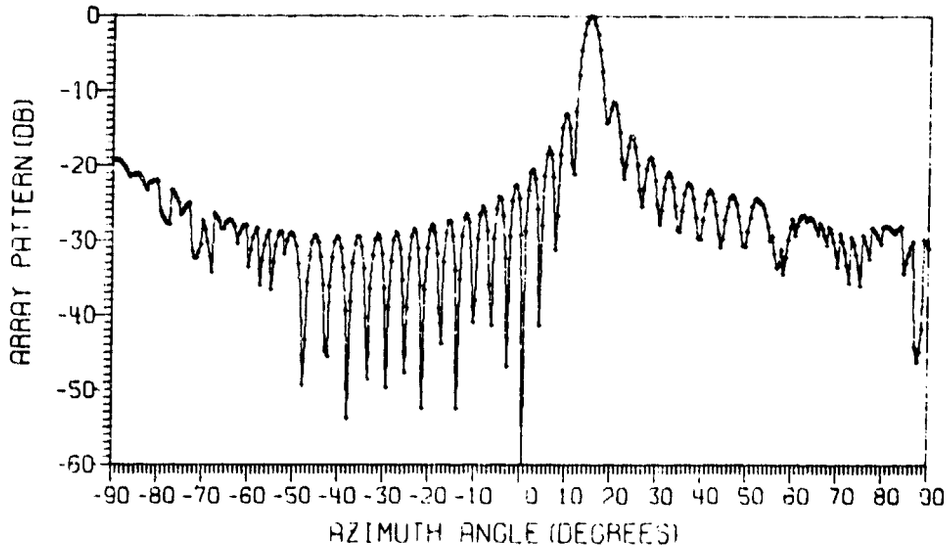

Fig. 52 — **Radiation pattern of a projected uniformly spaced circular-arc array, scanned to 15° by applying linear-array phase steering**

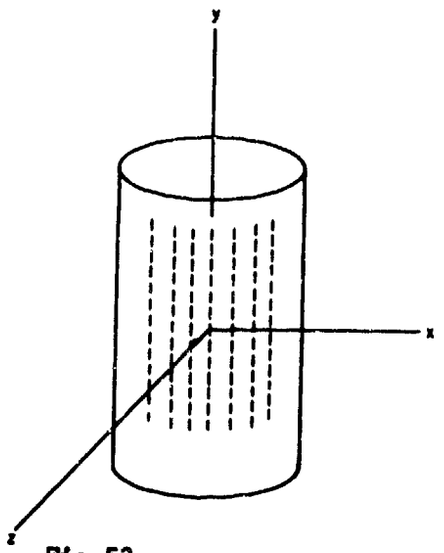

Fig. 53 — **Uniformly spaced circular-cylinder array**

Data Card 1: NE=0, NC=1, NP=361, LLL=2, LBP=1, NBP=11

Data Card 2: NCX=7, NRY=13, AX=3.0, AY=6.0, RX=5.1816, RY=0., LP=1

Data Card 3: FI(I)=0

Data Card 4: FIO=0., TAO=0., TAPI=-90°, TAPF=90°.

Using the subroutine ELAGPO for a doubly curved surface with uniformly spaced elements, the radiation pattern plotted by the computer is shown in Figure 54. The step changes noted in Figure 54 and some of the later figures are the result of the provision provided in the program which makes it possible to drop the element contribution whenever the element becomes invisible (due to the curved surface) from the point at which the radiation field is being computed.

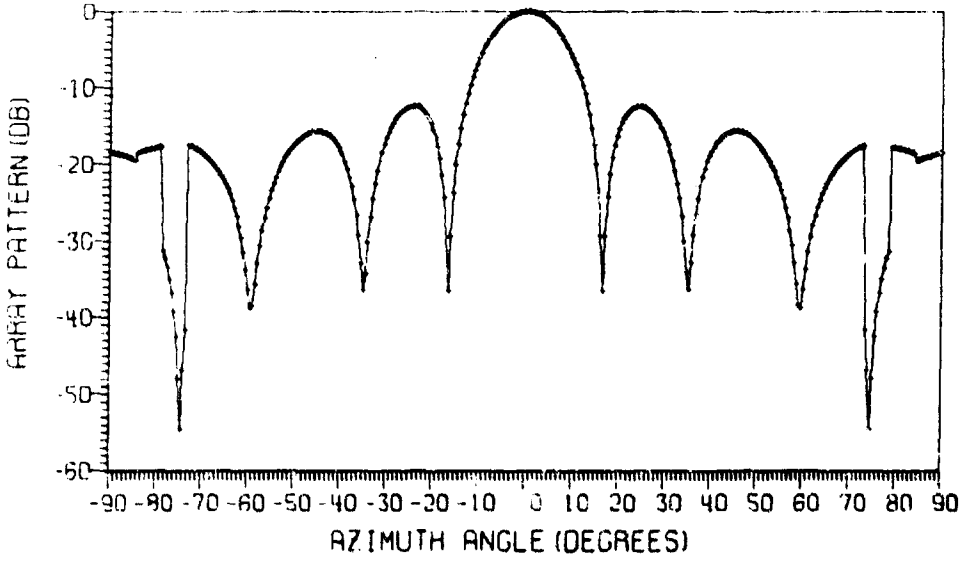

Figure 54 - Radiation pattern of a uniformly spaced circular-cylinder array

The fifth example is a 7-by-13-element, uniformly spaced planar array. The array apertures in the x and y directions are assumed to be the same as that of Example 4. The broadside pattern in the $\phi = 0$ plane for this planar array can be obtained using the same ELAGPO subroutine and data cards as those of Example 4 by simply changing the RX value to zero in Data Card 2. The radiation pattern for this planar array is shown in Figure 55.

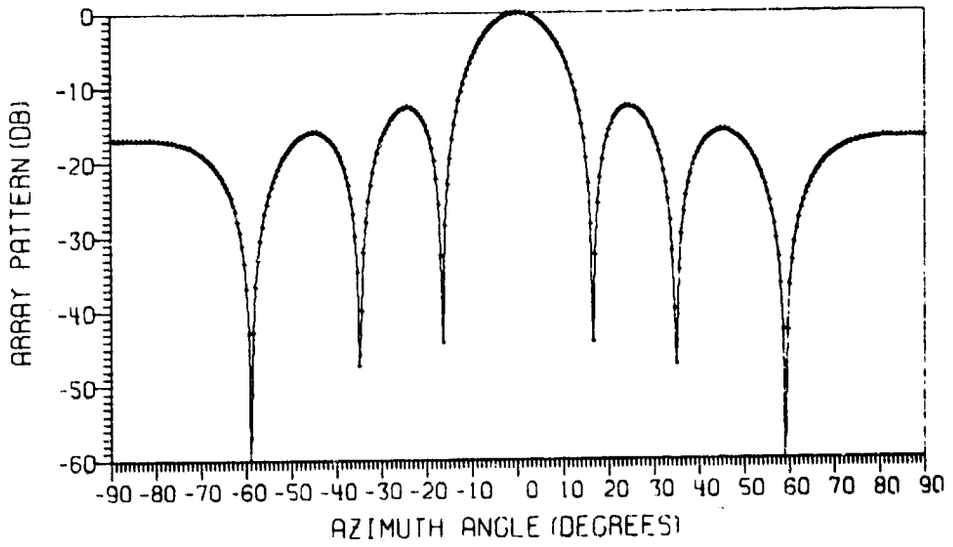

Figure 55. Radiation pattern of a uniformly spaced planar array

The sixth example is a 7-by-13-element array on a conic surface with a base radius of 137.46λ and a cone angle of 7°. There are seven rows, and each row contains 13 elements. The spacing between the rows is assumed to 0.5λ; the interelement spacing along the base arc is also assumed to be 0.5λ. It is assumed that the array elements are vertical dipoles and that a rectangular grid arrangement is used. The coordinate system applied to

this array is shown in Figure 56. The following values for the data cards are used to obtain a pattern in the $\phi = 0$ plane with zero scan angles:

Data Card 1: NE=0, NC=1, NP=361, LLL=2, LBP=1, NBP=11
Data Card 2: MM=7, RB=137.46, ARC=2.55, TC=7°, DX=0.5, DY=0.5, LP=1, LRT=0
Data Card 3: FI(I)=0
Data Card 4: FIO=0., TAO=0., TAPI=-90°, TAPF=90°.

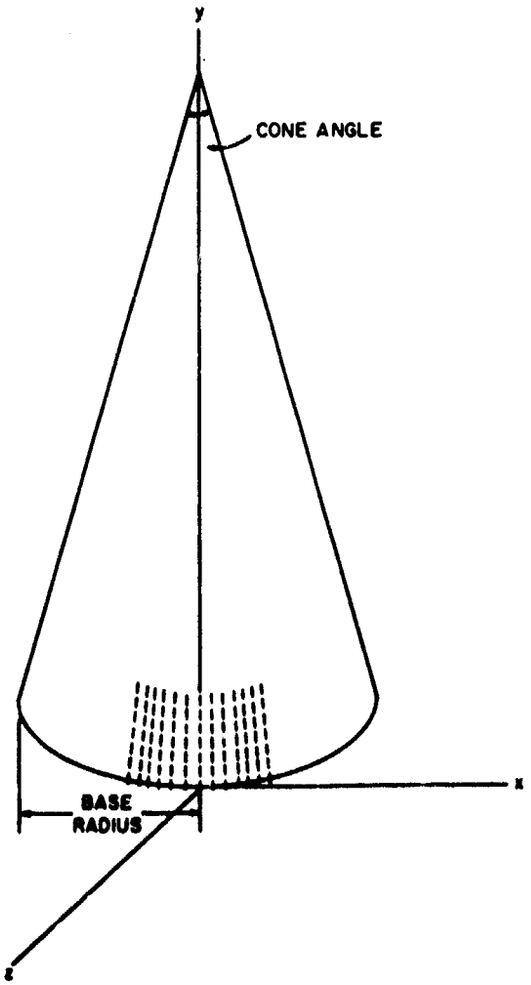

Figure 56. Conic-surface array

The radiation pattern, obtained by using these data cards and the subroutine ELAGPO for a conic surface, is shown in Figure 57. Because of the conic surface, there is a cross-polarization component which is plotted in the same figure as a separate curve. In this example, the crosspolarization component is quite low because the radius of curvature of the conic surface is large and the array surface approximates a planar surface.

The final example illustrates two additional and useful features of the subroutine ELAGPO for a conic surface. The first feature is that this subroutine can be used for the arrays on a circular cylinder by specifying the cone angle TC = 0. The second additional feature is that a triangular grid instead of a rectangular grid arrangement can be specified. In this example an array on a circular cylinder with a triangular grid is considered, as shown in Figure 58. To obtain a broadside pattern in the ϕ = 0 plane, the following data cards are used:

Data Card 1: NE=0, NC=1, NP=361, LLL=2, LBP=1, NBP=11
Data Card 2: MM=10, RB=5.1816, ARC=33.167, TC=0., DX=0.75, DY=.666, LP=1, LRT=1
Data Card 3: FI(I) = 0
Data Card 4: FIO=0., TAO=0., TAPI=-90°, TAPF=90°.

The radiation obtained by using these data cards with subroutine ELAGPO for a conic surface is shown in Figure 59. Because of the large value of DX(.75), the radiation pattern obtained by using a rectangular grid (not included here) will have high sidelobes. From Figure 59 it is clear that the triangular grid has the effect of reducing these sidelobes.

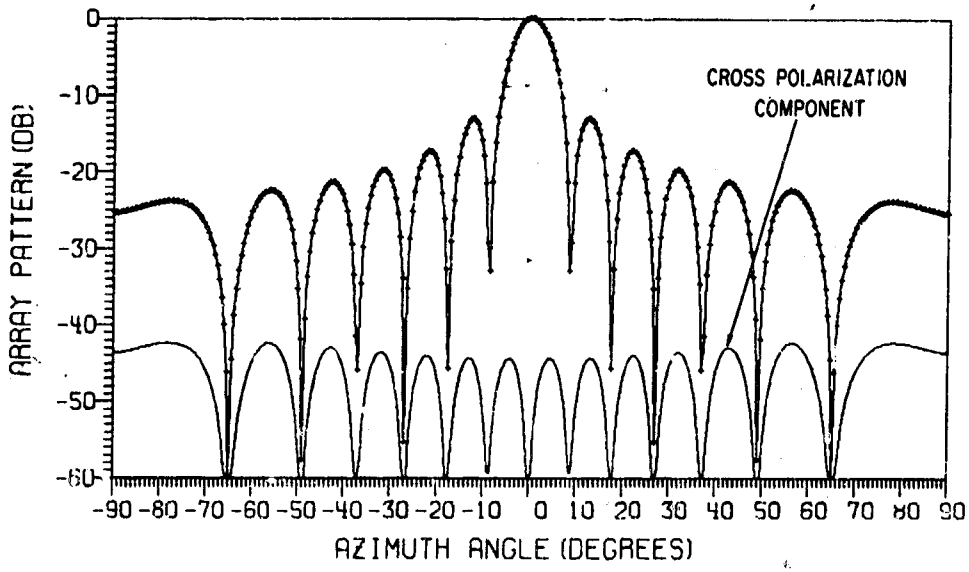

Figure 57. Radiation pattern of a conic-surface array

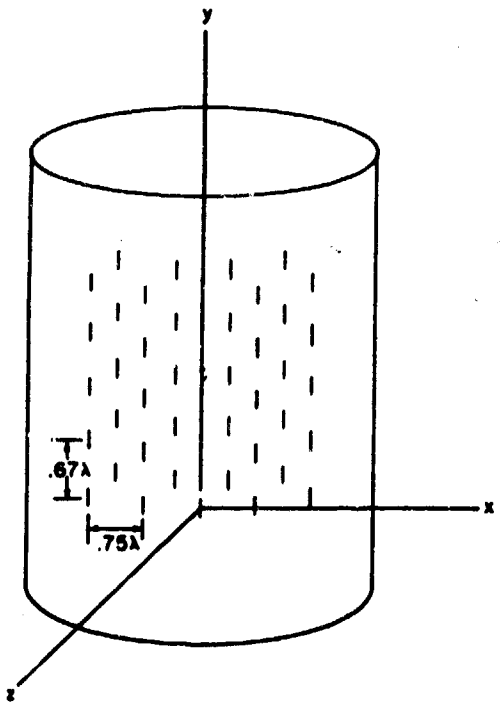

Figure 58. Triangular-grid array on a circular cylinder

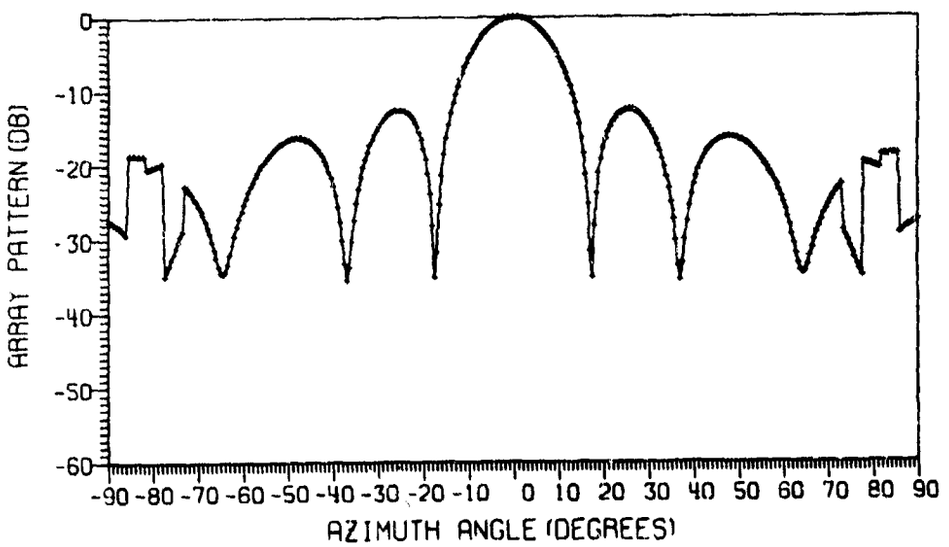

Figure 59. Radiation pattern of a triangular-grid array on a circular cylinder

APPENDIX A: DISCRETE APPROXIMATION

Suppose M identical elements are spaced on the cylinder at the angles

$$\alpha_p = \frac{2\pi}{M}(p+f)$$

where $p = 0, 1, \ldots M-1$, and f is some fraction of the spacing that defines the location of the first element with respect to the beam direction $\alpha = 0$. Let the excitation currents be

$$I(\alpha_p)\,\Delta\alpha = \frac{2\pi}{M}\sum_{n=0}^{N} I_n \cos n\,\alpha_p \tag{A-1}$$

The pattern of an element at α_p is

$$G(\varphi-\alpha_p) = \sum_{m=0}^{\infty} F_m \cos m(\varphi-\alpha_p) = \sum_{m=0}^{M} F_m \cos m(\varphi-\alpha_p) \tag{A-2}$$

The far-field pattern due to the M elements is thus

$$E_D(\varphi) = \sum_{p=0}^{M-1} I(\alpha_p)\Delta\alpha\, G(\varphi-\alpha_p)$$

$$= \frac{2\pi}{M} Kf(\theta) \sum_{p=0}^{M-1}\sum_{n=0}^{N} I_n \cos n\frac{2\pi(p+f)}{M} \sum_{m=0}^{M} F_m \cos m\left(\varphi - \frac{2\pi(p+f)}{M}\right) \tag{A-3}$$

$$= \frac{2\pi}{M} Kf(\theta) \sum_{n=0}^{N} I_n \sum_{m=0}^{M} F_m \sum_{p=0}^{M-1} \cos\frac{2\pi n(p+f)}{M}\left[\cos\frac{2\pi m(p+f)}{M}\cos m\varphi + \sin\frac{2\pi m(p+f)}{M}\sin m\varphi\right]$$

After consideration of the possible cases, one may show that

$$\sum_{p=0}^{M-1} \cos \frac{2\pi n\,(p+f)}{M} \cos \frac{2\pi m\,(p+f)}{M} = \frac{M}{\epsilon_n} \text{ if } m=n \text{ but } m+n \neq M$$

$$= \frac{M}{\epsilon_n} \cos 2\pi f \text{ if } m+n = M,\ m \neq n$$

$$= \frac{M}{2} + \frac{M}{2} \cos 2\pi f \quad \text{if } m=n \text{ and } m+n = M \tag{A-4}$$

$$= 0 \text{ otherwise}$$

Also, one may show that

$$\sum_{p=0}^{M-1} \cos \frac{2\pi n\,(p+f)}{M} \sin \frac{2\pi m\,(p+f)}{M} = \frac{M}{\epsilon_n} \sin 2\pi f \text{ if } m+n = M$$

$$= 0 \text{ otherwise} \tag{A-5}$$

Thus (A-3) may be written in the convenient form

$$E_D(\varphi) = 2\pi K f(\theta) \sum_{n=0}^{N} \frac{I_n F_n}{\epsilon_n} \cos n\varphi$$

$$+ 2\pi K f(\theta) \sum_{n=0}^{N} \frac{I_n}{\epsilon_n} F_{M-n} \left[\cos 2\pi f \cos (M-n)\varphi + \sin 2\pi f \sin (M-n)\varphi\right] \tag{A-6}$$

APPENDIX B

PROGRAM - COFLARAY

```
      PROGRAM CONFARRAY
      COMMON/1/PLTARRAY(254),FMAT(1000,3)
      COMMON/2/G(1000,3),W(1000,3)
      COMMON/3/RMAT(1000,3,3),DMAT(3,3),ENAT(3),TEMP(3)
      COMMON/4/FI(10)
      COMMON/5/DMATUP(3,3)
      COMMON/6/LG(3),A(3),B(3)
      DIMENSION CR(3),CI(3),BP(1000)
C
C ENTER PLOT FRAME PARAMETERS
      CALL PLOTS (PLTARRAY,254,18)
      XM=9.0
      YM=5.
      SY=2.
      SYM=SY+YM
      YSL=60.
      NY=60
C
C     ENTER RANDOM NUMBER SEED
      RS=TIMEF(X)
      CALL RANFSET(RS)
C
C INPUT DATA
C     G-ARRAY, THREE COORDINATE ROTATION ANGLES FOR EACH ELEMENT
C     W-ARRAY ELEMENT LOCATIONS
C     ROTATIONAL CONVENTION-CLOCKWISE FROM PRIMED TO UNPRIMED COORDINATE
C     IS CONSIDERED POSITIVE
C     ROTATIONAL SEQUENCES-X,Y,Z
C     LG ARRAY SECIFIES THE GROUND PLANE OF RADIATORS
C     LG(1)=1,LG(2)=LG(3)=0 ZY PLANE
C     LG(1)=LG(3)=0,LG(2)=1,XZ PLANE
C     LG(1=LG(2)=0,LG(3)=1,XY PLANE
C     NE-NUMBER OF ARRAY ELEMENT
C     NC-NUMBER OF ANTENNA PATTERN CUTS IN ANGLE FI PLANE
C     NP-NUMBER OF POINT OF ANTENNA PATTERN TO BE PLOTTED
C     LLL=0,SET PRINT-OUT FOR DIAGNOSTIC PURPOSE
C     IF LLL=1, PRINT ELEMENTS POSITIONS AND ROTATION ANGLES
C     IF LLL=2, PRINT PATTERN FUNCTION ONLY
C     IF LLL GREATER THAN 2 NO PRINT-OUT
C     LBP=0,APPROXIMATE BY A PLANAR ARRAY PHASE
C     LBP=1,WITH CORRECT CONFORMAL ARRAY PHASE
C     NBP, NO. OF PHSE SHIFT BITS,IF NBP.GT.10 CORRCET PHASES ARE USED
C     TAPI,PATTERN PLOT STARTING ANGLE
C     TAPF,PATTERN PLOT FINAL ANGLE
C
C ENTER INPUT DATA
      KK=0
 93   READ 100,NE,NC,NP,LLL,LBP,NBP
C
      IF(EOF,60)99,91
 91   IF(KK.EQ.0)GO TO 92
      CALL REZERO(XM)
 92   KK=1
      IF(NE.LE.0)GO TO 1
      READ 101,((W(I,J),I=1,NE),J=1,3)
      READ 101,((G(I,J),I=1,NE),J=1,3)
      READ 100,(LG(I),I=1,3)
      GO TO 2
 1    CALL FLAGPO(NE,LP)
```

```
 2     IF(LLL.GT.1)GO TO 201
       PRINT 104
       DO 202,I=1,3
 202   PRINT 102,(W(N,I),N=1,NE)
       PRINT 105
       DO 212 I=1,3
 212   PRINT 102,(G(N,I),N=1,NE)
 201   PI=3.14159265358979323846
       PI2=2.*PI
       ATR=PI/180.
C
C COMPUTE THE R-MATRIX
       DO 10 I=1,NE
  10   CALL COUTRF(I)
       IF(LLL.GT.0)GO TO 203
       DO 204 I=1,3
       DO 204 J=1,3
  204  PRINT 102,  (RMAT(L,I,J),L=1,NL,10)
C
C DETERMINE FIELD POINT ANGLES
  203  READ 101,(FI(I),I=1,NC)
  101  FORMAT( 8F10.6)
C
C ENTER SCAN ANGLES
       READ 101,FIO,TAO,TAPI,TAPF
       FIO=FIO*ATR
       TAO=TAO*ATR
       TAPIR=TAPI*ATR
       TAPFR=TAPF*ATR
       TAINC=(TAPFR-TAPIR)/(NP-1)
       TAAINC=TAINC/ATR
       JN=(NP-1)/3
       COTAO=COSF(TAO)
       SITAO=SINF(TAO)
       COFIO=COSF(FIO)
       SIFIO=SINF(FIO)
       XP=SITAO*COFIO
       YP=SITAO*SIFIO
       ZP=COTAO*LBP+1.0-LBP
       DO 70 K=1,NE
       BPK=W(K,1)*XP+W(K,2)*YP+ W(K,3)*ZP
       BPK=BPK-INTF(BPK)
       IF(NBP.GT.10) GOTO 73
       BP(K)=0.
       DO 71 N=1,NBP
       B1=1./2.**N
       IF(BPK.LE.B1)GO TO 72
       BPK=BPK-B1
       BP(K)=B1+BP(K)
  72   IF(N.NE.NBP)GO TO 71
       R=RANF(-1)
       IF(R.LT..5)GO TO 71
       BP(K)=B1+BP(K)
  71   CONTINUE
       GOTO 70
    73 BP(K)=BPK
  70   CONTINUE
C
C COMPUTE PATTERN
```

```
      DO 20 I=1,NC
      FI(I)=FI(I)*ATR
      TA=TAPIR
      COFIUP=COSF(FI(I))
      SIFIUP=SINF(FI(I))
      FNOR=0.
      DO 30 J=1,NP
      COTAUP=COSF(TA)
      SITAUP=SINF(TA)
      CALL DPRMAT(COFIUP,SIFIUP,COTAUP,SITAUP,DMATUP)
      IF(LLL.GT.0)GO TO 211
      JMOD=MOD(J,JN)
      IF(JMOD.NE.1)GO TO 211
      TAANG=TA/ATR
      PRINT 109,TAANG
      PRINT 102,((DMATUP(L,M),M=1,3),L=1,3)
 211  DO 31 L=1,3
 31   CR(L)=CI(L)=0.
      XF=SITAUP*COFIUP
      YF=SITAUP*SIFIUP
      ZF=COTAUP
C
C     SUM THE ELEMENT CONTRIBUTION
      DO 40 K=1,NE
      COFI=COFIUP
      SIFI=SIFIUP
      COTA=COTAUP
      SITA=SITAUP
C
C TRANSFER ANGEL FROM UNPRIMED COORDINATE TO PRIMED COORDINATE
      CALL ANGTRF(COFI,SIFI,COTA,SITA,K,LJG)
      IF(LLL.GT.0)GO TO 209
      KMOD=MOD(K,10)
      IF(KMOD.NE.1 .OR.JMOD.NE.1)GO TO 209
      PRINT 108,K
      PRINT 102,COFI,SIFI,COTA,SITA
      PRINT 102,(A(L),L=1,3),(B(L),L=1,3)
C
C  FORM D MATRIX
 209  IF(LJG.LE.0)GO TO 40
      CALL DPRMAT(COFI,SIFI,COTA,SITA,DMAT)
      IF(LLL.GT.0)GO TO 205
      IF(KMOD.NE.1 .OR.JMOD.NE.1)GO TO 205
      PRINT 102,((DMAT(L,M),M=1,3),L=1,3)
C
C ENTER ELEMENT PATTERN FUNCTION
 205  CALL ELPAT(COFI,SIFI,COTA,SITA,EP)
C
C PERFORM MATRIX MULTIPLICATIONS
      CALL MATMUT(K)
      IF(LLL.GT.0)GO TO 207
      IF(KMOD.NE.1 .OR.JMOD.NE.1)GO TO 207
      PRINT 102,(TEMP(L),L=1,3)
C
C FIND THE PHASE
 207  PHASE=      W(K,1)*XF+W(K,2)*YF+W(K,3)*ZF
      PHASE=PHASE-INTF(PHASE)
      PHASL=PI2*(PHASE-BP(K))
      PRE=COSF(PHASL)
```

```
      PIM=SINF(PHASE)
C
C FORM PATTERN FUNCTION
      DO 41 L=1,3
      CR(L)=CR(L)+TEMP(L)*PRE
 41   CI(L)=CI(L)+TEMP(L)*PIM
 40   CONTINUE
      DO 32 L=1,3
      FMAT(J,L)=CR(L)**2+CI(L)**2
 32   IF(FMAT(J,L).GT.FNOR)FNOR=FMAT(J,L)
 30   TA=TA+TAINC
      XSL=TAPF-TAPI
      NX=XSL
      IF(I.EQ.1)GO TO 21
      CALL REZERO
 21   CALL FRAME(XM,YM,XSL,YSL,NX,NY,TAPI)
      IF(LLL.GT.2)GO TO 213
      PRINT 107,FNOR
C
C PLOT ANTENNA PATTERN
 213  DO 60 K=1,3
      TA=TAPI
      LM=0
      DO 50 L=1,NP
      FMAT(L,K)=FMAT(L,K)/FNOR
      IF(K.LE.1)GO TO 50
      IF(FMAT(L,K).GT.0.0000001)GO TO 52
      FMAT(L,K)=-YSL
      GO TO 53
 52   FMAT(L,K)=10.*ALOG10(FMAT(L,K))
 53   Y=YM*(1.+FMAT(L,K)/YSL)+SY
      X=(TA+90.0)*XM/XSL
      IF(Y.GT.SY)GO TO 56
      Y=SY
      GO TO 54
 56   IF(Y.GT.SYM)Y=SYM
      IF(K.GT.2)GO TO 54
      IF(LM.GT.0)GO TO 55
      CALL SYMBOL(X,Y,.06,3,0.,-1)
      GO TO 57
 55   CALL SYMBOL(X,Y,.06,3,0.,-2)
      GO TO 57
 54   IF(LM.GT.0)GO TO 51
      CALL PLOT(X,Y,3)
      GO TO 57
 51   CALL PLOT(X,Y,2)
 57   LM=1
 50   TA=TA+TAAINC
      IF(LLL.GT.2)GO TO 60
      PRINT 103,K
      PRINT 106,(FMAT(J,K),J=1,NP)
 60   CONTINUE
 20   CONTINUE
      PRINT 110,(BP(K),K=1,NE)
  110 FORMAT(//,10X,*STEERING PHASE*,//,(10X,10F12.6))
      GO TO 93
 99   CALL STOP PLOT
 100  FORMAT(615)
 102  FORMAT( /,(10X,10E12.3))
 103  FORMAT(//,20X,*ARRAY PATTERN (DB)*,5X,*K=*,I5)
 104  FORMAT(//,20X,*ELEMENT LOCATIONS*)
 105  FORMAT(//,20X,*ELEMENT ROTATION ANGLES*)
 106  FORMAT(//,(10X,10F12.6))
 107  FORMAT(//,10X,*ARRAY NORMALIZING FACTOR*,5X,F15.6)
 108  FORMAT(//,10X,*ELEMENT*,I5)
 109  FORMAT(//,20X,*AZIMUTH ANGLE=*,F6.2)
      END
```

```
      SUBROUTINE ELAGPO(NE,LP)
C     THIS SUBROUTINE IS FOR A DOUBLY CURVED SURFACE
      COMMON/2/G(1000,3),W(1000,3)
      COMMON/6/LG(3),A(3),B(3)
C     GROUND PLANE IS ON XZ PLANE
      LG(1)=LG(3)=0
      LG(2)=1
C     NRY, NO OF ROWS IN Y DIRECTION
C     NCX, NO OF COLUMN IN X DIRECTION
C     AX, X-DIRECTION APERTURE, IN WAVELENGTHS
C     AY, Y-DIRECTION APERTURE, IN WAVELENGTHS
C     RX, RADIUS OF CURVATURE IN X DIRECTION
C     RY, RADIUS OF CURVATURE IN Y DIRECTION
      PI=3.14159265358979323846
      PIH=PI/2.
C     LP=0, HORIZONTAL DIPOLES, LP=1, VERTICAL DIPOLES
C     THE FIRST ELEMENT STARTED AT -X AND -Y
      READ 100,NCX,NRY,AX,AY,RX,RY,LP
  100 FORMAT(2I5,4F10.6,I2)
      PRINT 101,NCX,NRY,AX,AY,RX,RY,LP
  101 FORMAT(10X,2I5,4F10.4,I5)
      IF(RY.EQ.0.)GO TO 2
      ARCYH=ASINF(.5*AY/RY)
      ARCY=2.*ARCYH
      ARCYINC=ARCY/(NRY-1)
    2 IF(RX.EQ.0.)GO TO 3
      ARCXH=ASINF(.5*AX/RX)
      ARCX=2.*ARCXH
      ARCXINC=ARCX/(NCX-1)
    3 IF(NCX-1.EQ.0)GO TO 8
      DX=AX/(NCX-1)
    8 IF(NRY-1.EQ.0)GO TO 9
      DY=AY/(NRY-1)
    9 AUGY=AUGX=0.
      LL=0
      DO 10 I=1,NRY
      IF(RY.GT.0.)GO TO 4
      YS=(I-1)*DY-AY/2.
      ZS=0.
      AUGYY=0.
      GO TO 5
    4 AUGY=(I-1)*ARCYINC-ARCYH
      YS=RY*SINF(AUGY)
      ZS=RY*COSF(AUGY)-RY
      AUGYY=AUGY
    5 DO 10 J=1,NCX
      LL=LL+1
      IF(RX.GT.0.)GO TO 6
      XS=(J-1)*DX-AX/2.
      ZXS=0.
      AUGXX=0.
      GO TO 7
    6 AUGX=(J-1)*ARCXINC-ARCXH
      XS=RX*SINF(AUGX)
      ZXS=RX*COSF(AUGX)-RX
      AUGXX=AUGX
    7 W(LL,1)=XS
      W(LL,2)=YS
      W(LL,3)=ZS+ZXS
```

* When the array elements are uniformly spaced.

```
      IF(LP.GT.0)GO TO 1
      G(LL,1)=PIH+AUGX
      G(LL,2)=AUGYY
      G(LL,3)=PIH
      GO TO 10
1     G(LL,1)=PIH-AUGY
      G(LL,2)=AUGXX
      G(LL,3)=0.
10    CONTINUE
      NE=LL
      RETURN
      END
```

```
      SUBROUTINE ELAGPO(NE,LP)
C     THIS SUBROUTINE IS FOR A DOUBLY CURVED SURFACE
      COMMON/2/G(1000,3),W(1000,3)
      COMMON/6/LG(3),A(3),B(3)
C     GROUND PLANE IS ON XZ PLANE
      LG(1)=LG(3)=0
      LG(2)=1
C     NRY,NO OF ROWS IN Y DIRECTION
C     NCX, NO OF COLUMN IN X DIRECTION
C     AX, X-DIRECTION APERTURE, IN WAVELENGTHS
C     AY, Y-DIRECTION APERTURE, IN WAVELENGTHS
C     RX, RADIUS OF CURVATURE IN X DIRECTION.
C     RY, RADIUS OF CURVATURE IN Y DIRECTION
      PI=3.14159265358979323846
      PIH=PI/2.
C     LP=0, HORIZONTAL DIPOLES, LP=1, VERTICAL DIPOLES
C     THE FIRST ELEMENT STARTED AT -X AND -Y
      READ 100,NCX,NRY,AX,AY,RX,RY,LP
  100 FORMAT(2I5,4F10.6,I2)
      PRINT 101,NCX,NRY,AX,AY,RX,RY,LP
  101 FORMAT(10X,2I5,4F10.4,I5)
      IF(NRY-1.EQ.0) GOTO8
      DY=AY/(NRY-1)
      GOTO 20
    8 DY=0.0
   20 IF(NCX-1.EQ.0) GOTO 9
      DX=AX/(NCX-1)
      GOTO 22
    9 DX=0.0
   22 AUGY=AUGX=0.0
      LL=0
      DO 10 I=1,NRY
      YS=(I-1)*DY-AY/2.0
      IF(RY.GT.0.) GOTO 4
      ZS=0.0
      AUGYY=0.0
      GOTO 5
    4 AUGY=ASINF(YS/RY)
      ZS=RY*COSF(AUGY)-RY
      AUGYY=AUGY
    5 DO 10 J=1,NCX
      LL=LL+1
      XS=(J-1)*DX-AX/2.0
      IF(RX.GT.0.) GOTO 6
      ZXS=0.0
      AUGXX=0.0
      GOTO 7
    6 AUGX= ASINF(XS/RX)
      ZXS=RX*COSF(AUGX)-RX
      AUGXX=AUGX
    7 W(LL,1)=XS
      W(LL,2)=YS
      W(LL,3)=ZS+ZXS
      IF(LP.GT.0)GO TO 1
      G(LL,1)=PIH+AUGX
      G(LL,2)=AUGYY
      G(LL,3)=PIH
      GO TO 10
    1 G(LL,1)=PIH-AUGY
```

*When the array elements are projected uniformly spaced.

```
      G(LL,2)=AUGXX
      G(LL,3)=0.
10    CONTINUE
      NE=LL
      RETURN
      END
```

```
      SUBROUTINE ELAGPO(NE,LP)
C     THIS SUBROUTINE IS FOR CONIC ARRAY
      COMMON/2/G(1000,3),W(1000,3)
      COMMON/6/LG(3),A(3),B(3)
C     MM, NUMBER OF ROWS
C     RB, BASE RADIUS
C     ARC, CONE ARCH
C     TC CONE ANGLE
C     DX, SPACING IN X-DIRECTION
C     DY, SPACING IN Y DIRECTION
C     LP=0, HORIZONTAL DIPOLES, LP=1, VERTICAL DIPOLES
C     LRT=1, TRIANGULAR GRID
C     LRT=0, RECTANGULAR GRID
      READ 100,MM,RB,ARC,TC,DX,DY,LP,LRT
  100 FORMAT(I5,5F10.6,2I2)
      PRINT 101,MM,RB,ARC,TC,DX,DY,LP,LRT
  101 FORMAT(10X,I5,5F10.4,2I5)
C     GROUND PLANE IS ON XZ PLANE
      LG(1)=LG(3)=0
      LG(2)=1
    2 PI=3.14159265358979323846
      PIH=PI/2.
      ATR=PI/180.
      TC=TC*ATR
      ARC=ARC*ATR
      ARCH=ARC/2.
      TTC=TANF(TC)
      I=0
      DO 10 M=1,MM
      IMOD=MOD(M-1,2)*LRT
      R=RB-(M-1)*DY*TTC
      RL=R*ARC
      D=R*SINF(ARCH)
      NN=RL/DX+1
      ARCINC=ARC/(NN-1)
      NN=NN-IMOD
      DO 10 J=1,NN
      I=I+1
      AUG=(1.-J-.5*IMOD)*ARCINC+ARCH
      W(I,1)=COSF(PIH-AUG)*R
      W(I,2)=DY*(M-1)
      W(I,3)=SINF(PIH-AUG)*R-D
      IF(LP.GT.0)GO TO 3
      G(I,1)=AUG+PIH
      G(I,2)=TC
      G(I,3)=PIH
      GO TO 10
    3 G(I,1)=PIH-TC
      G(I,2)=AUG
      G(I,3)=0.
   10 CONTINUE
      NE=1
      RETURN
      END
```

```
      SUBROUTINE COORTRF(L)
      COMMON/1/PLTARRAY(254),FMAT(1000,3)
      COMMON/2/G(1000,3),W(1000,3)
      COMMON/3/RMAT(1000,3,3),DMAT(3,3),EMAT(3),TEMP(3)
      DIMENSION A(3,3),B(3,3),C(3,3)
      COX=COSF(G(L,1))
      COY=COSF(G(L,2))
      COZ=COSF(G(L,3))
      SIX=SINF(G(L,1))
      SIY=SINF(G(L,2))
      SIZ=SINF(G(L,3))
C FIND THE X RATATION MATRIX
      C(1,1)=1.
      C(1,2)=C(1,3)=C(2,1)=C(3,1)=0.
      C(2,2)=C(3,3)=COX
      C(3,2)=SIX
      C(2,3)=-SIX
C FIND THE Y ROTATION MATRIX
      B(1,1)=B(3,3)=COY
      B(1,3)=SIY
      B(3,1)=-SIY
      B(1,2)=B(2,1)=B(2,3)=B(3,2)=0.
      B(2,2)=1.
C FORM MATRIX PRODUCT
      DO 10 I=1,3
      DO 10 J=1,3
      A(I,J)=0.
      DO 10 K=1,3
 10   A(I,J)=A(I,J)+B(I,K)*C(K,J)
C FORM Z-AXIS ROTAT+ON MATRIX
      C(1,1)=C(2,2)=COZ
      C(2,1)=SIZ
      C(1,2)=-SIZ
      C(1,3)=C(3,1)=C(3,2)=C(2,3)=0.
      C(3,3)=1.
      DO 20 I=1,3
      DO 20 J=1,3
      RMAT(L,I,J)=0.
      DO 20 K=1,3
 20   RMAT(L,I,J)=RMAT(L,I,J)+C(I,K)*A(K,J)
      RETURN
      END
```

```
      SUBROUTINE DPRMAT(COFI,SIFI,COTA,SITA,DMAT)
      DIMENSION DMAT(3,3)
      DMAT(1,1)=SITA*COFI
      DMAT(1,2)=COTA*COFI
      DMAT(1,3)=-SIFI
      DMAT(2,1)=SITA*SIFI
      DMAT(2,2)=COTA*SIFI
      DMAT(2,3)=COFI
      DMAT(3,1)=COTA
      DMAT(3,2)=-SITA
      DMAT(3,3)=0.
      RETURN
      END
```

```
      SUBROUTINE ANGTRF(COFI,SIFI,COTA,SITA,L,LJG)
      COMMON/3/RMAT(1000,3,3),DMAT(3,3),EMAT(3),TEMP(3)
      COMMON/6/LG(3),A(3),B(3)
      LJG=1
      B(1)=SITA*COFI
      B(2)=SITA*SIFI
      B(3)=COTA
      DO 20 I=1,3
      A(I)=0.
      DO 10 K=1,3
10    A(I)=A(I)+RMAT(L,K,I)*B(K)
      IF(A(I).GE.0. .OR.LG(I).LT.1)GO TO 20
      LJG=0
      GO TO 9
20    CONTINUE
      COTA=A(3)
      IF(ABS(COTA).GT.1.)COTA=SIGN(1.,A(3))
      SITA=SQRT(1.-COTA**2)
      IF(ABS(A(1)).GT.1.E-10)GO TO 1
      COFI=0.
      SIFI=1.
      GO TO 2
1     TGFI=A(2)/A(1)
      COFI=SQRT(1./(1.+TGFI**2))
      SIFI=SQRT(1.-COFI**2)
2     COFI=SIGNF(COFI,A(1))
      SIFI=SIGNF(SIFI,A(2))
99    RETURN
      END
```

```
      SUBROUTINE ELPAT(COFI,SIFI,COTA,SITA,LP)
      COMMON/3/RMAT(1000,3,3),DMAT(3,3),EMAT(3),TEMP(3)
      EMAT(1)=0.
      EMAT(2)=-SITA*(LP-1)
      EMAT(3)=SITA*LP
      RETURN
      END
```

```
      SUBROUTINE MATMUT(L)
      COMMON 1/PLTARRAY(254),FMAT(1000,3)
      COMMON/3/RMAT(1000,3,3),DMAT(3,3),EMAT(3),TEMP(3)
      COMMON/5/DMATUP(3,3)
      DO 10 I=1,3
      TEMP(I)=0.
      DO 10 J=1,3
10    TEMP(I)=TEMP(I)+DMAT(I,J)*EMAT(J)
      DO 20 I=1,3
      EMAT(I)=0.
      DO 20 J=1,3
20    EMAT(I)=EMAT(I)+RMAT(L,I,J)*TEMP(J)
      DO 30 I=1,3
      TEMP(I)=0.
      DO 30 J=1,3
30    TEMP(I)=TEMP(I)+DMATUP(J,I)*EMAT(J)
      RETURN
      END
```

```
      SUBROUTINE FRAME(XM,YM,XSL,YSL,NX,NY,TAPI)
C NX,NUMBER OF DIVISIONS ON X-AXIS
C NY,NUMBER OF DIVISIONS ON Y-AXIS
C YM,MAX LENGTH OF Y-AXIS IN INCH
C XM,MAX LENGTH OF X-AXIS IN INCH
C SY=SHIFT OF ORIGIN ON Y-AXIS
C HN= HEIGHT OF LABELING CHARACTER IN MULTIPLES OF 0.035
CXSL,YSL-X-AXIS,Y-AXIS SCALE
C LL=1,FOR DB SCALE,LL=0,FOR ABSOLUTE VALUE
      COMMON/1/PLTARRAY(254),FMAT(1000,3)
      SY=2.
      HN=5.
      YMSY=YM+SY
      HLAB=HN*.035
      HLAS=HLAB+.035
      WLAB=4.*HLAB/7.
      XSCL=XSL/NX
      YSCL=YSL/NY
      DY=YM/NY
      Y=SY
      NNY=NY+1
      CALL PENCHG(12)
      CALL PLOT(0.,SY,3)
      CALL PLOT(XM,SY,2)
      CALL PLOT(XM,YMSY,2)
      CALL PLOT(0.,YMSY,2)
      CALL PLOT(0.,SY,2)
      CALL PENCHG(11)
      DO 10 J=1,NNY
      CALL PLOT(0.,Y,3)
      MODY=MOD(J-1,2
      IF(MODY.NE.0)GO TO 11
      CALL PLOT(-.2,Y,2)
      A=YSCL*(J-1)-YSL
      CALL NUMBER(-7.5*WLAB,Y-HLAB/2.,HLAB,A,0.,4HF4.0)
      GO TO 10
11    CALL PLOT(-.1,Y,2)
10    Y=Y+DY
      X=0.
      DX=XM/NX
      NNX=NX+1
      DO 20 K=1,NNX
      CALL PLOT(X,SY,3)
      MODX=MOD(K-1,10)
      IF(MODX.NE.0)GO TO 21
      CALL PLOT(X,SY-.2,2)
      A=(K-1)*XSCL+TAPI
      CALL NUMBER(X-3.5*WLAB,SY-HLAB*2.5,HLAB,A,0.,4HF4.0)
      GO TO 20
21    CALL PLOT(X,SY-.1,2)
20    X=X+DX
      CALL SYMBOL(.5*XM-20.5*WLAB,-5.*HLAB+SY,HLAS,22HAZIMUTH ANGLE(DEGR
     (EES),0.,22)
33    CALL SYMBOL (-9.0*WLAB,YM/2.+SY-13.7*WLAB,HLAS,17HARRAY PATTERN(DB
     (),90.,17)
32    CALL PLOT(0.,0.,3)
      END
```

```
      SUBROUTINE REZERO(XM)
      COMMON/1/PLTARRAY(254),FMAT(1000,3)
      CALL PLOT(XM+5.0,0.,-3)
99    END
```

```
      SUBROUTINE PENCHG(IP)
      RETURN
      END
```

CHAPTER 2

APERTURE SYNTHESIS

2.0 THE SYNTHESIS PROBLEM

Although some conformal arrays are used to provide omni-azimuth coverage, more often the objective is to produce a pencil beam for communications, radar, etc. Both fixed beams and electronically scanned beams are of interest. The desirable pattern is often a narrow beam with low sidelobes and sometimes a difference pattern with low sidelobes. The narrowest beam-width for a given sidelobe level is produced by a Chebyshev pattern; DuHamel (1951) developed a methodology of calculating the coefficients for ring arrays. However, equal sidelobe arrays tend to have a high Q so it is generally desirable to utilize a tapered sidelobe envelope in order to make the array excitation robust. The one-parameter modified sin x/x space factor developed by Taylor (see Hansen, 1964) is often used for arrays. This can be applied to circular arrays in several ways, by representing the array as a Fourier series, as a Bessel series, or as a polynomial. Then the coefficients are determined from the Chebyshev polynomial (Taylor, 1952; Tseng and Cheng, 1968). As in the case of linear arrays, a tapered amplitude excitation is required. If the beam must be electronically scanned, then the tapered excitation must be rotated, unless a mechanical coupler such as a goniometer is used. There have been attempts to reduce sidelobes via phase adjustments alone, but these are not satisfactory (Coleman, 1970; Goto and Tsunoda, 1977; Watanabe et al, 1980).

Sidelobe level and envelope taper are generally the qualities most important in array patterns. It is, however, possible to maximize the directivity or some other performance index. When continuous apertures are optimized, a constraint relationship is

needed, but with an array the constraint is provided by the fixed number of elements. When the array index is expressed as a ratio of quadratic Hermitian forms, it can be maximized and any combination of index parameters can be used (Cheng and Tseng, 1967). Difference pattern parameters such as slope (Powers, 1967) or directivity (Bayliss, 1968) can also be maximized at the expense of sidelobe level.

For an array on a cylinder, the pattern can be synthesized by using a constituent linear array along the axis and a constituent array in azimuth. However, as pointed out in Chapter One, the cylindrical array excitation is nonseparable. That is, to produce a given pattern (sidelobe level), the required excitation changes with angle between the pattern plane and cylinder axis. Arrays on surfaces of other shapes are even more difficult to handle. For spherical arrays the pattern may be expanded in a spherical harmonic series and the array coefficients determined from this. This is a laborious but straight forward procedure. A similar procedure can be used for conical arrays, but in the case of a cone it is not possible to cover the surface with a uniformly spaced lattice of elements. For both cases, the harmonic series approach to pattern synthesis becomes unwieldy when the radius of the sphere or cone base becomes large in wavelengths. For these cases, which include most practical arrays, a projective synthesis method is more useful. In this projective method, which is discussed in detail in the rest of this chapter for conical arrays, a fixed beam virtual planar array is located at the base of the cone with the planar array axis pointed in the desired beam direction. Using the Equivalence Principle of Schelkunoff the field on the cone can then be determined.

2.1 Projective Synthesis

In previous studies (Kummer, et al 1970, 1971, 1973; Munger et al, 1974), an equivalence principle was applied to the problem of determining the distribution of sources on a cone to produce a prescribed pattern. By this method, more conventional sources such as planar or linear arrays are replaced by sources on a conformal surface such as a cone. The method and patterns synthesized by it are reviewed in this section.

The problem of interest is that of forming various steerable antenna patterns by distributing sources over the surface of a vehicle. The patterns that are desirable are essentially those that would be obtained from a circular or an elliptical planar aperture. The beam would be steered electronically.

The initial problem is to produce the pattern of a conventional antenna such as is illustrated in Figure 1, by sources on an aerodynamic surface. The conventional antenna is represented by a source distribution $\bar{J}_i$, $\bar{M}_i$ of electric and magnetic currents that produce the desired fields $\bar{E}$, $\bar{H}$ as illustrated in Figure 2.

Figure 1. Array with conventional pattern.

Fig. 2. Sources & resulting fields

If the actual sources are surrounded by a closed mathematical surface S, the fields $\bar{E}$, $\bar{H}$ exterior to S will result if the actual sources are replaced by equivalent sources $\bar{J}_s$ and $\bar{M}_s$ on S where

$$\bar{J}_s = \bar{n} \times \bar{H} \tag{1a}$$

$$\bar{M}_s = \bar{E} \times \bar{n} \tag{1b}$$

and $\bar{n}$ is the exterior unit normal to S as illustrated in Figure 3 (Harrington, 1961)

The equivalent sources produce no fields within S. Consequently, the mathematical surface S may be replaced by a perfectly conducting surface that lies just inside the equivalent source currents $\bar{J}_s$ and $\bar{M}_s$ without affecting the external fields

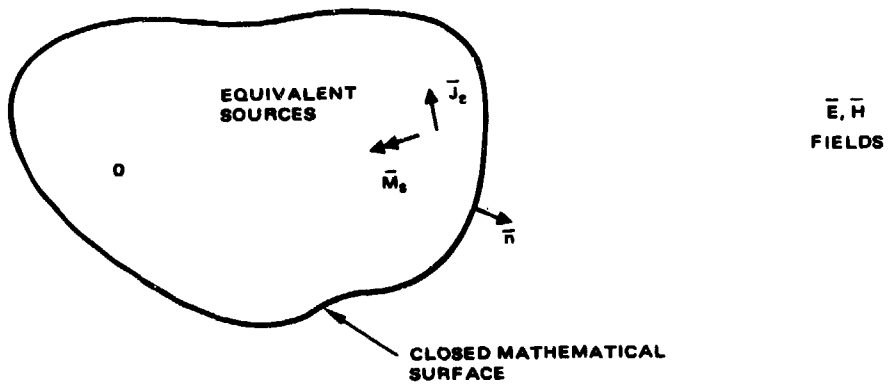

Figure 3. Equivalent sources on mathematical surface.

$\bar{E}$, $\bar{H}$ as shown in Figure 4. The perfectly conducting surface short circuits the electric source currents. Therefore, the total field outside the surface may then be found using only the magnetic currents $\bar{M}_s$ radiating in the presence of the conductor as shown in Figure 5.

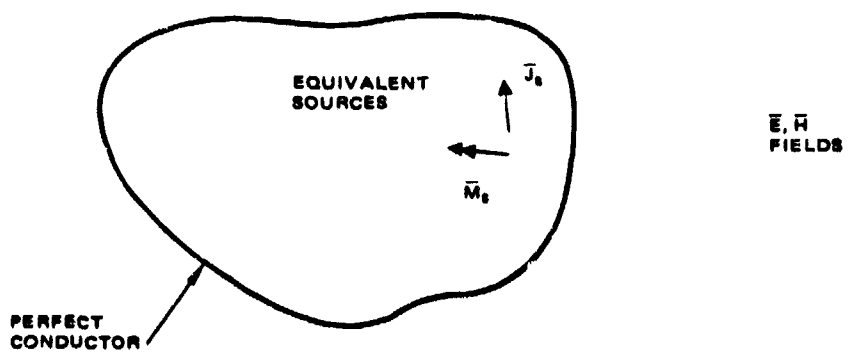

Figure 4. Equivalent sources on conducting surface

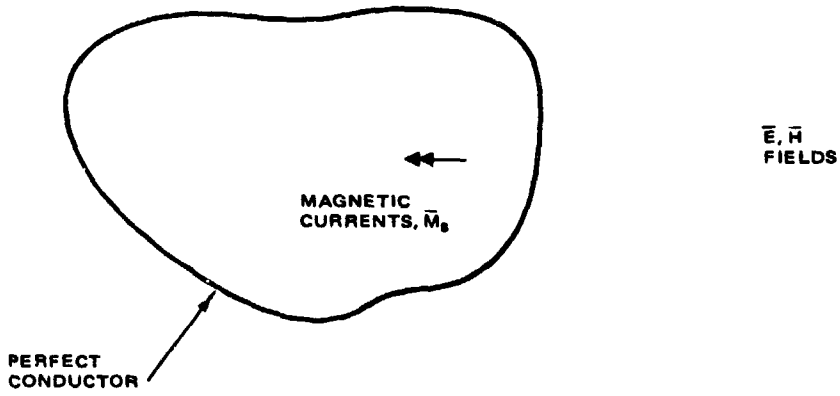

Figure 5. Equivalent magnetic sources on conducting surface

Consequently, if the proper equivalent magnetic source currents can be synthesized on the conducting surface, the original field will result at all points exterior to the surface. In the case of interest, the original source is a planar array and the metal surface is a conical or ogival surface. The magnetic current sheets are surface distributions of magnetic dipoles. A magnetic dipole can be approximated by slots on the metallic surface. By proper orientation and excitation of slots on the metallic surface, the desired exterior field can then be approximated. The required source distribution is known exactly since the initial fields are known. In the following discussion this approach is applied to finding the equivalent sources on a cone to reproduce the pattern of a planar array.

2.1.1 Description of Reference Antenna

The antenna utilized in determining the sources on a cone that are equivalent to a planar array is illustrated in Figure 6. It is a circular planar array of parallel slots that may

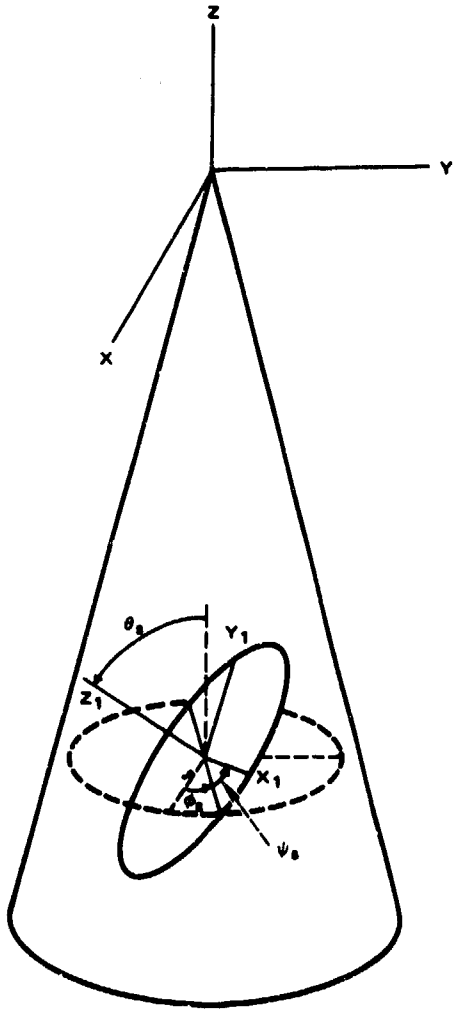

Figure 6. Planar array located within conical surface

be oriented arbitrarily within the conical surface. Its pivotal point is located far enough from the cone apex to permit arbitrary angular positioning of the array without intersecting the conical surface.

It is evident that the positioning of the equivalent planar array in Figure 6 does not take full advantage of the total

conical surface when the beam is pointing directly through the cone tip. However, this arrangement is a relatively simple one that provides an invariant pattern as the beam direction is changed. It is possible to take advantage of the total conical surface as the beam is moved through the cone tip by making the diameter of the equivalent planar array larger. The array may be moved back along the cone axis as a function of beam position so that the equivalent planar array just fills the cone base when it is looking through the cone tip.

2.1.2 Near Field of Planar Slot Array

In accordance with the field equivalence principle, the free space pattern of this array can be approximated by magnetic sources on the conducting cone that approximate the electric field strength that would be produced over the conical surface by the array. The coordinate system fixed with respect to the planar array is a rectangular system denoted by x_1, y_1, z_1, with its origin at the array center. The slots are directed parallel to the y_1 axis. In this coordinate system, the rectangular components of the electric field strength from a y_1 directed slot of length ℓ, located at x_{1a}, y_{1a}, 0 are

$$E_{x1}^{s} = -\frac{j\,V\exp(-jkr_{1a})}{\pi r_{1a}}\left[\frac{\cos\left(k\frac{\ell}{2}\frac{(y_1 - y_{1a})}{r_{1a}}\right) - \cos\left(k\frac{\ell}{2}\right)}{\left[(x_1 - x_{1a})^2 + z_1^2\right]}\right] r_{1a} z_1 \tag{2a}$$

$$E_{y1}^{s} = 0 \tag{2b}$$

$$E_{z1}^{s} = \frac{j\,V\exp(-jkr_{1a})}{\pi r_{1a}}\left[\frac{\cos\left(k\frac{\ell}{2}\frac{(y_1 - y_{1a})}{r_{1a}}\right) - \cos\left(k\frac{\ell}{2}\right)}{\left[(x_1 - x_{1a})^2 + z_1^2\right]}\right] r_{1a}(x_1 - x_{1a}) \tag{2c}$$

where

$$r_{1a} = \sqrt{(x_1 - x_{1a})^2 + (y_1 - y_{1a})^2 + z_1^2} \tag{3a}$$

$$k = 2\pi/\lambda \tag{3b}$$

λ = wavelength

V = voltage across center of slot

Consequently, the total electric field strength from an array of such slots is given by the following equations:

$$E_{x1} = \frac{-i}{\quad} \sum_n V_n \exp(-jkr_{1an}) \frac{\left[\cos\left(k \frac{\ell}{2} \frac{(y_1 - y_{1an})}{r_{1an}}\right) - \cos\left(k \frac{\ell}{2}\right)\right] z_1}{\left[(x_1 - x_{1an})^2 + z_1^2\right]} \tag{4a}$$

$$E_{y1} = 0 \tag{4b}$$

$$E_{z1} = \frac{i}{\quad} \sum_n V_n \exp(-jkr_{1an}) \frac{\left[\cos\left(k \frac{\ell}{2} \frac{(y_1 - y_{1an})}{r_{1an}}\right) - \cos\left(k \frac{\ell}{2}\right)\right] (x_1 - x_{1an})}{\left[(x_1 - x_{1an})^2 + z_1^2\right]} \tag{4c}$$

where

$$r_{1an} = \sqrt{(x_1 - x_{1an})^2 + (y_1 - y_{1an})^2 + z_1^2} \tag{5}$$

The summation is over all slots in the array. In the reference position of the planar array, its x_1, y_1, z_1 axes are parallel to the x, y, z axes of the cone but the origin of the x_1, y_1, z_1 coordinate system is located at $z = z_0$ in the x, y, z coordinate system. The position of the array relative to its reference position is described in terms of three Eulerian angles, θ_s, ϕ_s, and ψ_s as illustrated in Figure 7. The beam-pointing direction is along the positive z_1 axis. In the x, y, z coordinate system, the beam-pointing direction θ_p, ϕ_p is related to the two Eulerian angles θ_s, ϕ_s by the relations

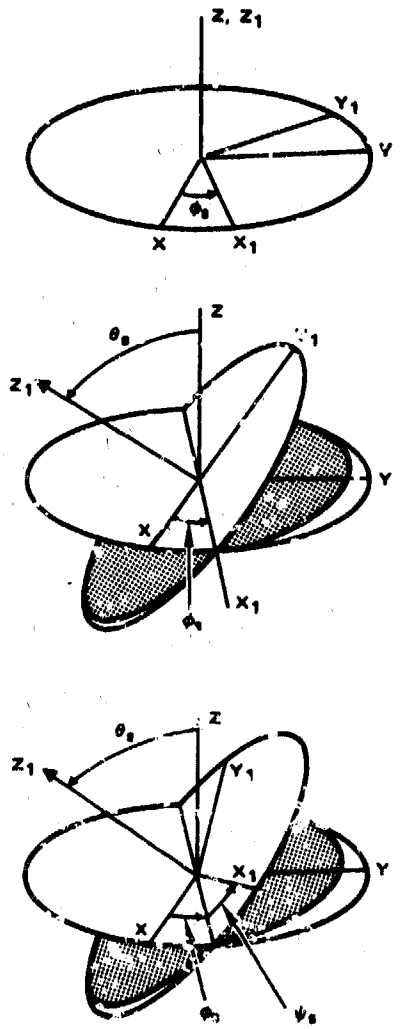

Figure 7. Illustration of Eulerian angles

$$\theta_p = \theta_s$$

$$\phi_p = \phi_s - \frac{\pi}{2}$$

In addition, the polarization of the far field depends on ψ_s, the third Eulerian angle. For example, if a vertically polarized beam is desired in the direction θ_p, ϕ_p then ψ_s must be either $\frac{\pi}{2}$ or $\frac{3\pi}{2}$; if a horizontally polarized beam is desired, ψ_s must be either 0 or π.

The coordinates of the x_1, y_1, z_1 system are related to the coordinates of the x, y, z system through the transformation

$$x_1 = (\cos \psi_s \cos \phi_s - \cos \theta_s \sin \phi_s \sin \psi_s)x + (\cos \psi_s \sin \phi_s + \cos \theta_s \cos \phi_s \sin \psi_s)\, y + \sin \psi_s \sin \theta_s (z - z_0) \tag{6a}$$

$$y_1 = -(\sin \psi_s \cos \phi_s + \cos \theta_s \sin \phi_s \cos \psi_s)\, x + (-\sin \psi_s \sin \phi_s + \cos \theta_s \cos \phi_s \cos \psi_s)\, y + \cos \psi_s \sin \theta_s (z - z_0) \tag{6b}$$

$$z_1 = \sin \theta_s \sin \phi_s\, x - \sin \theta_s \cos \phi_s\, y + \cos \theta_s (z - z_0) \tag{6c}$$

2.1.3 Equivalent Sources on Cone

The surface on which the calculation of electric field strength is desired is the conical surface, for which the x, y, z coordinates are expressible in spherical coordinates as

$$x = r \sin \theta_0 \cos \phi$$

$$y = r \sin \theta_0 \sin \phi$$

$$z = r \cos \theta_0$$

where θ_0 is the cone angle measured from the positive z-axis. Therefore, on the conical surface, the x_1, y_1, z_1 coordinates are given by

$$x_1 = r \left\{ \cos \psi_s \sin \theta_0 \cos (\phi - \phi_s) + \cos \theta_s \sin \psi_s \sin \theta_0 \sin (\phi - \phi_s) + \sin \psi_s \sin \theta_s \cos \theta_0 \right\} - z_0 \sin \psi_s \sin \theta_s \quad (7a)$$

$$y_1 = r \left\{ -\sin \psi_s \sin \theta_0 \cos (\phi - \phi_s) + \cos \theta_s \cos \psi_s \sin \theta_0 \sin (\phi - \phi_s) + \cos \psi_s \sin \theta_s \cos \theta_0 \right\} - z_0 \cos \psi_s \sin \theta_s \quad (7b)$$

$$z_1 = r \left\{ -\sin \theta_s \sin \theta_0 \sin (\phi - \phi_s) + \cos \theta_s \cos \theta_0 \right\} - z_0 \cos \theta_s \quad (7c)$$

If these expressions are used for the values of x_1, y_1, z_1 in Equations (4) and (5), then the values of E_{x1}, E_{y1}, and E_{z1} can be evaluated on the cone. The x, y, and z components of E can also be obtained from the x_1, y_1, z_1 components using the following equations.

$$E_x = (\cos \psi_s \cos \phi_s - \cos \theta_s \sin \phi_s \sin \psi_s) E_{x1} + \sin \theta_s \sin \phi_s E_{z1} \quad (8a)$$

$$E_y = (\cos \psi_s \sin \phi_s + \cos \theta_s \cos \phi_s \sin \psi_s) E_{x1} - \sin \theta_s \cos \phi_s E_{z1} \quad (8b)$$

$$E_z = \sin \theta_s \sin \psi_s E_{x1} + \cos \theta_s E_{z1} \quad (8c)$$

The equivalent magnetic source currents that must be set up on the conducting conical surface to provide the same external fields and, hence, the same pattern are given by

$$\bar{M} = \bar{E} \times \bar{n} = \bar{u}_\theta \times \bar{E} \quad (9)$$

When this operation is performed, the resulting radial and circumferential magnetic current densities on the cone are found to be

$$M_r = E_y \cos \phi - E_x \sin \phi \quad (10a)$$

$$M_\phi = - [E_x \sin \theta_o \cos \phi + E_y \sin \theta_0 \sin \phi + E_z \cos \theta_o] \quad (10b)$$

The far-field radiation pattern from these sources will be the same as that of the original planar array.

In any practical situation, the required magnetic current density can only be approximated by discrete magnetic sources distributed over the conical surface. Consequently, the pattern that will result from the placement of discrete magnetic sources will deviate from the desired pattern. The seriousness of this deviation will depend on the spacing of the sources on the conical surface. This spacing should be as large as possible to minimize the number of sources required but will be limited by the amount of allowable pattern deterioration.

2.1.4 Computer Program

A FORTRAN computer program has been written that implements the equivalence principle synthesis technique. The program approximates the pattern of a reference planar array of slot radiators by replacing the planar array by an approximate equivalent array of elements on a conducting cone. The elements on the cone are crossed slots whose arms can be independently excited. The radiation pattern of each slot is represented by a simple approximate expression that does not include tip diffraction. As presently implemented, the program accomplishes the following operations:

1. It positions the elements on the conical surface according to a specified algorithm. Presently the elements are equi-spaced on circumferential rings, with each ring separated by a selectable distance along the cone generatrix. The number of elements on each ring is selected according to the following rule: In the ring nearest the tip of the cone the number of elements is selected so that the spacing just exceeds a specified minimum allowable fraction of a wavelength. The same number of elements is used in succeeding rings until the

circumferential spacing exceeds some maximum allowable fraction of a wavelength. When this condition occurs, more elements are added until the spacing just exceeds the minimum allowable spacing, and so on. In addition, the positions in adjacent rings are rotated by one-half the element spacing to lessen any tendency to form grating lobes in azimuth.

2. At the locations of the elements on the conical surface, the program computes the electric field produced by a reference planar array of slots that fits within the conical surface. This array provides the reference pattern that is being synthesized. The pointing direction and orientation of the planar array determine the beam direction and the polarization.

   Two options are available. In one, the entire cone is excited forward of the plane containing the equivalent planar array. In the second, only that portion of the cone is excited that lies within a specified area of the cone.

   Monopulse difference excitations may also be obtained in the E-plane or the H-plane.

3. It computes the pattern of the conical array. In performing the computation it uses the electric fields computed in 2. as the element excitations, and uses an approximation for the patterns of the individual radiators. The phase of the element excitations may be quantized if desired.

A listing of the program is given in Appendix A.

An auxiliary computer program has been written that allows the study of the positioning of radiating elements on the cone relative to the orientation of the reference array. A listing of this program is given in Appendix B.

These programs were used in the design of an experimental array and for the computation of its excitation and predicted patterns as discussed in the next section.

2.2 Pattern Calculations

The computer programs described in the preceding section have been used as tools to study the equivalence principle synthesis technique through the computation of various array patterns using different reference planar arrays and different numbers and spacings of slots on the conical surface. These patterns are presented and discussed in this section. Several patterns are included for which the full conical surface is excited. Other patterns are included for which only a portion of the cone is excited. This second condition corresponds to a practical case in which those slots on the cone that would be weakly excited are turned off completely (i.e., short-circuited). It also corresponds to the situation that exists for the experimental cone to be described in Chapter Six. Patterns are also included that illustrate the effects of three-bit phase quantization. Additional pattern calculations are compared with measurements in Chapter Six.

The various calculated patterns are intended to simulate the patterns of several reference planar arrays. These reference arrays are illustrated along with their calculated E-plane and H-plane patterns in Figures 8 through 13. The patterns are calculated using the patterns of slots in an infinite groundplane and are therefore idealizations of the actual patterns that would be obtained, especially in the far-out sidelobe regions.

The coordinate system used for calculated patterns of the conical arrays is that shown in Figure 14. The desired beam pointing angles are θ_p, ϕ_p. In all calculated and measured patterns ϕ_p was set to zero. All patterns were calculated for vertical, i.e., θ-directed polarization at the peak of the beams. The angular coordinate for E-plane patterns is θ, while that for H-plane patterns is ψ. The E-plane patterns are plotted as functions of $\theta - \theta_p$. The various parameters and areas of cone excitations used in the calculations are summarized in Table 1.

TABLE 1. SUMMARY OF PARAMETERS FOR CALCULATED PATTERNS

Figure No.	Pattern Type	Beam Position θ_p Deg.	Beam Position ϕ_p Deg.	Ref. Planar Array Diam. Wvlths	Ref. Planar Array No. of Slots	Ref. Planar Array Dist. from Cone Tip-Wvlths	Element Spacings on Cone: Ring Separation Along Generatrix Wvlths	Element Spacings on Cone: Slot Separation in Azimuth Wvlths	Excited Region of Cone	Number of Active Slots	Phase Quantization	Cone Angle θ^o Degrees
15a b c d	E-plane sum H-plane sum E-plane diff H-plane diff	70	0	4.26	24	12.28	0.7	0.5 to 0.7	Full	228	None	170
16a b	E-plane sum H-plane sum	80	0	4.26	24	12.28	0.7	0.5 to 0.7	Full	219	None	170
17a b	E-plane sum H-plane sum	30	0	4.26	24	12.28	0.7	0.5 to 0.7	Planar array projection	45	None	170
19a b	E-plane sum H-plane sum	30	0	4.26	24	12.28	0.7	0.5 to 0.7	Full	219	3-bit	170
20a b	E-plane sum H-plane sum	30	0	4.26	24	12.28	0.7	0.5 to 0.7	Planar array projection	45	3-bit	170
21a b	E-plane sum H-plane sum	30	0	4.26*	24	12.28	0.7	0.5 to 0.7	Planar array projection	45	None	170
22a b	E-plane sum H-plane sum	50	0	4.26	40	12.28	0.5	1.0 to 1.4	Planar array projection	35	None	170
24a b c	E-plane sum H-plane sum E-plane diff	50	0	3.66	32	12.28	0.7	0.5 to 0.7	Planar array projection	35	None	170
26a b	E-plane sum H-plane sum	50	0	3.66	32	12.28	0.5	1.0 to 1.4	Full	153	None	170
27a b	E-plane sum H-plane sum	50	0	3.66	32	12.28	0.5	1.0 to 1.4	Planar array projection	35	None	170
28a b	E-plane sum H-plane sum	50	0	3.66	32	11.98	0.5	1.0 to 1.4	Planar array projection	35	None	169.75
29a b	E-plane sum H-plane sum	49.2	0	3.66	32	11.98	0.5	1.0 to 1.4	Planar array projection	35	None	169.75
30a b	E-plane sum H-plane sum	50	0	3.66	32	11.98	0.5	1.0 to 1.4	4.36λ diameter+	35	None	169.75
31a b	E-plane sum H-plane sum	50	0	3.66	32	11.98	0.5	1.0 to 1.4	4.36λ diameter+	37	None	169.75
32a b	E-plane sum H-plane sum	50	0	3.66	32	12.27	0.5	1.0 to 1.4	4.36λ diameter+	37	None	169.75
33a b	E-plane sum H-plane sum	79.75	0	3.66	32	11.98	0.5	1.0 to 1.4	4.36λ diameter+	37	None	169.75
34a b	E-plane sum H-plane sum	79.75	0	3.66	32	11.98	0.25	1.0 to 1.4	4.36λ diameter+	74	None	169.75

*Planar array had tapered distribution

$f(\rho) = 0.5 + [1 - (\frac{\rho}{a})^2]^2$

+Excited region of cone corresponds to the projection of a 4.36λ diameter circle onto cone.

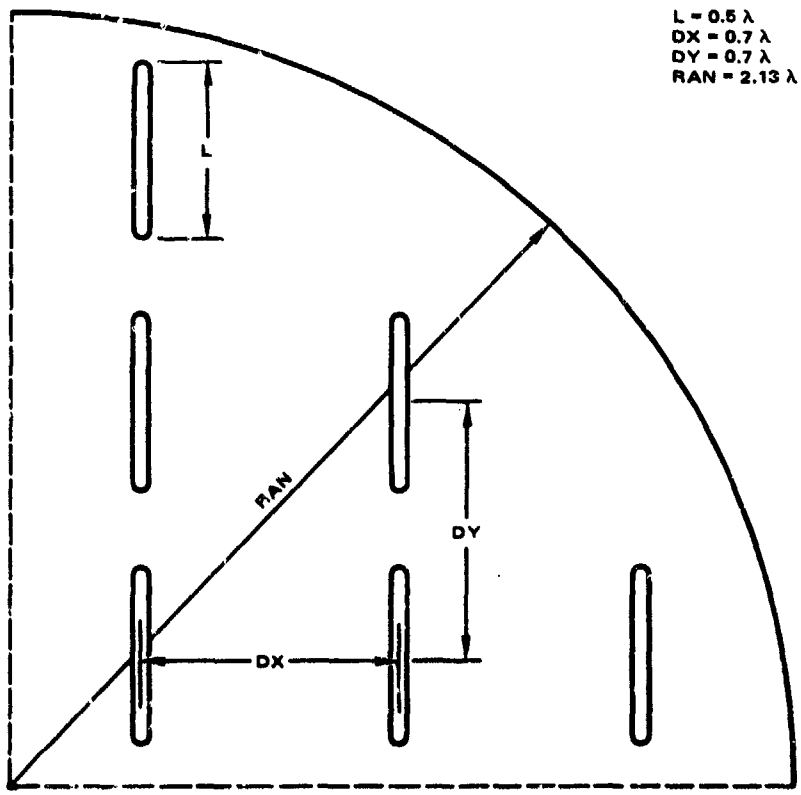

Figure 8. Quadrant of 24 element planar array

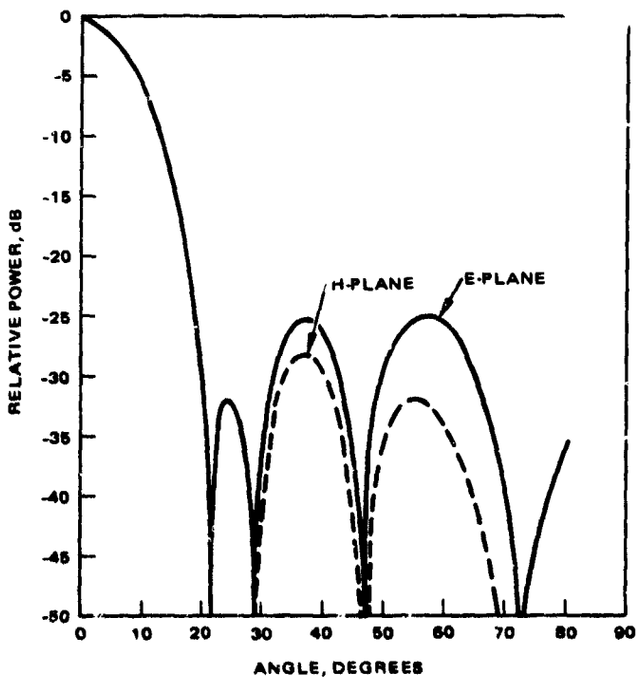

Figure 9. Calculated patterns of 24 element planar slot array.

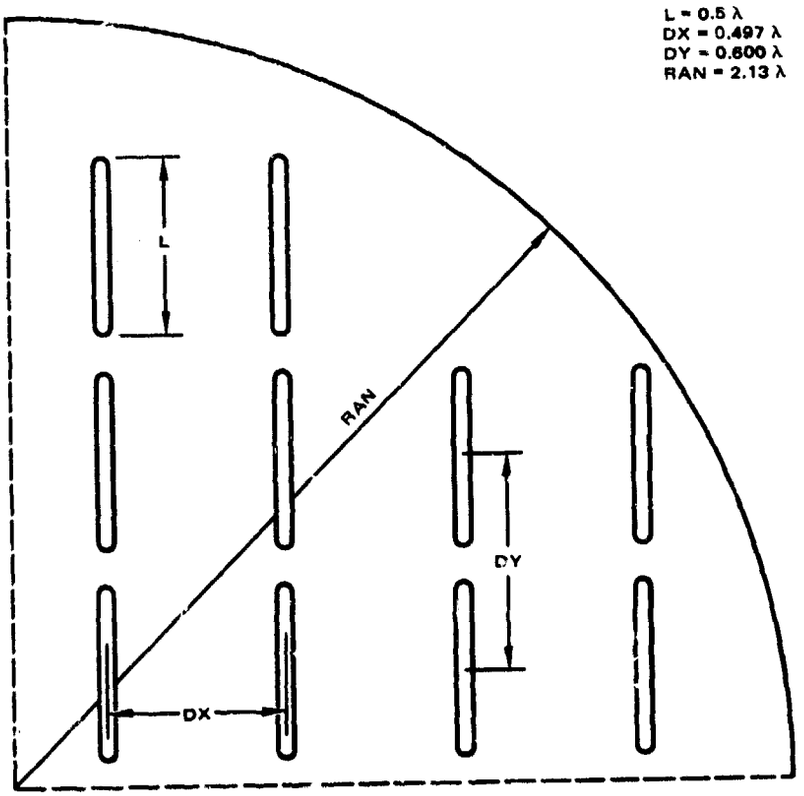

Figure 10. Quadrant of 40 element planar array

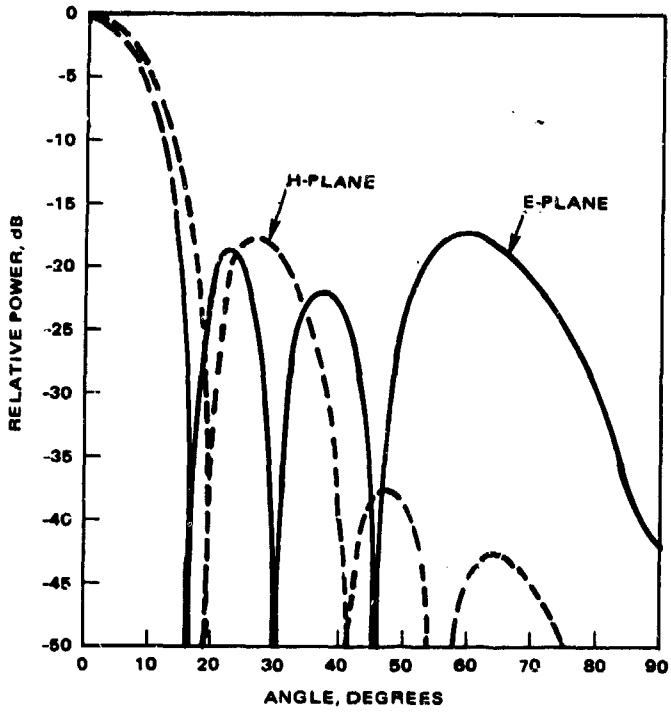

Figure 11. Calculated patterns of 40 element planar slot array.

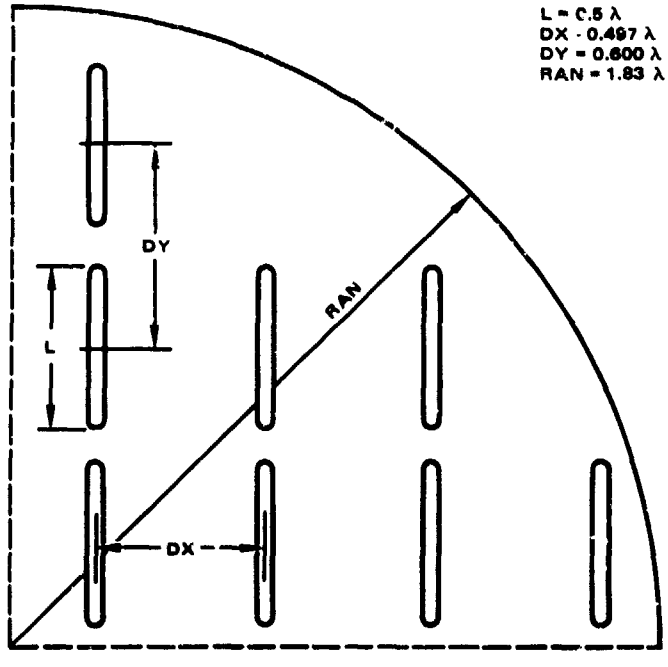

Figure 12. Quadrant of 32 element planar array.

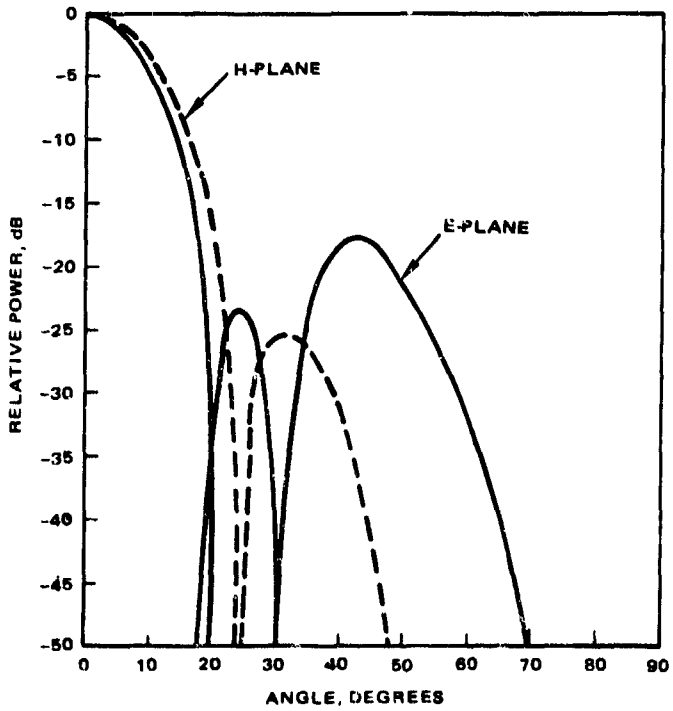

Figure 13. Calculated patterns of 32 element planar slot array.

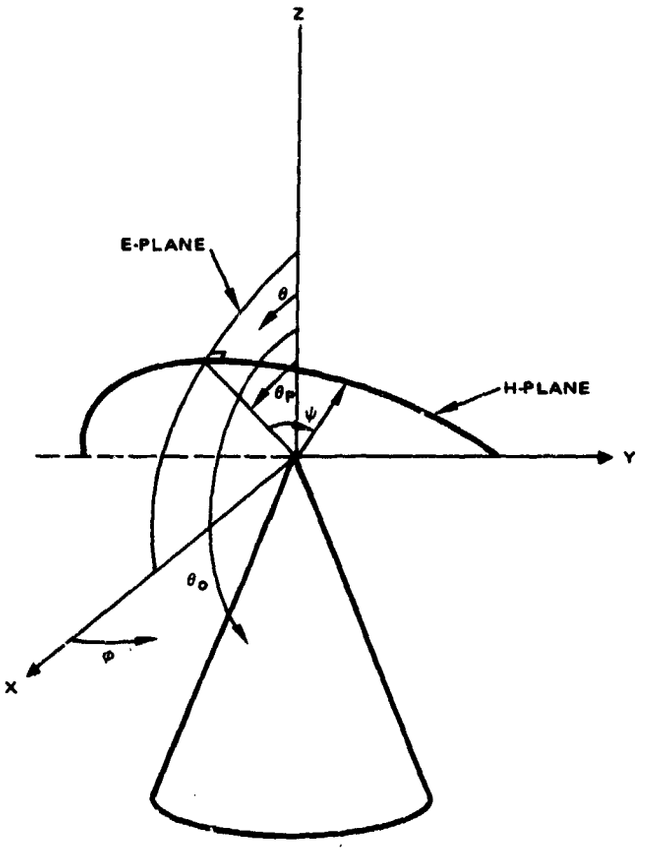

Figure 14. Coordinate system for patterns.

The radiating elements on the cone are positioned in accordance with the rule given in Section 2.1.4. The distance from the cone tip to the first ring of slots is in all cases 0.7 wavelengths and the separation of adjacent rings was varied. Figures 15 through 20 relate to the 24-slot planar array, and are for a cone half angle of 10 deg.

Figures 15a and b show the calculated E-plane and H-plane patterns for the cone using all the available slots to approximate the required distribution. It is seen that the main beams agree well with those of the reference planar array, but that the sidelobes of the conical array patterns are higher in the E-plane and the general sidelobe structure differs from that of the reference patterns. This difference is attributable to two main factors. First, the cone excitation consists of discrete slot fields rather than the continuous excitation dictated by the equivalence principle. The use of more slots spaced more closely on the cone should more nearly approximate the continuous distribution and improve agreement between conical array patterns and planar array patterns. However, since the design of an experimental array was the goal, and the number of slots that could be implemented was limited, no extensive set of pattern calculations was made for more closely packed slots. However, one such calculation was done for a slightly different cone angle ($\theta_0 = 169.75^\circ$); (see Figure 34). A marked improvement of the conical pattern was observed for that case. The second reason that the calculated conical array patterns do not agree with the calculated patterns of the reference planar array in sidelobe detail is that approximate radiation patterns were used for the slots on the cone. These slot patterns do not include tip diffraction effects.* These two conditions are common to all calculated conical array patterns.

*The discontinuities in the patterns result from the use of the approximate element patterns which have sharp cutoffs in certain cuts.

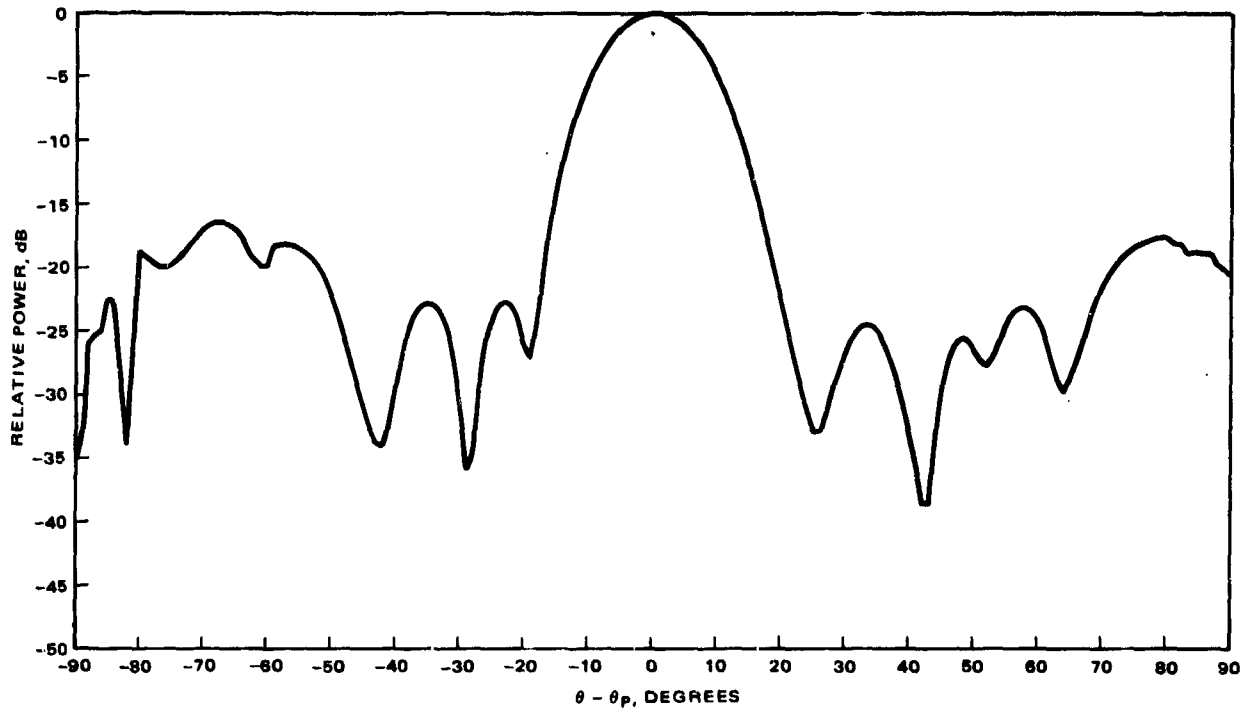

a) E-plane

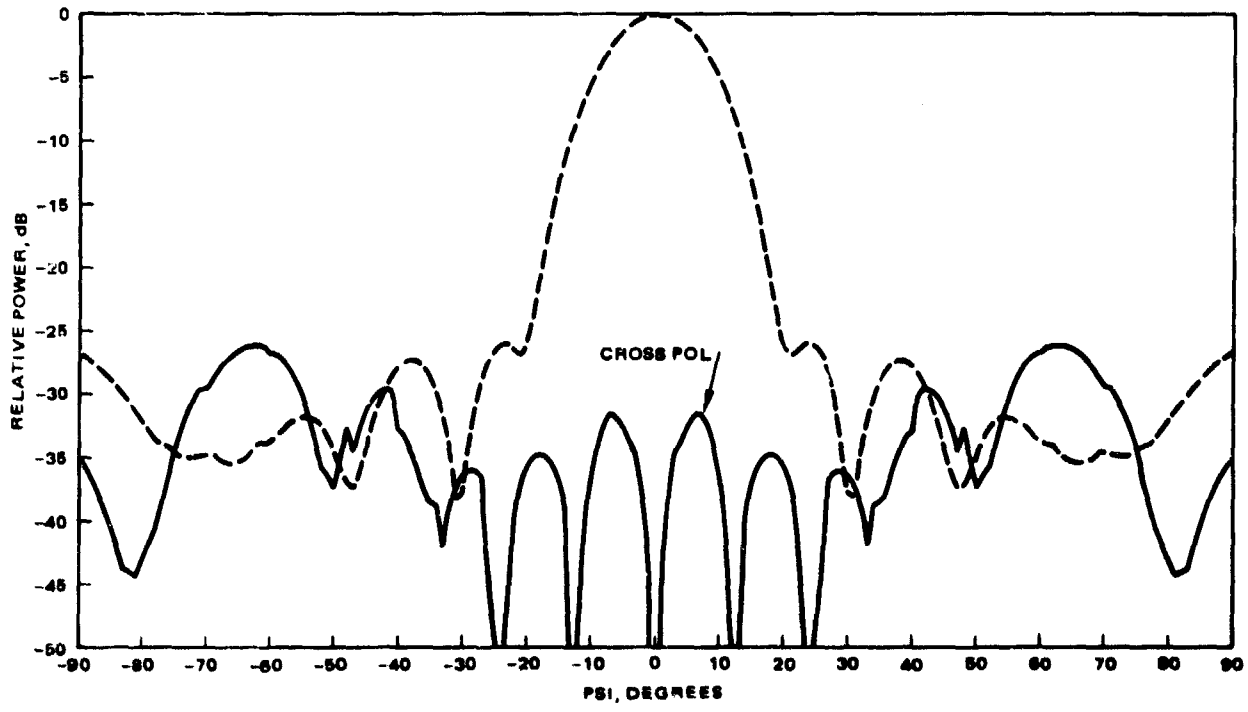

b) H-plane

Figure 15. Calculated patterns of 10^{O} conical slot array; full excitation ($\theta_P = 70^{O}$).

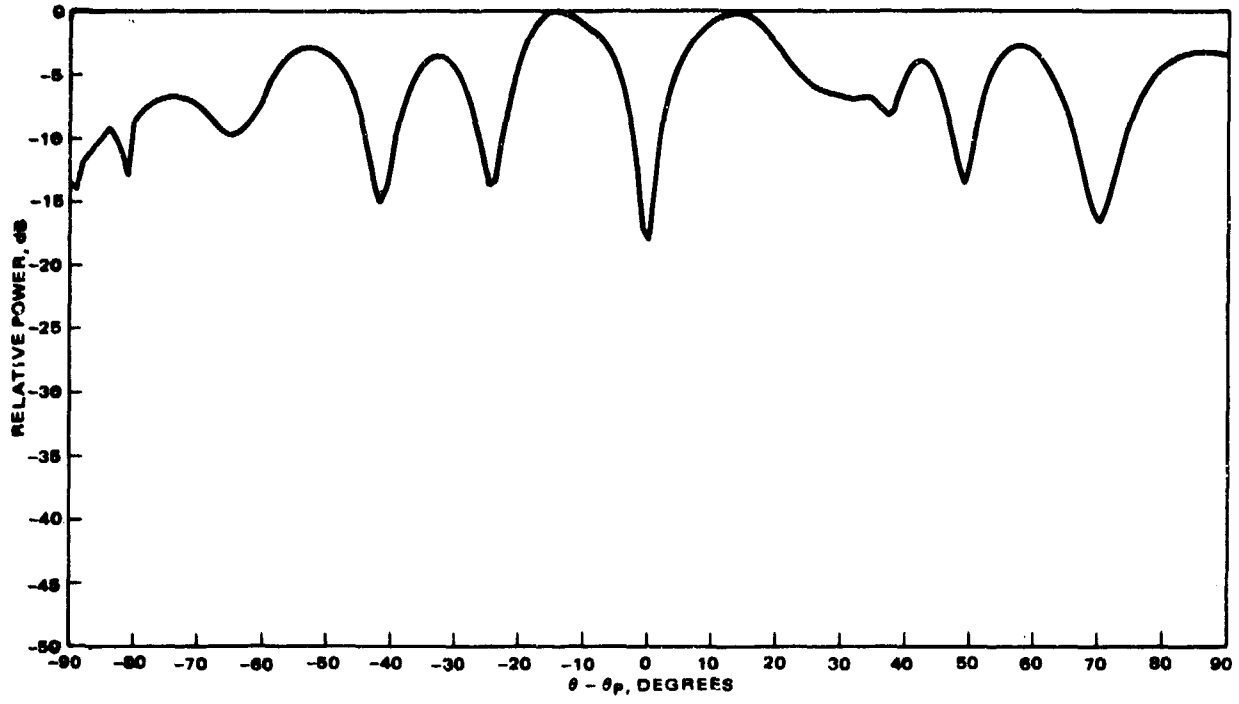

c) E-plane difference

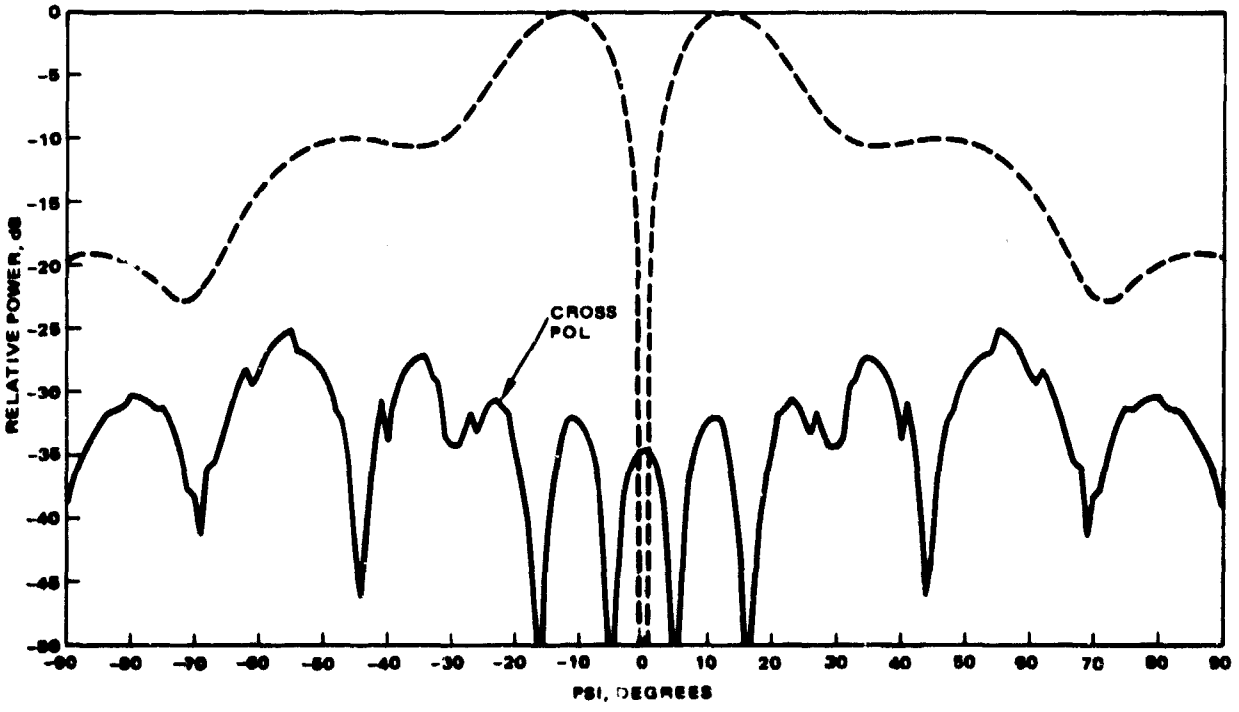

d) H-plane difference

Figure 15. Calculated patterns of 10^{O} conical slot array; full excitation ($\theta_p = 70^{O}$). (Continued)

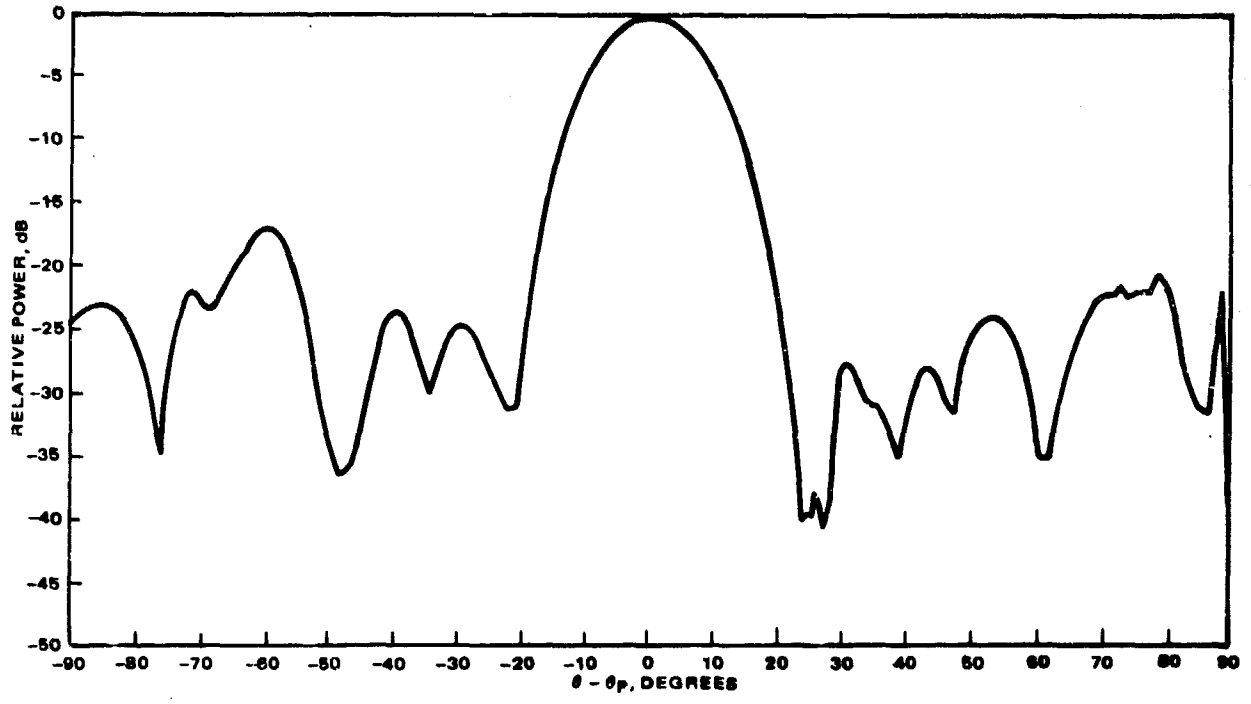

a) E-plane

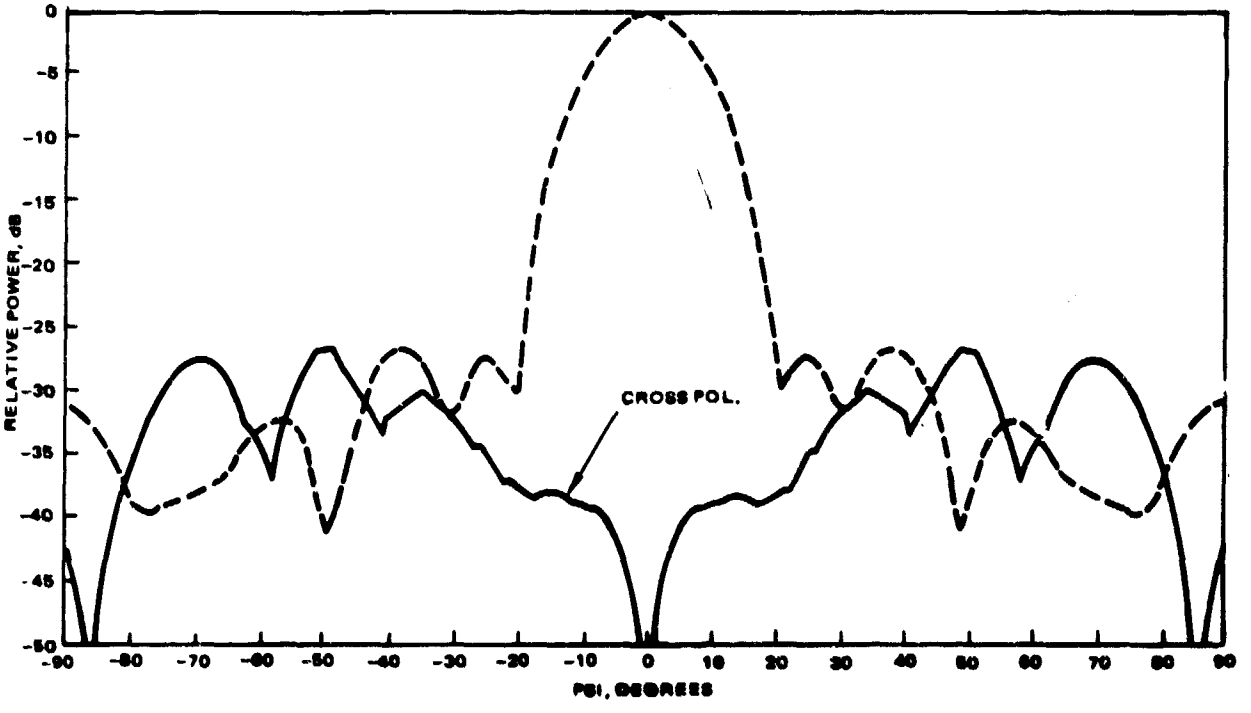

b) H-plane

Figure 16. Calculated patterns of 10^0 conical slot array; full excitation ($\theta_p = 80^0$)

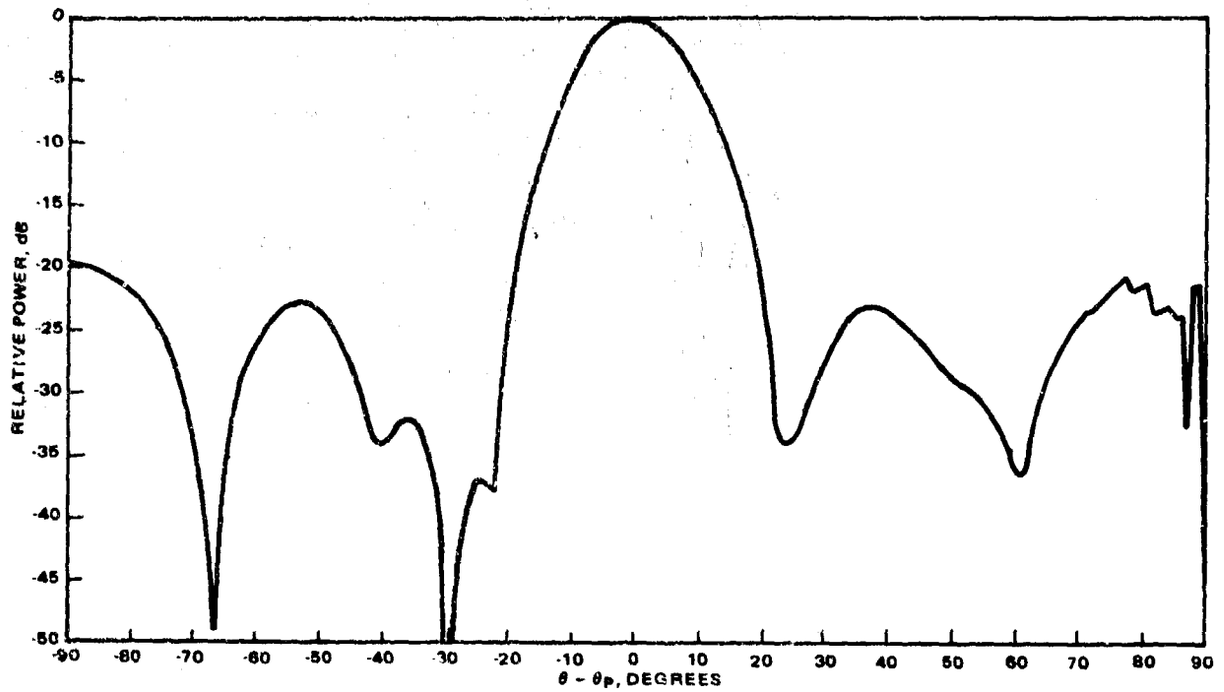

a) E-plane

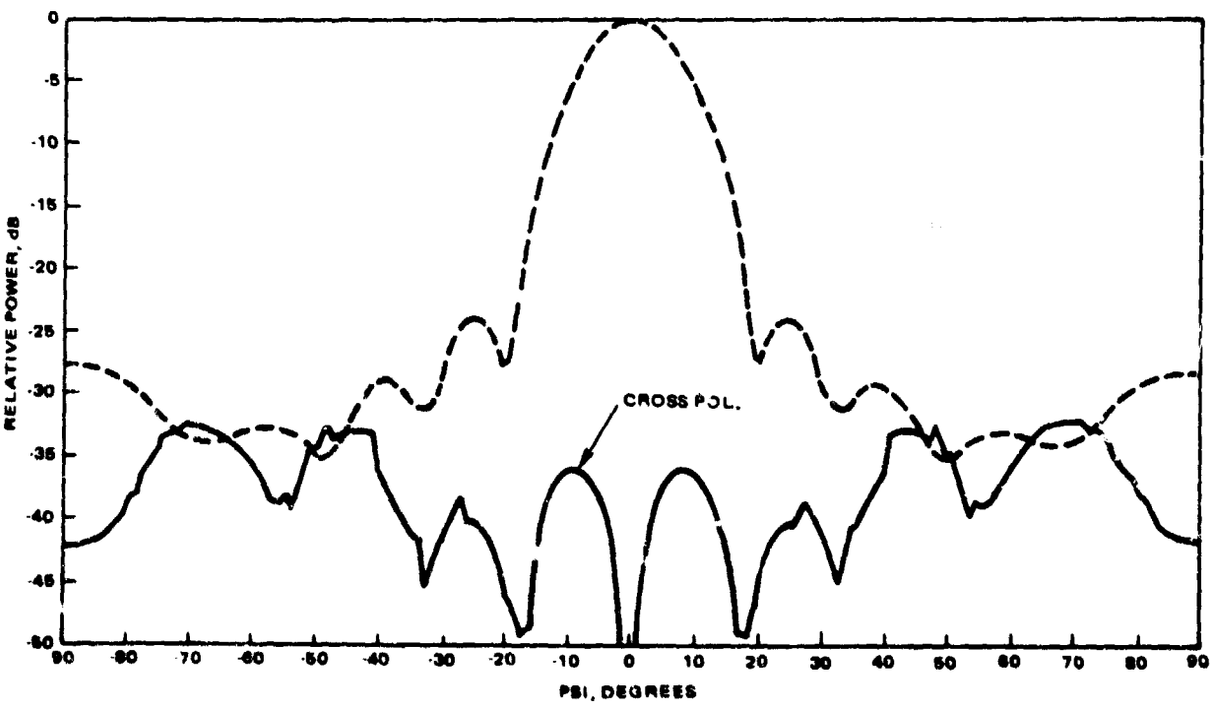

b) H-plane

Figure 17. Calculated patterns of 10° conical slot array; 45 elements ($\theta_p = 80^{\circ}$).

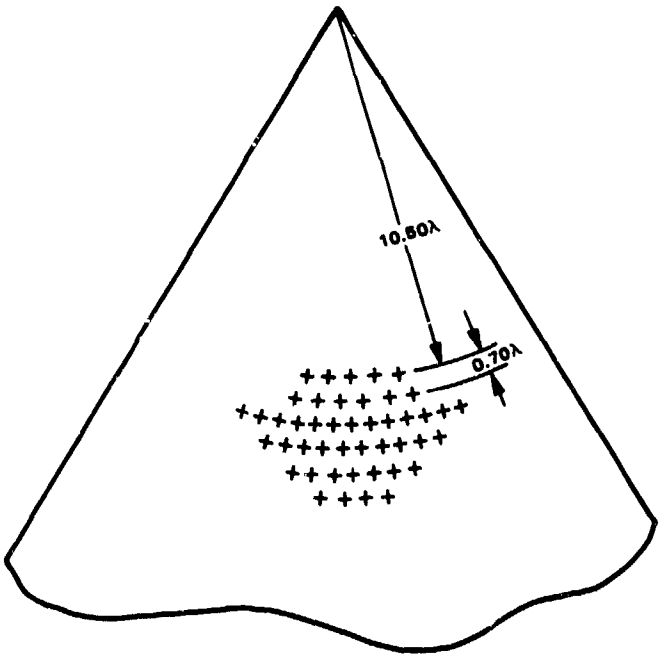

Figure 18. Locations of excited slots for the patterns of Figures 17, 20 and 21.

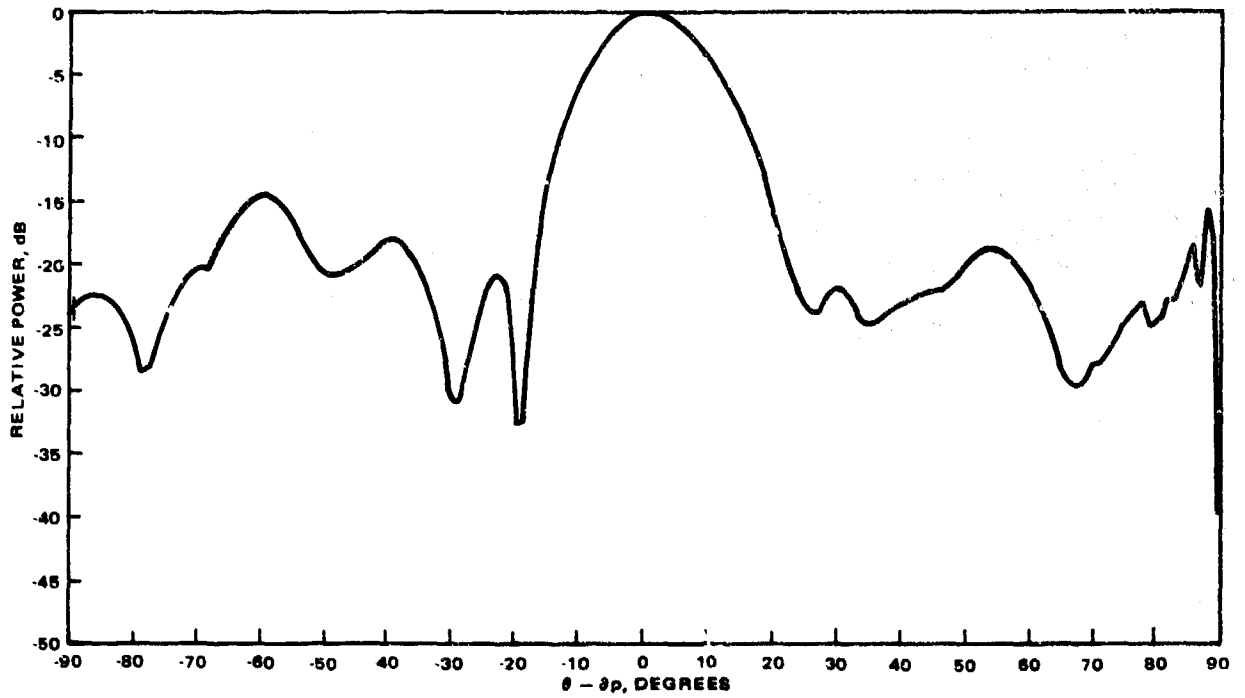

a) E-plane

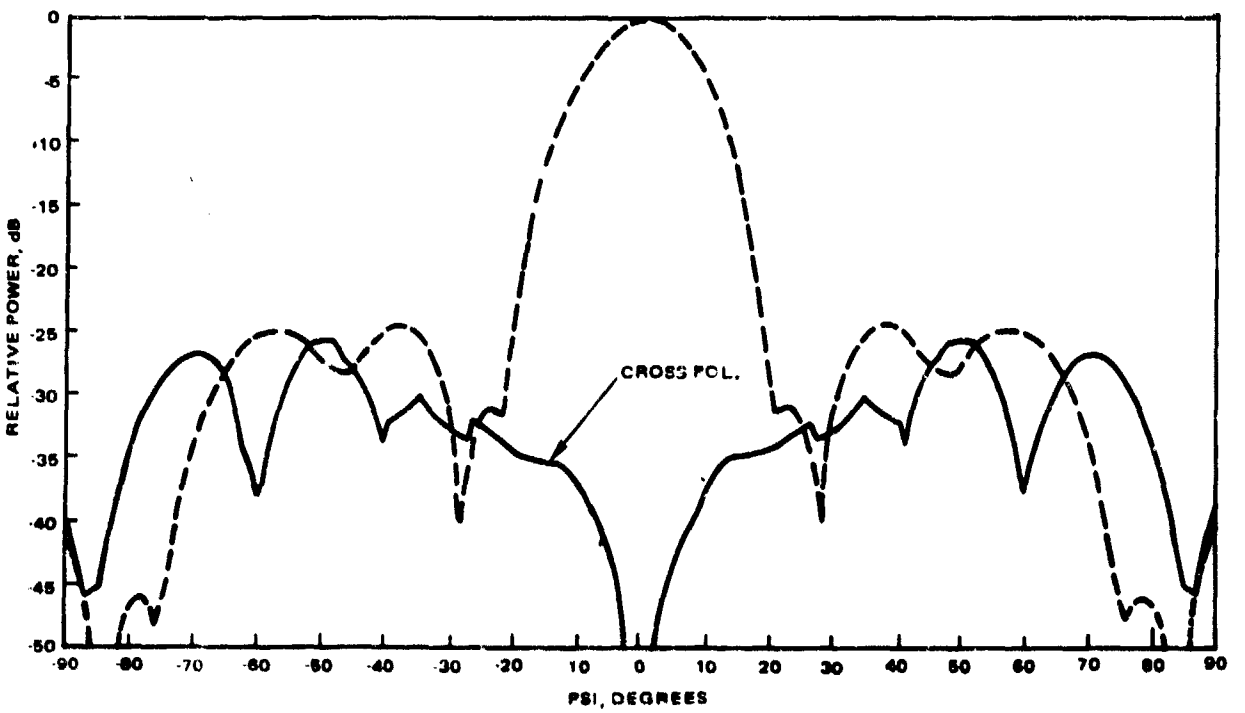

b) H-plane

Figure 19. Calculated patterns of 10° conical slot array; full excitation, 3 bit phase quantization. ($\theta_p = 80^\circ$)

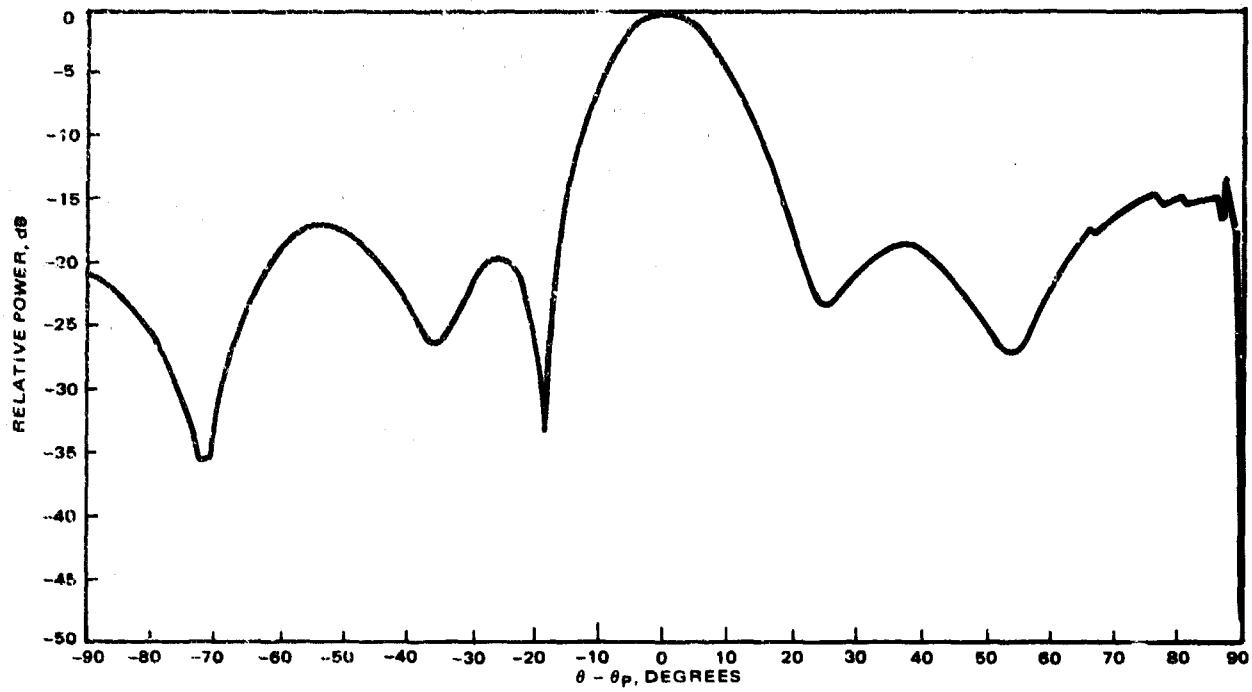

a) E-plane

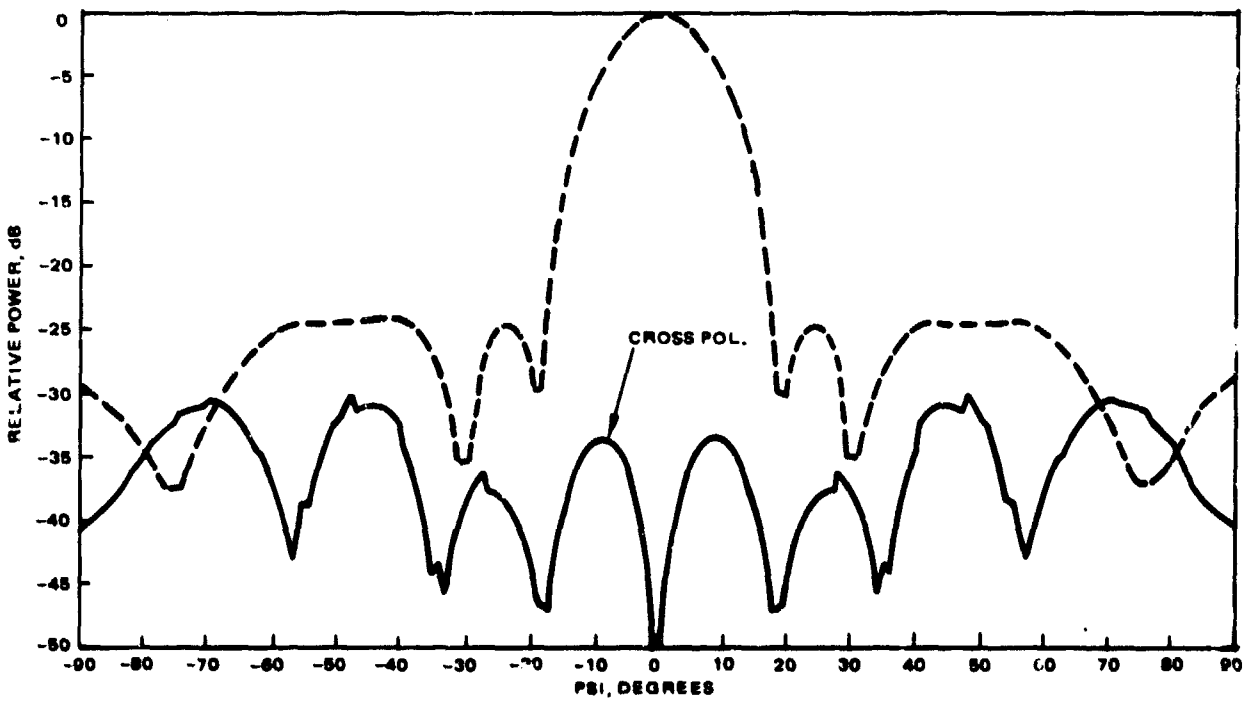

b) H-plane

Figure 20. Calculated patterns of 10^{o} conical slot array; 45 elements, 3-bit phase quantization ($\theta_p = 80^{o}$).

Figures 15c and 15d show E-plane and H-plane difference patterns, respectively, for the same array as in Figures 15a and b. Their excitations on the cone were obtained by exciting the reference planar array to produce E-plane and H-plane difference patterns and determining the resulting tangetial components of E at the conical surface. The difference patterns are shown normalized to their own peaks. The peak of the E-plane difference pattern is actually 3.47 dB below the peak of the sum pattern. Its "null" is therefore approximately 21.5 dB below the sum peak. Actually it appears that the true null may be slightly displaced from θ_p and was missed due to the one-degree step size used in the computations. The peak of the H-plane difference pattern is 3.58 dB below the peak of the sum pattern and the null in the desired polarization is a true null. The cross polarization in the null is down approximately 38 dB. Thus, the synthesis technique appears to permit generation of difference patterns without serious cross polarization problems, at least for the case where the null lies in a plane with azimuthal symmetry. Figures 16a and b illustrate the sum pattern for the same situation as in Figures 15a and b except that the beam is positioned at $\theta_p = 80^\circ$. The characteristics are very similar to those of Figures 15a and b. Figures 17a and b are for a case similar to Figures 16a and b except that only 45 slots within the direct projected area of the reference planar array were excited. Figure 18 shows the excited slots on the developed cone. The E-plane pattern is less symmetrical especially in the near-in lobes than for the fully excited cone. The H-plane sidelobes are raised somewhat. These effects result because the required excitation is truncated.

Figures 19a and b show the effect of 3-bit phase quantization on the pattern of a fully excited cone. Some deterioration of the sidelobe structure is evident. Figures 20a and b show

the effect of limiting the excited slots to the projection of the equivalent planar array and using 3-bit phase quantization. A further loss of detail of sidelobe structure is evident. Figures 21a and b illustrate the effect of aperture tapering on the patterns. A taper of the following form was placed on the aperture distribution of the reference planar array.

$$f(\rho) = 0.5 + \left(1 - \left(\frac{\rho}{a}\right)^2\right)^2$$

where a is the array radius and ρ is the distance from the array center. The main effect appears to be a lowering of the near-in sidelobes of the H-plane pattern and the far out sidelobes of both patterns.

Figures 22a and b illustrate patterns computed for a beam position at θ_p = 50 degrees and a reference planar array of 40 elements. The excited region of the cone is once again restricted to the projected area of the planar array. The spacing of slots on the cone is illustrated in Figure 23. Figures 24, 26, and 27 are also for a beam at θ_p = 50 degrees using a 32-slot reference planar array and various slot spacings on the 10 degree half-angle cone. Full cone excitation and limited cone excitations are used as illustrated in Table 1. Figure 25 shows the slot arrangement on a developed cone for the patterns of Figure 24. The peak of the difference pattern in Figure 24c is 1.93 dB below the sum pattern and the null, which is shifted by one degree from the desired location, is 23 dB down. Once again the actual location of the null was probably missed because of the one-degree step size used in the calculations.

The patterns in Figures 28 through 34 are for a half cone angle of 10.25°. This angle corresponds more closely to that of the experimental cone discussed in Chapter Six. The antennas whose patterns are shown in these figures have several different

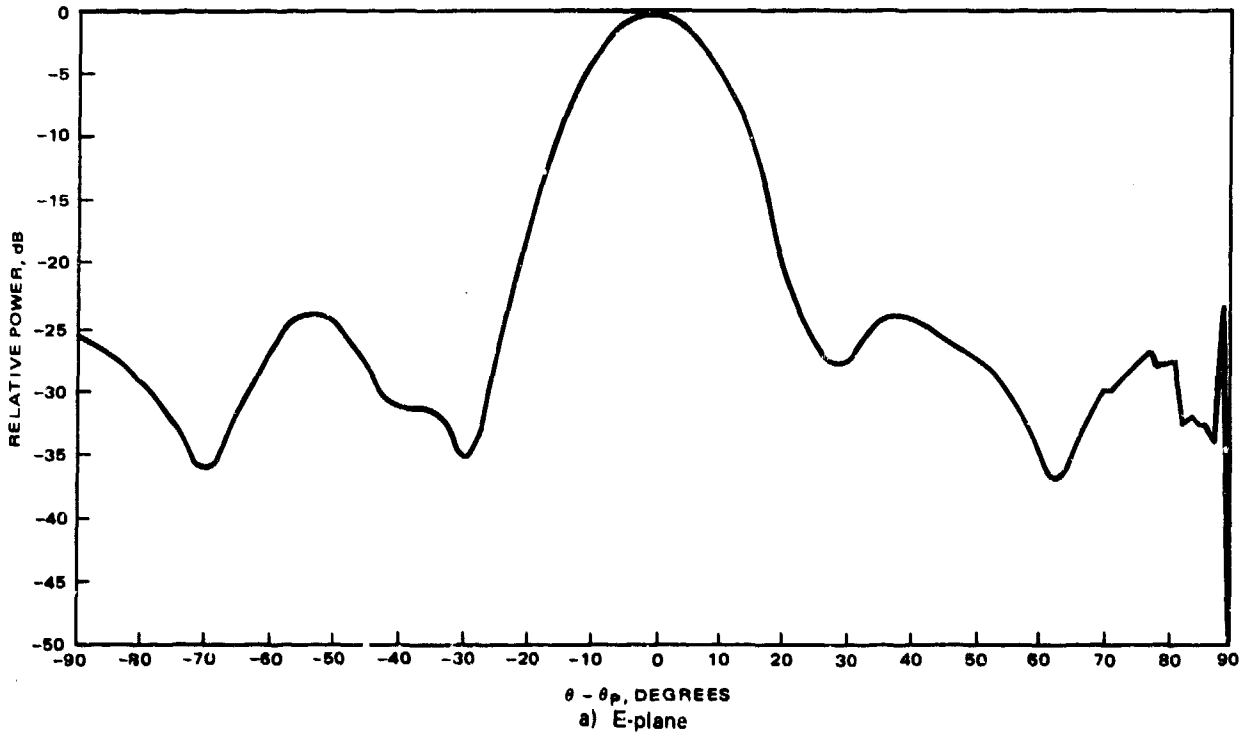

a) E-plane

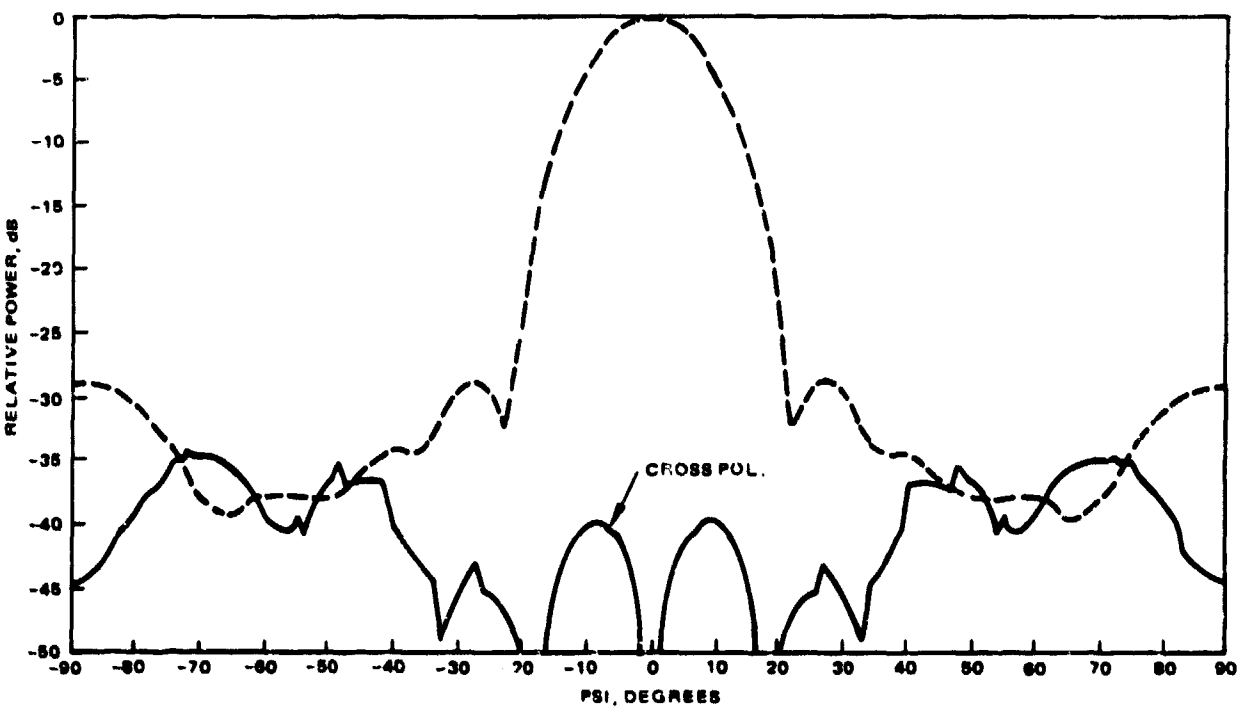

b) H-plane

Figure 21. Calculated patterns of 10^{o} conical slot array; 45 elements, tapered distribution ($\theta_p = 80^{o}$).

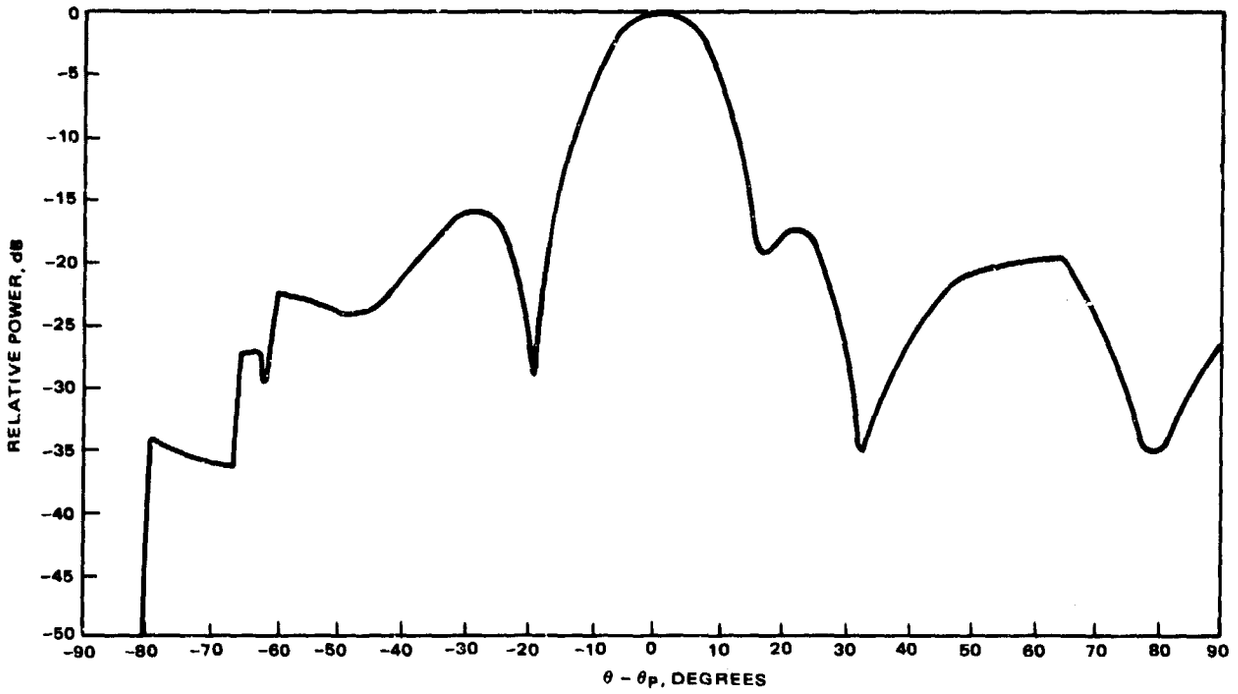

a) E-plane

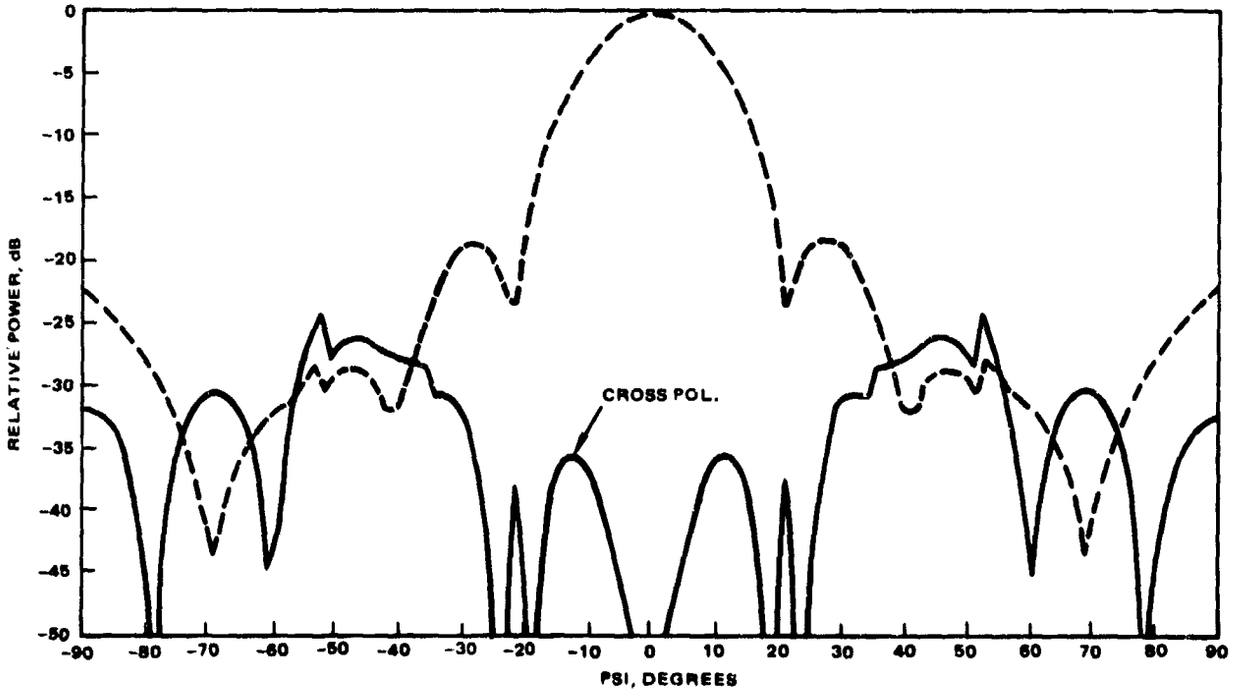

b) H-plane

Figure 22. Calculated pattern of 10^{o} conical slot array; 35 elements, modified spacing ($\theta_P = 50^{o}$).

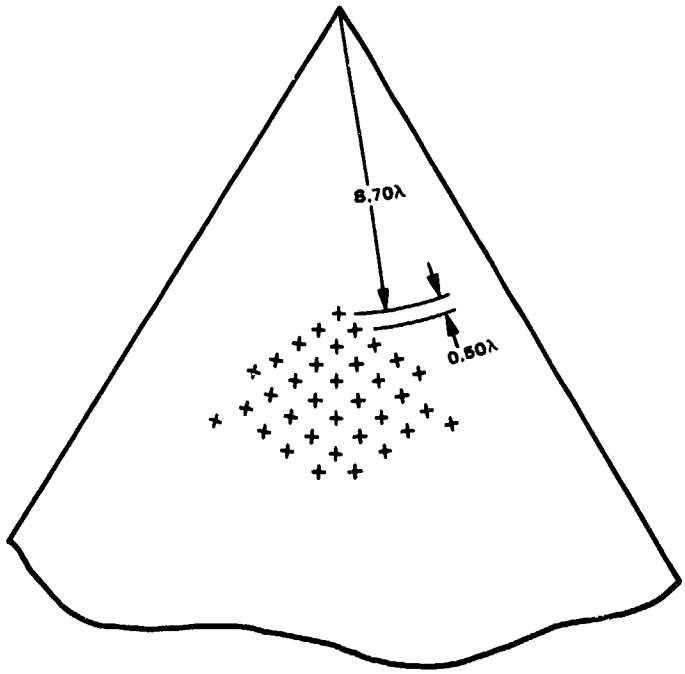

Figure 23. Location of excited slots for the patterns of Figures 22 and 27.

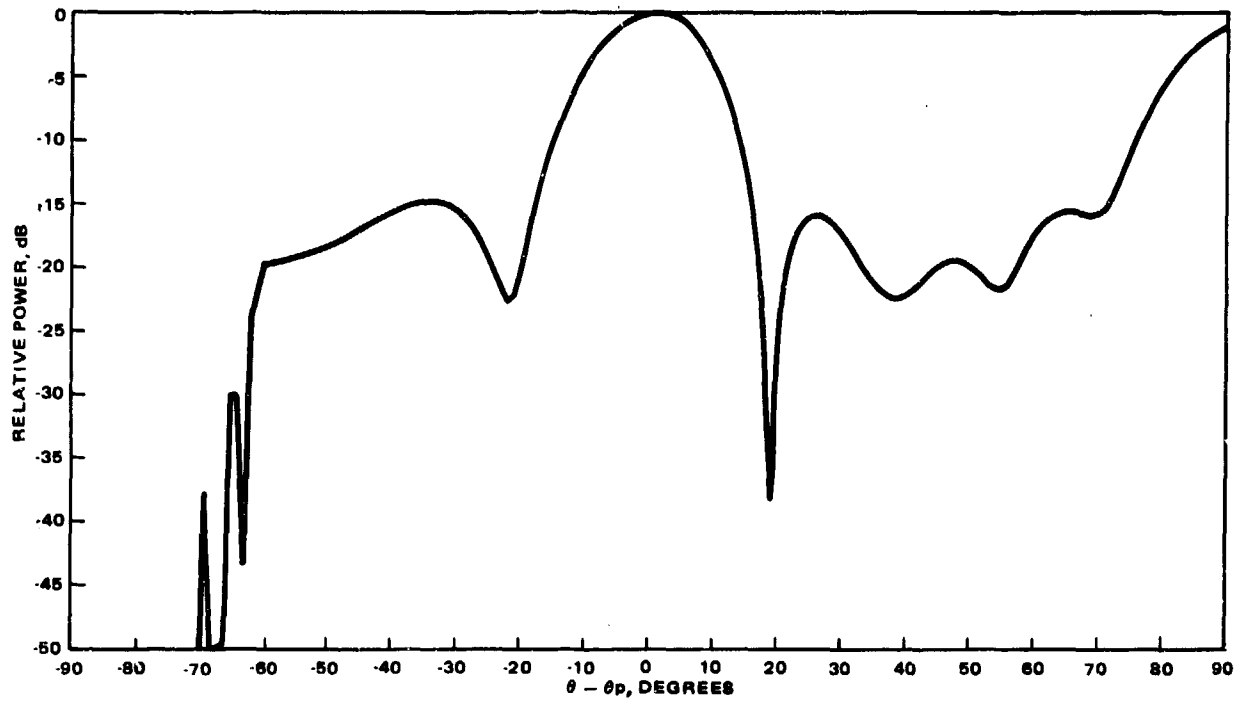

a) E-plane

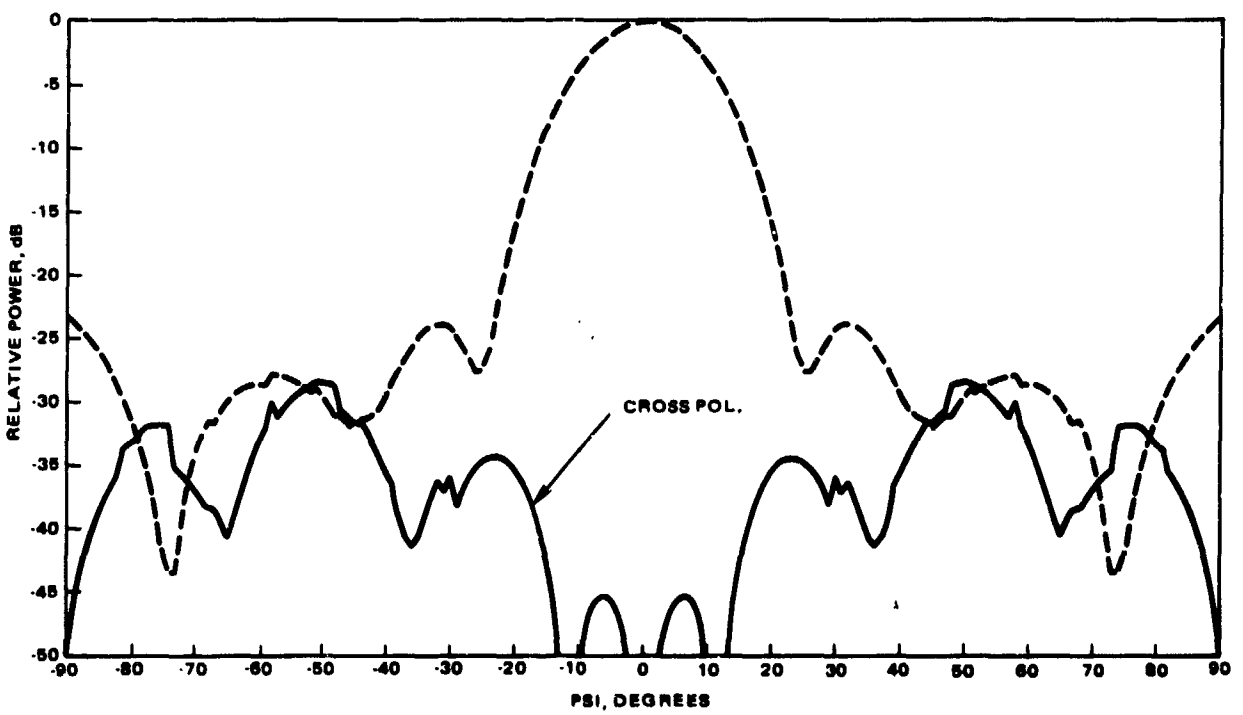

b) H-plane

Figure 24. Calculated pattern of 10^{o} conical slot array; limited excitation ($\theta_p = 50^{o}$).

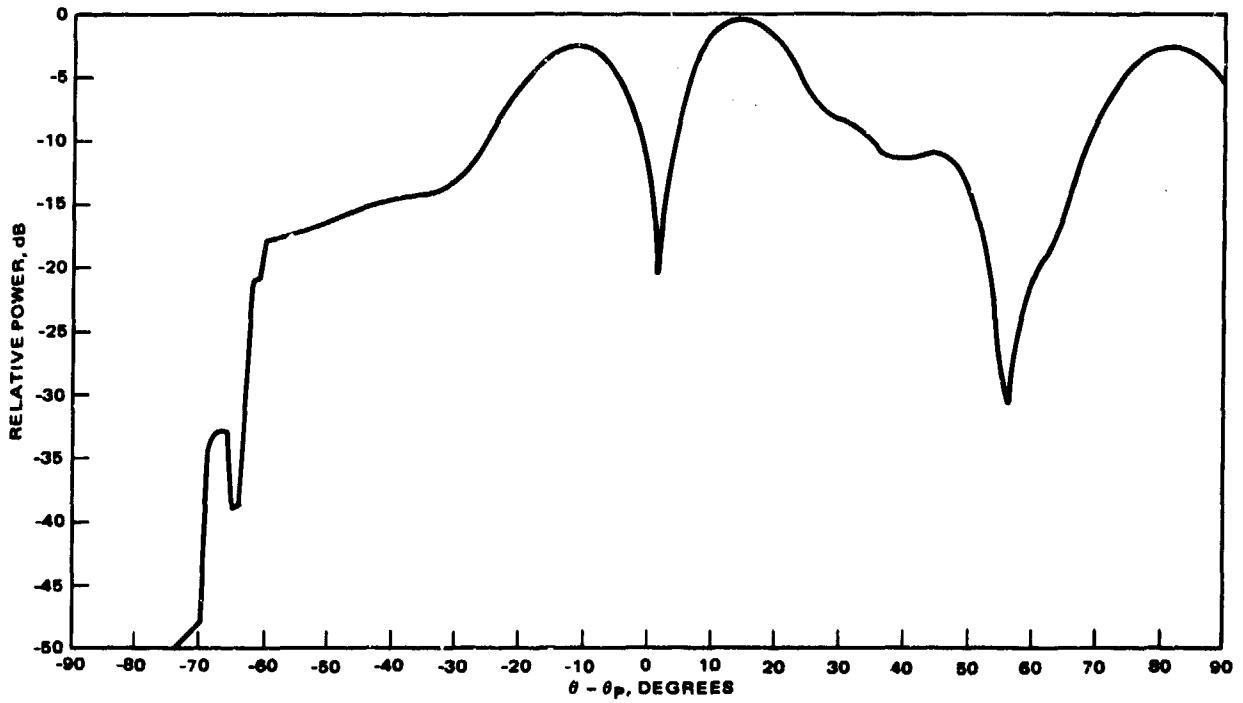

c) E-plane difference

Figure 24. Calculated pattern of 10^{o} conical slot array; limited excitation ($\theta_p = 50^{o}$). (Continued)

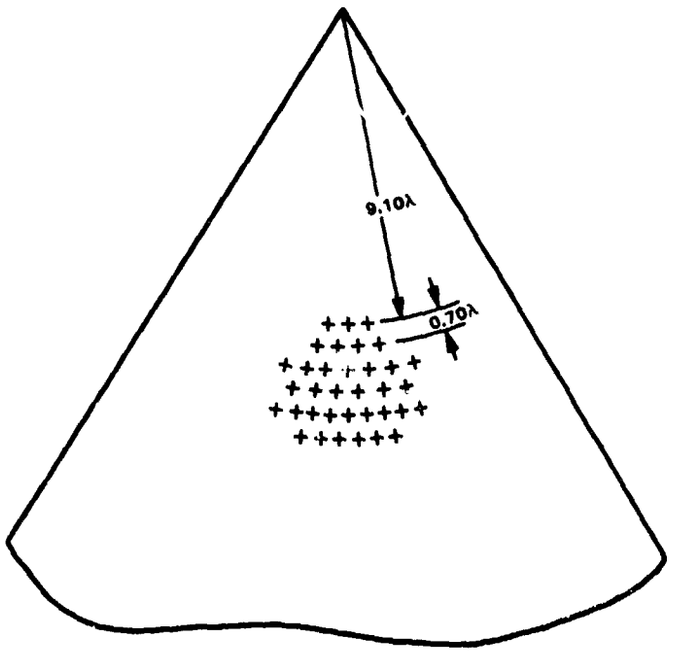

Figure 25. Locations of excited slots for the patterns of Figure 24.

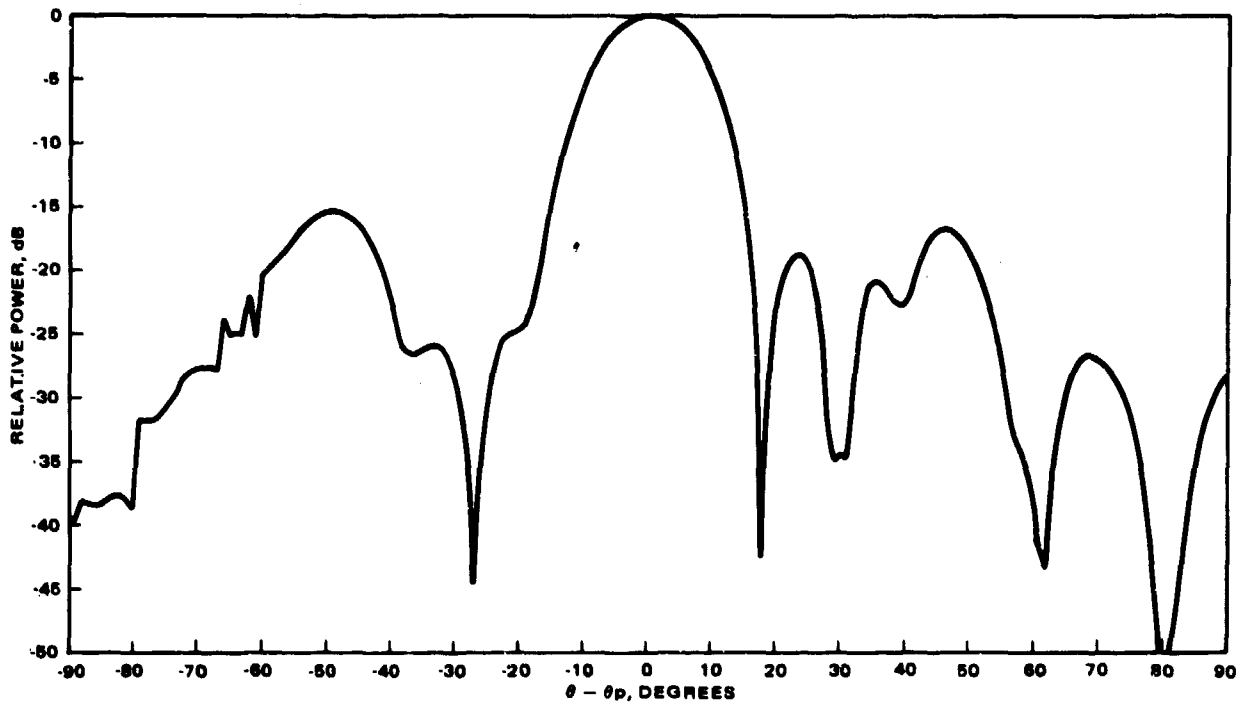

a) E-plane

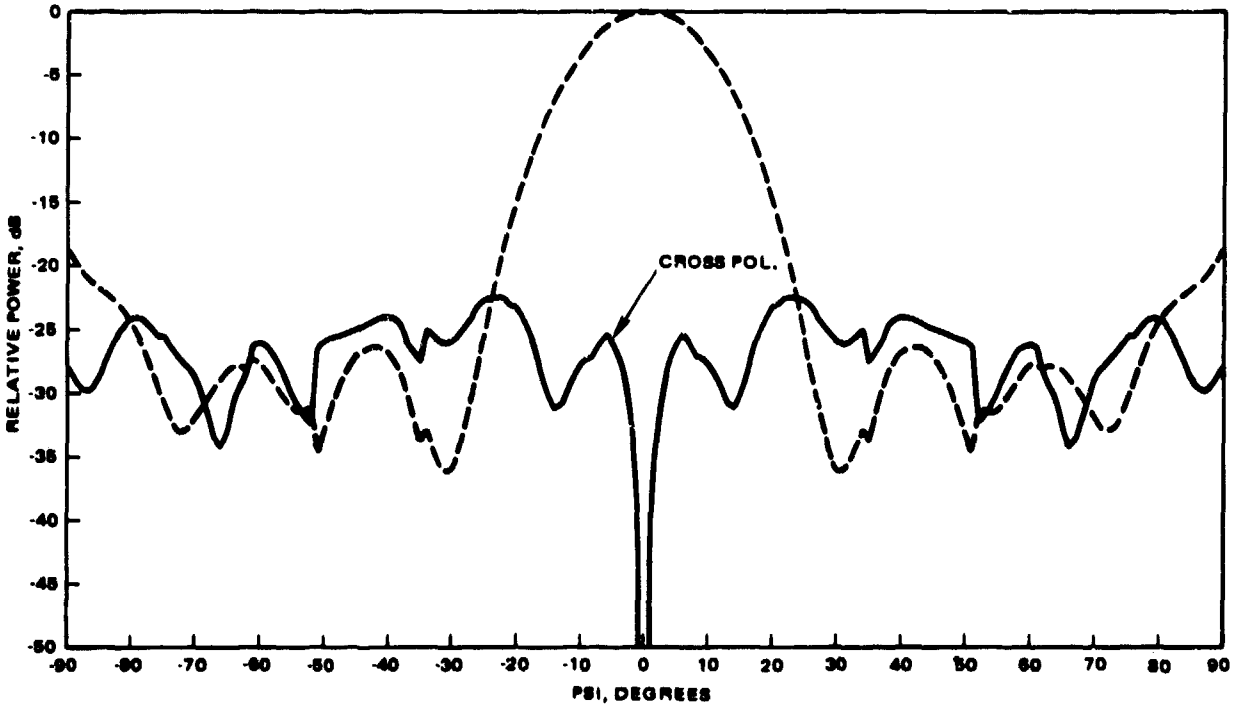

b) H-plane

Figure 26. Calculated patterns of 10° conical slot array; full excitation, modified spacing ($\theta_p = 50^\circ$).

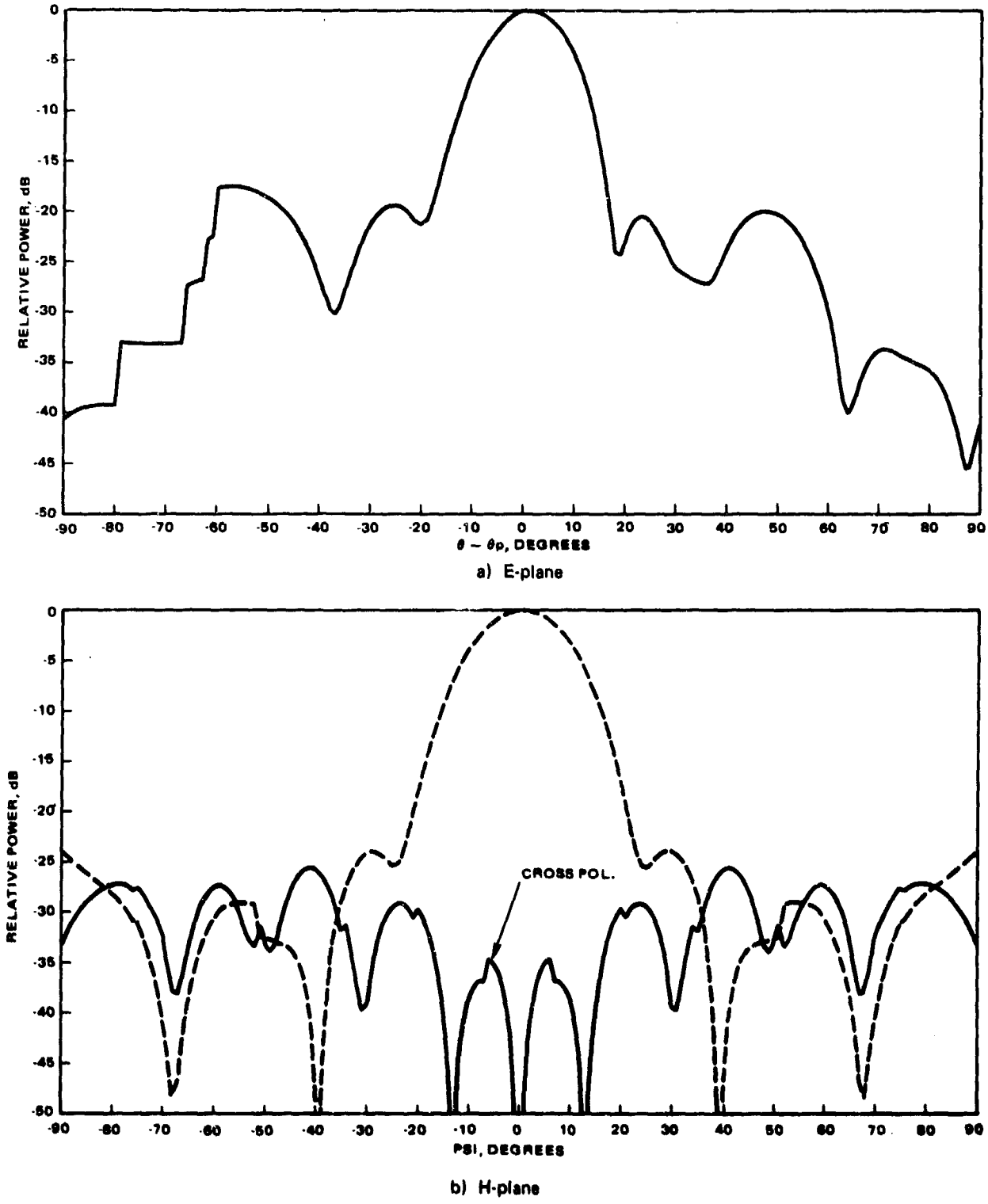

Figure 27. Calculated patterns of 10^{o} of conical slot array; 35 elements ($\theta_p = 50^{o}$).

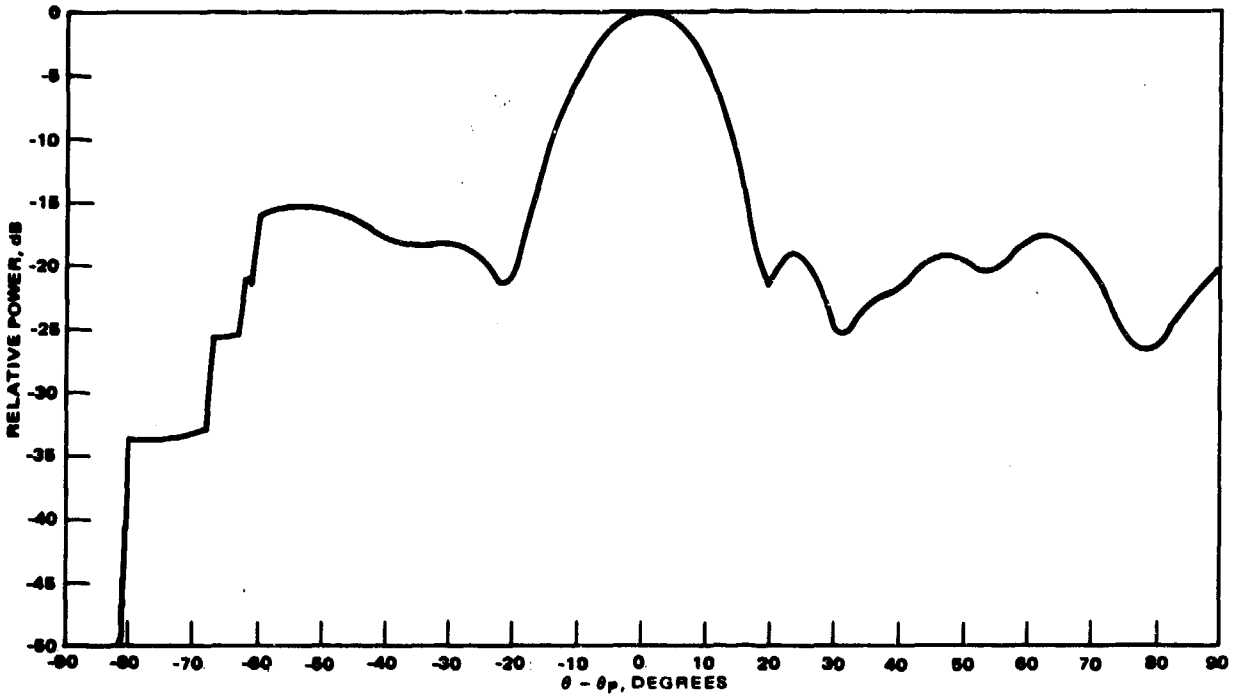

a) E-plane

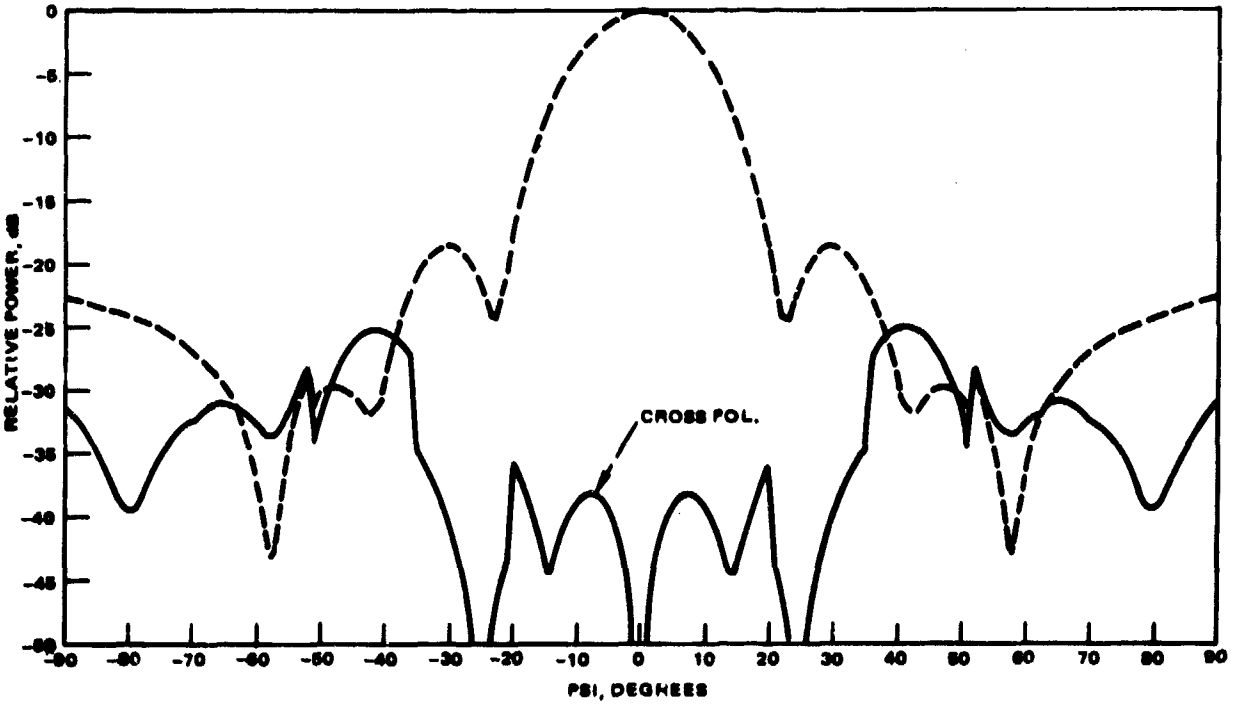

b) H-plane

Figure 28. Calculated patterns of 10.25° conical slot array; 35 elements ($\theta_p = 50^\circ$).

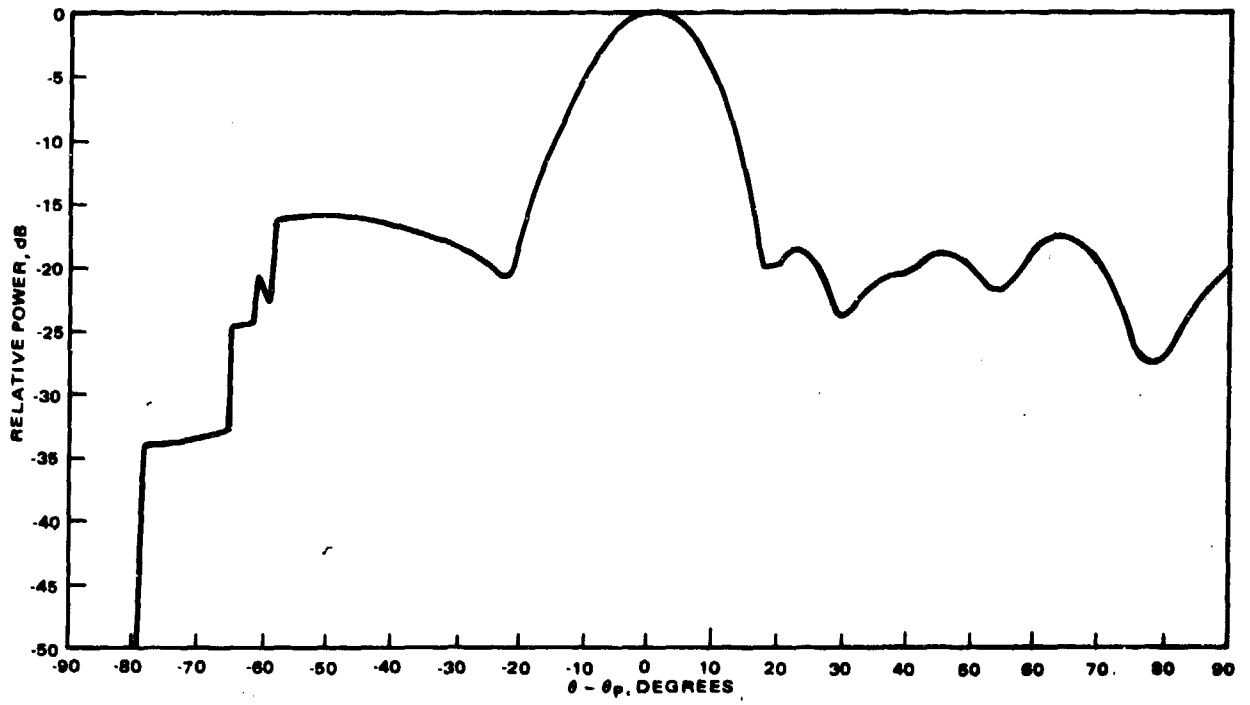

a) E-plane

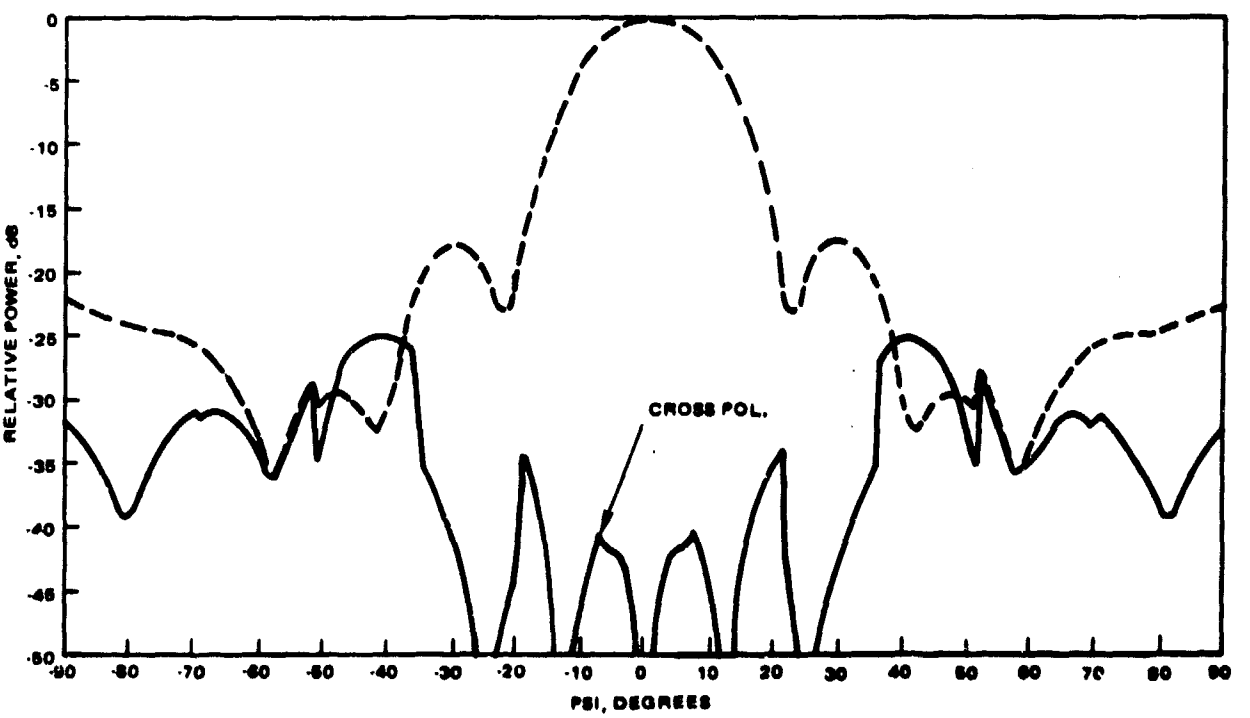

b) H-plane

Figure 29. Calculated patterns of 10.25° conical slot array; 35 elements (θ_p = 48.2°).

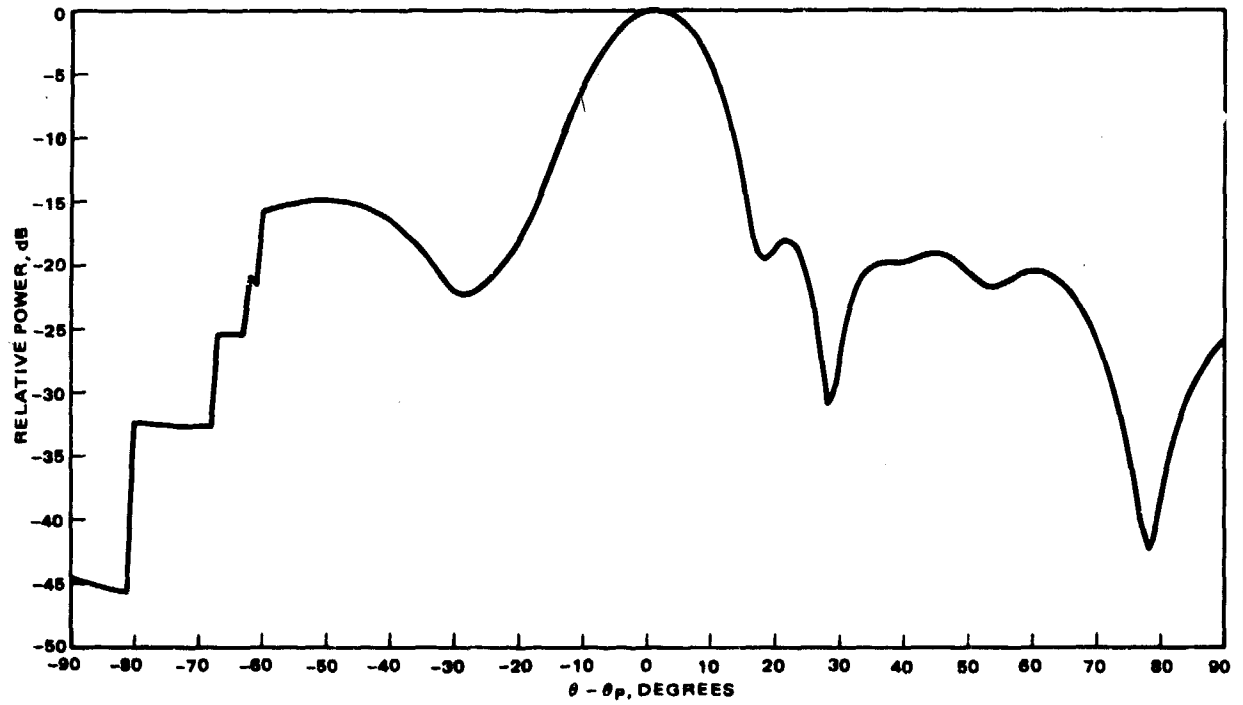

a) E-plane

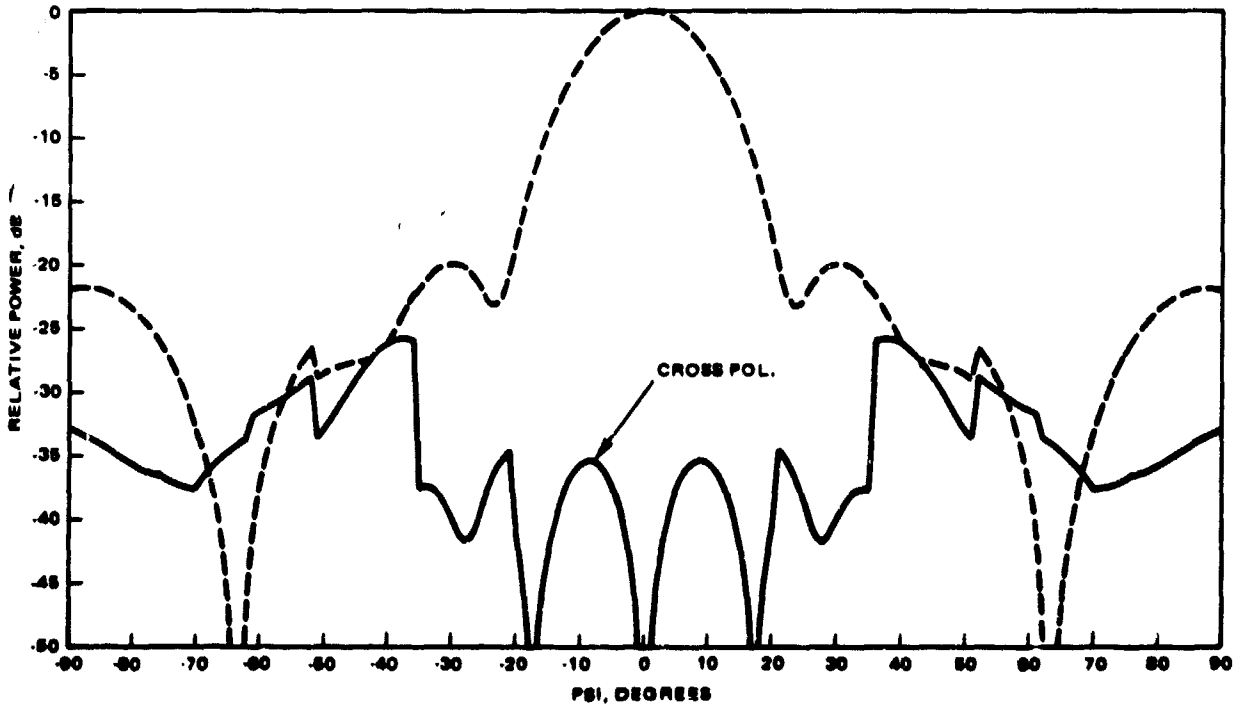

b) H-plane

Figure 30. Calculated patterns of 10.25° conical slot array; 35 elements, modified positions ($\theta_p = 50^\circ$).

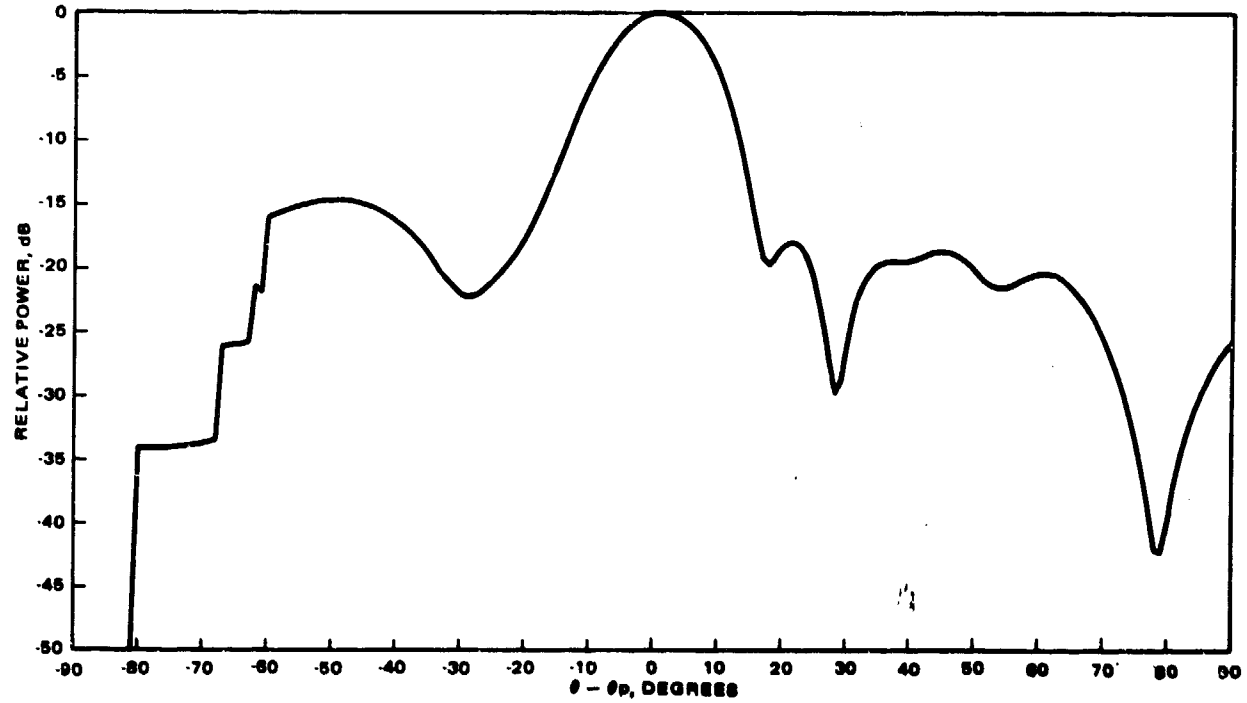

a) E-plane

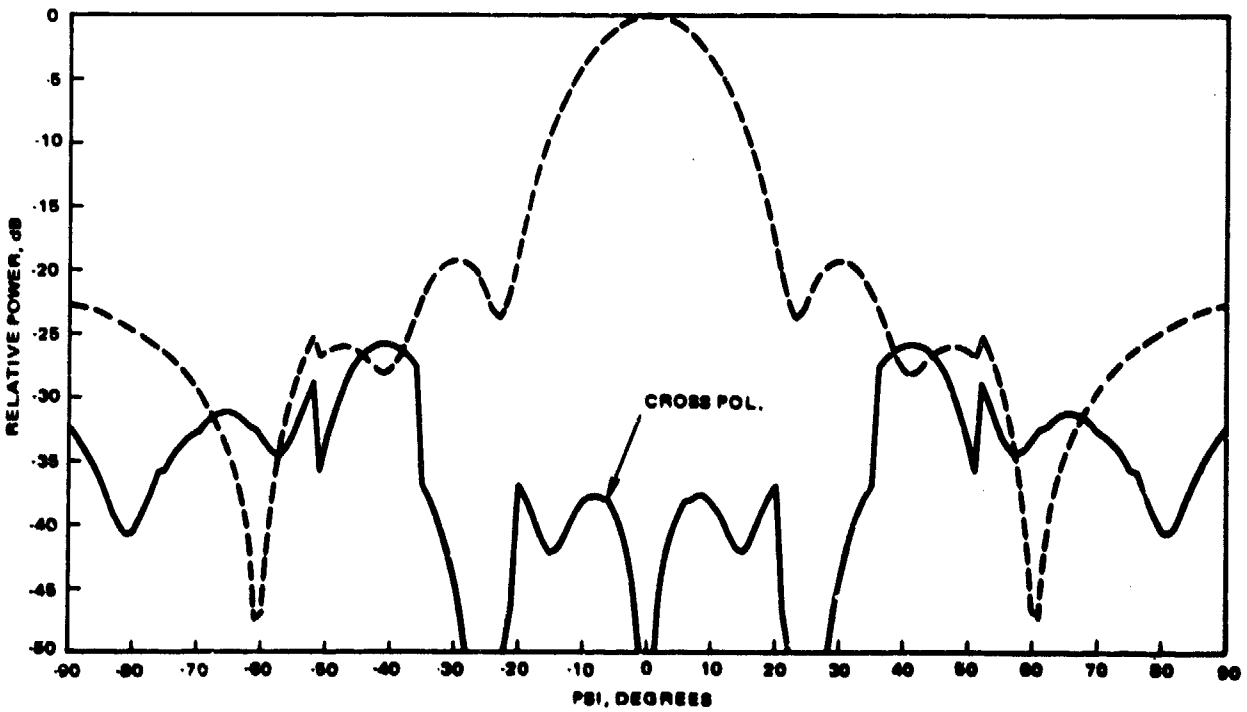

b) H-plane

Figure 31. Calculated patterns of 10.25° conical slot array; 37 elements (θ_p = 50°).

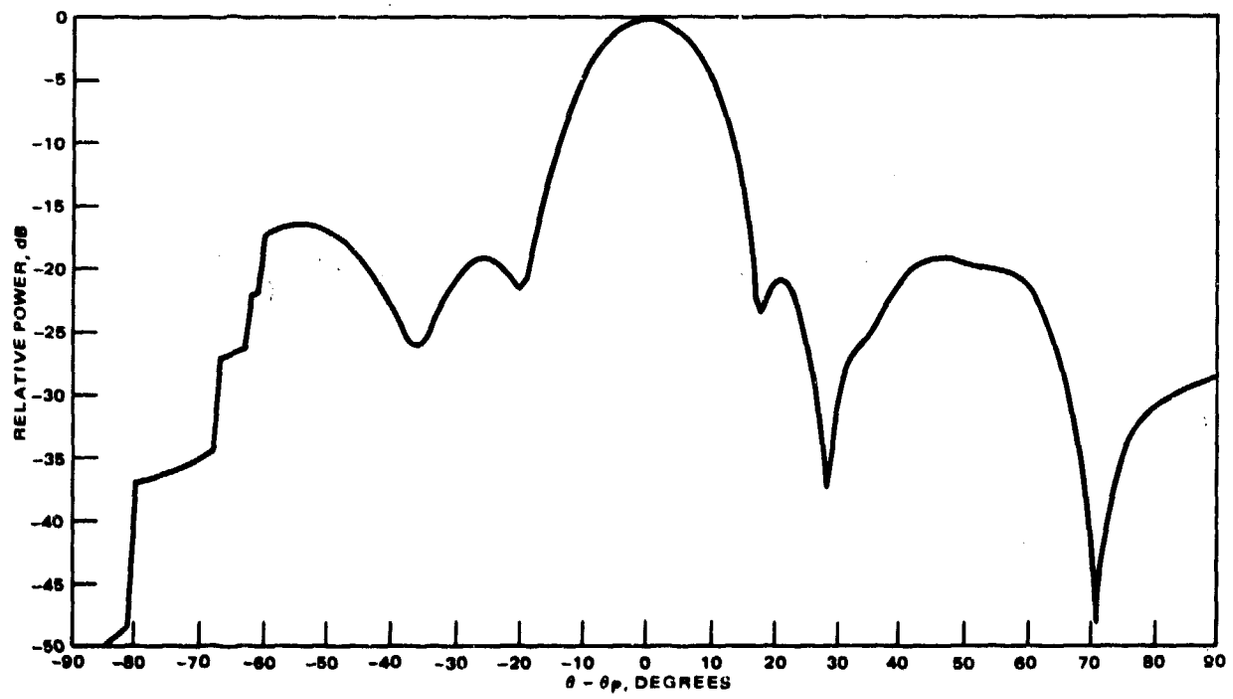

a) E-plane

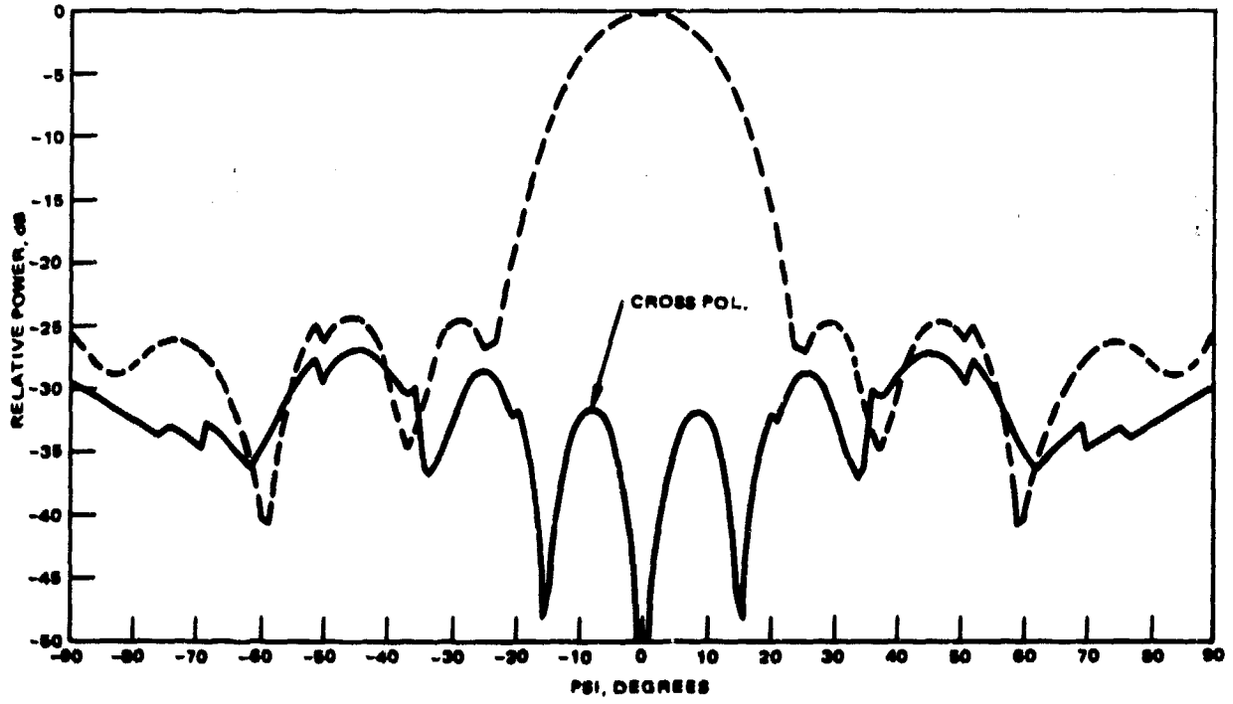

b) H-plane

Figure 32. Calculated patterns of 10.25° conical slot array; 37 elements, modified position of planar array ($\theta_p = 50°$)

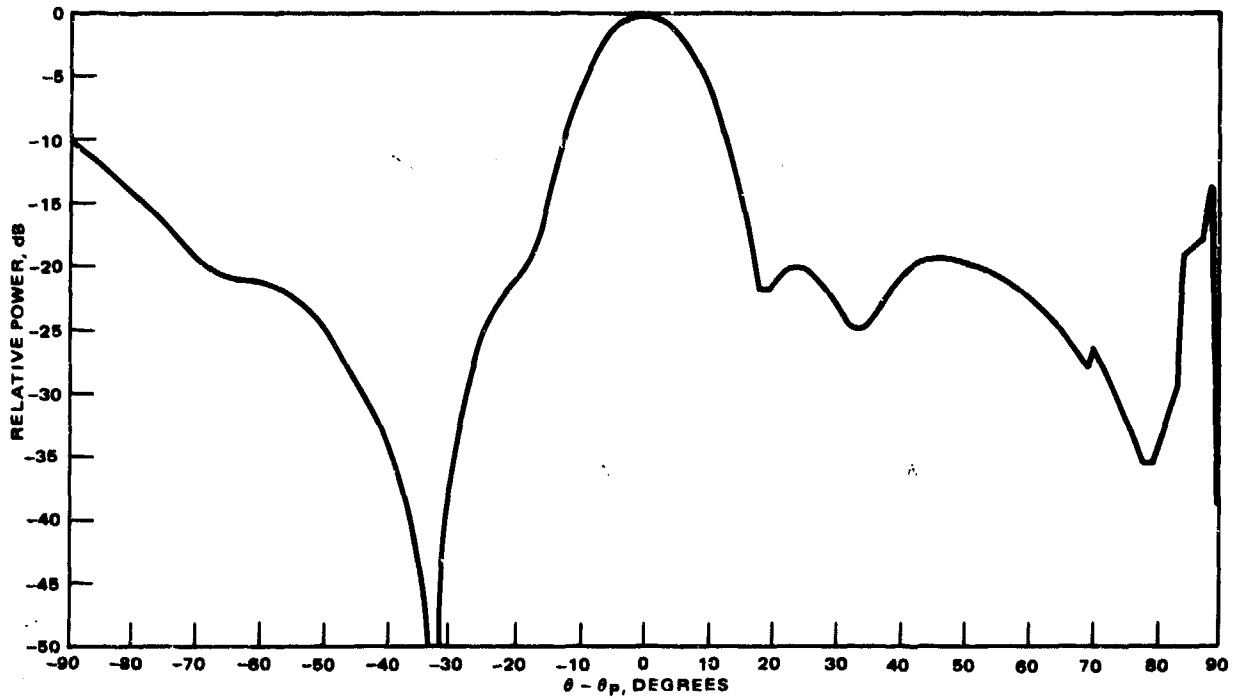

a) E-plane

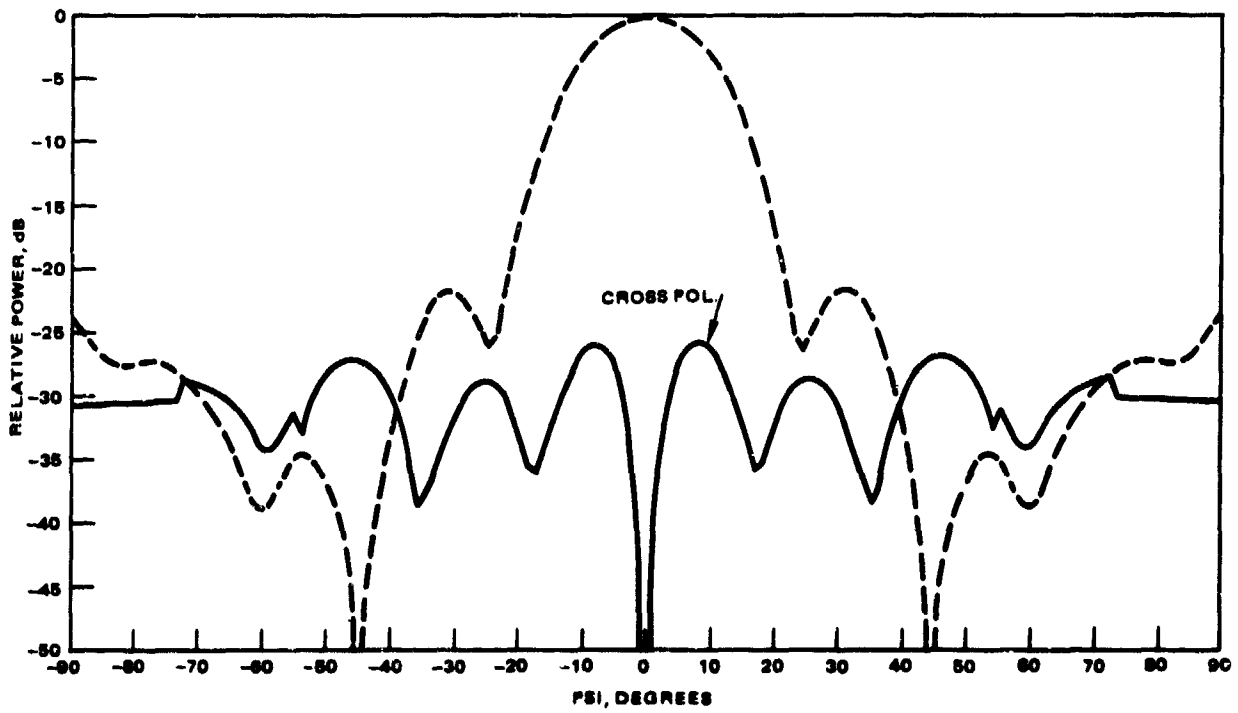

b) H-plane

Figure 33. Calculated patterns of 10.25° conical slot array; 37 elements (θ_p = 79.75°).

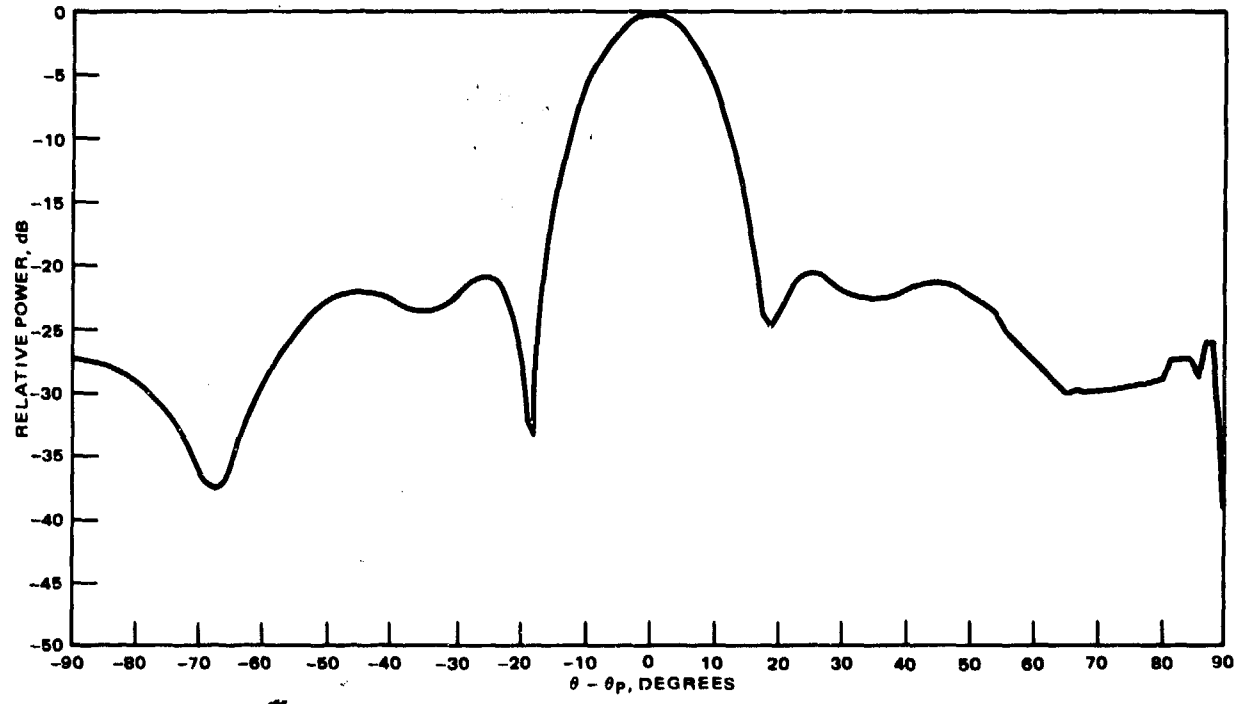

a) E-plane

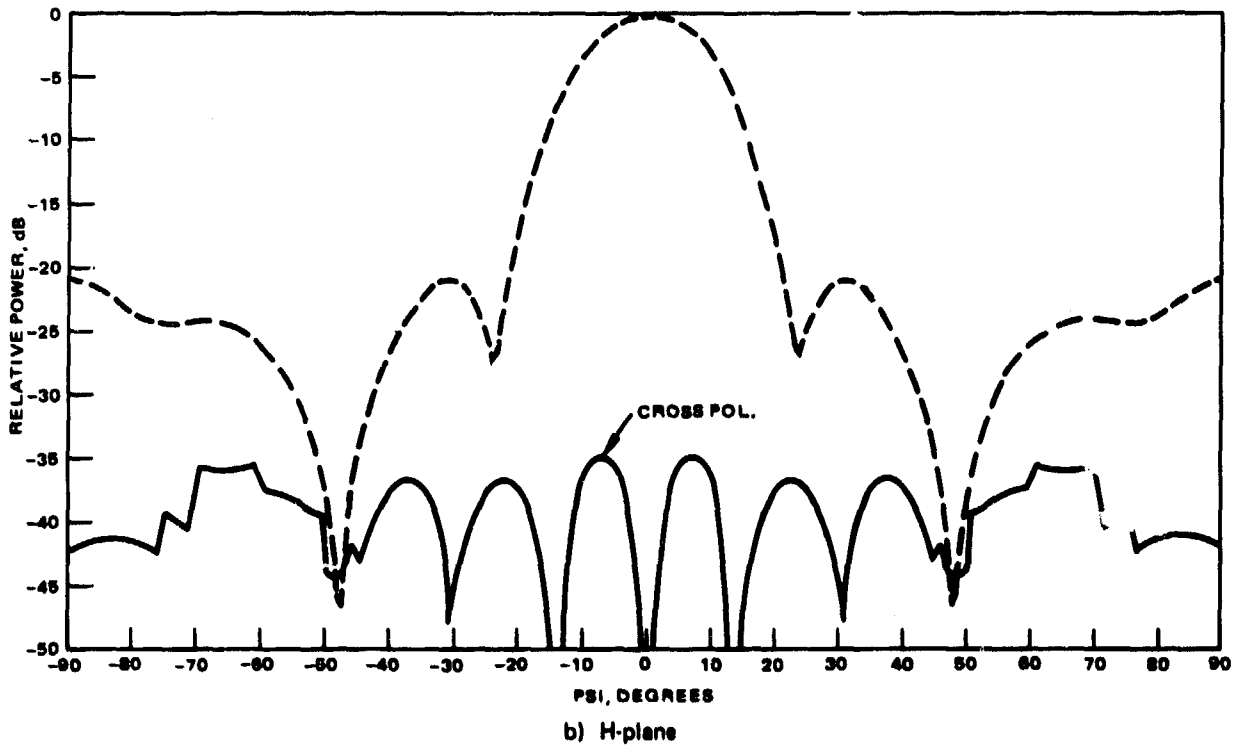

b) H-plane

Figure 34. Calculated patterns of 10.25° conical slot array; 74 elements (θ_p = 79.75°).

arrangements of excited elements. Figure 32 also has a somewhat different position of the reference planar array that determines the slot excitations. The arrangements of slots on the developed cones for the patterns in Figures 28 through 34 are shown in Figures 35, 36 and 37. The slot arrangement finally selected for the experimental array is that of Figure 37. This arrangement was selected as a compromise between number of slots and the quality of the patterns.

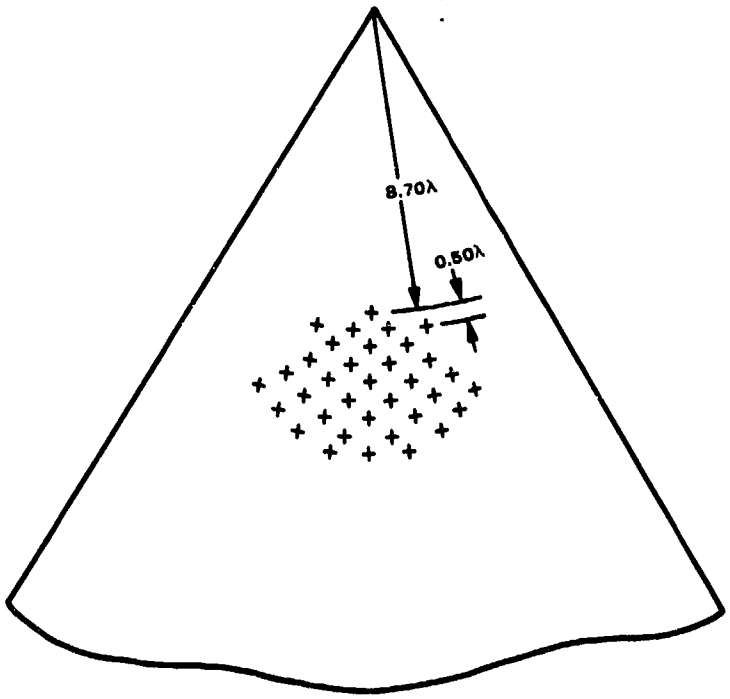

Figure 35. Locations of excited slots for the patterns of Figures 28 and 29.

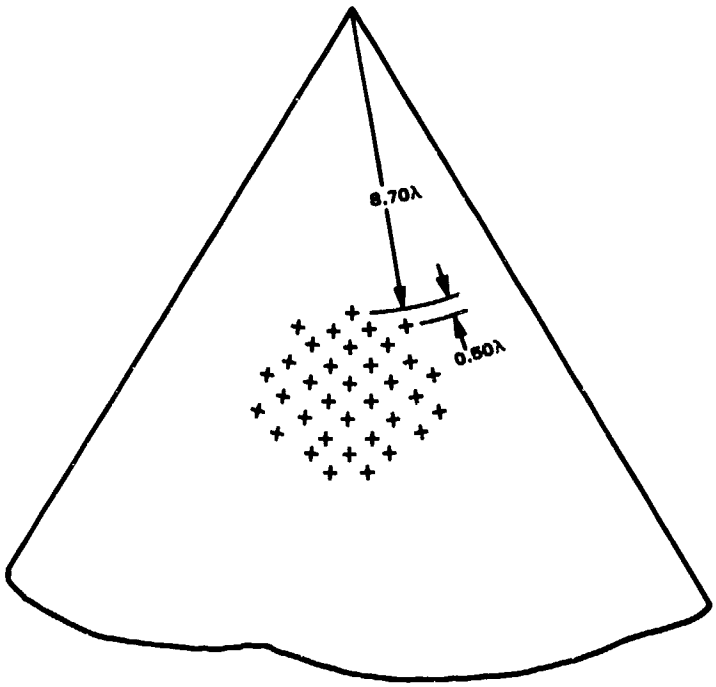

Figure 36. Locations of excited slots for the patterns of Figure 30.

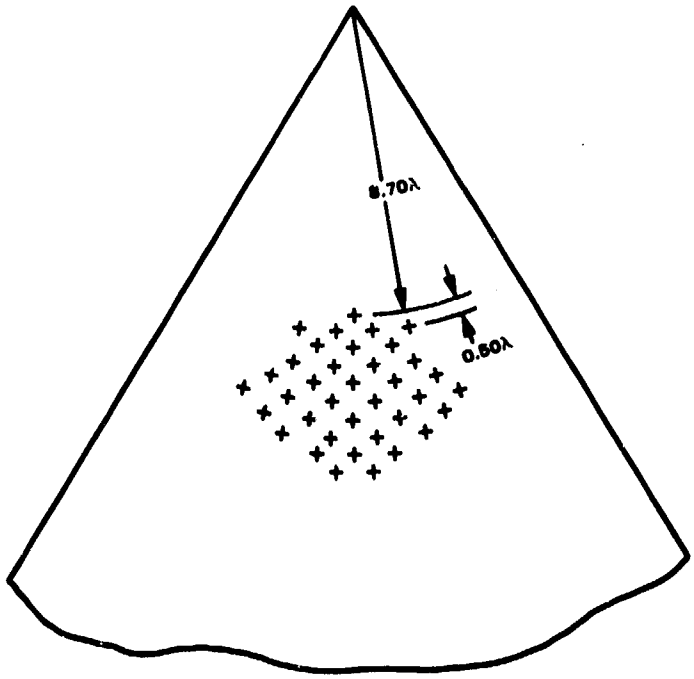

Figure 37. Locations of excited slots for the patterns of Figures 31, 32 and 33.

APPENDIX A

In this Appendix the first computer program described in Section 2.1.4 is listed. The program is CONEZ and a complete Fortran listing is given as well as a list of input variables, data formats, and output variables (Tables I, II and III).

```
C     THIS PROGRAM TAKES PLANAR ARRAY AND COMPUTES ITS NEAR FIELD ON
C     A CONICAL SURFACE SURROUNDING THE ARRAY. THIS FIELD IS THEN USED
C     AS AN EQUIVALENT SOURCE ON A CONDUCTING CONE TO REPRODUCE THE
C     ARRAY PATTERN. THE EQUIVALENT SOURCE IS APPROXIMATED BY
C     SHORT SLOTS ON THE CONE EXCITED IN PROPORTION TO THE
C     REQUIRED EQUIVALENT SOURCE AT THE SLOT LOCATION. APPROXIMATE
C     ELEMENT PATTERNS ARE USED FOR THE SLOTS.
C
C     MAIN PROGRAM
C
C     THE MAIN PROGRAM CONTROLS FLOW, READS DATA, AND CALLS VARIOUS
C     SUBROUTINES
C
      COMMON/OUTPUT/ EPDB(400),ETDB(400)
      COMMON/ALL/NSLOT,PI,PID2,THETA0,WVLTH
      COMMON/PATAU/NPSI,T2(400),P2(400),PSI(400),TAD
      COMMON/PELCON/P0(2000),R(2000),RMAX
      COMMON/PATCON/ER1(2000),EPHI1(2000)
      COMMON/TAU/PHIS,THETAS
      COMMON/REST/Z0,RN
      COMMON/LAST/ZTEST(2000)
      COMMON/ROT/ETPPDB(400),EPPPDB(400)
      COMMON/BEAM/PHIP,THETAP
      COMPLEX ER1,EPHI1
      DOUBLE PRECISION DATE
  100 CALL CLOCK(TIME,DATE)
      WRITE(6,11)TIME,DATE
   11 FORMAT(//1X,5HTIME ,A4,6X,5HDATE ,A8,//)
      READ(5,200)THETA0, WVLTH, NUMCUT
  200 FORMAT(2F10.5,I5)
      CALL ELLOC
      DO 400 NUMBER=1,NUMCUT
      IF (NUMBER.GT.1)WRITE(6,15)
   15 FORMAT(/////)
      CALL TAUCUT
      IF(NUMBER.GT.1) GO TO 300
      CALL CONDIS
  300 CALL PATCOM
      READ(5,12) NC,NP1,NP2,SX,XMIN,DELX,SY,YMIN,DELY
   12 FORMAT(3I5,6F10.5)
      CALL PLOTI
      CALL CPLOT3(NC,PSI,SX,XMIN,DELX,'PHPSI-DEG',7,SY,YMIN,DELY,
     +12HREL.PWR.(DB),12,NP1,EPPPDB,NP2,ETPPDB)
  400 CONTINUE
      STOP
      END
      SUBROUTINE ELLOC
C
C     THIS SUBROUTINE COMPUTES THE LOCATIONS OF ELEMENTS ON A CONE. THE
C     ELEMENTS ARRANGED ON RINGS WITH AZIMUTHAL SPACING OF BETWEEN SOME
C     MINIMUM VALUE, SPAZMN, AND SOME MAXIMUM VALUE SPAZMX. THE NUMBER
C     OF ELEMENTS IN A GIVEN RING IS DETERMINED BY THIS CRITERION. THE
C     RADIAL SPACING OF RINGS IS DEAD. THE INPUTS REQUIRED ARE THE
C     RADIUS OF THE LARGEST REFERENCE PLANAR ARRAY CONSIDERED, RN,
C     AND THE DISTANCE FROM THE CONE TIP TO THE FIRST
```

```
C     RING OF ELEMENTS. ADJACENT RINGS ARE SHIFTED BY ONE HALF THE
C     ELEMENT SEPARATION TO PROVIDE A TRIANGULAR LATTICE.
C
      COMMON/ALL/NSLOT,PI,PID2,THETA0,WVLTH
      COMMON/PELCON/P0(2000),R(2000),RMAX
      COMMON/REST/Z0,RN
      PI=4.*ATAN(1.)
      RAD=PI/180.
      READ(5,500) SPAZMX, SPAZMN
      SEPMAX = SPAZMX*WVLTH
      SEPMIN = SPAZMN*WVLTH
      READ(5,500)RN,RADMIN,DRAD
      WRITE(6,400) SEPMIN,SEPMAX
  400 FORMAT(//,1X,29HMINIMUM AZIMUTHAL SEPARATION=,F10.5,7H INCHES,/
     *1X,29HMAXIMUM AZIMUTHAL SEPARATION=,F10.5,7H INCHES,//)
      WRITE(6,600) DRAD
  600 FORMAT(1X,33HRING SEPARATION ALONG GENERATRIX=,F10.5,7H INCHES,//)
      T0=THETA0*RAD
  500 FORMAT(3F10.5)
      SIN0=SIN(T0)
      COS0=COS(T0)
      Z0=-RN/SIN0
      RMAX=(-RN*(1.+SIN0)/SIN0-2.*WVLTH)/COS0
      I=0
      RAD1=RADMIN
      NSLT=INT(2.*PI*RAD1*SIN0/(SEPMIN))
      IF(NSLT.EQ.0) NSLT=1
      DO 100 N=1,1000
      IF (RAD1.GT.RMAX) GO TO 300
      SEP=RAD1*2.*PI*SIN0/FLOAT(NSLT)
      IF (SEP.GE.SEPMAX) NSLT=INT(2.*PI*RAD1*SIN0/(SEPMIN))
      IF(NSLT.EQ.0) NSLT=1
      DELPHI=2.*PI/FLOAT(NSLT)
  123 FORMAT(1X,I3,3F10.4)
      M=1*(-1)**N
      DO 200 L=1,NSLT
      I=I+1
      R(I)=RAD1
      P0(I)=FLOAT(L-1)*DELPHI
      IF (M.EQ.2) P0(I)=P0(I)+DELPHI/2.
  200 CONTINUE
      RAD1=RAD1+DRAD
  100 CONTINUE
  300 NSLOT=I
      RETURN
      END
      SUBROUTINE TAUCUT
C
C     THIS SUBROUTINE SETS UP THE COORDINATE SYSTEM FOR PATTERN CALCULA-
C     TION. THE ANGLE TAU IS THE ANGLE OF THE CUT (TAU=0 CORRESPONDS TO
C     A CUT THROUGH THE CONE AXIS). PSI IS THE ANGULAR VARIABLE OF THE
C     CUT. THE ROUTINE USES THE BEAM POINTING DIRECTIONS PHIP AND
C     THETAP. THE OUTPUT IS ARRAYS OF ANGLES PSI(I),T2(I),AND P2(I).
C
      COMMON/DATAU/NPSI,T2(400),P2(400),PSI(400),TAU
```

```
      COMMON/TAU/PHIS,THETAS
      COMMON/BEAM/PHIP,THETAP
      READ(5,100)TAD,PL,PH,ST,PHIP,THETAP
  100 FORMAT(6F10.5)
      WRITE(6,200)THETAP,PHIP
  200 FORMAT(1X,26HPOINTING DIRECTION: THETA=,F7.2,3X,8HDEGREES,,3X,4HPH
     +I=,F7.2,3X,7HDEGREES,//)
      WRITE(6,19)
   19 FORMAT(//33H TAU CUT   PSI LO   PSI HI   STEP,/1X,F8.3,2F9.3,F7.3)
      WRITE(6,20)TAD,PL,PH,ST
   20 FORMAT(1X,F7.2,1X,F7.2,1X,F7.2,3X,F7.2)
      PI=4.*ATAN(1.)
      RA= 180./PI
      TA=TAD/RA
      THETAS=THETAP
      PHIS=PHIP+90.
      PHIR=PHIP/RA
      THETAR=THETAS/RA
      COSPHI=COS(PHIR)
      SINPHI=SIN(PHIR)
      SINTH=SIN(THETAR)
      COSTH=COS(THETAR)
      I9=0
      SINTA=SIN(TA)
      COSTA=COS(TA)
      PSID=PL
  260 I9=I9+1
      PSIR=PSID/RA
      PSI(I9)=PSIR
      SINP=SIN(PSIR)
      COSP=COS(PSIR)
      WN=SINP*COSTA*COSTH+COSP*SINTH
      XN=WN*COSPHI-SINP*SINTA*SINPHI
      YN=WN*SINPHI+SINP*SINTA*COSPHI
      IF(XN.EQ.0..AND.YN.EQ.0)XN=1.0E-18
      ZN=COSP*COSTH-SINP*COSTA*SINTH
      XY=SQRT(XN**2+YN**2)
      T2(I9)=ATAN2(XY,ZN)
      P2(I9)=ATAN2(YN,XN)
      PSID=PSID+ST
      IF(PSID.LE.PH)GO TO 260
      NPSI=I9
      RETURN
      END
      SUBROUTINE CONDIS
C
C     THIS SUBROUTINE COMPUTES THE RADIAL AND CIRCUMFERENTIAL ELECTRIC
C FIELDS AT SELECTED POINTS ON A CONICAL SURFACE. THE FIELDS COME FROM A
C PLANAR SLOT ARRAY LOCATED WITHIN THE CONICAL SURFACE. THE ARRAY
C ORIENTATION IS ARBITRARY. THE INPUTS REQUIRED ARE THE RADIUS OF THE
C CONE, THE SLOT SPACING IN THE PLANAR ARRAY, DX,DY,THE WAVELENGTH,
C WVLTH, THE CONE ANGLE, THETA0, AND THE RADIUS OF THE PLANAR ARRAY,RAN,
C AND THE RADIUS OF THE PROJECTED ACTIVE PORTION OF THE CONE, RAL.
C THE SLOTS ON THE ARRAY ARE PARALLEL TO THE Y-AXIS OF THE ARRAY.
C THE POLARIZATION IS CONTROLLED BY PSIS. (PSIS=-90 CORRESPONDS TO
```

```
C VERTICAL (THETA) POLARIZATION.)
C THE PLANAR ARRAY TAPER, FNA(R), MUST BE SPECIFIED.
C THE PHASE MAY BE QUANTIZED TO N BITS BY SETTING MQPH EQUAL TO N.
C MQPH=0 GIVES NO QUANTIZATION. THE ACTIVE PORTION OF THE ARRAY IS
C CONTROLLED BY ILIM. IF ILIM=0, ALL SLOTS ARE EXCITED ON THE CONE THAT
C DO NOT LIE BEHIND THE PLANE OF THE EQUIVALENT PLANAR ARRAY. IF ILIM>0
C ONLY THOSE SLOTS ARE EXCITED THAT LIE WITHTIN THE PROJECTION OF THE
C PLANAR ARRAY OUTLINE ONTO THE CONICAL SURFACE.
C SUM OR DIFFERENCE PATTERNS MAY BE OBTAINED BY ADJUSTING MONO.
C (MONO=0 GIVES SUM; MONO=1 GIVES H-PLANE DIFFERENCE; MONO=2 GIVES
C E-PLANE DIFFERENCE.)
C
C PRELIMINARY COMPUTATIONS AND SETUP OF INITIAL VALUES
      COMMON/ALL/NSLOT,PI,FID2,THETA0,WVLTH
      COMMON/PELCON/P0(2000),R(2000),RMAX
      COMMON/PATCON/ER1(2000),EPHI1(2000)
      COMMON/REST/Z0,RN
      COMMON/TAU/PHIS,THETAS
      COMMON/LAST/ZTEST(2000)
      COMPLEX EX2,EZ2,F,G,ZIM,EX0,EZ0,EX,EY,EZ,EPHI,ER,EPHI1,ER1
      REAL L, MAGR, MAGPHI
C SPECIFY THE APERTURE TAPER FNA(R).
      FNA(X)=1.
      RAD=PI/180.
      READ(5,100)DX,DY,PSIS,RAN,RAL,MONO,MQPH,ILIM
  100 FORMAT(5F10.3,3I5)
      WRITE(6,700) RN,RAN
  700 FORMAT(//,1X,28HMAXIMUM PLANAR ARRAY RADIUS=,F10.5,7H INCHES,/,
     +1X,27HACTUAL PLANAR ARRAY RADIUS=,F10.5,7H INCHES,//)
      WRITE(6,900) DX, DY
  900 FORMAT(1X,29HPLANAR ARRAY ELEMENT SPACING:,/,1X,3HDX=,
     +F10.5,12H INCHES, DY=,F10.5,7H INCHES,//)
      WRITE(6,800) WVLTH
  800 FORMAT(1X,11HWAVELENGTH=,F10.5,7H INCHES,//)
      DELTP=2.*PI/2.**MQPH
      T0=THETA0*RAD
      PHS=PHIS*RAD
      THTS=THETAS*RAD
      PSS=PSIS*RAD
      WRITE(6,110)THETA0
  110 FORMAT(/1X,19HCONE ANGLE, THETA0=1X,F6.2,6H DEGREES,//)
      WRITE(6,140)
  140 FORMAT(1X,49HPSI-SUB-S-DEG     PHI-SUB-S-DEG     THETA-SUB-S-DEG/)
      WRITE(6,150)PSIS,PHIS,THETAS
  150 FORMAT(F13.2,4X,F13.2,4X,F15.2,//)
      IF(MONO.EQ.0) WRITE(6,145)
  145 FORMAT(1X,11HSUM PATTERN,//)
      IF(MONO.EQ.1) WRITE(6,155)
  155 FORMAT(1X,26HH-PLANE DIFFERENCE PATTERN,//)
      IF(MONO.EQ.2) WRITE(6,165)
  165 FORMAT(1X,26HE-PLANE DIFFERENCE PATTERN,//)
      IF(MQPH.GT.0) WRITE(6,600) MQPH
  600 FORMAT(1X,19HPHASE QUANTIZED AT ,I5,5H BITS,//)
      IF(ILIM.EQ.0) WRITE(6,190)
  190 FORMAT(1X,18HFULL CONE EXCITED.,//)
```

```
      IF(ILIM.GT.0) WRITE(6,195) RAL
  195 FORMAT(1X,40HRADIUS OF PROJECTED ACTIVE AREA OF CONE=,F10.5,7H INC
     +HES,//)
      WRITE(6,160)
  160 FORMAT(1X,8HSLOT NO.,3X,8HRAD SLOT,2X,8HANG SLOT,3X,4HEPHI,5X,5HPH
     +ASE,5X,2HER,7X,5HPHASE)
      WRITE(6,170)
  170 FORMAT(13X,6HINCHES,5X,3HDEG,7X,3HMAG,6X,3HDEG,6X,3HMAG,7X,3HDEG,/
     +)
      L=WVLTH/2.
      A1=(1.-L/DY)/2.
      A2=(1.+L/DY)/2.
      SIN0=SIN(T0)
      COS0=COS(T0)
      SINPS=SIN(PSS)
      COSPS=COS(PSS)
      SINTS=SIN(THTS)
      COSTS=COS(THTS)
      SIPHS=SIN(PHS)
      COPHS=COS(PHS)
      RBAS=RMAX*SIN0
      M1=INT(SQRT(RAN**2-((DY+L)/2.)**2)/DX+.4999)
      M2=2*M1
      STH = SIN(THETA0*RAD)
      CTH = COS(THETA0*RAD)
      RR1 = COS(PHIS*RAD)*COS(PSIS*RAD)
     +-SIN(PHIS*RAD)*COS(THETAS*RAD)*SIN(PSIS*RAD)
      RR2 = SIN(PHIS*RAD)*COS(PSIS*RAD)
     ++COS(PHIS*RAD)*COS(THETAS*RAD)*SIN(PSIS*RAD)
      RR3 = -COS(PHIS*RAD)*SIN(PSIS*RAD)
     +-SIN(PHIS*RAD)*COS(THETAS*RAD)*COS(PSIS*RAD)
      RR4 = -SIN(PHIS*RAD)*SIN(PSIS*RAD)
     ++COS(PHIS*RAD)*COS(THETAS*RAD)*COS(PSIS*RAD)
      Q3 = -Z0
      RX1 = SIN(THETAS*RAD)*SIN(PSIS*RAD)
      RY1 = SIN(THETAS*RAD)*COS(PSIS*RAD)
      DO 10 N=1,NSLOT
C CONDITIONAL STATEMENTS TO REMOVE SELECTED SLOTS.
C     IF(N.EQ.85.OR.N.EQ.91.OR.N.EQ.135)GO TO 10
C     IF(N.EQ.140.OR.(N.GT.144.AND.N.LT.156)) GO TO 10
C     IF(N.EQ.158.OR.N.EQ.169) GO TO 10
C     IF(N.GT.94.AND.N.LT.101) GO TO 10
      ER1(N) = CMPLX(0.,0.)
      EPHI1(N) = CMPLX(0.,0.)
      Q1 = R(N)*STH*COS(P0(N))
      Q2 = R(N)*STH*SIN(P0(N))
      Q4 = R(N)*CTH
      X3P = Q1*RR1 + Q2*RR2 + (Q3+Q4)*RX1
      Y3P = Q1*RR3 + Q2*RR4 + (Q3+Q4)*RY1
      RHOXY = SQRT(X3P**2 + Y3P**2)
      IF (ILIM.GT.0.AND.RHOXY .GT. RAL)  GO TO 09
      AN=N
      RSLOT=R(N)
      PHI2=P0(N)
      PHID=PHI2/RAD
```

```
      SIND=SIN(PHI2-PHS)
      COSD=COS(PHI2-PHS)
      COPHI2=COS(PHI2)
      SIPHI2=SIN(PHI2)
      X2=RSLOT*(SIN0*(COSPS*COSD+COSTS*SINPS*SIND)+SINPS*SINTS*COS0)
     +-Z0*SINPS*SINTS
      Y2=RSLOT*(SIN0*(-SINPS*COSD+COSTS*COSPS*SIND)+COSPS*SINTS*COS0)
     +-Z0*COSPS*SINTS
      Z2=RSLOT*(-SINTS*SIN0*SIND+COSTS*COS0)-Z0*COSTS
      ZTEST(N)=Z2
      IF(Z2.LT.0.) GO TO 10
C
C   COMPUTATION OF FIELD DUE TO PLANAR ARRAY
C
      EX2=CMPLX(0.,0.)
      EZ2=CMPLX(0.,0.)
      DO 30 M=1,M2
      AM=M-M1-1
      X1=(AM+.5)*DX
      B=SQRT(RAN**2-((AM+.5)*DX)**2)/DY-.0001
      N2=INT(B+A1)+INT(B-A2)+1
      DO 30 J=1,N2
      BN=J-INT(B+A1)-1
      Y1=(BN+.5)*DY
      ANGLE=ATAN2(Y1,X1)
      R1=SQRT((X2-X1)**2+(Y2-Y1)**2+Z2**2)
      C=COS(PI*L*(Y2-Y1)/(R1*WVLTH))-COS(PI*L/WVLTH)
      RHO=SQRT(X1**2+Y1**2)
      V=FNA(RHO)
      IF(MONO.EQ.1.AND.ANGLE.LT.0.) V=-V
      IF(MONO.EQ.2.AND.ABS(ANGLE).LT.PI/2.) V=-V
      R4=SQRT((X2-X1)**2+Z2**2)
      F1=V*Z2*C/(PI*R4**2)
      F=CMPLX(0.,-F1)
      G1=V*(X2-X1)*C/(PI*R4**2)
      G=CMPLX(0.,G1)
      ZIM=CMPLX(0.,-2.*PI*R1/WVLTH)
      EX0=F*CEXP(ZIM)
      EZ0=G*CEXP(ZIM)
      EX2=EX2+EX0
   30 EZ2=EZ2+EZ0
C
C   TRANSFORM FIELD COMPONENTS TO COORDINATE SYSTEM OF CONE.
C
      EX=EX2*(COSPS*COPHS-COSTS*SIPHS*SINPS)+EZ2*SINTS*SIPHS
      EY=EX2*(COSPS*SIPHS+COSTS*COPHS*SINPS)-EZ2*SINTS*COPHS
      EZ=EX2*SINTS*SINPS+EZ2*COSTS
C
C   RADIAL AND CIRCUMFERENTIAL COMPONENTS
C
      ER=(EX*COPHI2+EY*SIPHI2)*SIN0+EZ*COS0
      EPHI=-EX*SIPHI2+EY*COPHI2
      IF(MOPH.GT.0) GO TO 80
      ER1(N)=ER
      EPHI1(N)=EPHI
```

```
   80   MAGR=CABS(ER)
        MAGPHI=CABS(EPHI)
        IF(MAGR.NE.0.) GO TO 40
        PHAR=0.
        GO TO 50
   40   PHAR=ATAN2(AIMAG(ER),REAL(ER))
   50   IF(MAGPHI.NE.0.) GO TO 60
        PHAPHI=0.
        GO TO 65
   60   PHAPHI=ATAN2(AIMAG(EPHI),REAL(EPHI))
   65   IF(MOPH.EQ.0) GO TO 70
        PHAR=-DELTP*AINT((PI-PHAR)/DELTP+0.5)
        PHAPHI=-DELTP*AINT((PI-PHAPHI)/DELTP+0.5)
        ER1(N)=CMPLX(MAGR*COS(PHAR),MAGR*SIN(PHAR))
        EPHI1(N)=CMPLX(MAGPHI*COS(PHAPHI),MAGPHI*SIN(PHAPHI))
   70   PHAPHD=PHAPHI/RAD
        PHARD=PHAR/RAD
        WRITE (6,180) N, RSLOT, PHID, MAGPHI, PHAPHD, MAGR, PHARD
  180   FORMAT(2X,I4,3X,F7.3,3X,F7.2,2X,E10.4,F8.2,2X,E10.4,F8.2)
   09   CONTINUE
   10   CONTINUE
        RETURN
        END
        SUBROUTINE PATCOM
C
C       THIS SUBROUTINE COMPUTES THE RADIATION PATTERN OF SLOTS ON CONE.
C       IT USES APPROXIMATE ELEMENT PATTERNS.IT USES THE SLOT POSITIONS
C       COMPUTED IN ELLOC, THE FIELD POSITIONS COMPUTED IN TAUCUT, AND
C       THE EXCITATIONS COMPUTED IN CONDIS.
C
        COMMON/OUTPUT/EPDB(400),ETDB(400)
        COMMON/ALL/NSLOT,PI,PID2,THETA0,WVLTH
        COMMON/PATAU/NPSI,T2(400),P2(400),PSI(400),TAD
        COMMON/PELCON/P0(2000),R(2000),RMAX
        COMMON/PATCON/ER1(2000),EPHI1(2000)
        COMMON/LAST/ZTEST(2000)
        COMMON/ROT/ETPPDB(400),EPPPDB(400)
        COMMON/BEAM/PHIP,THETAP
        DIMENSION EPM(400),ETM(400)
        COMPLEX EP0,ET0,EP,ET,COEF,ZIM,ER1,EPHI1,S
        COMPLEX ETPP(400),EPPP(400)
        RAD=PI/180.
        PID2 = PI/2.
        T0=THETA0*RAD
        PHT = PHIP*RAD + PID2
        PHP = PHIP*RAD
        THT = THETAP*RAD
        THP = THETAP*RAD
        PST = TAD*RAD - PID2
        TAU = TAD*RAD
        SIN0=SIN(T0)
        COS0=COS(T0)
C       WRITE(6,110)
  110 FORMAT(3X,7HPSI DEG,9X,5HE-PHI,14X,8HE-PHI DB,13X,7HE-THETA,11X,10
     *HE-THETA DB,/)
```

```
      ZIM=(0.,1.)
      DO 100 J=1,NPSI
      SINT=SIN(T2(J))
      COST=COS(T2(J))
      EP=(0.,0.)
      ET=(0.,0.)
      DO 90 I=1,NSLOT
      SW=1.
      IF(ZTEST(I).LT.0.) GO TO 90
      SINP=SIN(P2(J)-P0(I))
      COSP=COS(P2(J)-P0(I))
      TEST=-SINT*COS0*COSP+COST*SIN0
      IF (TEST.LT.0.)SW=0.
C COMPUTATION OF APPROXIMATE ELEMENT PATTERN
      ZNUM=SINT*SINP
      DEN=SIN0*COST-SINT*COS0*COSP
      PHI=ABS(ATAN2(ZNUM,DEN))
      SIN1=SQRT(ZNUM**2+DEN**2)
      ZKASIN=2.*PI*R(I)*SIN0*SIN1/WVLTH
      ZNU=5.*ZKASIN/64.+3.375
      PHI0=RAD*(90.+24.8*EXP(-.0179*ZKASIN))
      EPR=1./(1.+(PHI/PHI0)**ZNU)
      S=R(I)*2.*PI*(SINT*SIN0*COSP+COST*COS0)*ZIM/WVLTH
      COEF=CEXP(S)
      EP0=(EPHI1(I)*(COST*SIN0*COSP-COS0*SINT)*EPR-SW*ER1(I)*COST*SINP)*
     1COEF
      ET0=(EPHI1(I)*SIN0*SINP*EPR+SW*ER1(I)*COSP)*COEF
C CONTINUATION OF SUMMATION
      EP=EP+EP0
      ET=ET+ET0
   90 CONTINUE
      EPM(J)=CABS(EP)
      ETM(J)=CABS(ET)
      PSID= PSI(J)/RAD
C TRANSFORM TO COMPONENTS, ETPP(J),PERPENDICULAR TO PLANE OF CUT, AND
C EPPP(J), PARALLEL TO PLANE OF CUT.
      CALL TRNFRM (ET,EP,ETPP(J),EPPP(J),THP,PHP,TAU,T2(J),P2(J),PSI(J))
      PSI(J) = PSID
  120 FORMAT (1X,F8.2,4E20.7)
  100 CONTINUE
C NORMALIZE PATTERNS AND CONVERT TO DB
      CALL DECYBL (EPPP,EPPPDB,ETPP,ETPPDB,400,NPSI)
C     DO 150  J = 1,NPSI
C 150 WRITE (6,120) PSI(J),EPM(J),EPDB(J),ETM(J),ETDB(J)
      WRITE (6,200)
  200 FORMAT (/////4X,'PSI',12X,'EPPP',15X,'EPPPDB',15X,
     1                          'ETPP',15X,'ETPPDB',//)
      DO 300  J = 1,NPSI
      EPPPJ = CABS(EPPP(J))
      ETPPJ = CABS(ETPP(J))
  300 WRITE (6,120) PSI(J),EPPPJ,EPPPDB(J),ETPPJ,ETPPDB(J)
      RETURN
      END
      SUBROUTINE TRNFRM(ET,EP,ET3P,EP3P,THP,PHP,TAU,T2,P2,PSI)
C
```

```
C THIS SUBROUTINE TRANSFORMS THE THETA AND PHI COMPONENTS OF THWE FIELDS
C TO COMPONENTS PERPENDICULAR TO AND PARALLEL TO THE PLANE OF THE CUT.
C THE COMPONENT PERPENDICULAR TO THE PLANE OF THE CUT IS ET3P.
C THE COMPONENT PARALLEL TO THE PLANE OF THE CUT IS EP3P.
C
      COMPLEX ET,EP,ET3P,EP3P,EX3P,EY3P,EZ3P
C
      DPH = PHP - P2
      CTHP = COS(THP)
      STHP = SIN(THP)
      CTHA = COS(T2)
      STHA = SIN(T2)
      CDPH = COS(DPH)
      SDPH = SIN(DPH)
      CTAU = COS(TAU)
      STAU = SIN(TAU)
      CPSI = COS(PSI)
      SPSI = SIN(PSI)
C
      EX3P = ET*(STHP*CTHA*CDPH-CTHP*STHA)
     1     + EP*(STHP*SDPH)
      EY3P = ET*((CTHP*CTHA*CDPH+STHP*STHA)*CTAU-CTHA*SDPH*STAU)
     1     + EP*(CTHP*SDPH*CTAU+CDPH*STAU)
      EZ3P = -ET*(CTHA*SDPH*CTAU+(CTHP*CTHA*CDPH+STHP*STHA)*STAU)
     1     + EP*(CDPH*CTAU-CTHP*SDPH*STAU)
C
      ET3P = -EZ3P
      EP3P = -EX3P*SPSI + EY3P*CPSI
C
      RETURN
      END
      SUBROUTINE DECYBL (A,B,C,D,N,M)
C
C THIS SUBROUTINE NORMALIZES THE FIELDS TO THE LARGEST VALUE AND
C CONVERTS POWER LEVELS TO DB.
C
      DIMENSION A(N),B(N),C(N),D(N)
      COMPLEX A,C
      CM = 0.
      DO 100  I = 1,M
      B(I) = CABS(A(I))
      CM = AMAX1(CM,B(I))
  100 CONTINUE
      DO 300 I=1,M
      D(I)=CABS(C(I))
      CM=AMAX1(CM,D(I))
  300 CONTINUE
      DO 200  I = 1,M
      B(I) = 20.*ALOG10(B(I)/CM)
      D(I)=20.*ALOG10(D(I)/CM)
  200 CONTINUE
      RETURN
      END
```

TABLE I. LIST OF INPUT VARIABLES

THETAO	θ_o Cone Angle - Degrees
WVLTH	λ Wavelength
SPAZMX	Maximum Azimuthal Element Spacing in Wavelengths
SPAZMN	Minimum Azimuthal Element Spacing in Wavelengths
RN	Maximum Radius of Equivalent Planar Array
RADMIN	Distance Along Generatrix from Cone Tip to First Ring of Radiating Elements
DRAD	Separation of Adjacent Rings. Measured Along Generatrix.
TAD	τ Angle of Plane of Cut - Degrees
PL	Initial Angle of Pattern Cut - Degrees (0 Corresponds to Beam Pointing Direction)
PH	Final Angle of Pattern Cut - Degrees
ST	Step Size on Pattern Cut - Degrees
PHIP	ϕ_p Azimuth Beam Pointing Direction - Degrees
THETAP	θ_p Elevation Beam pointing Direction - Degrees. Measured from +Z
DX	X - Spacing of Slots in Equivalent Planar Array
DY	Y - Spacing of Slots in Equivalent Planar Array
PSIS	Angle of Polarization Vector at Peak of Beam (0^o - Horizontal, -90^o Vertical)
RAN	Actual Radius of Equivalent Array
MONO	Switch for Selecting Sum or Difference Patterns (0 - Sum; 1 - H-Plane Difference; 2 - E-Plane Difference)

TABLE I. LIST OF INPUT VARIABLES (Continued)

MQPH	Number of Bits of Phase Quantization (MQPH=0 - No Quantization)
ILIM	Switch to Indicate Whether Full Cone or Limited Region of Cone is Excited (0 - Full Cone, > 0 - Limited Region)
RAL	Radius of Projection of Excited Region (If ILIM > 0)
NC	Number of Curves to be Plotted on Same Set of Axes
NP1	Number of Points to be Plotted in Curve 1
NP2	Number of Points to be Plotted in Curve 2
SX	Length (Inches) and Type of Independent Axis (If SX is Positive, a Linear Scale will be Drawn; if SX is Negative, a Log Scale will be Drawn)
XMIN	Smallest Value to be Shown on Independent Axis
DELX	Scale Increment per Inch for Linear Scale; Length in Inches of Log Cycle for Log Scale
SY	Length (Inches; $1.0 \leq \lvert SY \rvert \leq 10.$) and Type of Dependent Axis (see SX)
YMIN	Smallest Value to be Shown on Dependent Axis
DELY	Scale Increment for Dependent Axis (see DELX)

TABLE II. DATA FORMAT FOR CONEZ

Card No.	Parameter	Columns	Format
1	THETAO	1-10	F10.5
1	WVLTH	11-20	F10.5
1	NUMCUT	21-25	I5
2	SPAZMX	1-10	F10.5
2	SPAZMN	11-20	F10.5
3	RN	1-10	F10.5
3	RADMIN	11-20	F10.5
3	DRAD	21-30	F10.5
4	TAD	1-10	F10.5
4	PL	11-20	F10.5
4	PH	21-30	F10.5
4	ST	31-40	F10.5
4	PHIP	41-50	F10.5
4	THETAP	51-60	F10.5
5	DX	1-10	F10.3
5	DY	11-20	F10.3
5	PSIS	21-30	F10.3
5	RAN	31-40	F10.3
5	RAL	41-50	F10.3
5	MONO	51-55	I5
5	MQPH	56-60	I5
5	ILIM	61-65	I5
6	NC	1-5	I5
6	NP1	6-10	I5
6	NP2	11-15	I5
6	SX	16-25	F10.5
6	XMIN	26-35	F10.5
6	DELX	36-45	F10.5
6	SY	46-55	F10.5
6	YMIN	56-65	F10.5
6	DELY	66-75	F10.5

Repeat Cards 4 and 6 for Each Cut to be Computed.

TABLE III. LIST OF OUTPUT DATA

1. Maximum and minimum azimuthal slot separations.
2. Separation distance of adjacent rings measured along generatrix.
3. Beam pointing directions in the coordinates of the cone, ϕ and θ.
4. The cut computed (τ), the beginning and ending values of ψ, and the step size in ψ.
5. Maximum planar array diameter, RN
6. Actual Planar array diameter, RAN
7. Planar array element spacing DX, DY
8. Wavelength
9. Cone angle, θ_o
10. The Eulerian angles (ψ_s, ϕ_s, θ_s) that describe the angular position of the planar array coordinate system relative to the coordinate system of the cone.
11. The type of patterns calculated (sum, E-plane difference, H-plane difference)
12. Slot locations and excitations
13. Amplitudes of field components parallel to the plane of the cut (EPPP) and perpendicular to the plane of the cut (ETPP), versus angle, ψ, along cut. Relative powers in dB of the same components (normalized to peak value).
14. Plots of same variables as in 13.

APPENDIX B

In this Appendix the Fortran program LOCEL is listed. This program was used to study the relationships between reference planar array size, position and orientation, and the location of excited elements on a conical surface when only a limited region of the cone is excited. The inputs required are given in the listing. The outputs are the element numbers, their radial distances from the cone tip, their azimuthal positions ϕ_p, and then angular positions, ψ, on the developed cone.

```
C     THIS PROGRAM COMPUTES THE LOCATIONS OF ELEMENTS ON A CONE. THEY
C     ARE ARRANGED ON RINGS WITH AZIMUTHAL SPACING OF BETWEEN SOME
C     MINIMUM VALUE, SPAZMN, AND SOME MAXIMUM VALUE SPAZMX. THE NUMBER
C     OF ELEMENTS IN A GIVEN RING IS DETERMINED BY THIS CRITERION. THE
C     RADIAL SPACING OF RINGS IS DRAD. OTHER INPUTS REQUIRED ARE THE
C     RADIUS OF THE LARGEST REFERENCE PLANAR ARRAY CONSIDERED, RN, THE
C     RADIUS OF THE PROJECTION OF THE EXCITED PORTION OF THE CONE, RAN,
C     THE DISTANCE FROM THE CONE TIP TO THE FIRST RING OF ELEMENTS,
C     RADMIN, THE WAVELENGTH, THE POINTING ANGLES, THETAP AND PHIP, THE
C     CONE ANGLE, THETA0. ADJACENT RINGS ARE SHIFTED BY ONE HALF THE
C     ELEMENT SEPARATION TO PROVIDE A TRIANGULAR LATTICE.
C
      DIMENSION P0(2000),R(2000)
      PI=4.*ATAN(1.)
      RAD=PI/180.
      READ(5,500) SPAZMX, SPAZMN, WVLTH
      WRITE(6,800)
  800 FORMAT(//,1X,3X,6HSPAZMX,4X,6HSPAZMN,4X,5HWVLTH,/)
      WRITE(6,500) SPAZMX, SPAZMN, WVLTH
      SEPMAX = SPAZMX*WVLTH
      SEPMIN = SPAZMN*WVLTH
      READ(5,500)RN,RADMIN,DRAD,THETAP,PHIP,THETA0,RAN
      WRITE(6,700)
  700 FORMAT(//,1X,3X,2HRN,7X,6HRADMIN,5X,4HDRAD,6X,6HTHETAP,5X,
     *4HPHIP,5X,6HTHETA0,7X,3HRAN,/)
      WRITE(6,500)RN,RADMIN,DRAD,THETAP,PHIP,THETA0,RAN
      TC=THETA0*RAD
      THTP=THETAP*RAD
      PHP=PHIP*RAD
  500 FORMAT(7F10.5)
      SIN0=SIN(T0)
      COS0=COS(T0)
      COSP=COS(THTP)
      SINP=SIN(THTP)
      COPHP=COS(PHP)
      SIPHP=SIN(PHP)
      Z0=-RN/SIN0
      RMAX=(-RN*(1.+SIN0)/SIN0-2.*WVLTH)/COS0
      WRITE(6,600)
  600 FORMAT(//,1X,4H  N ,35H R-INCHES    PHI-DEG    PSI-DEG     NT,/)
      I=1
      J=0
      RAD1=RADMIN
      NSLT=INT(2.*PI*RAD1*SIN0/(SEPMIN))
      IF(NSLT.EQ.0) NSLT=1
      DO 100 N=1,1000
      IF (RAD1.GT.RMAX) GO TO 300
      SPF=RAD1*2.*PI*SIN0/FLOAT(NSLT)
      IF (SPF.GE.SEPMAX) NSLT=INT(2.*PI*RAD1*SIN0/(SEPMIN))
      IF(NSLT.EQ.0) NSLT=1
      DELPHI=2.*PI/FLOAT(NSLT)
  123 FORMAT(1X,I3,3F10.4,I6)
      DO 200 L=1,NSLT
      J=J+1
      M=1+(-1)**N
```

```
      R(I)=RAD1
      PO(I)=FLOAT(L-1)*DELPHI
      IF (M.EQ.2) PO(I)=PO(I)+DELPHI/2.
      X=R(I)*SINO*COS(PO(I))
      Y=R(I)*SINO*SIN(PO(I))
      Z=R(I)*COSO
      XP=X*COPHP+Y*SIPHP
      YP=-X*SIPHP+Y*COPHP
      ZP=Z-ZO
      XPP=XP*COSP-ZP*SINP
      YPP=YP
      ZPP=XP*SINP+ZP*COSP
      RHOXY=SQRT(XPP**2+YPP**2)
      IF(RHOXY.GT.RAN.OR.ZPP.LT.0.) GO TO 200
      PD=PO(I)/RAD
      POD=PD
      IF(POD.GT.180.) POD=POD-360.
      PSI=POD*SINO
      WRITE(6,123) I,R(I),PD,PSI,J
      I=I+1
  200 CONTINUE
      RAD1=RAD1+DRAD
  100 CONTINUE
  300 NSLOT=I-1
      WRITE (6,400)NSLOT
  400 FORMAT(//,1X,18HNUMBER OF SLOTS = ,I4,//)
      END
```

CHAPTER 3

SLOTS ON CYLINDER: PATTERN AND ADMITTANCE

3.0 INTRODUCTION

This chapter is concerned with the pattern and input admittance of a single slot on a conducting circular cylinder, and with the mutual admittance between two identical slots on a cylinder. The curvature of the cylinder affects both patterns and admittance; these effects are determined through application of a modal representation, a vector cylindrical harmonic series that satisfies all boundary conditions over the cylindrical surface. This type of solution is useful for cylinders of small to moderate radius in wavelengths, while the GTD approach of Chapter 5 is useful for large diameter cylinders.

3.1 Pattern

The boundary value problem of radiation from a slot (with a sinusoidal distribution) on a metallic cylinder was solved exactly several decades ago. (Carter, 1943; Harrington & Lepage, 1952; Knudsen, 1959). The solution is a harmonic series of functions appropriate for the cylinder: Bessel and Hankel functions. A standard cylindrical coordinate system is used, where z, θ, ϕ are the axial, polar, and circumferential coordinates. Finite width of the slot has a small effect upon the patterns, but the appropriate factor can be included if desired (Collin and Zucker, 1969). With slot voltage V and cylinder radius a, the fields for an axial half wave slot are (Wait, 1959): $E_\theta = 0$, and;

$$E_\theta = \frac{V \cos\left(\frac{\pi}{2}\cos\theta\right)}{2\pi^2 \, ka \sin^2\theta} \sum_{m=0} \frac{\epsilon_m \, j^m \cos m\phi}{H_m'(ka \sin\theta)} \qquad \text{(1a)}$$

This pattern is that of a half wave dipole modified by the summation. For a circumferential half wave slot, again thin, the fields are:

$$E_\theta = \frac{2ka\ V}{\pi^2 \sin\theta \cos\theta} \sum_{m=0}^{\infty} \frac{\varepsilon_m\, j^{m+1} \cos m\phi \cos m\pi/2ka}{(k^2a^2 - m^2)\, H_m(ka \sin\theta)} \qquad (1b)$$

$$E_\phi = \frac{2\ V \cos\theta}{\pi^2 \sin^2\theta} \sum_{m=0}^{\infty} \frac{m\, j^{m+1} \sin m\phi \cos m\pi/2ka}{(k^2a^2 - m^2)\, H_m'(ka \sin\theta)} \qquad (1c)$$

Convergence of these series is controlled by ka, where $k = 2\pi/\lambda$. Between ka and 2ka terms are usually needed. Large cylinders thus require many terms but with current computer capability many tens of terms can be included. However, for such large cylinders the Watson transformation has been used to convert the harmonic series above, which results from an evaluation of an integral at real poles, to a residue series of complex order Hankel functions, evaluated at the complex poles. For large cylinders the residue series, which is analogous to the Regge pole series in quantum mechanics, converges with only a few terms (Collin and Zucker, 1969). Wait (1959) has computed the sum for the azimuth patterns of primary interest: E_ϕ for an axial slot, and E_θ for a circumferential slot. His results are given in Figures 1 and 2. It is interesting to note the axial slot electric field produces diffraction interference behind the cylinder whereas the circumferential slot pattern exhibits a smooth decay. Computer code listings or descriptions are not included as the formulas are straight forward. These patterns are used with the

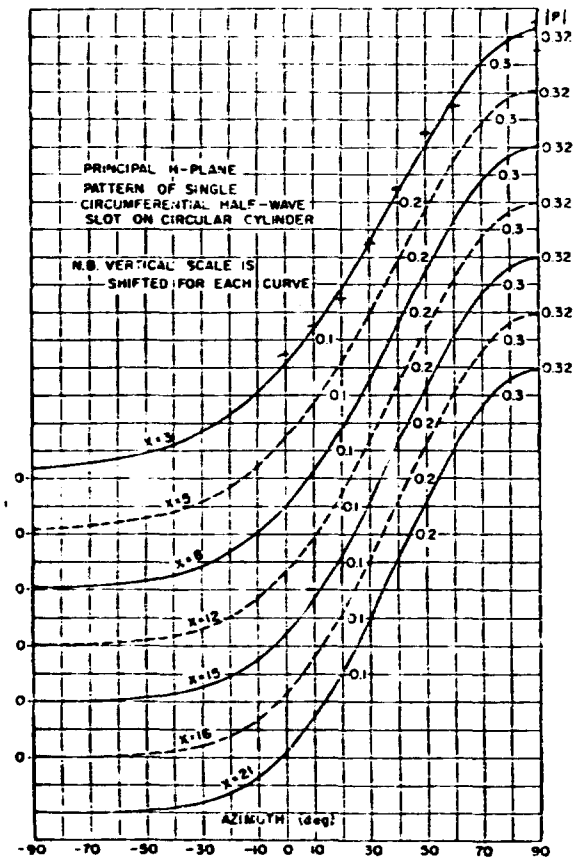

Figure 1

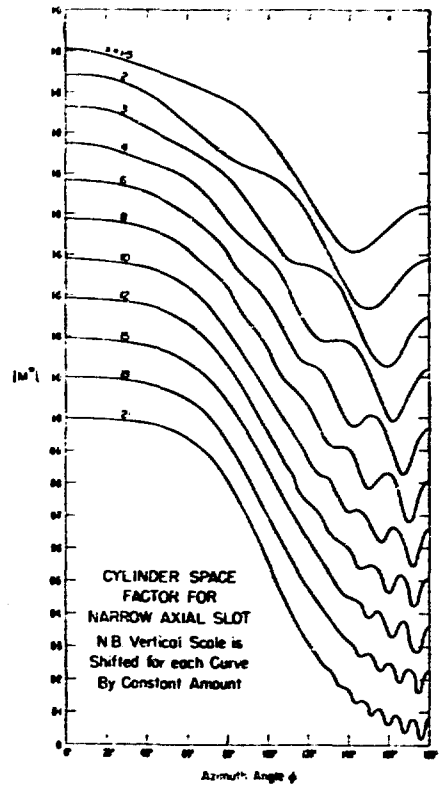

Figure 2

array factor and active reflection coefficient to produce the complete pattern.

3.2 Admittance

3.2.1 Definition of Slot Admittance

In the design of a conformal slot array on the surface of a conducting cylinder, the calculation of the mutual admittance Y_{12} is a crucial step, which has been studied extensively in recent years. Referring to Figure 3, two identical slots, circumferential or axial, are located on the surface of an infinitely long cylinder. The geometrical parameters are

R = radius of the cylinder

(a,b) = dimensions of the slot along (ϕ,z) directions (a is the arc length along the cylinder)

$(z_0, R\phi_0)$ = center-to-center distances between slots

$$s_0 = \sqrt{z_0^2 + (R\phi_0)^2}$$

$$\theta_0 = \tan^{-1}(z_0/R\phi_0)$$

The problem is to determine the mutual admittance between these two slots when kR is large.

First define mutual admittance. Throughout this work it is assumed that

(i) the slots are thin, and

(ii) their length is roughly a half-wavelength.

Then the aperture field in each slot can be adequately approximated by a simple cosine distribution, which is the so-called "one-mode" approximation. For example, if slot 1 is circumferential (lower slot in Figure 3a), its aperture field under the "one-mode" approximation is given by (exp + jωt time convention)

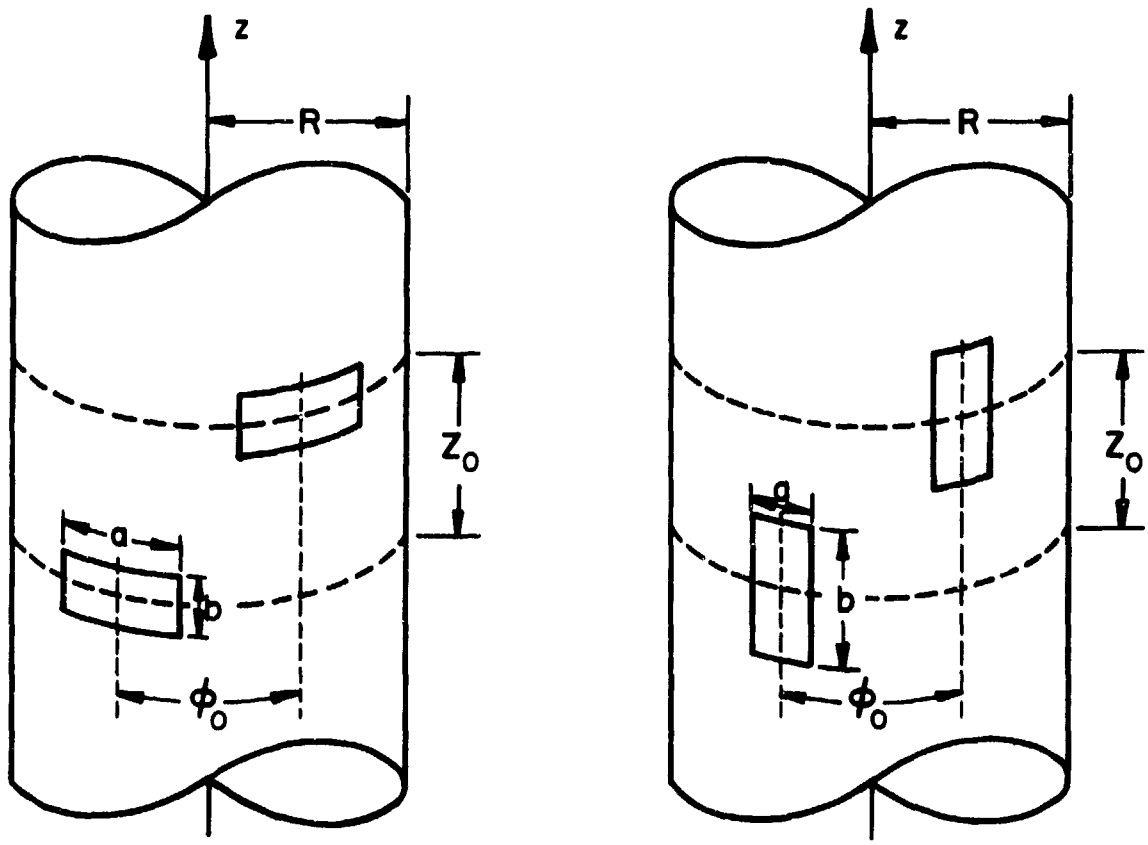

(a) CIRCUMFERENTIAL SLOTS (b) AXIAL SLOTS

Figure 3. Two identical slots on the surface of a cylinder.

$$\bar{E} = V_1\bar{e}_1, \quad \bar{H} = I_1\bar{h}_1 \tag{2}$$

where

$$\bar{e}_1 = \hat{z}\sqrt{\frac{2}{ab}}\cos\frac{\pi}{a}y \ , \quad h_1 = \hat{x}\cdot e_1$$
$$y = R\phi \ . \tag{3}$$

(V_1, I_1) are respectively the modal (voltage, current) of slot 1. The mutual admittance Y_{12} is defined by

$$Y_{12} = Y_{21} = \frac{I_{21}}{V_1} \tag{4}$$

where I_{21} is the induced current in slot 2 when slot 1 is excited by a voltage V_1 and slot 2 is short-circuited. An alternative expression for Y_{12} is

$$Y_{12} = \frac{1}{V_1V_2}\iint_{A_2}\bar{E}_2 \times \bar{H}_1 \cdot d\bar{s}_2 \tag{5}$$

where

A_2 = aperture of slot 2

$\bar{H}_1$ = magnetic field when slot 1 is excited with voltage V_1, and slot 2 is covered by a perfect conductor.

$\bar{E}_2$ = electric field when slot 2 is excited with voltage V_2, and slot 1 is covered by a perfect conductor.

Because $\bar{H}_1 = I_{21}\bar{h}_2$ and $\bar{E}_2 = V_2\bar{e}_2$, it is a simple matter to verify that (4) and (5) are equivalent (Richmond, 1961).

There is an alternative definition of mutual admittance. Instead of (2), a modal voltage $\underline{V}_1$ (with a bar) may be defined through the expression for the aperture field of slot 1 as follows:

$$\bar{E} = \bar{z}\,\frac{1}{b}\,\underline{V}_1 \cos\frac{\pi}{a}\,y \tag{6}$$

or equivalently

$$\underline{V}_1 = \int_{-b/2}^{b/2} (\bar{z}\cdot\bar{E})_{y=0}\,dz\ . \tag{7}$$

Then a different mutual admittance $\underline{Y}_{12}$ is defined by (5) after replacing (V_1,V_2) by $(\underline{V}_1\underline{V}_2)$. It can be easily shown that

$$\underline{Y}_{12} = \frac{a}{2b}\ Y_{12} \tag{8}$$

Two remarks are in order: (i) In the limiting case that $b \to 0$, Y_{12} goes to zero as b , whereas $\underline{Y}_{12}$ approaches a constant independent of b. (ii) For the special case $a = \lambda/2$ and $R \to \infty$, it is $\underline{Y}_{12}$ that is identical to the mutual impedance Z_{12} between two corresponding dipoles calculated by the classical Carter's method (Jordan and Balmain, 1968; Hansen, 1972). (iii) When the slots are excited by waveguides (transmission lines), one often uses Y_{12} $(\underline{Y}_{12})$. From here on, attention will be given to Y_{12} instead of $\underline{Y}_{12}$.

The mutual admittance defined in (4) and (5) includes the self admittance Y_{11} as a special case which occurs when two slots coincide. (All the formulas of Y_{12} given in this section, except for the one developed by Lee in Section 3.2.2, can be used for calculating Y_{11} by setting $\phi_0 \to 0$ and $z_0 \to 0$.)

3.2.2 Mutual Admittance Using Modal Series

A canonical geometry that yields insight into the behavior of slots on a cylinder is an array of infinitely long axial thin slots (slits) deployed all around the cylinder. Sureau and Hessel (1969, 1971, 1972; Hessel and Sureau, 1971, 1973: Hessel, 1972) derived active element patterns using the unit cell approach of Oliner and Malech (1966) identifying a direct component

associated with the integrated saddle point, and a set of leaky waves representing complex poles (natural resonances) of the periodic cylinder. Pattern nulls due to external dielectric sheet covers were also exhibited. The unit cell approach was extended by Munger et al (1971) who considered an infinitely long cylinder covered with a regular array of axial slots. A different approach gives insight into coupling between azimuthal modes. Borgiotti and Balzano (1970, 1972A, 1972B; Balzano, 1974) decomposed a ring of slots into a sum of eigen excitations (modes) and then computed coupling between modes on adjacent rings. If this were generalized to obtain mutual admittance between two slots, each on a different ring, the result would be the modal series admittance, using the cylindrical Green's function (Bowman et al, 1969). This approach, developed by Pridmore-Brown and Stewart, and extended by Lee is the most useful as it gives mutual admittance between slots directly. It is the subject of the next part of this chapter.

A modal series was developed by Golden, Stewart, and Pridmore-Brown of Aerospace Corp. (1974)*, utilizing a series for the azimuth poles in the Green's function, and an integral for the continuous spectrum in z. This series has been used extensively by Hughes in obtaining Y_{12} for slots on a cylinder. The infinite integral must be approximated, and this is facilitated by assumption of a small loss in the medium via a small negative imaginary part of k. This becomes less satisfactory as z becomes larger, but a modified solution for that regime will be discussed later.

The mutual admittance formulas as used by Hughes are as follows:

*See also Golden and Stewart, 1971.

Circumferential slots

(9)

$$Y_{12} = \int_{-\infty}^{\infty} dk_z \sum_{m=-\infty}^{\infty} \psi(m,k_z) G(m,k_z) e^{-j(m\phi_0 + k_z z_0)}$$

where

$$\psi(m,k_z) = \frac{ab}{8\pi^2 R} \frac{\sin^2(k_z b/2)}{(k_z b/2)^2} \cdot \left\{ \frac{\sin(m\phi_a + \pi/2)}{(m\phi_a + \pi/2)} + \frac{\sin(m\phi_a - \pi/2)}{(m\phi_a - \pi/2)} \right\}^2$$

$$\phi_a = (a/2R)$$

$$G(m,k_z) = Y_0 \left[\frac{jk}{k_t} \frac{H_m^{(2)'}(k_t R)}{H_m^{(2)}(k_t R)} + \left(\frac{mk_z}{k_t^2 R} \right)^2 \frac{k_t}{jk} \frac{H_m^{(2)}(k_t R)}{H_m^{(2)'}(k_t R)} \right] .$$

$$k_t = \begin{cases} \sqrt{k^2 - k_z^2} & , \text{ if } k \geq k_z \\ -j\sqrt{k_z^2 - k^2} & , \text{ if } k \leq k_z \end{cases} .$$

Axial slots

(10)

$$Y_{12} = \int_{-\infty}^{\infty} dk_z \sum_{m=-\infty}^{\infty} \phi(m,k_z) F(m,k_z) e^{-j(m\phi_0 + k_z z_0)}$$

where

$$\phi(m,k_z) = \frac{ab}{8R} \left(\frac{\sin(m\phi_a)}{(m\phi_a)} \cdot \frac{\cos(k_z b/2)}{(k_z b/2)^2 - (\pi/2)^2} \right)^2$$

$$F(m,k_z) = Y_0 \frac{k_t}{jk} \frac{H_m^{(2)}(k_t R)}{H_m^{(2)'}(k_t R)}$$

Lee and Mittra (1976) developed an alternate modal series, suitable for large z. Consider first circumferential slots. Rewrite Y_{12} in terms of its real and imaginary parts.

$$Y_{12} = G + jB \ .$$

It can be shown that G is given by

$$G = \int_0^{k_0} \sum_{m=0}^{\infty} \frac{\cos m\phi_0}{\varepsilon_m} \cos k_z z_0 \ \psi(m,k_z) R(m,k_z) \ dk_z \qquad (11)$$

where

$$R(m,k_z) = \frac{2}{\pi k_t R} \cdot \frac{k_0}{k_t} \cdot \left[\frac{1}{M_m^2(k_t R)} + \left(\frac{m k_z}{k_t k_0 R} \right)^2 \frac{1}{N_m^2(k_t R)} \right]$$

$$M_m^2(\chi) = J_m^2(\chi) + Y_m^2(\chi)$$

$$N_m^2(\chi) = J_m'^2(\chi) + Y_m'^2(\chi)$$

$$\varepsilon_m = \begin{cases} 2 \ , & m = 0 \\ 1 \ , & m \neq 0 \end{cases} .$$

Note that G contains a *finite* integral and can be evaluated in a straightforward manner by standard numerical integration techniques. The imaginary part of Y_{12} is given by

$$B = \int_{C_1} \sum_{m=0}^{\infty} \frac{\cos m\phi_0}{\varepsilon_m} \cdot \cos k_z z_0 \cdot \psi(m,k_z) \cdot W(m,k_z) \ dk_z \qquad (12)$$

where the integration contour C_1 is shown in Fig. 4 and

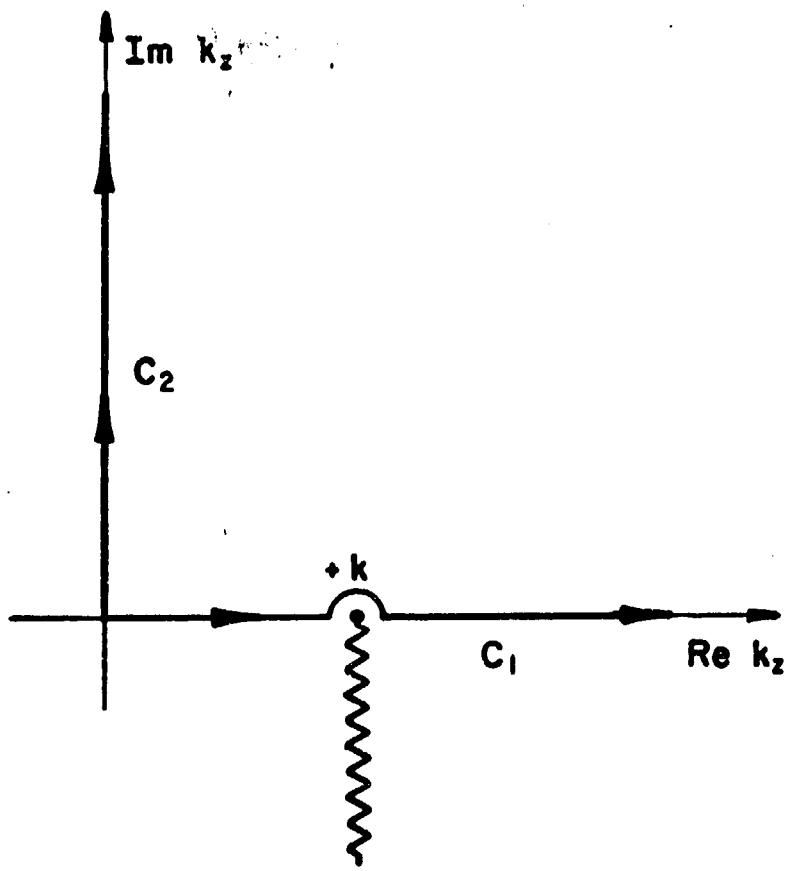

Figure 4. Contours in the complex k_z-plane for the integral in (14)

$$W(m,k_z) = \begin{cases} \dfrac{k_0}{k_t}\,(J_m J_m' + Y_m Y_m')\left[\dfrac{1}{M_m^2(k_t R)} - \left(\dfrac{mk_z}{k_t k_0 R}\right)^2 \dfrac{1}{N_m^2(k_t R)}\right], & \text{if } k_0 > k_z \\ \dfrac{-k_0}{|k_t|}\left[\dfrac{K_m'(|k_t|R)}{K_m(|k_t|R)} - \left(\dfrac{mk_z}{|k_t|k_0 R}\right)^2 \dfrac{K_m(|k_t|R)}{K_m'(|k_t|R)}\right], & \text{if } k_0 < k_z \end{cases} \tag{13}$$

The computation of B as given in(12) can be quite laborious because (i) the integration with respect to k_z is of infinite range, and the factor $\cos k_z z_0$ is highly oscillatory for large $k_0 z_0$, (ii) $W(m,k_z)$ has nonintegrable singularities of opposite sign on both sides of $k_z = k_0$, (iii) $W(m,k_z)$ decays slowly with respect to m and k_z.

To circumvent the above difficulties in evaluating B, a method introduced by Duncan (1962) in the study of cylindrical antenna problems is adopted. Rewrite (12) as

$$B = \mathrm{Im}\left\{\sum_{m=0}^{\infty} \frac{\cos m\phi_0}{\epsilon_m}\left[-j\int_{C_1} F(m,k_z)\sin k_z z_0\, dk_z + \int_{C_1} F(m,k_z) e^{jk_z z_0}\, dk_z\right]\right\} \tag{14}$$

where

$$F(m,k_z) = [R(m,k_z) + jW(m,k_z)]\psi(m,k_z) \quad .$$

The imaginary part of the first term inside the bracket of (14) is

$$\mathrm{Im}\left\{-j\int_{C_1} F(m,k_z)\sin k_z z_0\, dk_z\right\} = -\int_0^{k_0} R(m,k_z)\psi(m,k_z)\sin k_z z_0\, dk_z \quad . \tag{15}$$

In order to compute the imaginary part of the second term of (14), the integration contour C_1 is deformed into C_2 (Fig. 4) according to the theory of complex variables. This manipulation leads to

$$\mathrm{Im}\int_{C_1} F(m,k_z)e^{jk_z z_0}\,dk_z = \mathrm{Im}\int_{C_2} F(m,k_z)e^{jk_z z_0}\,dk_z \,. \qquad (16)$$

Make the change of variable $k_z = j\eta$ in (16). Substitution of the resultant equation and (15) into (14) gives

$$B = \sum_{m=0}^{\infty} \frac{\cos m\phi_0}{\epsilon_m}\left(-\int_0^{k_0} R(m,k_z)\,\psi(m,k_z)\,\sin k_z z_0\,dk_z\right.$$

$$\left.+\int_0^{\infty} R(m,j\eta)\psi(m,j\eta)e^{-\eta z_0}\,d\eta\right) . \qquad (17)$$

The final expression for Y_{12} is given by the real part G in (11) and the imaginary part B in (17). Several remarks are in order: (i) Not only G but also B is determined by $R(m,k_z)$, which is much simpler than $W(m,k_z)$ defined in (13). (ii) G contains only a finite integral. (iii) The infinite integral in B, i.e., the second integral in (9a), contains an exponentially decaying factor $\exp[-(z_0 - a)\eta]$ in its integrand. Thus the larger z_0, the faster convergence in the evaluation of B. This is in contrast to the original expression of Y_{12}. (iv) There is no nonintegrable singularity in (11) or (17).

The same method applies to the derivation of an alternative expression of Y_{12} for two axial slots ($a < b$ as shown in Fig. 1b). Only the final result is given:

$$Y_{12}^{a} = -\frac{abY_0}{\pi k_0 R^2} \sum_{m=0}^{\infty} \frac{\cos m\phi_0}{\epsilon_m} \left[\int_0^{k_0} \phi(m,k_z) e^{-jk_z z_0} \frac{dk_z}{N_m^2(k_t R)} + j \int_0^{\infty} \phi(m,j\eta) e^{-\eta z_0} \frac{d\eta}{N_m^2\left(R\sqrt{k_z^2 + k_0^2}\right)} \right]$$

where

$$\phi(m,k_z) = \left[\frac{\sin (m\phi_a/2)}{(m\phi_a/2)} \cdot \frac{\cos (k_z b/2)}{(k_z b/2)^2 - (\pi/2)^2} \right]^2$$

$$\phi_a = 2 \sin^{-1} (a/2R) .$$

3.2.3 Mutual Admittance Data -- Slots on Cylinder

Using the computer codes described, slot mutual impedance data have been calculated for both axial and circumferential slots. All data are at 9 Ghz, for two slot dimensions: .9 x .4 in, and .9 x .2 in. A summary of the data set parameters is:

Data Set A	Circumferential	.9 x .4	Radius 1.991 in.
Data Set B	Axial	.9 x .4	Radius 1.991 in.
Data Set C	Circumferential	.9 x .2	Radius 1,2,4,10 λ
Data Set D	Axial	.9 x .2	Radius 1,2,4,10 λ

DATA SET A

Circumferential slot	9. x .4 in
Cylinder radius	1.991 in except as noted
Frequency	9 Ghz

Table A1 gives mutual admittance amplitude and phase for spacings from 0 to 30 in., and rotation angles 0 to 90 deg. See Fig. 3. Fig. A1 shows Y_{12} versus rotation angle ϕ_0 for an axial spacing of 2 in. Figure A2 shows the important result that slot coupling is stronger for two parallel slots on a cylinder than on a plane. That is, the mutual admittance depends upon transverse curvature. This result led to a search for a quantification in terms of geometric diffraction, and for physical mechanism; the results are given in Chap. 5. The ratio of cylindrical to planar coupling, in terms of transverse curvature, is depicted in Fig. A3. This data set, and that which follows, are for open end waveguide slots, and thus are useful for validating simple experiments.

TABLE A1

Y_{12} FOR CIRCUMFERENTIAL SLOTS

z_0	ϕ_0 0 deg	30	60	90
0 in		-81.33 db -77 deg	-101.97 - 49	
.5	-62.62 db -72 deg			
1	-66.82 155			
2	-71.78 -117	-77.60 175	- 89.98 - 4	-103.15 116
4	- 76.89 54			
8	- 81.84 34			
12	- 84.61 15			
16	- 86.48 - 4			
20	- 87.91 - 24			
30	- 90.33 110			

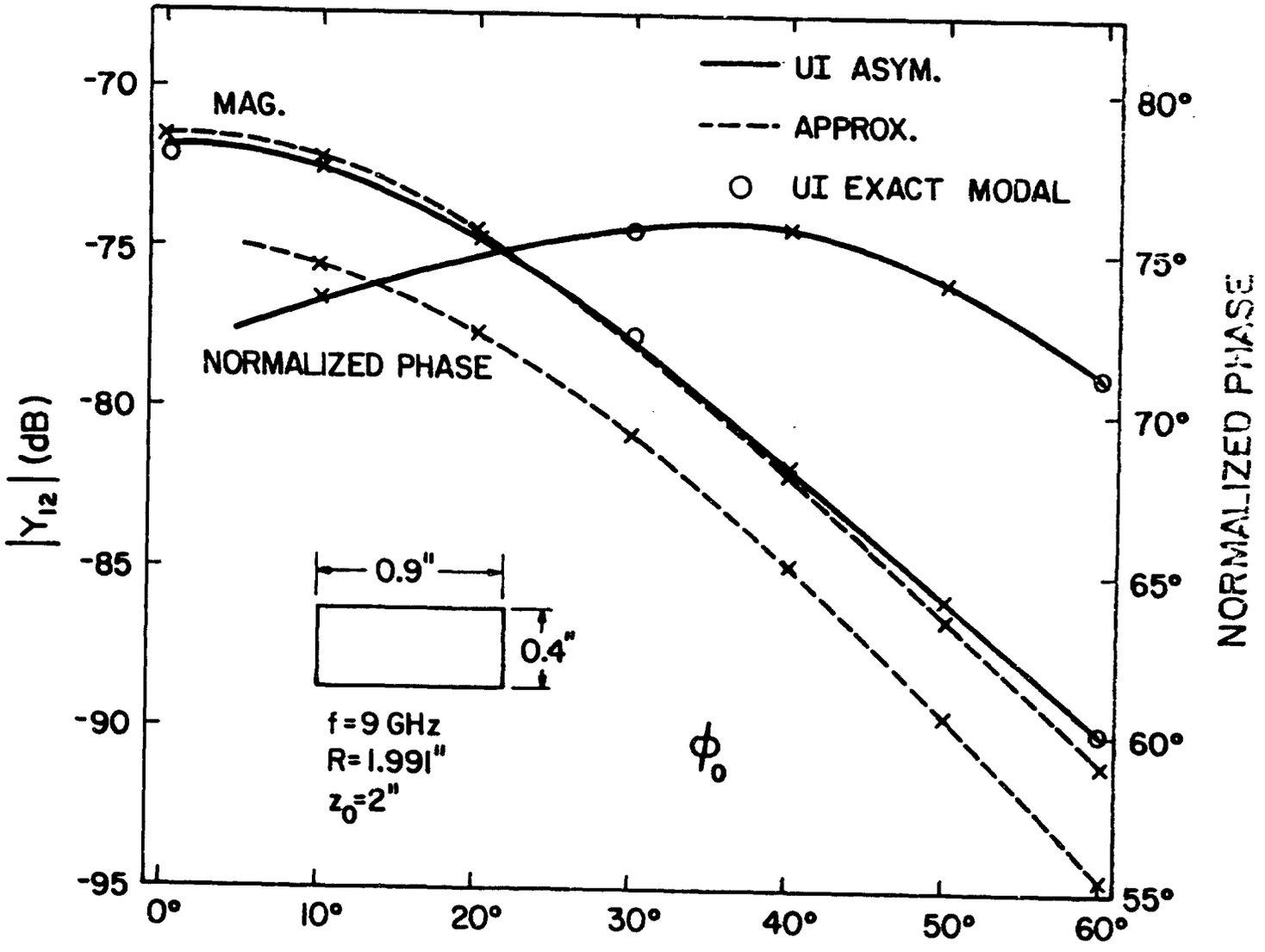

Figure A-1. Mutual admittance Y_{12} between two circumferential slots as a function ϕ_0.

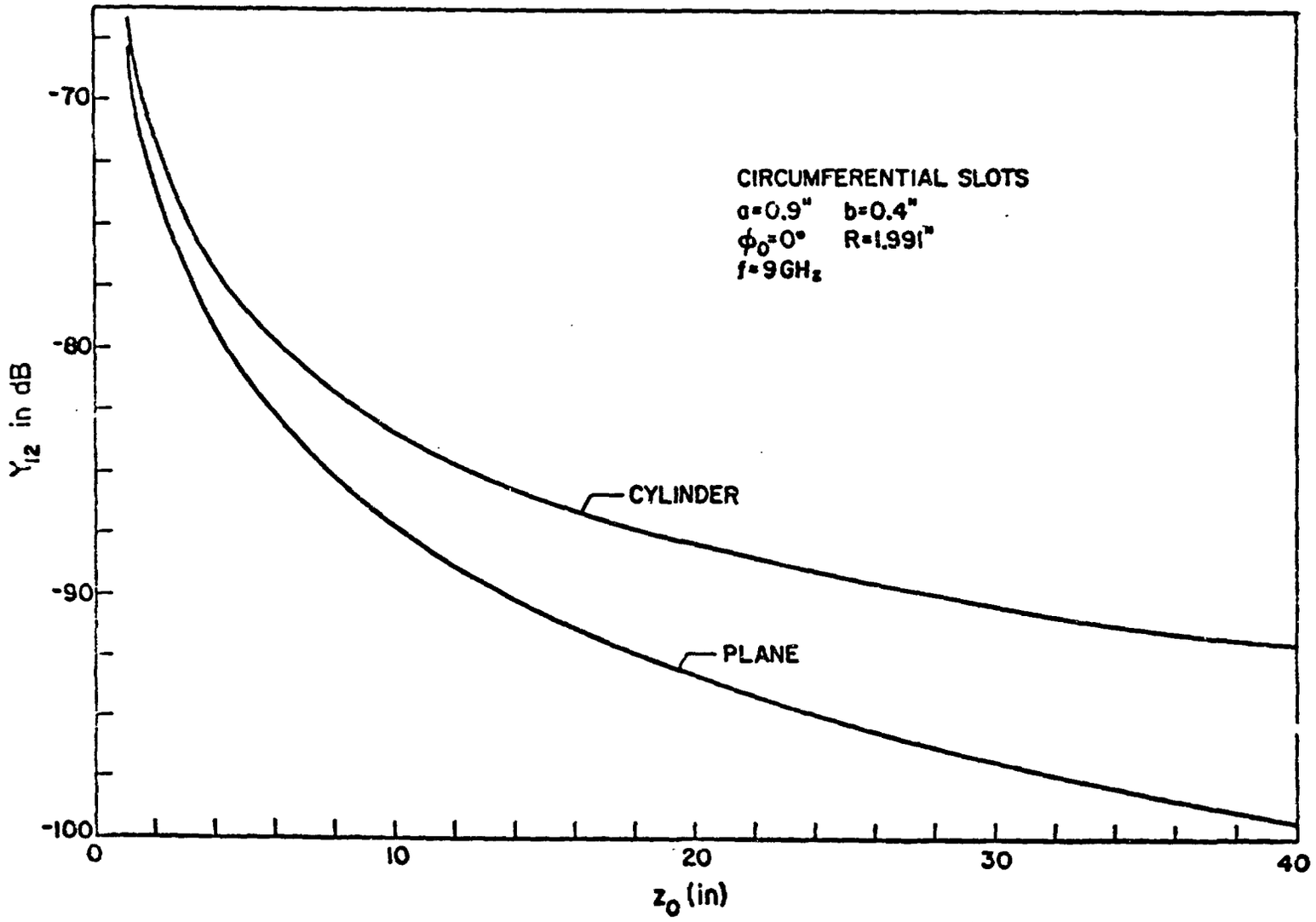

Figure A-2: Y_{12} on a cylinder (UI modal solution) and that on a plane as a function of z_0.

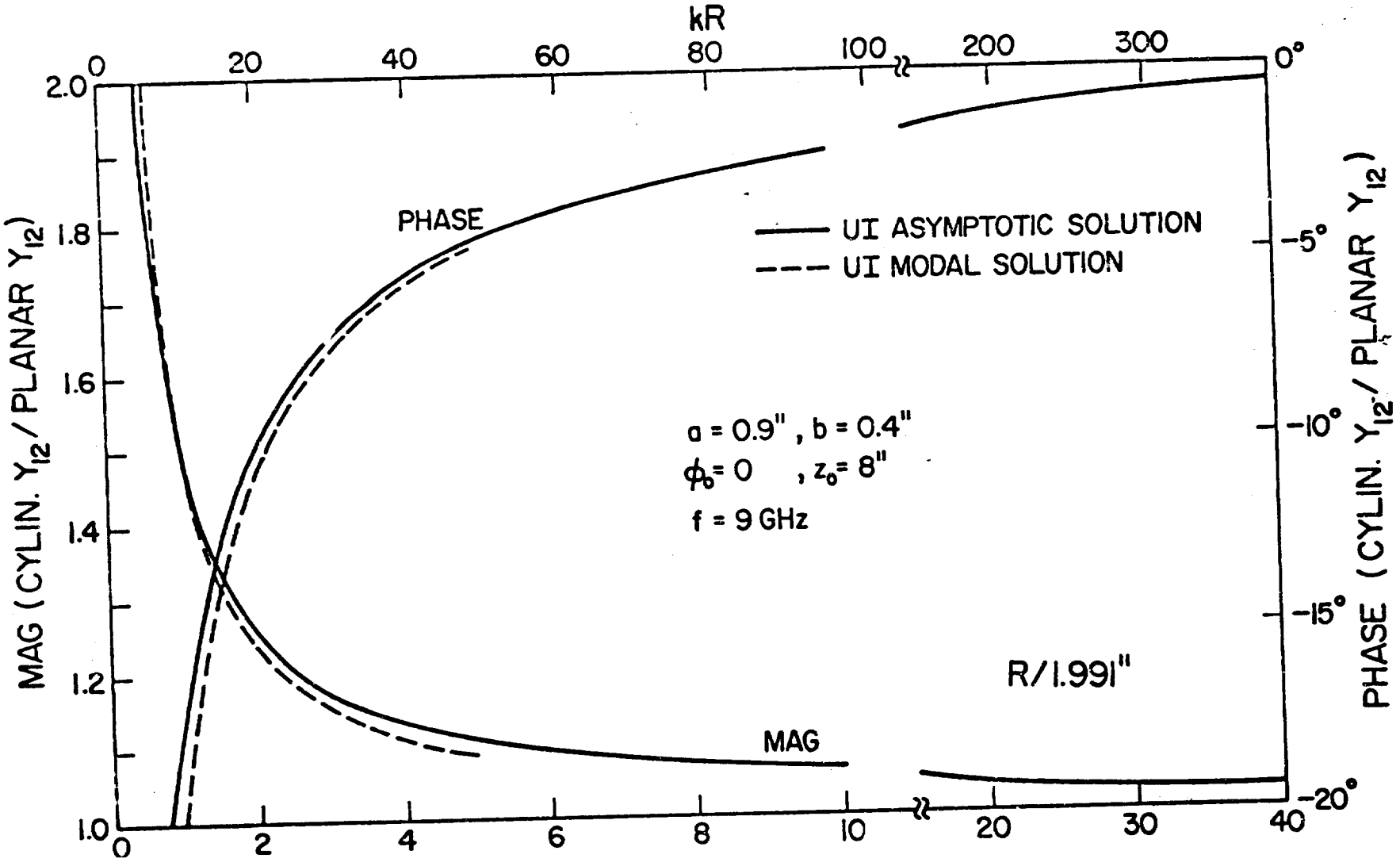

Figure A-3: Y_{12} on a cylinder as a function of the radius R of the cylinder. Y_{12} is normalized by Y_{12} on a plane, which is $5.37 \times 10^{-5} \exp(j53.55^{\circ})$ mho.

DATA SET B

Axial slot	.9 x .4 in
Cylinder radius	1.991 in except as noted
Frequency	9 Ghz

Tables B1 and B2 give mutual admittance as a function of axial and circumferential slot separation, as before. Fig. B1 compares admittance versus axial separation for slots on a cylinder and on a plane. Here unlike the circumferential case the two are nearly equal, and the difference is perhaps the calculation error. Transverse curvature thus does not affect axial slots significantly.

TABLE B1

Y_{12} FOR AXIAL SLOTS

$\phi_0 = 0$

z_0	Y_{12}	
1 in	- 77.38 db	- 59 deg
2	- 92.00	8
4	-104.68	172
8	-116.93	151
12	-123.86	134
16	-128.96	115
24	-136.07	81
32	-141.24	59

TABLE B2

Y_{12} FOR AXIAL SLOTS

$z_0 = 1.5$ in

ϕ_0	Y_{12}	
0 deg	- 86.58 db	151 deg
30	- 86.41	- 26
60	- 87.43	84
90	- 93.02	169

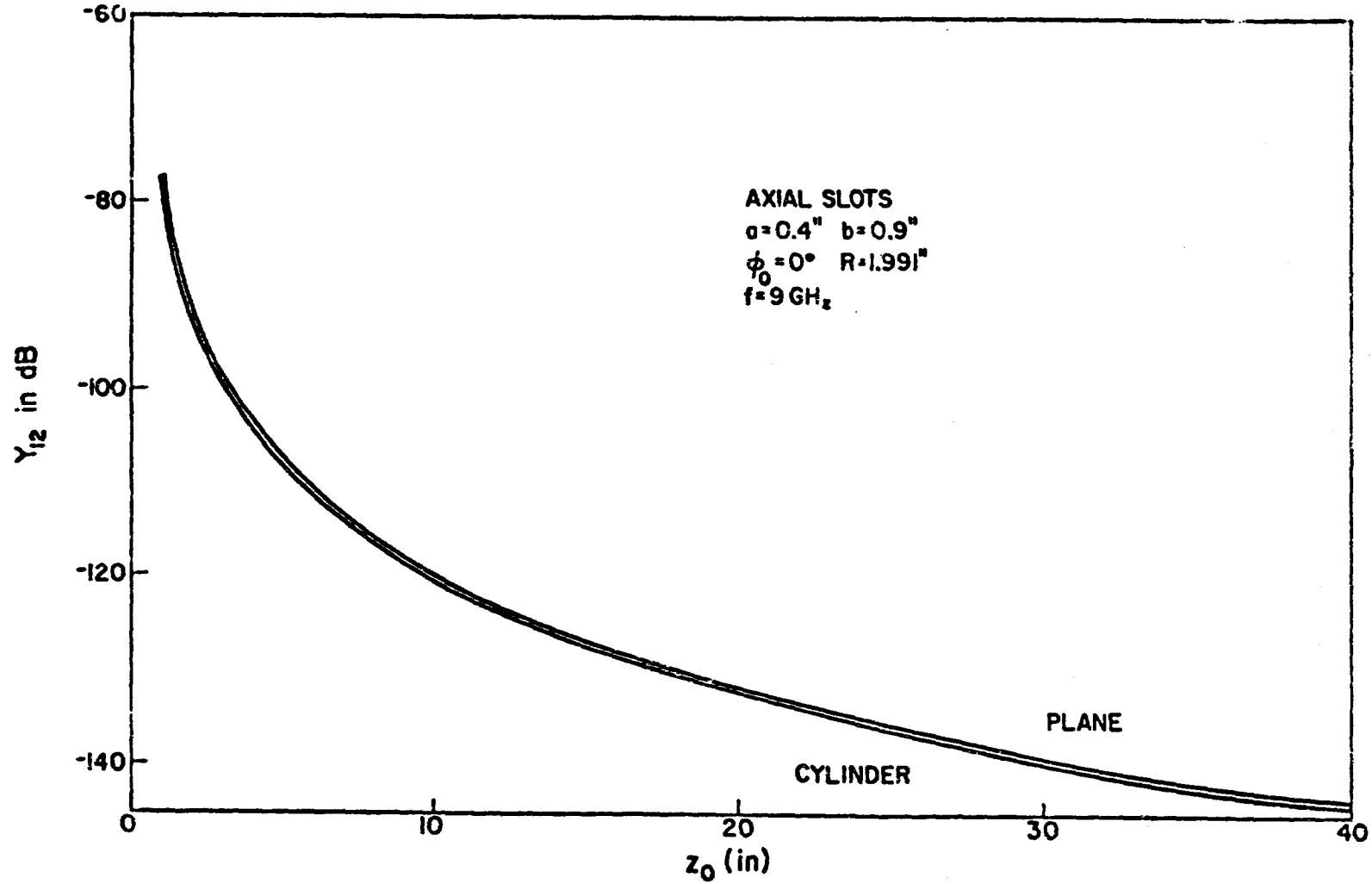

Figure B-1: Y_{12} on a cylinder (UI modal solution) and that on plane as a function of z_0.

DATA SET C

Circumferential slot	.5 x .2 λ
Cylinder radius	1,2,4,10 λ

Table C1 gives mutual admittance versus axial and circumferential slot separation; the coupling is considerably weaker than for the .9 x .4 in slots of Data Set A as those slots are considerably larger. Figs. C1, C2, and C3 give variation of Y_{12} versus angular and axial separation. This data set is useful as such small slots (smaller than waveguide) may be necessary to achieve a lattice spacing that will obviate grating lobes, and to achieve crossed slots for dual polarization.

TABLE C1

Y_{12} OF CIRCUMFERENTIAL SLOTS

	ϕ_0, R=λ			ϕ_0, R=2λ		
z_0	0 deg	30	60	0	30	60
.5λ	- 67.87 db			-68.69		
	-117 deg			-114		
1	- 72.54	-77.34	-88.05	-73.64	-86.37	-103.77
	67	25	-91	73	-77	- 41
2	- 77.46			-78.98		
	68			75		
4	- 82.22			-84.30		
	66			75		
8	- 86.65			-89.41		
	62			72		

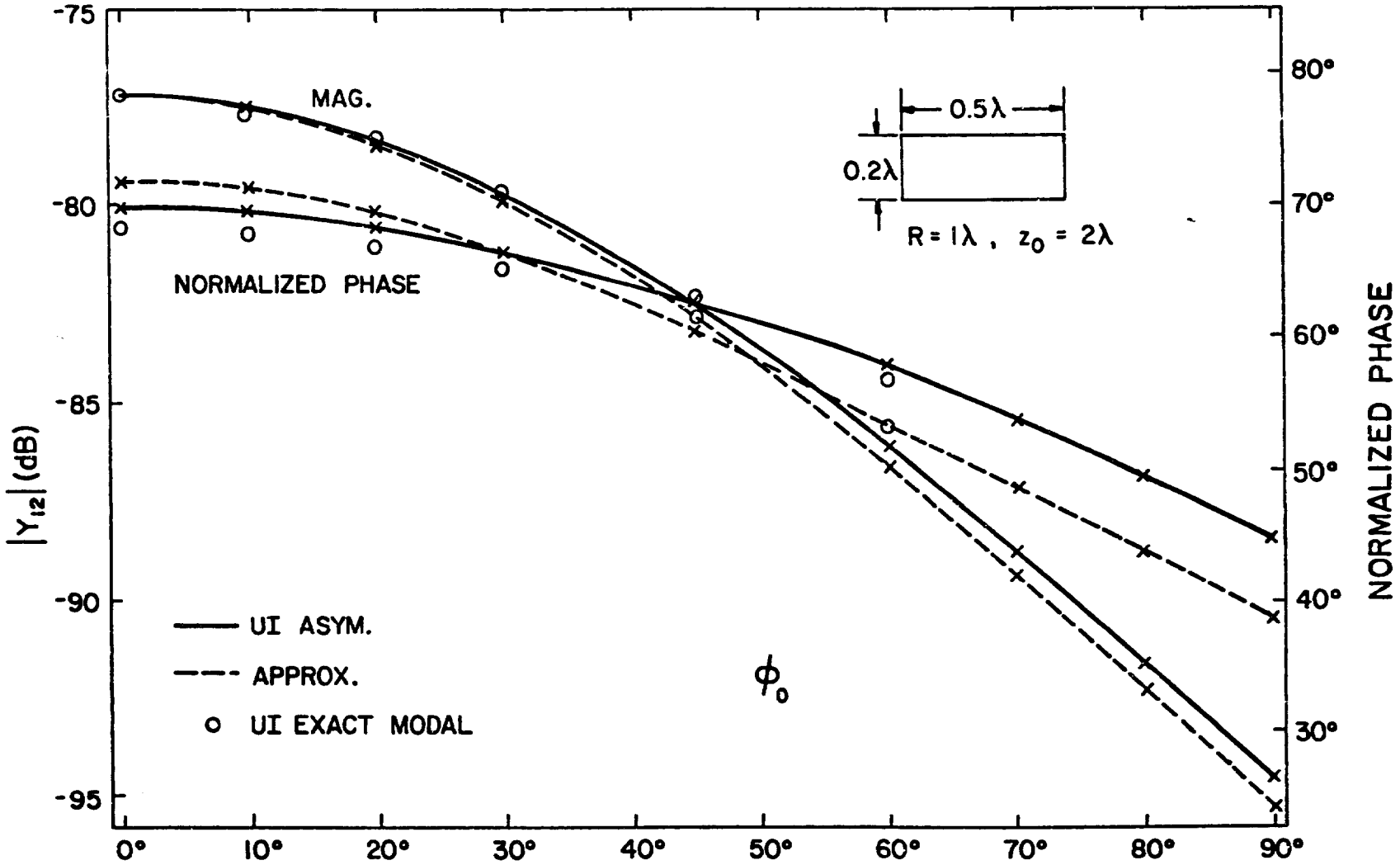

Figure C-1. Mutual admittance Y_{12} between two circumferential slots as a function of ϕ_0.

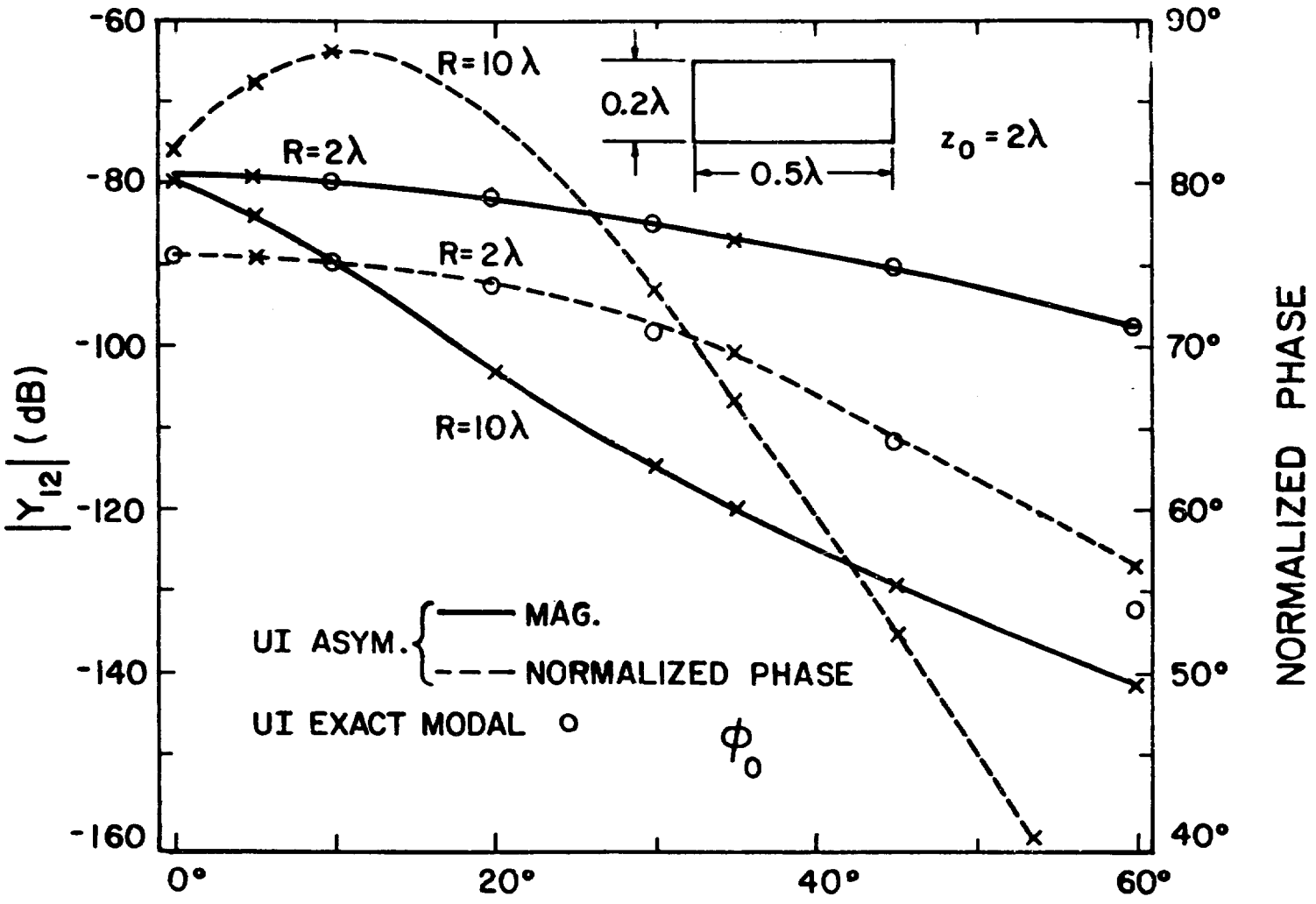

Figure C-2. Mutual admittance Y_{12} between two circumferential slots as a function of ϕ_0.

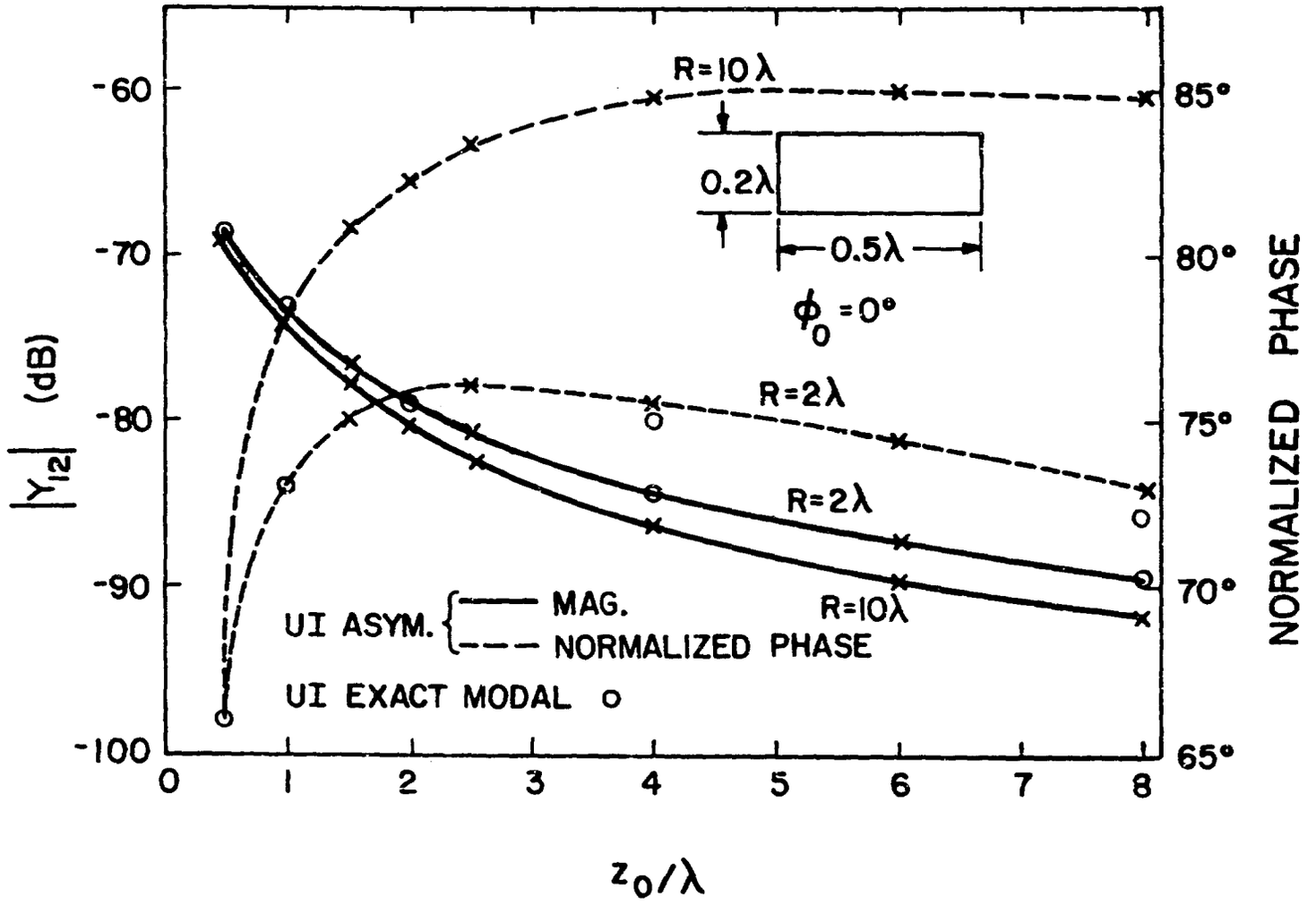

Figure C-3. Mutual admittance Y_{12} between two circumferential slots as a function of z_0.

DATA SET D

Axial slot	.5 x .2λ
Cylinder radius	1, 2, 4, 10λ

Table D1 gives data for a few combinations of angular and axial separations, for radii of one and two wavelengths. Fig. D1 gives Y_{12} versus axial spacing.

TABLE D1

Y_{12} OF AXIAL SLOTS

	ϕ_0, R = λ			ϕ_0, R = 2λ		
z_0	0 deg	30	60	0	30	60
1λ	- 87.06 db	-89.40	-89.84	-86.83	-87.01	-91.86
	-171 deg	85	-83	-172	-72	-61
2	- 99.97			-99.61		
	-174			-176		
4	-112.43			-111.93		
	-175			-177		
8	-124.33			-124.12		
	-174			-177		

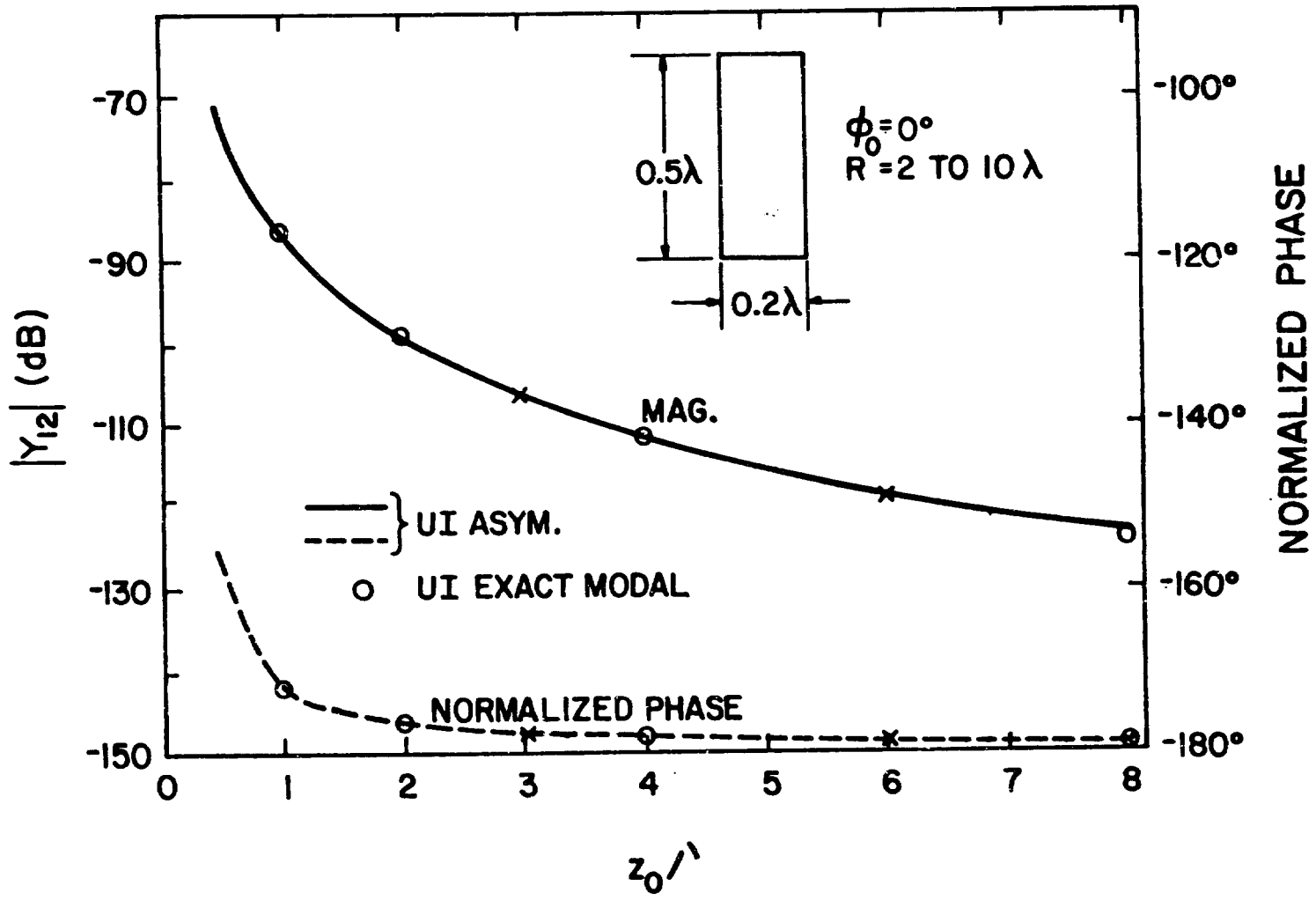

Figure D-1. Mutual admittance Y_{12} between two axial slots as a function of z^0.

4.3 Computer Program

The UI computer subroutine for mutual admittance between axial slots on a cylinder is PROG1, while that for circumferential slots is PROG2. Both subroutines may be imbedded into a simple main program that loops as desired over any of the input parameters. These subroutines utilize a subroutine FMFN which computes Bessel factors in the sum; Bessel function subroutines are also included as some extant subroutines are insufficiently accurate. Test case data follow the code listings, which are in standard FORTRAN 4.

```
      SUBROUTINE PROG1(RHO,AMPY,PHASEY,AMPYDB,PHASNM)
      PROGRAM TO COMPUTE THE MUTUAL ADMITTANCE BETWEEN TWO IDENTICAL
      AXIAL SLOTS ON A CYLINDER ( UI MODAL SOLUTION)
      REAL    KO,KZ,KT,I2,KZKTRO
      COMPLEX  I1,Y12,PSIEXP,YN12
      REAL     F1(400), FM(400),FN(400),AIMAG,REAL,ATAN2
      COMMON/DATA3/KO,NCYCLE,PHIO,ZO,Y11,MMAX,A,B
```

```
C      INPUT PARAMETERS:
C      KO=WAVE NUMBER IN FREE SPACE IN TERMS OF 1/INCH
C      NCYCLE=NO. OF SUBSECTIONS BETWEEN ANY TWO  SUCCESSIVE ZEROS OF INTEGRAND
C      IN TRAPEZOIDAL RULE FOR NUMERICAL INTEGRATION
C      A*B= SLOT DIMENSION  B>A      <INCH>
C      RHO=RADIUS OF CYLINDER  <INCH>
C      PHIO=ANGULAR SEPARATION OF THE SLOTS (CENTER TO CENTER) <RADIAN>
C      ZO= SEPARATION OF THE SLOTS IN Z-DIRECTION   <INCH>
C      Y11= NORMALIZATION FACTOR
C      MMAX= MAXIMUM NO. OF TERMS WHICH HAS BEEN USED IN CALCULATION OF
C      INFINITE SERIES
       PI=3.14159265
       YO=1./(120.*PI)
       FREQ=3.E10*KO/(2.*PI*2.54)
       AKA=KO*A
       BKB=KO*B
       RK=KO*RHO
C      PHIA=HALF ANGULAR WIDTH OF THE SLOT
       PHIA=2.*ASIN(A/(2.*RHO))
C      COMPUTATION OF INFINITE SERIES
       MMAX12=MMAX+1
       DO 100 M=1,MMAX12
       M1=M-1
       IF(M.EQ.1) GO TO 99
       F1(M)=COS(M1*PHIO)*(SIN(M1*PHIA/2.)/(M1*PHIA/2.))**2
       GO TO 100
    99 F1(M)=0.5
   100 CONTINUE
C      INTEGRATION OF PSI(KZ)*R1(M,KZ)*EXP(-J*KZ*ZO) BETWEEN 0 AND KO
C      DELTA= NEIGHBOURHOOD OF THE SINGULAR POINT KZ=KO IN WHICH THE INTEGRAL
C      HAS BEEN CALCULATED ANALYTICALLY
       DELTA=1.E-7*KO
C      NSECT1=NO. OF SAMPLES IN THE INTERVAL (0.,KO-DELTA).
       NSECT1=(IFIX((B+ZO+RHO)*KO/PI)+2)*NCYCLE
       DKZ=(KO-DELTA)/NSECT1
       NSECT=NSECT1+1
       I1=(0.,0.)
C      I1=FIRST INTEGRAL (BETWEEN 0. AND KO)
       DO 200 I=1,NSECT
       KZ=(I-1)*DKZ
       IF(KZ.EQ.0) KZ=0.00001*KO
       CIN=1.
       IF((I.EQ.1).OR.(I.EQ.NSECT)) CIN=0.5
       KT=SQRT(KO*KO-KZ*KZ)
       IF(ABS(KZ*B/2.-PI/2.).LE.1.E-8) KZ=1.000001*KZ
       PSIEXP=(COS(KZ*B/2.)/((KZ*B/2.)**2-(PI/2.)**2))**2*CIN*DKZ
      &*CEXP((0.,-1.)*KZ*ZO)
       MMAX1=MMAX
       ROKT=RHO*KT
C      COMPUTATION OF FM(N)=1./(JN(X)**2+YN(X)**2) AND FN(N)=1./(DJN(X)**2+
C      DYN(X)**2) FOR X=ROKT AND N=0 TO MMAX1 ; WHERE MMAX1 IS A NUMBER AFTER
C      WHICH  THE CONTRIBUTIONS OF FM(N) AND FN(N) TO THE INFINITE SUM
```

```
C      BECOME NEGLIGIBLE. MMAX1 IS A FUNCTION OF  THE ARGUMENT X AND IS ALWAYS
C      LESS THAN OR EQUAL TO MMAX. MMAX1, FM(N) AND FN(N) ARE CALCULATED
C      BY SUBROUTINE FMFN(X,MMAX1,FM,FN).
       CALL FMFN(ROKT,MMAX1,FM,FN)
       DO 200 M=1,MMAX1
       M1=M-1
  200  I1=I1+FN(M)*PSIEXP*F1(M)
C      COMPUTATION OF I2 (BETWEEN ZERO AND ETAMAX ; WHERE ETAMAX  IS A NUMBER
C      AFTER WHICH THE INTEGRAND BECOMES VERY SMALL)
       I2=0.
       ETAMAX=14./(ZO-B)
C      THE INTEGRATION IS CARRIED OUT BY TRAPEZOIDAL RULE. AT FIRST THE WHOLE
C      RANGE OF INTEGRATION (0.,ETAMAX) IS DEVIDED INTO TWO SUBINTERVALS :
C      (0.,ETA1) AND (ETA1,ETAMAX) , WHERE ETA1=ETAMAX/2.. THEN THE NUMERICAL
C      COMPUTATION OF THE  INTEGRAL IS PERFORMED IN THESE SUBINTERVALS WITH THE
C      NO. OF SAMPLES IN THE FIRST SUBINTERVAL TWO TIMES THAT IN THE SECOND ONE.
       ETA1=7./(ZO-B)
       NSECT1=(IFIX(SQRT(KO*KO+ETA1**2)*RHO/PI)+2)*NCYCLE
       DETA1=ETA1/NSECT1
       DETA2=2.*DETA1
       NSECT2=IFIX((ETAMAX-ETA1)/DETA2)+1
       NSECT=NSECT1+NSECT2+2
       DO 300 I=1,NSECT
       IF(I.LE.NSECT1+1) GO TO 220
       ETA=ETA1+(I-NSECT1-2)*DETA2
       DETA=DETA2
       GO TO 240
  220  ETA=(I-1)*DETA1
       IF(ETA.EQ.0.) ETA=0.0001/A
       DETA=DETA1
  240  CIN=1.
       IF((I.EQ.1).OR.(I.EQ.NSECT1+1).OR.(I.EQ.NSECT1+2).OR.(I.EQ.NSECT)
      &) CIN=0.5
       PSEX=(COSH(ETA*B/2.)/((ETA*B/2.)**2+(PI/2.)**2))**2*DETA*CIN
      &*EXP(-ETA*ZO)
       KT=SQRT(KO*KO+ETA**2)
       MMAX1=MMAX
       CALL FMFN(RHO*KT,MMAX1,FM,FN)
       DO 300 M=1,MMAX1
       M1=M-1
  300  I2=I2+FN(M)*PSEX*F1(M)
       Y12=(I1+(0.,1.)*I2)*A*B*YO/(PI*KO*RHO**2)
C      NORMALIZATION OF THE PHASE OF Y12
       YN12=Y12*CEXP((0.,1.)*(KO*SQRT(ZO*ZO+(RHO*PHIO)**2)))
C      COMPUTATION OF THE ACTUAL PHASE 'PHASEY' AND NORMALIZED PHASE 'PHASNM'
C      OF Y12.
       PHASEY=ATAN2(AIMAG(Y12),REAL(Y12))*180./PI
       PHASNM=ATAN2(AIMAG(YN12),REAL(YN12))*180./PI
C      COMPUTATION OF THE MAGNITUDE OF THE Y12 IN TERMS OF <MHO> AND <DB>.
       AMPY=CABS(Y12)
       AMPYDB=ALOG10(AMPY/ABS(Y11))*20.
       RPHIK=KO*RHO*PHIO
```

```
      ZOK=KO*ZO
      PHIOD=PHIO*180./PI
      RETURN
      END
      SUBROUTINE PROG2(RHO,AMPY,PHASEY,AMPYDB,PHASNM)
C     PROGRAM FOR COMPUTATION OF THE MUTUAL ADMITTANCE BETWEEN TWO
C     IDENTICAL CIRCUMFERENTIAL SLOTS ON A CYLINDER(UI MODAL SOLUTION)
      REAL   KO,KZ,KT,I2,KZKTRO
      COMPLEX  I1,Y12,PSIEXP,YN12
      REAL    F1(400), FM(400),FN(400),AIMAG,REAL,ATAN2
      COMMON/DATA3/KO,NCYCLE,PHIO,ZO,Y11,MMAX,A,B
C     INPUT PARAMETERS :
C     KO=WAVE NUMBER IN FREE SPACE IN TERMS OF 1/INCH
C     RHO=RADIUS OF CYLINDER <INCH>
C     PHIO=ANGULAR SEPARATION OF THE SLOTS (CENTER TO CENTER) <RADIAN>
C     ZO= SEPARATION OF THE SLOTS IN Z-DIRECTION   <INCH>
C     Y11= NORMALIZATION FACTOR
C     MMAX= MAXIMUM NO. OF TERMS WHICH HAS BEEN USED IN CALCULATION OF
C     INFINITE SERIES
C     NCYCLE=NO. OF SUBSECTIONS BETWEEN ANY TWO  SUCCESSIVE ZEROS OF INTEGRAND
C     IN TRAPEZOIDAL RULE FOR NUMERICAL INTEGRATION
      PI=3.14159265
      YO=1./(120.*PI)
      FREQ=3.E10*KO/(2.*PI*2.54)
      AKA=KO*A
      BKB=KO*B
      RK=KO*RHO
C     PHIB=HALF ANGULAR WIDTH OF THE SLOT
      PHIB=ASIN(A/(2.*RHO))
C     COMPUTATION OF INFINITE SERIES
      MMAX12=MMAX+1
      DO 100 M=1,MMAX12
      M1=M-1
      EPM=1.
      IF(M.EQ.1) EPM=2.
      PHIB1=PHIB
      IF(ABS(PHIB*M1-PI/2.).LE.1.E-7) PHIB1=PHIB*1.001
  100 F1(M)=COS(M1*PHIO)*(-PI*COS(M1*PHIB1)/(((M1*PHIB1)**2-(PI/2.)**2
     &)))**2*(1./EPM)
C     INTEGRATION OF PSI(KZ)*R1(M,KZ)*EXP(-J*KZ*ZO) BETWEEN 0 AND KO
C     DELTA= NEIGHBOURHOOD OF THE SINGULAR POINT KZ=KO IN WHICH THE INTEGRAL
C     HAS BEEN CALCULATED ANALYTICALLY
      DELTA=0.0001*KO
C     DELTA1= NEIGHBOURHOOD OF THE SINGULAR POINT KZ=KO WHERE THE INTEGRAND
C     VARIES RAPIDLY AND 'NDELTA' SAMPLES HAVE BEEN USED.
      DELTA1=0.01*KO
      NDELTA=100
      DKZ2=(DELTA1-DELTA)/NDELTA
C     NSECT1= NO. OF SUBSECTIONS BETWEEN  0 AND KO-DELTA1
      NSECT1=(IFIX((B+ZO+RHO)*KO/PI)+2)*NCYCLE
      DKZ1=(KO-DELTA1)/NSECT1
      NSECT=NSECT1+NDELTA+2
```

```
C       I1=FIRST INTEGRAL (BETWEEN 0. AND KO)
        I1=(0.,0.)
        DO 200 I=1,NSECT
        IF(I.LE.NSECT1+1) GO TO 120
        KZ=KO-DELTA1+(I-NSECT1-2)*DKZ2
        DKZ=DKZ2
        GO TO 140
  120   KZ=(I-1)*DKZ1
        IF(KZ.EQ.0) KZ=0.00001*KO
        DKZ=DKZ1
  140   CIN=1.
        IF((I.EQ.1).OR.(I.EQ.NSECT1+1).OR.(I.EQ.NSECT1+2).OR.(I.EQ.NSECT)
       &) CIN=0.5
        KT=SQRT(KO*KO-KZ*KZ)
        PSIEXP=(SIN(KZ*B/2.)/(KZ*B/2.))**2*CIN*DKZ*CEXP((0.,-1.)*KZ*ZO)
        MMAX1=MMAX
        ROKT=RHO*KT
C       COMPUTATION OF FM(N)=1./(JN(X)**2+YN(X)**2) AND FN(N)=1./(DJN(X)**2+
C       DYN(X)**2) FOR X=ROKT AND N=0 TO MMAX1 ; WHERE MMAX1 IS A NUMBER AFTER
C       WHICH  THE CONTRIBUTIONS OF FM(N) AND FN(N) TO THE INFINITE SUM
C       BECOME NEGLIGIBLE. MMAX1 IS A FUNCTION OF  THE ARGUMENT X AND IS ALWAYS
C       LESS THAN OR EQUAL TO MMAX. MMAX1, FM(N) AND FN(N) ARE CALCULATED
C       BY SUBROUTINE FMFN(X,MMAX1,FM,FN).
        CALL FMFN(ROKT,MMAX1,FM,FN)
        KZKTRO=(KZ/(KT*KO*RHO))**2
        DO 200 M=1,MMAX1
        M1=M-1
        R1=(1./KT**2)*(FM(M)+M1**2*KZKTRO*FN(M))
  200   I1=I1+R1*PSIEXP*F1(M)
        I1=(2.*KO/(PI*RHO))*(I1-F1(1)*CEXP((0.,-1.)*KO*ZO)*(PI*PI/(2.*KO))
       &*(SIN(KO*B/2.)/(KO*B/2.))**2/(2.*(0.5772156649+ALOG(RHO*SQRT
       &(KO/2.)))+ALOG(DELTA)))
C       COMPUTATION OF I2 (BETWEEN ZERO AND ETAMAX ; WHERE ETAMAX  IS A NUMBER
C       AFTER WHICH THE INTEGRAND BECOMES VERY SMALL)
        I2=0.
        ETAMAX=14./(ZO-B)
C       THE INTEGRATION IS CARRIED OUT BY TRAPEZOIDAL RULE. AT FIRST THE WHOLE
C       RANGE OF INTEGRATION (0.,ETAMAX) IS DEVIDED INTO TWO SUBINTERVALS :
C       (0.,ETA1) AND (ETA1,ETAMAX) , WHERE ETA1=ETAMAX/2.. THEN THE NUMERICAL
C       COMPUTATION OF THE  INTEGRAL IS PERFORMED IN THESE SUBINTERVALS WITH THE
C       NO. OF SAMPLES IN THE FIRST SUBINTERVAL TWO TIMES THAT IN THE SECOND ONE.
        ETA1=7./(ZO-B)
        NSECT1=(IFIX(SQRT(KO*KO+ETA1**2)*RHO/PI)+2)*NCYCLE
        DETA1=ETA1/NSECT1
        DETA2=2.*DETA1
        NSECT2=IFIX((ETAMAX-ETA1)/DETA2)+1
        NSECT=NSECT1+NSECT2+2
        DO 300 I=1,NSECT
        IF(I.LE.NSECT1+1) GO TO 220
        ETA=ETA1+(I-NSECT1-2)*DETA2
        DETA=DETA2
        GO TO 240
```

```
  220 ETA=(I-1)*DETA1
      IF(ETA.EQ.0.) ETA=0.0001/B
      DETA=DETA1
  240 CIN=1.
      IF((I.EQ.1).OR.(I.EQ.NSECT1+1).OR.(I.EQ.NSECT1+2).OR.(I.EQ.NSECT)
     &) CIN=0.5
      PSEX=(SINH(ETA*B/2.)/(ETA*B/2.))**2*EXP(-ETA*ZO)*DETA*CIN
      KT=SQRT(KO*KO+ETA**2)
      ETKTRO=(ETA/(RHO*KO*KT))**2
      MMAX1=MMAX
      CALL FMFN(RHO*KT,MMAX1,FM,FN)
      DO 300 M=1,MMAX1
      M1=M-1
      R1=(1/(KT*KT))*(FM(M)-M1*M1*ETKTRO*FN(M))
  300 I2=I2+F1(M)*R1*PSEX
      I2=I2*2.*KO/(PI*RHO)
      Y12=(I1+(0.,1.)*I2)*A*B*YO/(2.*PI*PI*RHO)
C     NORMALIZATION OF THE PHASE OF Y12
      YN12=Y12*CEXP((0.,1.)*(KO*SQRT(ZO*ZO+(RHO*PHIO)**2)))
C     COMPUTATION OF THE ACTUAL PHASE 'PHASEY' AND NORMALIZED PHASE 'PHASNM'
C     OF Y12.
      PHASEY=ATAN2(AIMAG(Y12),REAL(Y12))*180./PI
      PHASNM=ATAN2(AIMAG(YN12),REAL(YN12))*180./PI
C     COMPUTATION OF THE MAGNITUDE OF THE Y12 IN TERMS OF <MHO> AND <DB>.
      AMPY=CABS(Y12)
      AMPYDB=ALOG10(AMPY/ABS(Y11))*20.
      RPHIK=KO*RHO*PHIO
      ZOK=KO*ZO
      PHIOD=PHIO*180./PI
      RETURN
      END
      SUBROUTINE FMFN(X,N,FM,FN)
      REAL DUM1(400),DUM2(400)
      REAL FJ(400),XB,BSSY(400),FM(400),FN(400)
      PI=3.14159265
      XB=X
      IF(X-0.1) 10,10,20
   10 GAMLOG=ALOG(X/2.)+0.5772156649
      X2=X*X
      X3=X2*X
      X4=X*X3
      X5=X*X4
      BSSY1=2.*(GAMLOG*(1.-X2/4.+X4/64.)+X2/4.-3.*X4/128.)/PI
      BSSY2=-2./(PI*X)+2.*(GAMLOG*(X/2.-X3/16.+X5/384.)-X/4.+1.25*X3/16.
     &-3.33333*X5/768.)/PI
      GO TO 25
   20 CALL BESY(X,0,BSSY1,IER)
      CALL BESY(X,1,BSSY2,IER)
   25 CONTINUE
      BSSY(1)=BSSY1
      BSSY(2)=BSSY2
      DBSSY1=-BSSY(2)
      I=1
   80 I=I+1
      BSSY(I+1)=2.*(I-1)*BSSY(I)/X-BSSY(I-1)
      BSSYI1=BSSY(I+1)
```

```
      IF(ABS(BSSYI1).GE.1.E10) GO TO 100
      GO TO 80
  100 NMAX=I+1
      IF(NMAX.GE.N) NMAX=N
      N1=N-1
      CALL BSLJZ(XB,FJ,NMAX+1,0.D00,7,IERR,DUM1,DUM2)
      DFJ1=-FJ(2)
      FM(1)=1./(BSSY(1)**2+FJ(1)**2)
      FN(1)=1./(DBSSY1**2+DFJ1**2)
      DO 200 I=1,N1
      IF(I.GE.NMAX) GO TO 250
      DBSSY=BSSY(I)-I*BSSY(I+1)/X
      DFJ=FJ(I)-I*FJ(I+1)/XB
      FM(I+1)=1./(BSSY(I+1)**2+FJ(I+1)**2)
      FN(I+1)=1./(DBSSY**2+DFJ**2)
  200 CONTINUE
  250 CONTINUE
      N=NMAX
      RETURN
      END
C     SUBROUTINE 'BESY'
C        PURPOSE                                                        BES
C           COMPUTE THE Y BESSEL FUNCTION FOR A GIVEN ARGUMENT AND ORDERBES
C                                                                       BES
C        USAGE                                                          BES
C           CALL BESY(X,N,BY,IER)                                       BES
C                                                                       BES
C        DESCRIPTION OF PARAMETERS                                      BES
C           X  -THE ARGUMENT OF THE Y BESSEL FUNCTION DESIRED           BES
C           N  -THE ORDER OF THE Y BESSEL FUNCTION DESIRED              BES
C           BY -THE RESULTANT Y BESSEL FUNCTION                         BES
C           IER-RESULTANT ERROR CODE WHERE                              BES
C              IER=0  NO ERROR                                          BES
C              IER=1  N IS NEGATIVE                                     BES
C              IER=2  X IS NEGATIVE OR ZERO                             BES
C              IER=3  BY HAS EXCEEDED MAGNITUDE OF 10**70               BES
C                                                                       BES
C        REMARKS                                                        BES
C           VERY SMALL VALUES OF X MAY CAUSE THE RANGE OF THE LIBRARY   BES
C           FUNCTION ALOG TO BE EXCEEDED                                BES
C           X MUST BE GREATER THAN ZERO                                 BES
C           N MUST BE GREATER THAN OR EQUAL TO ZERO                     BES
C                                                                       BES
C        SUBROUTINES AND FUNCTION SUBPROGRAMS REQUIRED                  BES
C           NONE                                                        BES
C                                                                       BES
C        METHOD                                                         BES
C           RECURRENCE RELATION AND POLYNOMIAL APPROXIMATION TECHNIQUE  BES
C           AS DESCRIBED BY A.J.M.HITCHCOCK,'POLYNOMIAL APPROXIMATIONS  BES
C           TO BESSEL FUNCTIONS OF ORDER ZERO AND ONE AND TO RELATED    BES
C           FUNCTIONS', M.T.A.C., V.11,1957,PP.86-88, AND G.N. WATSON,  BES
C           'A TREATISE ON THE THEORY OF BESSEL FUNCTIONS', CAMBRIDGE   BES
```

```
C            UNIVERSITY PRESS, 1958, P. 62                                  BES
C                                                                           BES
C     ..................................................................... BES
C                                                                           BES
      SUBROUTINE BESY(X,N,BY,IER)                                           BES
C                                                                           BES
C     CHECK FOR ERRORS IN N AND X                                           BES
C                                                                           BES
      IF(N)180,10,10                                                        BES
   10 IER=0                                                                 BES
      IF(X)190,190,20                                                       BES
C                                                                           BES
C     BRANCH IF X LESS THAN OR EQUAL 4                                      BES
C                                                                           BES
   20 IF(X-4.0)40,40,30                                                     BES
C                                                                           BES
C       COMPUTE Y0 AND Y1 FOR X GREATER THAN 4                              BES
C                                                                           BES
   30 T1=4.0/X                                                              BES
      T2=T1*T1                                                              BES
      P0=((((-.0000037043*T2+.0000173565)*T2-.0000487613)*T2                BES
     1  +.00017343)*T2-.001753062)*T2+.3989423                              BES
      Q0=((((.0000032312*T2-.0000142078)*T2+.0000342468)*T2                 BES
     1  -.0000869791)*T2+.0004564324)*T2-.01246694                          BES
      P1=((((.0000042414*T2-.0000200920)*T2+.0000580759)*T2                 BES
     1  -.000223?03)*T2+.002921826)*T2+.3989423                             BES
      Q1=((((-.0000036594*T2+.00001622)*T2-.0000398708)*T2                  BES
     1  +.0001064741)*T2-.0006390400)*T2+.03740084                          BES
      A=2.0/SQRT(X)                                                         BES
      B=A*T1                                                                BES
      C=X-.7853982                                                          BES
      Y0=A*P0*SIN(C)+B*Q0*COS(C)                                            BES
      Y1=-A*P1*COS(C)+B*Q1*SIN(C)                                           BES
      GO TO 90                                                              BES
C                                                                           BES
C       COMPUTE Y0 AND Y1 FOR X LESS THAN OR EQUAL TO 4                     BES
C                                                                           BES
   40 XX=X/2.                                                               BES
      X2=XX*XX                                                              BES
      T=ALOG(XX)+.5772157                                                   BES
      SUM=0.                                                                BES
      TERM=T                                                                BES
      Y0=T                                                                  BES
      DO 70 L=1,15                                                          BES
      IF(L-1)50,60,50                                                       BES
   50 SUM=SUM+1./FLOAT(L-1)                                                 BES
   60 FL=L                                                                  BES
      TS=T-SUM                                                              BES
      TERM=(TERM*(-X2)/FL**2)*(1.-1./(FL*TS))                               BES
   70 Y0=Y0+TERM                                                            BES
      TERM = XX*(T-.5)                                                      BES
      SUM=0.                                                                BES
```

```
      Y1=TERM                                                          BES
      DO 80 L=2,16                                                     BES
      SUM=SUM+1./FLOAT(L-1)                                            BES
      FL=L                                                             BES
      FL1=FL-1.                                                        BES
      TS=T-SUM                                                         BES
      TERM=(TERM*(-X2)/(FL1*FL))*((TS-.5/FL)/(TS+.5/FL1))              BES
   80 Y1=Y1+TERM                                                       BES
      PI2=.6366198                                                     BES
      Y0=PI2*Y0                                                        BES
      Y1=-PI2/X+PI2*Y1                                                 BES
C                                                                      BES
C     CHECK IF ONLY Y0 OR Y1 IS DESIRED                                BES
C                                                                      BES
   90 IF(N-1)100,100,130                                               BES
C                                                                      BES
C     RETURN EITHER Y0 OR Y1 AS REQUIRED                               BES
C                                                                      BES
  100 IF(N)110,120,110                                                 BES
  110 BY=Y1                                                            BES
      GO TO 170                                                        BES
  120 BY=Y0                                                            BES
      GO TO 170                                                        BES
C                                                                      BES
C    PERFORM RECURRENCE OPERATIONS TO FIND YN(X)                       BES
C                                                                      BES
  130 YA=Y0                                                            BES
      YB=Y1                                                            BES
      K=1                                                              BES
  140 T=FLOAT(2*K)/X                                                   BES
      YC=T*YB-YA                                                       BES
      IF(ABS(YC)-1.0E70)145,145,141                                    BES
  141 IER=3                                                            BES
      RETURN                                                           BES
  145 K=K+1                                                            BES
      IF(K-N)150,160,150                                               BES
  150 YA=YB                                                            BES
      YB=YC                                                            BES
      GO TO 140                                                        BES
  160 BY=YC                                                            BES
  170 RETURN                                                           BES
  180 IER=1                                                            BES
      RETURN                                                           BES
  190 IER=2                                                            BES
      RETURN                                                           BES
      END                                                              BES
C     SUBROUTINE BSLJZ(X , FJ , NMAX , A , ND , IERR , FJAPRX , RR)
C
C THIS IS ONE OF THREE ROUTINES, "BSLJZ", "BSLIZ", AND "BSCJZ",
C BASED ON ALGORITHM 236 FROM "COMMUNICATIONS OF THE A.C.M.",
C AUGUST 1964. THIS ONE EVALUATES THE BESSEL FUNCTIONS OF THE
C FIRST KIND FOR REAL ORDERS AND NON-NEGATIVE REAL ARGUMENTS.
```

```
C
C THE PARAMETERS ARE DESCRIBED AS FOLLOWS, WITH "(I)", "(O)", AND
C "(I/O)" INDICATING, RESPECTIVELY, THAT A PARAMETER IS TO BE SET ON
C ENTRY, WILL BE SET BY THE ROUTINE, OR BOTH :
C
C *** ALL PARAMETERS EXCEPT "ND" , "IERR" , "NMAX" ARE ***
C *** SINGLE PRECISION REAL NUMBERS OR ARRAYS.          ***
C
C (I)   X        --  THE (NON-NEGATIVE) ARGUMENT TO THE BESSEL FUNCTIONS.
C (O)   FJ       --  AN ARRAY IN WHICH THE VALUES OF THE BESSEL FUNCTIONS
C                    ARE STORED, AS FOLLOWS: LET J(X;B) DENOTE THE VALUE
C                    OF THE BESSEL FUNCTION OF ORDER B WITH ARGUMENT X.
C                    THEN, FOR I = 1 TO ABS(NMAX)+1,
C                        FJ(I) = J(X;A + (I-1)*SIGN(NMAX)) .
C (I)   NMAX     --  REFER TO "FJ".
C (I)   A        --  REFER TO "FJ". NORMALLY, 0 <= A < 1, BUT THE ALGOR-
C                    ITHM WORKS, WITH SOME LOSS OF ACCURACY, FOR A >= 1.
C                    SEE THE PROGRAM NOTES BELOW.
C (I)   ND       --  THIS GIVES THE NUMBER OF SIGNIFICANT FIGURES OF
C                    ACCURACY DESIRED IN THE FUNCTION VALUES.
C (O)   IERR     --  THIS IS AN ERROR FLAG WHICH IS SET TO 0 IF THE
C                    INPUT PARAMETERS ARE OKAY, AND TO SOME POSITIVE
C                    VALUE IF ONE OF THE PARAMETERS IS INVALID. REFER
C                    TO THE ERROR EXITS AT THE END OF THE CODE FOR A
C                    DETAILED LIST OF THE VALUES OF IERR.
C (O)   FJAPRX   --  A SCRATCH ARRAY USED BY THE ROUTINE. IT MUST HAVE
C                    AT LEAST ABS(NMAX)+1 ENTRIES.
C (O)   RR       --  ANOTHER SCRATCH ARRAY. IT TOO MUST HAVE AT LEAST
C                    ABS(NMAX)+1 ENTRIES
C
C OTHER ROUTINES CALLED: ( * INDICATES A LOCAL ROUTINE )
C  *    NBS01Z -- INVERSE FUNCTION OF X*LOG(X)
C  *    UNDERZ -- ROUTINE TO CONTROL UNDERFLOW INTERRUPTS ON THE IBM 360.
C       MGAMMA -- GAMMA FUNCTION FROM THE IMSL LIBRARY.
C       ALOG   -- LOGARITHM
C       ABS    -- ABSOLUTE VALUE
C       MOD    -- REMAINDER
C       AMAX1  -- MAXIMUM OF 2 REALS
C
C NOTES:
C       THE METHOD OF COMPUTATION IS A VARIANT OF THE BACKWARD
C       RECURRENCE ALGORITHM OF J.C.P.MILLER (REFERENCE 1). THE
C       PURPORTED ACCURACY IS OBTAINED BY A JUDICIOUS SELECTION
C       OF THE INITIAL VALUE "NU" OF THE RECURSION INDEX (REP-
C       RESENTED IN THE CODE BY THE VARIABLE "XNU"), TOGETHER
C       WITH AT LEAST ONE REPETITION OF THE RECURSION WITH "NU"
C       REPLACED BY "NU"+5. NEAR A ZERO OF ONE OF THE BESSEL
C       FUNCTIONS, THE ACCURACY OF THAT PARTICULAR BESSEL FUNCTION
C       MAY DETERIORATE TO LESS THAN "ND" SIGNIFICANT DIGITS. THE
C       ALGORITHM IS MOST EFFICIENT WHEN X IS SMALL OR MODERATELY
C       LARGE.
C
```

```
C       THE ABOVE PARAGRAPH IS TAKEN FROM GAUTSCHI'S PRESENTATION
C       OF ALGORITHM 236 IN C.A.C.M. THE SELECTION OF THE INITIAL
C       "NU" IS DONE WITH THE AID OF THE FUNCTION NBS01Z, ALSO
C       BY GAUTSCHI (AND CALLED "T" BY HIM). IN THIS CODE, THE
C       FOLLOWING SPECIAL CASES HAVE BEEN ADDED:
C               A. X=0 WHEN NMAX > 0 OR A=0
C               B. A=0 AND NMAX < 0
C               C. A >= 1 : THE ALGORITHM WORKS IN THIS CASE, BUT THE
C                           INITIAL CHOICE OF "NU" IS NO LONGER
C                           OPTIMAL, AND SOME ACCURACY IS LOST. SIMPLE
C                           TESTS INDICATE THAT ONLY A FEW DECIMAL
C                           PLACES ARE SACRIFICED AT WORST. A LIMIT OF
C                           "ABIG" IS PLACED ON A TO AVOID OVERFLOW IN
C                           THE GAMMA FUNCTION. TO AVOID COMPLICATIONS,
C                           NMAX IS REQUIRED TO BE NON-NEGATIVE IF A > 1.
C
C REFERENCES:
C       1. GAUTSCHI, W. "RECURSIVE COMPUTATION OF SPECIAL FUNCTIONS",
C               UNIVERSITY OF MICHIGAN ENGINEERING SUMMER CONFER-
C               ENCES, NUMERICAL ANALYSIS, 1963.
C
C*********************************************************************
      SUBROUTINE BSLJZ(X , FJ , NMAX , A , ND , IERR , FJAPRX , RR)
      REAL NBS01Z
      DIMENSION FJ(1) , FJAPRX(1) , RR(1)
      LOGICAL   NEVEN , AFLAG
      DATA      ONE/1D0/        , TWO/2D0/      , HALF/.5D0/    ,
     *          TEN/10D0/       , SMALL/1D-15/  , C1/.73576D0/  ,
     *          C2/1.3591D0/    , C3/2.3026D0/  , C4/1.3863D0/  ,
     *          ZERO/0D0/       , ABIG/55D0/    , TWOP5/2.5D0/  ,
     *          ALEPH/3777 0000 0000 0000 0000B/, FOUR/4D0/     ,
     *          C5/2000 4000 0000 0000 0000B/
C******
C INITIALIZE THE ERROR PARAMETER , TURN UNDERFLOW OFF , AND CHECK
C THE PARAMETERS FOR VALIDITY AND FOR THESE SPECIAL CASES:
C       A. X=0 WITH NMAX > 0 OR A=0
C       B. A=0 AND NMAX < 0
C
C THE CODE DELIBERATELY AVOIDS TESTING MORE THEN ONE THING IN EACH
C LOGICAL "IF" BELOW BECAUSE OF I.B.M. FORTRAN INEFFICIENCY IN THIS
C REGARD.
C
C IF A>1, NMAX MUST NOT BE NEGATIVE.
C******
      IERR = 0
C     CALL UNDERZ('OFF',SAVE)
      IF(A    .LT. ZERO) GOTO 999
      IF(A    .GT. ABIG) GOTO 998
      IF(X    .LT. ZERO) GOTO 997
      IF(NMAX .GE. 0   ) GOTO 10
      IF(A    .EQ. ZERO) GOTO 10
      IF(A    .LE. SMALL) GOTO 996
```

```
      IF(A     .GE. ONE   ) GOTO 994
10    IF(X     .GT. ZERO) GOTO 40
      IF(NMAX .GE. 0    ) GOTO 20
      IF(A     .GT. ZERO) GOTO 995
C******
C IF NMAX < 0, NMAXT IS SET HERE SO THAT ONLY J(X;A) IS CALCULATED.
C THE LOOP FOLLOWING STATEMENT 800 THEN CALCULATES THE REMAINING
C FUNCTIONS BY A SIMPLE RECURRENCE.
C IF A=0, NMAXT IS SET SO THAT J(X;A+N), N=0,...,-NMAX ARE
C CALCULATED; THE CODE AFTER 800 THEN REVERSES THE SIGN OF EVERY
C OTHER ONE.
C
C WE FIRST HANDLE THE CASE X=0.
C******
20    NTEMP = IABS(NMAX) + 1
      DO 30 I = 1,NTEMP
30    FJ(I) = ZERO
      IF(A .EQ. ZERO) FJ(1) = ONE
      GOTO 1000
C******
40    AFLAG = (A .EQ. ZERO) .AND. (NMAX .LT. 0)
      NMAXT = NMAX
      IF(NMAX .LT. 0) NMAXT = 1
      NTEMP = MAX0(NMAX+1,1)
      IF(.NOT. AFLAG) GOTO 60
      NMAXT = - NMAX
      NTEMP = NMAXT + 1
60    EPSLON = TEN**(-ND)/2
      DO 80 I = 1,NTEMP
80    FJAPRX(I) = ZERO
      CALL MGAMMA(ONE+A , RESULT , IER)
      SUM = (X/TWO)**A/RESULT
      D1  = C3*ND + C4
      R   = ZERO
      IF(NMAXT .GT. 0) R = NMAXT * NBS01Z(HALF*D1/NMAXT)
      S    = C2 * X * NBS01Z(C1*D1/X)
C******
C THE RECURSION INDEX 'NU' IS DELIBERATELY CALCULATED AS A FLOATING
C POINT NUMBER RATHER THAN AN INTEGER, AND ALL COMPARISONS WITH IT
C ARE DONE AS FLOATING POINT COMPARISONS.
C******
      XNU  = ONE + AMAX1(R,S)
      XLIMIT = XNU/2
      TWOA = A + A
      XN   = ZERO
      FL   = ONE
C******
C THE OUTER ITERATION LOOP STARTS HERE.
C
C
C THE FOLLOWING LOOP IS DONE ENTIRELY IN FLOATING POINT FOR
C EFFICIENCY.
```

```
C******
200     XN = XN + ONE
        FL = FL * (XN + A)/(XN + ONE)
        IF(XN .LT. XLIMIT) GOTO 200
        OLDFL = FL
        OLDXN = XN
C
        N  = 2*XN
        XN = N
        NEVEN = .TRUE.
        R = ZERO
        S = ZERO
        TEMP1 = TWO/X
C******
C IN THE FOLLOWING LOOP, THE SUCCESSIVE VALUES OF "R" ARE PARTIAL
C FRACTIONS OF A CONTINUED FRACTION.
C******
300     DENOM = TEMP1 * (A + XN) - R
        IF(ABS(DENOM) .LE. SMALL) DENOM = DENOM + SMALL
        R = ONE/DENOM
        FLMBDA = ZERO
        IF(.NOT. NEVEN) GOTO 400
        FL     = FL * (XN + TWO)/(XN + TWOA)
        FLMBDA = FL * (XN + A)
400     S = R * (FLMBDA + S)
        IF(N .LE. NMAXT) RR(N) = R
        N  = N - 1
        XN = XN - ONE
        NEVEN = .NOT. NEVEN
        IF(N .GE. 1) GOTO 300
C******
        FJ(1) = SUM/(ONE + S)
        IF(NMAXT .EQ. 0) GOTO 600
        DO 500 N = 1,NMAXT
500     FJ(N+1) = RR(N) * FJ(N)
C******
C THE LATEST APPROXIMATIONS ARE CHECKED FOR IMPROVEMENT:
C******
600     DO 800 N = 1,NTEMP
          IF(ABS(FJ(N) - FJAPRX(N)) .LE. ABS(FJ(N))*EPSLON) GOTO 800
          DO 700 M = 1,NTEMP
700       FJAPRX(M) = FJ(M)
          XN     = OLDXN
          FL     = OLDFL
          XLIMIT = XLIMIT + TWOP5
          GOTO 200
800     CONTINUE
        IF(NMAX .GE. 0) GOTO 1000
C******
C IF NMAX<0, WE HAVE FINISHED OBTAINING J(X;A) , AND NOW
C ITERATE TO FIND ALL THE DESIRED FUNCTIONS.
C
```

```
C FIRST WE CHECK FOR THE SPECIAL CASE A=0.
C******
      IF(.NOT. AFLAG) GOTO 850
      NMAXT = -NMAX + 1
      DO 820 N = 2,NMAXT,2
820   FJ(N) = - FJ(N)
      GOTO 1000
C******
850   FJ(2) = TWO * A * FJ(1)/X - FJ(2)
      IF(NMAX .EQ. -1) GOTO 1000
C******
C THE FOLLOWING CODE IS A RENDITION OF THE LOOP
C                DO 900 N = 2,NMAXT
C       900      FJ(N+1) = (2/X)*(A-N)*FJ(N) - FJ(N-1)
C
C WITH OVERFLOW DETECTION. AS SOON AS THE NUMBERS GET TOO BIG, THEY
C ARE SCALED DOWN (BY A POWER OF THE MACHINE BASE, SO AS TO AVOID
C LOSS OF PRECISION) AND THE CALCULATION CONTINUES. A SEPARATE LOOP
C TRANSFORMS THE SCALED VALUES TO THE CORRECT OUTPUT VALUES, SETTING
C TOO-LARGE ONES TO PLUS OR MINUS INFINITY.
C******
      NMAXT = -NMAX + 1
      FJNM2 = FJ(1)
      FJNM1 = FJ(2)
      TEMP1 = TWO/X
      OVER  = ZERO
      XNM1  = TWO
C
      DO 880 N = 3,NMAXT
      FJN   = TEMP1 * (A - XNM1) * FJNM1   -   FJNM2
      FJNM2 = FJNM1
      FJNM1 = FJN
      FJ(N) = FJN
      XNM1  = XNM1 + ONE
      RR(N) = OVER
      IF(ABS(FJN) .LT. C5) GOTO 880
      OVER  = OVER + ONE
      FJNM1 = FJNM1/C5
      FJNM2 = FJNM2/C5
880   CONTINUE
C
      IF(NMAXT .LE. 3) GOTO 1000
      OVER  = ZERO
      SCALE = ONE
C
      DO 900 N = 4,NMAXT
      IF(OVER .LT. FOUR) GOTO 890
      FJ(N) = SIGN(ALEPH,FJ(N))
      GOTO 900
890   IF(RR(N) .GT. OVER) SCALE = SCALE * C5
      FJ(N) = FJ(N) * SCALE
      OVER  = RR(N)
```

```
900    CONTINUE
       GOTO 1000
C******
C ERROR EXITS FOLLOW. MEANINGS OF THE EXIT VALUES OF "IERR" ARE:
C        0 : NO ERROR
C        1 : A < 0
C        2 : A > ABIG
C        3 : X < 0
C        4 : NMAX < 0 AND 0 < A < SMALL
C        5 : X=0, NMAX < 0, AND A > 0
C        6 : NMAX < 0 AND A >= 1
C******
994    IERR = IERR + 1
995    IERR = IERR + 1
996    IERR = IERR + 1
997    IERR = IERR + 1
998    IERR = IERR + 1
999    IERR = IERR + 1
1000   CONTINUE
C      CALL UNDERZ('S',SAVE)
       RETURN
       END
       REAL FUNCTION NBS01Z(X)
C******
C THIS IS A NUCLEUS FOR THE THREE BESSEL FUNCTION ROUTINES
C "BSLJZ" , "BSLIZ" , "BSCJZ" BASED ON ALGORITHM 236 FROM
C "COMMUNICATIONS OF THE A.C.M.".
C IT EVALUATES THE INVERSE FUNCTION OF X*LOG(X) FOR X >= 1 TO AN
C ACCURACY OF ABOUT ONE PER CENT.
C FOR THE INTERVAL 0 <= X <= 10 A FIFTH DEGREE APPROXIMATION IS
C USED, OBTAINED BY TRUNCATING AN EXPANSION IN CHEBYCHEV POLYNOMIALS.
C FOR X > 10, A DIFFERENT APPROXIMATION IS GIVEN, AS CAN BE SEEN.
C******
       DATA       C1/.00057941D0/          , C2/-.00176148D0/       ,
      *           C3/.0208645D0/           , C4/-.129013D0/         ,
      *           C5/.85777D0/             , C6/1.10125D0/          ,
      *           ALPHA/.775D0/            , TEN/10D0/
       IF(X .GT. TEN) GO TO 10
       NBS01Z = ((((C1*X + C2)*X + C3)*X + C4)*X + C5)*X + C6
       RETURN
10     TEMP1 = ALOG(X)-ALPHA
       TEMP2 = (ALPHA-ALOG(TEMP1))/(1+TEMP1)
       NBS01Z = X/((1+TEMP2)*TEMP1)
       RETURN
       END
```

AXIAL TEST CASE

Inputs

K = 6.283185307	Y11 = 1
A = .2	PHI = 30
B = .5	ZO = 1
NCYCLE = 40	RADIUS = 1
MMAX = 480	

Outputs

Y12 = .3386E-4 mho 85.48 deg

DB = -.8941

NORM PHASE = 131.84 deg.

CIRCUMFERENTIAL TEST CASE

Inputs

K = 6.283185307	Y11 = 1
A = .5	PHI = 30
B = .2	ZO = 1
NCYCLE = 40	RADIUS = 1
MMAX = 480	

Outputs

Y12 = .1358E-3 mho 24.82 deg

DB = -.7734E+2

NORM PHASE = 71.18 deg.

CHAPTER 4

MODAL CALCULATION OF SLOTS ON CONE

4.0 SLOT MODAL FIELDS

Expressions for the radiation fields from slot-excited conical antennas were first obtained by Bailin and Silver (1956). The fields were expressed in terms of normal-mode expansions using the orthogonal properties of the eigenfunctions. Although some corrections modifying the first results appeared in the literature (Bailin and Silver, 1956, 1957), the expressions for the fields need additional examination. More recently Pridmore-Brown and Stewart (1972) presented a more rigorous calculation of the θ-polarized electric field component of circumferential slots. Their numerical calculation is based on expressions derived from integral transform methods.

In this section, complete expressions of two potential functions representing the modal fields will be presented for both the circumferential and the radial slot. The electric field components will then be obtained from the potential functions and will be available for calculation of radiation patterns of the individual slots or arrays of slots of any desired configuration.

Figure 1 shows typical circumferential and radial slots and the conical geometry. The usual spherical coordinate system centered at the cone tip is associated with the structure. The cone axis coincides with the z-axis of the rectangular coordinates (x, y, z) associated with (r, θ, ϕ). Primes denote coordinates of the apertures on the structure.

The two scalar potential functions in question are Π^{TE} and Π^{TM}, TE and TM to the radial direction, respectively. For an assumed time dependence of exp (jwt) both satisfy the wave equation:

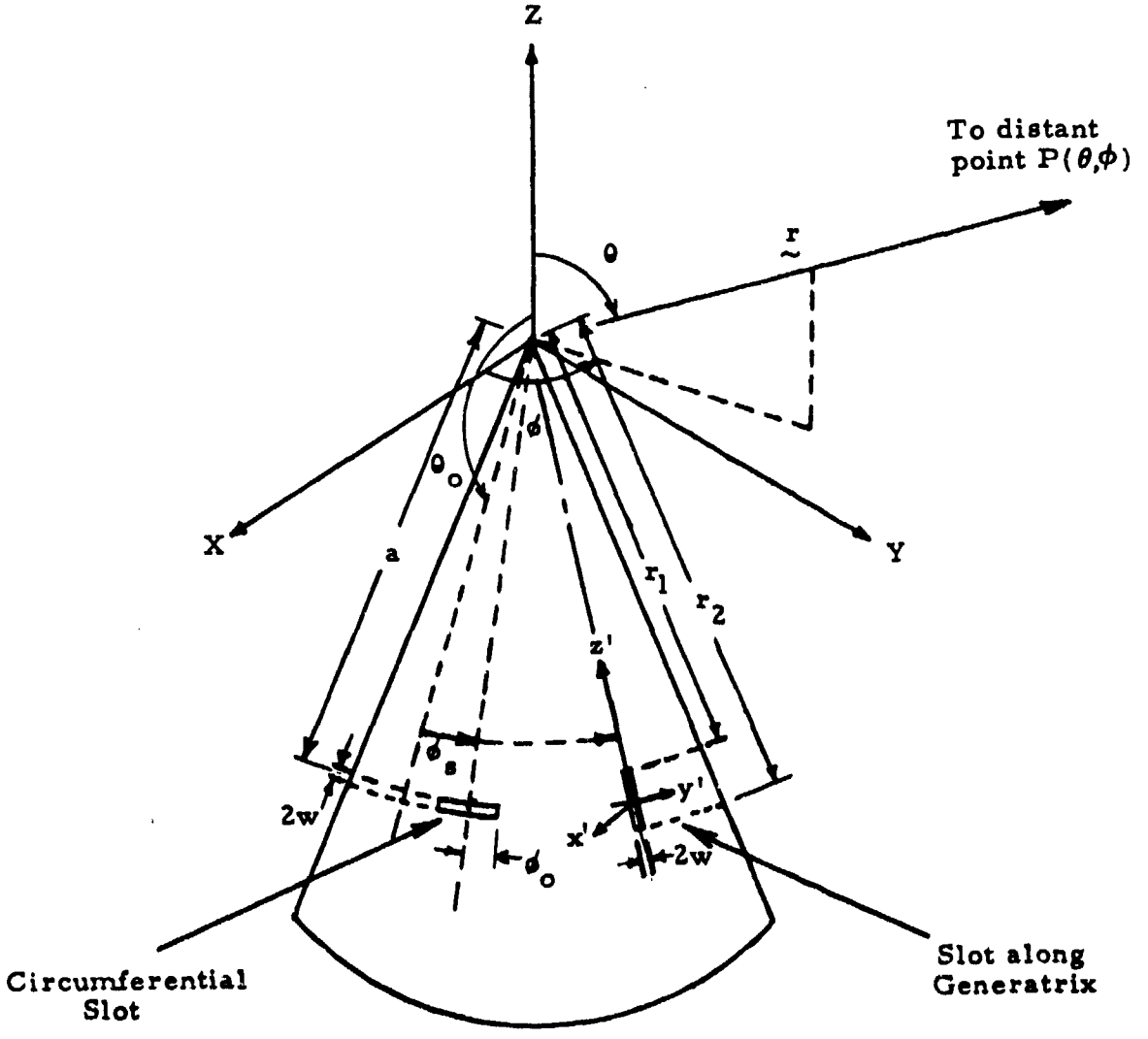

Figure 1. Conical Geometry and Slot Coordinates

$$(\nabla^2 + k^2)\ \Pi = 0. \qquad (1)$$

The electric and magnetic field components are then conveniently given by superposition of TE and TM partial fields obtained from the potential functions as follows:

TM - Partial Fields:

$$E_r = \frac{\partial^2}{\partial r^2}(r\Pi^{TM}) + k^2 (r\Pi^{TM}) \qquad H_r = 0$$

$$E_\theta = \frac{1}{r}\frac{\partial^2}{\partial r \partial \theta}(r\Pi^{TM}) \qquad H_\theta = \frac{j\omega\epsilon}{r\sin\theta}\frac{\partial}{\partial \phi}(r\Pi^{TM}) \qquad (2)$$

$$E_\phi = \frac{1}{r\sin\theta}\frac{\partial^2}{\partial r \partial \phi}(r\Pi^{TM}) \qquad H_\phi = \frac{-j\omega\epsilon}{r}\frac{\partial}{\partial \theta}(r\Pi^{TM})$$

TE - Partial Fields:

$$E_r = 0 \qquad H_r = \frac{\partial^2}{\partial r^2}(r\Pi^{TE}) + k^2 (r\Pi^{TE})$$

$$E_\theta = -\frac{j\omega\mu}{r\sin\theta}\frac{\partial}{\partial \phi}(r\Pi^{TE}) \qquad H_\theta = \frac{1}{r}\frac{\partial^2}{\partial r \partial \theta}(r\Pi^{TE}) \qquad (3)$$

$$E_\phi = \frac{j\omega\mu}{r}\frac{\partial}{\partial \theta}(r\Pi^{TE}) \qquad H_\phi = \frac{1}{r\sin\theta}\frac{\partial^2}{\partial r \partial \phi}(r\Pi^{TE})$$

For an arbitrarily shaped source excitation the expression for the Π^{TM} is given by Bailin and Silver (1956) (There is a (-) sign in their expression.)

$$\Pi^{TM} = \sum_{m=0}^{\infty} \sum_{i=1}^{\infty} \frac{(jk)(2\nu_i + 1) P_{\nu_i}^m(\cos\theta)}{\nu_i(\nu_i+1)(1+\delta_{om})\pi \sin\theta_o \left.\frac{\partial P_\nu^m}{\partial \nu}\right|_{\substack{\theta=\theta_o \\ \nu=\nu_i}}} \cdot \int_{r_1}^{r_2}\int_{\phi_1}^{\phi_2} f_1(r',\phi') \cos m(\phi' - \phi)\, j_{\nu_i}(k r_<)\, h_{\nu_i}(k r_>)\, r' \sin\theta_o \, dr'\, d\phi' \tag{4}$$

where r>, r< symbolizes the larger and smaller of the coordinates r, r', respectively. $P_\nu^m(\cos\theta)$ is the associated Legendre function and

$$j_\nu(kr) = \sqrt{\frac{\pi}{2kr}}\, J_{\nu+1/2}(kr) \tag{5}$$

$$h_\nu^{(2)}(kr) = \sqrt{\frac{\pi}{2kr}}\, H_{\nu+1/2}^{(2)}(kr) \tag{6}$$

are the spherical Bessel and spherical Hankel functions, respectively. J_ν is the Bessel function of the first kind and order ν and $H_\nu^{(2)}$ is the Hankel function of the second kind and order ν. δ_{om} is the Kronecker delta function

$$\delta_{om} = \begin{cases} 1 & m = 0 \\ 0 & m \neq 0 \end{cases} \tag{7}$$

while the ν_i are the roots of the equation

$$P_\nu^m (\cos \theta_0) = 0 \tag{8}$$

The function $f_1(r', \phi')$ in equation (4) is the electric field source excitation in the r direction. Following the general procedure described by Bailin and Silver where the boundary conditions are applied in conjunction with the Lorentz reciprocity theorem to the modal fields, an expression for Π^{TE} is obtained. The TE scalar function with arbitrary source excitation is given by,

$$\Pi^{TE} = \frac{1}{\eta} \sum_{m=o}^{\infty} \sum_{i=1}^{\infty} \frac{(2\nu_i' + 1)\, P_{\nu_i'}^m(\cos \theta)}{\pi (1+\delta_{om})\, \nu_i'(\nu_i' + 1) \sin \theta_o \frac{\partial^2 P_\nu^m}{\partial \nu \partial \theta}} \Bigg|_{\substack{\theta = \theta_o \\ \nu = \nu_i'}}$$

$$\cdot \left\{ \int_{r_1}^{r_2} \int_{\phi_1}^{\phi_2} m f_1(r', \phi')\, \Gamma_1(r, r') \sin m(\phi' - \phi)\, dr'\, d\phi' \right. \tag{9}$$

$$\left. + \int_{r_1}^{r_2} \int_{\phi_1}^{\phi_2} \nu_i'(\nu_i' + 1) \sin \theta_o f_2(r', \phi')\, j_{\nu_i'}(kr<) h_{\nu_i'}^{(2)}(kr>) \cos m(\phi' - \phi)\, dr'\, d\phi' \right\}$$

$$\text{where } \Gamma_1(r, r') = \begin{cases} j_{\nu_i'}(kr) \frac{d}{dr'} [r' h_{\nu_i'}^{(2)}(kr')] & r < r' \\ h_{\nu_i'}^{(2)}(kr) \frac{d}{dr'} [r' j_{\nu_i'}(kr')] & r > r' \end{cases} \tag{10}$$

and η is the free space wave impedance $\sqrt{\mu/\epsilon}$. The ν_i' are the roots of the equation

$$\frac{\partial P_\nu^m (\cos \theta_0)}{\partial \theta} = 0 \qquad (11)$$

and f_2 (r', $\emptyset$') is the $E_\emptyset$ component of the source excitation. All other quantities are as defined for the TM case. It is interesting to observe that, unlike the TM mode, the TE mode is excited by both the r- and $\emptyset$- components of the source excitation in the aperture. Conversely, the r- component of the source excitation excites both the TM and the TE modes. It should also be noted that the expression in Equation (9) differs from the expression given by Bailin and Silver (1956) in the expression for Γ_1 (r, r') and a common factor of 1/sin θ_0.

The modal functions and the corresponding field components from particular aperture configurations on the cone structure with appropriate field excitations are given in Sections 4.1 and 4.2 below:

4.1 Circumferential and Radial Slots

Only circumferential and radial slots are considered. Inclined slot values can be interpolated from these two.

4.1.1 Circumferential Slot

A narrow circumferential slot of width $2w \ll \lambda$ is considered as shown in Figure 1. The narrow slot has an azimuthal length $d = 2\emptyset_0 a \sin \theta_0$ where $2\emptyset_0$ is the azimuthal angle subtended by the slot, θ_0 is the cone exterior angle measured from the axis, a is the distance from the cone tip to the center of the slot and λ is the operating wavelength. The slot is assumed to be excited by a voltage V_0 across its center and has a resulting field across it in the r direction given by

$$E_r(r', \phi') = \begin{cases} V_0 \cos\left[\dfrac{\pi(\phi' - \phi_s)}{2\phi_0}\right] \delta(r' - a), & |\phi' - \phi_s| < \phi_0 \\ 0 & |\phi' - \phi_s| > \phi_0 \end{cases} \tag{12}$$

where $\delta(r' - a)$ is the Dirac delta function.

Substituting the expression of $E_r(r', \phi')$ in Equations (4) and (9) for $f_1(r', \phi')$ and integrating over the primed coordinates, we obtain the explicit expression for Π^{TM} and Π^{TE}. The function $f_2(r', \phi')$ is set equal to zero in the TE case, as only the E_r component of the source excitation is assumed. Thus,

$$\underset{\sim}{\Pi}^{TM}(\underset{\sim}{r}) = \sum_{m=0}^{\infty}\sum_{i=1}^{\infty} \frac{(j k a V_o)(2\nu_i + 1) P_{\nu_i}^m(\cos\theta)}{\nu_i(\nu_i + 1)(1 + \delta_{om})\pi \dfrac{\partial P_\nu^m(\cos\theta)}{\partial \nu}\Big|_{\substack{\theta = \theta_o \\ \nu = \nu_i}}} j_{\nu_i}(kr<)\, h_{\nu_i}^{(2)}(kr>)$$

$$\cdot \frac{2k a \sin\theta_o \cos\left(\dfrac{m\pi}{2k a \sin\theta_o}\right) \cos m(\phi - \phi_s)}{(k a \sin\theta_o)^2 - m^2} \tag{13}$$

and

$$\underset{\sim}{\Pi}^{TE}(\underset{\sim}{r}) = \frac{1}{\eta}\sum_{m=0}^{\infty}\sum_{i=1}^{\infty} \frac{(2\nu_i' + 1) P_{\nu_i'}^m(\cos\theta)}{\pi(1 + \delta_{om})\nu_i'(\nu_i' + 1)\sin\theta_o \dfrac{\partial^2 P_\nu^m(\cos\theta)}{\partial\nu\,\partial\theta}\Big|_{\substack{\theta = \theta_o \\ \nu = \nu_i'}}}$$

$$\cdot \left\{ \frac{-2k a \sin\theta_o \cos\left(\dfrac{m\pi}{2k a \sin\theta_o}\right) \; m \sin m(\phi - \phi_s)}{(k a \sin\theta_o)^2 - m^2} \right\} \cdot \Gamma_1(r, a) \tag{14}$$

$$\text{where } \Gamma_1(r, a) = \begin{cases} h^{(2)}_{\nu'_i}(kr)\,\frac{d}{dr}\left(r' j_{\nu'_i}(kr')\right)\Big|_{r'=a} & r > a \\ j_{\nu'_i}(kr)\,\frac{d}{dr}\left(r' h^{(2)}_{\nu'_i}(kr')\right)\Big|_{r'=a} & r < a \end{cases} \tag{15}$$

The radiation fields are readily found by substituting the expression of Π^{TM} and Π^{TE} corresponding to r>a into Equations (2) and (3). On using the asymptotic expansion for the spherical Hankel functions,

$$h_\nu^{(2)}(k\,r) = \sqrt{\frac{\pi}{2\,k\,r}}\sqrt{\frac{2j}{\pi\,k\,r}}\; j^{\nu+1/2} e^{-j\,k\,r} \qquad (16)$$

$k\,r \to \infty$

and noting that

$$\frac{\partial}{\partial r}\left(r\,h_\nu^{(2)}(kr)\right) = j^\nu\, e^{-jkr} \tag{17}$$

the following expressions are obtained for the electric field components:

$$E_\theta = \sum_{m=0}^{\infty} \frac{V_o\, e^{-j(kr - \pi/4)}}{r\pi(1+\delta_{om})} \sqrt{2\pi ka}\; \frac{2\,k\,a \sin\theta_o \cos\left(\frac{m\pi}{2\,k\,a\sin\theta_o}\right)}{(k\,a\sin\theta_o)^2 - m^2} \cos m\phi \cdot \tag{18}$$

$$\left\{ P_{1\theta} + \frac{j\,m^2}{\sin\theta_o \sin\theta} P_{2\theta} \right\}$$

$$\text{where } P_{1\theta} = \sum_{i=1}^{\infty} j^{\nu_i} \frac{\nu_i}{\nu_i^2 - 1/4} J_{\nu_i}(ka)\; \frac{\frac{\partial}{\partial\theta} P^{-m}_{\nu_i - 1/2}(\cos\theta)}{\frac{\partial P^{-m}_{\nu-1/2}(\cos\theta)}{\partial\nu}}\Bigg|_{\substack{\theta=\theta_o \\ \nu=\nu_i}} \tag{19}$$

$$\text{and } P_{2\phi} = \sum_{i=1}^{\infty} j^{\nu_i'} \frac{\nu_i'}{\nu_i'^2 - 1/4} \left. \frac{P_{\nu_i' - 1/2}^{-m}(\cos\theta)}{\frac{\partial^2 P_{\nu - 1/2}^{-m}(\cos\theta)}{\partial\nu\,\partial\theta}} \right|_{\substack{\theta = \theta_o \\ \nu = \nu_i'}} \left[\frac{\left(\nu_i' + \frac{1}{2}\right) J_{\nu_i'}(ka)}{ka} - J_{\nu_i'+1}(ka) \right] \tag{20}$$

$$E_\phi = \sum_{m=0}^{\infty} m \frac{V_o e^{-j(kr - \pi/4)}}{r\pi} \sqrt{2\pi ka} \cdot \frac{2ka \sin\theta_o \cos\left(\frac{m\pi}{2ka \sin\theta_o}\right)}{(ka \sin\theta_o)^2 - m^2} \sin m\phi \tag{21}$$

$$\cdot \left\{ \frac{-j}{\sin\theta} P_{1\phi} + \frac{1}{\sin\theta_o} P_{2\phi} \right\} \tag{22}$$

where

$$P_{1\phi} = \sum_{i=1}^{\infty} \frac{\nu_i}{\nu_i^2 - 1/4} j^{\nu_i} J_{\nu_i}(ka) \left. \frac{P_{\nu_i - 1/2}^{-m}(\cos\theta)}{\frac{\partial P_{\nu - 1/2}^{-m}(\cos\theta)}{\partial\nu}} \right|_{\substack{\theta = \theta_o \\ \nu = \nu_i}}$$

$$\text{and } P_{2\phi} = \sum_{i=1}^{\infty} \frac{\nu_i'}{\nu_i'^2 - 1/4} j^{\nu_i'} \left. \frac{\frac{\partial}{\partial\theta} P_{\nu_i' - 1/2}^{-m}(\cos\theta)}{\frac{\partial^2 P_{\nu - 1/2}^{-m}(\cos\theta)}{\partial\nu\,\partial\theta}} \right|_{\substack{\theta = \theta_o \\ \nu = \nu_i'}} \left[\frac{(\nu_i' + 1/2) J_{\nu_i'}(ka)}{ka} - J_{\nu_i'+1}(ka) \right] \tag{23}$$

It is pointed out that the θ-dependence is represented by the Legendre function $P^{-m}_{\nu-1/2}(\cos\theta)$ instead of $P^{m}_{\nu}(\cos\theta)$ as originally derived. This choice simplifies the evaluation of the Legendre function in the digital computer and is preferred. Also, except for a constant factor of $1/\pi$, the expression for E_θ agrees with that reported by Pridmore-Brown and Stewart (1972) derived by the Kontorovitch-Lebedev transform method.

4.1.2 Radial Slot

A narrow slot of width 2 w<<circumference is assumed to be positioned along a generatrix of the cone and extends from r_1 to r_2 as shown in Figure 1. It is further assumed that the length of the slot, $(r_2 - r_1)$, is such as to allow definition of the ends of the slot by constant ϕ'. The slot is excited by a voltage V_0' resulting in an electric field in the ϕ-direction given by

$$E_\phi = V_0' \frac{g(r')\delta(\phi')}{r'\sin\theta_0} \tag{24}$$

The function g(r') describes the variation of the source excitation in the r' direction. Clearly, since $f_1(r', \phi') = 0$, i.e., no source excitation in the r'-direction, the TM mode of the potential function is not supported. The TE mode, on the other hand, is obtained only from the contribution of $f_2(r', \phi')$ in Equation (9). Substitution of Equation (24) into Equation (9) results in the following expression for Π^{TE} for the radial slot:

$$\underset{\sim}{\Pi}^{TE}(r) = \frac{V_o'}{\eta}\sum_{m=0}^{\infty}\sum_{i=1}^{\infty}\frac{(2\nu_i'+1)\,P^m_{\nu_i'}(\cos\theta)\cos m\phi}{\sin\theta_o\,\pi(1+\delta_{om})\dfrac{\partial^2 P^m_\nu(\cos\theta)}{\partial\nu\,\partial\theta}\Bigg|_{\substack{\theta=\theta_o\\ \nu=\nu_i'}}} \cdot \int_{r_1}^{r_2}\frac{\underline{E}(r')}{r'}\, j_{\nu_i'}(kr'<)\, h^{(2)}_{\nu_i'}(k\,r>)\,d\,r' \tag{25}$$

The electric field components are obtained from Equation (2) operating on Equation (25) giving:

$$E_\theta = \frac{V_o' e^{-j(kr - \pi/4)}}{r \sin \theta_o} \sum_{m=1}^{\infty} j \sqrt{\frac{2}{\pi}} \; m \sin m\phi \; \frac{1}{\sin \theta} P_\theta \tag{26}$$

$$E_\phi = \frac{V_o' e^{-j(kr - \pi/4)}}{r \sin \theta_o} \sum_{m=0}^{\infty} j \sqrt{\frac{2}{\pi}} \; \frac{\cos m\phi}{(1 + \delta_{om})} P_\phi \tag{27}$$

where

$$P_\theta = \sum_{i=1}^{\infty} \nu_i' j^{\nu_i'} \left. \frac{P_{\nu_i'}^{-m} - 1/2 (\cos \theta)}{\frac{\partial^2 P_{\nu - 1/2}^{-m}(\cos \theta)}{\partial \nu \partial \theta}} \right|_{\substack{\theta = \theta_o \\ \nu = \nu_i'}} \cdot \int_{r_1}^{r_2} \frac{g(r')}{r'} \frac{J_{\nu_i'}(k r')}{\sqrt{k r'}} \, dr' \tag{28}$$

$$P_\phi = \sum_{i=1}^{\infty} \nu_i' j^{\nu_i'} \left. \frac{\frac{\partial}{\partial \theta} P_{\nu_i'}^{-m} - 1/2 (\cos \theta)}{\frac{\partial^2 P_{\nu - 1/2}^{-m}(\cos \theta)}{\partial \nu \partial \theta}} \right|_{\substack{\theta = \theta_o \\ \nu = \nu_i'}} \cdot \int_{r_1}^{r_2} \frac{g(r')}{r'} \frac{J_{\nu_i'}(k r')}{\sqrt{k r'}} \, dr' \tag{29}$$

and the ν_i' are the roots of the equation

$$\frac{\partial P_{\nu - 1/2}^{-m}(\cos \theta_o)}{\partial \theta} = 0 \tag{30}$$

4.2 COMPUTATIONAL PROCEDURES

4.2.1 Legendre Functions

The calculation of radiation patterns from slots on a cone requires the evaluation of the associated Legendre function P_ν^m (cos θ) and its derivatives with respect to ν and θ. For numerical computations, however, it is more convenient to work with the related function P_ν^{-m} (cos θ). There are numerous representations available in the literature which can be used for the numerical computation of the function P_ν^{-m} (cos θ). However, the different representations vary in computational precision and are often expensive in terms of computer time. In addition, some representations are only valid for specific ranges of their independent variables and the choice must be made with extreme care.

We have chosen the expansion (Erdelyi, 1953, p. 147):

$$P_\nu^{-m}(\cos\theta) = \sqrt{\frac{2}{\pi \sin\theta}}\ \Gamma(\nu - m + 1) \sum_{k=o}^{\infty} (-1)^k \frac{(1/2 + m)_k\ (1/2 - m)_k}{k!\ (2 \sin\theta)^k\ (\nu + 3/2)_k}$$

$$\sin\left[(\nu + k + 1/2)\,\theta + \pi\,(1/2\,k + 1/2\,m + 1/4)\right] \qquad (31)$$

where $(b)_k = \frac{\Gamma(b+k)}{\Gamma(b)}$ and $\frac{\pi}{6} < \theta < 5\,\frac{\pi}{6}$ to compute the function for all $\theta \geq \frac{9}{72 + 2\,m}$ radians by increasing the degree of the function to at least $\nu = 72 + m$ prior to the use of the expansion in the numerical computation. The value of the function of the desired degree is then obtained by backward recursion. This in effect extends the usefulness of the expansion for numerical evaluation of the function to a new range for θ, $\frac{9}{72 + 2\,m} \leq \theta < \pi$ radians. The validity of the extension in the lower limit

was verified by comparing the calculated values in this θ-range with calculated values from an expansion suitable for small values of θ.

The verification that the asymptotic expansion of Equation (31) gives satisfactory results for $\theta \geq 5\pi/6$ under the above modification is somewhat more involved. As stated earlier, there are many representations of the associated Legendre functions, but only certain ones will lead to satisfactory results. Since the value of the argument of the associated Legendre functions of interest is near -1, the representation of the associated Legendre function P_ν^0 (cos ($\pi - \alpha$)), where $\alpha = \pi - \theta$, developed by Hille with small modification (Gray, 1953) was selected as an alternate representation of the function and suitable for computation. The representation used for computation of the zeroth order and for $0 \leq \nu \leq 2$ and small α is

$$P_\nu^0 \left[\cos(\pi-\alpha)\right] = \left[2\frac{\sin\nu\pi}{\pi}\log(\sin\alpha/2) + \cos\nu\pi \right] P_\nu^0 (\cos\alpha) + \frac{\sin\nu\pi}{\pi} \sum_{r=0}^{\infty} \frac{(-1)^r (\nu+r)!}{(\nu-r)!} \cdot \left[\psi(\nu+r) + \psi(\nu-r) - 2\psi(r)\right] \frac{(\sin\alpha/2)^{2r}}{r!\,r!} \tag{32}$$

where

$$P_\nu^0 (\cos\alpha) = \sum_{r=0}^{\infty} \frac{(-1)^r (\nu+r)!}{(\nu-r)!\,r!\,r!} (\sin\alpha/2)^{2r}$$

and

$$\psi(\xi) = \frac{d}{d\xi} (\log \xi!)$$

is the logarithmic derivative of the factorial function.

The series in Equation (32) converges very rapidly for $0 \leq \nu \leq 2$ and allows great computational precision. All other values of $P_\nu^m(\cos\theta)$ and $(\partial P_\nu^m(\cos\theta)/\partial\theta)$, $135^\circ \leq \theta \leq 180^\circ$, are then obtained by employing the recurrence formulas (Erdelyi, 1953, p. 161) given in Equations (33) and (34). The recurrence relationships for ν and m are, respectively,

$$P_{\nu+1}^m(x) = \frac{1}{(\nu-m+1)}\left[(2\nu+1)xP_\nu^m(x) - (\nu+m)P_{\nu-1}^m(x)\right] \qquad (33)$$

and

$$P_\nu^{m+1}(x) = \frac{1}{\sqrt{1-x^2}}\left[(\nu-m)xP_\nu^m(x) - (\nu+m)P_{\nu-1}^m(x)\right] \qquad (34)$$

The expression of Equation (32) was programmed together with the recurrence relationships of Equations (33) and (34) to obtain values of the associated Legendre functions. In the range of ν between 0 and 2 the computed values using Equation (32) agreed very well with computed values using the modified expansion of Equation (1). As the recurrence relationships were used to obtain values for higher order and higher degree functions, however, the agreement was no longer maintained. It appears that the recurrence relationships lead to imprecise values of the desired functions. Since the two representations give results in excellent agreement for small values of ν in the θ-range of interest, it is concluded that the modified expansion of Equation (31) gives satisfactory results for all values of ν of interest in the same θ-range.

From the expressions of the field components given in Section 4.1 it is seen that the calculation of radiation patterns requires the evaluation of the function $P_\nu^m(\cos\theta)$ and its derivatives with respect to ν and θ. As stated previously, we have chosen to work with the function $P_\nu^{-m}(\cos\theta)$ rather than $P_\nu^m(\cos\theta)$. The two functions are related by (Erdelyi, 1953, p.144):

$$P_\nu^m(\cos\theta)\cos(m\pi) = \frac{\Gamma(\nu+m+1)}{\Gamma(\nu-m+1)} P_\nu^{-m}(\cos\theta) \qquad (35)$$

where $\Gamma(k)$ is Euler's gamma function. Using the above relationship, it is easy to show that the ratio

$$\frac{\frac{\partial}{\partial\theta} P_\nu^m(\cos\theta)}{\frac{\partial}{\partial\nu} P_\nu^m(\cos\theta_0)} \qquad (36)$$

can be replaced by

$$\frac{\frac{\partial}{\partial\theta} P_\nu^{-m}(\cos\theta)}{\frac{\partial}{\partial\nu} P_\nu^{-m}(\cos\theta_0)} \qquad (37)$$

in the expression of the functions Π^{TM} and Π^{TE}. From the equation it is also evident that the roots of $P_\nu^m(\cos\theta_0)$ are also roots of $P_\nu^{-m}(\cos\theta_0)$. The same holds true for the derivatives of the two functions with respect to θ. Derivatives of the Legendre Functions with respect to θ are computed by the recurrence formula (Erdelyi, 1953, p. 161).

$$\frac{d}{d\theta} P_\nu^m(\cos\theta) = m\frac{\cos\theta}{\sin\theta} P_\nu^m(\cos\theta) + P_\nu^{m+1}(\cos\theta) \qquad (38)$$

The derivatives $\frac{d}{d\nu} P_\nu^m$ are computed numerically using the formula (Carnahan et al, 1969):

$$\frac{d}{d\nu} f(\nu_i) = \frac{1}{12h} \left[f(\nu_0) - 8 f(\nu_1) + 8f(\nu_2) - f(\nu_3) \right] \quad (39)$$

where $\nu_i = \nu_0 + i\,h$, h is a selected increment in ν, and $f(\nu_i)$ are the values of the Legendre functions of order m and degree ν_i, $P_{\nu_i}^m(\cos\theta)$.

4.2.2 Spherical Bessel Functions

The computation of the fields involves the spherical Bessel function $j_\nu(x)$ and the spherical Hankel function $h_\nu^{(2)}(x)$. Since these functions are related to corresponding cylindrical functions, Equations (5) and (6), the cylindrical functions are computed instead. For the Hankel function, $h_\nu^{(2)}(x)$, the asymptotic expansion has been used.

The computation of the radiation field from a slot along a generator of the conical surface requires the evaluation of the integral

$$\int_{r_1}^{r_2} \frac{g(r)}{r} \frac{J_\nu(k\,r)}{k\,r}\, d\,r \quad . \quad (40)$$

A series solution of the indicated integral when g(r') is a polynomial in r' is obtained from the formula (Abramowitz & Stegun, 1956): (41)

$$\int_0^z t^\mu J_\nu(t)\,dt = \frac{z^\mu\,\Gamma\left(\frac{\nu+\mu+1}{2}\right)}{\Gamma\left(\frac{\nu-\mu+1}{2}\right)} \sum_{k=0}^{\infty} (\nu+2k+1) \frac{\Gamma\left(\frac{\nu-\mu+1}{2}+k\right)}{\Gamma\left(\frac{\nu+\mu+3}{2}+k\right)} J_{\nu+2k+1}(z)$$

with Real part $(\mu + \nu + 1) > 0$. Alternatively, the indicated integral may be evaluated with sufficient accuracy by known numerical integration techniques. The latter method, using Simpson's "3/8 Rule", has been chosen for the present program. Either method, however, requires the evaluation of the Bessel function $J_\nu(x)$.

4.3 Analysis of Computed Element Patterns for Slots on a Cone

The convergence of the modal series representing the far fields of the circumferential and radial slots was examined by looking at the pattern change in the sequential summation of higher order modes. In each case, patterns were calculated for every 10° in azimuth and every 5° in elevation for both the θ-polarization and the ϕ-polarization. However, elevation cuts were plotted only at $\phi = 0^\circ$ and $\phi = 180$ degrees. These two cuts have been plotted on an extended θ scale to give a single view of the elevation cut. Since the cone under study has a 10° half angle, the position of $\theta = 80^\circ$ was selected for azimuthal cuts. This corresponds to the broadside of the conical surface. Figure 1 shows the relative position of slots in the coordinate system.

The patterns to be shown subsequently have been normalized to the largest value computed for both polarizations for the particular modal sum or individual mode. For convenience, we shall refer to the individual mode patterns by the small letter "m" and to the sum patterns by the capital letter "M".

4.3.1 Radiation Patterns of Circumferential Slots

A slot of azimuthal length $d = \lambda/2$ located at $ka = 39$ radians ($k = 2\pi/\lambda$) from the tip of the 10° half angle cone was selected for pattern computations. This particular location was selected because it corresponds to a case of a circumferential slot at 8.15 GHz and 9 inches from the cone tip previously

investigated experimentally (Pridmore-Brown & Stewart, 1972). The computed results will be compared with the available experimental results where appropriate. The slot is assumed to be excited by a voltage across its center and has a resulting field across it in the r direction given by Equation (12). Near the tip of the cone this excitation function may be represented by a few terms of a cosine series with appropriate coefficients. A greater number of terms are required for adequate representation of the same function when the slot is located many wavelengths away from the tip. It will be seen later that there is a correlation between the number of expansion terms in the excitation function and the number of terms required for convergence of the modal series representing the fields. However, this correlation is not easily determined beforehand. The dominant TE_{10} mode of a rectangular waveguide may be used to excite the slot.

Figures 2 and 3 show the θ-polarized pattern of the lowest two modes, $m = 0$ and $m = 1$, respectively, for $\phi = 0^{\circ}$ and $\phi = 180^{\circ}$. As expected, the modal patterns for $\phi = 180^{\circ}$ are identical to the $\phi = 0^{\circ}$ patterns, since the variation of the fields in the ϕ-direction is purely sinusoidal. The pattern corresponding to the $m = 0$ mode shows significant variation at broadside with extrema at $\theta = 0^{\circ}$ and $\theta = \theta_o = 170$ degrees. The peaks at $\theta = 12^{\circ}$ and $\theta = 30^{\circ}$ of this particular mode are particularly noteworthy. In contrast to the $m = 0$ mode pattern, the $m = 1$ mode pattern of Figure 3 exhibits a relatively small and smooth variation at the broadside region. The maximum now occurs at $\theta = 0^{\circ}$ with a pronounced first minimum at $\theta = 15^{\circ}$ followed by a local maximum at $\theta = 25$ degrees. Also, the pattern is about 1 dB down at $\theta = \theta_o$.

The total or sum θ-polarized pattern of the first two modes, $M = 1$, is also shown in Figure 2 for $\phi = 0^{\circ}$ and for $\phi = 180^{\circ}$

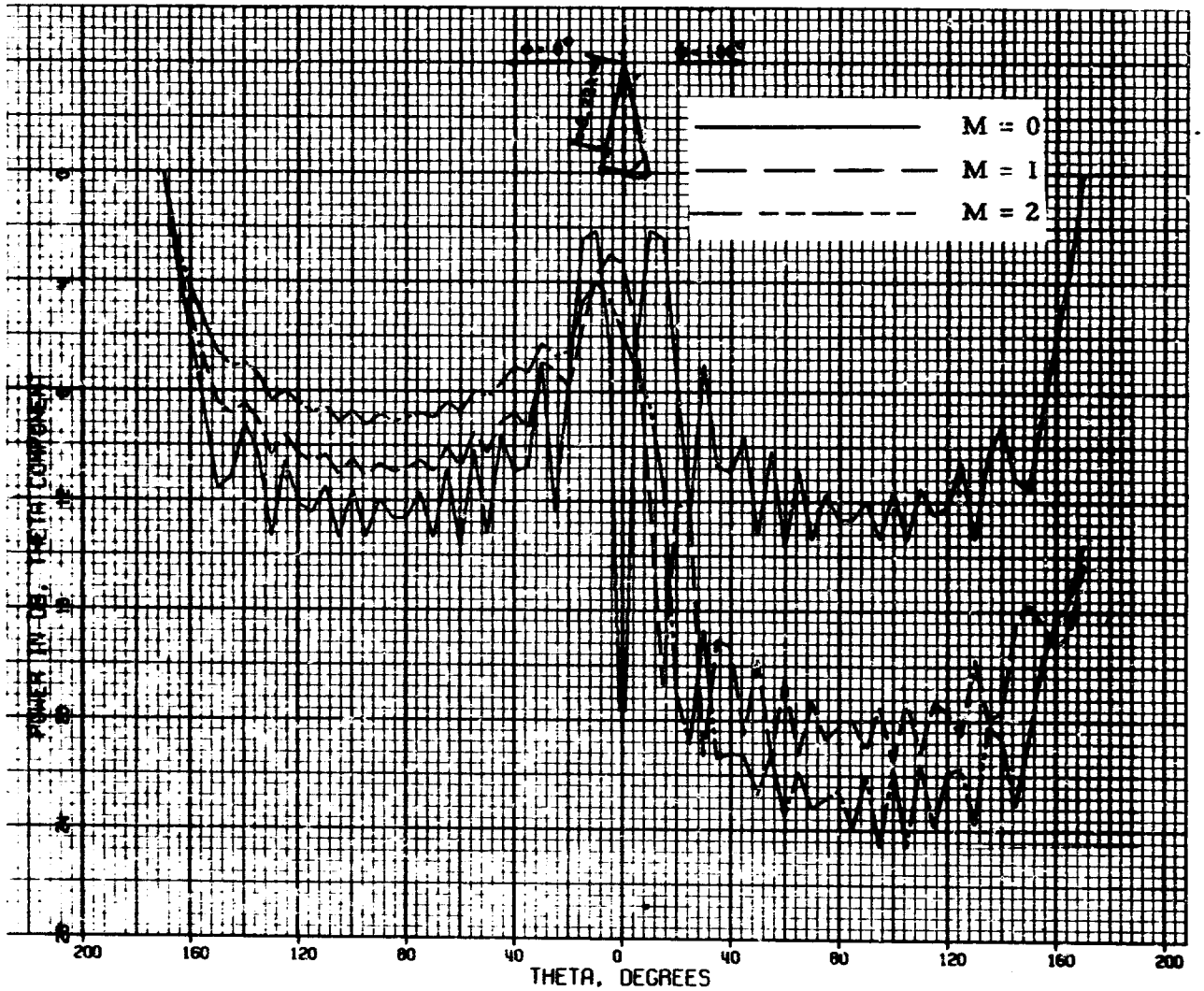

Figure 2. θ-Polarized Total Patterns of λ/2 Circumferential Slot for $\phi = 0^{\circ}$, $\phi = 180^{\circ}$, M = 0, 1, and 2

Figure 3. θ-Polarized Modal Pattern of λ/2 Circumferential Slot for m = 1, $\phi = 0^{\circ}$, $\phi = 180^{\circ}$

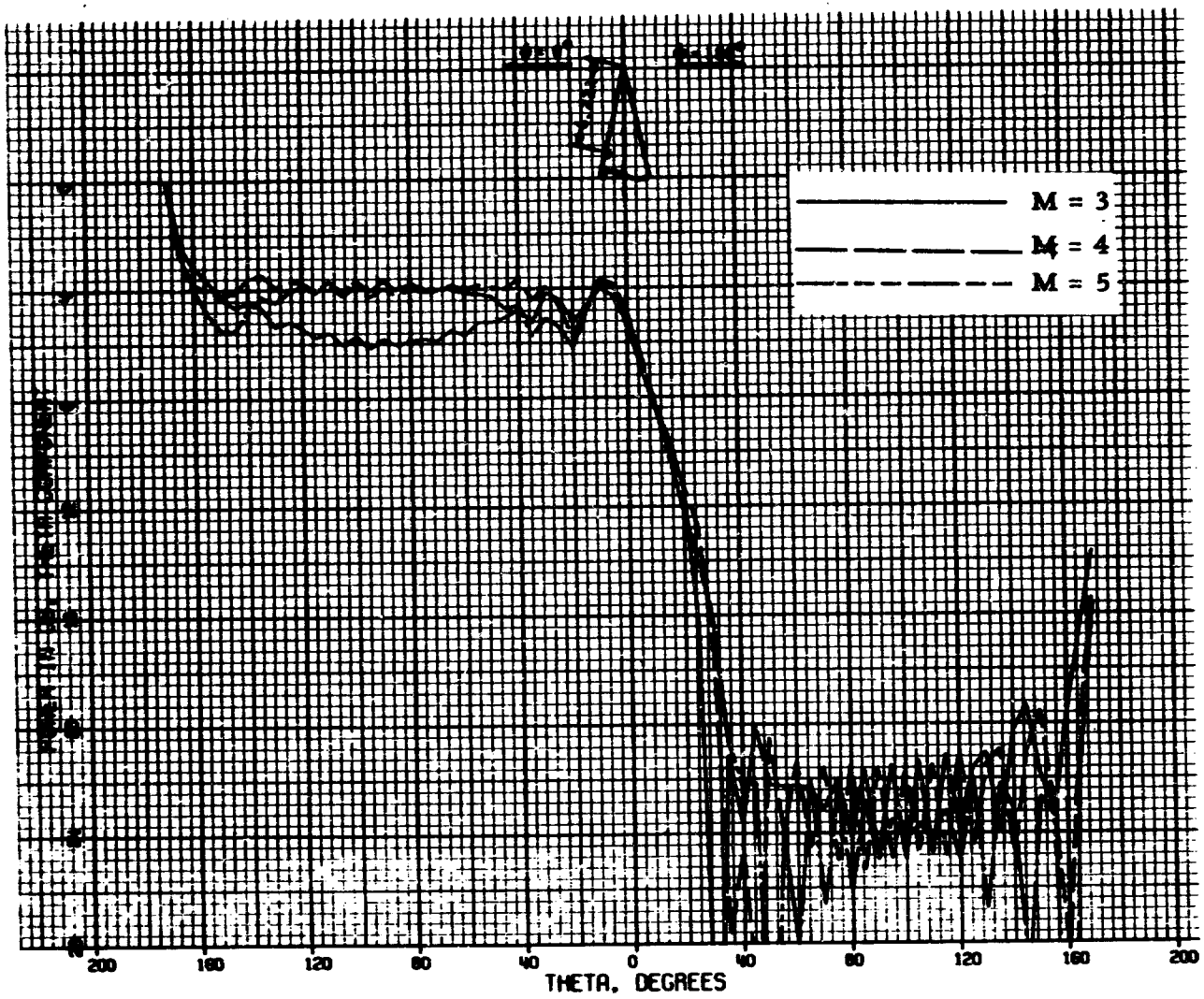

Figure 4. θ-Polarized Total Patterns of /2 Circumferential Slot for $\phi = 0^{\circ}$, $\phi = 180^{\circ}$, M = 3, 4 and 5

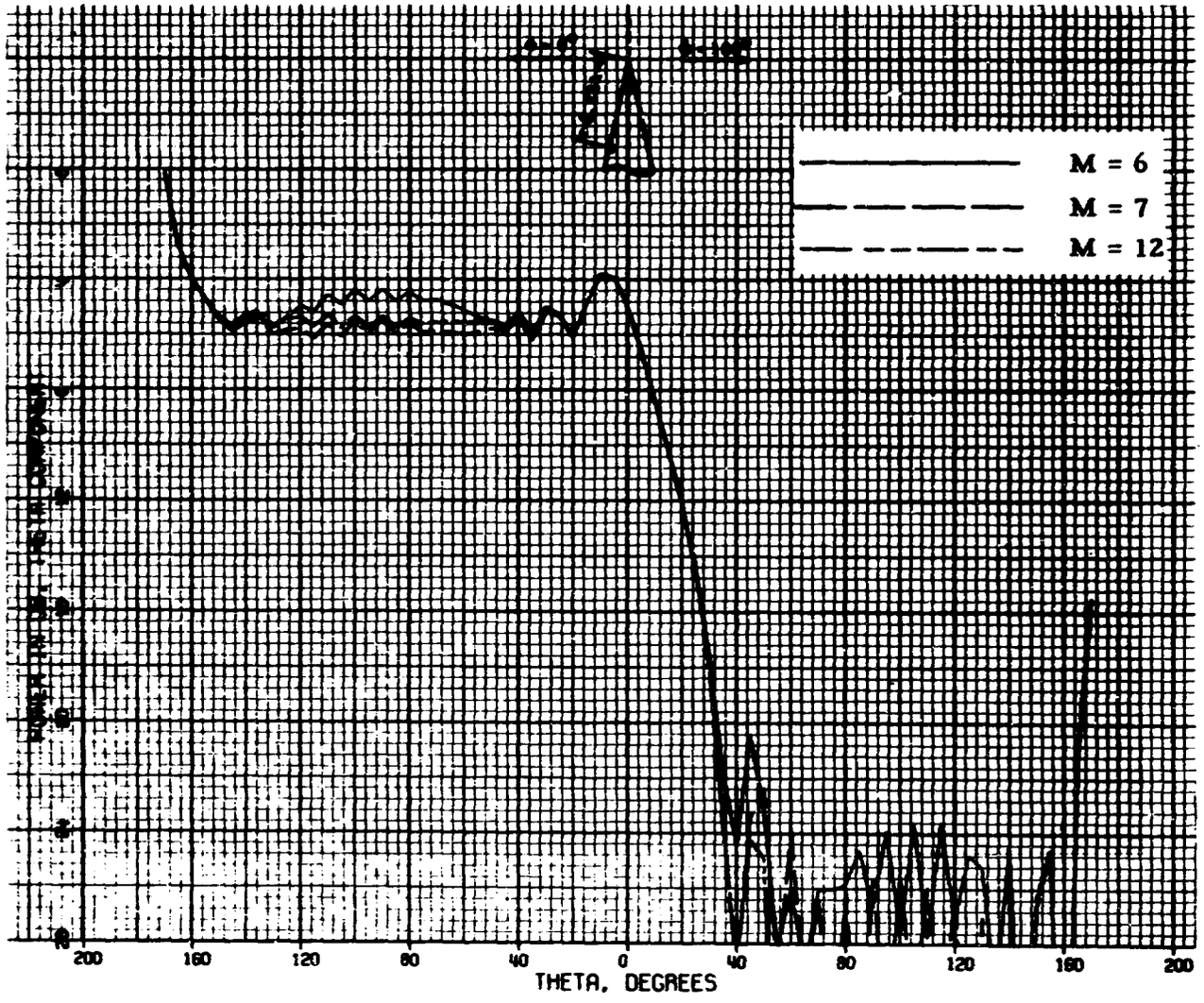

Figure 5. θ-Polarized Total Pattern of λ/2 Circumferential Slot for $\phi = 0^{o}$, $\phi = 180^{o}$, M = 6, 7, and 12

together with the M = 2 pattern. The addition of the second mode, m = 1, to the first mode, in effect dominates the resulting pattern. The effect of the m = 0 mode, however, is still evident in the region near the cone axis with a -3.5 dB value at θ = 1 degree. The forward-back difference varies from 1 dB at $\theta = 1^{\circ}$ to 9 dB at $\theta = 80^{\circ}$ and to 14 dB at $\theta = \theta_o$.

Higher order mode sum patterns, M = 3 through M = 5, for both $\phi = 0^{\circ}$ and $\phi = 180^{\circ}$ are shown in Figure 4 . In each case, the sequential summation of a higher order mode in the sum series effectively decreases the variation at the broadside region with the average level of the $\phi = 0^{\circ}$ patterns at -9 dB for M = 2 and -4 dB for M = 4. Addition of the m = 5 mode raises the pattern level only slightly at broadside while in the vicinity of $\theta = 40^{\circ}$ and $\theta = 150^{\circ}$ changes of about -1.5 dB are noted. The next significant changes in the pattern are seen in the M = 7 modal sum shown in Figure 5 for $\phi = 0^{\circ}$. At the same time, the $\phi = 180^{\circ}$ pattern shows that the pattern level decreases with increased modes at the broadside region while maintaining the level of about -5.5 dB and -15.5 dB at $\theta = 1^{\circ}$ and $\theta = \theta_o$, respectively.

The addition of the next five modes, m = 8 through m = 12, to the M = 7 total pattern gives the total pattern of M = 12. The patterns for this case are also shown in Figure 5 . Comparison of this pattern with the M = 7 total pattern shows that the addition of these five modes results in a decrease of the pattern level of less than .4 dB in the range of $\theta = 40^{\circ}$ to θ = 140 degrees. Similarly, the $\phi = 180^{\circ}$ pattern for this case shows only a slight decrease in the same range. There is no significant change to either pattern outside this range.

To study further effects of the higher order modes to the total pattern, the m = 13 mode was added to M = 12 pattern. The resulting M = 13 sum pattern in elevation is shown in Figure

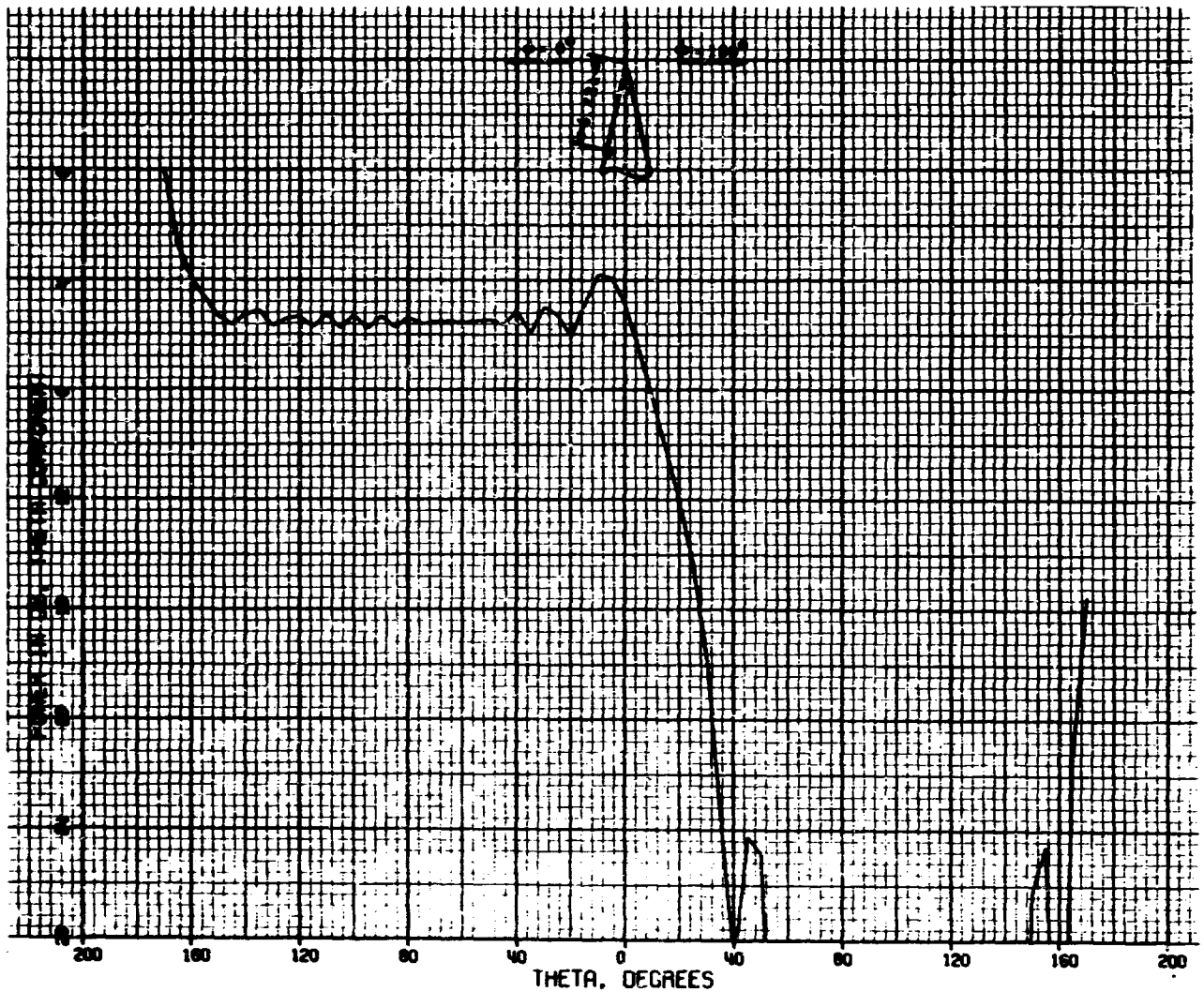

Figure 6. θ-Polarized Total Patterns of λ/2 Circumferential Slot for $\phi = 0^{\circ}$, $\phi = 180^{\circ}$, M = 13

6 . There are no noticeable changes in either the elevation or the azimuthal patterns with the addition of the m = 13 mode. It should be pointed out, however, that the normalized θ-polarized pattern of the m = 13 mode, has its maximum at θ = 90 degrees rather than at broadside. This is a consequence of the θ-dependence of the associated Legendre functions and their derivatives. This also explains why only the broadside range of the pattern is changed with increased higher order modes. Thus, it is concluded that about 13 terms of the modal series are required to correctly represent the radiation from this slot configuration. Furthermore, the tip diffraction effects are generally accounted by the lower order modes of the series.

4.3.2 Radiation Patterns of a Radial Slot

In the present section we consider the narrow slot along a generatrix of the cone which was described in Section 4.1.2. For the present study the length of the slot has been chosen as one-half wavelength at the operating frequency. The cone characteristics and the operating frequency, as well as the location of the center of the slot remain the same as for the circumferential slot described in Section 4.3.1. The slot is excited by a voltage V_o' resulting in an electric field in the Ø-direction given by

$$E_{\emptyset} = V_o' \frac{\cos (kr' - ka)}{r' \sin \theta_o} \delta (\emptyset') \qquad (42)$$

It is interesting to follow the convergence of the modal series of the radial slot in the same manner that was done for the circumferential slot. We first look at the M = 0 and M = 1 mode patterns of the Ø-polarized components at $\emptyset = 0^o$ depicted in Figure 7 . The effect of the cone's tip on the modal patterns is clearly seen by the behavior of the patterns near the axis of the cone. This effect continues to persist also through

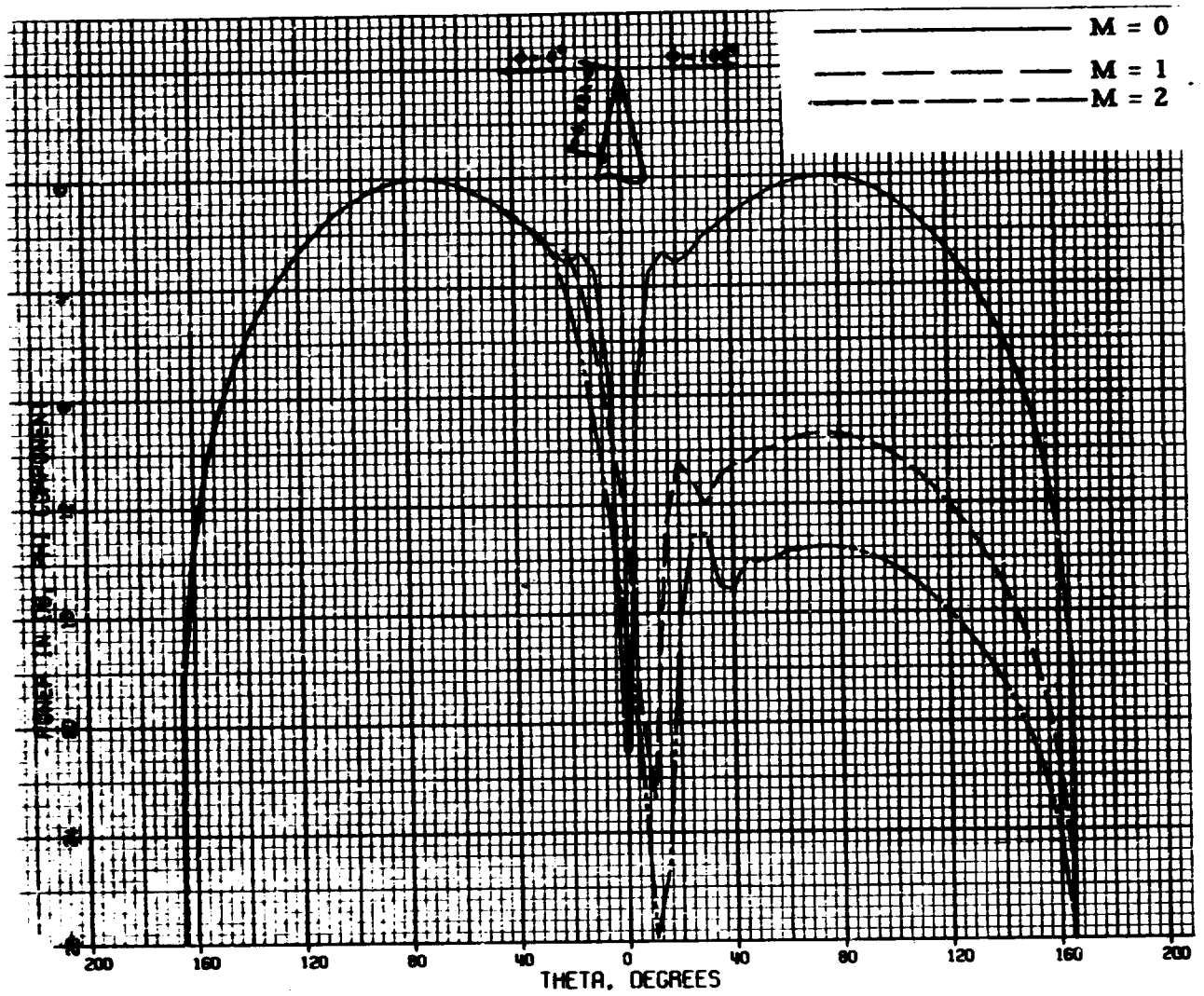

Figure 7. Ø-Polarized Total Patterns of λ/2 Radial Slot for Ø = 0°, Ø = 180°, M = 0, 1, and 2

M = 5. It is evident from the Figures that the total patterns are dominated by the m = 1 mode. Both the patterns for $\phi = 0^{\circ}$ and $\phi = 180^{\circ}$ exhibit a local maximum at about 20 degrees from the axis. This maximum moves toward the broadside region with increased number of terms of the modal series. Also, the higher order total patterns are increasingly narrower.

The M = 12 for $\phi = 0^{\circ}$ pattern shows a minimum of -18 dB at $\theta = 1^{\circ}$ and has its maximum at exactly broadside. The pattern for $\phi = 180^{\circ}$ of the same case dips to a minimum near $\theta = 15^{\circ}$ and then increases to about -14 dB at $\theta = 100$ degrees. Both patterns decrease rapidly near $\theta = \theta_{o}$. The irregularities noticed in all the previous total patterns are not present at all in the M = 12 patterns.

Azimuth patterns for the radial slot are not shown. However, all of the low order sum patterns for both polarizations exhibit considerable variation in azimuth. This can be viewed as an indication of the slow convergence of the modal series and the requirement for additional terms in the series representation. On the other hand, the M = 12, ϕ-polarized total pattern shows a smooth transition from 0 dB at $\phi = 0^{\circ}$ to -13 dB at $\phi = 140^{\circ}$ while maximum of the θ-polarized pattern occurs near broadside at about -17 dB.

From the above considerations, it appears that more than eight but less than fourteen terms of the modal series are required to represent the fields of this slot configuration correctly. The upper limit was further checked by looking at the M = 13 patterns and comparing them with the M = 12 patterns. There were no noticeable changes in either the elevation or the azimuthal patterns.

4.4 Measured Patterns

The computed patterns, using the first fourteen modes of the modal series, have been normalized to the largest value computed for both polarizations for either the circumferential or radial case. Computed and measured elevation cuts are shown on an extended θ -scale to give a single view of the elevation cuts. Since the cone under study has a 10° half-angle, the position of $\theta=80^{\circ}$ was selected for the computed azimuthal cuts. This corresponds to the broadside of the conical surface.

Measurements were made on an experimental 10° half-angle cone at a frequency of 10.38 GHz with the slots 6.22 wavelengths from the cone tip. This slot location corresponds to ka = 39 radians from the cone tip for which a complete set of patterns have been computed with the modal series program. In both the circumferential and the radial case, the slots were fed by a half height X-band waveguide. Where possible, computed pattern values are shown on the same scale for comparison.

4.4.1 Radiation Patterns of Circumferential Slot

Figure 8 shows the θ-polarized patterns for $\phi = 0^{\circ}$ and $\phi = 180^{\circ}$ together with corresponding computed patterns. There is excellent agreement between the measured and computed patterns throughout the cone tip region and the broadside region where both patterns are quite uniform. The measured pattern drop-off for $\phi = 0^{\circ}$ and θ greater than 140° is due to shadowing at the base of the cone by the absorbent material in which the cone was set. Similar drop-off is observed in the measured pattern for $\phi = 180^{\circ}$ for the same θ values except that this is not as noticeable since the computed pattern in this region is at a much lower level relative to the $\phi = 0^{\circ}$ pattern. Measured θ-polarized patterns are also shown for $\phi = 45^{\circ}$, $\phi = 225^{\circ}$ and $\phi = 90^{\circ}$, $\phi = 270^{\circ}$ in Figures 9 and 10 , respectively. In Figure 10 the corresponding computed pattern values are also

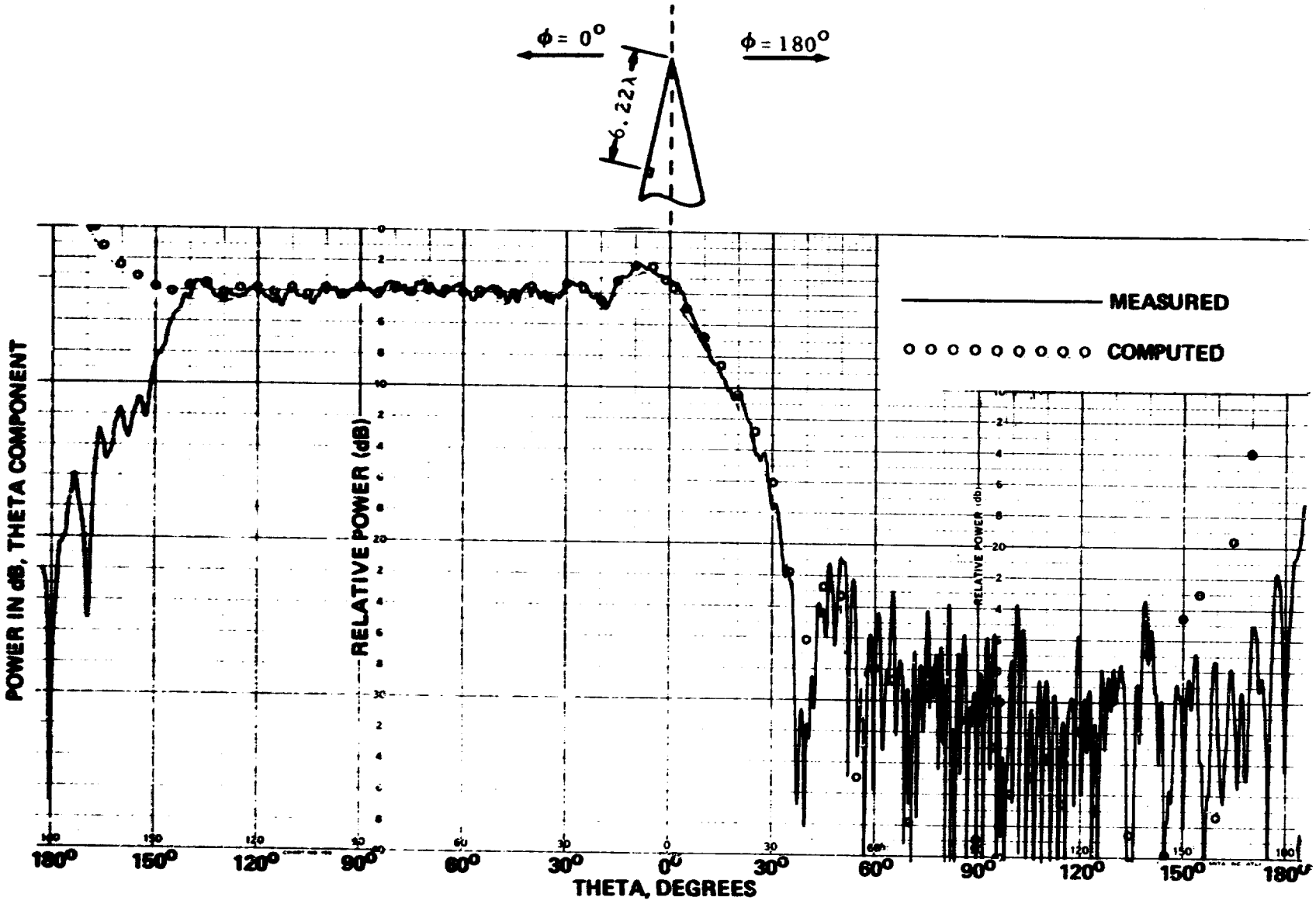

Figure 8. Measured and Computed (M = 13) θ-Polarized Patterns of λ/2 Circumferential Slot for $\phi = 0^o$, $\phi = 180^o$

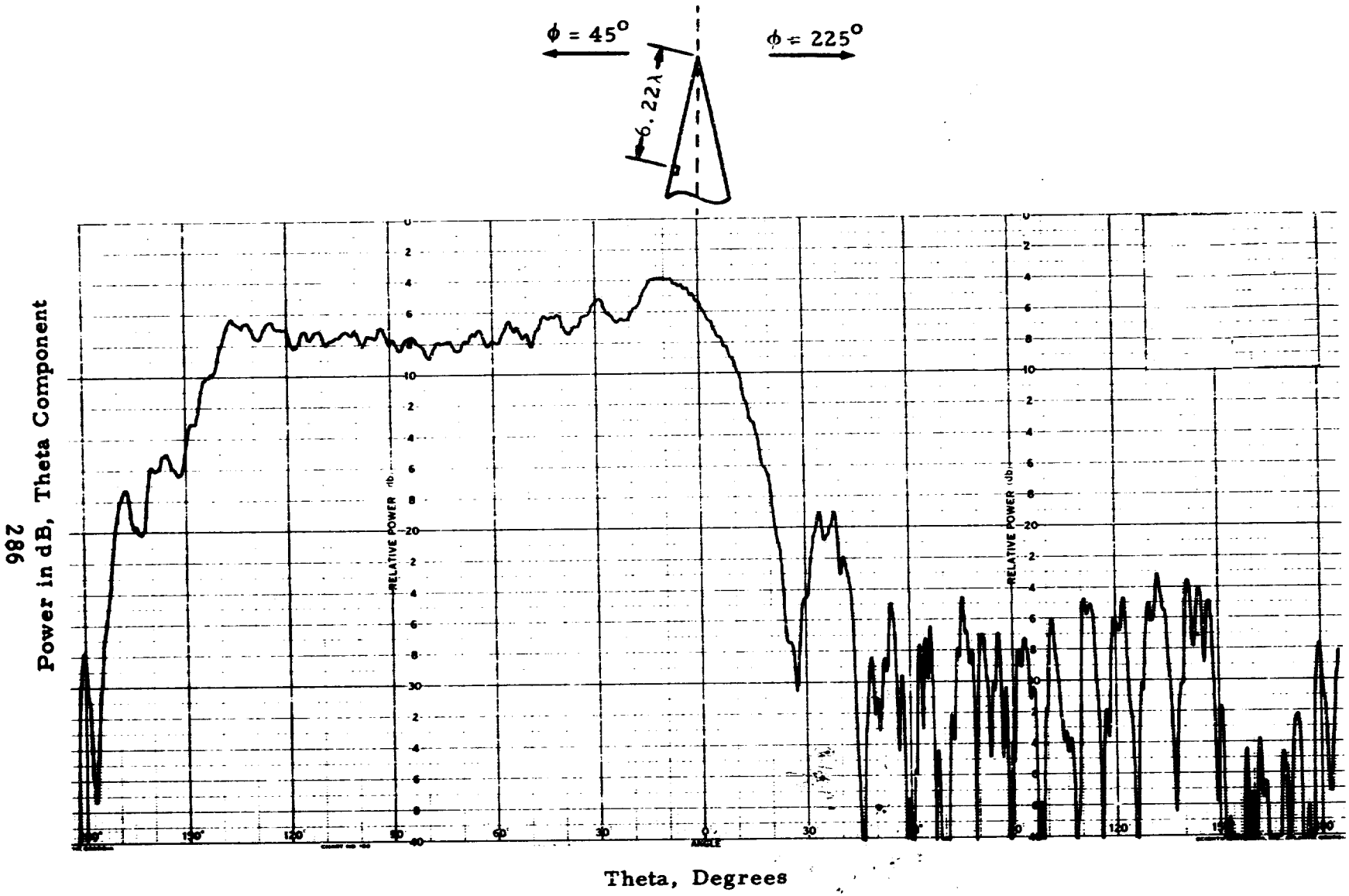

Figure 9. Measured θ-Polarized Patterns of λ/2 Circumferential Slot for $\phi = 45^{\circ}$, $\phi = 225^{\circ}$.

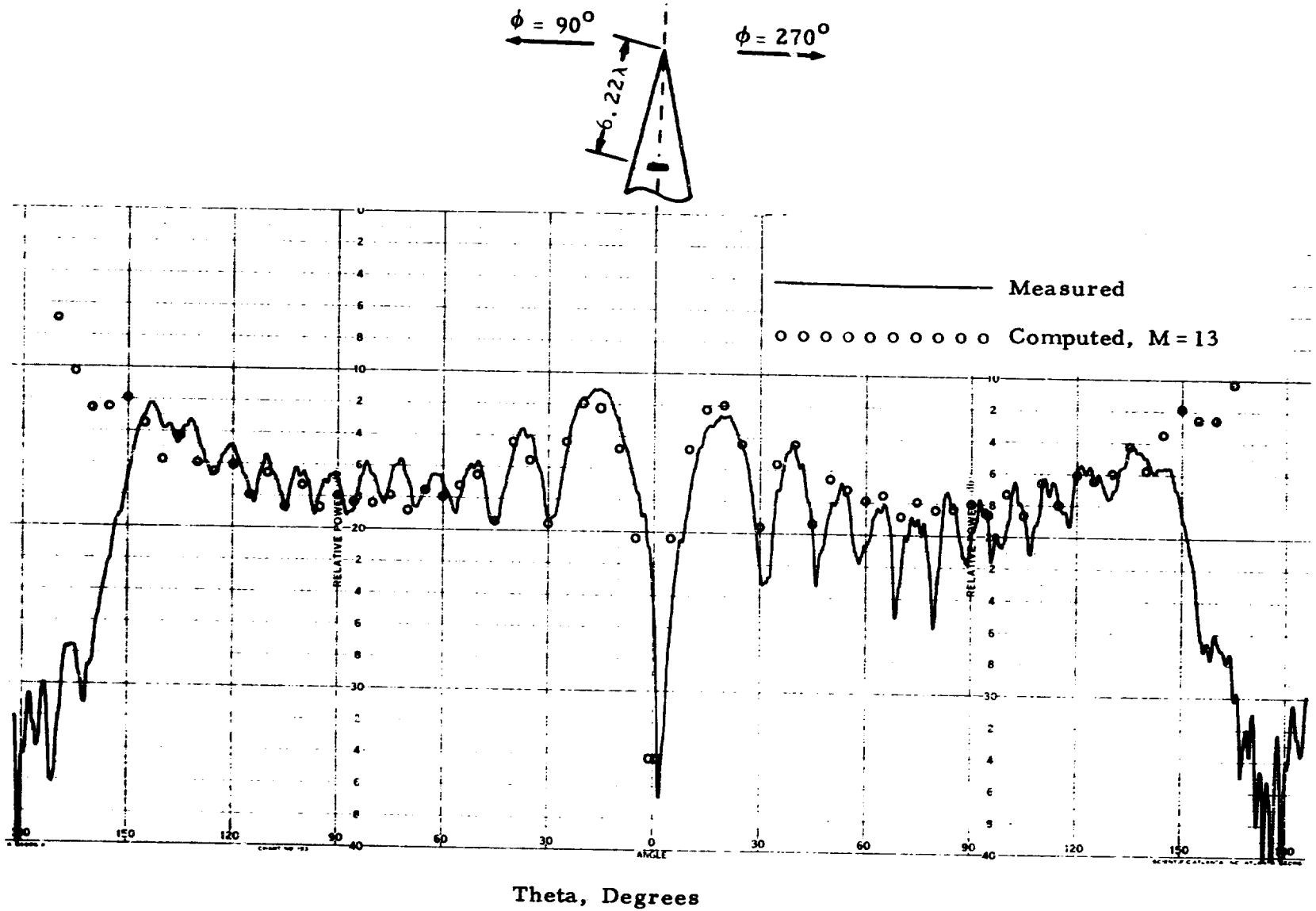

Figure 10. Measured and Computed (M = 13) θ-Polarized Patterns of λ/2 Circumferential Slot for $\phi = 90^\circ$, $\phi = 270^\circ$.

shown. There appears to be a 2° difference in the position of the null between the computed and measured patterns but this is probably caused by inaccurate alignment between the transmitter and receiving antennas. This also explains the slight asymmetry in the measured pattern. The shadowing by the absorbent material for θ greater than 140° is evident in all measured patterns. The above two patterns also show that the pattern level at $\phi = 135^{\circ}$ is approximately 10 dB below that of $\phi = 90^{\circ}$.

The ϕ-polarized patterns in elevation are shown in Figures 11 through 13 for the same azimuth positions as for the θ polarized patterns. Azimuthal patterns for both polarizations at $\theta = 80^{\circ}$ are shown in Figure 14 . Excellent agreement is seen between computed and measured patterns of Figures 13 and 14 considering the fact that computed pattern values were made every 5 degrees in θ and 10 degrees in ϕ.

4.4.2 Radiation Patterns of Radial Slot

The tip section of the 10° half-angle cone was modified to accommodate a radial slot 6.22 wavelengths from the cone tip. The edges of the waveguide were carefully taped to obtain one-half wavelength at the operating frequency.

The computed patterns shown together with the measured patterns have been normalized to the largest value computed for both polarizations using the first fourteen modes of the modal series. This largest value was computed at the field point $P(\phi,\theta) = P(0^{\circ}, 80^{\circ})$. As expected, this point is broadside to the conical surface and lies on the plane normal to the conical surface and containing the radial axis of the slot element. For meaningful comparison of measured and computed patterns, the reference level of the measured patterns was also taken at broadside at $\phi = 0^{\circ}$.

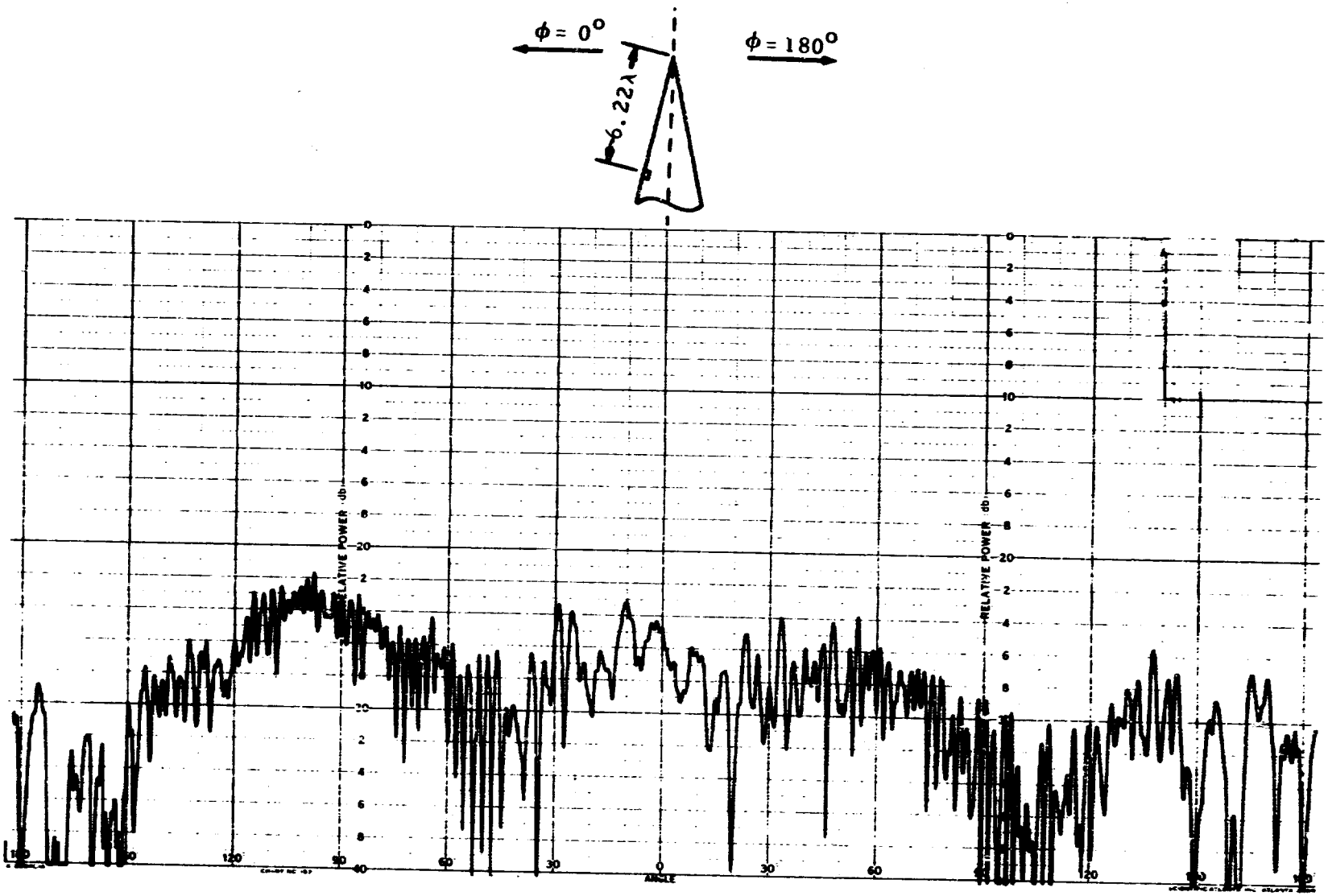

Figure 11. Measured Ø-Polarized Patterns of λ/2 Circumferential Slot for $\phi = 0^\circ$, $\phi = 180^\circ$.

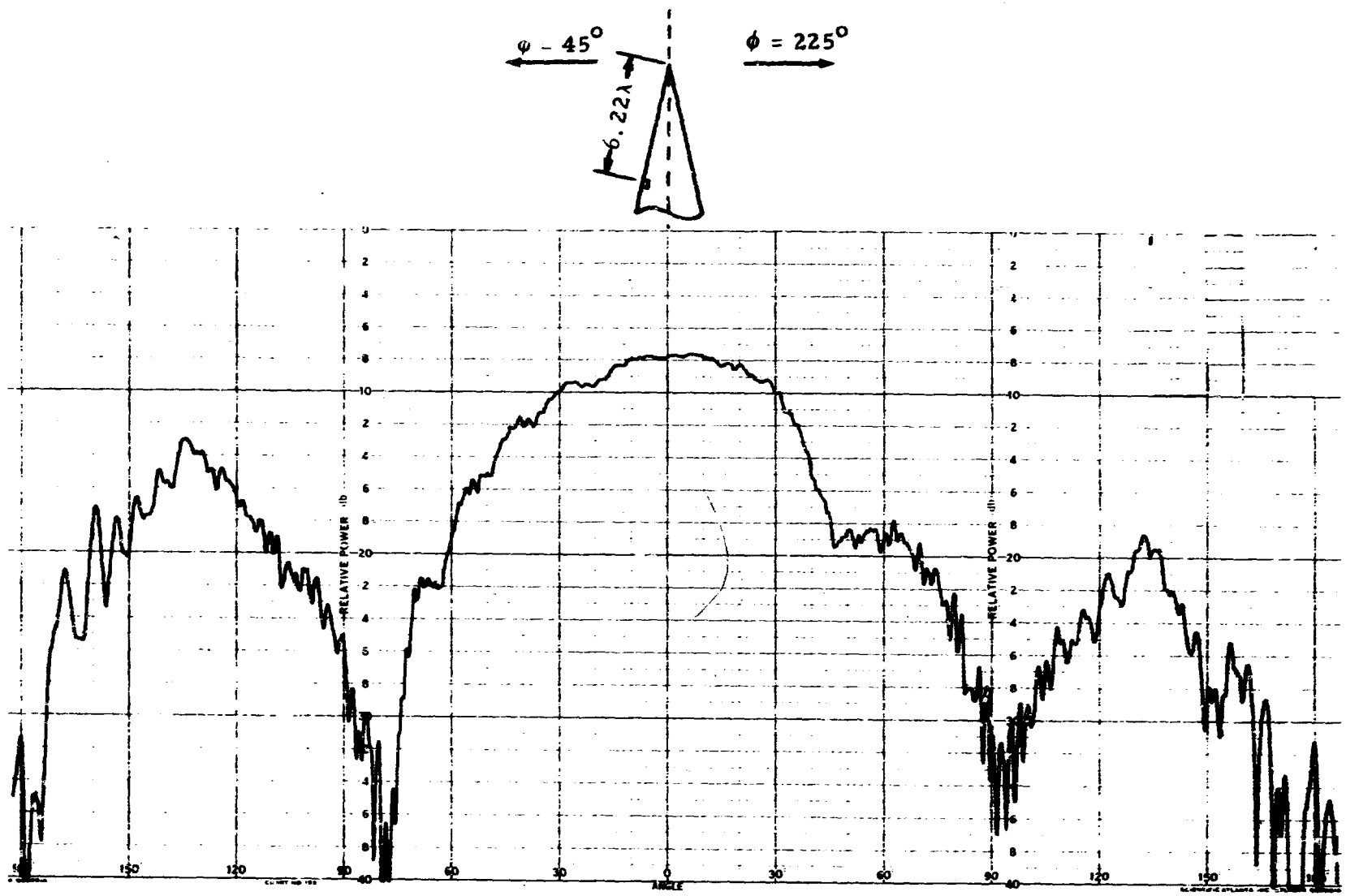

Figure 12. Measured ∅-Polarized Patterns of λ/2 Circumferential Slot for ∅ = 45°, ∅ = 225°

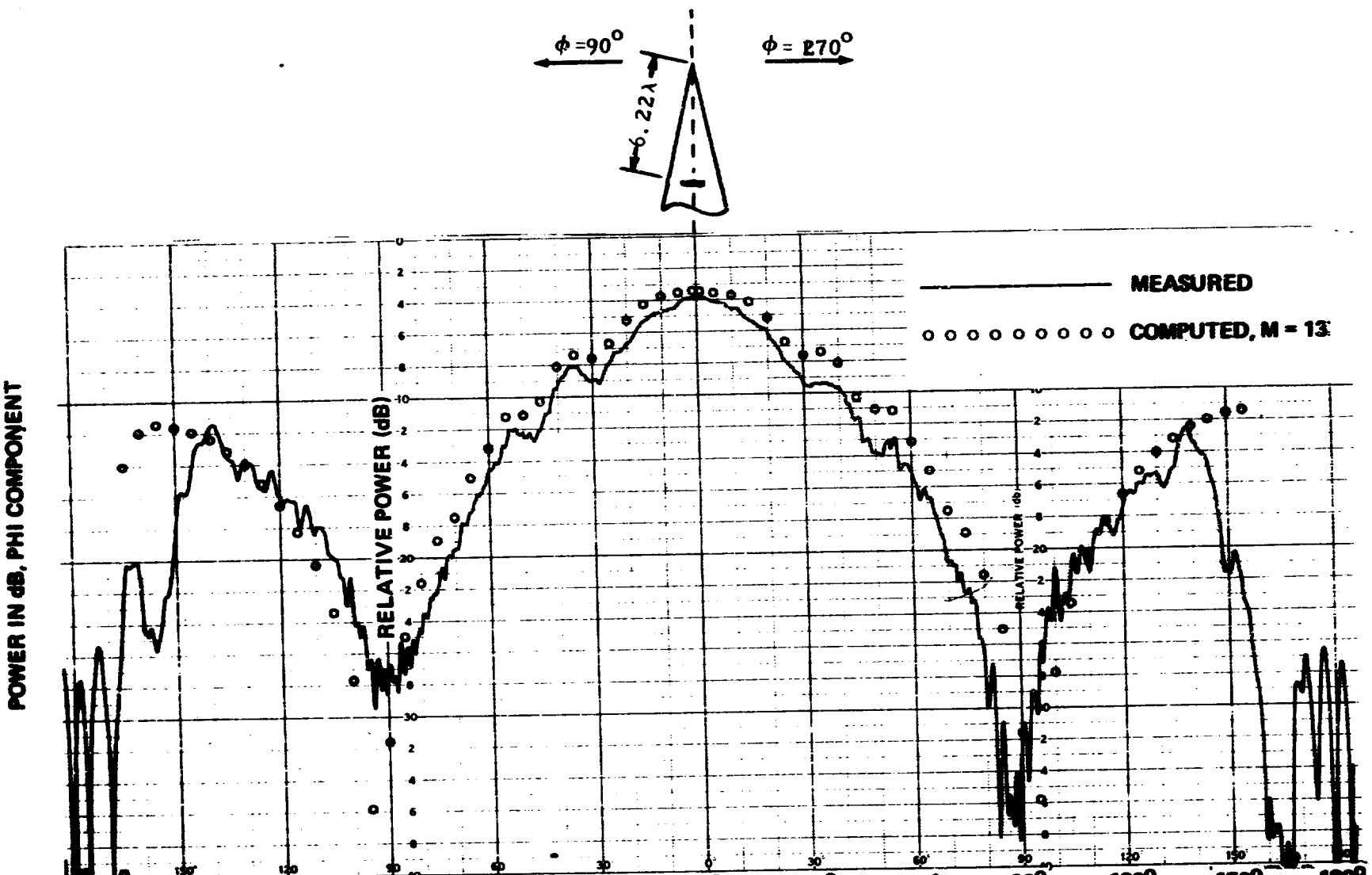

Figure 13. Measured and Computed (M = 13) Ø-Polarized Patterns of λ/2 Circumferential Slot for Ø = 90°, Ø = 270°.

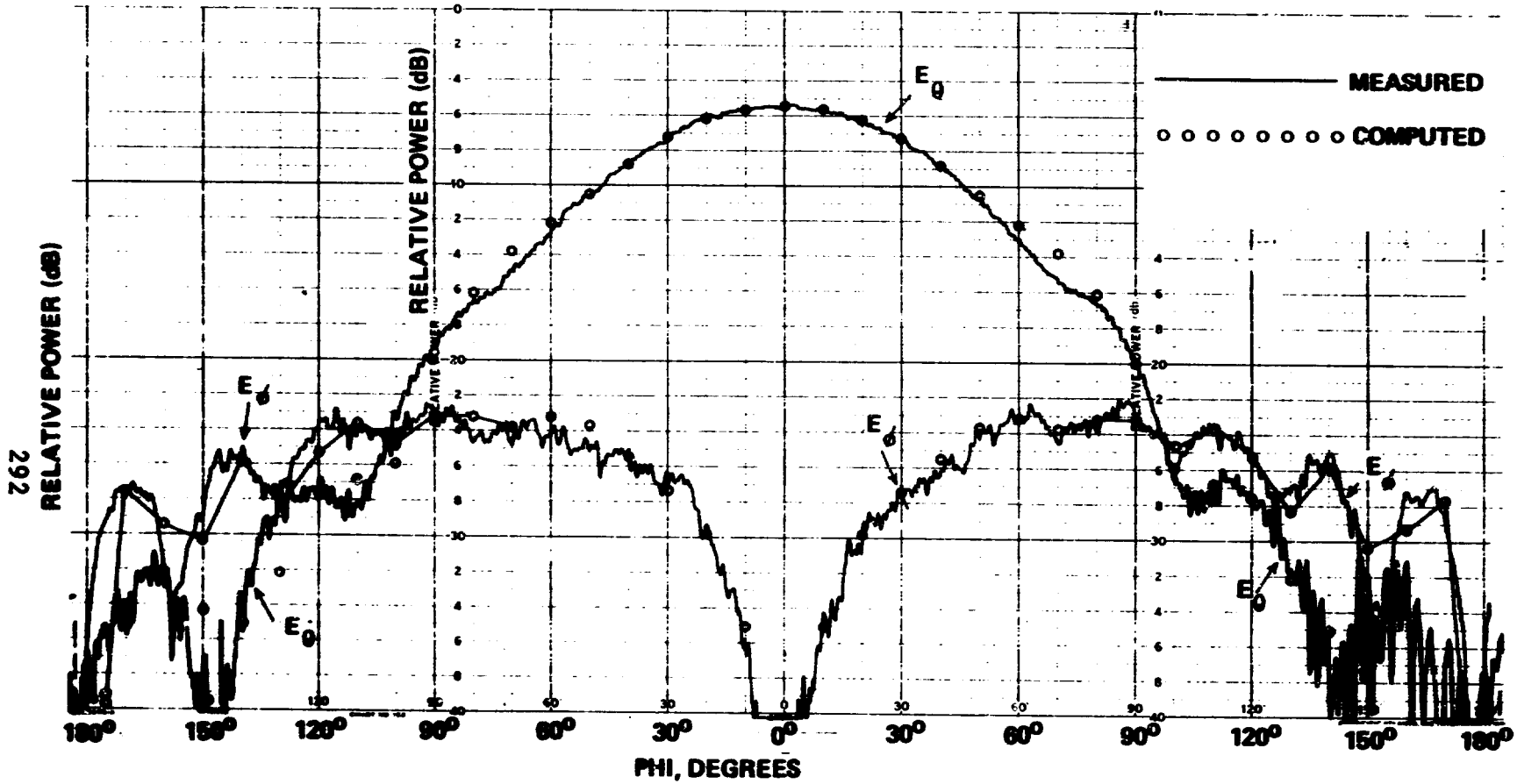

Figure 14. Measured and Computed (M = 13) Patterns of $\lambda/2$ Circumferential Slot for θ and ϕ Polarizations at $\theta = 80^{\circ}$.

Figure 15 shows the ϕ-polarized patterns for $\phi = 0^{\circ}$ and $\phi = 180^{\circ}$ together with corresponding computed patterns. There is excellent agreement between the measured and computed patterns throughout the cone tip region and the broadside region where both patterns are quite broad.

Measured ϕ-polarized patterns are also shown for $\phi = 10^{\circ}$, $\phi = 190^{\circ}$, $\phi = 40^{\circ}$, $\phi = 220^{\circ}$, $\phi = 90^{\circ}$ and $\phi = 270^{\circ}$ in Figures 16 and 17 . Computed pattern values are also shown in the same figures for comparison. Figure (17) shows a 3° difference in the position of the null between the computed and measured patterns but this is probably caused by misalignment between the transmitter and receiving antennas. It would also explain the slight asymmetry in the measured pattern. The shadowing by the absorbent material for θ greater than 140° is again evident here. The above figures also show that there is a difference of 4 dB in the maxima of $\phi = 0^{\circ}$ and $\phi = 90^{\circ}$ patterns, whereas the pattern maxima at $\phi = 180^{\circ}$ are approximately 14 dB below that at $\phi = 0^{\circ}$. As mentioned earlier, the maxima occur at the broadside to the conical surface.

The θ-polarized patterns in elevation are shown in Figures 18 and 19 for the same azimuth positions as for the ϕ-polarized patterns. These figures clearly show that unlike the patterns of a circumferential slot on a similar cone, the cross-polarization is well below the dominant polarization at the same azimuthal angles. The shadowing by the absorbent material at the base of the cone is clearly identified in these patterns. Since the pattern levels of this polarization are approximately 18 dB below the reference level, the misalignment of the transmitter and receiver antennas is also more apparent.

Azimuthal cuts at various angles, including the broadside of the antenna element, are shown for both polarizations in Figures 20 through 22 . From Figure 21 it is seen that the

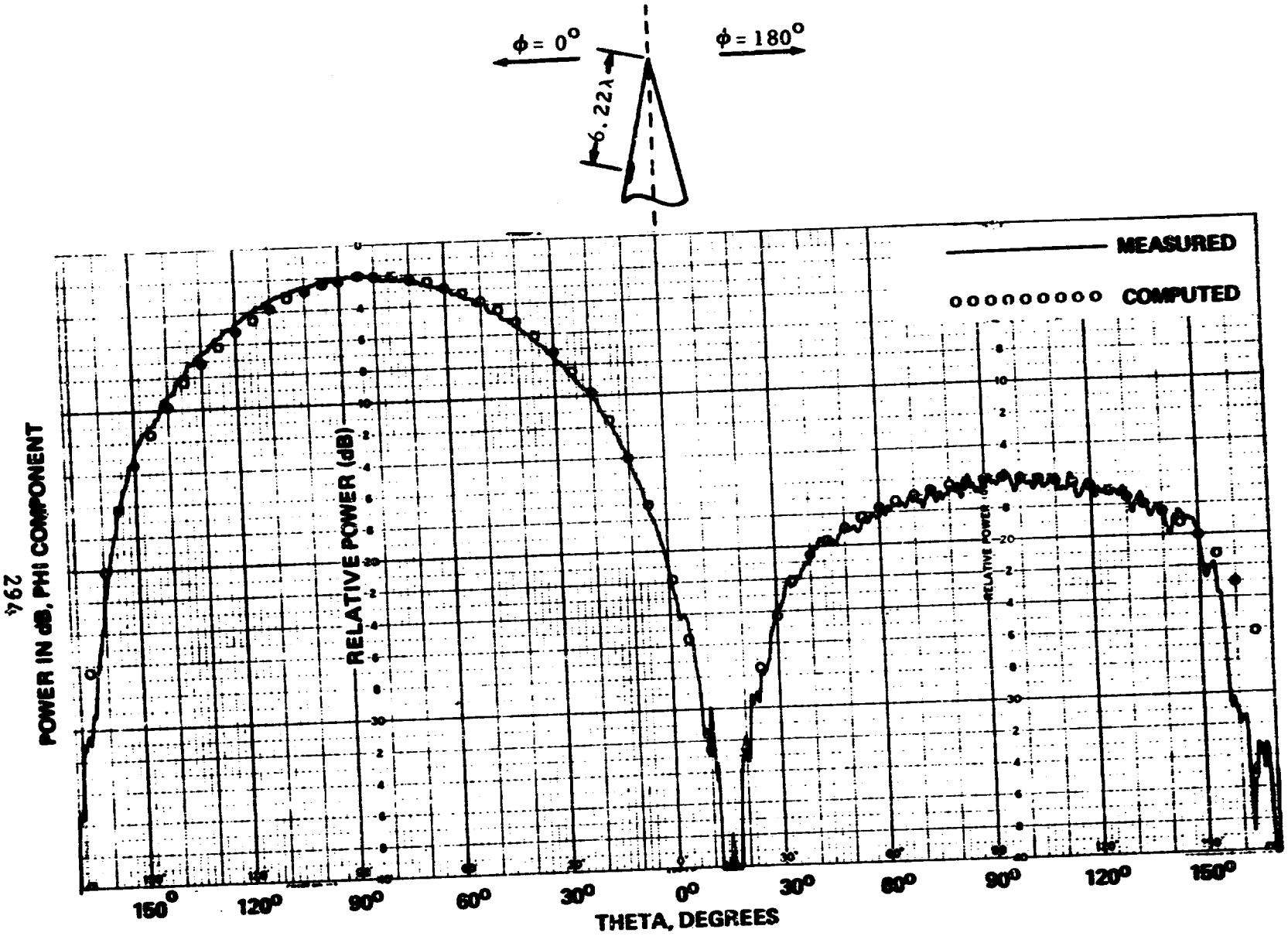

Figure 15. Measured and Computed (M = 13) ∅-Polarized Patterns of λ/2 Radial Slot for $\emptyset = 0^o$, $\emptyset = 180^o$

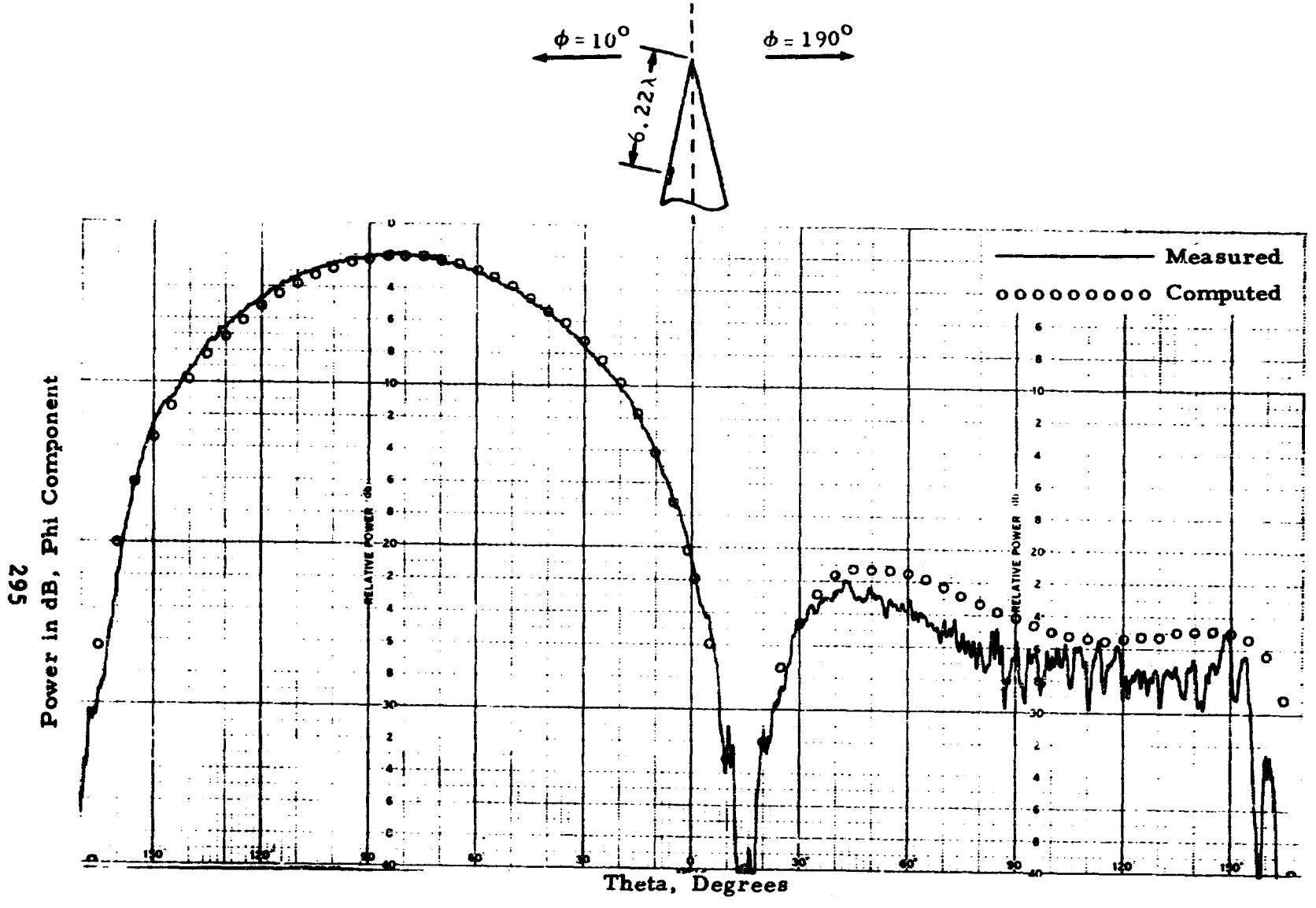

Figure 16. Measured and Computed (M = 13) $\emptyset$-Polarized Patterns of $\lambda/2$ Radial Slot for $\emptyset = 10^{\circ}$, $\emptyset = 190^{\circ}$

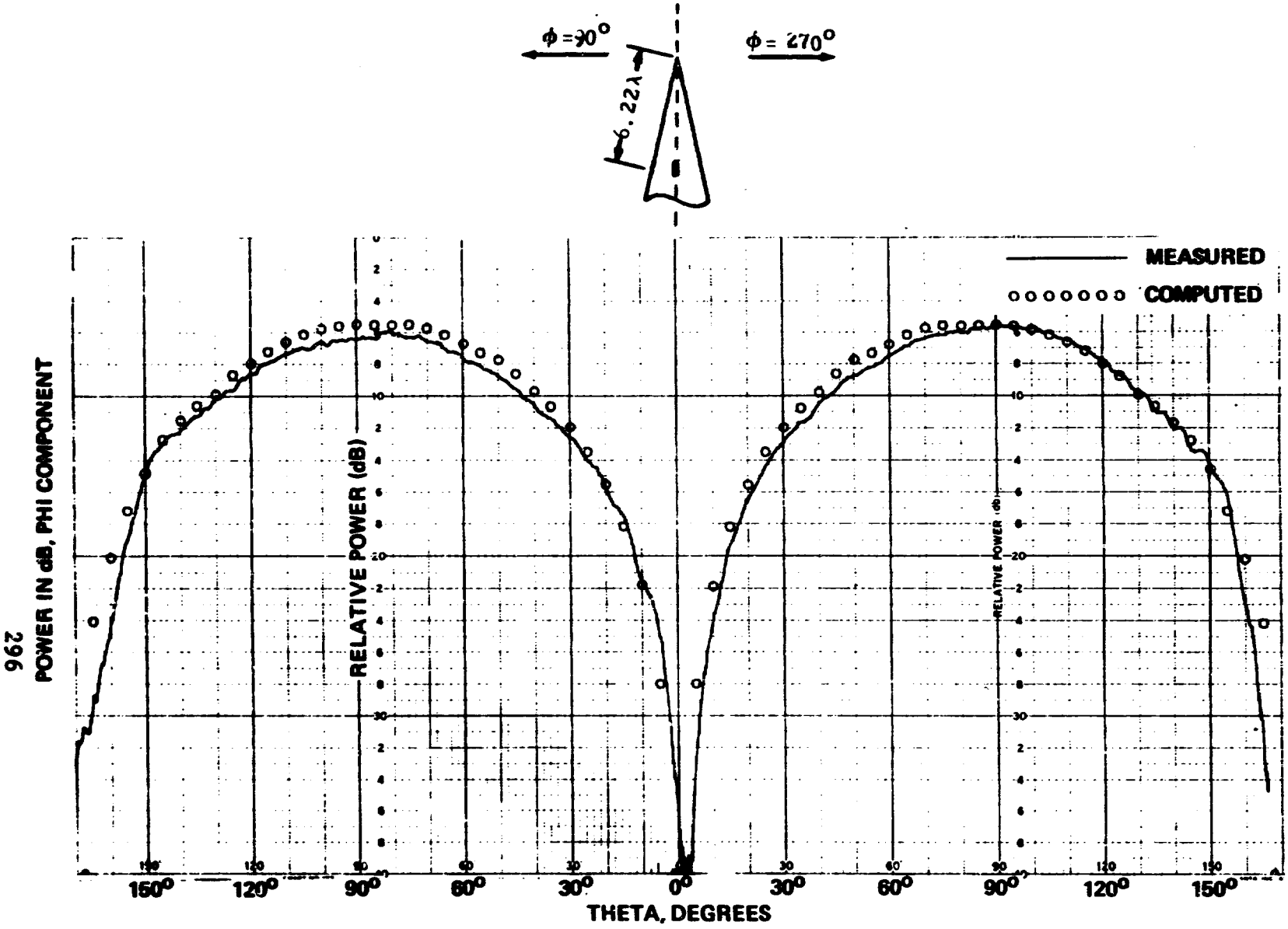

Figure 17. Measured and Computed (M = 13) $\emptyset$-Polarized Patterns of $\lambda/2$ Radial Slot for $\emptyset = 90^{\circ}$, $\emptyset = 270^{\circ}$

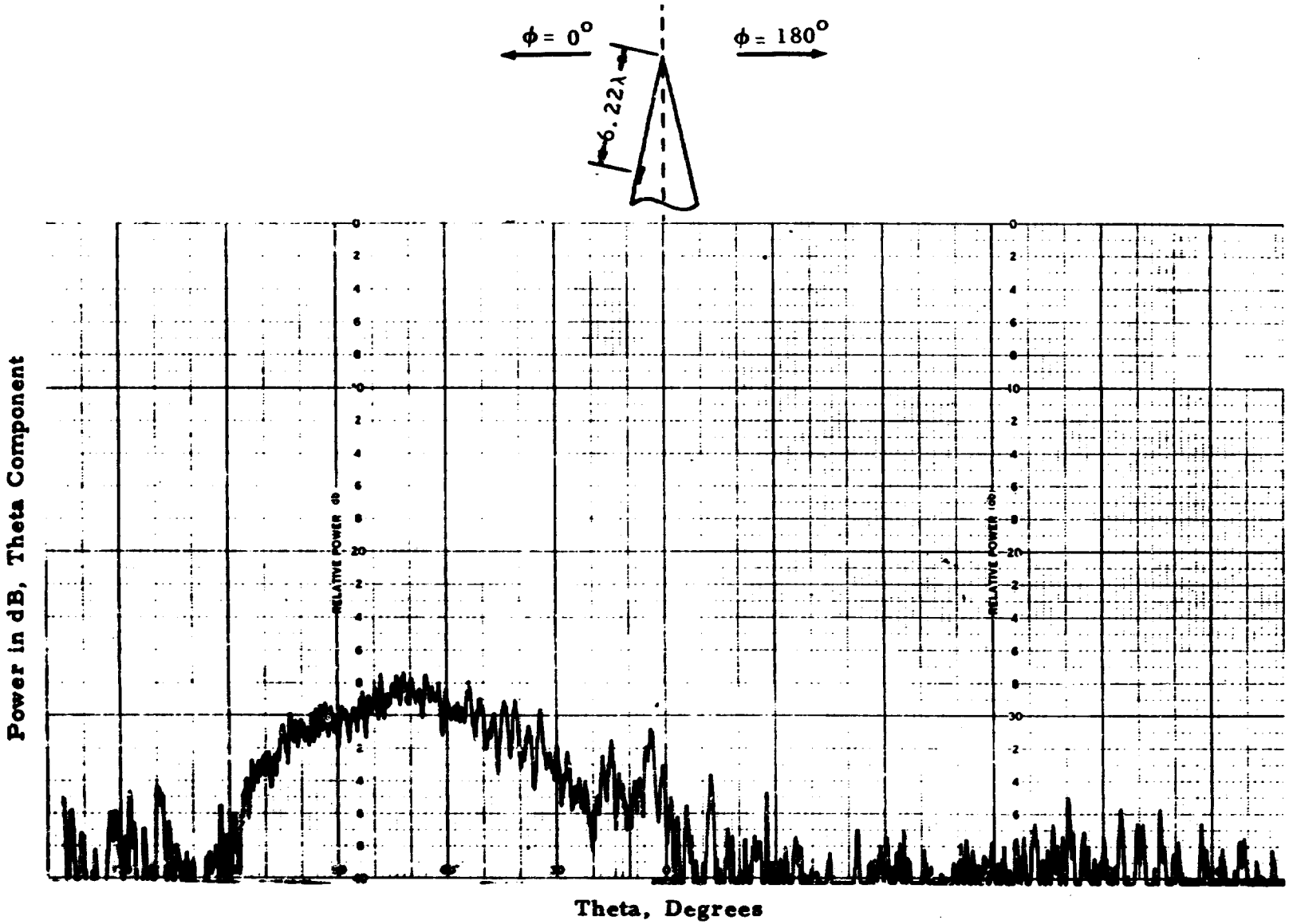

Figure 18. Measured θ-Polarized Patterns of λ/2 Radial Slot for $\phi = 0^\circ$, $\phi = 180^\circ$

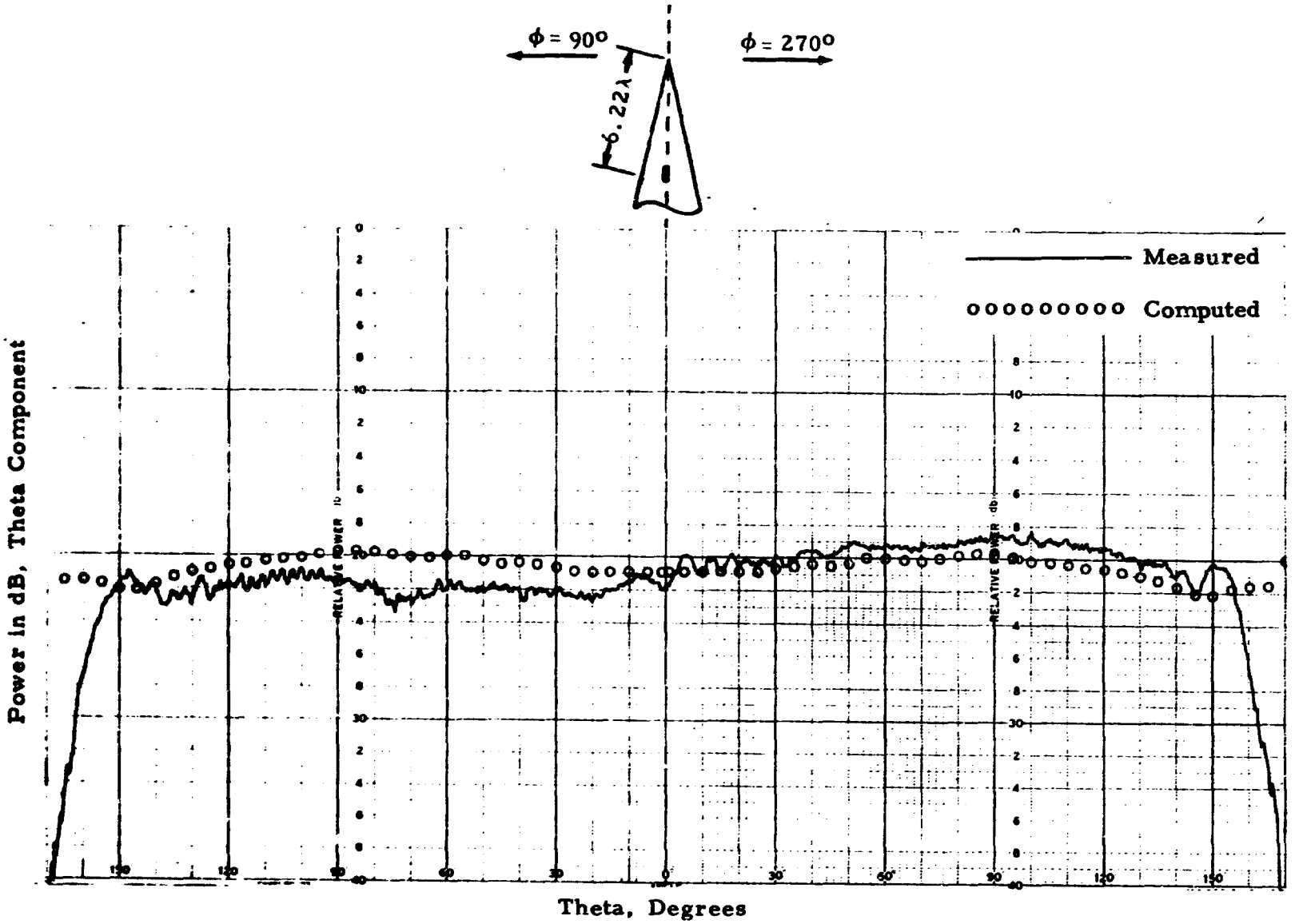

Figure 19. Measured and Computed (M = 13) θ-Polarized Patterns of λ/2 Radial slot for $\phi = 90^{\circ}$, $\phi = 270^{\circ}$

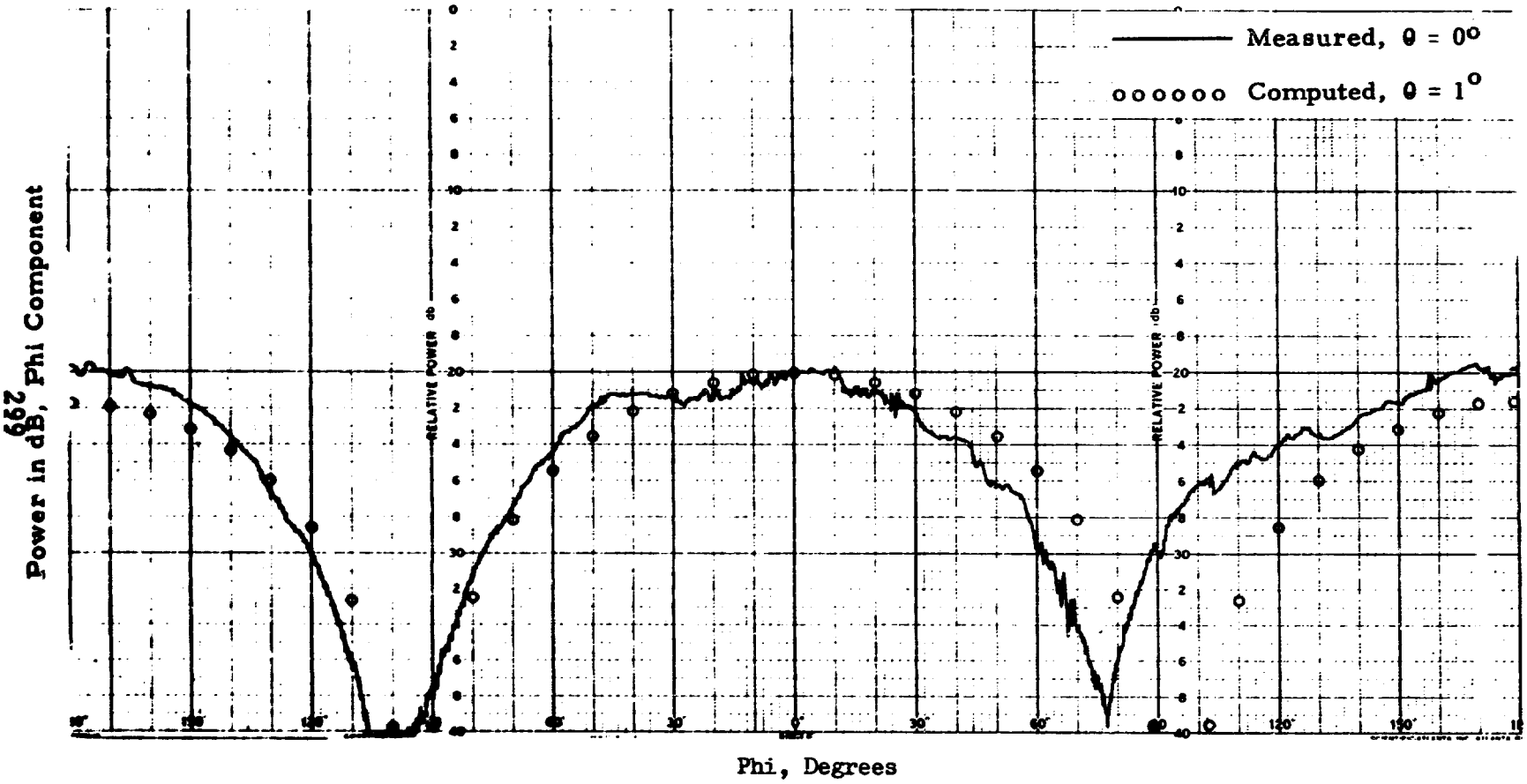

Figure 20. Measured and Computed (M = 13) Ø-Polarized Patterns of λ/2 Radial Slot for Ø = 0°, θ = 1°

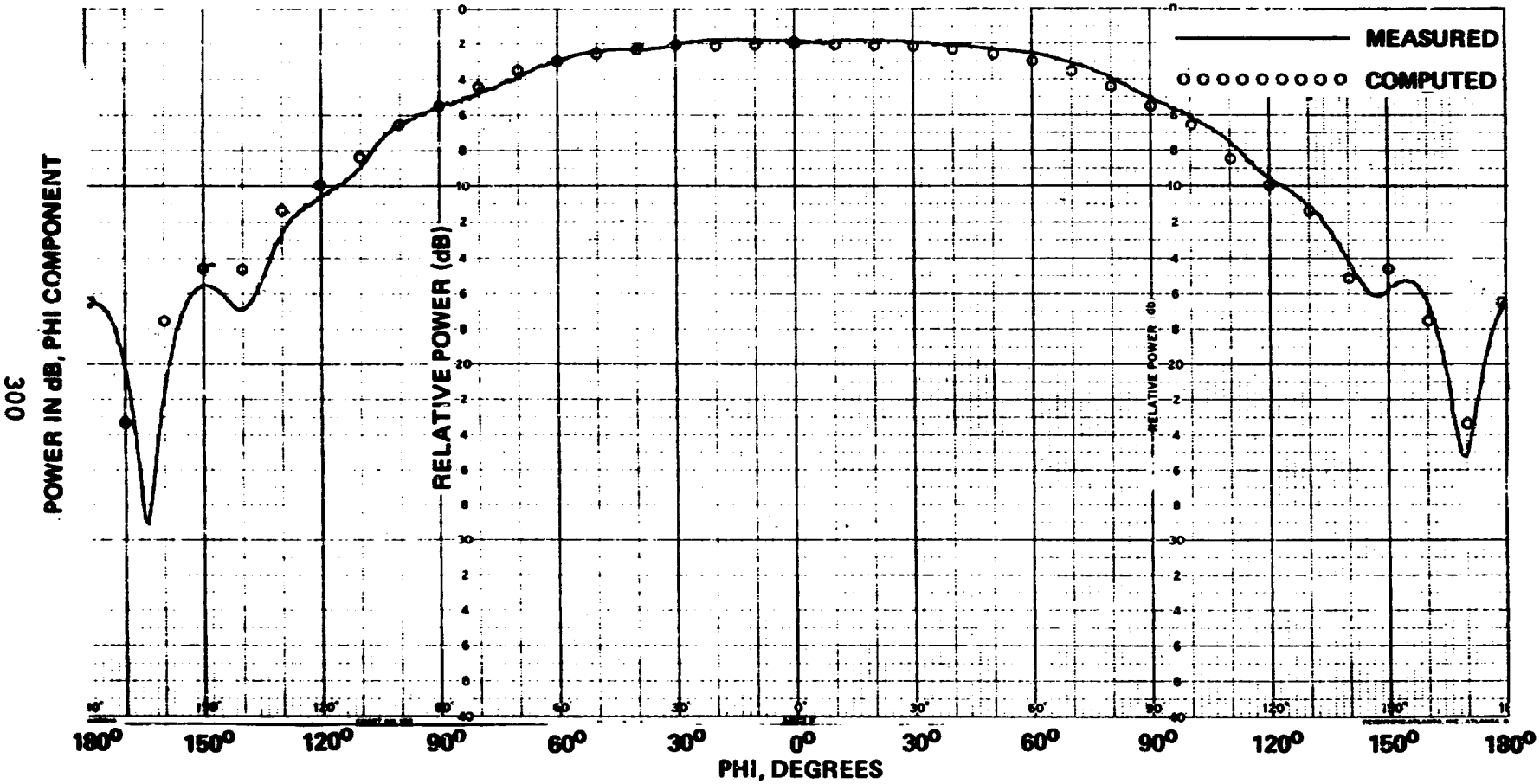

Figure 21. Measured and Computed (M = 13) Ø-Polarized Patterns of λ/2 Radial Slot for $\theta = 80^{\circ}$

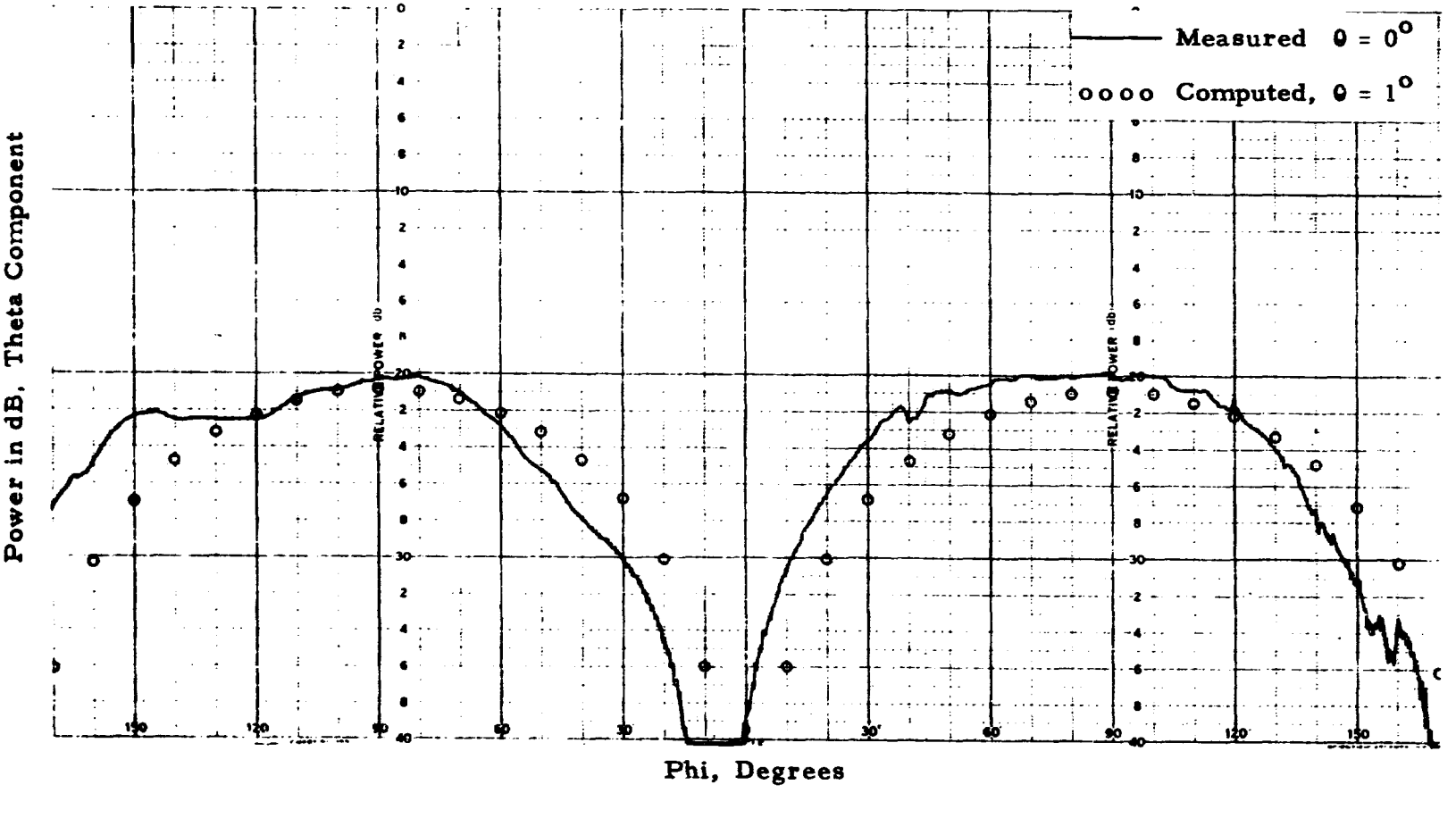

Figure 22. Measured and Computed (M = 13) θ-Polarized Patterns of λ/2 Radial Slot for $\phi = 0^{\circ}$, $\theta = 1^{\circ}$

measured broadside pattern of the $\emptyset$-polarization exhibits a broad maximum at $\emptyset = 0^{o}$ and is in very good agreement with the computed pattern. As stated earlier, this has been selected as the reference point for all patterns. In the θ-polarized azimuthal cuts, where the levels are considerably lower than the reference level, the shift of the null between measured and computed patterns is more apparent. At other points, however, the agreement between measured and computed values is very good. The θ-polarized pattern levels are in all cases at least 18 dB below the reference level.

4.5 Admittance

The harmonic series formulation gives exact circumferential slot near fields when the potential functions equations (13) and (14) are used with the field equations (2) and (3), but without the far field approximation equation (16). Similarly for axial slots: use of equation (3) and the exact potential function gives exact near field expressions. A delta function slot distribution can also be assumed for the 'sink' slot, and the electric field expression can be (approximately) integrated over the slot to get mutual admittance. The mutual coupling expressions for axial or circumferential slots are expressed as double sums over the azimuthal index m which is the degree of the Associated Legendre Functions and the radial index n which is the order of the ALF. n also indicates the proper real Spherical Bessel and Hankel Function order ν_n. All Y_{12} expressions involve derivatives of the ALF with respect to both argument and degree, and Spherical Bessel and Hankel Functions and their derivatives (Bowman et al, 1969). Unfortunately, the cone is not as simple as the sphere or cylinder. The vector Green's function for the sphere has the singularity explicitly separated, while the essential singularity in the cylindrical expression (see Chap. 3) can be handled for small axial separations by assuming a small loss in the medium. The cone mutual admittance

expressions however diverge whenever the kr's (distance from slot center to tip) are equal, even if the ϕ's are different. Thus two slots on opposite sides of a circle on the cone will have a small coupling, but the Y_{12} formula diverges. Rate of convergence is affected by the relative kr for the two slots; if the kr's differ by only a small amount the series may require thousands of terms to converge. Of course round off and the difficulty of accurately computing fractional order Associated Legendre and Spherical Hankel functions make multiple precision essential for such an endeavor. In practice then the series (modal) approach to exact mutual admittance on a cone is limited to slot circle diameters of a few wavelengths, with appreciable separations between slots (in cone radius). Narrow angle cones with elements spaced $\lambda/2$ along a generator may not afford sufficient change in cone radius to produce satisfactory convergence. And in any case the mutual between slots on the same circle cannot be found from the series expressions.

Two options remain for the calculation of mutual admittance.* One assumes the two slots are on a cylinder of mean diameter between the diameters of the two circles containing the slots. Then if a slot is close to the tip, a tip correction calculated from tip diffraction can be added (Golden et al, 1974). The second option uses the Green's function in integral form, and makes an approximation. GTD, as a short wavelength approximation is one approach (see Chap. 5) to this.

* Another scheme computes coupling between rings of slots, mode pair by mode pair (Balzano & Dowling, 1974).

CHAPTER 5

GTD CALCULATION OF PATTERN AND ADMITTANCE

5.0 INTRODUCTION

The modal technique described in the two previous chapters is not attractive for large diameter cylinders or conical regions due to slow convergence of the series. In some cases the situation is even more difficult: the modal series for mutual admittance on a cone with equal kr's diverges. Fortunately GTD techniques are applicable when the radius of curvature is large. GTD (Hansen, 1981) is based on surface rays, first introduced by Keller in his Geometric Theory of Diffraction. It normally yields an asymptotic solution valid for high frequencies (body large in wavelengths), but often provides excellent results for smaller bodies as well. Because of its simplicity and wide applicability, GTD is a most attractive tool for conformal array problems. This chapter will use GTD for calculating mutual admittance, and will consider rectangular slot elements.

5.1 Slot Array Analysis

5.1.1 Circuit Description

Consider an array of N slots over a curved conducting surface, see Figure 1. Each slot is fed by a rectangular waveguide, see Figure 2, where only the dominant TE_{10} mode propagates and all other modes attenuate. The electromagnetic properties of the array can be conveniently described by circuit parameters detailed below.

Consider a typical element n in the array. At a sufficiently large distance ℓ from the aperture, only the dominant TE_{10} mode is present. Then the transverse field vectors in the n^{th} guide can be represented by

$$\bar{E}(x,y,z=-\ell) = V_n \bar{e}(x,y) \qquad (1a)$$

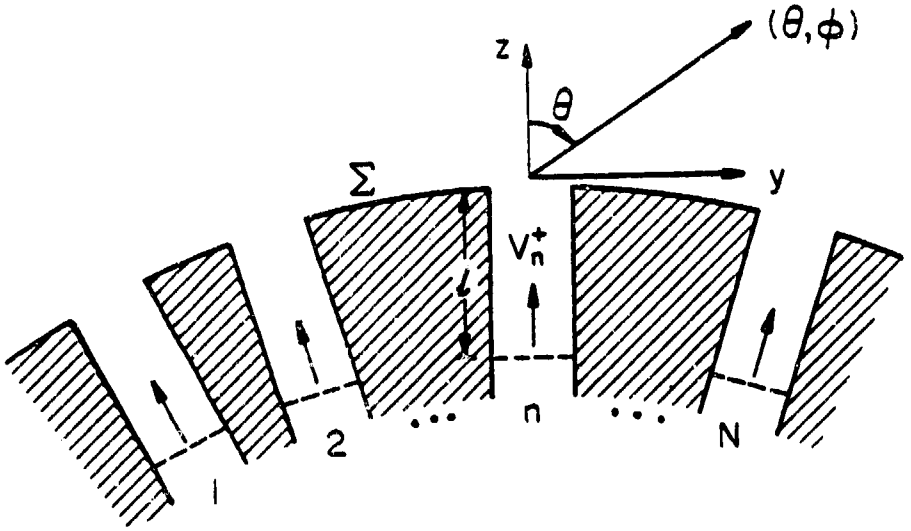

Figure 1. Array of N identical slots which are fed by waveguides.

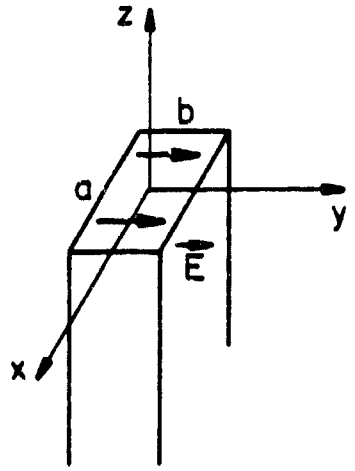

Figure 2. A slot fed by a rectanguide waveguide of the same cross-section (a x b).

$$\bar{H}(x,y,z=-\ell) = I_n(\hat{z} \times \bar{e}) \qquad (1b)$$

where

$$\bar{e}(x.y) = \hat{y}\left(\frac{2}{ab}\right)^{1/2} \cos\left(\frac{\pi}{a} x\right) \quad . \qquad (2a)$$

V_n = modal voltage in n^{th} element (2b)

I_n = modal current in n^{th} element (2c)

Note that the field in (1) is the total field consisting of waves traveling in both +z and -z directions. Because of the linearity of the Maxwell's equations, the current in the m^{th} element is linearly proportional to the voltages in all elements in the array, i.e.,

$$I_m = \sum_{n=1}^{N} Y_{mn} V_n \quad , \quad m = 1,2\ldots,N \quad . \qquad (3)$$

In matrix notation, (3) may be rewritten as

$$[I] = [Y][V] \qquad (4)$$

where [I] and [V] are column matrices with elements $\{I_n\}$ and $\{V_n\}$, and [Y] is a square matrix with elements $\{Y_{mn}\}$.

The proportional constant Y_{12} in (3), for example, is called the mutual admittance between slots 1 and 2. By reciprocity, $Y_{12} = Y_{21}$. One may calculate (measure) Y_{12} from the setup of Figure 3, where:

(i) Element 1 is excited so that the (total) voltage at the reference plane ($z = -\ell$) is V_1.

(ii) Conducting planes are placed at the reference planes of all other elements so that $V_n = 0$ for $n \neq 1$.

Then it follows from (3) that

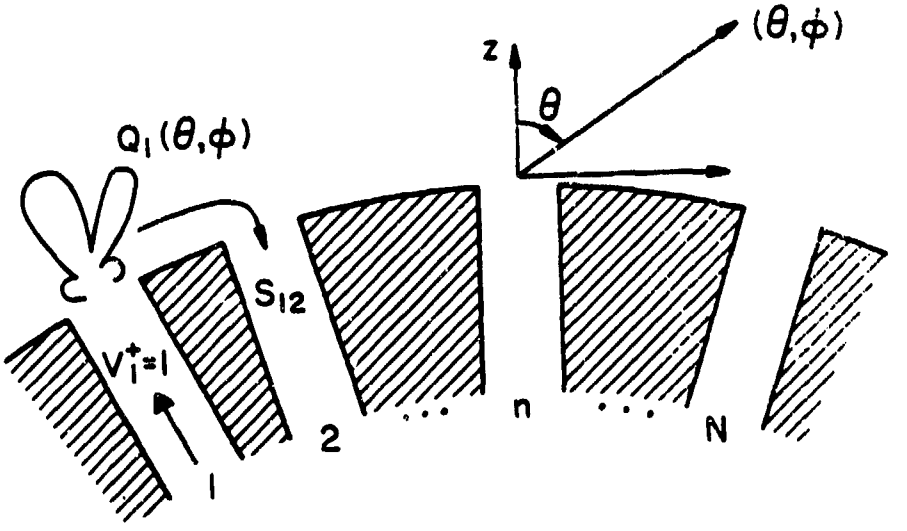

Figure 3. With $V_1^+ = 1$ and all other elements match-loaded, the radiation pattern is called match-loaded active element pattern Q_1.

$$Y_{12} = \left.\frac{I_2}{V_1^-}\right|_{\text{short all except 1}} \tag{5}$$

which may be considered as the definition of Y_{12}.

As a transmitting antenna, the n^{th} element in the slot array in Figure 1 is excited by an incident TE_{10} mode with voltage V_n^+, where the superscript "+" signifies that the wave propagates toward the aperture in the +z direction. The discontinuity at the aperture causes a reflected TE_{10} mode with voltage V_n^-, which travels in the -z direction. Then the (total) voltage at the reference plane ($z = -\ell$) is

$$V_n = V_n^+ + V_n^- \tag{6a}$$

while its corresponding current is

$$I_n = Y_c(V_n^+ - V_n^-) \quad . \tag{6b}$$

where Y_c is the characteristic admittance of TE_{10} mode

$$Y_c = \frac{1}{120\pi}\left[1 - \left(\frac{\pi}{ka}\right)^2\right]^{1/2} \quad . \tag{7}$$

For a given set of incident voltages $\{V_n^+\}$, one can determine the reflected voltages $\{V_n^-\}$ and the (total) voltages $\{V_n\}$ from (6) and (4). The results are

$$[V^-] = \left([I] + [Y_c]^{-1}[Y]\right)^{-1}\left([I] - [Y_c]^{-1}[Y]\right)[V]^+ \tag{8}$$

$$[V] = 2\left([I] + [Y_c]^{-1}[Y]\right)^{-1}[V]^+ \tag{9}$$

where $[I]$ is an identity matrix, and $[Y_c] = Y_c[I]$

5.1.2 Scattering Description of Slot Array

For the same slot array in Figure 1, a different and equivalent description may be given in terms of scattering parameters, instead of circuit parameters.

Parallel to (3), the basic relation in the second description is

$$V_m^- = \sum_{n=1}^{N} \left[S_{mn}\right]\left[V_n^+\right], \quad m = 1,2,\ldots,N \quad , \tag{10a}$$

or in matrix notation,

$$[V] = [S][V]^+ \tag{10b}$$

Here $[S] = [S_{mn}]$ is a scattering matrix. $S_{12} = S_{21}$, for example, is the induced voltage at element 2 when

(i) element 1 is excited with $V_1^+ = 1$ (not $V_1 = 1$), and

(ii) all other elements are terminated with a matched load, in the manner sketched in Figure 3. Sometimes, S_{12} is also known as the coupling coefficient between elements 1 and 2. The comparison of (10b) with (8) leads immediately to

$$[S] = ([I] + [Y_c]^{-1}[Y])^{-1}\,([I] - [Y_c]^{-1}[Y]) \tag{11}$$

which relates [S] to the admittance matrix [Y]. For the special case N = 2;

$$S_{12} = \frac{-2Y_c Y_{12}}{(Y_c + Y_{11})^2 - Y_{12}^2} \tag{12}$$

For a given incident voltage vector $[V]^+$, the (voltage) reflection coefficient in element m is defined by

$$R_m = \frac{V_m^-}{V_m^+} \quad , \quad m = 1,2,\ldots,N \tag{13a}$$

and is found from (10a) to be

$$R_m = \sum_{n=1}^{N} S_{mn}(V_n^+/V_m^+) \quad . \tag{13b}$$

The input admittance of the TE_{10} mode in element m is given by

$$Y_m^{(in)} = \frac{V_m}{I_m} = Y_c \frac{1 + R_m}{1 - R_m} \quad . \tag{14}$$

Unlike Y_{mn}, R_m and $Y_m^{(in)}$ are functions of the array excitations.

Under the condition sketched in Figure 3 the radiation pattern is called the match-loaded active element pattern $Q_1(\theta,\phi)$. For a given incident voltage vector $\bar{V}^+$, the pattern of the whole array is given by

$$P_{array}(\theta,\phi) = \sum_{n=1}^{N} V_n^+ Q_n(\theta,\phi) = (\bar{V}^+)^T \bar{Q} \quad . \tag{15}$$

5.1.3 One-Mode Approximation

In the previous discussion, the reference plane for voltage and current is taken to be a distance ℓ from the aperture as shown in Figure 1. Specifically, ℓ should be chosen sufficiently large so that all reflected modes other than TE_{10} attentuate to negligible values within ℓ. As an example, the following parameters are used for the dimensions in Figure 2:

$$a = 0.9", \; b = 0.4", \; f = 9 \text{ GHz} \quad ,$$

ℓ should be at least 0.45" in order that the next higher-order mode TE_{20} attenuate to one-tenth of its magnitude within ℓ.

For finite ℓ, the calculation of $\{Y_{mn}\}$ and other scattering parameters is quite difficult. Hence, in practice, an approximation is often used:

$$\ell = 0 \quad . \tag{16}$$

When (16) is used, all of the analysis becomes approximate. This approximation is valid if, despite the discontinuity of the guide and the coupling in the array, the aperture field of the slot essentially contains no other modes than TE_{10}. For this reason, the approximation in (16) is known as the "one-mode approximation." It has been verified experimentally and theoretically that the one-mode approximation is good if (i) the slots are thin, and (ii) their length is roughly a half-wavelength.

Under the one-mode approximation, the expression of mutual admittance in (5) can be replaced by

$$Y_{12} = \frac{1}{V_1 V_2} \int_{A_2} \bar{E}_2 \times \bar{H}_1 \cdot d\bar{s}_2 \tag{17}$$

where

A_2 = aperture of slot 2

$\bar{H}_1$ = magnetic field when slot 1 is excited with voltage V_1, and all other slots are covered by perfect conductors at their openings ($\ell = 0$ in Figure 2)

$\bar{E}_2$ = electric field when slot 2 is excited with voltage V_2, and all other slots are covered by perfect conductors at their openings.

Because $\bar{H}_1 = I_2 \bar{h}_2$ and $\bar{E}_2 = V_2 \bar{e}_2$, it is a simple matter to verify that (17) and (5) are equivalent under the one-mode approximation.

5.2 Slots on a Cylinder

5.2.1 GTD Green's Function for Surface Field on a Cylinder

Under the one-mode approximation, the mutual admittance between two slots in an array can be calculated from (17). It will now be applied to a slot array on an infinitely long conducting cylinder. The key step lies in the calculation of $\bar{H}_1$, the magnetic field at the aperture of slot 2 due to a voltage excitation in slot 1. To this end, consider the following Green's function problem.

At point Q' on the surface of the cylinder of radius R, see Figure 4a, there is a tangential magnetic dipole source described by a magnetic current density (for exp +jωt time convention)

$$\bar{K}(r) = \bar{M} \frac{1}{R} \delta(r - R)\delta(\phi)\delta(z) \tag{18}$$

where $\bar{M}$ is the magnetic dipole moment, and ($r = R$, $\phi = 0$, $z = 0$) are the cylindrical coordinates of Q'. The problem is to determine $\bar{H}$ at another point $Q = (R,\phi,z)$ on the same surface. The ray technique described below applies when kR is large (say 10 or more).

According to GTD (Keller, 1962; Pathak and Kouyoumjian, 1974; Kouyoumjian, 1975; Hansen, 1981), the dominant contribution of $\bar{H}$ at Q is the field on the surface ray from Q' to Q. The surface ray is a geodesic on the conducting surface, and in the present case is a helical path, Figure 4. The arclength of the surface ray is

$$s = \sqrt{(R\phi)^2 + z^2} \quad . \tag{19}$$

The tangent, normal, and binormal of the surface ray are ($\hat{t}'$, $-\hat{n}'$, $-\hat{b}'$) at Q', and ($\hat{t}$, $-\hat{n}$, $-\hat{b}$) at Q. Thus, ($\hat{t}$, $\hat{n}$, $\hat{b}$) form a moving trihedron along a surface ray, pointing toward the longitudinal and two transverse directions. At any point on the

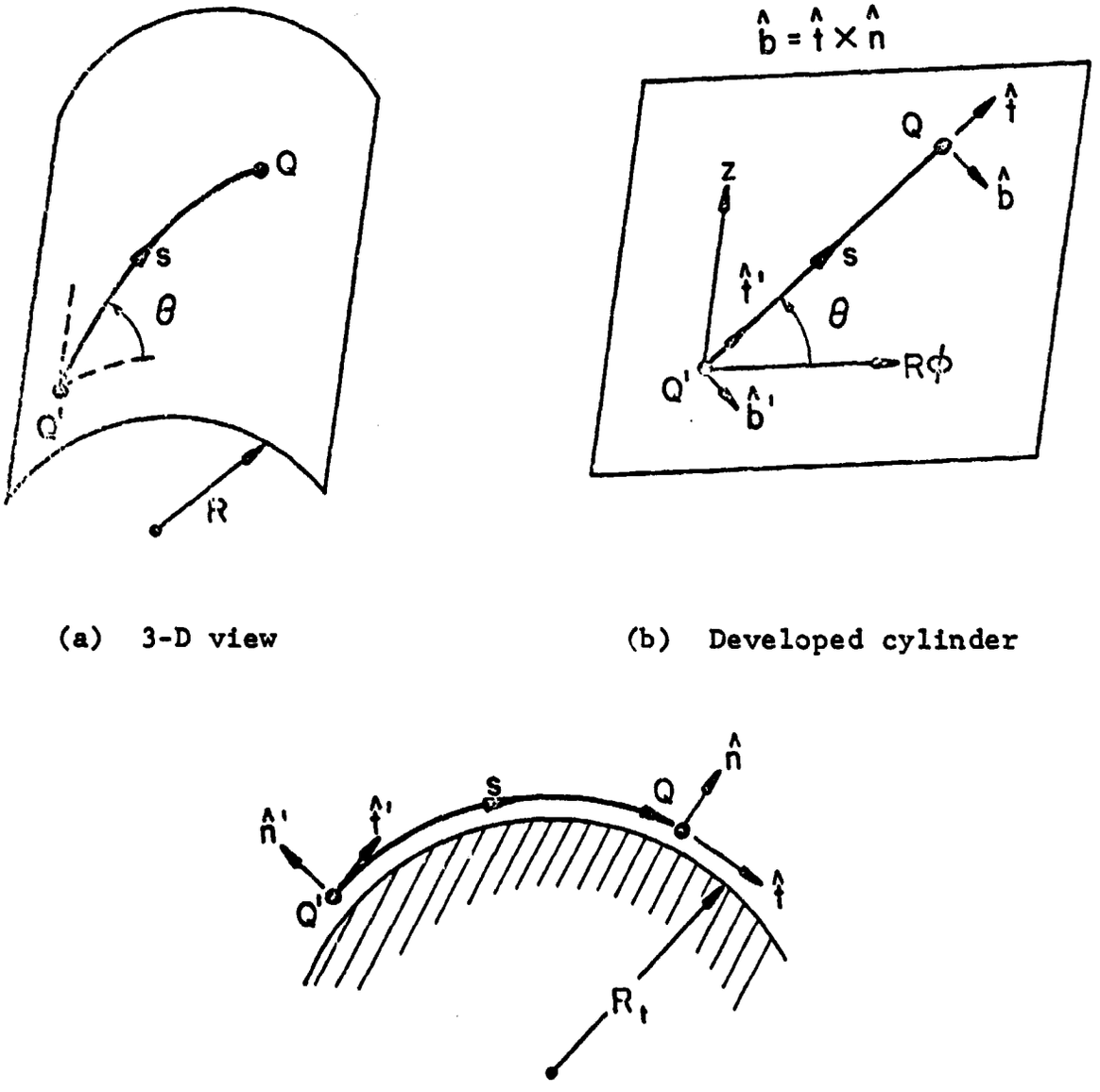

(a) 3-D view

(b) Developed cylinder

(c) Cut along θ-direction

Figure 4. A surface ray from source point Q' to observation point Q on a cylinder of radius R.

surface ray, the curvature of the conducting surface is described by two parameters:

R_t = the radius of curvature in the direction of $\hat{t}$ (or that in the longitudinal direction of the surface ray), and

R_b = the radius of curvature in the direction of $\hat{b}$ (or that in the transverse direction of the surface ray).

On a convex surface, both R_t and R_b are nonnegative. For the present case of a conducting cylinder, one has

$$R_t = \frac{R}{\cos^2 \theta} \quad , \qquad R_b = \frac{R}{\sin^2 \theta} \tag{20}$$

where θ is measured from the $R\phi$-axis in Figure 4b, and takes a value between 0 and 2π. The large parameter for the asymptotic expansion is

$$m = (\tfrac{1}{2} kR_t)^{1/3} \quad . \tag{21}$$

Thus, the solution to be presented is an approximate asymptotic solution valid for $m \to \infty$. Furthermore, introduce a distance parameter

$$\xi = \frac{ms}{R_t} = (k/2R_t^2)^{1/3} s = \frac{ks}{2m^2} \tag{22}$$

which is the arclength normalized by k and R_t. Note that $\xi = 0$ defines the lit region ($\theta = \pi/2$), $\xi \simeq 1$ defines the penumbra region, and $\xi >> 1$ defines the deep shadow region. The solution is uniformly valid for all $\xi \geq 0$.

Due to the point source in (18), the final asymptotic solution for the magnetic field on the surface derived in (Lee and Safavi-Naini, 1978; Mittra and Safavi-Naini, 1979) is given by

$$\bar{H}(Q) \simeq \bar{M} \cdot (\hat{b}'\hat{b}H_b + \hat{t}'\hat{t}H_t) \tag{23a}$$

where the transverse component is

$$H_b(Q) \sim [(1 - \frac{j}{ks})v(\xi) - (\frac{1}{ks})^2 u(\xi) + j(\sqrt{2}\, kR_t)^{-2/3} v'(\xi)$$

$$+ j(\sqrt{2}\, kR_t)^{-2/3} (R_t/R_b)u'(\xi)]\, G(s) \qquad (23b)$$

the longitudinal component is

$$H_t(Q) \sim (\frac{j}{ks})[v(\xi) + (1 - \frac{2j}{ks})\, u(\xi) + j(\sqrt{2}\, kR_t)^{-2/3} u'(\xi)]\, G(s) \qquad (23c)$$

and the function G(s) is

$$G(s) = \frac{k^2 Y_0}{2\pi j} \frac{e^{-jks}}{ks} \qquad (23d)$$

$Y_0 = (\varepsilon_0/\mu_0)^{1/2} = (120\pi)^{-1}$, v and u are defined in the Appendix, and v' is the derivative of v. The solution in (23) is largely based on the classic work of Fock (1965).

Consider several limiting cases of the solution given in (23). If the radius of the cylinder becomes infinite

$$kR \to \infty \qquad (24)$$

the use of (A-11) through (A-15) in the Appendix in (23) leads to

$$H_b(Q) \sim [1 - \frac{j}{ks} - (\frac{1}{ks})^2]\, G(s) \quad , \quad kR \to \infty \qquad (25a)$$

$$H_t(Q) \sim (\frac{2j}{ks})\, (1 - \frac{j}{ks}) G(s) \quad , \quad kR \to \infty \quad . \qquad (25b)$$

When (25) is substituted into (23a), we find that $\bar{H}$ in (23a) is identical to the *exact* solution of the surface field due to a magnetic dipole on a flat ground plane (Felsen and Marcuvitz, 1973).

The second limiting case occurs when

$$\theta \to \pi/2 \quad . \tag{26}$$

It is found from (23) that H_t is again given by (25a), but H_b becomes

$$H_b(Q) \sim [1 - \frac{j}{ks} - (\frac{1}{ks})^2 + \frac{3}{4}(\frac{\pi}{2})^{1/2} e^{-j\pi/4} \frac{(ks)^{1/2}}{kR}] G(s) \quad , \quad \theta = \frac{\pi}{2} \; . \tag{27a}$$

In terms of the planar solution in (25a), rewrite (27a) as

$$H_b(Q) \sim [H_b(Q)]_{planar} + \frac{3}{8}\sqrt{\frac{1}{2\pi}}\, k^2 Y_0 e^{-j3\pi/4} \frac{1}{kR} \frac{e^{-jks}}{\sqrt{ks}} \quad , \quad \theta = \frac{\pi}{2} \; . \tag{27b}$$

The result in (27) is most interesting and, in fact, somewhat surprising. The surface ray traveling in direction $\theta = \pi/2$ Fig. 4 is *a straight* line ($kR_t \to \infty$). However, due to the finite curvature in the binormal direction ($R_b = R$), H_b on the cylindrical surface differs from its counterpart on a planar surface by the additional term in (27b). At a large distance away from the source ($ks \to \infty$) in the direction $\theta = \pi/2$, and for a fixed kR, we find that H_b on a planar surface and that on a cylindrical surface are given by, respectively,

$$[H_b(Q)]_{planar} \sim A \frac{e^{-jks}}{ks} \tag{28}$$

$$H_b(Q) \sim B \frac{1}{kR} \frac{e^{-jks}}{\sqrt{ks}} + A \frac{e^{-jks}}{ks} \quad , \tag{29}$$

where A and B are constants independent of s and R. Thus, for large ks, H_b on a cylinder is *stronger* than that on a plane.

As a third limiting case, let

$$\xi \to \infty \tag{30}$$

which occurs when observation point Q is in the deep shadow. Making use of (A-6) through (A-10), one can derive from (23):

$$H_b(Q) \sim \frac{k^2 \cos^{2/3}\theta}{1528(kR)^{1/3}(ks)^{1/2}} \exp\left[-0.88\xi - j\left(\frac{5\pi}{12} + 0.51\xi + ks\right)\right] , \quad \xi \to \infty \qquad (31a)$$

$$H_t(Q) \sim \frac{j}{ks} H_b(Q) \quad , \quad \xi \to \infty \quad . \qquad (31b)$$

Therefore, in the deep shadow, the field is a slow wave and decays exponentially along the surface ray.

5.2.2 Mutual Admittance Between Slots on a Cylinder

Return to the calculation of Y_{12} from (17) for two identical circumferential slots on a cylinder, Figure 5a. To calculate H_1, the voltage excitation V_1 in slot 1 can be replaced by an equivalent magnetic surface current density, see Figure 6.

$$\bar{K}_1 = \bar{E}_1 x\hat{x} = \hat{z} V_1 \cos\left(\frac{\pi}{a}y\right) , \text{ for } (y,z) \text{ in slot 1} , \qquad (32)$$

which radiates in a completely filled cylinder (Harrington, 1961). In (32), $y = R\phi$. Making use of the Green's function in (23a), $\bar{H}_1$ is calculated from the superposition integral

$$\bar{H}_1 = \int_{A_1} dy_1 dz_1 \left[V_1\sqrt{\frac{2}{ab}} \cos\left(\frac{\pi}{a} y_1\right)\right]\left[\hat{b}\, H_b \sin\theta + \hat{t}\, H_t \cos\theta\right] \qquad (33)$$

where the source point (y,z) is written as (y_1, z_1). Making use of (33) and the electric field distribution of slot 2 in (17), the final expression for Y_{12} between two identical circumferential slots on a cylinder is obtained namely:

$$Y_{12} = \frac{-2}{ab}\int_{A_1} dy_1 dz_1 \int_{A_2} dy_2 dz_2 \left[\cos\frac{\pi}{a} y_1\right]\left[\cos\frac{\pi}{a}(y_2 - R\phi_0)\right] g_{\phi}(1,2) . \qquad (34)$$

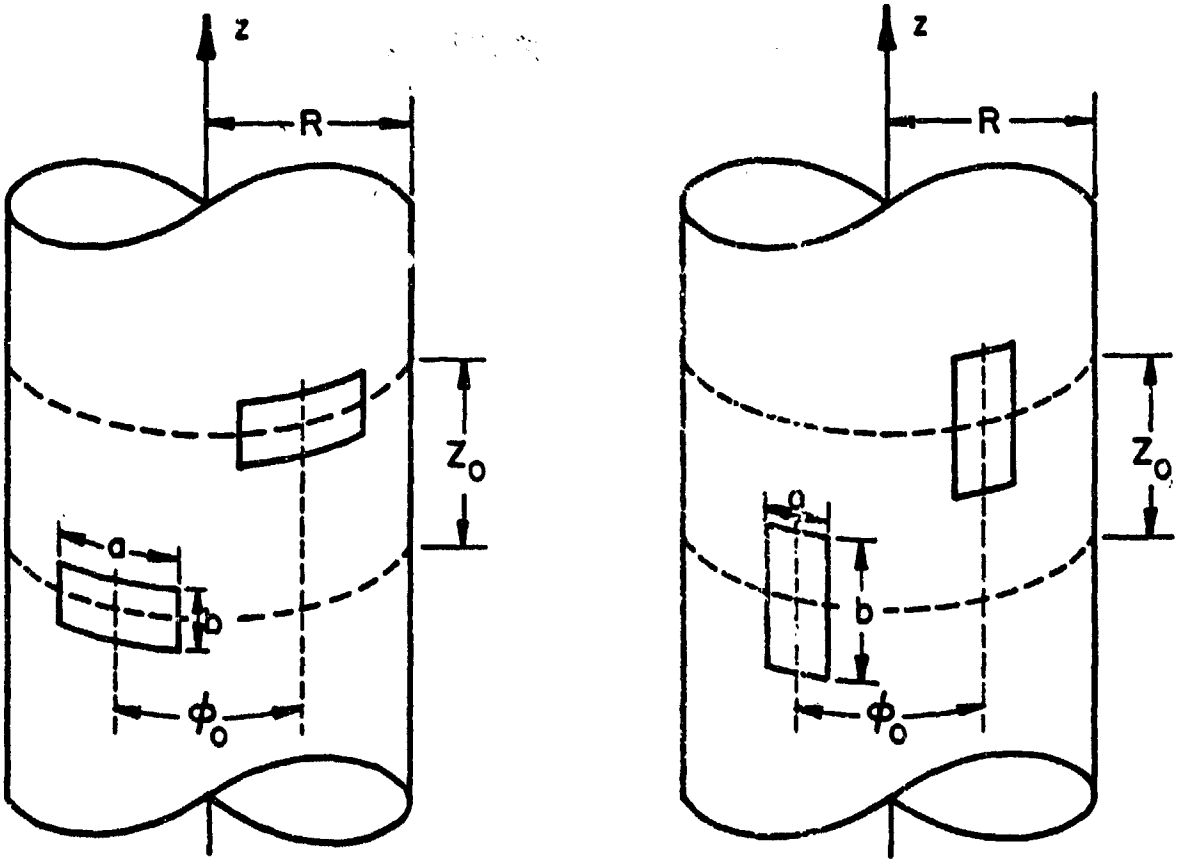

(a) CIRCUMFERENTIAL SLOTS (b) AXIAL SLOTS

Figure 5. Two identical slots on the surface of a cylinder.

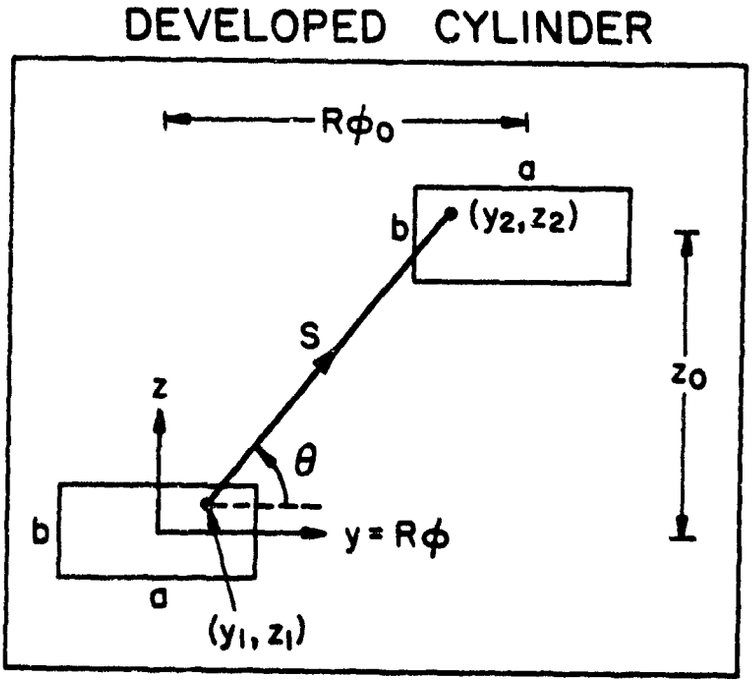

Figure 6. Two identical circumferential slots on the surface of a cylinder. The figure shows the developed cylinder.

Here (y_1,z_1), and (y_2,z_2) are two typical points in slots 1 and 2, respectively. The Green's function g_ϕ is

$$g_\phi(1,2) = H_b \sin^2 \theta + H_t \cos^2 \theta \tag{35}$$

where (H_b,H_t) are given in (23) with

$$s = \sqrt{(y_2 - y_1)^2 + (z_2 - z_1)^2} \tag{36a}$$

$$\theta = \tan^{-1}[(z_2 - z_1)/(y_2 - y_1)] \tag{36b}$$

In a very similar manner, the mutual admittance between two identical axial slots, Figure 5b, can be derived. The final result reads

$$Y_{12} = \frac{-2}{ab}\int_{A_1} dy_1 dz_1 \int_{A_2} dy_2 dz_2 \left[\cos \frac{\pi}{b} z_1\right]\left[\cos \frac{\pi}{b}(z_2 - z_0)\right] g_z(1,2) \tag{37}$$

where the Green's function g_z is

$$g_z(1,2) = H_b \cos^2 \theta + H_t \sin^2 \theta \quad . \tag{38}$$

The two surface integrals in (34) or (37) must be evaluated numerically. Extensive numerical results are given by Lee and Mittra (1977), while some representative examples are quoted below. All values of Y_{12} are presented in (db, phase in degrees) format, where db = 20 $\log_{10}$ (Y_{12} in mho). See also Chiang and Cheng (1968), Sureau and Hessel (1971), Stewart and Golden (1971), Felsen et al (1974), Pathak (1975), Hwang and Kouyoumjian (1975), Steyskal (1977), Lee and Eichmann (1980), and Hessel et al (1979).

Agreement between GTD and exact modal solutions. Under the one-mode approximation, an exact solution of Y_{12} on a cylinder can be found in terms of cylindrical functions (the so-called "exact modal solution") see Chapter 4. Consider two identical circumferential slots with parameters

$$a = 0.9" \quad , \quad b = 0.4" \quad , \quad R = 1.991" \tag{39a}$$

$$f = 9 \text{ GHz} \quad , \quad \lambda = 1.3123" \tag{39b}$$

For various slot separations, values of Y_{12} calculated by GTD solutions in (34) and by the exact modal solution are presented in Table A. Note that they are in excellent agreement.

Effect of transverse curvature term. As explained in the discussion of (26) through (29), the ray traveling along the generator of the cylinder is straight. However, the field H_b on it is stronger than that on a ray traveling on a planar conducting surface. Such a dependence on the surface curvature in the transverse direction of the ray is most interesting, and can be seen in Figure 7, where the ratio

$$\frac{Y_{12} \text{ on a cylinder with radius R}}{Y_{12} \text{ on a plane}}$$

is plotted as a function of R for $z_0 = 8"$ and $\phi_0 = 0$. Note that the convergence rate of the cylindrical Y_{12} to the planar Y_{12} is not as rapid as one would normally expect. For example, at $kR = 50$, the cylindrical Y_{12} is still about 10 percent higher than the planar one. The exact modal solution in this figure is truncated at $kR = 50$, because beyond this radius, it becomes extremely slowly convergent.

Additional numerical results of Y_{12} between two identical slots on a cylinder are given in Figures 7 to 11. The normalized phase is defined by the phase of $Y_{12} \exp(+jks_0)$, where s_0 is the center-to-center distance of the slots and is equal to $(z_0^2 + R^2\phi_0^2)^{1/2}$.

This investigation on the effects of transverse curvature was initiated after the discovery by Hughes and PINY workers that coupling was stronger for circumferential slots along a cylinder than for slots on a flat plane. At that time there

TABLE A. Y_{12} OF CIRCUMFERENTIAL SLOTS ON A CYLINDER

ϕ_0(deg.)	z_0(inch)	Modal Solution	GTD Solution
0	0.5"	-62.62 db -72°	-62.54 -72°
	2.0"	-71.78 -117°	-71.66 -116°
	8.0"	-81.84 34°	-81.83 37°
	40.0"	-91.95 -115°	-92.46 -110°
30°	2"	-77.42 175°	-77.69 177°
60°		-90.00 -3°	-90.17 -1°
90°		-102.52 120°	-103.10 116°
30°	9	-81.33 -77°	-81.34 -75°
40°		-89.87 168°	-90.02 170°
60°		-101.97 -49°	-102.48 -47°

Parameters of slots are given in (39).

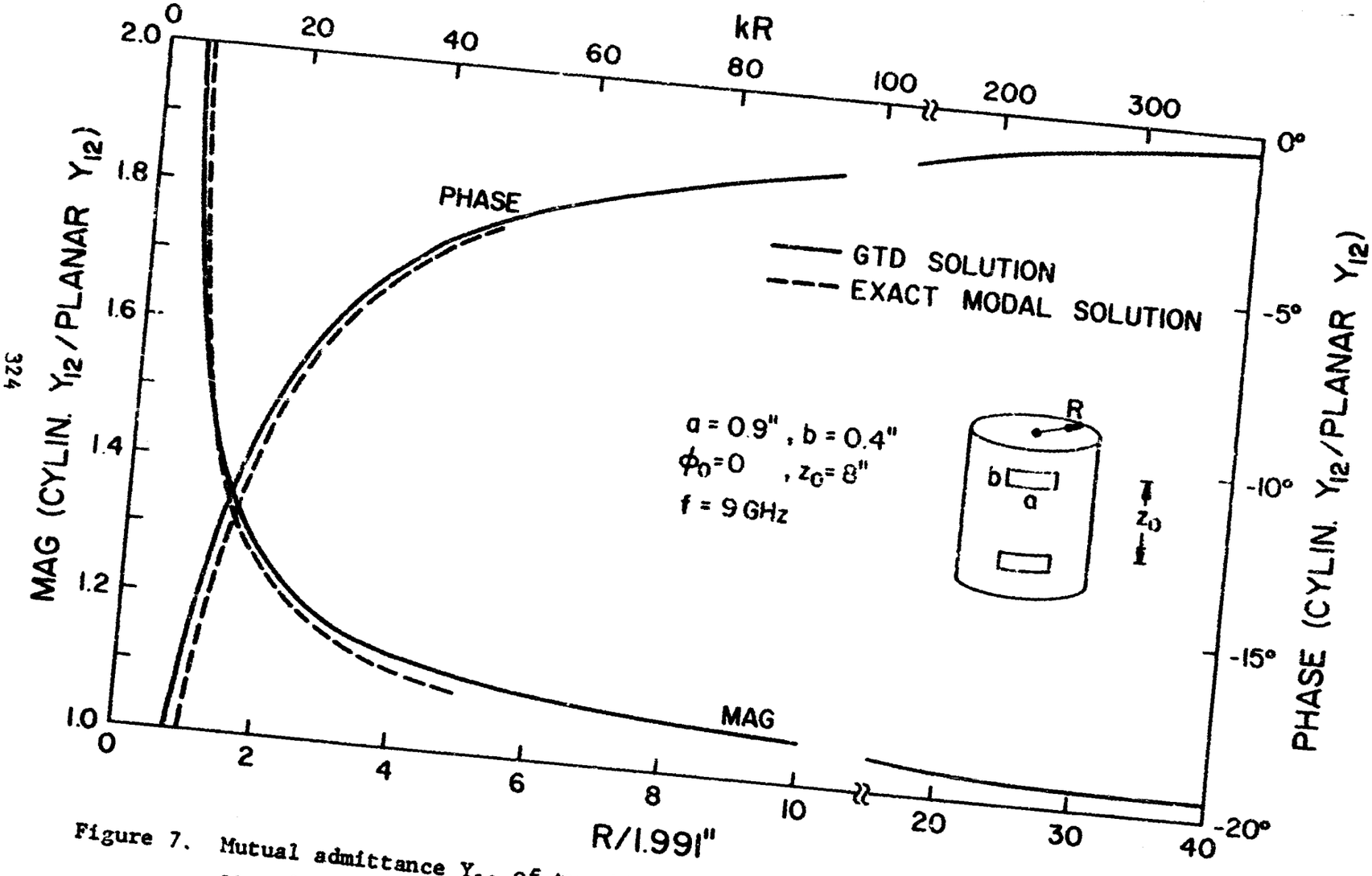

Figure 7. Mutual admittance Y_{12} of two identical circumferential slots on a cylinder as a function of the radius R of the cylinder. Y_{12} is normalized by Y_{12} on a plane which is 5.37×10^{-5} exp(J53.55°) mho.

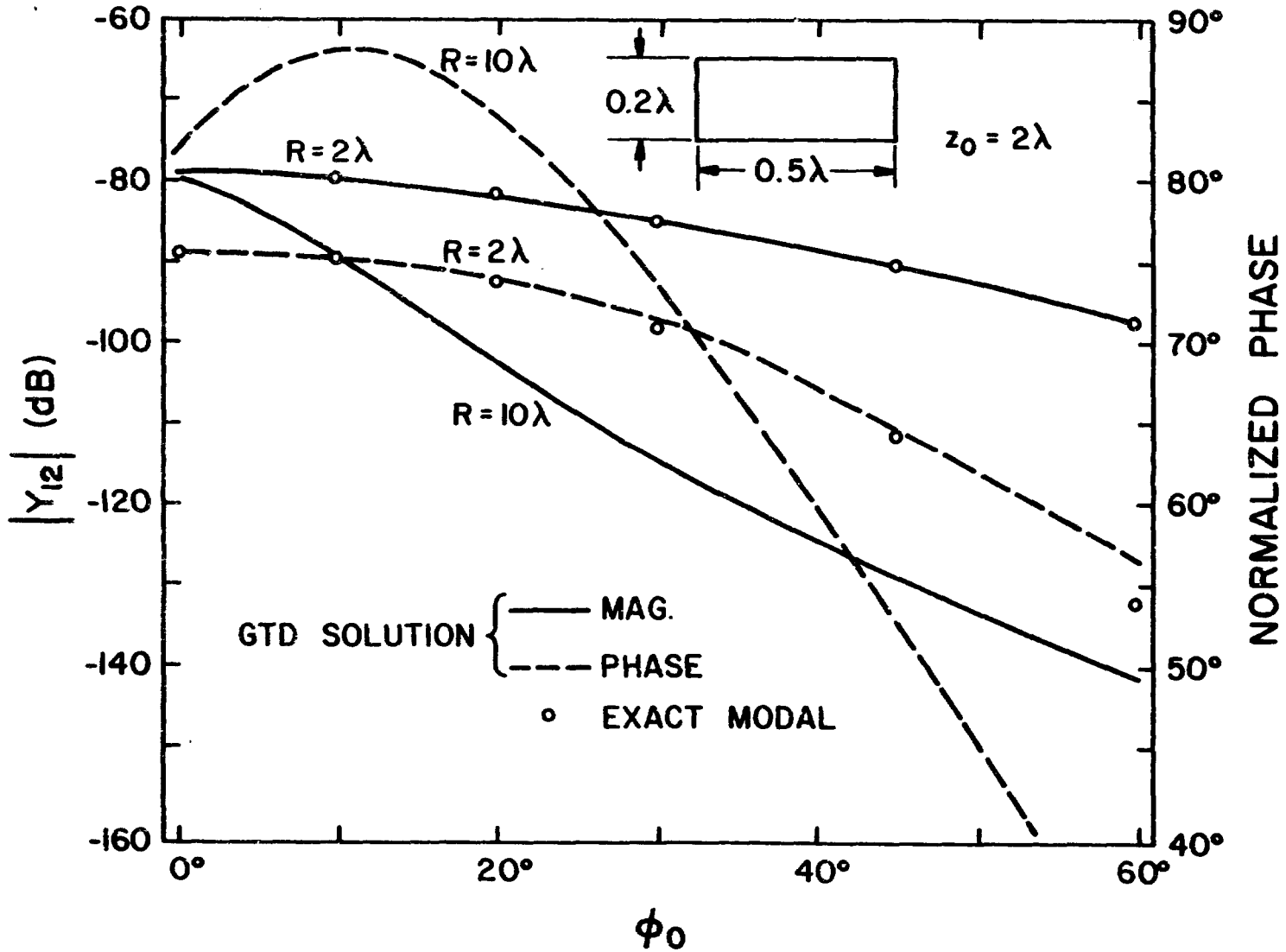

Figure 8. Mutual admittance Y_{12} between two circumferential slots as a function of ϕ_0.

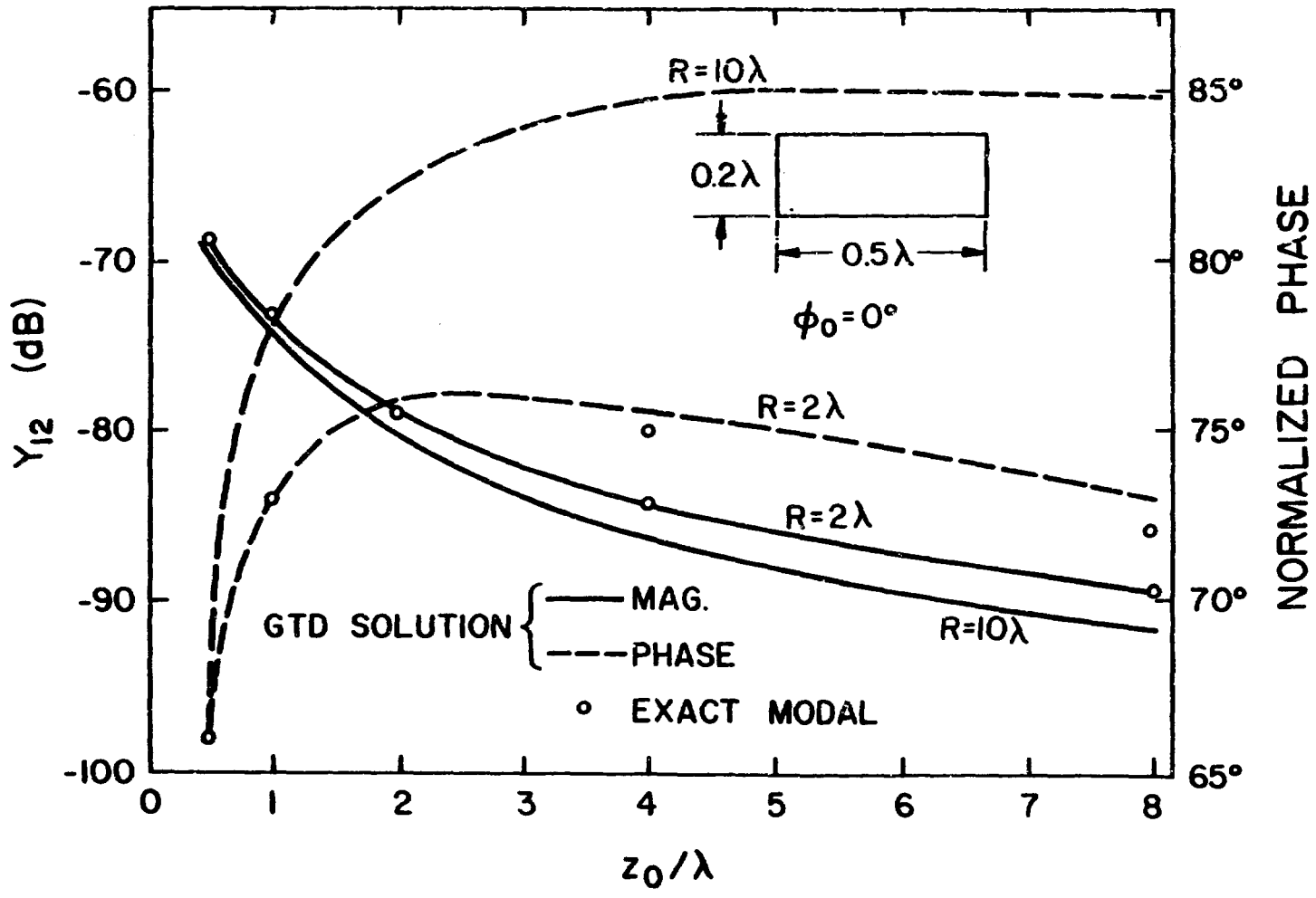

Figure 9. Mutual admittance Y_{12} between two circumferential slots as a function of z_0.

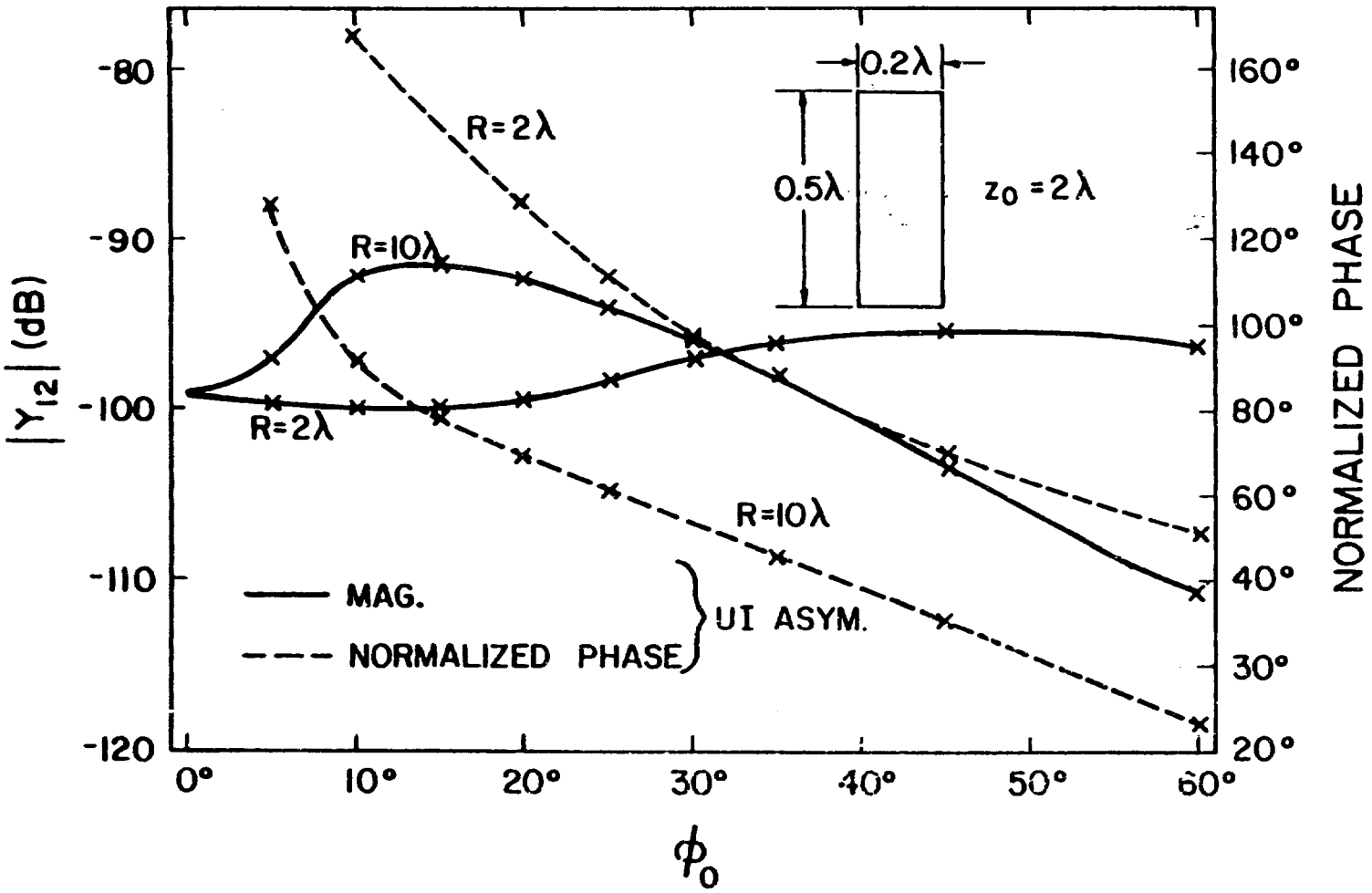

Figure 10. Mutual admittance Y_{12} between two axial slots as a function of ϕ_0.

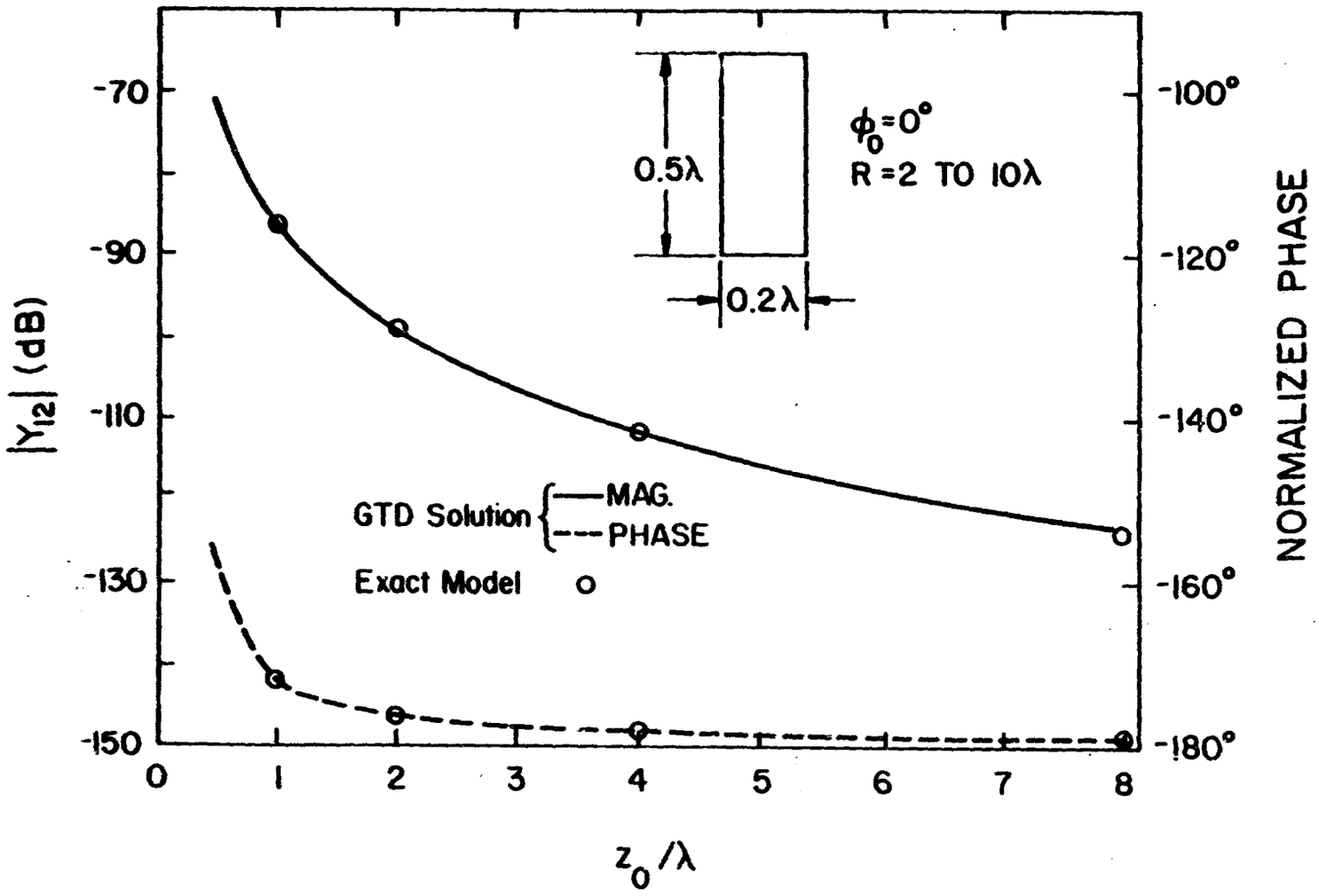

Figure 11. Mutual admittance Y_{12} between two axial slots as a function of z_0.

was no physical or mathematical explanation of this interesting phenomenon.

5.2.3 GTD Green's Function for a Surface Field on a General Convex Surface

To Calculate the mutual admittance between slots on a general convex surface, the GTD Green's function for the cylinder in (23) is generalized. Referring to Figure 12 consider a perfectly conducting convex surface Σ , whose radii of curvature at any point are large in terms of wavelength. At a point Q_1, described by position vector r_1 on Σ, there is a tangential magnetic dipole source described by a magnetic current density

$$\bar{K}(r) = \bar{M}\delta(r - r_1) \tag{40}$$

where M is the magnetic dipole moment and lies in the tangent plane of Σ. The problem is to determine a high-frequency asymptotic solution of H at a general point Q_2 described by position vector r_2 on Σ. In other words, the GTD Green's function for the surface magnetic field for points r_1 and r_2 is to be found.

Before presenting the solution, several definitions and parameters are introduced. According to GTD (Keller, 1962; Kouyoumjian, 1975; Hansen, 1981), (Shapira, Felsen, and Hessel, 1974A and 1974B), the dominant high-frequency contribution to $H(r_2)$ is the field on the surface ray from $r_1$to r_2. The surface ray is a geodesic of Σ. Some of the geometrical properties are described by Figure 12 (i) the arc length $\bar{s}$ which is chosen such that $\bar{s} = 0$ at the source point r_1 and $\bar{s} = s$ at the observation point r_2; (ii) the tangent, normal, and binormal, denoted by $(\hat{t}_n, -\hat{n}_n, -\hat{b}_n)$ at r_n where $n = 1,2$; and (iii) its two radii of curvature $R_t(\bar{s})$, and $R_b(\bar{s})$ of Σat point $\bar{s}$ in the directions of tangent and binormal, respectively. (On a general convex surface, both radii are nonnegative.)

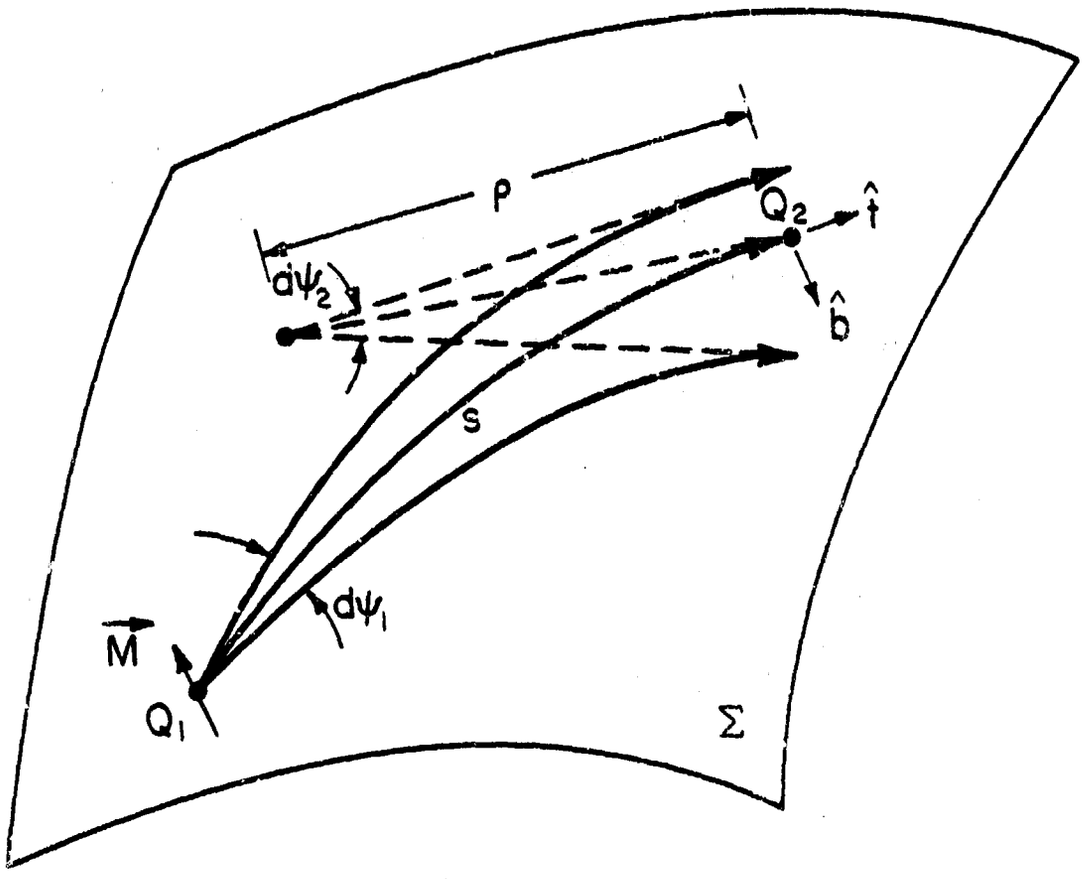

Figure 12. A surface ray pencil originating from the magnetic dipole source at Q_1. The central ray of the pencil passes through the observation point Q_2. The angle extended by the pencil is $d\psi_1$ at Q_1 and $d\psi_2$ at Q_2.

From the above parameters, one may calculate the following quantities that are needed for the solution of the Green's function:

(i) The large parameter in the asymptotic expansion of the Green's function is

$$m(\bar{s}) = [\tfrac{1}{2} kR_t(\bar{s})]^{1/3} \tag{41}$$

which is a function of position along the ray from r_1 to r_2.

(ii) A distance parameter from r_1 to r_2 is defined by

$$\xi = \int_{r_1}^{r_2} \frac{k}{2m^2(\bar{s})}\, d\bar{s} \quad . \tag{42}$$

For the special case when R_t is not a function of $\bar{s}$ (constant ray curvature), ξ is reduced to $(ks/2m^2)$, a well-known parameter introduced first by Fock (1965).

(iii) The ray curvatures at the source and observation points enter in a parameter defined by

$$\tau = [\frac{ks}{2m(0)\, m(s)\, \xi}]^{1/2} \quad , \tag{43}$$

which is positive real for a convex surface, and is reduced to unity for the special case of a constant ray curvature.

(iv) Consider a small pencil of surface rays originating from r_1 and propagating toward r_2, Figure 12. The angle extended by the pencil at r_1 is $d\psi_1$, and that at r_2 is $d\psi_2$. The divergence factor DF of the pencil is defined by

$$DF = \left(\frac{s\, d\psi_1}{\rho\, d\psi_2} \right)^{1/2} \tag{44}$$

where ρ is the caustic distance of the wavefront at r_2 and is always positive. For example, if Σ is a sphere and r_1 is the north pole, DF at point $r_2 = (r, \theta, \phi)$ is

$$DF = \left[\frac{\theta}{\sin\theta}\right]^{1/2}$$

which varies from one at the north pole ($\theta = 0$) to infinity at the south pole ($\theta = \pi$) as r_2 moves along a great circle.

(v) The "mean" radii of curvature between r_1 and r_2 are defined by

$$\bar{R}_t = [R_t(0)\ R_t(s)]^{1/2} \tag{45a}$$

$$\bar{R}_b = [R_b(0)\ R_b(s)]^{1/2} \quad . \tag{45b}$$

Throughout this work, it is assumed that Σ is a smooth surface with a slowly varying curvature. Then $(\bar{R}_t, \bar{R}_b)$ represents a sort of average value of radii of curvature along the ray.

Return to the electromagnetic problem in Figure 12. Assume that $m(\bar{s})$ is large and is slowly varying for all $\bar{s}$ in the range $0 \leq \bar{s} \leq s$. Then an approximate asymptotic solution for the surface magnetic field at r_2 due to the dipole source in (40) is given by

$$\bar{H}(r_2) \simeq \bar{M} \cdot (\hat{b}_1\hat{b}_2 H_b + \hat{t}_1\hat{t}_2 H_t)\ (DF) \tag{46a}$$

where

$$H_b = G(s)\{(1 - \tfrac{j}{ks})\ \tau v(\xi) - (\tfrac{1}{ks})^2\ \tau^3 u(\xi) + j(\ \bar{2}k\bar{R}_t)^{-2/3} \cdot [\tau v'(\xi) + (\bar{R}_t/\bar{R}_b)\ \tau^3 u'(\xi)]\} \tag{46b}$$

$$H_t = G(s)(\tfrac{j}{ks})[\tau v(\xi) + (1 - \tfrac{2j}{ks})\ \tau^3 u(\xi) + j(\ \bar{2}k\bar{R}_t)^{-2/3}\ \tau^3 u'(\xi)] \tag{46c}$$

$$G(s) = \frac{k^2 Y_0}{2\pi j}\ \frac{e^{-jks}}{ks}\ , \quad Y_0 = (120\pi)^{-1}. \tag{46d}$$

The Fock functions u and v and their derivatives u' and v' are described in the Appendix. Several remarks about the solution in (46) are in order.

(i) It is derived in an approximate manner from the classic work of Fock (1965) and the recipe of GTD, as detailed in Lee (1978). All traditional GTD solutions depend on $\bar{R}_t$, not $\bar{R}_b$. In (46b), the term containing $(\bar{R}_t/\bar{R}_b)$ was introduced through an Ansatz suggested in (Lee and Safavi-Naini, 1978). Because of the fact that u' decays faster than v', this term is important only if $\bar{R}_t$ is very large and $\bar{R}_b$ is finite. An example occurs in the axial propagation along a cylinder, where $\bar{R}_t \to \infty$ and $\bar{R}_b$ is equal to the radius of the cylinder. For this particular example, it is only with this additional term that (46b) agrees with the rigorous asymptotic solution (derived recently by J. Boersma in an unpublished note). Thus, the Ansatz is at least partially verified.

(ii) For the special case that Σ is a planar surface ($R_t = R_b \to \infty$), (46) recovers the known exact solution given in (25). When Σ is a cylinder, (46) is reduced to (23).

(iii) The solution is valid for any combination of r_1 and r_2. In the penumbra region (r_2 is close to r_1 and $\xi << 1$), (46) gives approximately the known planar solution. In the deep shadow ($\xi >> 1$), the residue series representation of the Fock functions can be used, and (46) is identified as the creeping-wave contribution.

(iv) Except for the very simple surfaces such as a cylinder, cone or sphere, no explicit parameter equations can be found for the geodesics (Lee, 1977). Thus, for a general surface, one may have to rely on numerical techniques for determining the geodesics and the divergent factor.

5.3 Slots on a Cone

5.3.1 Green's Function of a Cone

Let us apply the formula (46) to the field on an infinite cone, described by the equations, Figure 13a.

$$x = r \sin\theta_0 \cos\phi \quad , \quad y = r \sin\theta_0 \sin\phi \quad , \quad z = r \cos\theta_0 \tag{47}$$

where θ_0 is the half-cone angle ($0 < \theta_0 < \pi/2$). Since the cone is a developable surface, the rays (geodesics) on a developed cone, Figure 13b, are straight lines (Lee, 1977.) Due to the source at $r_1 = (r_1, \theta_0, \phi_1)$, the main contribution of the field at $r_2 = (r_2, \theta_0, \phi_2)$ comes from the shortest ray described by

$$r_1 \sin\Omega_1 = r_2 \sin\Omega_2 \quad . \tag{48}$$

As the ray propagates away from the source point r_1, it reaches the highest altitude at M where $\Omega_2 = \pi/2$. After M, the ray travels downward away from the cone tip. The various parameters defined in Section 5.2.3 can be simply calculated from the cone geometry, and expressed in terms of coordinates (r_1, ϕ_1) and (r_2, ϕ_2). The arclength is

$$s = \{r_1^2 + r_2^2 - 2r_1 r_2 \cos[(\phi_1 - \phi_2)\sin\theta_0]\}^{1/2} \quad . \tag{49}$$

The angle Ω_1 at r_1 is

$$\Omega_1 = \sin^{-1}\left\{\frac{r_2}{s}\sin[(\phi_2 - \phi_1)\sin\theta_0]\right\} \quad . \tag{50}$$

Choose $\Omega_1 < \pi/2$ if $r_2^2 < s^2 + r_1^2$, and $\Omega_1 > \pi/2$ if otherwise. The other parameters are

$$\Omega_2 = \Omega_1 + (\phi_2 - \phi_1)\sin\theta_0 \tag{51}$$

$$\bar{R}_t = \frac{r_1 r_2 \tan\theta_0}{\sin\Omega_1 \sin\Omega_2} \quad , \quad \bar{R}_b = \frac{r_1 r_2 \tan\theta_0}{\cos\Omega_1 \cos\Omega_2} \tag{52}$$

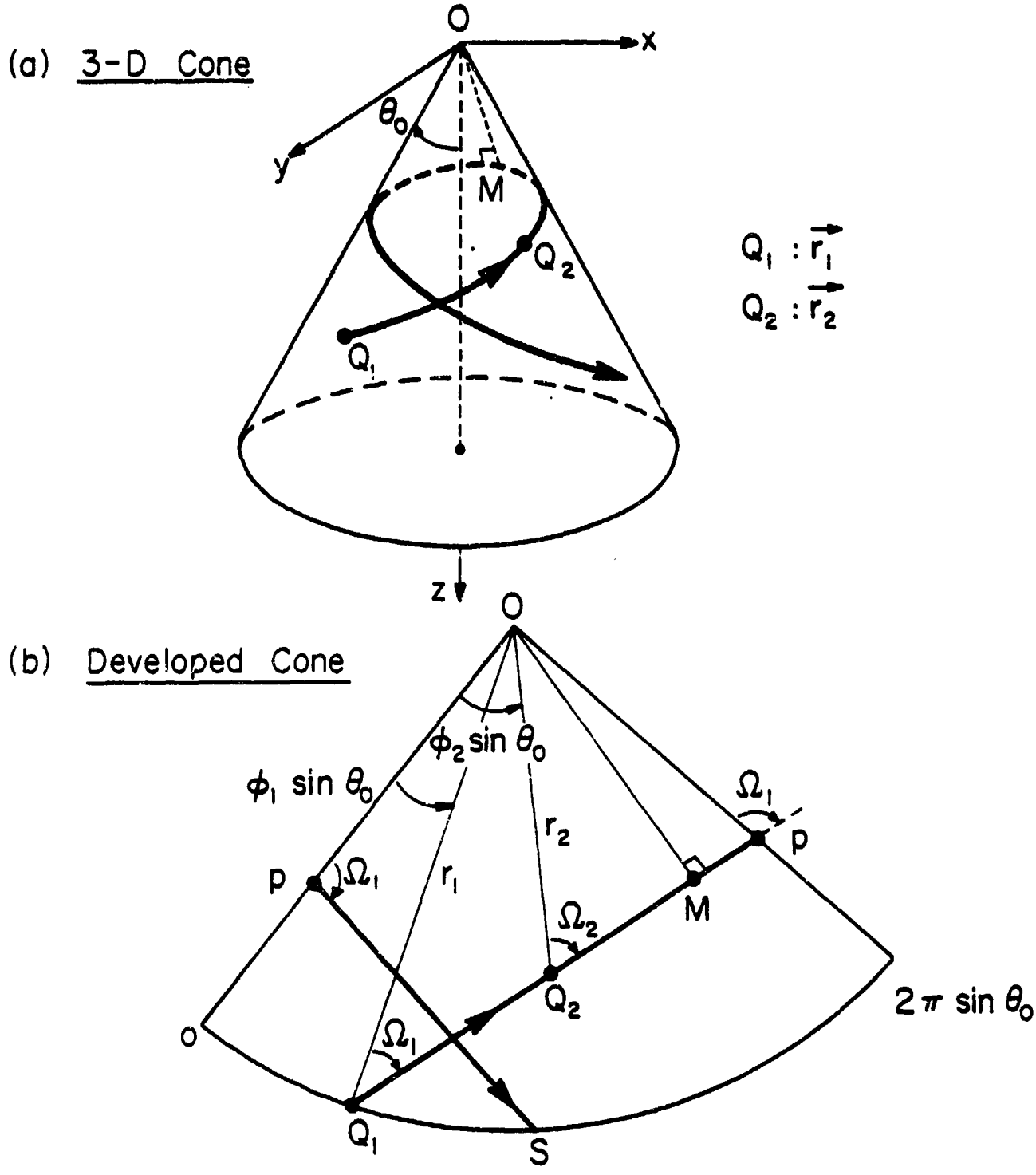

Figure 13. A surface ray from source point Q_1 to observation point Q_2 on a cone with half cone angle θ_0.

$$\xi = (\tfrac{1}{2} kr_1 \sin \Omega_1 \sin \theta_0)^{1/3} \left| \phi_2 - \phi_1 \right| \cos^{2/3} \theta_0 \qquad (53)$$

$$\tau = (ks/\xi)^{1/2} (2k^2 r_1 r_2)^{-1/6} (\sin \Omega_1 \sin \Omega_2 \cos \Omega_0)^{1/3} \qquad (54)$$

$$DF = 1 \quad . \qquad (55)$$

When the above parameters in (49) through (55) are substituted into (46), we obtain an approximate solution for the surface field on a cone due to a direct surface ray contribution. Let us consider a special observation point r_2 such that

$$ks >> 1 \quad , \quad \Omega_1 \text{ and } \Omega_2 \text{ are not close to zero} \quad . \qquad (56)$$

After making use of the residue series representation for the Fock functions (Appendix) and keeping only the leading terms, then the two components of the field in (46) are reduced to

$$H_b \sim \frac{k^2 (\sin \Omega_1 \sin \Omega_2 \cot \theta_0)^{1/3}}{1528 (k^2 r_1 r_2)^{1/6} (ks)^{1/2}} \exp\left[-0.88\xi - j\left(\frac{5\pi}{12} + 0.51\xi + ks\right)\right] \qquad (57a)$$

$$H_t \sim O[(ks)^{-3/2}] \qquad (57b)$$

which agree with the rigorous asymptotic solutions given in Equations (50) and (53) of (Chan et al, 1977). (In making the comparison, note the corresponding notations used in (Felsen et al, 1974) and here: $-i \to j$, $\theta_c \to \theta_0$, $L_1 \to s$, $r_> \to r_1$, $r_< \to r_2$, $\beta_{s>} \to \pi/2 - \Omega_1$, and $\bar{q}_1 \to t_1'$.) Note that the result in (57) or that in (Chan et al, 1977) is valid only under the conditions in (56). For an arbitrarily located observation point, (46) should be used.

Two final remarks about the formula in (46) are in order. (i) For a given source and observation point, there are infinitely many rays (geodesics) passing through them. The contribution from each ray can be calculated from (46), and the final

field solution is the superposition of all ray contributions. In most practical problems (all the numerical computations presented in this paper), only the ray with the shortest arclength gives the significant contribution to the field solution, whereas all other rays may be ignored. (ii) Depending on the polarization and the distances of the source and observation points from the cone tip, there may be another significant contribution to the field from the diffraction at the tip. In such a case, the total field at any point contains two dominant contributions: one from the direct ray according to formula (46), and one from the tip-diffracted ray (Pridmore-Brown, 1972, 1973). More about the latter will be given next.

5.3.2 Mutual Admittance Between Slots on a Cone

On the surface of a cone, let us consider two arbitrarily oriented slots. Under the assumption that the dimensions of the slots are relatively small compared with the radii of curvature of the cone surface, the shapes of slots are taken to be rectangular on a developed cone.

Referring to Figure 14, describe the dimensions and the positions of the two slots by (a_n, b_n) and $[c_n, (n-1)\phi_0, \omega_n]$, $n = 1,2$. Thus, the radial separation of the two slots is $(c_2 - c_1)$ and the angular separation is ϕ_0. The angle ω_n measures the deviation of the longitudinal direction of slot n from the radial direction of the cone. As usual, assume that the slots are thin, and that their lengths are roughly a half-wavelength. Then the aperture field in each slot can be adequately approximated by a simple cosine distribution, which is the "one-mode" approximation described in Section 5.1.3. Y_{12} has two dominant high-frequency contributions: one from the direct rays going from slot 1 to slot 2, and the other from the rays diffracted at the tip of the cone, viz.,

$$Y_{12} \sim Y_{12}^d + Y_{12}^t \quad . \tag{58}$$

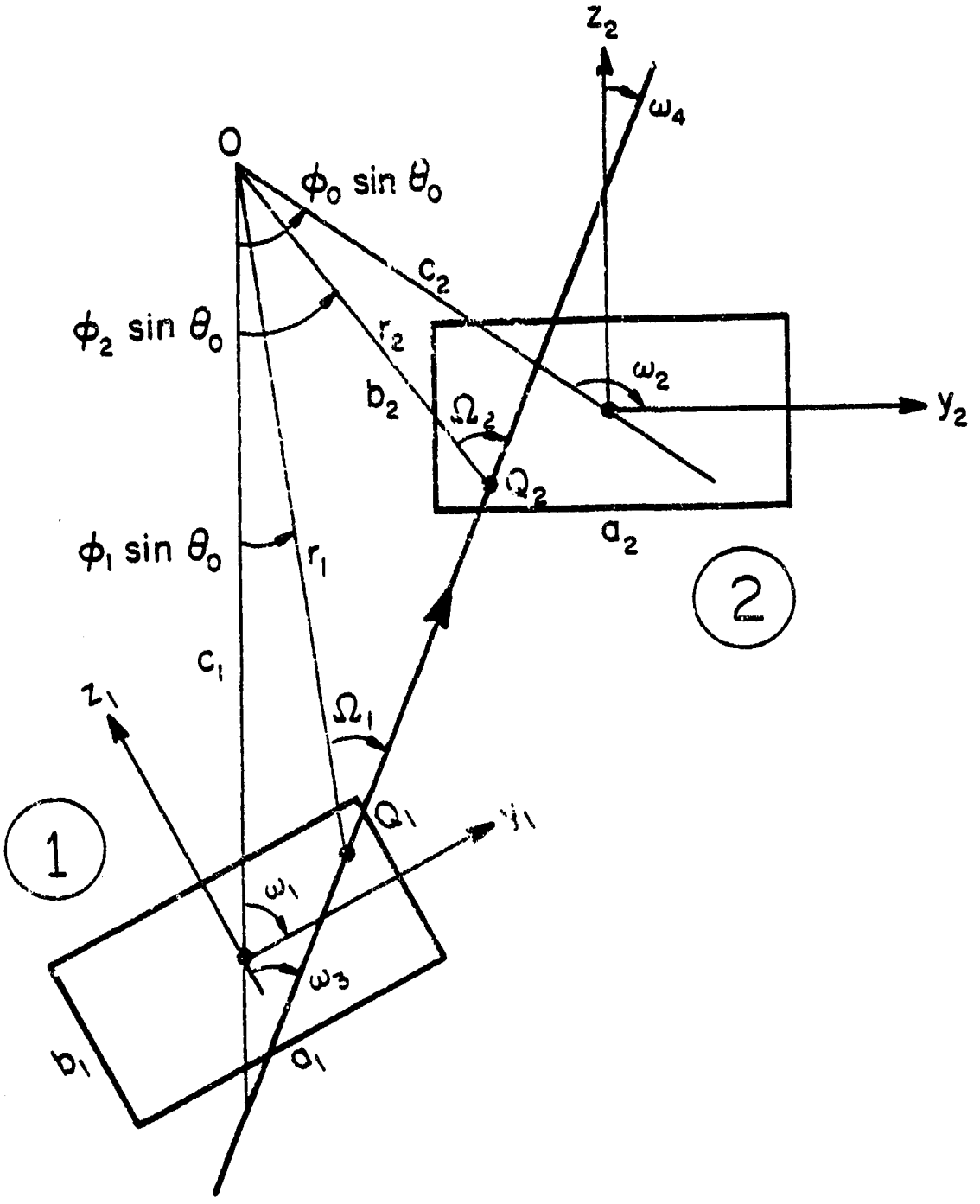

Figure 14. Two rectangular slots on a developed cone.

The first term Y_{12}^d may be explicitly written as *

$$Y_{12}^d = \frac{-2}{(a_1 b_1 a_2 b_2)^{1/2}} \int_{-a_1/2}^{a_1/2} dy_1 \int_{-b_1/2}^{b_1/2} dz_1 \int_{-a_2/2}^{a_2/2} dy_2 \int_{-b_2/2}^{b_2/2} dz_2$$

$$\times \left(\cos \frac{\pi}{a_1} y_1\right) \left(\cos \frac{\pi}{a_2} y_2\right) g(1,2) \qquad (59a)$$

where

$$g(1,2) = H_b \cos \omega_3 \cos \omega_4 + H_t \sin \omega_3 \sin \omega_4 \quad . \qquad (59b)$$

The Green's function components (H_b, H_t) are given in (46), and angles (ω_3, ω_4) are shown in Figure 14. In evaluating the integrals in (64), for two given points (y_1, z_1) and (y_2, z_2), one must calculate some geometrical parameters appearing in H_b and H_t. Those calculations lead to the following results

$$r_n = [c_n^2 + y_n^2 + z_n^2 - 2c_n\sqrt{y_n^2 + z_n^2} \cos(\omega_n - \omega_{n+4})]^{1/2} \qquad (60a)$$

$$\phi_n = (\sin \theta_0)^{-1} \sin^{-1} [\sqrt{y_n^2 + z_n^2}\, r_n^{-1} \sin(\omega_n - \omega_{n+4})] \qquad (60b)$$

$$\omega_{n+4} = \tan^{-1}(z_n/y_n) \qquad (60c)$$

$$\omega_{n+2} = \Omega_n + (\pi/2) - \omega_n - \phi_n \sin \theta_0 + (n-1)\phi_0 \sin \theta_0 \qquad (60d)$$

where n = 1 and 2. One may evaluate the integrals in (59a) with the aid of a computer.

*Coordinates (y_2, z_2) here have their origin at the center of slot 2 Figure 14, not at the center of slot 1 as in the cylinder case Figure 6.

Next, consider Y_{12}^t, the part of mutual admittance due to the rays diffracted at the cone tip. Approximate it by

$$Y_{12}^t \simeq T \sin \omega_1 \sin \omega_2 \tag{61}$$

where T is derived in (Golden et al, 1974) and is given by

$$T = \sigma_0 \frac{(a_1 b_1 a_2 b_2)^{1/2}}{30\pi^4 c_1 c_2 \sin \theta_0} \left[\frac{\tan \theta_0}{2\pi}\right]^{1/2} \frac{\sin (kb_1/2) \sin (kb_2/2)}{(kb_1/2)(kb_2/2)}$$

$$\cdot \exp j\left(\frac{\pi}{4} - kc_1 - kc_2\right) \quad . \tag{62}$$

Here σ_0 is the zeroth-order tip diffraction coefficient and is a function of the half-cone angle θ_0. A numerical table of σ_0 for several typical values of θ_0 is given by Golden et al (1974). Those values are fitted by a simple expression, viz.,

$$\sigma_0 = A \exp (jB) \quad , \tag{63}$$

where

$$A = 1.3057\theta_0^{-1} - 1.755\theta + 2.772\theta_0 - 1.459\theta_0^2$$

$$B = 2.7195 + 1.4608\theta_0 - 1.1295\theta_0^2 + 0.6566\theta_0^3 \quad .$$

Both θ and B are in radians. It has been checked that the numerical values of σ_0 calculated from (63) are in excellent agreement with those tabulated in Golden et al (1974).

The final solutions for Y_{12} (total mutual admittance) and Y_{12}^d (partial mutual admittance) are given in (58), (59), and (61). For a given geometry of the slots and cone, the two surface integrals in (59a) are evaluated numerically by choosing an integration grid roughly equal to $0.05\lambda \times 0.05\lambda$. Unless specified otherwise, all numerical computations are based on two identical slots with slot length = 0.5λ and width = 0.2λ.

"Equivalent" cylinder. It has been conjectured by Golden et al (1974) calculating Y_{12}^d (the contribution from the direct rays) approximately, the cone may be replaced by an "equivalent" cylinder with radius

$$R = \frac{1}{2}(c_1 + c_2) \sin \theta_0 \quad . \tag{64}$$

This conjecture has been quantitatively checked out (Lee and Mittra, 1977). The conclusion is that the "equivalent" cylinder gives a good approximation for a small-angled cone, e.g., $\theta_0 = 15^\circ$. However, the error in Y_{12}^d calculated from the "equivalent" cylinder can be as large as 2.5 db for a large-angled cone ($\theta_0 = 30^\circ$, for example).

Comparison with experiments. A set of experimental data on the mutual coupling between two X-band open-ended waveguides (0.9" x 0.4") on a cone was reported by Golden et al (1974). As a function of frequency, measurements were done on the coupling coefficient S_{12}, which is related to Y_{12} through the formula in (12). In Figures 15 and 16, three sets of data are presented: (i) the experimental data; (ii) the theoretical results from the present analysis in which the calculation of Y_{12}^d is based on a cone, e.g., Equation (59); (iii) the theoretical results of Golden et al (1974) in which Y_{12}^d is calculated from the exact modal solution of an "equivalent" cylinder. Several observations can be made. (a) Both theoretical results are in good agreement with the experimental data (with the present result being slightly better). As explained in (59a), the "equivalent" cylinder method works because the cone angles ($\theta_0 \sim 10^\circ$) are small. (b) The peaks and valleys are caused by the interference between Y_{12}^d and Y_{12}^t, which are of comparable magnitudes due to the large angular separations (60.3° and 80°). (c) There exists a slight shift in frequency ($\Delta f/f \approx 3$ percent) between the theoretical and experimental valleys in Figure 15.

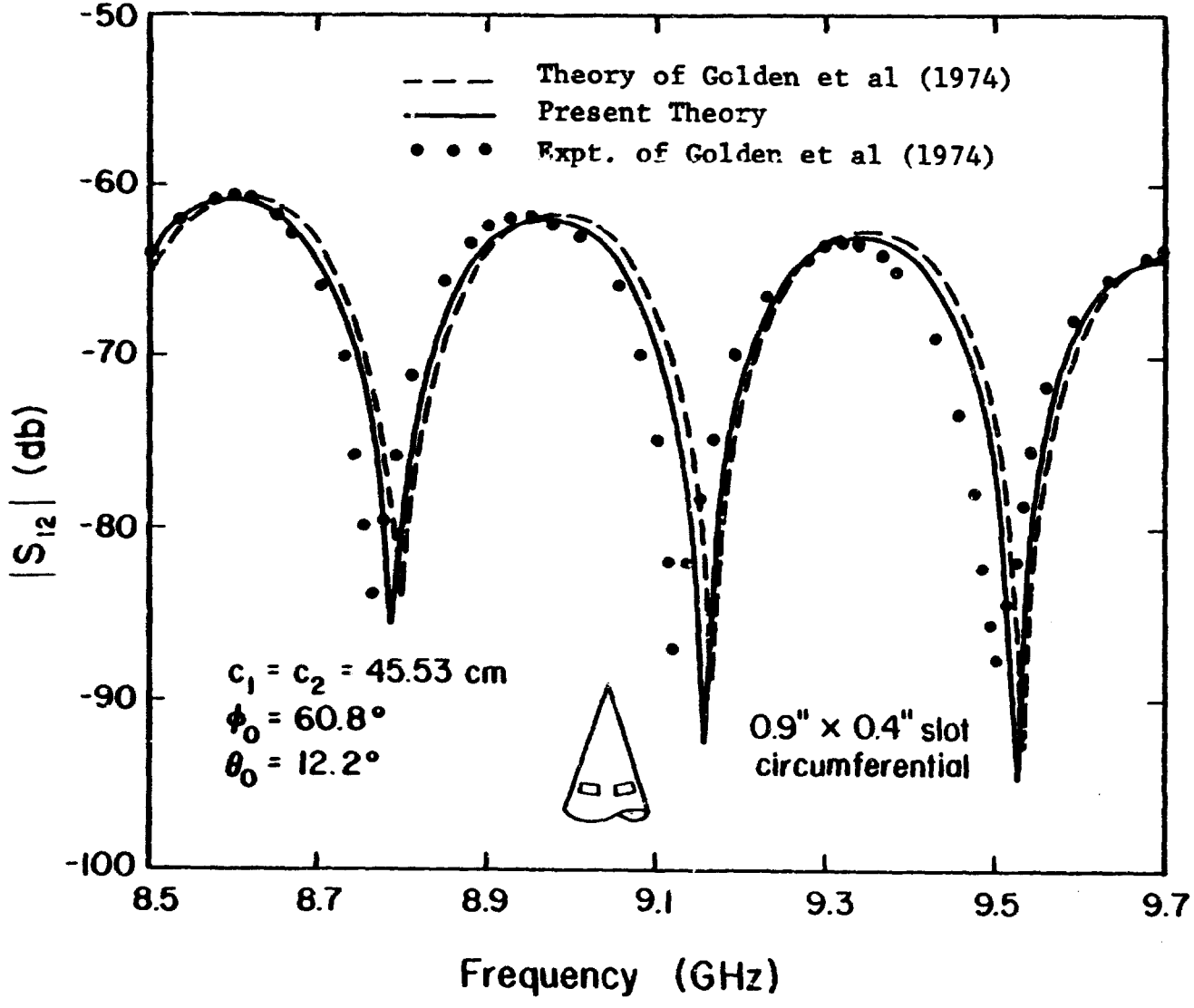

Figure 15. Coupling coefficient S_{12} between two circumferential slots on a cone as a function of frequency.

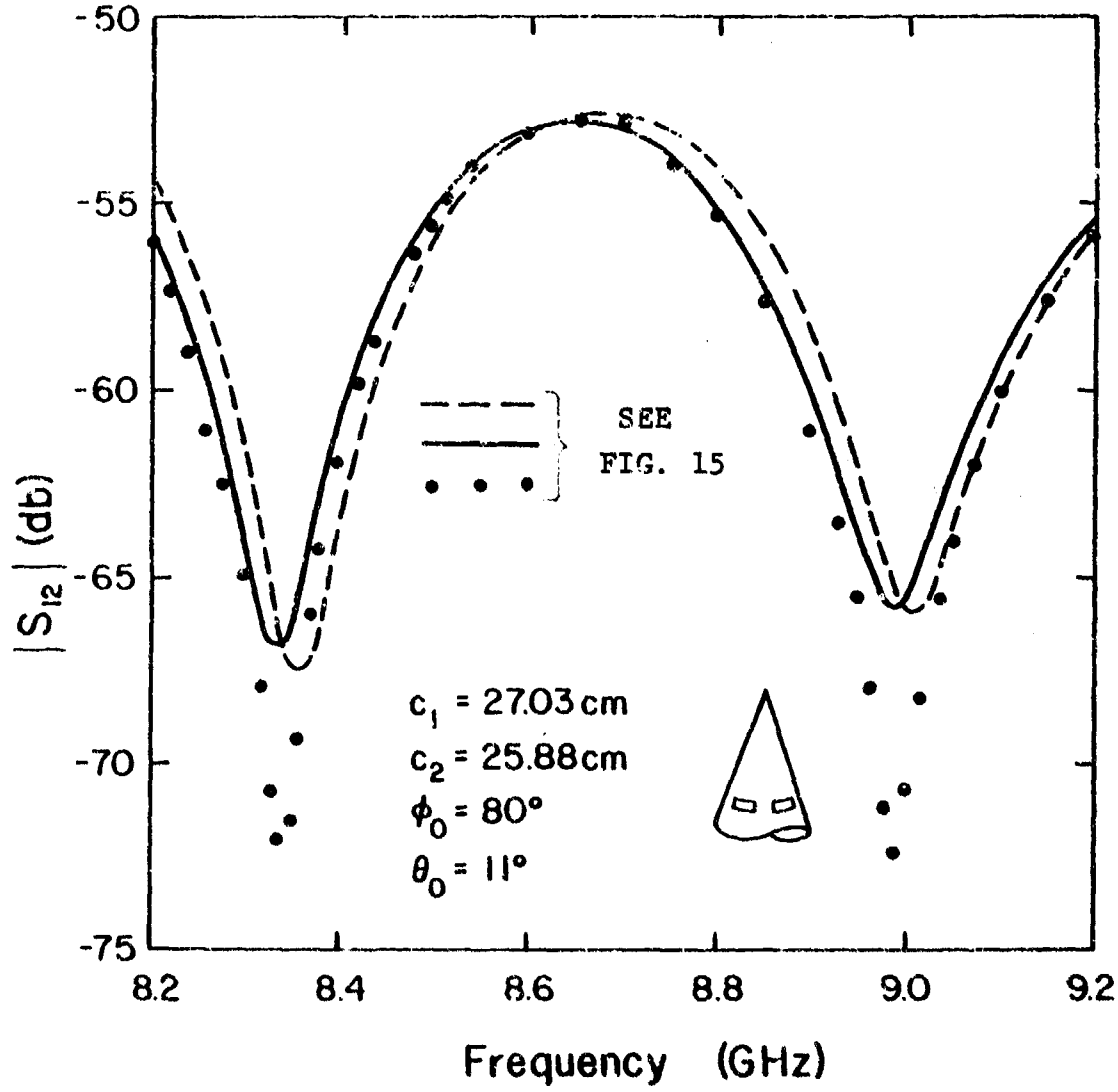

Figure 16. Coupling coefficient S_{12} between two circumferential slots on a cone as function of frequency.

This may be due to a slight phase inaccuracy in Y_{12}^t.

Mutual admittances of circumferential slots. In Figures 17 to 19, Y_{12} and Y_{12}^d for two circumferential slots are displayed as functions of angular separation θ_0 and the radial separation $(c_1 - c_2)$. Note that the effect of Y_{12}^t can modify the curves of Y_{12} in several different ways. When the slots are at the same latitude, Figure 17, the direct coupling is weak. Thus, tip contribution is noticeable even at a small angular separation. As the radial separation is increased, Figure 18, the tip contribution is almost negligible for $\theta_0 < 65^\circ$. When the two slots are widely separated in the radial direction with one slot near the tip, Figure 19, the tip contribution gets stronger, the direct contribution gets stronger, and the direct contribution becomes insensitive to θ_0. Hence, the oscillation on the Y_{12} curve has a much larger period. In fact, there is only a half-"cycle" in the range $0 < \theta_0 < 90^\circ$, and Y_{12} appears to be shifted from Y_{12}^d by a fixed amount.

Effect of slot orientation on mutual admittance. Consider two slots separated by 1 λ along the radial direction. The magnitude of Y_{12} as functions of the slot orientation angles ω_1 and ω_2 is plotted in Figure 20. As expected, the maximum value (-73 db) occurs when both slots are circumferential ($\omega_1 = \omega_2 = 90^\circ$). This value is above 14 db, higher than that when both slots are radial ($\omega_1 = \omega_2 = 0$). The minimum value (-113 db) of Y_{12} occurs when the top slot is radial and the bottom one is circumferential. This result confirms a common belief that the mutual coupling between two orthogonal slots is generally negligible.

5.3.3 Self Admittance of a Slot on a Cylinder or Cone

The formula for calculating mutual admittance Y_{12} in (17) can be used to calculate the self-admittance Y (or the alternative notation Y_{11}), provided that slot 1 coincides with slot 2.

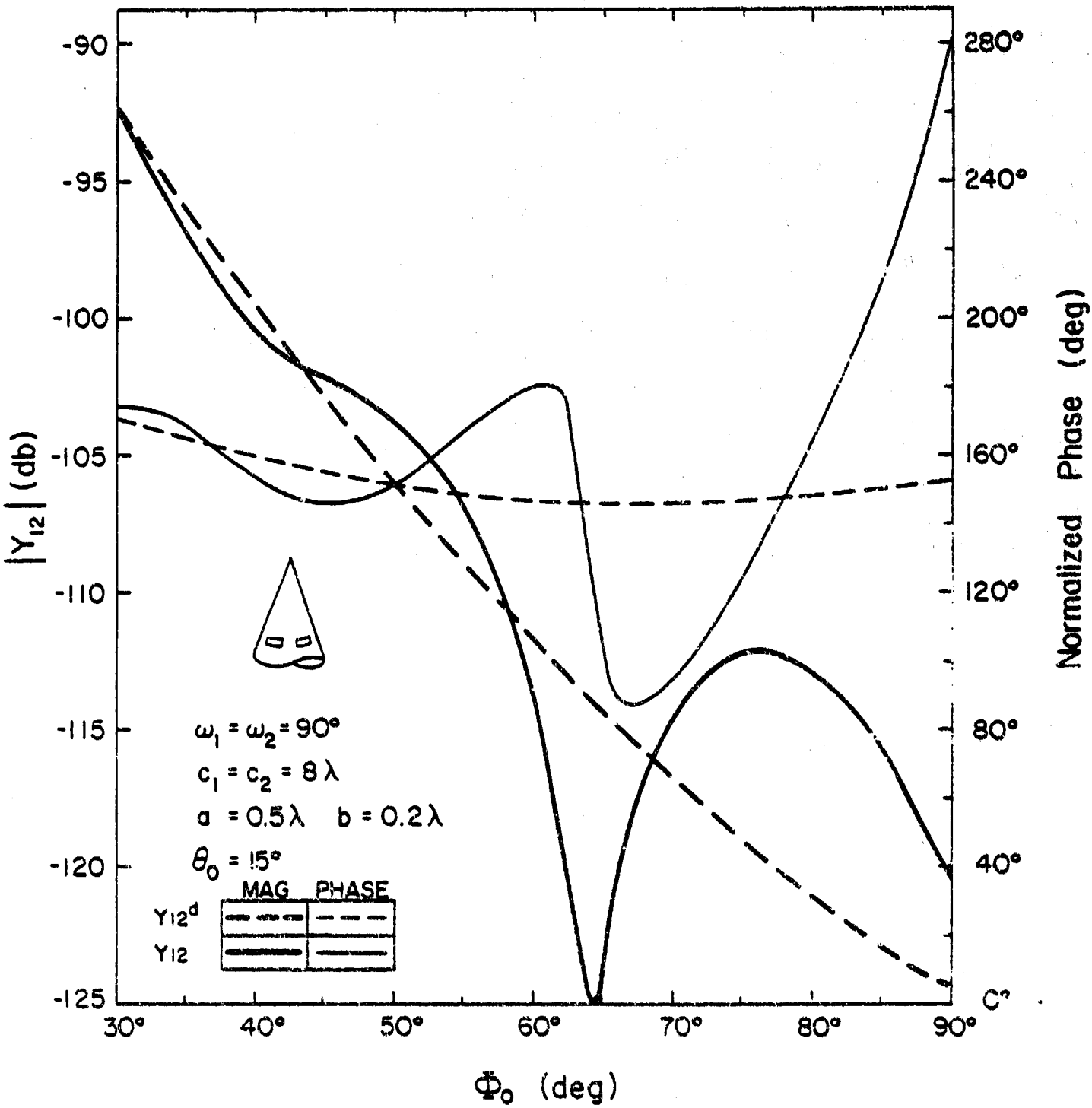

Figure 17. Mutual admittances Y_{12} between two circumferential slots on a cone calculated from GTD solution.

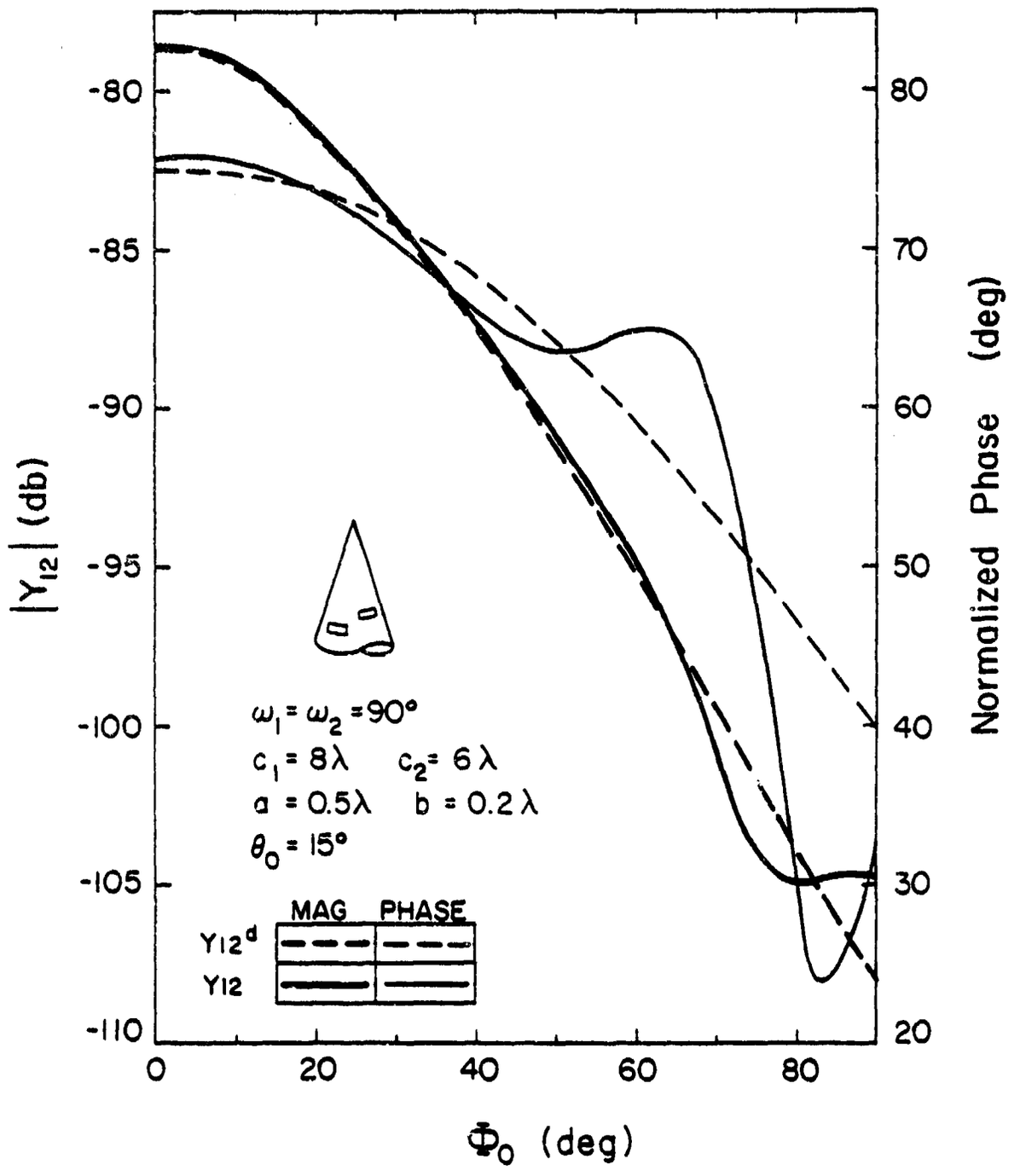

Figure 18. Mutual admittances Y_{12} between two circumferential slots on a cone calculated from GTD solution.

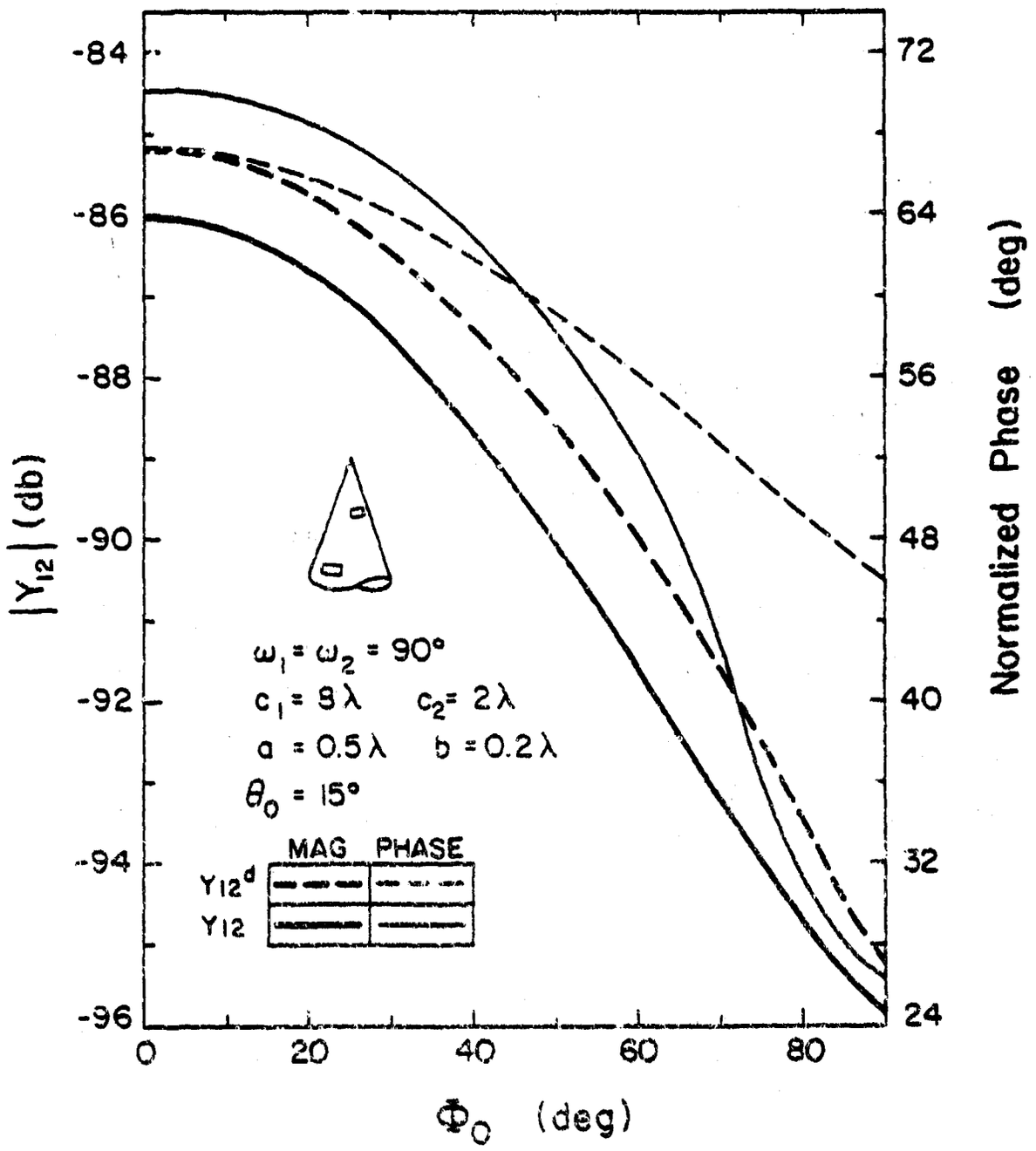

Figure 19. Mutual admittance Y_{12} between two circumferential slots on a cone calculated from GTD solution.

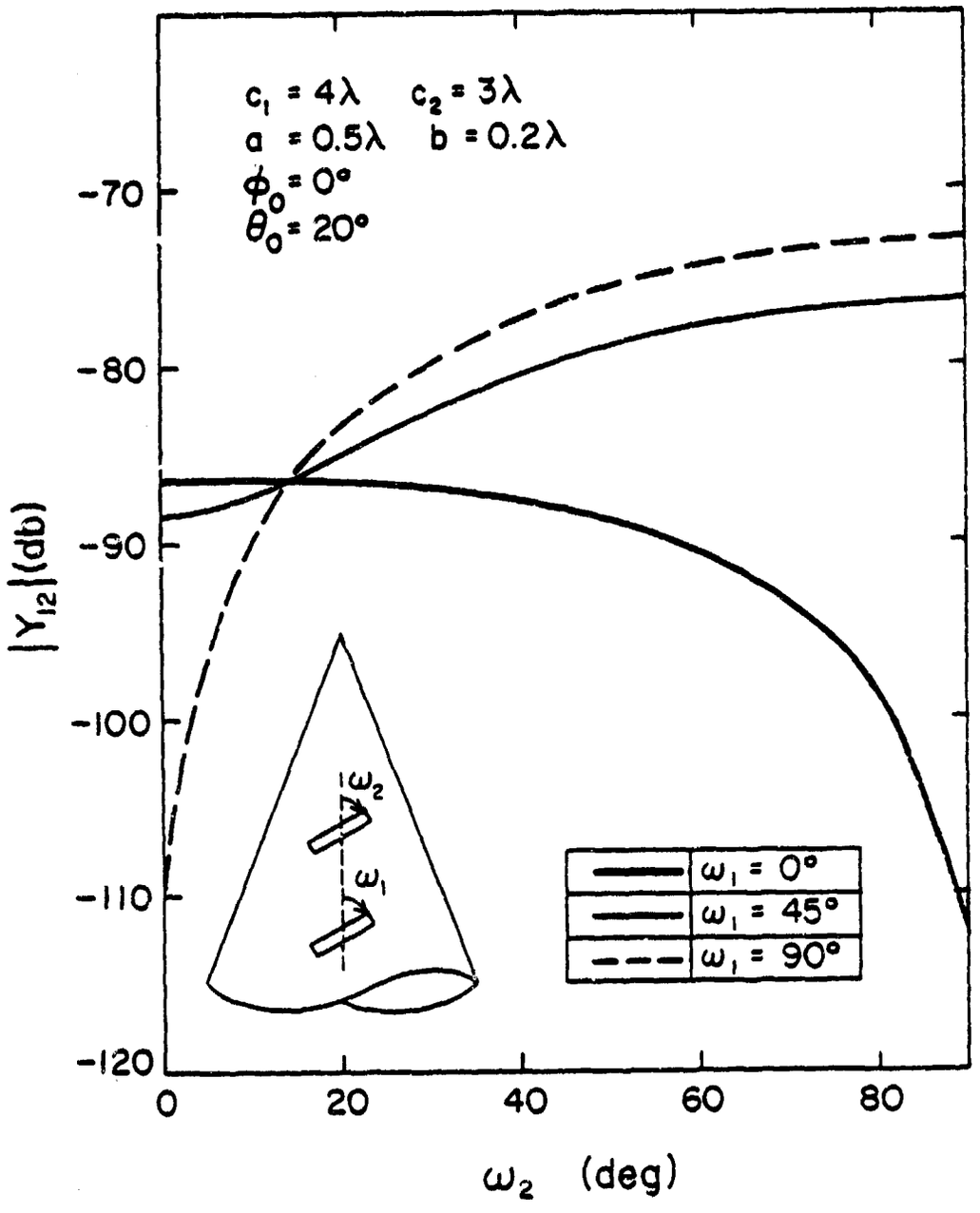

Figure 20. Mutual admittance Y_{12} between two arbitrarily oriented slots on a cone calculated from GTD solution.

However, in the actual numerical evaluation of GTD expressions such as (34), (37), and (59), a mathematical difficulty arises as explained below.

Concentrate on (59) with $a_1 = b_1$, $a_2 = b_2$, $c_1 = c_2$, and $\phi_0 = 0$, which is the direct ray contribution Y^d to the self-admittance of a slot on a cone. This integral is <u>divergent</u>, due to the fact that, as point Q_1 approaches point Q_2, Figure 14, the Green's function in (59b) becomes infinite as

$$g(1,2) \simeq Cs^{-3} \quad , \quad s \to 0 \quad , \tag{65a}$$

where s, defined in (49), is the distance between the two points, and the parameter C is

$$C = \frac{1}{j240\pi^2 k} \left(2 - 3\cos^2 \Omega_1\right) \quad . \tag{65b}$$

It is well-known that the singularity of cubic power is non-integrable with respect to a surface integral. This difficulty can be traced back to the derivation of the Green's function g. Strictly speaking, g is a distribution and can be wrtten as

$$g = D\bar{g} \quad , \tag{66}$$

where D is a second-order differential operator with respect to coordinates of point Q_2, and $\bar{g}$ is the Green's function of a vector potential component. A "legitimate" expression corresponding to (59a) should read

$$Y^d = -\frac{2}{ab}\iint dy_2 dz_2 \left(\cos\frac{\pi y_2}{a}\right) \{D\left[\iint dy_1\, dz_1 \left(\cos\frac{\pi y_1}{a}\right) \bar{g}\right]\} \quad . \tag{67}$$

which is convergent, and Y^d has a well-defined finite value. However, in writing (59a), we have interchanged the differential operator D and the second surface integration operator in (67).

This interchanging is not permissible and, therefore, leads to the divergent integral in (59a).

Since (67) contains a differential operator and is not suitable for numerical evaluation, it is better to work with (59a) provided of course that one can extract the correct finite part from the divergent integral. To this end, rewrite Green's function in (59a) as

$$g = g_0 + g_1 \quad . \tag{68}$$

The first term g_0 in (68) is the Green's function of an infinite ground plane, and is given by the well-known expression, c.f. (25),

$$g_0 = G(s) \left[\cos^2 \Omega_1 + \frac{j}{ks}\left(1 - \frac{j}{ks}\right) (2 - 3 \cos^2 \Omega_1)\right] \quad . \tag{69}$$

Note that, as $s \to 0$, g_0 has exactly the same singular behavior in (65) as g. This is expected, because in the sufficiently small neighborhood of a point source, the cone can be approximated by its tangent plane. The second term $g_1 (g_1 = g - g_0)$ in (68) is the difference between the Green's function of a cone and that of a plane. Near the source, it can be shown from (59a) and (69) that

$$g_1 \approx C_1 s^{-3/2} \quad , \quad s \to 0 \quad , \tag{70a}$$

where

$$C_1 = (1920\bar{R}_t)^{-1} k^{-1/2} \pi^{-3/2} (1 - j) (2 - 3 \sin^2 \Omega_1) \quad . \tag{70b}$$

When (68) is substituted into (59a), the self-admittance Y^d on a cone is decomposed into two components, namely,

$$Y^d = Y_0^d + Y_1^d \quad . \tag{71}$$

The singularity of g_1 at the source point specified in (70) is integrable. Thus, there is no difficulty in evaluating Y_1^d numerically.

The first term Y_0^d is the admittance of a slot on a plane. It is defined by (59a) after replacing g by g_0 in (69). From (23d) and (69), recognize the following identity:

$$g_0 = (1 + \frac{1}{k^2} \frac{\partial^2}{\partial y_2^2}) G(s) \quad . \tag{72}$$

Note that (72) is in the form of (66). Substituting (72) into (59a) and interchanging integration and differentiation operators, one obtains:

$$Y_0^d = - \frac{2}{ab} \iint dy_2 \, dz_2 \cos (\frac{\pi y_2}{a}) \{(1 + \frac{1}{k^2} \frac{\partial^2}{\partial y_2^2})[\iint dy_1 \, dz_1 \cdot \cos (\frac{\pi y_1}{a}) G(s)]\} \quad . \tag{73}$$

The integral in (73) is now convergent, and can be considered as the "finite part" of the divergent integral in (59a). For numerical evaluation, (73) in the space domain is converted to that in the Fourier transform domain. Following Rhodes (1964), it is simplified and the final result reads

$$\mathrm{Re}Y_0^d = \frac{a}{15\pi^4 k} \int_0^k d\alpha \, C(\alpha) \beta \{ \int_0^{\beta b} J_0(t) dt - J_1(\beta b)]\} \quad , \tag{74a}$$

$$\mathrm{Im}Y_0^d = \frac{-a}{15\pi^4 k} \int_0^k d\alpha \, C(\alpha) \beta \left(\int_0^{\beta b} Y_0(t) dt - Y_1(\beta b) - \frac{2}{\pi \beta b} \right) + \frac{2}{\pi} \int_k^\infty d\alpha \, C(\alpha) \gamma \int_0^{\gamma b} K_0(t) dt + K_1(\gamma b) - \frac{1}{\gamma b} \Big] \Big) \quad , \tag{74b}$$

where $\beta = (k^2 - \alpha^2)^{1/2}$, $\gamma = (\alpha^2 - k^2)^{1/2}$, and

$$C(\alpha) = \frac{\cos^2 (\alpha a/2)}{1 - (\alpha a/\pi)^2} \quad . \tag{75}$$

This is no difficulty in evaluating (74) numerically.

In summary, the direct ray contribution of Y^d for self-admittance of a slot on a cone as given in (59a) is divergent, due to an "illegal" interchange of integration and differentiation operators in the derivation process. The (correct) finite part of the divergent integral is given in (71), where Y_0^d is given in (74), and Y_1^d in (59a) after replacing g by g_1. The same difficulty arises in the case of a cylinder, and it is treated by the same procedure as in the case of a cone.

The self-admittance Y of a slot on three types of surfaces has been derived: (i) For an infinite plane, the final solution $Y = Y^d$ is given in (74). (ii) For an infinite cylinder, $Y = Y^d$ is given in (71). For a circumferential slot, Y_1^d is given by the integral in (34) after replacing g_ϕ by $(g_\phi - g_0)$, and recognizing that $\Omega_1 = (\pi/2) - \theta$ and $A_1 = A_2$. For an axial slot, Y_1^d is given by the integral in (37) after replacing g_z by $(g_z - g_0)$, and $\Omega_1 = \theta$ and $A_1 = A_2$. (iii) For an infinite cone, Y has two contributions as described in (58). If one realized that the two slots in Figure 14 are identical, and occupy the same position on the cone, Y^t is given in (61) and Y^d in (71). To calculate Y_1^d, we use (59a) after replacing g by g_1, where g_1 can be gathered from (68), (59b), and (69). Numerical results of Y on the above three surfaces are presented below.

Slot on a plane. As a function of slot length a, we plot (a/2b)Y in Figure 21 for three different values of slot width b. Those curves are practically linear, and can be described for $0.4 \leq (a/\lambda) \leq 0.6$ to a good accuracy by

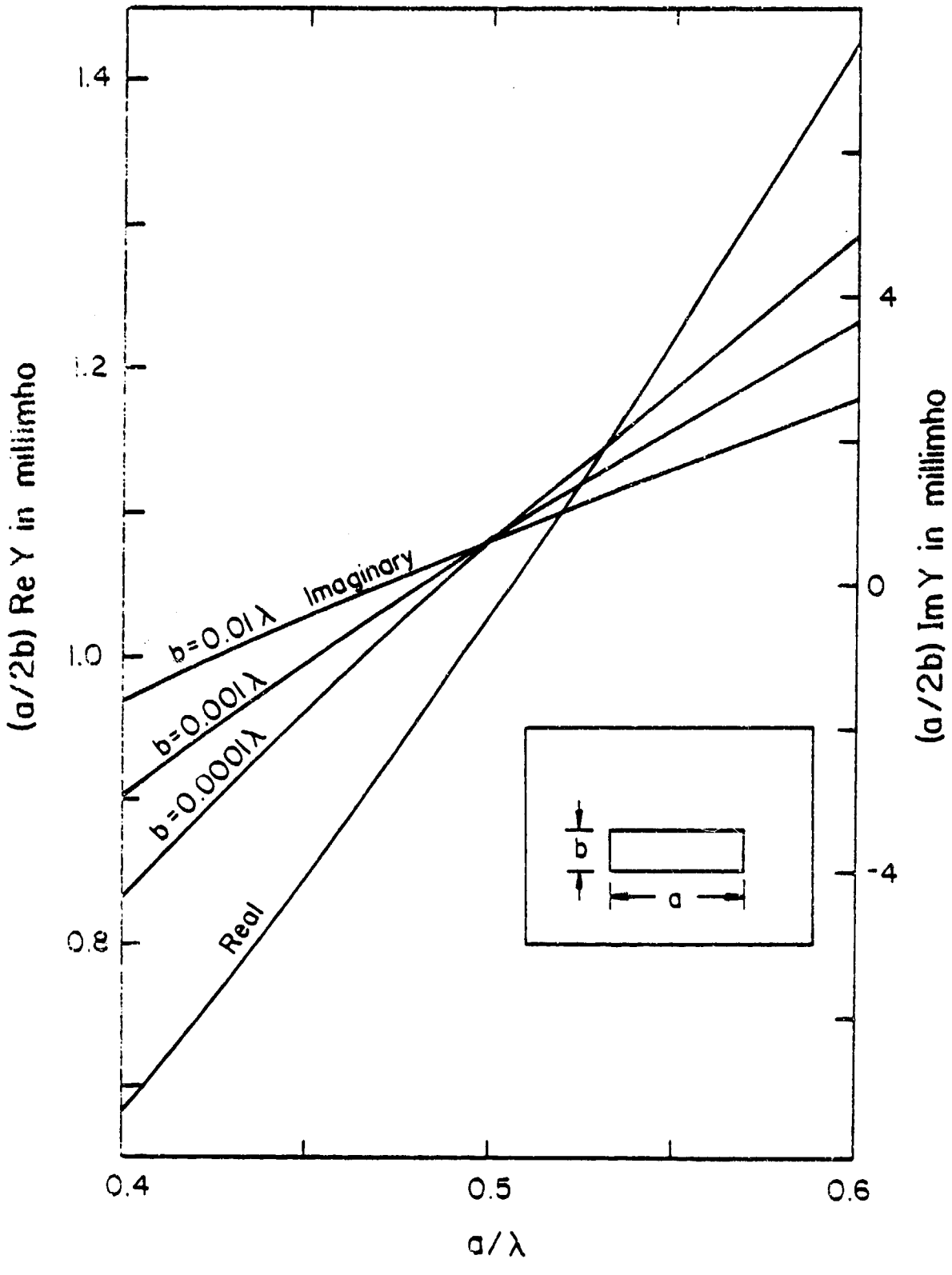

Figure 21. Self-admittance Y of a slot on an infinite plane.

$$Y \approx \frac{2b}{a}\{[\,1.029 + j0.596\,] + (3.75 + jB)(\frac{a}{\lambda} - 0.5)\} \quad \text{millimho} \qquad (76)$$

where B = 44, 33, and 21 for b = .0001, 0.001λ, and 0.01λ, respectively.

Relation to dipole impedance. There is an alternative definition for the (self- or mutual) admittance of a slot. This alternative self-admittance $\bar{Y}$ is related to the present Y by

$$\bar{Y} = (a/2b)Y \quad . \qquad (77)$$

From the duality relation in Maxwell's equations, it can be shown (Jordan and Balmain, 1968, p. 519) that for the special case a = λ/2,

$$\bar{Z} = \frac{1}{4}(120\pi)^2(2\bar{Y}) \quad , \qquad (78)$$

when $\bar{Z}$ is the input impedance of a centrally fed, half-wavelength dipole radiating in the free space (not in a half-space as in the case of a waveguide-fed slot). From (76) through (78), we find that for a half-wavelength dipole,

$$\bar{Z} = 73.12 + j\ 42.36 \text{ ohm} \quad , \qquad (79)$$

which agrees with the results in Rhodes, (1964) and Jordan and Balmain (1968).

Slot on a cylinder. Consider a circumferential slot of dimension 0.9" x 0.4" on an infinitely long cylinder whose radius is 3.8". Figure 22 shows Y calculated by the present GTD solution and that by the exact modal series solution in (Golden et al, 1974). These two solutions are in agreement within 0.5% in magnitude and one degree in phase. Note that, under the "one-mode approximation," the modal series solution is exact. It is amazing that the present GTD solution gives such an accurate result for kR = 18.

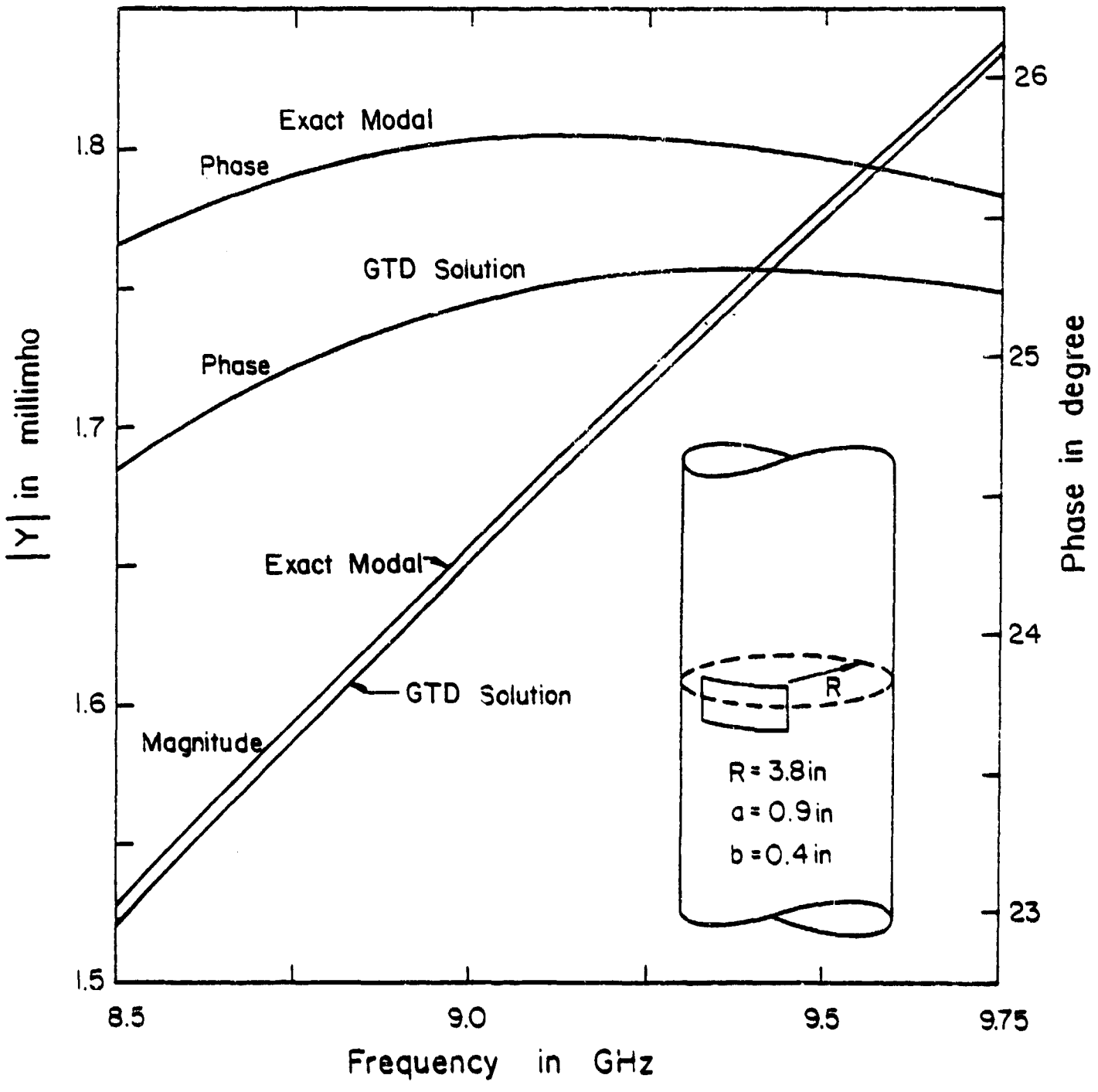

Figure 22. Self-admittance Y of a slot on an infinitely long cylinder.

Slot on a cone: variation with radial distance. In all of the following cone calculations, the slot has the dimensions of $0.5\lambda \times 0.05\lambda$, except when stated otherwise. In Figures 23 and 24, the slot is circumferentially oriented on a cone with $\theta_0 = 30^\circ$, and the variation of Y with the radial distance c is presented. Two effects are observed: (i) As c is increased, the radius $R = c \sin \theta_0$ of the "equivalent" cylinder becomes larger and larger. The magnitude of Y decreases and approaches the asumptotic value of the slot on a plane. (ii) At $c = 2\lambda$, the tip contribution Y^t is less than 1% of the Y , and this contribution diminishes as c increases.

Slot on a cone: variations with cone angle. As θ_0 is increased, the cone surface becomes flatter. Therefore, Y in Figure 25 approaches its value on a plane.

Slot on a cone: variations with slot length. It is interesting to observe from Figure 26 that the minimum values of Y for both the cone and plane cases occur roughly at $a = 0.45\lambda$, not at the resonant length $a = 0.5\lambda$.

Slot on a cone: variation with slot orientation angle. Figure 27, shows that there is about 10% increase in Y as ω varies from 0 (radial slot) to $\pi/2$ (circumferential slot).

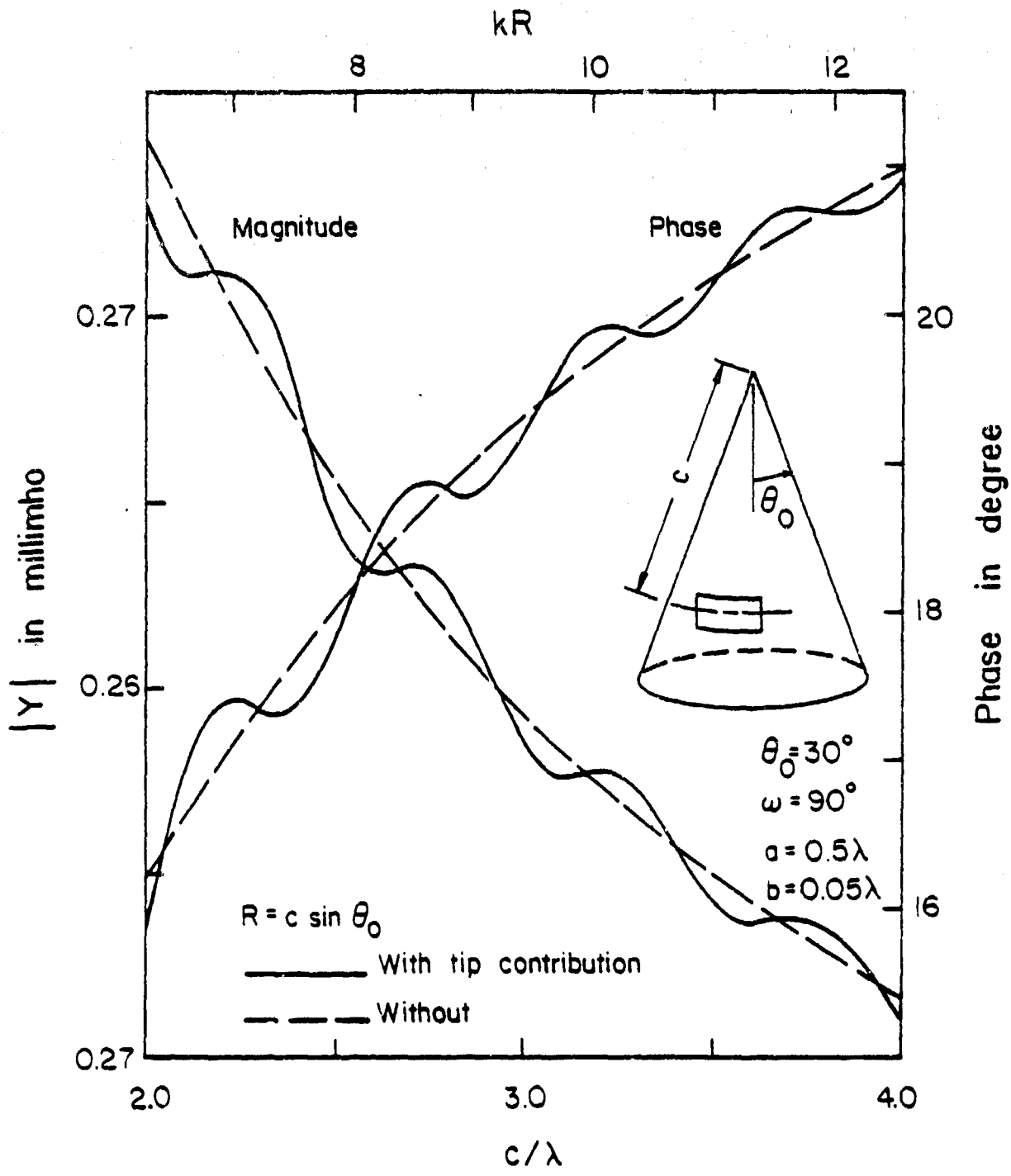

Figure 23. Self-admittance Y of a slot on a cone as a function of radial distance c.

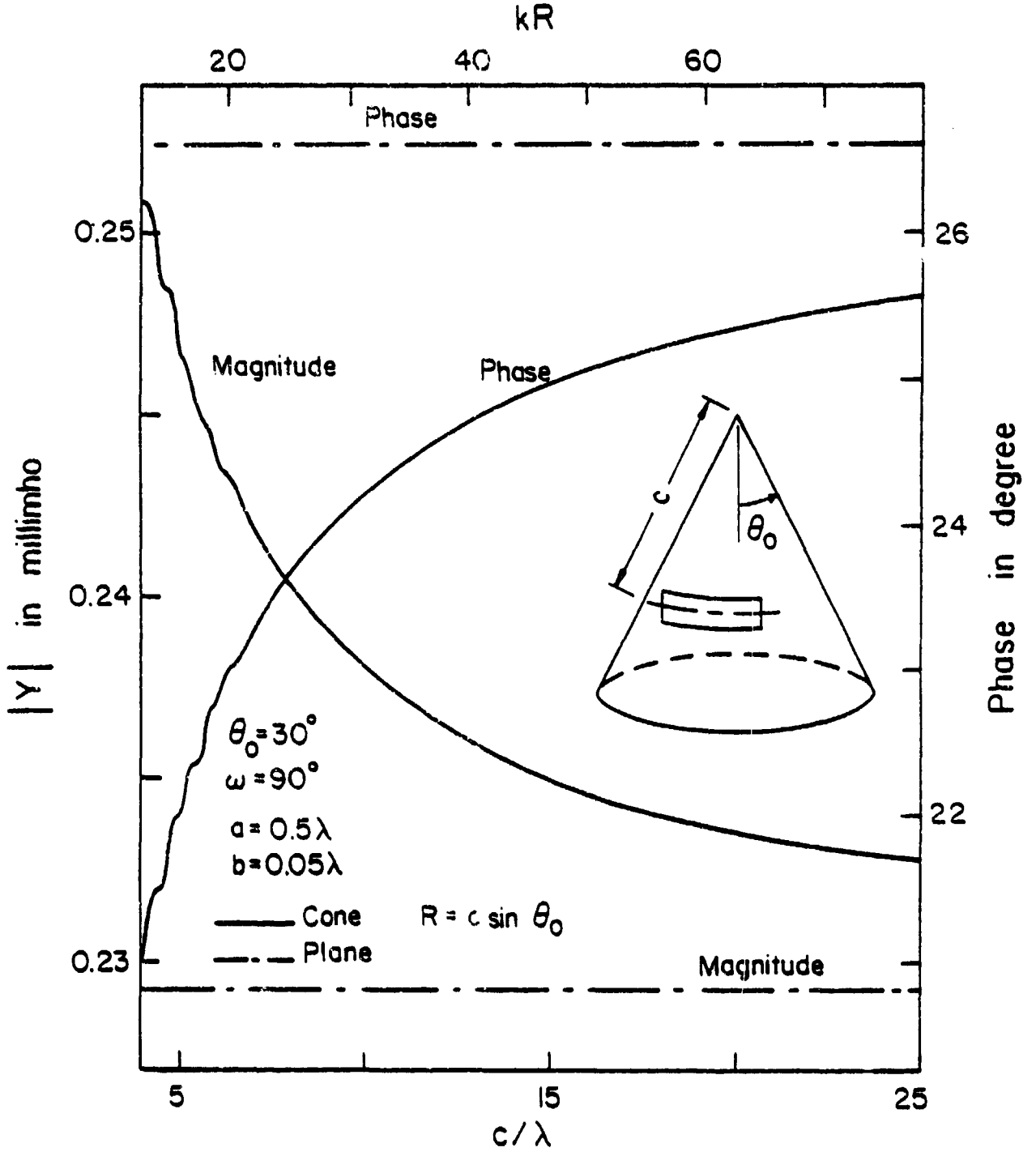

Figure 24. Same as Fig. 23, except with larger radial distance c.

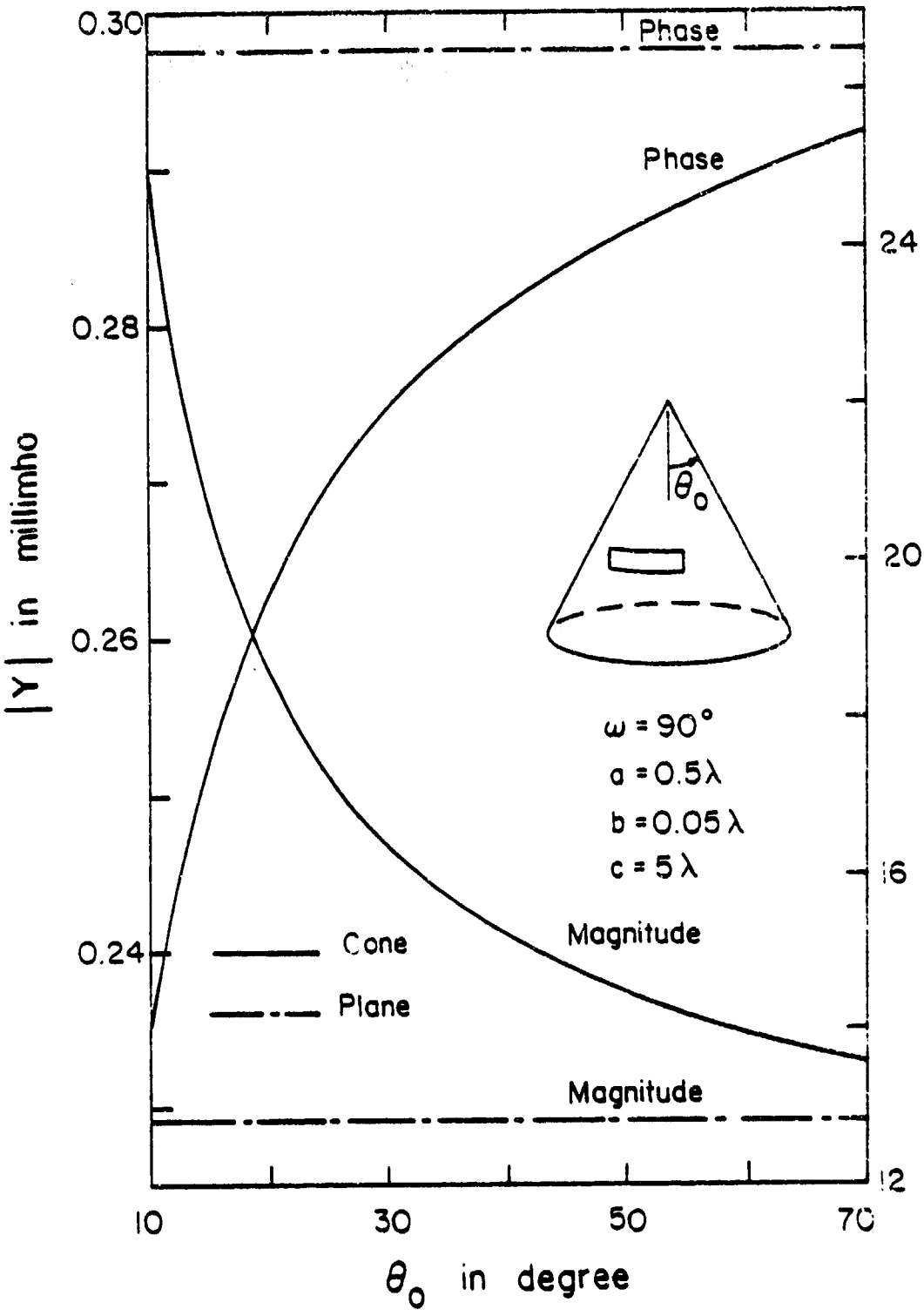

Figure 25. Self-admittance of a slot on a cone as a function of half-cone angle θ_0.

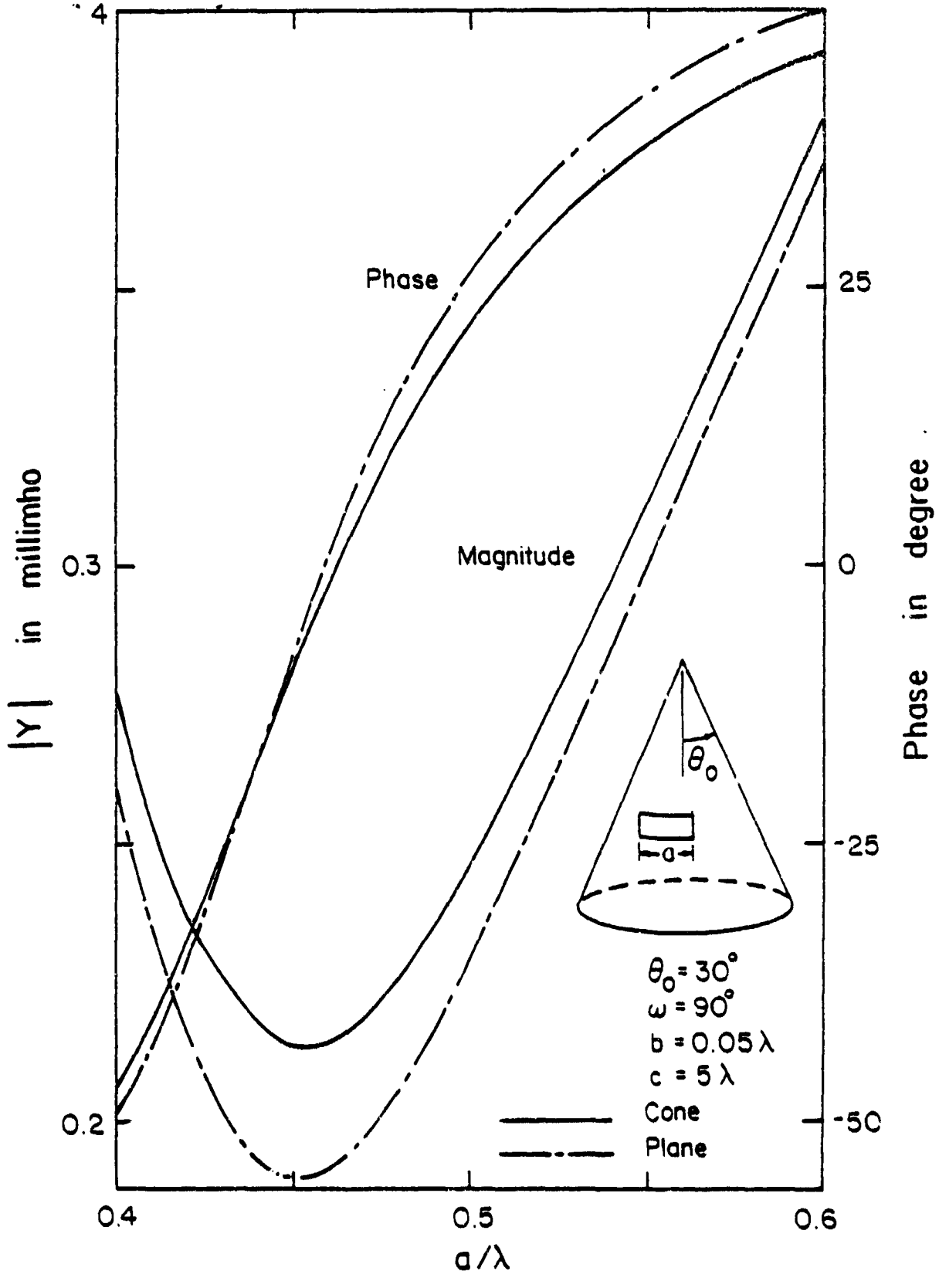

Figure 26. Self-admittance Y of a slot on a cone as a function of slot length a.

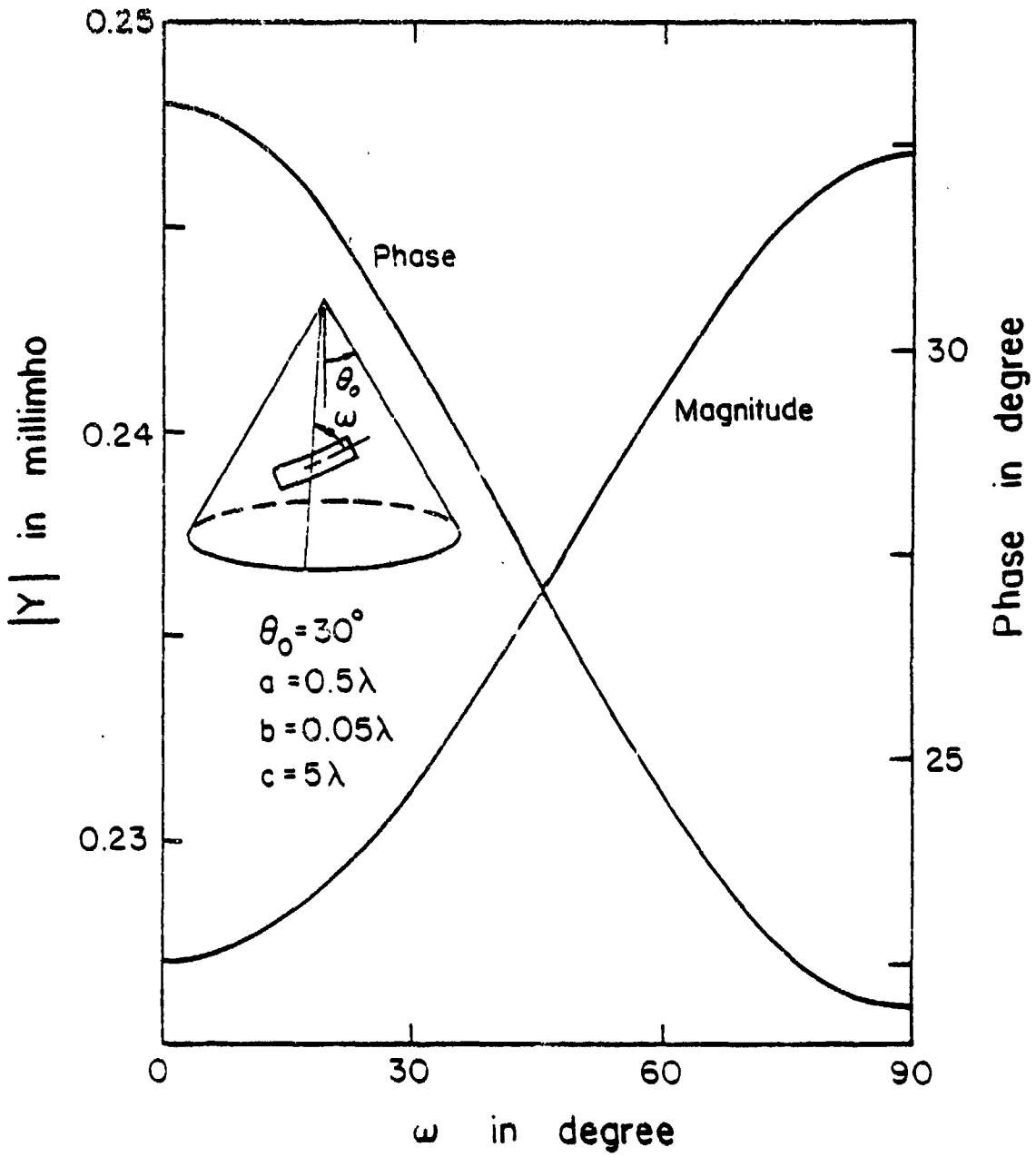

Figure 27. Admittance Y of a slot on a cone as a function of orientation angle ω.

APPENDIX
FOCK FUNCTIONS

In this Appendix some useful formulas of the functions $w_1(t)$, $w_2(t)$, $v(\xi)$, $u(\xi)$, and $v_1(\xi)$ are defined and listed. These functions are commonly known as Fock functions.

Definition: For a complex t and a real ξ

$$w_1(t) = \frac{1}{\pi} \int_{\Gamma_1} dz \exp\left[tz - \frac{1}{3} z^3 \right] \tag{A-1}$$

$$w_2(t) = \frac{1}{\pi} \int_{\Gamma_2} dz \exp\left[tz - \frac{1}{3} z^3 \right] = w_1^*(t) \tag{A-2}$$

$$v(\xi) = \frac{1}{2} e^{j\pi/4} \xi^{1/2} \frac{1}{\sqrt{\pi}} \int_{\Gamma_1} \frac{w_2(t)}{w_2'(t)} e^{-j\xi t} dt \tag{A-3}$$

$$u(\xi) = e^{j3\pi/4} \xi^{3/2} \frac{1}{\sqrt{\pi}} \int_{\Gamma_1} \frac{w_2'(t)}{w_2(t)} e^{-j\xi t} dt \tag{A-4}$$

where integration contour $\Gamma_1(\Gamma_2)$ goes from ∞ to 0 along the line Arg $z = -2\pi/3$ $(+2\pi/3)$ and from 0 to ∞ along the real axis. Because of different time conventions, $w_1(w_2)$ above is equal to $w_2(w_1)$ defined in (Fock, 1965).

Residue series representation: For real positive ξ,

$$v(\xi) = e^{-j\pi/4}\sqrt{\pi}\,\xi^{1/2} \sum_{n=1}^{\infty} (t_n')^{-1} e^{-j\xi t_n'} \tag{A-6}$$

$$u(\xi) = e^{j\pi/4}2\sqrt{\pi}\,\xi^{3/2} \sum_{n=1}^{\infty} e^{-j\xi t_n} \tag{A-7}$$

$$v_1(\xi) = e^{j\pi/4}2\sqrt{\pi}\,\xi^{3/2} \sum_{n=1}^{\infty} e^{-j\xi t_n'} \tag{A-8}$$

$$v'(\xi) = \frac{1}{2} e^{-j\pi/4}\sqrt{\pi}\,\xi^{-1/2} \sum_{n=1}^{\infty} (1 - j2\xi t_n')(t_n')^{-1} e^{-j\xi t_n'} \tag{A-9}$$

$$u'(\xi) = e^{j\pi/4}3\sqrt{\pi}\,\xi^{1/2} \sum_{n=1}^{\infty} \left[1 - j\,\frac{2}{3}\,\xi t_n\right] e^{-j\xi t_n} \quad . \tag{A-10}$$

where $t_n = |t_n| \exp(-j\pi/3)$, $t'_n = |t'_n| \exp(-j\pi/3)$, and

n	$\lvert t_n \rvert$	$\lvert t_n' \rvert$
1	2.33811	1.01879
2	4.08795	3.24820
3	5.52056	4.82010
4	6.78671	6.16331
5	7.99413	7.37218

n	$\lvert t_n \rvert$	$\lvert t_n' \rvert$
6	9.02265	8.48849
7	10.04017	9.53545
8	11.00852	10.52766
9	11.93602	11.47506
10	12.82878	12.38479

Small argument asymptotic expansion: For real positive ξ and $\xi \to 0$,

$$v(\xi) \sim 1 - \frac{\sqrt{\pi}}{4} e^{j\pi/4}\xi^{3/2} + \frac{7j}{60}\xi^3 + \frac{7\sqrt{\pi}}{512} e^{-j\pi/4}\xi^{9/2} - 4.141 \times 10^{-3}\xi^6 + \ldots \quad \text{(A-11)}$$

$$u(\xi) \sim 1 - \frac{\sqrt{\pi}}{2} e^{j\pi/4}\xi^{3/2} + \frac{5j}{12}\xi^3 + \frac{5\sqrt{\pi}}{64} e^{-j\pi/4}\xi^{9/2} - 3.701 \times 10^{-2}\xi^6 + \ldots \quad \text{(A-12)}$$

$$v_1(\xi) \sim 1 + \frac{\sqrt{\pi}}{2} e^{j\pi/4}\xi^{3/2} - \frac{7j}{12}\xi^3 - \frac{7\sqrt{\pi}}{64} e^{-j\pi/4}\xi^{9/2} + 4.555 \times 10^{-2}\xi^6 + \ldots \quad \text{(A-13)}$$

$$v'(\xi) \sim \frac{3\sqrt{\pi}}{8} e^{-j3\pi/4}\xi^{1/2} + \frac{7j}{20}\xi^2 + \frac{63\sqrt{\pi}}{1024} e^{-j\pi/4}\xi^{7/2} - 2.485 \times 10^{-2}\xi^5 + \ldots \quad \text{(A-14)}$$

$$u'(\xi) \sim \frac{3}{4}\sqrt{\pi}\, e^{-j3\pi/4}\xi^{1/2} + \frac{5j}{4}\xi^2 + \frac{45\sqrt{\pi}}{128} e^{-j\pi/4}\xi^{7/2} - 2.221 \times 10^{-1}\xi^5 + \ldots \quad \text{(A-15)}$$

Numerical evaluation: For $\xi \geq \xi_0$, the residue series representation with the first ten terms in the summation can be used. For $\xi \geq \xi_0$, the small argument asymptotic expansion with the first five terms can be used. It has been indicated by Chang et al (1976) that the smoothest crossover is obtained if $\xi_0 = 0.6$. In the present study, ξ_0 has been set to 0.7, where the difference in the two representations is less than 0.1% in magnitude and 0.9° in phase.

AXIAL TEST CASE

Inputs

XK	= 6.28319	Y11	= 1
AA	= .2	PHI	= 0
BB	= .5	ZO	= 8
IPA	= 3	RADIUS	= 2
PIB	=14		

Outputs

Y12	= .6595E - 6	/-179.21
DB	= -.12362E3	
NORM PHASE	= - 179.21	

CIRCUMFERENTIAL TEST CASE

Inputs

XK	= 6.28319	Y11	= 1
AA	= .5	PHI	= 30
AB	= .2	ZO	= 0
IPA	= 14	RADIUS	= 2
IPB	= 1		

Outputs

Y12	= .1340E - 5	/155.34
DB	= - .11745E3	
NORM PHASE	= 172.34	

```
C       MAIN PROGRAM SHOULD INCLUDE THE FOLLOWING
        IMPLICIT COmPLEX C H Z
        DIMENSION TN(10),TNPI(10)
        REAL Z0,MAG
        COMMON PI TZ1,TZ2,TY1,TY2,R,THETHA
        COMMON /DATA1/ TN,TNPI,RHO,C1,C2,F2,IOP
        COMMON /DATA2/ A0,B0,Z0,Y0
        DATA TN/2.33811,4.08795,5.52156,6.78671,7.99417,
     1  9.02265,10.04017,11.00852,11.93602,12.82878/
        DATA TNPI/1.01879,3.24820,4.82010,6.16331,7.37218,
     1  8.48849,9.53545,10.52766,11.47506,12.38479/
C       INPUT PARAMETERS HERE
C       FOR AXIAL SLOT SET:
        A=BB
        B=AA
        IJ=2
        A0=B*XK
        B0=A*XK
C       FOR CIRCUMFERENTIAL SLOT SET:
        A=AA
        B=BB
        IJ=1
        A0=A*XK
        B0=B*XK
C       FOLLOWING FOR BOTH CASES
        ZY1=CMPLX(Y11,0.)
C       MAY LOOP OVER Z0,RADIUS,PHI
        PHI0=PHI
        WIDTH1=A0/IPA
        WIDTH2=B0/IPB
        C1=CEXP(CMPLX(0.,-PI/3))
        C2=CEXP(CMPLX(0.,PI/4))
        F2=SQRT(PI)
        Y1=-.5*(A0-WIDTH1)
        Z1=-.5*(B0-WIDTH2)
        RHO=RADIUS*XK
        Z0=Z*XK
        Y0=RHO*PI*PHI/180
        IF (PHI.EQ.0) Y0=.001
        Y=Y0/XK
        Y2=Y0-Y1
        Z2=Z0-Z1
        DO 80 K=1,IPA
        TY1=Y1+K*WIDTH1
        DO 90 L=1,IPB
        TZ1=Z1+L*WIDTH2
        DO 100 M=1,IPA
        TY2=Y2+M*WIDTH1
        DO 110 N=1,IPB
        TZ2=Z2+N*WIDTH2
        R=SQRT((TY2-TY1)**2+(TZ2-TZ1)**2)
        THETHA=ATAN2((TZ2-TZ1),(TY2-TY1))
```

```
      IOP=1
      CALL CYLIND(IJ,ZSUM)
110   CONTINUE
100   CONTINUE
90    CONTINUE
80    CONTINUE
      ZY2=-2*ZSUM*(WIDTH1*WIDTH2)**2/(A0*B0)
      MAG=CABS(ZY2)
      PHASE=ATAN2(AIMAG(ZY2),REAL(ZY2))*180/PI
      ZEXPON=CEXP(CMPLX(0.,SQRT(Y0*Y0+Z0*Z0)))
      ZPROD=ZY2*ZEXPON
      PHN=ATAN2(AIMAG(ZPROD),REAL(ZPROD))*180/PI
      DB=20*ALOG10(CABS(ZY2/ZY1))
C     OUTPUT RESULTS AS DESIRED
      END
```

```
      SUBROUTINE CYLIND(IJ,ZSUM)
      IMPLICIT COMPLEX(C,H,Z),REAL(A-B,D-G,P-Y)
      REAL Z0,KA
      REAL TN(10),TNPI(10)
      COMMON PI,TZ1,TZ2,TY1,TY2,R,THETHA
      COMMON/CF/CVF,CUF,CV1F,CVPF,CUPF
      COMMON/DATA1/TN,TNPI,RHO,C1,C2,F2,IOP
      COMMON/DATA2/A,B,Z0,Y0
      ZGR=(0.,-1.)*CEXP(CMPLX(0.E0,-R))/(240.*R*PI**2)
      ANGLE=ATAN2(ABS(TZ2-TZ1),ABS(TY2-TY1))*180./PI
      IF(ANGLE.LT.89.99) GO TO 10
      IT=1
      THETHA=PI*89.99/180.
      ZW=(0.,1.)/R+CEXP(CMPLX(0.E0,-PI/4.E0))*SQRT(PI*R/2.)/RHO
10    RHOG=RHO/COS(THETHA)**2
      KA=R*ABS((1./(2.*RHOG**2))**(1./3.))
      IF(KA.LT.0.7) GO TO 20
      CALL FOCK(KA)
      GO TO 30
20    CALL FOCK1(KA)
30    IF(I.EQ.1) GO TO 40
      ZW=(0.,1.)*(1./COS(THETHA)**2)/R*(CUF-CV1F*SIN(THETHA)**2)
40    GO TO (21,22,23),IOP
21    ZHB1=CMPLX(1.E0,-1./R)*CVF
      ZHB2=CUF/R**2
      ZHB3=(0.,1.)*CVPF/(SQRT(2.E0)*RHOG)**(2./3.)
      ZHB4=(0.,1.)*(1./(SQRT(2.E0)*RHOG))**(2./3.)*CUPF*TAN(THETHA)**2
      HB=ZGR*(ZHB1-ZHB2+ZHB3+ZHB4)
      ZTM1=(0.,1.)*CUPF/(SQRT(2.E0)*RHOG)**(2./3.)
      HT=(0.,1.)*ZGR/R*(CVF+CMPLX(1.E0,-2./R)*CUF+ZTM1)
      HZ=HB*COS(THETHA)**2+HT*SIN(THETHA)**2
      HPHI=HB*SIN(THETHA)**2+HT*COS(THETHA)**2
      GO TO 500
22    HB=ZGR*CVF
      HT=(0.,1.)*ZGR*CUF/R
      HZ=HB*COS(THETHA)**2+HT*SIN(THETHA)**2
      HPHI=HB*SIN(THETHA)**2+HT*COS(THETHA)**2
      GO TO 500
23    ZTM2=(0.,1.)*(1.-3.*SIN(THETHA)**2)/R
      HZ=ZGR*CVF*(COS(THETHA)**2+(0.,1.)*(2.-3.*COS(THETHA)**2)/R)
      HPHI=ZGR*(CVF*(SIN(THETHA)**2+ZTM2)+ZW)
500   ZGREEN=HPHI
      IF(IJ.EQ.2) ZGREEN=HZ
      FACTOR=COS(PI*TY1/A)*COS(PI*(TY2-Y0)/A)
      IF(IJ.EQ.2) FACTOR=COS(PI*TZ1/B)*COS(PI*(TZ2-Z0)/B)
      ZSUM=ZSUM+FACTOR*ZGREEN
      RETURN
      END
```

```
      SUBROUTINE FOCK(X)
      IMPLICIT COMPLEX (C,Z),REAL(A-B,D-H,P-Y)
      REAL TN(10),TNPI(10)
      COMMON/CF/CVF,CUF,CV1F,CVPF,CUPF
      COMMON FI,TZ1,TZ2,TY1,TY2,R,THETHA
      COMMON/DATA1/TN,TNPI,RHO,C1,C2,F2,IOF
      F1=SQRT(X)
      F3=X**(3./2.)
      CVF=0.
      CUF=0.
      CV1F=0.
      CVPF=0.
      CUPF=0.
      DO 20 N=1,10
      ZTN=TN(N)*C1
      ZTNPI=TNPI(N)*C1
      C3=CEXP(CMPLX(0.E0,-X)*ZTNPI)
      C4=CEXP(CMPLX(0.E0,-X)*ZTN)
      CVF=CVF+C3/ZTNPI
      CV1F=CV1F+C3
      CVPF=(1.E0-CMPLX(0.E0,2*X)*ZTNPI)*C3/ZTNPI+CVPF
      CUPF=(1.E0-CMPLX(0.E0,2*X/3.)*ZTN)*C4+CUPF
20    CONTINUE
      CVF=F2*F1*CVF/C2
      CUF=2.*F2*F3*C2*CUF
      CV1F=2.*F2*F3*C2*CV1F
      CVPF=F2*CVPF/(2.*F1*C2)
      CUPF=3.*F2*F1*C2*CUPF
      RETURN
      ENTRY FOCK1
      F1=SQRT(X)
      F3=X**3
      Z1=F2*C2*SQRT(F3)
      Z2=CMPLX(0.E0,1.E0/60.)*X**3
      Z3=F2*X**(9./2.)/(C2*64.)
      F4=F3**2
      CVF=1.E0-Z1/4.+7*Z2+7.*Z3/8.-4.141D-3*F4
      CUF=1.E0-Z1/2.+25.*Z2+5.*Z3-3.701D-2*F4
      CV1F=1.E0+Z1/2.-35.*Z2-7.*Z3+4.555D-2*F4
      CVPF=3.*F2*F1/(8.*C2**3)+21.*Z2/X+63*Z3/(16.*X)-2.485D-2*F4/X
      CUPF=3.*F2*F1/(4.*C2**3)+CMPLX(0.E0,5.E0/4.E0)*X**2+45.*Z3/(2*X)
     1  -2.221D-1*F4/X
      RETURN
      END
```

CHAPTER 6

CONICAL ARRAY EXPERIMENTS

6.0 INTRODUCTION

The Hughes Aircraft Company conformal array program for Navair culminated in a conical array test bed. This experimental measurement program was designed to validate the theoretical calculations and to explicate features of cone diffraction. The array consisted of a conical structure with crossed slot radiators fed by a stripline feed network that provided controllable amplitude and phase excitations of each arm of the crossed slots. For ease of design and construction the frequency of operation was selected in the S-band region. The actual frequency of operation was 3.185 GHz. The array is described in the following sections. See bibliography for HAC reports; also Villeneuve et al (1974).

Other work on the care and feeding of conformal arrays includes ring arrays at HF (Longstaff and Davies, 1968), scanning of ring arrays via local oscillator phase (Davies, 1965; Davies and McCartney, 1965; Fenby and Davies, 1968), scanning of ring arrays via Rotman or Butler beam forming network (Davies, 1965; Sheleg, 1968; Sheleg, 1973; Skahill and White, 1975). Lens feeds for ring arrays use an R-2R lens (Boyns et al, 1968; Boyns et al, 1970), and a geodesic lens (Holley et al, 1974). Other conformal array hardware includes a wrap around microstrip array (Munson, 1974), a small array on a cone (Thiele and Donn, 1974), measurement of mutual admittance of slots on a cone (Golden et al, 1943), a TACAN array with space harmonics (Christopher, 1974; Shestag, 1974), a cylindrical despun microstrip array using switches (Gregorwich, 1974), a spherical retrodirective array (Rutz-Philipp, 1964), the dome antenna which is a hemispherical bootlace lens, (Schwartzman & Stangel, 1975) and finally a survey of rotationally symmetric arrays (Provencher, 1972).

6.1 Feed Network

The feed network is a 76-way variable power divider* with independently variable amplitude and phase control at each output and is capable of feeding 38 variable polarization radiators, although only 37 such radiators were actually used in the experiment. It is built in modular form and consists of 5 five-way variable power dividers feeding 19 four-way power dividers whose power division and phase shifts are variable. The networks are fabricated in stripline using one-eighth inch ground plane spacings. Semi-rigid coaxial lines 0.141 inch in diameter are used as interconnections between modules as well as between the feed network and the radiating elements. The arrangements of the modules are shown in Figures 1 and 2. They consist of combinations of quadrature hybrids. By adjusting the lengths of the open circuited coaxial stubs the amplitudes and phases of the element excitations can be arbitrarily adjusted. Figures 3 and 4 are photographs of the physical layout of the units. Figure 5 is a schematic of how the units are interconnected.

*For a description of VPD, see Teeter and Bushore (1957), and Vaillancourt (1958).

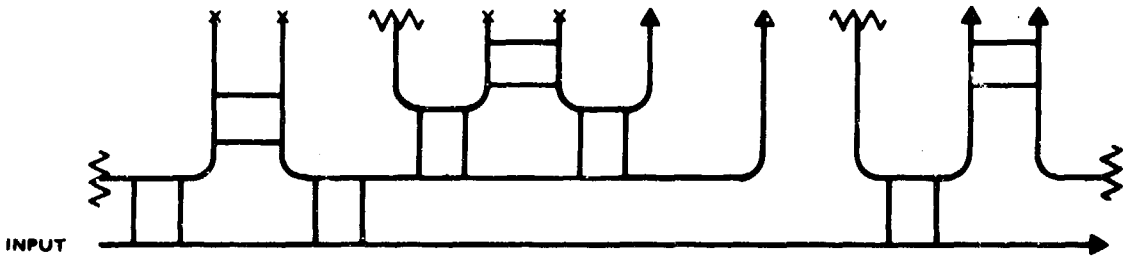

LEGEND:

3DB HYBRID

X OPEN CIRCUITED STUBS FOR AMPLITUDE CONTROL

OUTPUT LINES

Fig.1 Variable power divider module.

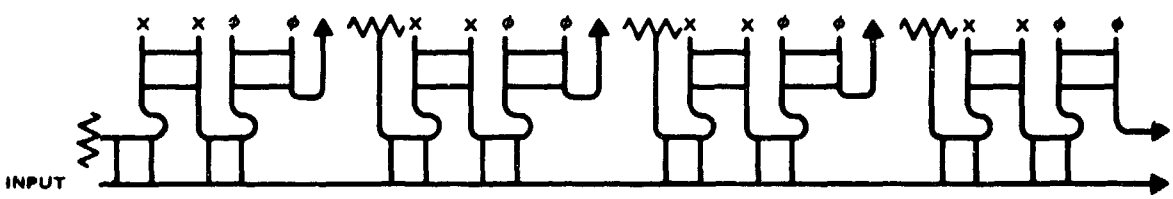

LEGEND:

3DB HYBRID

X OPEN CIRCUITED STUBS FOR AMPLITUDE CONTROL

ϕ OPEN CIRCUITED STUBS FOR PHASE CONTROL

OUTPUT LINES

Fig.2 Amplitude and phase control module.

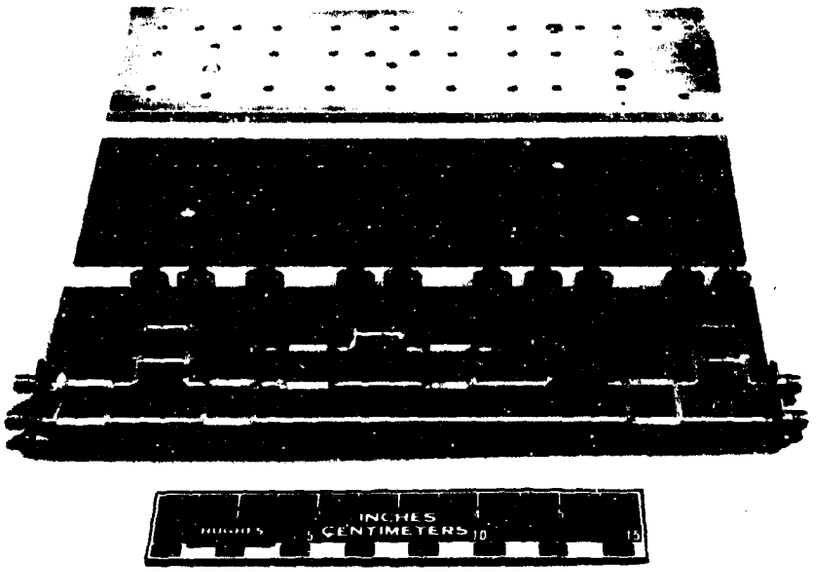

Fig. 3 Physical layout of power divider module (4R-53937).

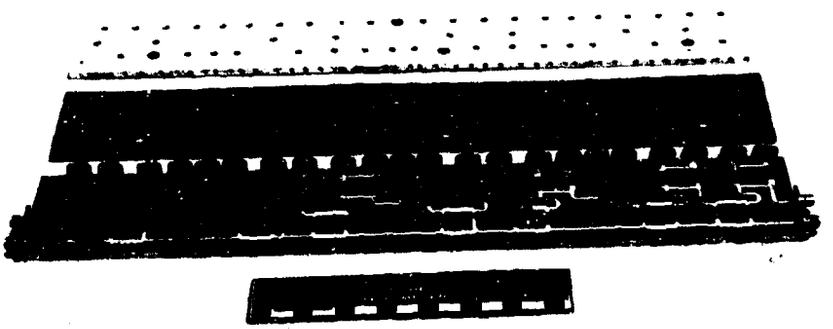

Fig. 4 Physical layout of amplitude and phase control module (4R-53941).

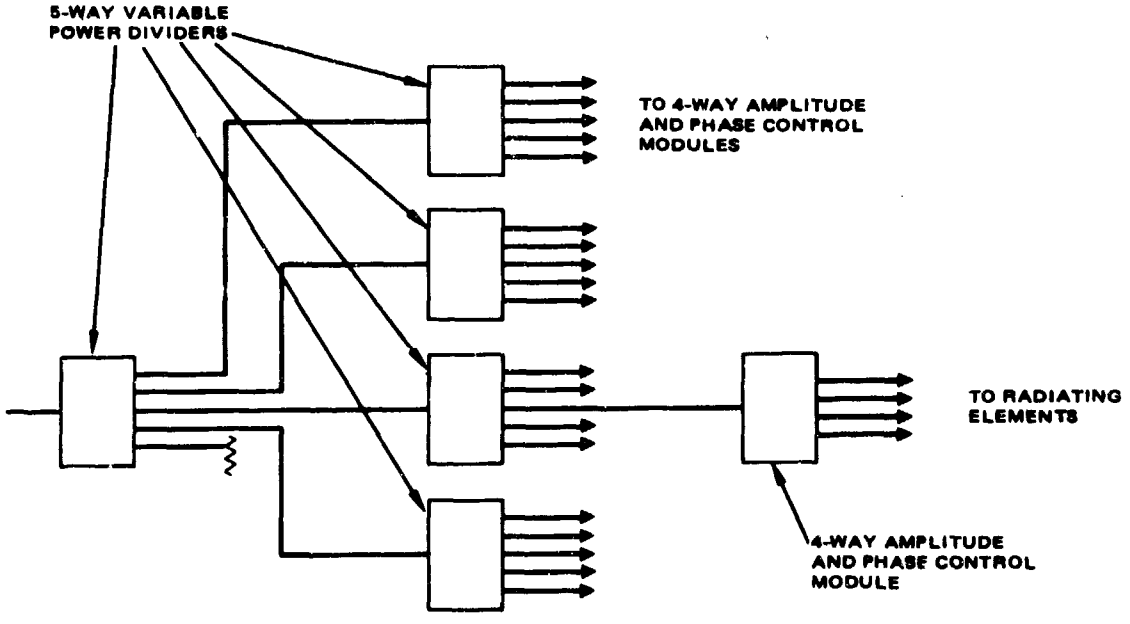

Fig. 5 Schematic of feed network interconnection.

6.2 Variable Polarization Radiating Element

The radiating element consists of two dielectrically-loaded, crossed-slot radiators independently excited through stripline matching networks. The element is illustrated in Figure 6. The stripline matching networks are shown shaded. Each matching network is excited from the rear through a coaxial connector and is coupled to its corresponding slot. The printed circuit board material also acts as dielectric loading for the radiating slots. The assembly is machined from aluminum. Figure 7 shows the assembled radiator and its various components. The elements were adjusted for individual VSWR's of approximately 1.2 or better when in a groundplane and isolated from other elements.

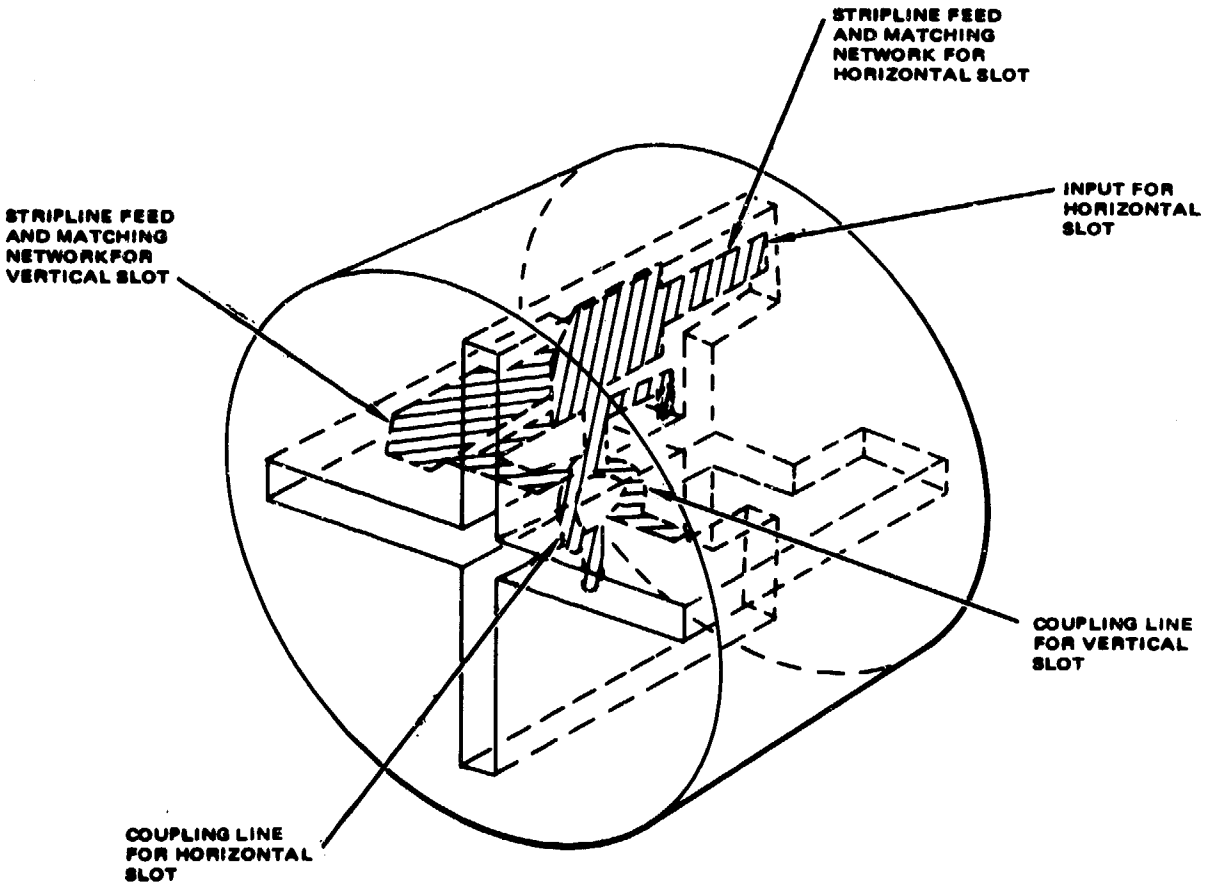

Fig. 6 Crossed slot radiating element.

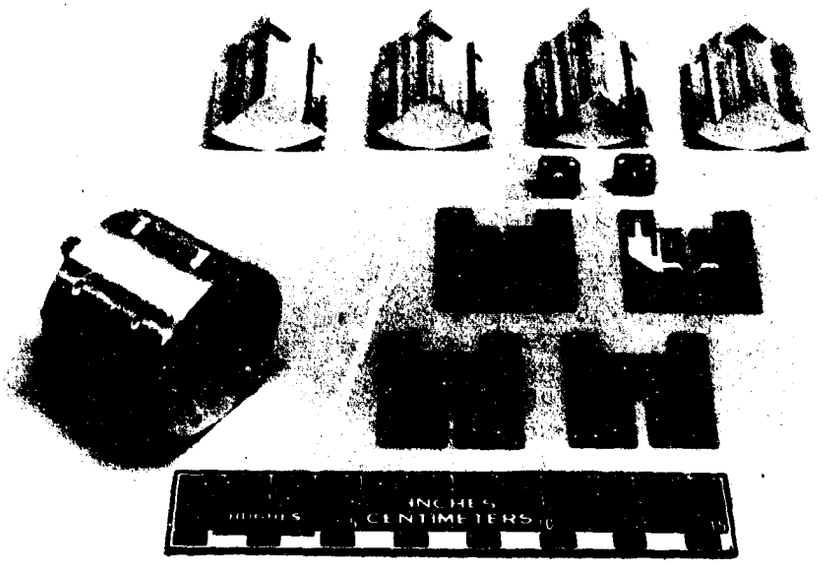

Fig. 7 Components and assembled crossed-slot radiating element (4R-53938).

6.3 Structural Configuration

The array and feed network are packaged as a self-contained structure. The unit is a cone approximately seven feet in length with a half-cone angle of 10.25^{o}. It is constructed in several sections. The lower portion contains the feed network which is accessible by removing cover panels. The central portion contains the radiating elements. A removable cover panel is located on the side opposite the radiators for easy access. Table 1 gives the locations of the various elements in terms of their distance along the slant height from the tip and their angular position about the cone axis. The upper portion of the structure includes the tip which is machined from solid aluminum. Figure 8 shows a front view of the completed unit. It may be seen that the radiating elements are not contoured to the cone surface, but have flat faces. This arrangement

TABLE 1. POSITION OF ELEMENTS ON EXPERIMENTAL CONE

Element No.	Slant Distance from Tip, inches	Angular Position About Cone Axis, Degrees
1	32.241	0.0
2	34.094	18.0
3	34.094	54.0
4	34.094	306.0
5	34.094	342.0
6	35.947	0.0
7	35.947	36.0
8	35.947	324.0
9	37.800	18.0
10	37.800	54.0
11	37.800	306.0
12	37.800	342.0
13	39.653	0.0
14	39.653	36.0
15	39.653	72.0
16	39.653	288.0
17	39.653	324.0
18	41.506	18.0
19	41.506	54.0
20	41.506	90.0
21	41.506	270.0
22	41.506	306.0
23	41.506	342.0
24	43.359	0.0
25	43.359	36.0
26	43.359	72.0
27	43.359	288.0
28	43.359	324.0
29	45.212	18.0
30	45.212	54.0
31	45.212	306.0
32	45.212	342.0
33	47.065	0.0
34	47.065	25.714
35	47.065	334.286
36	48.918	12.857
37	48.918	347.143

Note: The actual cone has two additional unused elements located at slant distance 45.212 inches and at angular positions 90° and 270°.

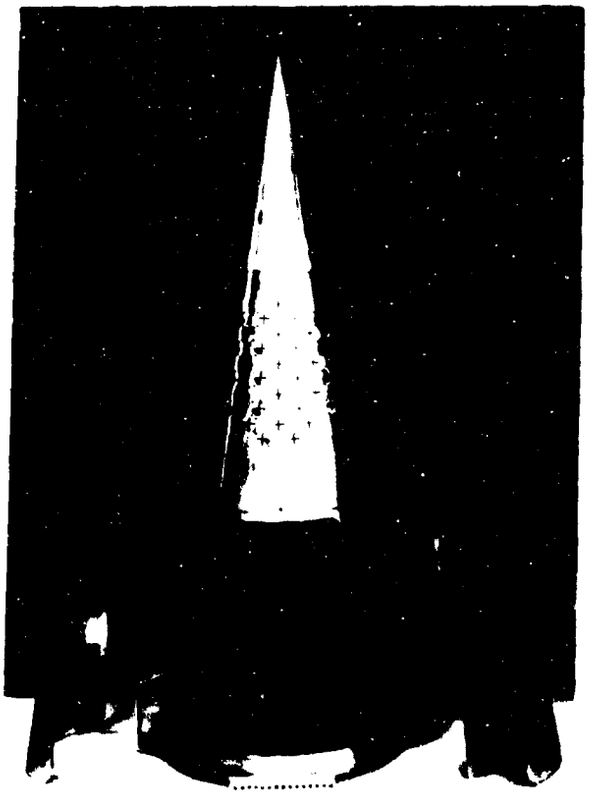

Fig. 8 Front view of completed conical array (4R-54192).

allowed all the radiators to be identical and interchangeable and, because the surface discontinuities are small in terms of wavelength, they had a negligible effect on measured radiation patterns. The coaxial cables connecting the feed network to the radiating elements are evident in the lower section. Fixtures for mounting the unit are also shown attached to the base.

A rear view of the unit is shown in Figure 9. The assembled feed network is visible in the lower section. The rear portions of the radiating elements are partially visible in the central section. Figures 10, 11 and 12 show close up views of the front and rear of the installed radiating elements and of the feed with open circuited stubs, respectively.

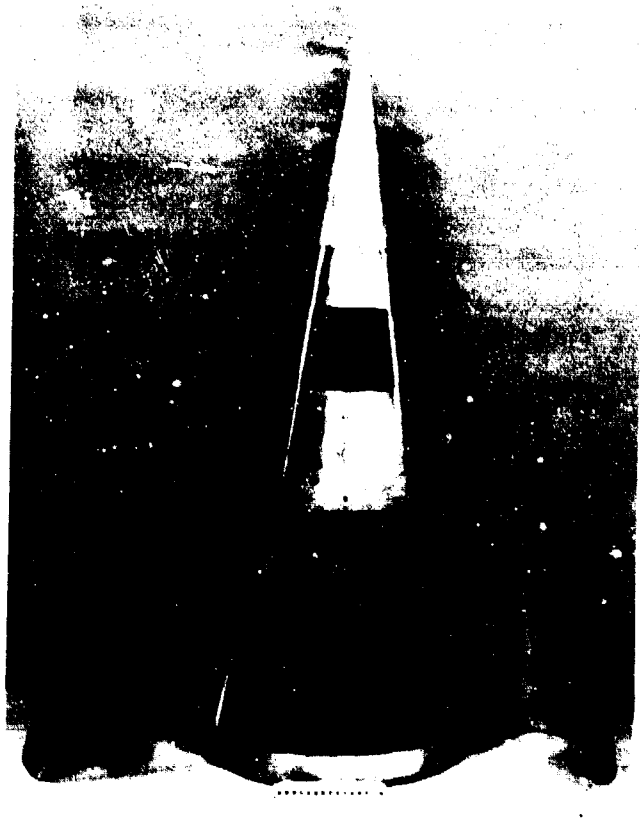

Fig. 9 Rear view of completed conical array (4R-54194).

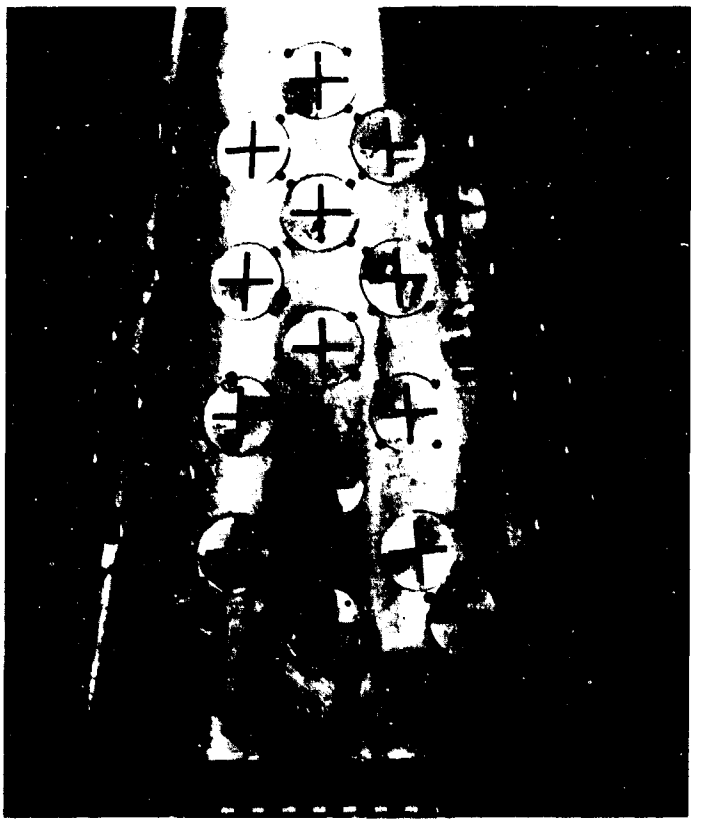

Fig. 10 Locations of radiating elements on cone (4R-54196).

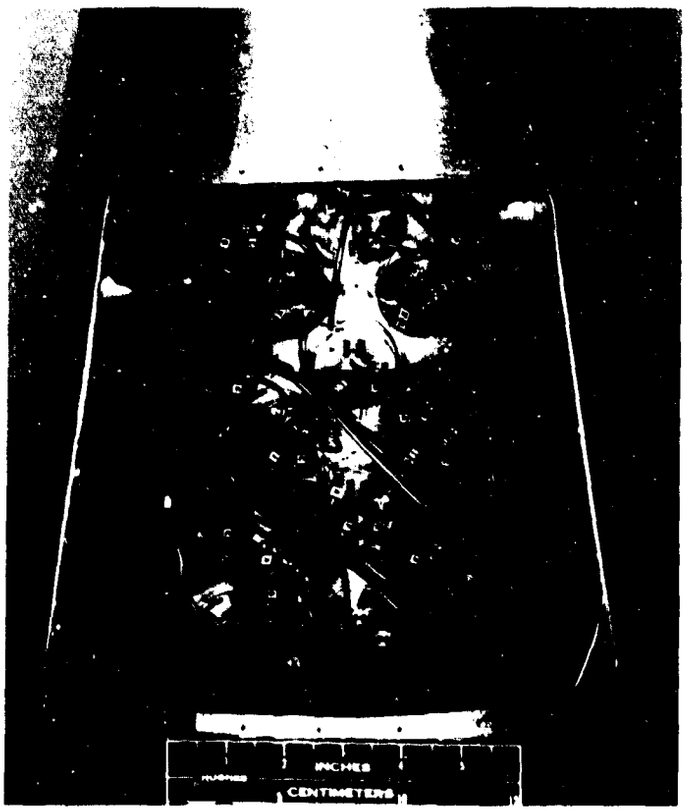

Fig. 11 Rear view of radiating elements and feed cables installed in cone (4R-54197).

Fig.12 Feeding network with open circuited stubs for amplitude and phase control. (4R-54376)

6.4 Experimental Measurements

Pattern measurements on the experimental array were made for two selected beam positions, θ_p equal to 50^o and θ_p equal to 79.75^o. The azimuth angle ϕ_p was zero in both cases. The patterns were θ-polarized on the peak of the beam. The two experimental cases correspond to the computed cases of Figures 32 and 33 respectively of Chapter 2.

6.4.1 Aperture Distributions

The experimental element excitations were obtained by an iterative procedure in which the fields directly in front of the slots were measured with a probe and compared to the required

relative values. Three iterations were made in both cases. Several probes were tested and the most repeatable results were obtained with a stripline dipole that was fitted into a dielectric tube and held snugly over the slots. Figure 13 shows a close-up of the probe. The dipole arms have been trimmed down to almost zero length and the actual coupling method is uncertain. Some difficulty was experienced with the probe, in that it appeared to have some cross polarized component. However, as a matter of expediency this probe was used for setting up the required aperture distributions. The measured radiation patterns had a corresponding slight polarization rotation but were otherwise in close agreement with the calculated patterns. Figure 14 shows the probe held in position for setting up the required aperture distributions. Tables 2 and 3 give the desired and measured slot excitations for the two beam positions. Excellent agreement for most slots is evident, though some errors exist, primarily at

Fig. 13 View of probe used for setting aperture distribution. (4R-54372)

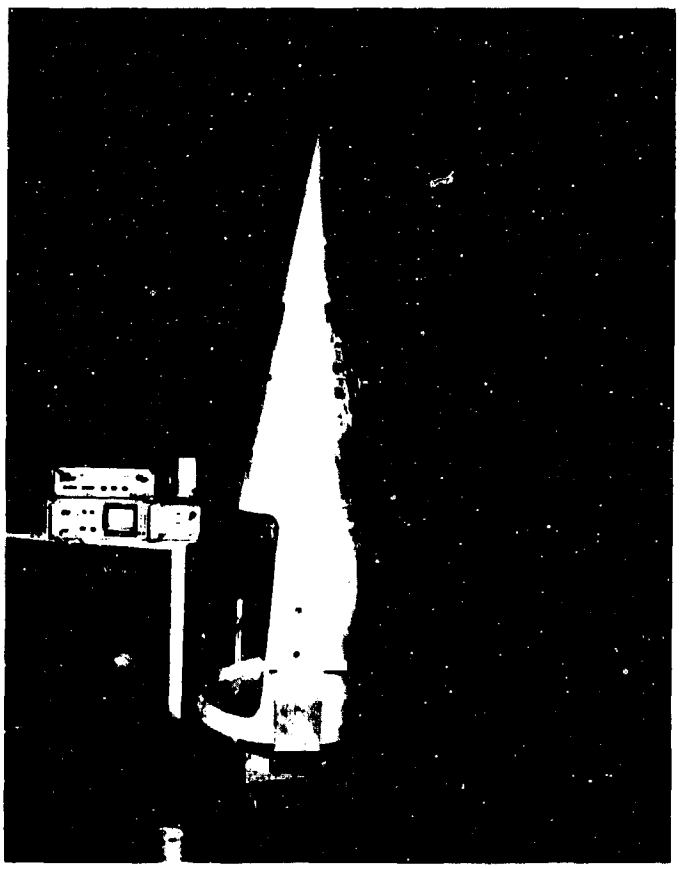

Fig. 14 Probe in position on conical array. (4R-54373)

TABLE 2. DESIRED AND MEASURED EXCITATIONS OF CIRCUMFERENTIAL AND RADIAL SLOTS FOR BEAM AT $\theta_p = 50^\circ$

Element No.	Circumferential Slot				Radial Slot			
	Ampl. dB		Phase Deg.		Ampl. dB		Phase Deg.	
	Desired	Measured	Desired	Measured	Desired	Measured	Desired	Measured
1	-13.14	-13.8	34.89	34	- ∞	-31	-	- 40
2	- 9.41	- 9.5	145.33	147	-20.49	-18	- 47.75	- 44
3	-17.56	-17.8	-119.58	-119	-19.13	-18.1	25.30	36
4	-17.56	-18.0	-119.58	-118	-19.13	-18.2	205.30	208
5	- 9.41	- 9.2	145.33	148	-20.49	-22.1	132.26	127
6	- 4.93	- 4.6	-144.92	-146	- ∞	-26	-	60
7	- 8.82	- 8.6	- 74.84	- 77	-13.13	-13.5	96.25	92
8	- 8.82	- 8.1	- 74.84	- 78	-13.13	-12.6	- 83.75	- 93
9	- 3.92	- 4.1	- 43.62	- 53	-18.84	-17.3	132.94	145
10	-13.46	-13.4	111.70	114	-15.57	-14.3	- 82.89	- 85
11	-13.46	-13.1	111.70	107	-15.57	-16.3	97.11	96
12	- 3.92	- 3.9	- 43.62	- 52	-18.84	-18.4	- 47.06	- 55
13	0.00	- 0.3	0.00	0	- ∞	-28	-	103
14	- 8.44	- 8.1	130.14	136	-13.43	-12.9	- 42.85	- 46
15	-16.74	-17.0	- 31.17	- 32	-12.42	-11.7	163.15	165
16	-16.74	-16.5	- 31.17	- 30	-12.42	-13.5	- 16.85	- 14
17	- 8.44	- 9.3	130.14	133	-13.43	-12.3	137.15	136
18	- 5.62	- 4.2	130.90	123	-16.74	-16.7	- 55.05	- 55
19	-12.18	-13.3	- 30.72	- 46	-17.48	-16.5	140.18	138
20	-22.14	-22.2	-147.16	-126	-13.57	-13.8	- 33.17	- 27
21	-22.14	-23.0	-147.16	-148	-13.57	-14	146.82	160
22	-12.18	-12.1	- 30.72	- 16	-17.49	-16.9	- 39.82	- 21
23	- 5.62	- 5.3	130.90	134	-16.74	-16.5	124.95	120
24	- 3.54	- 4.0	196.25	195	- ∞	-30	-	192
25	- 7.16	- 7.7	- 54.37	- 52	-16.28	-16.5	141.49	135
26	-22.66	-22.0	-116.94	-105	-15.53	-14.2	69.82	70
27	-22.66	-22.2	-116.94	-114	-15.53	-15.3	-110.18	-102
28	- 7.16	- 7.3	- 54.37	- 41	-16.28	-17.5	- 38.51	- 32
29	- 6.96	- 6.5	- 60.65	- 58	-18.92	-22.4	146.25	-151
30	-10.26	-10.8	155.12	146	-19.83	-20	- 56.48	- 59
31	-10.26	-10.5	155.12	156	-19.83	-19.0	123.52	120
32	- 6.96	- 6.8	- 60.56	- 65	-18.92	-17.6	- 33.75	- 40
33	- 4.94	- 5.4	24.60	8	- ∞	-30	-	150
34	-13.92	-14.8	71.79	59	-22.80	-24.5	-106.58	-116
35	-13.92	-13.9	71.79	66	-22.80	-28	73.42	62
36	-11.51	-11.8	100.52	97	-30.84	-29.5	- 51.19	- 22
37	-11.51	-11.5	100.52	98	-30.84	-28	128.81	131

TABLE 3. DESIRED AND MEASURED EXCITATION OF CIRCUMFERENTIAL AND RADIAL SLOTS FOR BEAM AT $\theta_p = 79.75^\circ$

Element No.	Circumferential Slot				Radial Slot			
	Ampl. dB		Phase Deg.		Ampl. dB		Phase Deg.	
	Desired	Measured	Desired	Measured	Desired	Measured	Desired	Measured
1	- 9.78	- 9.4	2.72	4	- ∞	- 31	-	-
2	- 8.63	- 8.3	67.67	70.5	-30.94	- 33	-126.19	-
3	-17.19	-17.8	-158.54	-157	-29.18	- 33	- 16.32	-
4	-17.19	-17.6	-158.54	-156	-29.18	- 31.5	163.68	-
5	- 8.63	- 8.4	67.67	70.5	-30.94	- 32	53.82	-
6	- 2.75	- 3.2	48.92	49	- ∞	- 31	-	-
7	- 9.89	- 9.8	131.35	129.5	-27.02	- 29	-113.96	-110
8	- 9.89	-10.0	131.35	131	-27.02	-30.5	66.04	120
9	- 1.37	- 1.1	60.76	61.5	-25.60	-32	-119.66	-
10	- 7.91	- 7.5	- 78.51	- 76	-15.41	-15.5	103.63	106
11	- 7.91	- 7.5	- 78.51	- 79	-15.41	-15.4	- 76.37	- 76
12	- 1.37	- 1.2	60.76	63	-25.60	-28.5	60.34	40
13	0.00	+ 0.2	0.00	1	- ∞	-31	-	-
14	- 3.62	- 3.5	171.11	171	-19.11	-17.8	- 29.67	- 24
15	-15.14	-15.9	121.54	129	-11.72	-11.7	- 61.48	- 60.5
16	-15.14	-14.8	121.54	123	-11.72	-11.6	118.52	123
17	- 3.62	- 3.0	171.11	171	-19.11	-19.3	150.33	155
18	- 2.61	- 2.5	65.36	62	-25.55	-31	-150.42	-
19	-11.86	-11.8	- 20.30	- 25.5	-22.80	-27	96.50	120
20	-37.96	-32	- 30.59	-	-22.88	-26	13.31	20
21	-37.96	-30	- 30.59	0	-22.88	-24	-166.69	-163
22	-11.86	-12.0	- 20.30	- 18.5	-22.80	-22.5	- 83.50	- 85
23	- 2.61	- 2.4	65.36	64	-25.55	-31	29.58	-
24	- 0.78	- 0.8	34.39	36.5	- ∞	-31	-	-
25	- 7.02	- 6.8	169.61	169.5	-26.33	-32	37.11	-
26	-17.81	-20.0	91.17	80	-16.90	-18.7	100.22	89
27	-17.81	-18.2	91.17	90	-16.90	-15.8	- 79.78	- 72
28	- 7.02	- 6.5	169.61	173	-26.33	-30	-142.89	- 60
29	- 6.56	- 6.5	63.77	63.5	-25.14	-30.5	- 66.60	-
30	-12.41	-12.0	-107.48	-106	-17.56	-18.8	-138.45	-143
31	-12.41	-11.9	-107.48	-107	-17.56	-17.2	41.55	48
32	- 6.56	- 6.5	63.77	60	-25.14	-29	113.40	150
33	- 6.23	- 6.5	43.16	46	- ∞	-30	-	-
34	-14.15	-15.4	99.01	99	-34.64	-31	- 90.03	-
35	-14.15	-14.8	99.01	101	-34.64	-32	89.97	-
36	-13.56	-13.7	12.94	17	-35.61	-28.5	- 35.90	36
37	-13.56	-13.6	12.94	14	-35.61	-26	144.10	-100

low levels, which would tend to have a minor effect on pattern characteristics. Some errors in the more strongly excited slots also exist but it was decided to make pattern measurements with these distributions rather than to attempt further refinement.

6.4.2 Pattern Measurements

E-plane and H-plane pattern measurements were made in an anechoic chamber. The cone was mounted horizontally for E-plane measurements. Its base was sealed with aluminum foil and covered with microwave absorbing material. The supporting structure was also covered with absorber. For H-plane patterns the cone was mounted vertically and then tilted forward by $90^{\circ}-\theta_p$. The unit was then rotated about a vertical axis thereby giving the cut illustrated in Figure 14 of Chapter 2. The base was covered with microwave absorber. The array is shown mounted for this cut in Figure 15.

The measured E-plane and H-plane patterns for the beam 50 degrees off the cone axis are shown in Figures 16a and b. The calculated patterns are superimposed for comparison. It is seen that the agreement is excellent although the sidelobe levels of the measured patterns are somewhat higher than those of the calculated patterns. In addition the polarization was found to be tilted from the correct value by approximately 13 degrees. It is believed that an improved probe design would eliminate the polarization tilt and that a more accurate setting of the relative slot excitations would improve the agreement between measured and calculated sidelobes. Some of the fine detail on the sidelobes may be due to low level reflections in the chamber. Some of the ripples near θ equal to zero may also be due to tip diffraction, which is not accounted for in the calculated patterns. The cross polarized patterns in the E-plane and H-plane relative to the tilted polarization are shown in Figures 17a and b. If the

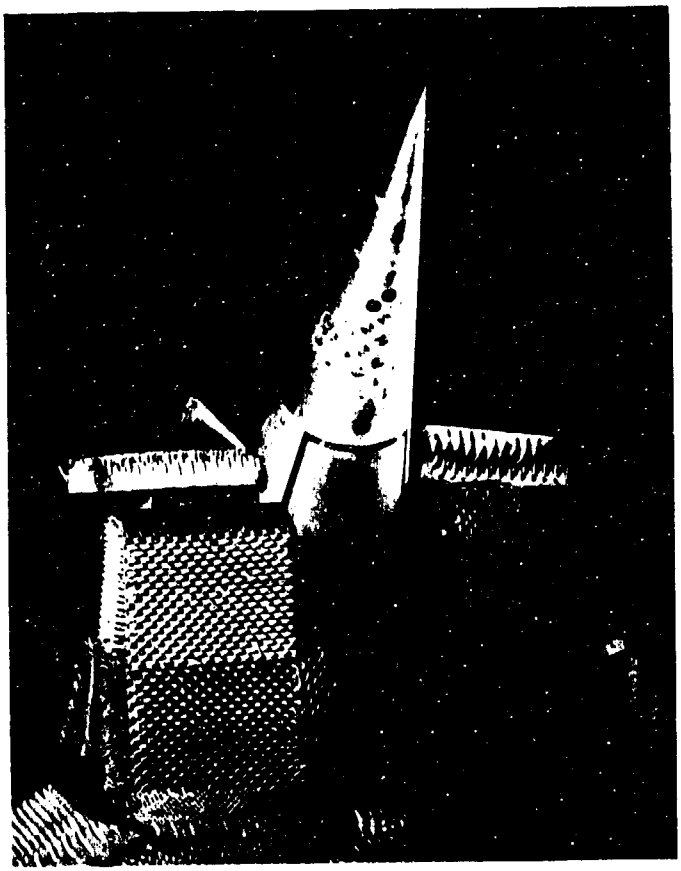

Fig. 15 *Array positioned for measurement of H-plane pattern. (4R-54374)

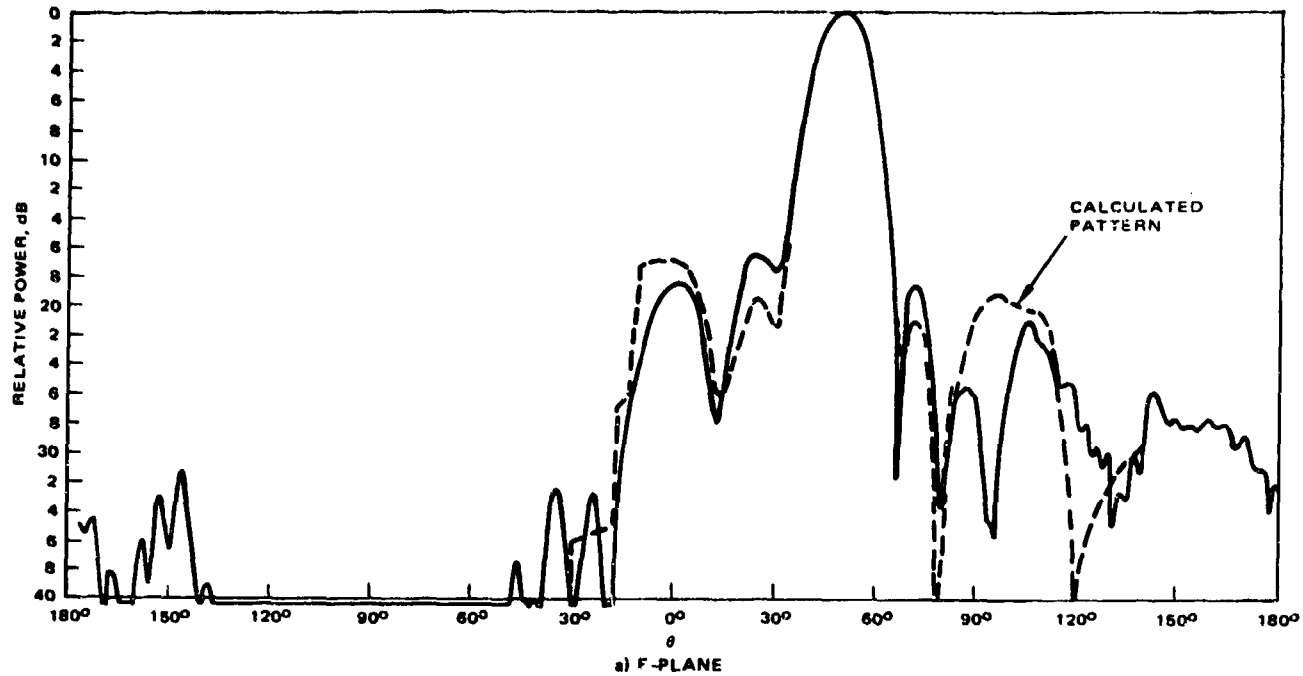

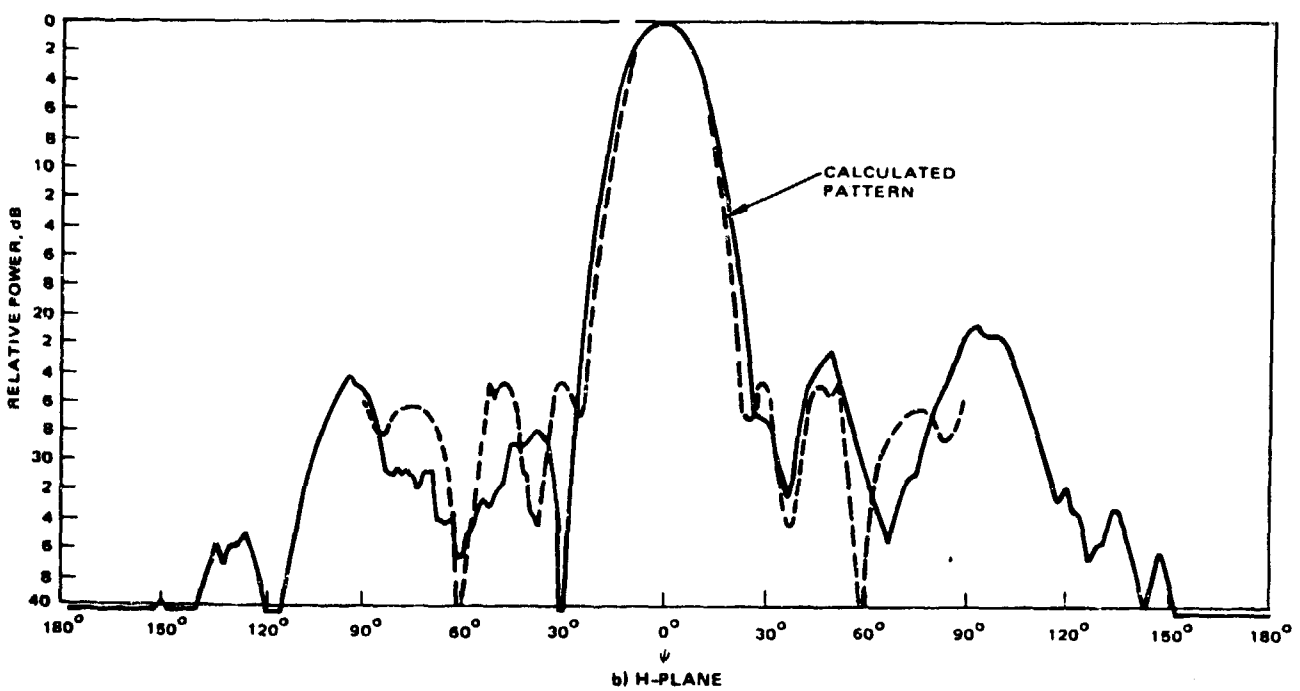

Figure 16. Measured E-plane and H-plane patterns of conical array (θ_p=50°).

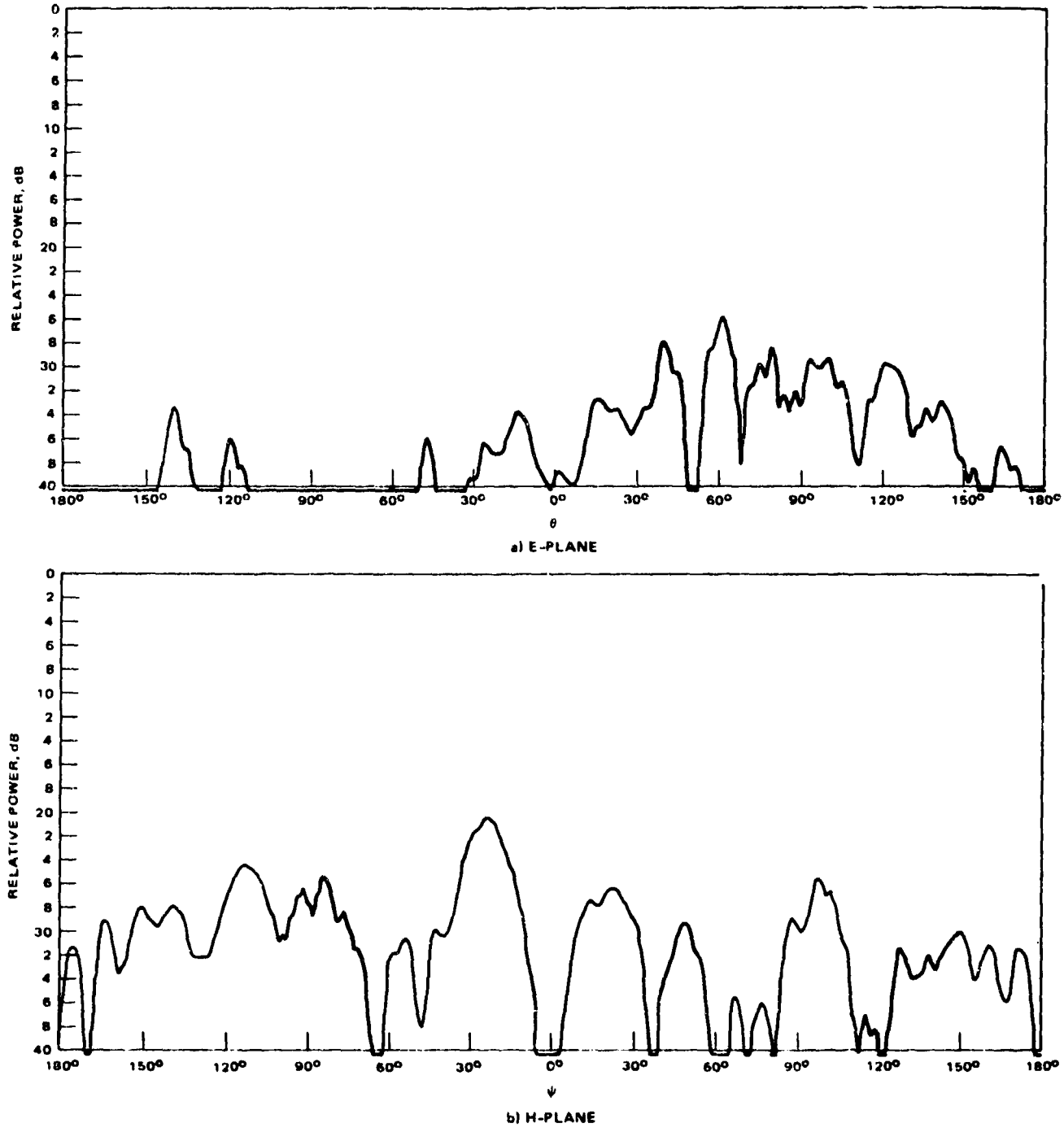

Figure 17. Measured cross-polarized patterns of conical array ($\theta_p = 50^\circ$).

excitation were truly correct there would be no cross polarized radiation in the E-plane. However, excitation errors introduce some cross polarization.

A similar set of patterns was made for the beam directed normal to the cone generatrix ($\theta_p = 79.75^o$). The patterns are shown in Figures 18 and 19. The calculated patterns are also superimposed on Figures 18a and b for comparison. Once again agreement is excellent. As before, a polarization tilt was measured. Its value was approximately 8 degrees. In Figure 18a the calculated pattern appears to rise to a relatively high value at θ equals -10.25^o, that is, along the extension of the cone generatrix. However the measured pattern falls approximately 6 dB below the calculated pattern at that point. This difference is to be expected since the calculated pattern does not account for tip diffraction. The tip diffraction effect in the E-plane cut is analogous to diffraction of slot radiation by the edge of a finite groundplane where the field along the extension of the groundplane is reduced by 6 dB from the value it would have if no diffraction were present.

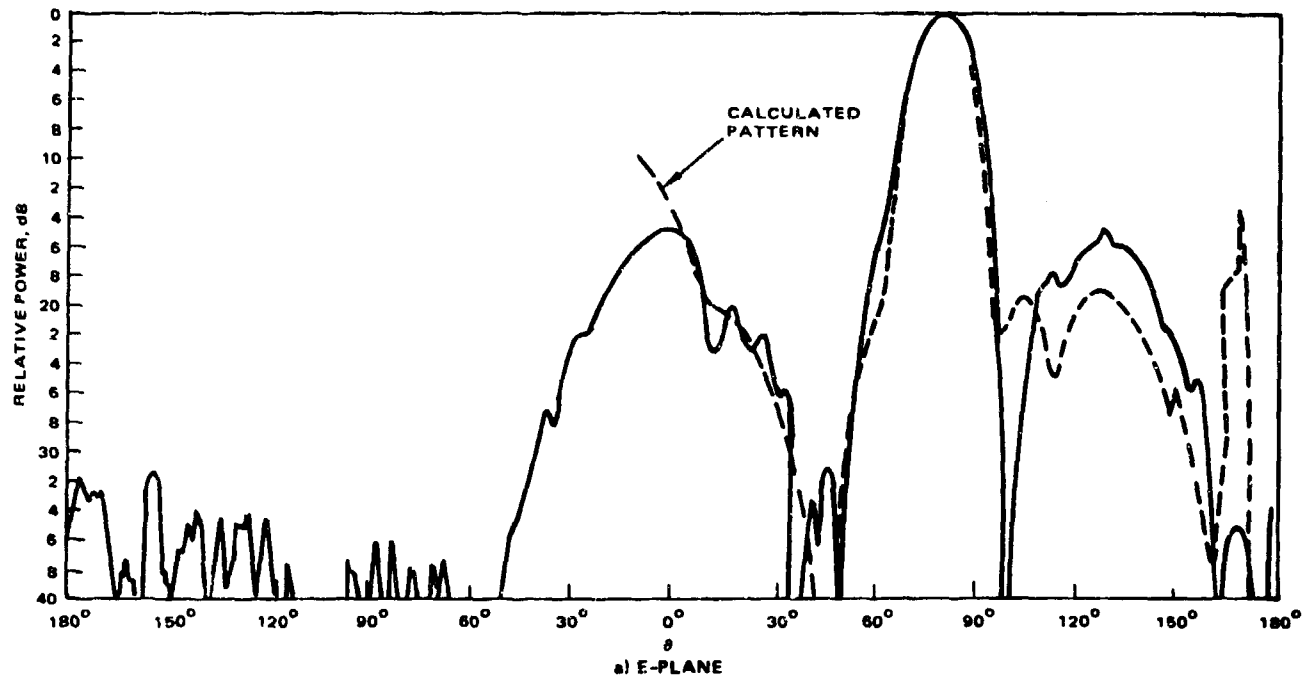

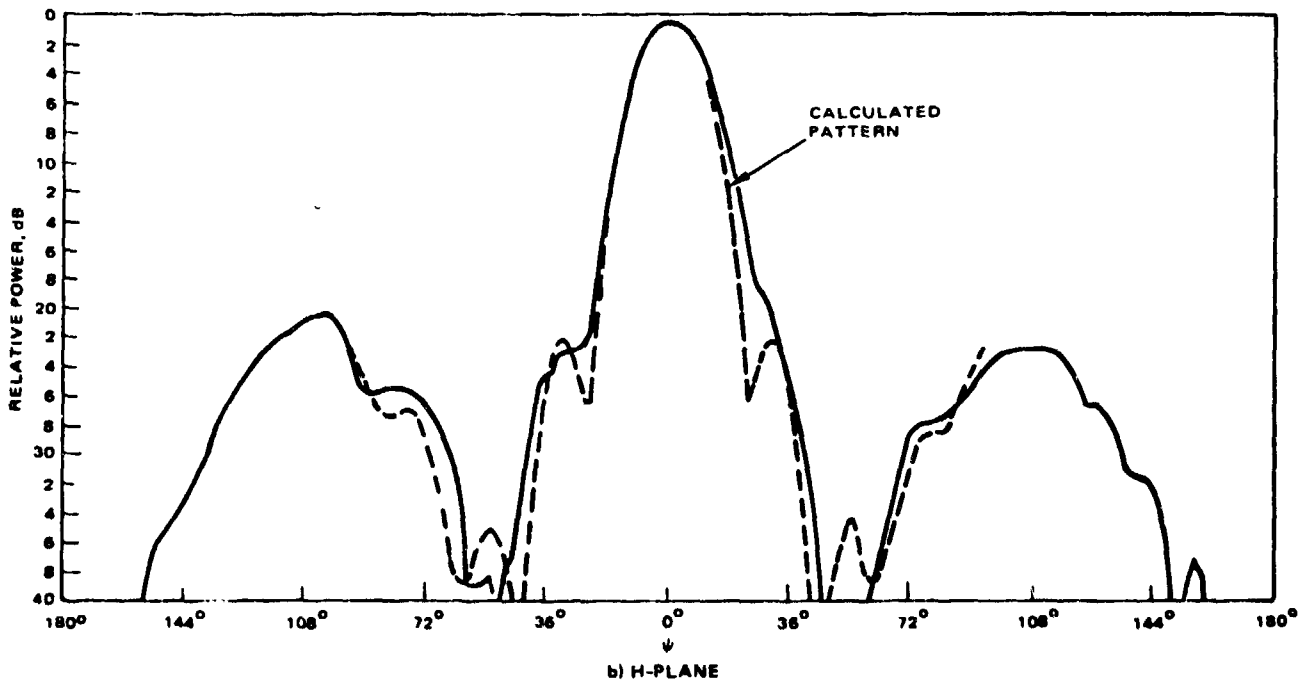

Figure 18. Measured E-plane and H-plane patterns of conical array ($\theta_p = 79.75^\circ$).

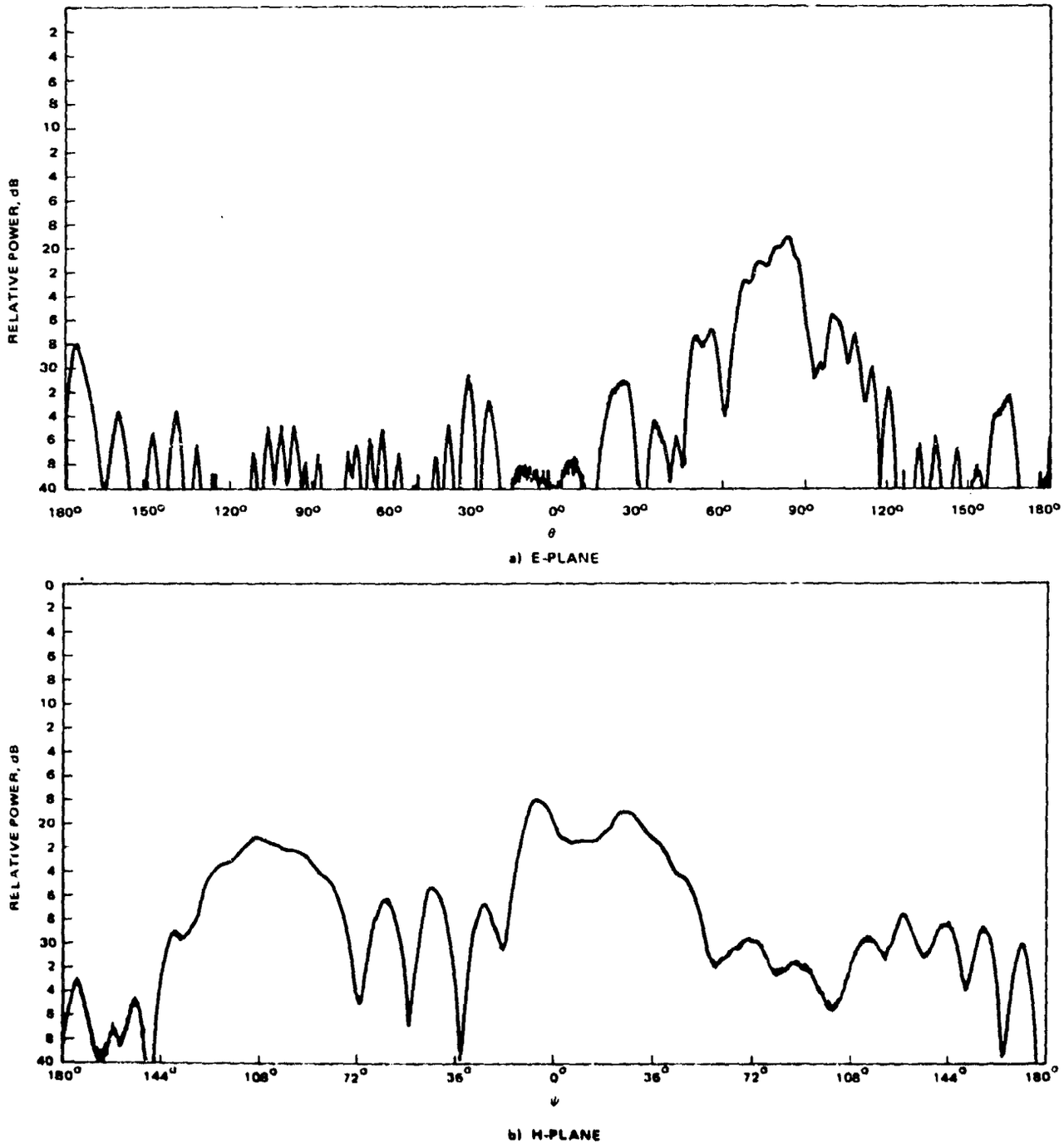

Figure 19. Measured cross-polarized patterns of conical array (θ_p=79.75°).

6.4.3 NOSC Measurements

The HAC conical array and projective synthesis computer code were transferred to NOSC, where additional calculations and measurements were made. These measurements were for a beam angle of 20 degrees from the axis, thereby complementing the previous 5 and 80 degree cases. The 80 degree patterns were duplicated as a check of the experimental setup. For the 20 degree beam angle, the phase and amplitude of the 32 element virtual base array were projected to the conical surface using the code described in Chapter 2. Array excitations were then adjusted using an iterative procedure with a sampling probe to the projected values. An improvement was made in the synthesis code wherein the equivalent cylinder element patterns were replaced by measured element patterns. To allow various inclined patterns to be measured, the cone axis was mounted 20 degrees above horizontal. Behind the wedge holding the cone was a roll axis (axis horizontal), and this rotator was mounted on an azimuth over elevation rotator. See Figure 20. The patterns are great circle cuts through the beam peak made in an inclined plane of inclination angle τ from vertical. τ is measured at the beam peak between the inclined plane and the E_θ vector. Figure 20 shows the θ - ϕ relationship for τ = 0, 30, 60, 90 degrees; supplementary values of τ simply reverse ϕ.

In the following graphs the computer pattern (using the projected distribution) and the corresponding measured pattern are presented as consecutive pairs. The patterns are in ψ (see Figure 14 of Chapter 2) for values of τ of 0 through 90 degrees at 15 degree intervals. Again supplementary τ values should give the same pattern with reversed ψ. The measured patterns for 180-τ have some discrepancies in the sidelobe region, as do the calculated patterns, since the latter uses measured element patterns.

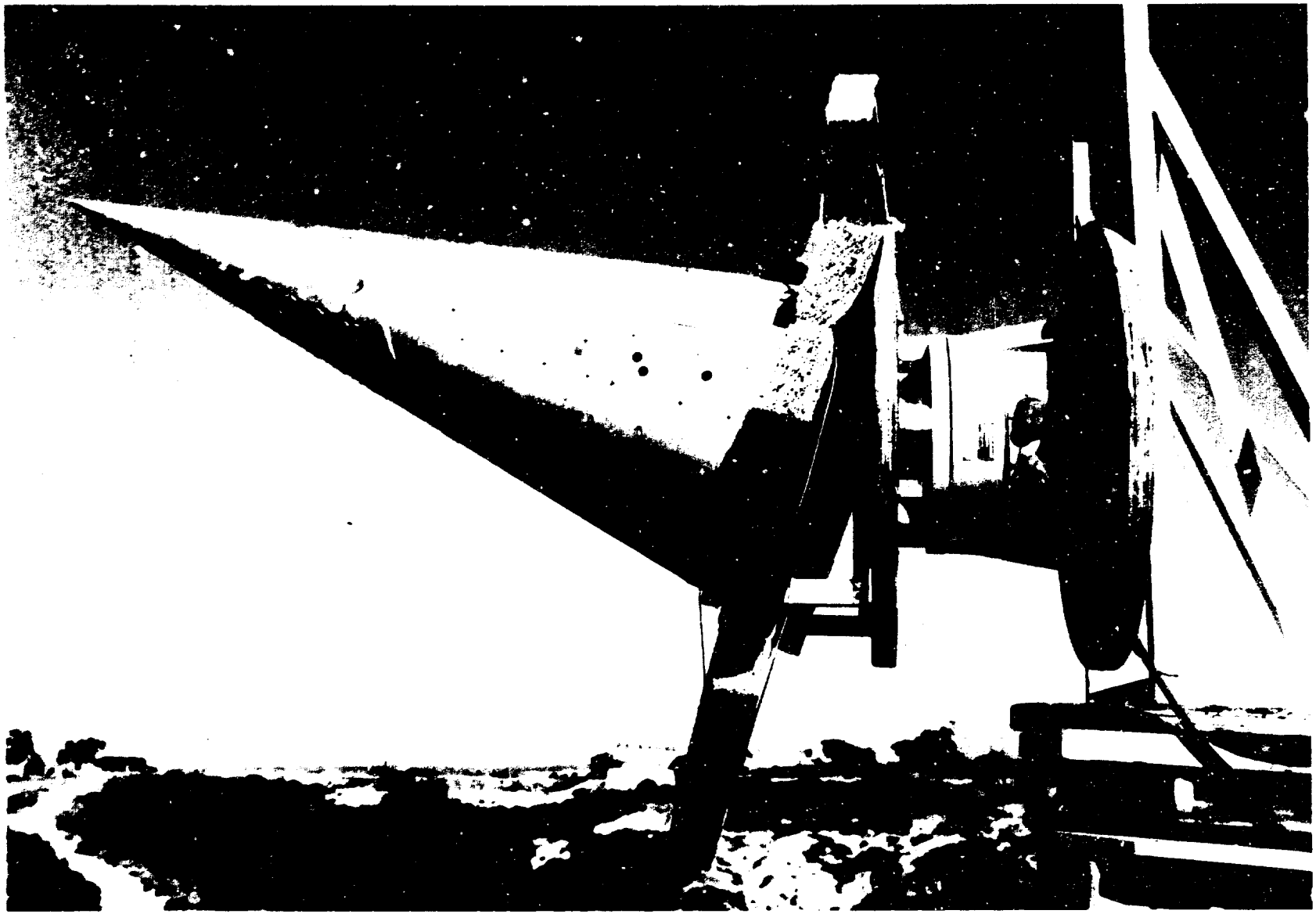

Figure 20. Conical array on NOSC range.

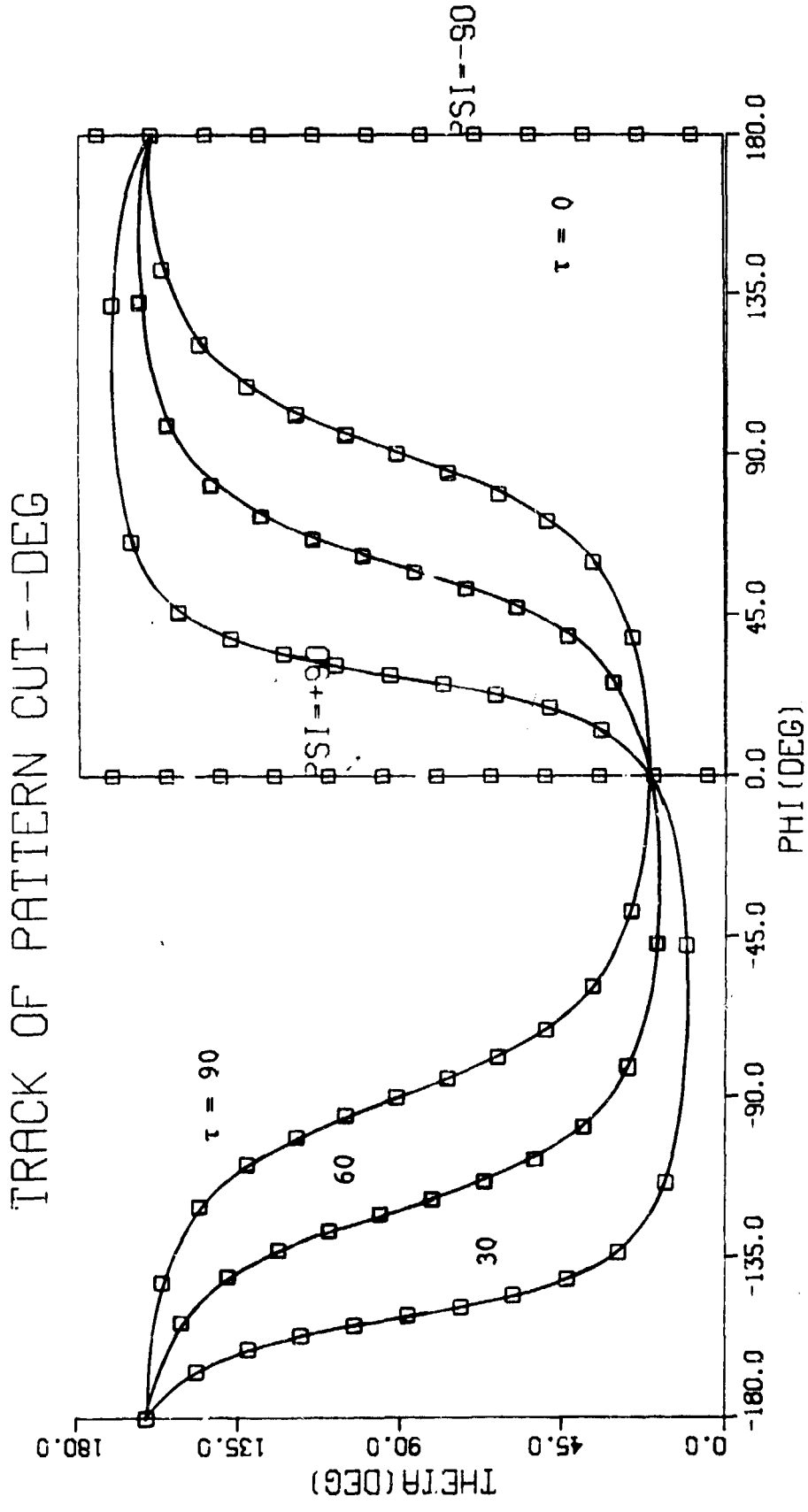
TRACK OF PATIERN CUT--DEG
PSI=-90
PSI=+90
τ = 0
τ = 90
60
30
THETA(DEG)
PHI(DEG)
0.0
45.0
90.0
135.0
180.0
-45.0
-90.0
-135.0
-180.0

Figure 21

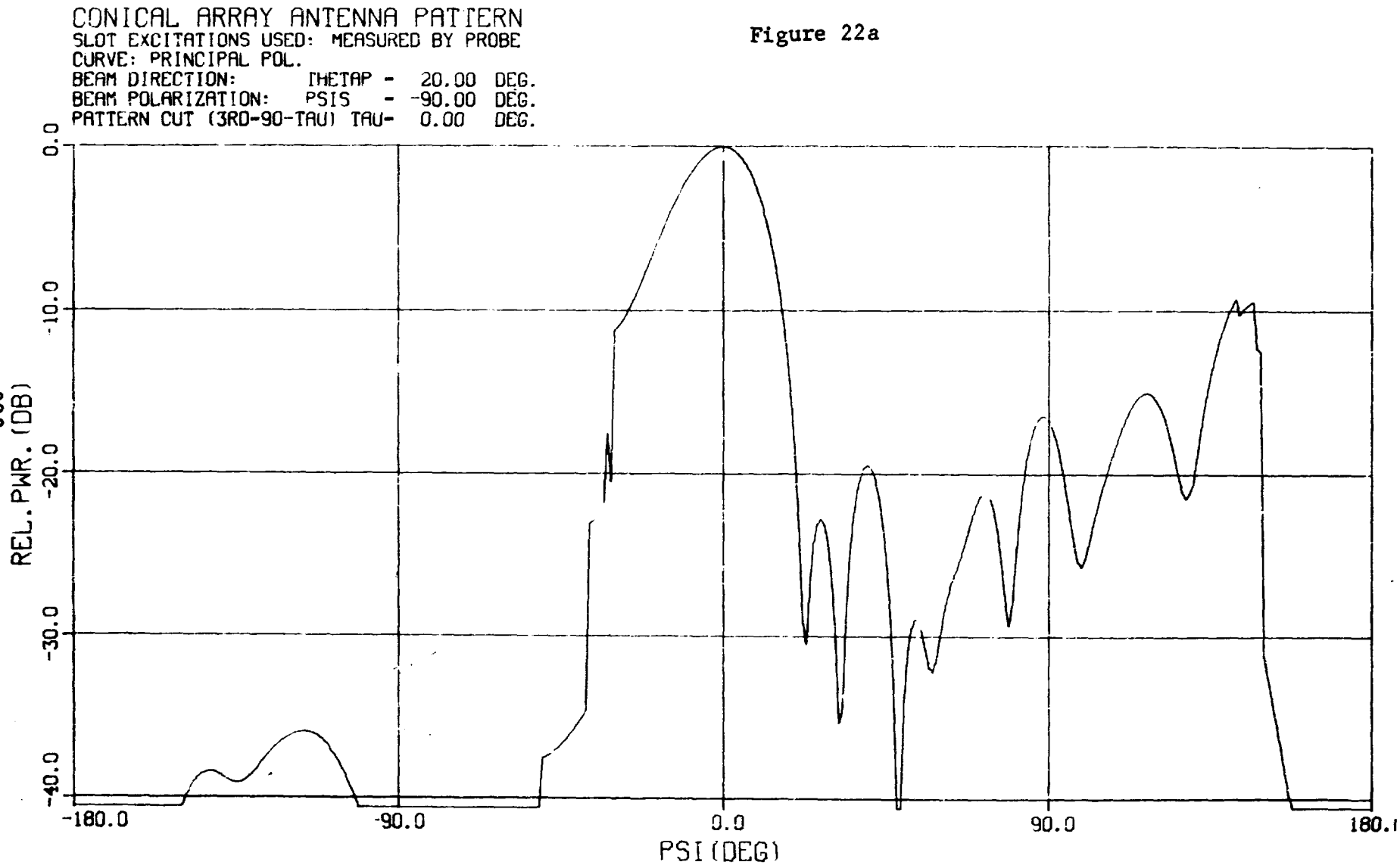
CONICAL ARRAY ANTENNA PATTERN
SLOT EXCITATIONS USED: MEASURED BY PROBE
CURVE: PRINCIPAL POL.
BEAM DIRECTION: THETAP - 20.00 DEG.
BEAM POLARIZATION: PSIS - -90.00 DEG.
PATTERN CUT (3RD-90-TAU) TAU- 0.00 DEG.
0.0
-10.0
-20.0
-30.0
-40.0
REL. PWR. (DB)
-180.0
-90.0
0.0
90.0
180.0
PSI (DEG)

Figure 22a

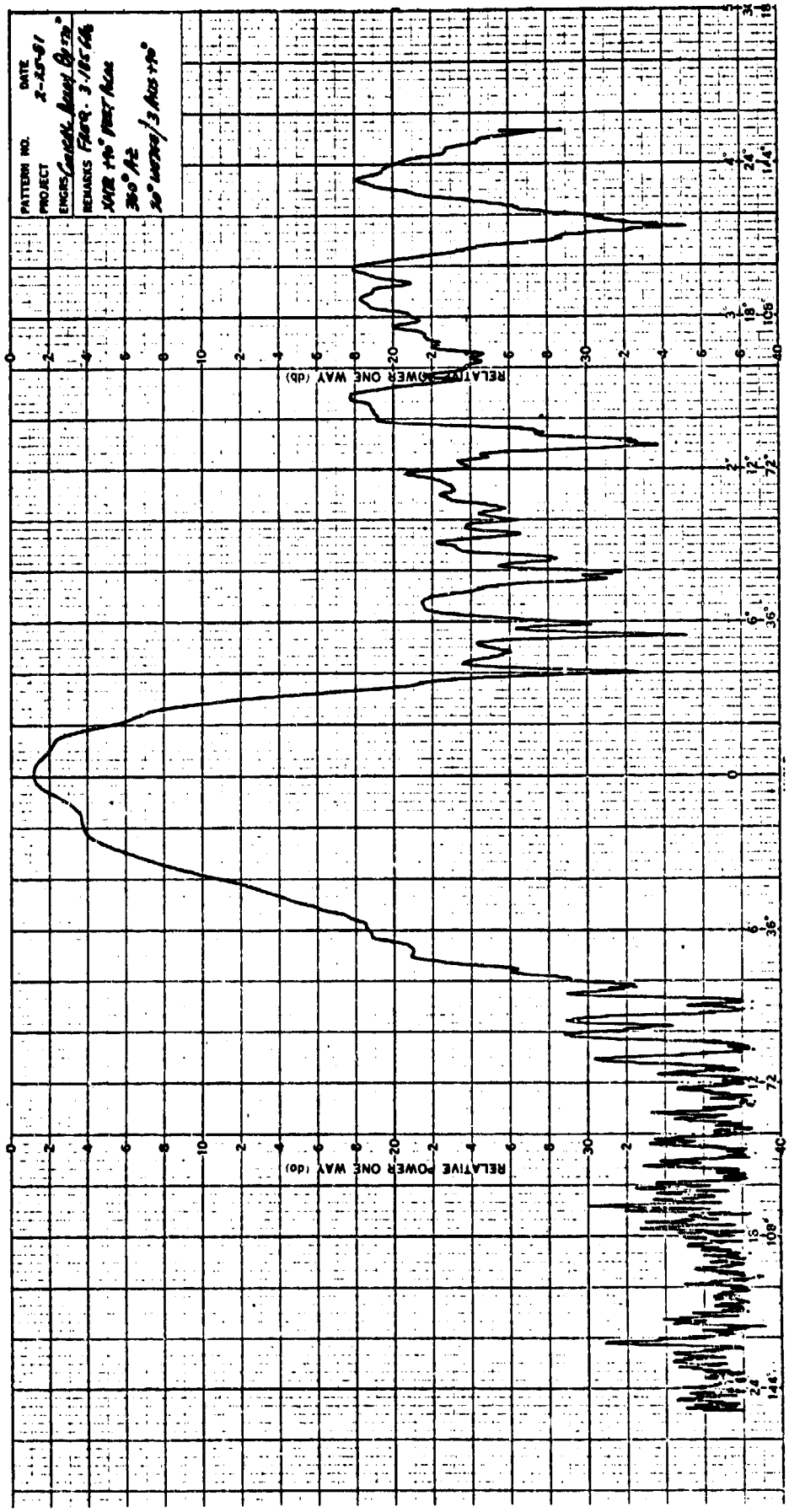
PATTERN NO.
DATE
2-25-61
PROJECT
ENGRS
REMARKS
RELATIVE POWER ONE WAY (db)
RELATIVE POWER ONE WAY (db)

Figure 22b

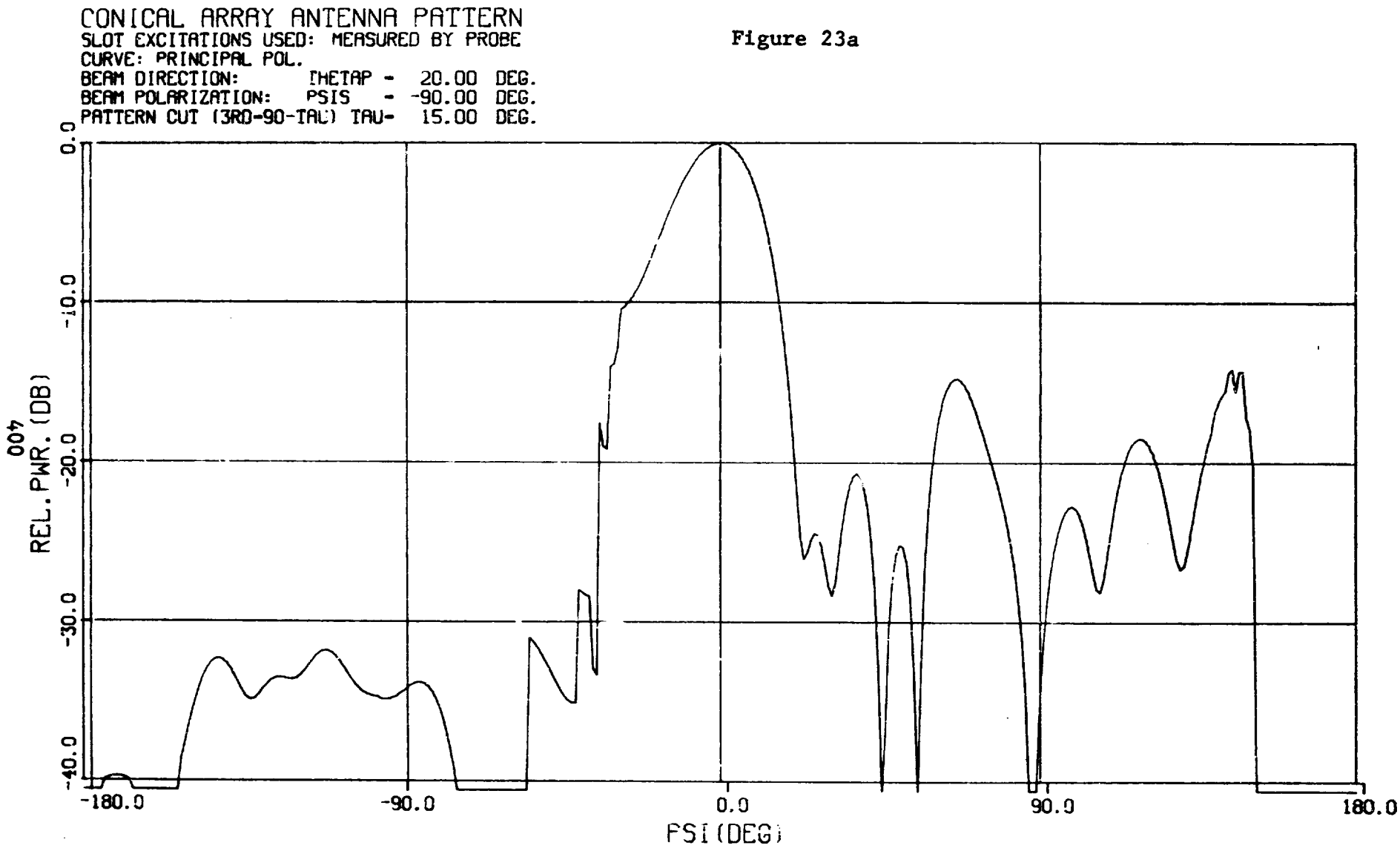
CONICAL ARRAY ANTENNA PATTERN
SLOT EXCITATIONS USED: MEASURED BY PROBE
CURVE: PRINCIPAL POL.
BEAM DIRECTION: THETAP - 20.00 DEG.
BEAM POLARIZATION: PSIS - -90.00 DEG.
PATTERN CUT (3RD-90-TAU) TAU- 15.00 DEG.
0.0
-10.0
-20.0
-30.0
-40.0
REL. PWR. (DB)
400
-180.0
-90.0
0.0
90.0
180.0
PSI (DEG)

Figure 23a

Figure 23b

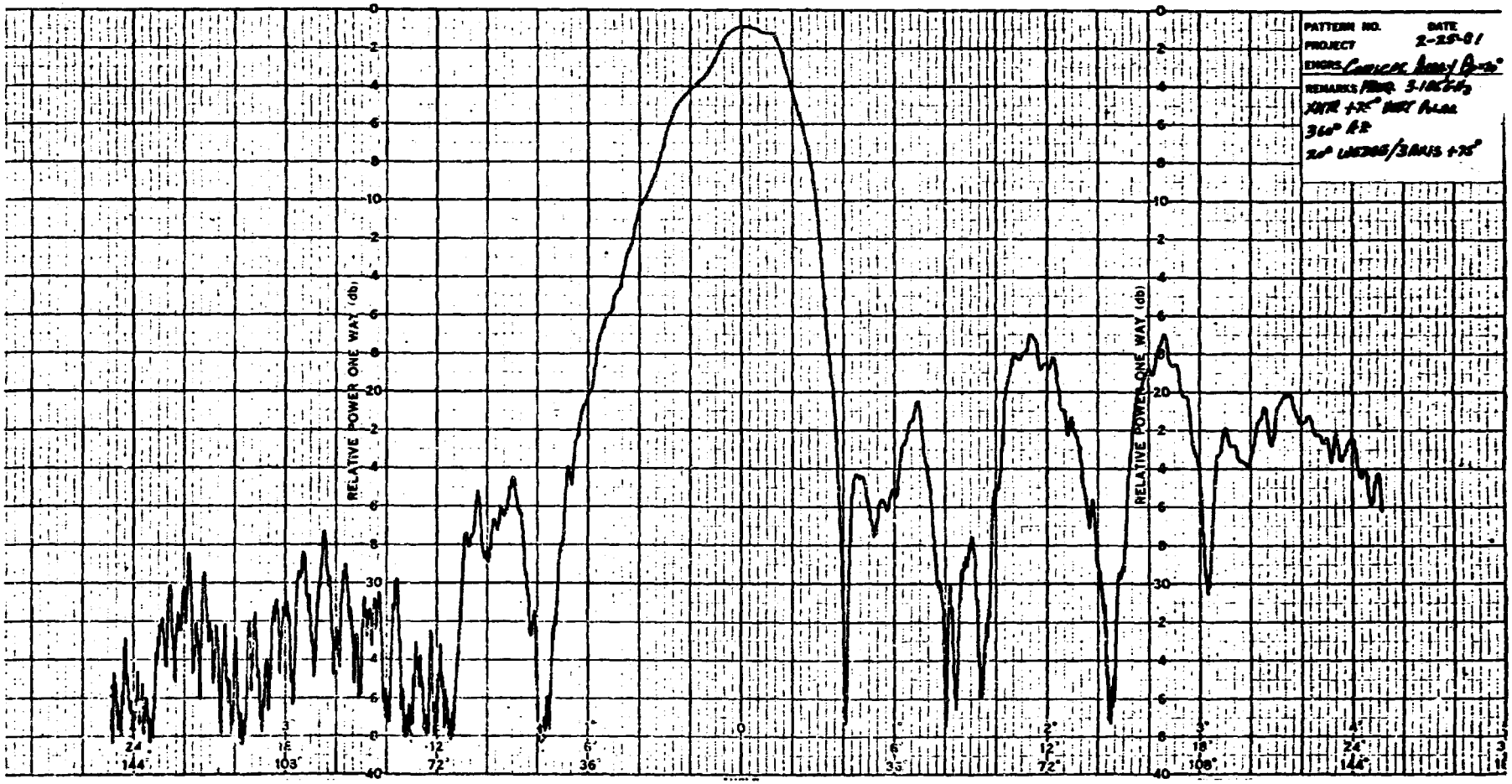
RELATIVE POWER ONE WAY (db)
RELATIVE POWER ONE WAY (db)
PATTERN NO.
DATE
PROJECT
2-25-81
ENGRS.
REMARKS

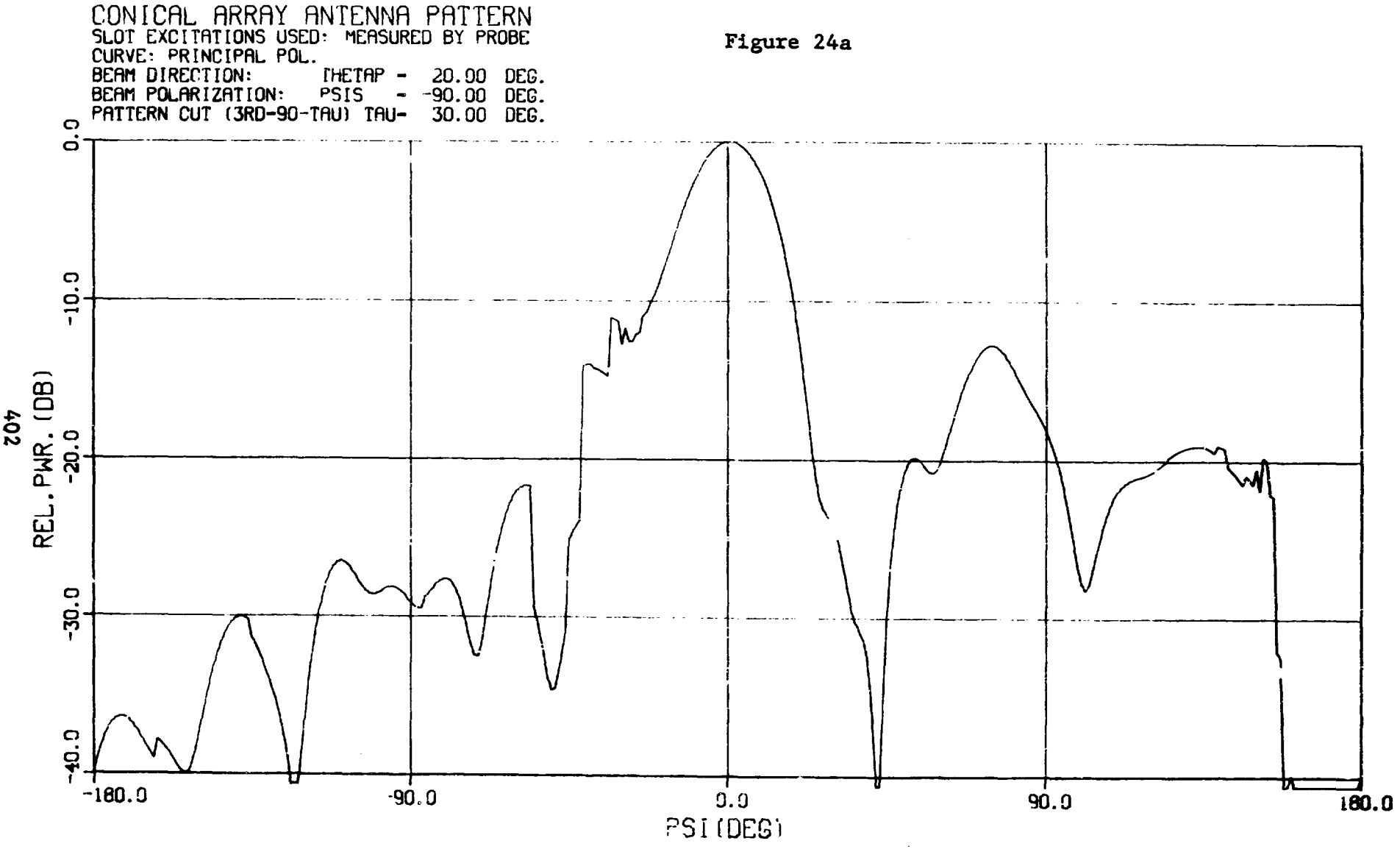
CONICAL ARRAY ANTENNA PATTERN
SLOT EXCITATIONS USED: MEASURED BY PROBE
CURVE: PRINCIPAL POL.
BEAM DIRECTION: THETAP - 20.00 DEG.
BEAM POLARIZATION: PSIS - -90.00 DEG.
PATTERN CUT (3RD-90-TAU) TAU- 30.00 DEG.
0.0
-10.0
-20.0
-30.0
-40.0
REL. PWR. (DB)
-180.0
-90.0
0.0
90.0
180.0
PSI (DEG)

Figure 24a

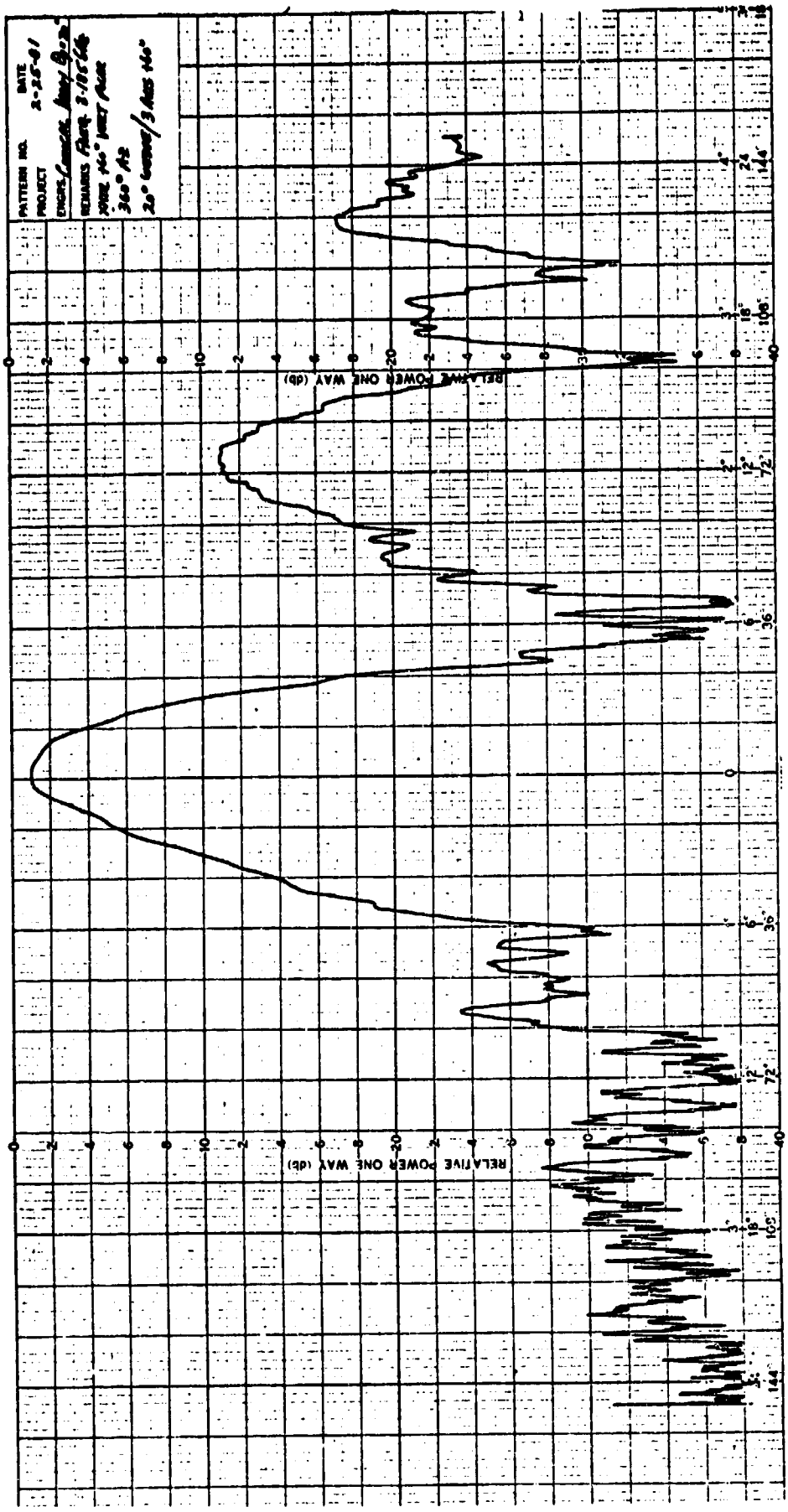
PATTERN NO.
DATE
PROJECT
RELATIVE POWER ONE WAY (db)
RELATIVE POWER ONE WAY (db)

Figure 24b

Figure 25a

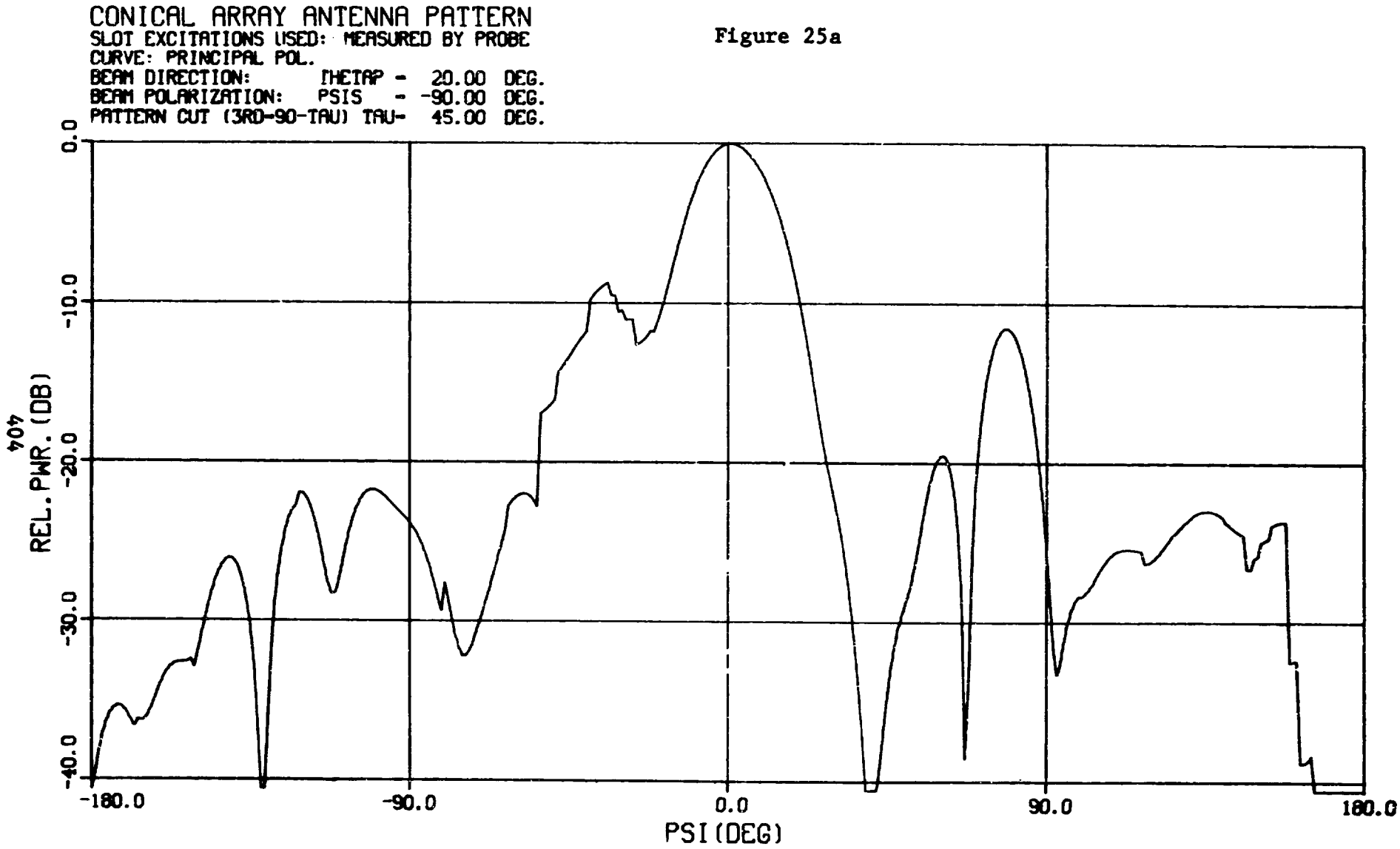
CONICAL ARRAY ANTENNA PATTERN
SLOT EXCITATIONS USED: MEASURED BY PROBE
CURVE: PRINCIPAL POL.
BEAM DIRECTION: THETAP = 20.00 DEG.
BEAM POLARIZATION: PSIS = -90.00 DEG.
PATTERN CUT (3RD-90-TAU) TAU= 45.00 DEG.
0.0
-10.0
-20.0
-30.0
-40.0
REL. PWR. (DB)
-180.0
-90.0
0.0
90.0
180.0
PSI (DEG)

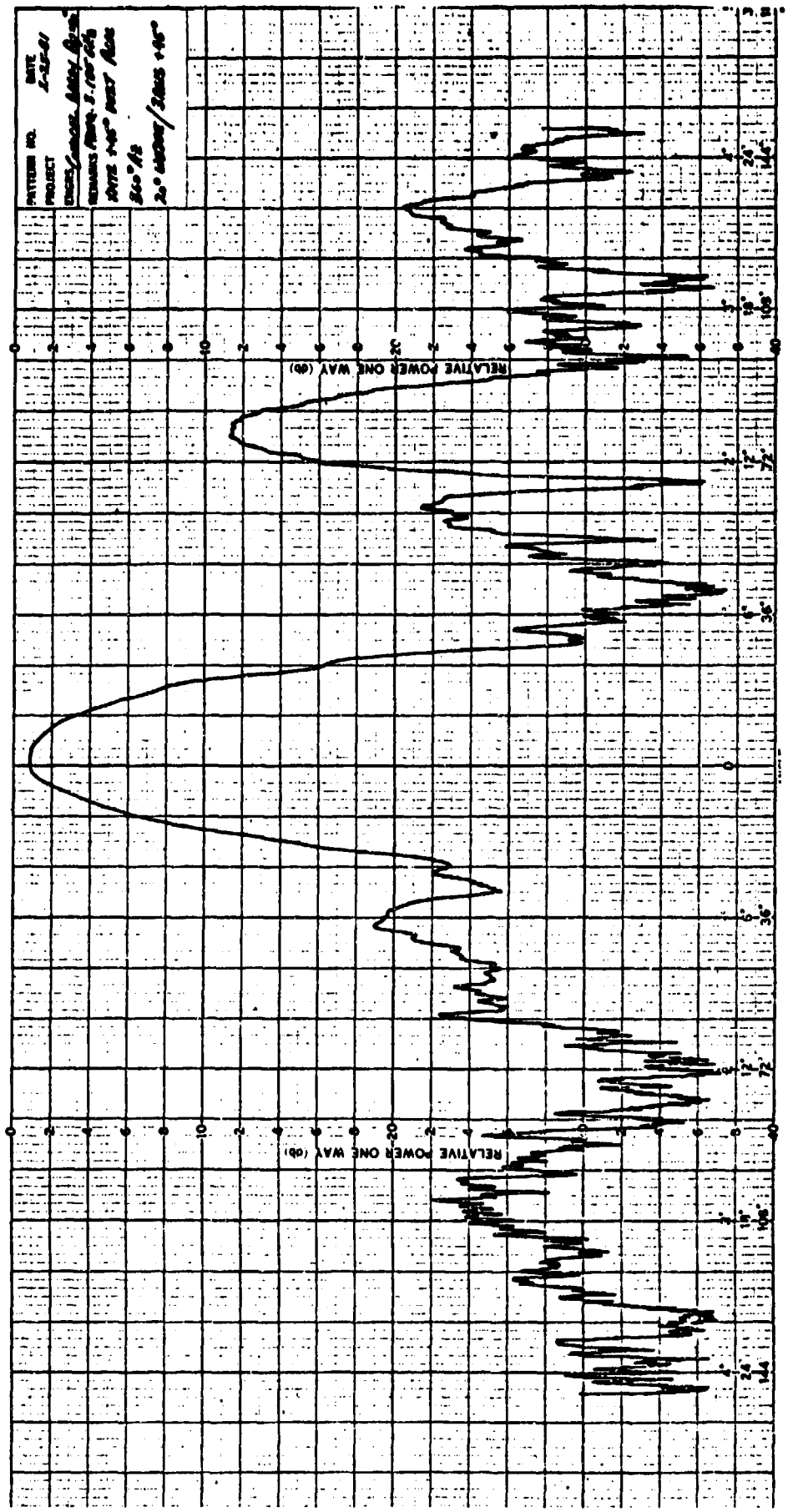

Figure 25b

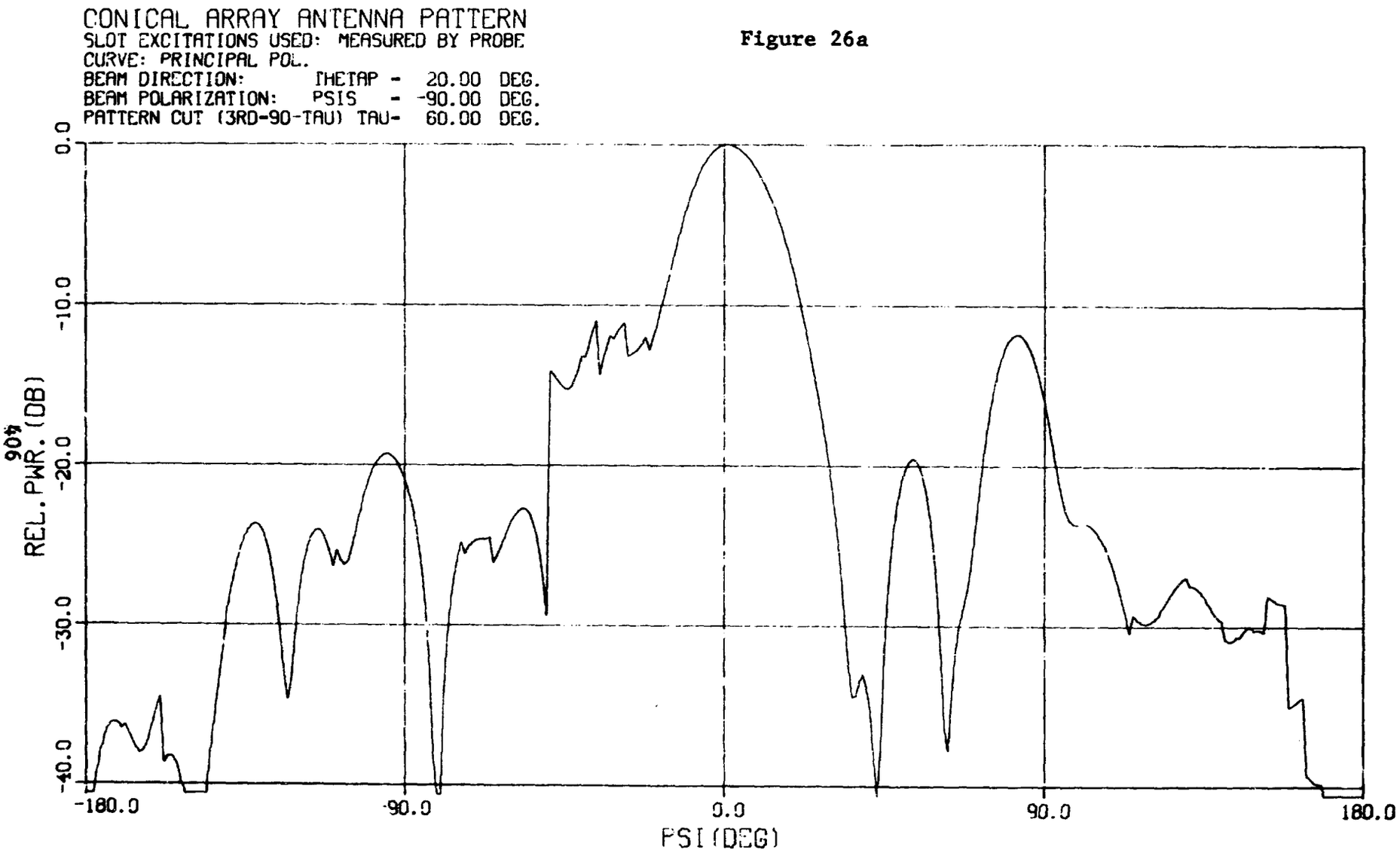
CONICAL ARRAY ANTENNA PATTERN
SLOT EXCITATIONS USED: MEASURED BY PROBE
CURVE: PRINCIPAL POL.
BEAM DIRECTION: THETAP - 20.00 DEG.
BEAM POLARIZATION: PSIS - -90.00 DEG.
PATTERN CUT (3RD-90-TAU) TAU- 60.00 DEG.
0.0
-10.0
-20.0
-30.0
-40.0
REL. PWR. (DB)
90%
-180.0
-90.0
0.0
90.0
180.0
PSI (DEG)

Figure 26a

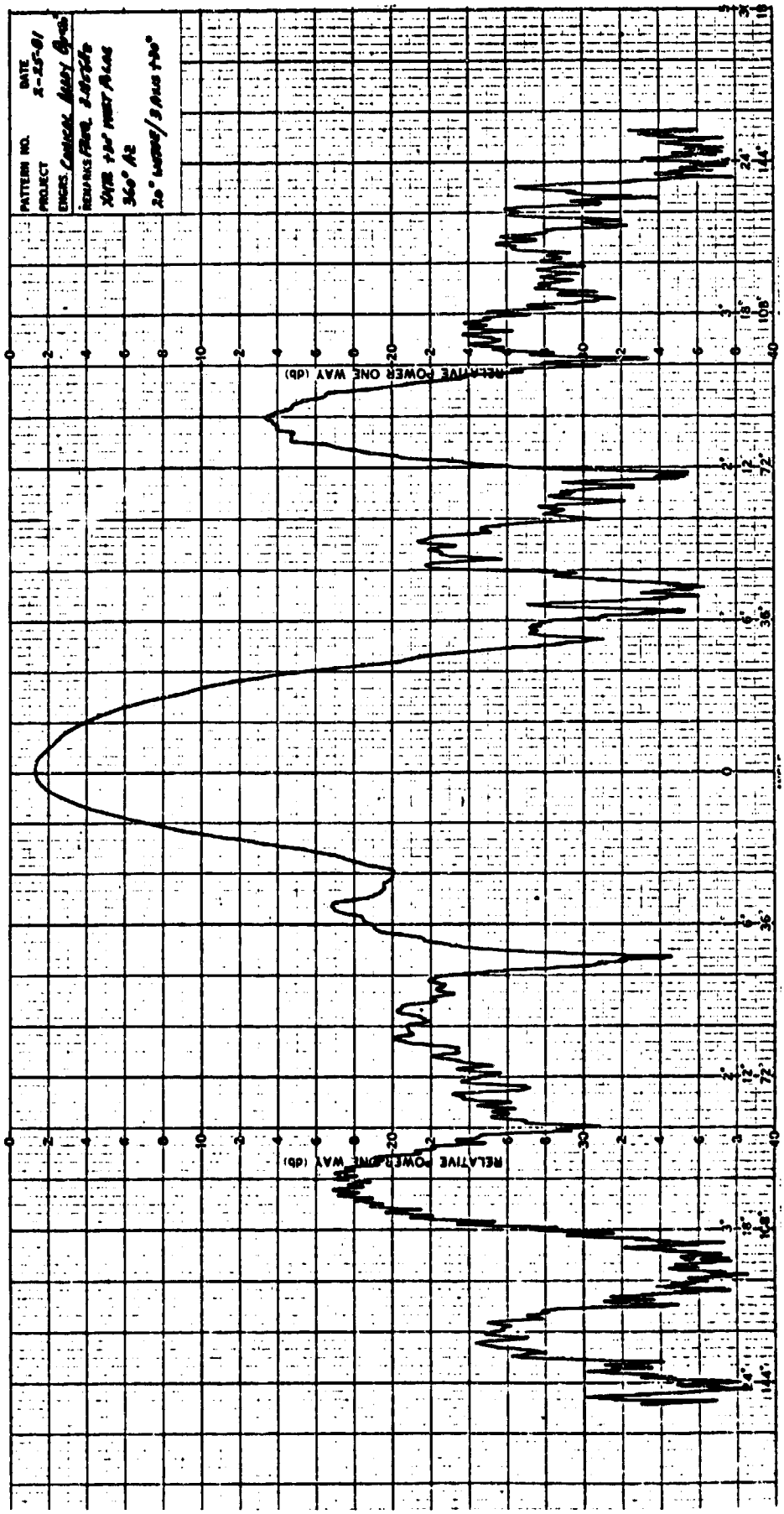
PATTERN NO.
DATE 2-25-81
PROJECT
RELATIVE POWER ONE WAY (db)
RELATIVE POWER ONE WAY (db)

Figure 26b

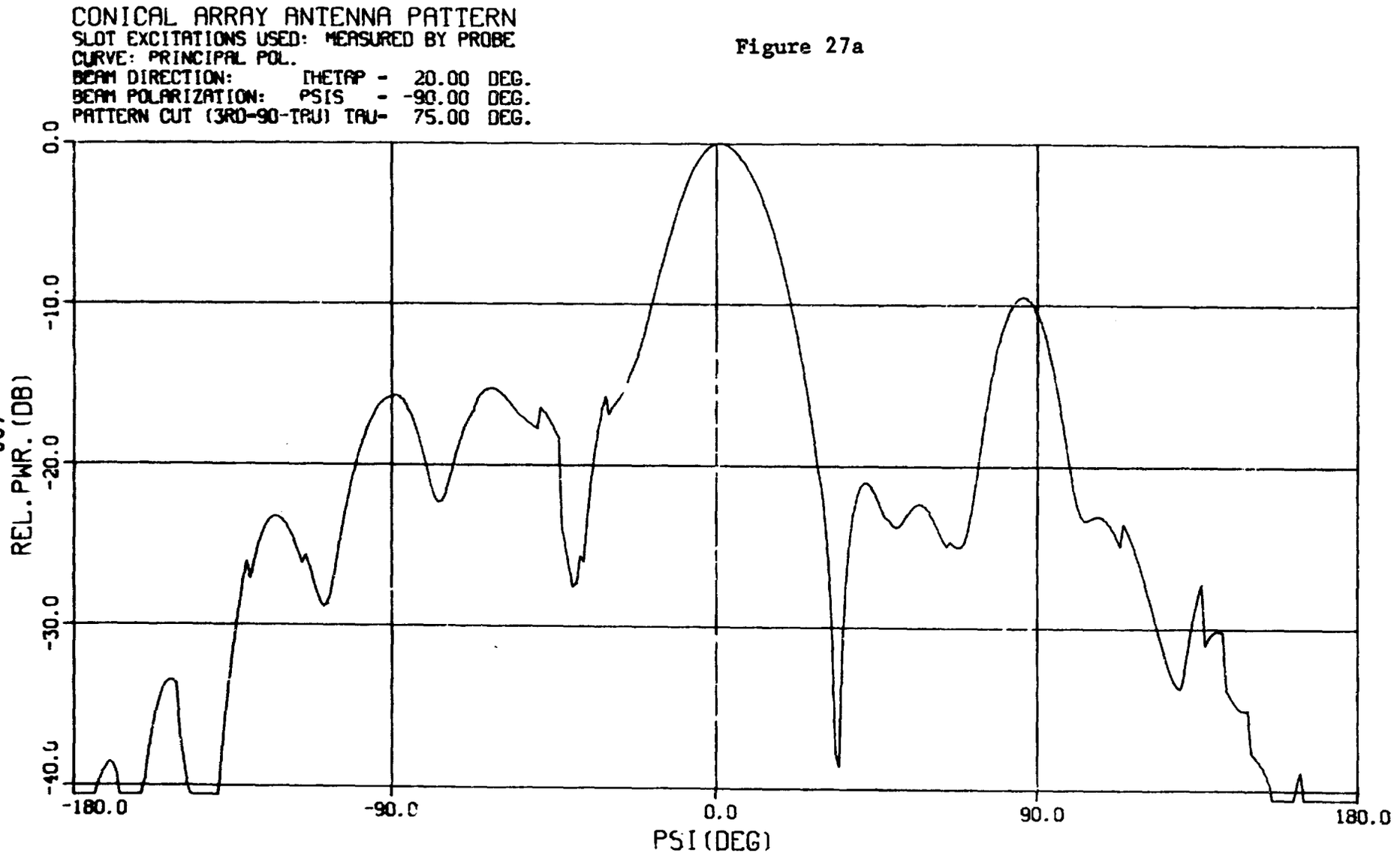
CONICAL ARRAY ANTENNA PATTERN
SLOT EXCITATIONS USED: MEASURED BY PROBE
CURVE: PRINCIPAL POL.
BEAM DIRECTION: THETAP - 20.00 DEG.
BEAM POLARIZATION: PSIS - -90.00 DEG.
PATTERN CUT (3RD-90-TAU) TAU- 75.00 DEG.
0.0
-10.0
-20.0
-30.0
-40.0
REL. PWR. (DB)
-180.0
-90.0
0.0
90.0
180.0
PSI (DEG)

Figure 27a

Figure 27b

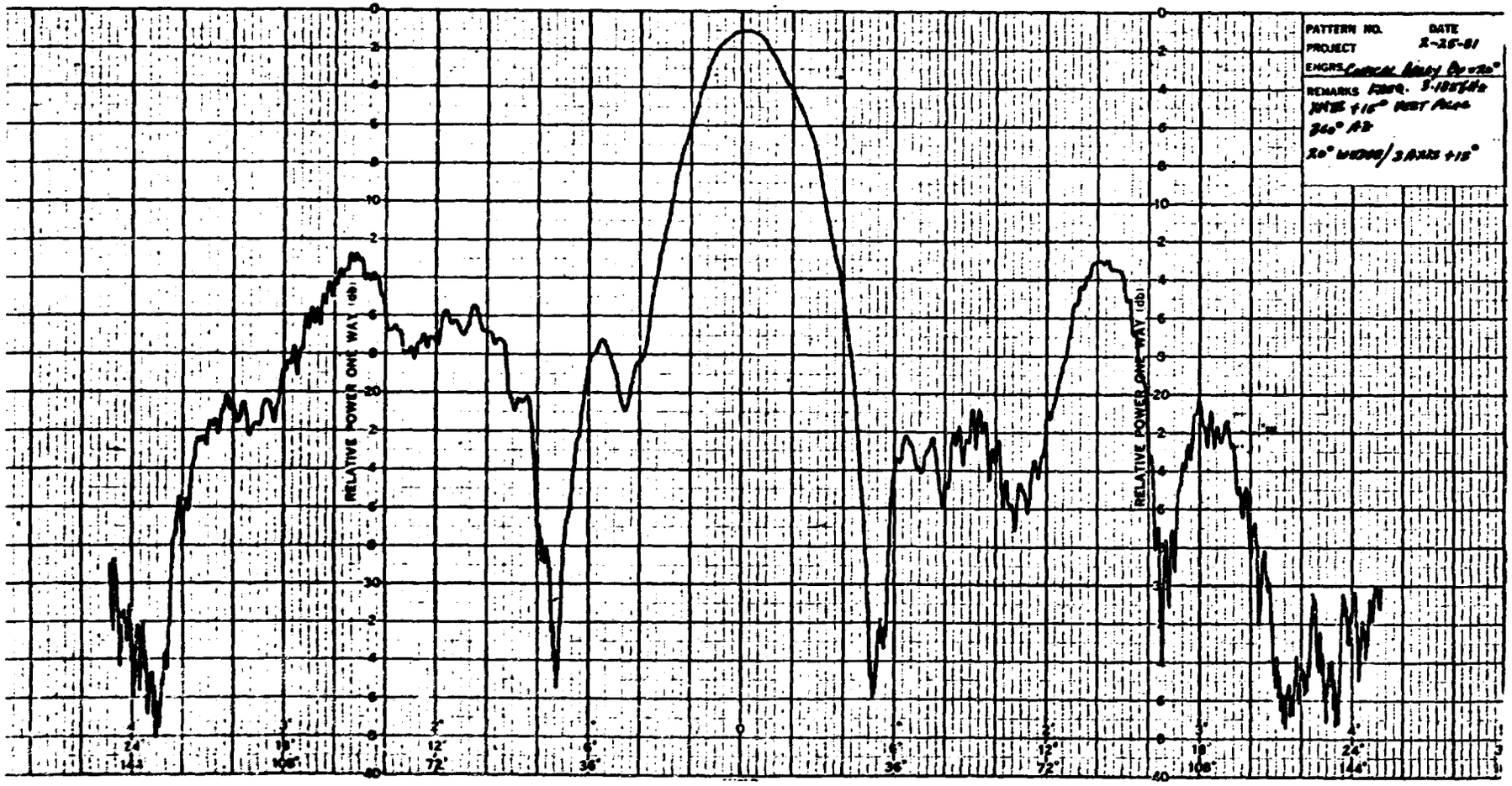
PATTERN NO.
DATE
PROJECT
RELATIVE POWER ONE WAY (db)
RELATIVE POWER ONE WAY (db)

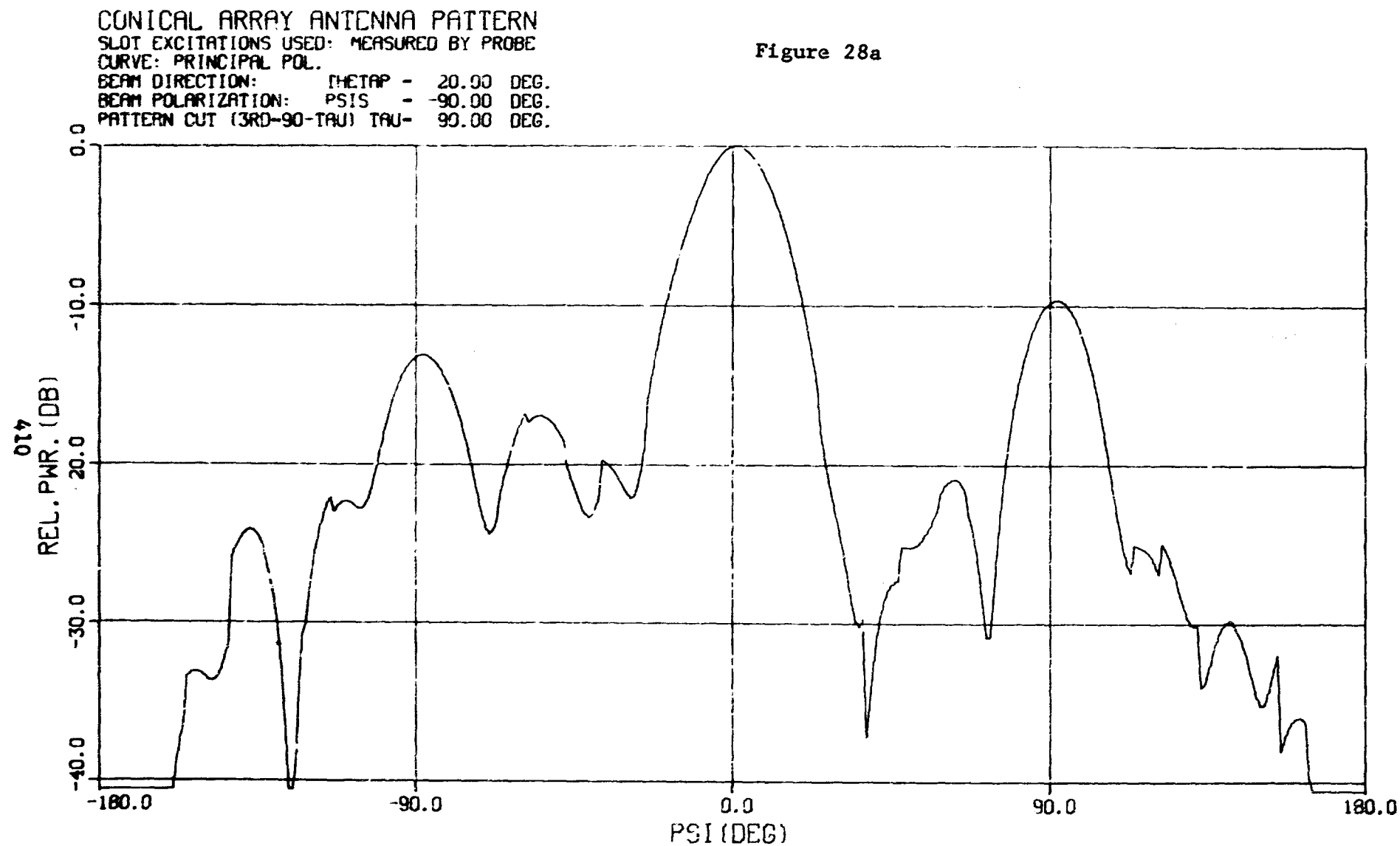
CONICAL ARRAY ANTENNA PATTERN
SLOT EXCITATIONS USED: MEASURED BY PROBE
CURVE: PRINCIPAL POL.
BEAM DIRECTION: THETAP - 20.00 DEG.
BEAM POLARIZATION: PSIS - -90.00 DEG.
PATTERN CUT (3RD-90-TAU) TAU- 90.00 DEG.
0.0
-10.0
-20.0
-30.0
-40.0
REL. PWR. (DB)
-180.0
-90.0
0.0
90.0
180.0
PSI (DEG)

Figure 28a

Figure 28b

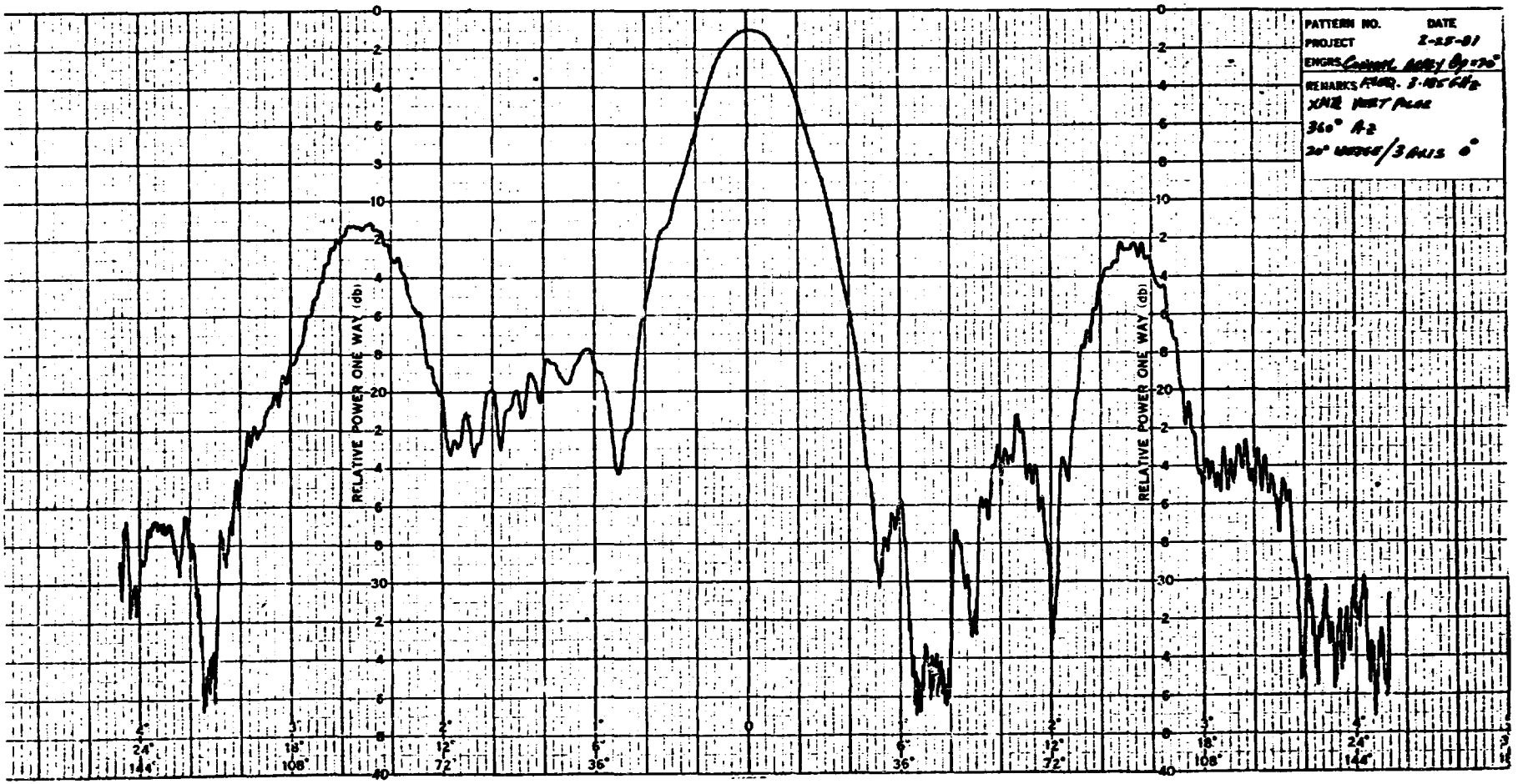
PATTERN NO.
DATE
PROJECT
2-25-81
ENGRS.
REMARKS
RELATIVE POWER ONE WAY (db)
RELATIVE POWER ONE WAY (db)

6.4.4 Conclusions from Measurements

Agreement between calculated and measured conical array patterns was excellent for main beam regions, and satisfactory for sidelobe regions. Both excitation errors and measurement (site or chamber) errors contribute to the sidelobe discrepancies. Effects of diffraction were reduced by using element patterns that were a function of distance from the cone tip; tip diffraction for this model, which had no slots close to the tip, was difficult to identify. Effects of mutual coupling were removed by the adjustment of excitation to the prescribed amplitude and phase. The program has demonstrated that the synthesis technique provides slot excitations that will produce patterns approximating desired patterns, and that such patterns can be obtained experimentally.

REFERENCES

M. Abramowitz & I. A. Stegun, "Handbook of Mathematical Functions", U.S. Department of Commerce NBS, 1956, p. 480.

N. Amitay, V. Galindo & C. P. Wu, "Theory and Analysis of Phased Array Antennas", Wiley-Intersci., New York, 1972.

Array Antenna Conference Proc., Feb. 1972, Naval Electronics Laboratory Center, San Diego, CA, Parts 1 & 2.

L. L. Bailin & S. Silver, "Exterior Electromagnetic Boundary Value Problems for Spheres and Cones", Trans. IRE, Vol. AP-4, Jan. 1956, pp. 5-16.

L. L. Bailin & S. Silver, "Exterior Electromagnetic Boundary Value Problems for Spheres and Cones", Trans. IRE, Vol. AP-4, Jan. 1956, pp. 5-16, corrections, Vol. AP-5, July 1957, p. 313.

Q. Balzano, "Analysis of Periodic Arrays of Waveguide Apertures on Conducting Cylinders Covered by Dielectric", Trans. IEEE, Vol. AP-22, Jan. 1974, pp. 25-34.

Q. Balzano & T. B. Dowling, "Mutual Coupling Analysis of Arrays of Apertures on Cones", Trans. IEEE, Vol. AP-22, Jan. 1974, pp. 92-97.

E. T. Bayliss, "Design of Monopulse Antenna Difference Patterns with Low Sidelobes," Bell Sys. Tech. J., Vol. 47, No. 5, May-June 1968, pp. 623-650.

D. E. Biswell & J. K. Butler, "Synthesis Functions for Circular Arc Arrays", Proc. IEEE, Vol. 56, Sept. 1968, pp. 1585-1586.

J. Blass, "An Analysis of the Radiation from Circular Arrays of Directive Elements", Trans. IEEE, Vol. AP-22, Jan. 1974, pp. 84-87.

G. Borgiotti & Q. Balzano, "Mutual Coupling Analysis of a Conformal Array of Elements on a Cylindrical Surface", Trans. IEEE, Vol. AP-18, Jan. 1970, pp. 55-63.

G. V. Borgiotti & Q. Balzano, "Conformal Arrays on Surfaces with Rotational Symmetry" in "Phased Array Antennas", A. A. Oliner & G. H. Knittel, eds., Proc. of 1970 Symposium at PIB, Artech House, 1972, p. 301-314.

G. V. Borgiotti & Q. Balzano, "Analysis and Element Pattern Design of Periodic Arrays of Circular Apertures on Conducting Cylinders," Trans. IEEE, Vol. AP-20, Sept. 1972, pp. 547-555.

J. J. Bowman, T.B.A. Senior & P.L.E. Uslenghi, "Electromagnetic and Acoustic Scattering by Simple Shapes", Wiley, 1969, Chap. 2.4.

J. E. Boyns, A.D. Munger, J. H. Provencher, J. Reindel, and B.I. Small; "A Lens Feed for a Ring Array", Trans. IEEE, Vol. AP-16, March 1968, pp. 264-267,

J. E. Boyns, C. W. Gorham, A. D. Munger, J. H. Provencher, J. Reindel, & B. I. Small; "Step-Scanned Circular-Array Antenna", Trans. IEEE, Vol. AP-18, Sept. 1970, pp. 590-595.

B. Carnahan, H. A. Luther & J. O. Wilkes, "Applied Numerical Methods", John Wiley and Sons, Inc., New York, 1969, p. 139.

P. S. Carter, "Antenna Arrays Around Cylinders", Proc. IRE Vol. 31, Dec. 1943, pp. 671-693.

A. K. Chan, A. Ishimaru & R. A. Sigelmann, "Equally Spaced Spherical Arrays", Radio Sci., Vol. 3, May 1968, pp. 401-404.

K. K. Chan, L. B. Felsen, A. Hessel & J. Schmoys, "Creeping Waves on a Perfectly Conducting Cone", Trans. IEEE, Vol. AP-25, 1977, pp. 661-670.

D. K. Cheng & F. I. Tseng, "Maximization of Directive Gain for Circular and Elliptic Arrays", Proc. IEE, Vol. 114, May 1967, pp. 589-594.

B. Chiang & D.H.S. Cheng, "Curvilinear Arrays", Radio Sci., Vol. 3, May 1968, pp. 405-409.

E. J. Christopher, "Electronically Scanned TACAN Antenna", Trans. IEEE, Vol. AP-22, Jan. 1974, pp. 12-16.

H. P. Coleman, "An Iterative Technique for Reducing Sidelobes of Circular Arrays", Trans. IEEE, Vol. AP-18, July 1970, pp. 566-567.

R. E. Collin & F. J. Zucker, "Antenna Theory", Part 1, McGraw-Hill Book Company, 1969, p. 574.

Conformal Array Antenna Conference Proc., NELC, San Diego, 1970, Report TD-95.

D.E.N. Davies, "Beam-Positioning Radar Systems Utilizing Continuous Scanning Techniques", Proc. IEE, Vol. 112, March 1965, pp. 493-496.

D.E.N. Davies, "A Transformation Between the Phasing Techniques Required for Linear and Circular Aerial Arrays", Proc. IEE, Vol. 112, Nov. 1965, pp. 2041-2045.

D.E.N. Davies & B. S. McCartney, "Cylindrical Arrays with Electronic Beam Scanning", Proc. IEE, Vol. 112, March 1965, pp. 497-505.

R. H. DuHamel, "Antenna Pattern Synthesis", PhD thesis, Univ. of Ill., 1951.

R. H. Duncan, "Theory of the Infinite Cylindrical Antenna including the Feedpoint Singularity in Antenna Current", J. Res. N.B.S., Vol. 66D, March-April 1962, pp. 181-188.

R. S. Elliott, "On Discretizing Continuous Aperture Distributions", Trans. IEEE, Vol. AP-25, Sept. 1977, pp. 617-621.

A. Erdelyi, et al., "Higher Transcendental Functions", Vol. 1, McGraw-Hill, New York, 1953.

L. B. Felsen & N. Marcuvitz, "Radiation and Scattering of Waves", Prentice-Hall, New Jersey, 1973, pp. 477 and 483.

R. G. Fenby, "Limitations on Directional Patterns of Phase-Compensated Circular Arrays," Radio Electronic Engr., Vol. 30, 1965, pp. 206-222.

R. G. Fenby & D.E.N. Davies, "Circular Array Providing Fast 360° Electronic Beam Rotation", Proc. IEE, Vol. 115, Jan. 1968, pp. 78-86.

V. A. Fock, "Electromagnetic Diffraction and Propagation Problems", Pergamon Press, New York, 1965.

A. Gerlin, "Polynomial Approach to Study of Single-Ring Circular Antenna Array", Proc. IEE, Vol. 121, April 1974, pp. 255-256.

J. F. Gobert & R.F.H. Yang, "A Theory of Antenna Array Conformal to Surface of Revolution", Trans. IEEE, Vol. AP-22, Jan. 1974, pp. 87-91.

K. E. Golden, G. E. Stewart & D.C. Pridmore-Brown, "Approximation Techniques for the Mutual Admittance of Slot Antennas on Metallic Cones", Trans. IEEE, Vol. AP-22, Jan. 1974, pp. 43-48.

K. E. Golden & G. E. Stewart, "Self and Mutual Admittances for Axial Rectangular Slots on a Conducting Cylinder in the Presence of an Inhomogeneous Plasma Layer", Trans. IEEE, Vol. AP-19, March 1971, pp. 296-299.

N. Goto & Y. Tsunoda, "Sidelobe Reduction of Circular Arrays with a Constant Excitation Amplitude", Trans. IEEE, Vol. AP-25, Nov. 1977, pp. 896-898.

M. C. Gray, "Legendre Functions of Fractional Order", Quart. of Appl. Math, Vol. 511, Oct. 1953, pp. 311-318.

W. S. Gregorwich, "An Electronically Despun Array Flush-Mounted on a Cylindrical Spacecraft", Trans. IEEE, Vol. AP-22, Jan. 1974, pp. 71-74.

R. C. Hansen, "Microwave Scanning Antennas", Vol. 1, 1964; Vols. 2 & 3, 1966; Academic Press, New York.

R. C. Hansen, ed. Special Issue on Electronic Scanning, Proc. IEEE, Vol. 56, Nov. 1968, pp. 1761-2075.

R. C. Hansen, "Formulation of Echelon Dipole Mutual Impedance for Computer", Trans. IEEE, Vol. AP-20, 1972, pp. 780-781.

R. C. Hansen, "Significant Phased Array Papers", Artech House, Inc., Dedham, MA, 1973.

R. C. Hansen, "Linear Arrays", and "Planar Arrays", in Handbook of Antenna Design, A.W. Rudge et al eds., Peregrinus, 1981.

R. C. Hansen, "Geometric Theory of Diffraction", IEEE Press, 1981.

R. F. Harrington, "Time Harmonic Electromagnetic Fields", Mc-Graw-Hill, New York, 1961, p. 110.

R. F. Harrington & W. R. Lepage, "Directional Antenna Arrays of Elements Circularly Disposed about a Cylindrical Reflector", Proc. IRE, Vol. 40, Jan. 1952, pp. 83-86.

A. Hessel, "Mutual Coupling Effects in Circular Arrays on Cylindrical Surfaces - Aperture Design Implications and Analysis" in "Phased Array Antennas", A. A. Oliner & G. H. Knittel, eds., Proc. of 1970 Symposium at PIB, Artech House, 1972, p. 273-291.

A. Hessel & J. C. Sureau, "On the Realized Gain of Arrays", Trans. IEEE, Vol. AP-19, Jan. 1971, pp. 122-124.

A. Hessel & J. C. Sureau, "Resonances in Circular Arrays with Dielectric Sheet Covers", Trans. IEEE, Vol. AP-21, March 1973, pp. 159-164.

A. Hessel et al, "Mutual Admittance Between Circular Apertures on a Large Conducting Sphere", Rad. Sci. Vol. 14, Jan-Feb. 1979, pp. 35-42.

C. E. Hickman, H. P. Neff & J. D. Tillman, "The Theory of a Single-Ring Circular Antenna Array", Trans. AIEE, Vol. 80, Part 1, May 1961, pp. 110-114.

J. L. Hilburn, "Circular Arrays of Radial and Tangential Dipoles for Turnstile Antennas", Trans. IEEE, Vol. AP-17, Sept. 1969, pp. 658-660.

J. L. Hilburn & C. E. Hickman, "Circular Arrays of Tangential Dipoles", J. Appl. Phys., Vol. 39, Dec. 1968, pp. 5953-5959.

M. Hoffman, "Conventions for the Analysis of Spherical Arrays", Trans. IEEE, Vol. AP-11, July 1963, pp. 390-393.

A. E. Holley, E. C. DuFort & R. A. Dell-Imagine, "An Electronically Scanned Beacon Antenna", Trans. IEEE, Vol. AP-22, Jan. 1974, pp. 3-12.

J. K. Hsiao & J.B.L. Rao, "Computation of Far-Field Pattern and Polarization of Conformal Arrays", Trans. IEEE, Vol. AP-26, March 1976, p. 259.

P. W. James, "Polar Patterns of Phase-Connected Circular Arrays", Proc. IEE, Vol. 112, 1965, pp. 1839, 1947.

E. C. Jordan & K. G. Balmain, "Electromagnetic Waves and Radiating Systems", Prentice-Hall, Inc., 1960, Chapter 14, pp. 535-600.

W. K. Kahn, "Efficiency of a Radiating Element in Circular Cylindrical Arrays", Trans. IEEE, Vol. AP-19, Jan. 1971, pp. 115-117.

J. B. Keller, "Geometrical Theory of Diffraction", J. Opt. Soc. Amer., Vol. 52, 1962, pp. 116-130.

H. Knudsen, "The Necessary Number of Elements in a Directional Ring Aerial", Jr. of Applied Physics, Vol. 22, Nov. 1951, pp. 1299-1306.

H. L. Knudsen, "Field Radiated by Ring Quasi-Array of an Infinite Number of Tangential or Radial Dipoles", Proc. IRE, Vol. 41, June 1953, pp. 781-789.

H. L. Knudsen, "Radiation from Ring Quasi-Arrays", Trans. IRE, Vol. AP-4, July 1956, pp. 452-472.

H. Knudsen, "Antennas on Circular Cylinders", Trans. IRE, Vol. AP-7, Dec. 1959, pp. S361-S370.

R. G. Kouyoumjian, "The Geometrical Theory of Diffraction and Its Application", in "Topics in Applied Physics", R. Mittra, ed. New York: Springer-Verlag, 1975.

A. Ksienski, "Equivalence Between Continuous and Discrete Radiating Arrays", Can. J. Phys., Vol. 29, 1961, pp. 335-349.

W. H. Kummer, "Conical Arrays", Paper No. 34, Array Antenna Conference, Naval Electronics Laboratory Center, San Diego, CA, Feb. 1972.

W. H. Kummer ed., "Special Issue on Conformal Arrays", Trans. IEEE, Vol. AP-22, Jan. 1974, pp. 1-103.

K. S. Lee & G. Eichmann, "Elementary Patterns for Conformal Dipole Arrays Mounted on Dielectrically Clad Conducting Cylinders", Trans. IEEE, Vol. AP-28, Nov. 1980, pp. 811-818.

S.W. Lee, "Mutual Admittance of Slots on a Cone: Solution by Ray Technique", Trans. IEEE, Vol. AP-26, 1978, pp. 768-773.

S.W. Lee & Y. T. Lo; "Pattern Function of Circular Arc Arrays", Trans. IEEE, Vol. AP-13, July 1965, pp. 649-650.

S.W. Lee & S. Safavi-Naini, "Approximate Asymptotic Solution of Surface Field due to a Magnetic Dipole on a Cylinder", Trans. IEEE, Vol. AP-26, July 1978, pp. 593-598.

J. C. Lim & D.E.N. Davies, "Synthesis of a Single Null Response in an Otherwise Omnidirectional Pattern Using a Circular Array", Proc. IEE, Vol. 122, April 1975, pp. 349-352.

Y. T. Lo & H. C. Hsuan, "Equivalence Theory Between Elliptical and Circular Arrays", Trans. IEEE, Vol. AP-13, March 1965, pp. 247-256.

I. D. Longstaff et al, "Directional Properties of Circular Arrays", Proc. IEE, Vol. 114, June 1967, pp. 713-718.

I. D. Longstaff & D.E.N. Davies, "A Wideband Circular Array for H.F. Communications", Radio and Electronic Engineer, June 1968, Vol. 35, pp. 321-327.

M. T. Ma ed., Special Issue on Theory of Antenna Arrays, Radio Science, Vol. 3, May 1968, pp. 401-522.

M. T. Ma, "Theory and Application of Antenna Arrays", Wiley, New York, 1974, Chapter 3.

M. T. Ma & L. C. Walters, "Theoretical Methods for Computing Characteristics of Wullenweber Antennas", Proc. IEE, Vol. 117, Nov. 1970, pp. 2095-2101.

R. H. MacPhie, "The Element Density of a Spherical Antenna Array", Trans. IEEE, Vol. AP-16, Jan. 1968, pp. 125-127.

R. J. Mailloux, "Phased Array Aircraft Antennas", Microwave J., Vol. 20, Oct. 1977, pp. 38-42.

R. Mittra & S. Safavi-Naini, "Source Radiation in the Presence of Smooth Convex Bodies", Rad. Sci. Vol. 14, March-April 1979, pp. 217-238.

A.D. Munger, J. H. Provencher, & B. R. Gladman, "Mutual Coupling on a Cylindrical Array of Waveguide Elements", Trans. IEEE, Vol. AP-19, Jan. 1971, pp. 131-134.

A. D. Munger, G. V. Vaughn, J. H. Provencher, & B. R. Gladman, "Conical Array Studies", Trans. IEEE, Vol. AP-22, Jan. 1974, pp. 35-43.

R. E. Munson, "Conformal Microstrip Antennas and Microstrip Phased Arrays", Trans. IEEE, Vol. AP-22, Jan. 1974, pp. 74-78.

A. A. Oliner & R. G. Malech, "Mutual Coupling in Infinite Scanning Arrays", Chapter III of "Microwave Scanning Antennas", Vol. II, R. C. Hansen, ed., Academic Press Inc., 1966.

A. A. Oliner & G. H. Knittel, "Phased Array Antennas", Artech House, Inc., Dedham, MA, 1972.

H. Page, "Radiation Resistance of Ring Aerials", Wireless Eng., Vol. 25, April 1948, pp. 102-109.

H. Page, "Ring Aerial Systems", Wireless Eng., Vol. 25, Oct. 1948, pp. 308-315, and Corr. Dec. 1948, p. 402.

A. R. Panicali & Y. T. Lo, "A Probabilistic Approach to Large Circular and Spherical Arrays", Ieee, Vol. AP-17, July 1969, pp. 514-522.

P. H. Pathak & R. G. Kouyoumjian, "An Analysis of the Radiation from Apertures in Curved Surfaces by the Geometric Theory of Diffraction," Proc. IEEE, Vol. 62, Nov. 1974, pp. 1438-1461.

E. J. Powers, "Utilization of the Lambda Functions in the Analysis and Synthesis of Monopulse Antenna Difference Patterns", IEEE Trans., Vol. AP-15, Nov. 1967, pp. 771-777.

D. C. Pridmore-Brown & G. Stewart, "Radiation from Slot Antennas on Cones", Trans. IEEE, Vol. AP-20, Jan. 1972, pp. 36-39.

D. C. Pridmore-Brown, "Diffraction Coefficients for a Slot-Excited Conical Antenna", Trans. IEEE, Vol. AP-20, Jan. 1972, pp. 40-49.

D. C. Pridmore-Brown, "The Transition Field on the Surface of a Slot-Excited Conical Antenna", Trans. IEEE, Vol. AP-21, Nov. 1973, pp. 889-890.

J. H. Provencher, "A Survey of Circular Symmetric Arrays", in "Phased Array Antennas", A. A. Oliner & G. H. Knittel, eds., Proc. of 1970 Symposium at PIB, Artech House, 1972, pp. 292-300.

R. W. Redlich, "Sampling Synthesis of Ring Arrays", Trans. IEEE, Vol. AP-18, Jan. 1970, pp. 116-188.

D. R. Rhodes, "On a Fundamental Principle in the Theory of Planar Antennas", Proc. IEEE, Vol. 52, 1964, pp. 1013-1021.

Richmond, "A Reaction Theorem and Its Application to Antenna Impedance Calculations", Trans. IRE, Vol. AP-9, Nov. 1961, pp. 515-520.

G. M. Royer, "Directive Gain and Impedance of a Ring Array of Antennas", Trans. IEEE, Vol. AP-14, Sept. 1966, pp. 566-573.

E. M. Rutz-Philipp, "Spherical Retrodirective Array", Trans. IEEE, Vol. AP-12, March 1964, pp. 187-194.

D. H. Schaubert, H. S. Jones, Jr. & F. Reggia, "Conformal Dielectric-Filled Edge-Slot Antennas with Inductive-Post Tuning", Trans. IEEE, Vol. AP-27, Sept. 1979, pp. 713-716.

H. E. Schrank, "Basic Theoretical Aspects of Spherical Phased Arrays" in"Phased Array Antennas", A. A. Oliner & G. H. Knittel, eds., Proc. of 1970 Symposium at PIB, Artech House, 1972, pp. 323-327.

L. Schwartzman & W. K. Kahn, "Maximum Efficiency for Cylindrically Disposed Multiple-Beam Antenna Arrays," Trans. IEEE, Vol. AP-12, Nov. 1964, pp. 795-797.

L. Schwartzman & J. Stangel, "The Dome Antenna", Microwave J., Vol. 18, Oct. 1975, pp. 31-34.

D. L. Sengupta, T. M. Smith & R. W. Larson, "Radiation Characteristics of a Spherical Array of Circularly Polarized Elements", Trans. IEEE, Vol. AP-16, Jan. 1968, pp. 2-7.

D. L. Sengupta, L. Dipak, J. E. Ferris, & T. M. Smith, "Experimental Study of a Spherical Array of Circularly Polarized Elements", Proc. IEEE, Vol. 56, Nov. 1968, pp. 2048-2051.

J. Shapira, L. B. Felsen & A. Hessel, "Ray Analysis of Conformal Antenna Arrays", Trans. IEEE, Vol. AP-22, Jan. 1974, pp. 49-63.

J. Shapira, L. B. Felsen, & A. Hessel, "Surface Ray Analysis of Mutually Coupled Arrays on Variable Curvature Cylindrical Surfaces", Proc. IEEE, Vol. 62, March 1974, pp. 1482-1492.

B. Sheleg, "A Matrix-Fed Circular Array for Continuous Scanning", Proc. IEEE, Vol. 56, July 1968, pp. 2016-2027.

B. Sheleg, "Butler Submatrix Feed Systems for Antenna Arrays", Trans. IEEE, Vol. AP-21, March 1973, pp. 228-229.

L. N. Shestag, "A Cylindrical Array for the TACAN System", Trans. IEEE, Vol. AP-22, Jan. 1974, pp. 17-25.

D. H. Sinnott & R. F. Harrington, "Analysis and Design of Circular Antenna Arrays by Matrix Methods," Trans. IEEE, Vol. AP-21, Sept. 1973, pp. 610-614.

G. Skahill & W. D. White, "A New Technique for Feeding a Cylindrical Array", Trans. IEEE, Vol. AP-23, March 1975, pp. 253-256.

G. E. Stewart & K. E. Golden, "Mutual Admittance for Axial Rectangular Slots in a Large Conducting Cylinder", Trans. IEEE, Vol. AP-19, pp. 120-133, 1971.

H. Steyskal, "Analysis of Circular Waveguide Arrays on Cylinders", Trans. IEEE, Vol. AP-25, Sept. 1977, pp. 610-616.

J. C. Sureau & A. Hessel, "Element Pattern for Circular Arrays of Axial Slits on Large Conducting Cylinders", Trans. IEEE, Vol. AP-17, Nov. 1969, pp. 799-803.

J. C. Sureau and A. Hessel, "Element Pattern for Circular Arrays of Waveguide-Fed Axial Slits on Large Conducting Cylinders", Trans. IEEE, Vol. AP-19, Jan. 1971, pp. 64-74.

J. C. Sureau and A. Hessel, "Realized Gain Function for a Cylindrical Array of Open-Ended Waveguides" in "Phased Array Antennas", A. A. Oliner & G. H. Knittel, eds., Proc. of 1970 Symposium at PIB, Artech House, 1972, p. 315-322.

T. T. Taylor, "A Synthesis Method for Circular and Cylindrical Antennas Composed of Discrete Elements", Trans. IRE, Vol. PGAP-1, Aug. 1952, pp. 251-261.

W. L. Teeter & K. R. Bushore, "A Variable-Ratio Microwave Power Divider and Multiplexer", Trans. IRE, Vol. MTT-5, Oct. 1957, pp. 227-229.

G. A. Thiele & C. Donn, "Design of a Small Conformal Array", Trans. IEEE, Vol. AP-22, Jan. 1974, pp. 64-70.

J. D. Tillman, W. T. Patton, C. E. Blakely, & F. V. Schultz, "The Use of a Ring Array as a Skip Range Antenna", Proc. IEEE, Vol. 43, June 1955, pp. 1655-1660.

J. D. Tillman, Jr., "The Theory and Design of Circular Antenna Arrays", Univ. of Tenn. Eng. Exp. Station, 1968.

G. N. Tsandoulas & G. H. Knittel, "The Analysis and Design of Dual-Polarization Square-Waveguide Phased Arrays", Trans. IEEE, Vol. AP-21, Nov. 1973, pp. 796-808.

F. Tseng & D. K. Cheng, "Pattern Synthesis of Circular Arrays with Many Directive Elements", Trans. IEEE, Vol. AP-16, Nov. 1968, pp. 758-759.

R. M. Vaillancourt, "Analysis of the Variable-Ratio Microwave Power Divider", Trans. IRE, Vol. MTT-6, April 1958, pp. 238-239.

A. T. Villeneuve, M. C. Behnke & W. H. Kummer, "Wide-Angle Scanning of Linear Arrays Located on Cones", Trans. IEEE, Vol. AP-22, Jan. 1974, pp. 97-103.

J. R. Wait, "Electromagnetic Radiation From Cylindrical Structures", Pergamon Press, 1959, pp. 30, 45.

J. E. Walsh, "Radiation Patterns of Arrays on a Reflecting Cylinder", Proc. IRE, Vol. 39, Sept. 1951, pp. 1074-1081.

F. Watanabe, N. Goto, A. Nagayama & G. Yoshida, "A Pattern of Synthesis of Circular Arrays by Phase Adjustment", Trans. IEEE, Vol. AP-28, Nov. 1980, pp. 857-863.

C. F. Winter, "Using Continuous Aperture Illuminations Discretely", Trans. IEEE, Vol. AP-25, Sept. 1977, pp. 695-700.

Workshop on Conformal Antennas Proc., April 1975, Naval Air Systems Command, Washington, D.C.

REPORTS

J. E. Howard, W. H. Kummer & A. T. Villeneuve, "Integrated Conformal Arrays', Final Report on Contract N00019-68-C-0214, 1969, Hughes Aircraft Co., Culver City.

W. H. Kummer, A. T. Villeneuve, J. E. Howard & A. F. Seaton, "Integrated Conformal Arrays", Final Report on Contract N00019-69-C-0281, 1970, Hughes Aircraft Co., Culver City.

A. T. Villeneuve & W. H. Kummer, "Integrated Conformal Arrays", Final Report on Contract N00019-70-C-0397, 1971, Hughes Aircraft Co., Culver City.

M. C. Behnke, A. T. Villeneuve, & W. H. Kummer, "Advanced Conformal Array Antenna Techniques", Final Report on Contract N00019-71-C-0197, 1972, Hughes Aircraft Co., Culver City.

W. H. Kummer, A. F. Seaton & A. T. Villeneuve, "Conformal Antenna Arrays Study", Final Report on Contract N00019-72-C-0212, 1973, Hughes Aircraft Co., Culver City.

P. C. Bargeliotes et al, "Dynamic Impedance Matching in Conformal Arrays", Contract N00019-73-C-0217, Quarterly Report Jan. - April 1973; April - July 1973; July - Oct. 1973; Final Report Jan. 1974, Hughes Aircraft Co., Culver City.

P. C. Bargeliotes et al, "Pattern Synthesis of Conformal Arrays", Contract N00019-74-C-0127, Quarterly Report, Jan. - April 1974; April - July, 1974; July - Oct., 1974; Final Report Jan. 1975, Hughes Aircraft Co., Culver City.

P. C. Bargeliotes et al, "Phased Array Antennas Scanned Near Endfire", Contract N00019-75-C-0160, Quarterly Report Jan. - April, 1975; April - July, 1975; July - October, 1975; Final Report March 1976, Hughes Aircraft Co., Culver City.

P. C. Bargeliotes et al, "Conformal Phased Array Breadboard", Contract N00019-76-C-0495, Quarterly Report May - Aug. 1976; Aug. - Nov. 1976; Final Report Jan. 1977, Hughes Aircraft Co., Culver City.

A. T. Villeneuve et al, "Conical Phased Array Antenna Investigations", Contract N00019-77-C-0358, Quarterly Report Oct. - Dec. 1977; Jan. - March, 1978; April - June, 1978; July - Sept. 1978; Final Report April 1979, Hughes Aircraft Co., Culver City, CA.

S. W. Lee & S. Safavi-Naini, "Asymptotic Solution of Surface Field due to a Magnetic Dipole on a Cylinder, Contract N00019-76-M-0622, Nov. 1976, Electromagnetics Lab., Univ. of Ill., Urbana.

S. W. Lee & R. Mittra, "Study of Mutual Coupling Between Two Slots on a Cylinder", Final Report on Contract No. N00019-76-M-0622, Nov. 1976, Electromagnetics Lab., Univ. of Ill., Urbana.

S. W. Lee & R. Mittra, "Investigation on Characterizing Mutual Admittance Between Two Antenna Slots on a Cylinder", Quarterly Report, Contract No. N00019-77-C-0127, Feb. 1977, Electromagnetics Lab, Univ of Ill., Urbana.

S. W. Lee, S. Safavi-Naini, & R. Mittra, "Mutual Admittance Between Slots on a Cylinder", Contract N00019-77-C-0127, March 1977, Electromagnetics Lab., Univ. of Ill., Urbana.

S. W. Lee & S. Safavi-Naini, "Simple Approximate Formula for Mutual Admittance Between Slots on a Cylinder", Contract N00019-77-C-0127, July 1977, Electromagnetics Lab, Univ. of Ill., Urbana.

J. Boersma & S. W. Lee, "Asymptotic Solution of a Surface Field Due to a Magnetic Dipole on a Cylinder", Contract No. N00019-78-C-0064, Nov. 1978, Electromagnetics Lab., Univ. of Ill., Urbana.

J. Boersma & S. W. Lee, "Surface Field Due to a Magnetic Dipole on a Cylinder: Asymptotic Expansion of Exact Solution", Contract N00019-78-C-0064, Dec. 1978, Electromagnetics Lab., Univ. of Ill., Urbana.

S. W. Lee, R. Mittra, J. Boersma, & E. Yung, "An Investigation on Characterizing Mutual Coupling Between Two Antenna Slots on a Cone", Contract No. N00019-78-C-0064, Jan. 1979, Electromagnetics Lab., Univ. of Ill., Urbana.

G. V. Vaughn, "Analysis of Arrays on a Conducting Conical Surface", June 1975, NOSC, San Diego.

J. Reindel, "Multithrow Microwave Diode Switch," NOSC Report 1468, June 1967, San Diego.

J. H. Provencher & B. I. Small, "Circular Array Radar Antenna", Report 1501, 7 July 1967, NOSC, San Diego.

A. D. Munger, "Current Distributions and Radiation Patterns for Circular-Array Radar Antenna: Theory", Report 1521, 26 Oct. 1967, NOSC, San Diego.

J. E. Boyns, "Circular-Array Radar Antenna: CARAMBA 1 Experimental Results", Report 1535, 2 February 1968, NOSC, San Diego.

J. H. Provencher & A. D. Munger, "Circular-Array Radar Antenna: Pencil-Beam Forming and Phasing Techniques", Report 1543, 12 March 1968, NOSC, San Diego.

A. D. Munger, "Circular-Array Radar Antenna: Cylindrical-Array Theory", Report 1608, 15 Jan. 1969, NOSC, San Diego.

J. B. L. Rao & J. K. Hsiao, "Phased Array Antenna Analysis for PMR Instrumentation Aircraft", Report 7806, Sept. 1974, NRL, Washington, D.C.

J. K. Hsiao & J. B. L. Rao, "Computer Analysis of Conformal Phased Arrays", Report 7826, 15 Nov. 1974, NRL, Washington, D.C.

Y. Hwang & R. G. Kouyoumjian, "The Mutual Coupling Between Slots on an Arbitrary Convex Cylinder", Semi-Annual Report 2902-21, Grant NGL 36-003-138, 1975, ElectroScience Lab. Dept. of EE, Ohio State Univ.

P. H. Pathak, "Analysis of a Conformal Receiving Array of Slots in a Perfectly-Conducting Circular Cylinder by the Geometrical Theory of Diffraction", Report ESL 3735-2, Contract N00140-74-C-6017, 1975, ElectroScience Lab, Dept. of EE, The Ohio State Univ.

L. B. Felsen, A. Hessel, J. Shapira, & J. Shmoys, "Ray Analysis of Mutual Coupling in Conformal Arrays," Final Report, March 1974, Contract N00123-73-C-1481, Polytechnic Institute of New York.

Z. W. Chang, L. B. Felsen, & A. Hessel, "Surface Ray Methods for Mutual Coupling in Conformal Arrays on Cylinder and Concical Surface", Final Report, July 1976, Contract N00123-76-C-0236, Polytechnic Institute of New York.

D. E. Biswell, "Circular and Cylindrical Array Antenna Investigation", 1 Feb. 1968, Texas Instruments, Inc.

GLOSSARY OF MAJOR SYMBOLS

a	slot length, cylindrical radius
b	slot width
C_n	Chebyshev coefficient
d	ring-to-ring spacing
E	electric field
F_n	element pattern Fourier coefficient
G	element pattern
H	magnetic field
H_n	Hankel function
h_ν	spherical Hankel function
I	current or excitation
J	electric current source
J_ν	Bessel function
j_ν	spherical Bessel function
k	free space wave number
ℓ	slot length
M	number of elements, magnetic current source
N	number of elements
P_ν^m	associated Legendre function
Q	active element pattern
r,θ,ϕ	spherical coordinates
S_{ij}	scattering coefficient
s	interelement spacing, arc length
T_n	Chebyshev polynomial
u,v	Fock function
V	applied voltage
x,y,z	rectangular coordinates
$\hat{x},\hat{y},\hat{z}$	unit vectors
Y	admittance

α	angular location of element
δ_{mo}	Kronecker delta
ε_n	Neumann number
λ	wavelength
ξ	distance parameter
ρ	cylindrical radius
τ	ray curvature parameter, pattern inclination angle
ψ	Eulerian angle

☆U.S. GOVERNMENT PRINTING OFFICE: 1981 505 099 1671